FUNCTIONAL SUPRAMOLECULAR NANOASSEMBLIES OF π-CONJUGATED MOLECULES

EDITED BY: Penglei Chen and Bin Wu
PUBLISHED IN: Frontiers in Chemistry

frontiers Research Topics

ISSN 1664-8714
ISBN 978-2-88963-360-9
DOI 10.3389/978-2-88963-360-9

About Frontiers

Frontiers is more than just an open-access publisher of scholarly articles: it is a pioneering approach to the world of academia, radically improving the way scholarly research is managed. The grand vision of Frontiers is a world where all people have an equal opportunity to seek, share and generate knowledge. Frontiers provides immediate and permanent online open access to all its publications, but this alone is not enough to realize our grand goals.

Frontiers Journal Series

The Frontiers Journal Series is a multi-tier and interdisciplinary set of open-access, online journals, promising a paradigm shift from the current review, selection and dissemination processes in academic publishing. All Frontiers journals are driven by researchers for researchers; therefore, they constitute a service to the scholarly community. At the same time, the Frontiers Journal Series operates on a revolutionary invention, the tiered publishing system, initially addressing specific communities of scholars, and gradually climbing up to broader public understanding, thus serving the interests of the lay society, too.

Dedication to Quality

Each Frontiers article is a landmark of the highest quality, thanks to genuinely collaborative interactions between authors and review editors, who include some of the world's best academicians. Research must be certified by peers before entering a stream of knowledge that may eventually reach the public - and shape society; therefore, Frontiers only applies the most rigorous and unbiased reviews.
Frontiers revolutionizes research publishing by freely delivering the most outstanding research, evaluated with no bias from both the academic and social point of view. By applying the most advanced information technologies, Frontiers is catapulting scholarly publishing into a new generation.

What are Frontiers Research Topics?

Frontiers Research Topics are very popular trademarks of the Frontiers Journals Series: they are collections of at least ten articles, all centered on a particular subject. With their unique mix of varied contributions from Original Research to Review Articles, Frontiers Research Topics unify the most influential researchers, the latest key findings and historical advances in a hot research area! Find out more on how to host your own Frontiers Research Topic or contribute to one as an author by contacting the Frontiers Editorial Office: researchtopics@frontiersin.org

FUNCTIONAL SUPRAMOLECULAR NANOASSEMBLIES OF Π-CONJUGATED MOLECULES

Topic Editors:
Penglei Chen, Institute of Chemistry (CAS), China
Bin Wu, Institute of Chemistry (CAS), China

Π-conjugated systems of delocalized aromatic electrons along their backbones, including conjugated small molecules, oligomers, polymers, and carbonaceous materials, etc., have received considerable attention from a wide variety of scientific and technical communities. Compared to inorganic materials, the advantages of those based on π-tectons lie in their broad diversity, flexibility, and tunability with regard to structure/geometry/morphology, processability, composition, functionality, electronic/band structure, etc. In terms of sophisticated molecular engineering, these features endow them not only with excellent self-assembly properties but also with unique optical, electrical, mechanical, photophysical, photochemical, and biochemical attributes. This renders them promising scaffolds for advanced functional materials (AFMs) in numerous areas of general interest such as electronics, optics, optoelectronics, photovoltaics, magnetic and piezoelectric devices, sensors, catalysts, biomedicines, and others.

With regard to the design/synthesis of novel π-tectons, the launch of diverse assembly/fabrication protocols, theoretical calculations, etc., the past several decades have witnessed tremendous advancements along this direction. Thus far, a vast array of high-performance π-tectons-based AFMs have been initiated. To some extent, the cooperative principle of π-πstacking and other noncovalent interactions has been revealed, and the structure-property relationships have been disclosed. Despite the existing progress, this field still faces challenges, for example:

(i) the need for scalable assembly/manufacture under ambient conditions—with low-cost, facile, environmentally-friendly protocols
(ii) clearer correlations bridging the underlying intricate relationships of each successive step in assembly/manufacture
(iii) corresponding theoretical calculations for guiding the rational design of π-tectons that elucidate the cooperative principle of π-π stacking and other noncovalent interactions, as well as the principle of structure-performance correlation
(iv) stability and durability, among the most important concerns regarding their commercialization

The advancements accumulated during the past decades have established a solid foundation for the further development of π-conjugated systems-based AFMs. We believe that with unrelenting efforts from both scientific and technical communities of various backgrounds, their practical applications will eventually be fulfilled.

This Research Topic aims to address the above-mentioned challenges

Citation: Chen, P., Wu, B., eds. (2020). Functional Supramolecular Nanoassemblies of Π-Conjugated Molecules. Lausanne: Frontiers Media SA.
doi: 10.3389/978-2-88963-360-9

Table of Contents

frontiers in Chemistry

ORIGINAL RESEARCH
published: 23 January 2019
doi: 10.3389/fchem.2019.00011

Cyclohexyl-Substituted Anthracene Derivatives for High Thermal Stability Organic Semiconductors

Yicai Dong[1,2], *Yuan Guo*[2,3], *Hantang Zhang*[2,4], *Yanjun Shi*[2,3], *Jing Zhang*[2,3], *Haiyang Li*[2,3], *Jie Liu*[2]*, *Xiuqiang Lu*[2,5], *Yuanping Yi*[2], *Tao Li*[1]*, *Wenping Hu*[6] *and Lang Jiang*[2]*

[1] *Shanghai Key Laboratory of Electrical Insulation and Thermal Aging, School of Chemistry and Chemical Engineering, Shanghai Jiao Tong University, Shanghai, China,* [2] *Beijing National Laboratory for Molecular Sciences, Key Laboratory of Organic Solids, Institute of Chemistry, Chinese Academy of Sciences, Beijing, China,* [3] *University of the Chinese Academy of Sciences, Beijing, China,* [4] *College of Chemistry and Material Science, Shandong Agricultural University, Taian, China,* [5] *School of Ocean Science and Biochemistry Engineering, Fuqing Branch of Fujian Normal University, Fuzhou, China,* [6] *Tianjin Key Laboratory of Molecular Optoelectronic Sciences, Department of Chemistry, School of Science, Tianjin, China*

OPEN ACCESS

Edited by:
John Stephen Fossey, University of Birmingham, United Kingdom

Reviewed by:
Tsuyoshi Minami, The University of Tokyo, Japan
Tsukuru Minamiki, National Institute of Advanced Industrial Science and Technology (AIST), Japan
Jonathan Hill, National Institute for Materials Science, Japan

***Correspondence:**
Jie Liu
liujie2009@iccas.ac.cn
Tao Li
litao1983@sjtu.edu.cn
Lang Jiang
ljiang@iccas.ac.cn

Specialty section:
This article was submitted to Supramolecular Chemistry, a section of the journal Frontiers in Chemistry

Received: *19 October 2018*
Accepted: *07 January 2019*
Published: *23 January 2019*

Citation:
Dong Y, Guo Y, Zhang H, Shi Y, Zhang J, Li H, Liu J, Lu X, Yi Y, Li T, Hu W and Jiang L (2019) Cyclohexyl-Substituted Anthracene Derivatives for High Thermal Stability Organic Semiconductors. Front. Chem. 7:11. doi: 10.3389/fchem.2019.00011

A novel p-type organic semiconductor with high thermal stability is developed by simply incorporating cyclohexyl substituted aryl groups into the 2,6-position of anthracene, namely 2,6-di(4-cyclohexylphenyl)anthracene (DcHPA), and a similar compound with linear alkyl chain, 2,6-di(4-*n*-hexylphenyl)anthracene (DnHPA), is also studied for comparison. DcHPA shows sublimation temperature around 360°C, and thin film field-effect transistors of DcHPA could maintain half of the original mobility value when heated up to 150°C. Corresponding DnHPA has sublimation temperature of 310°C and the performance of its thin film devices decreases by about 50% when heated to 80°C. The impressing thermal stability of the cyclohexyl substitution compounds might provide guidelines for developing organic electronic materials with high thermal stability.

Keywords: organic semiconductors, anthracene derivatives, thermal stability, organic field-effect transistors, mobility

INTRODUCTION

Organic field-effect transistors (OFETs) with organic semiconductors as key elements have been extensively studied and believed to play a prominent role in future organic electronics, such as flexible displays (Tang et al., 2009), the radio frequency identity tags (RFID) (Subramanian et al., 2005), and various sensors (Huang et al., 2008, 2017; Knopfmacher et al., 2014; Lu et al., 2017b). High mobility and great stability in ambient conditions are two prerequisites of organic semiconductors for high-performance OFETs. In recent years, remarkable progress has been achieved in improving mobility by design and synthesis of new molecules. In this process, it was found that, tailoring molecular structures is quite effective in tuning the molecular packing motifs and energy levels, which meanwhile influences the field-effect performance (Dong et al., 2010; Watanabe et al., 2012; Mori et al., 2013).On the other hand, great efforts have been devoted to improving the stability of OFETs, including environment stability (air and photo stability; Liu et al., 2015a), operating stability, and stability in some extreme conditions like under high temperatures.

Among the diverse organic semiconductors developed so far, anthracene derivatives (Meng et al., 2006; Klauk et al., 2007; Jiang et al., 2008a,b, 2009; Liu et al., 2009, 2016; Li et al., 2015; Chen et al., 2017, 2018) generally exhibit high environment stability and are supposed to have more commercial potential compared with the benchmark material of pentacene, but the thermal

stability of anthracene derivatives have rarely been addressed. Usually organic devices are prone to thermal degradation at the elevated operating temperature (Kuribara et al., 2012). Using organic semiconductor with great thermal stability is a straightforward approach for fabricating thermally stable organic transistors. To date, many researches on improving the thermal stability of semiconductors have been reported. For instance, DBTTT, which was derived from DNTT (Park et al., 2015) by replacing the terminal benzene rings of DNTT with two thiophene rings, exhibited good thermal stability with the sublimation temperature above 350°C, and the electrical characteristics of its thin film transistors (TFTs) remained unchanged when elevating the operating temperature from room temperature to 140°C. Similarly, another DNTT derivative, namely, DPh-DNTT (Yokota et al., 2013), was designed and corresponding TFTs showed that the mobility of devices decreased by no more than 20% upon annealing to 250°C. Despite these advancements, most of them were tested at room temperature after annealing to various temperatures (Sekitani et al., 2004; Yi et al., 2016; Seifrid et al., 2017). There is very few research on the thermal stability of simultaneous testing an OFET during heating (Fan et al., 2018; Gumyusenge et al., 2018), let alone possible strategies for improving the thermal stability of OFETs under elevated testing temperatures.

In this study, we developed a novel p-type organic semiconductor 2,6-di(4-cyclohexylphenyl)anthracene (DcHPA) by simply incorporating cyclohexyl-phenyl groups into the 2,6-position of the molecular skeleton of anthracene, and corresponding *n*-hexyl-phenyl substituted compound 2,6-di(4-*n*-hexylphenyl) anthracene (DnHPA) was also studied for systematical comparison. It was found that, the DcHPA showed sublimation temperature of 360°C (5% weight loss) and only 8% performance degradation for DcHPA thin film FETs when heated to 80°C, and it still maintained half of its original value up to about 150°C. DnHPA showed 50°C lower sublimation temperature, and the mobility of DnHPA TFTs decreased by 50% when heated to 80°C, then rapidly degraded, and failed to work at 120°C. Moreover, single crystal OFETs of DcHPA exhibited an average mobility of 1.98 $cm^2V^{-1}s^{-1}$ and maximum mobility up to 3.16 $cm^2V^{-1}s^{-1}$, which was comparable to that of DnHPA (Xu et al., 2016). All these results indicate that the cyclohexyl-phenyl substitution obviously improves the thermal stability without sacrificing the mobility, and it might provide guidelines for the design and investigation of high-performance semiconductors with high thermal stability in the future.

EXPERIMENTAL

Materials and Characterization

All reagents and chemicals were obtained from commercial resources and used without further purification.

The synthesis of the DcHPA is illustrated in **Scheme 1**. The final product can be easily synthesized through three simple steps with high yields (Lu et al., 2017a). Firstly a reduction reaction was carried out getting the intermediate of 2,6-dihydroxyl anthracene, and then esterification reaction was done getting 2,6-diyl bis (trifluoromethanesulfonate) anthracene as a yellowish-white crystalline powder, finally by coupling the intermediate 2 with (4-cyclohexylphenyl) boronic acid under the presence of $Pd(PPh_3)_4$ gave the target molecular DcHPA with a yield of 84%. The compound was confirmed by MS (EI): m/z 494 (M^+), NMR (**Figure S1**) and elemental analysis calculated for $C_{38}H_{38}$ (%): C 92.26, H 7.74. Found: C 91.96, H 7.74.

^{1}HNMR spectra were recorded on Advance 400 MHz spectrometer in deuterated chloroform with tetramethylsilane (TMS) as an internal reference. All chemical shifts were reported relative to TMS at 0.0 ppm. Elemental analysis was carried out by Flash EA 1112. The UV-vis spectra were obtained on a Jasco V-570 UV-vis spectrometer with solution concentration of 1×10^{-5} mol/L. Cyclic voltammetry (CV) was run on a CHI660C electrochemistry station in THF solution using tetrabutylammonium hexafluorophosphate (Bu_4NPF_6) as electrolyte at a scan speed of 100 mVs^{-1}, and glassy carbon was used as the working electrode and Pt wire as the counter electrode and ferrocene as inner standard. Thermogravimetric analysis (TGA) was carried out on a Perkin Elmer TGA7 under nitrogen. Differential scanning calorimetry (DSC) was carried out on DSC 250 under nitrogen with the heating rate of 10°C/min. X-ray diffraction (XRD) measurement was performed in reflection mode at 40 kV and 200 mA with Cu Ka radiation using a 2 kW Rigaku D/max-2500 X-ray diffractometer. Atomic force microscopy (AFM) images of single crystal were obtained by using a Digital Instruments Nanoscope III atomic force microscope in air. Transmission electron microscopy (TEM) and selected area electron diffraction (SAED) measurements were carried out on a JEM 1011 (Japan). HR-AFM images were obtained by the instrument of Asylum Research AFM.

Thin Film Transistors, Fabrication and Characterization

The films were imaged in air using a Digital Instruments Nanoscope III atomic force microscope operated in tapping mode. Thin film devices were fabricated with bottom-gate top-contact configuration. Fifty nanometer thin films of DcHPA and DnHPA were grown on the octadecytrichlorosilane (OTS)-treated Si/SiO_2 (300 nm) substrate by vacuum deposition with the speed of 0.1–0.4 Å/s at different substrate temperature (T_{sub}). Twenty nanometer thick gold source and drain electrodes were deposited successively using the shadow masks with width-to-length ratio (W/L, 240/30 μm) of cal. 8/1. OFET characteristics of DcHPA were obtained in air under different temperatures on a Keysight 1,500 A and Signatone 1,160 probe station, and the heating temperature was varied from 20 to 220°C in steps of 20°C. Then the mobility was calculated by using the equation: $I_{DS} = (W/2L) \times C_i \times u \times (V_G - V_T)^2$ where W and L are the width and length of channels, respectively, and *Ci* is the capacitance of the gate-dielectric capacitance per unit area.

Single Crystal Transistors, Fabrication and Characterization

High quality ribbon-like single crystals were grown on OTS-treated Si/SiO_2 substrate by physical vapor transport (PVT) method in a horizontal tube furnace under argon atmosphere (Wang et al., 2018). In a tube furnace, DcHPA was placed in a quartz boat at the high temperature zone of 180°C, and ribbon-like single crystals could be obtained on substrate down the

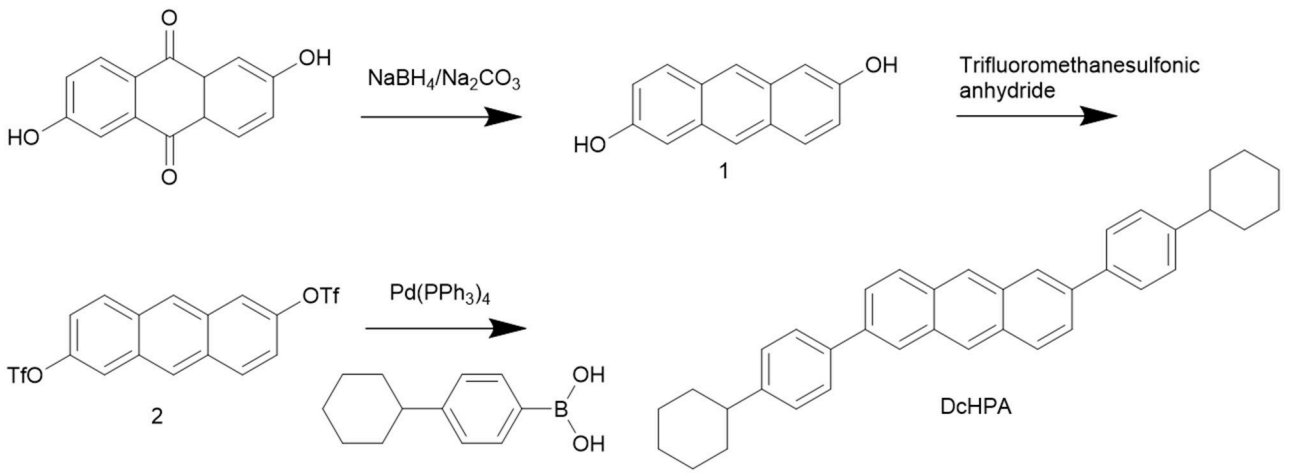

SCHEME 1 | Synthetic route to 2,6-di(4-cyclohexylphenyl)anthracene (DcHPA).

argon stream at the low temperature. The temperature of the tube furnace was gradually increased to 180°C, then maintained for 3 h. After cooling down to room temperature, single crystal transistors were fabricated using the "organic ribbon mask" technique (Jiang et al., 2008b).

RESULTS AND DISCUSSIONS

Figure 1A shows the molecular structure of DcHPA and DnHPA. Cyclic voltammetry measurement of DcHPA was performed in dichloromethane solution (with 10^{-3} M, $BuNPF_6$ as electrolyte) to investigate the electrochemical properties. As shown in **Figure 1B**, it exhibited one quasi-reversible oxidative wave. The highest occupied molecular orbital (HOMO) energy level of DcHPA was calculated from the onset of the oxidation peak with reference to Fc^+/Fc (4.8 eV) using the equation of $E_{HOMO} = [4.8\text{-}E_{Fc}+E_{onsetox}]$ eV, and HOMO level of 5.6 eV was determined, which was similar to that of 2,6-diphenyl-anthracene (DPA) (Liu et al., 2015a,b). UV-vis measurements of DcHPA in dilute solution (10^{-5} M in CH_2Cl_2) and in the form of thin film (50 nm) were performed as shown in **Figure 1C**. All the spectra of DcHPA exhibited fine vibronic structures of typical anthracene derivatives. The optical bandgap calculated from the onset absorption using the equation of $Eg = 1,240/\lambda$, and bandgap of 3 eV was estimated. Besides, frontier orbitals were estimated by theoretical calculation. Firstly, the molecular geometric structures of DnHPA and DcHPA were optimized by density functional theory (DFT) at the B3LYP/6-31G** level. As seen in **Figures 1D,E**, the electron density distribution of the HOMO and the lowest unoccupied molecular orbital (LUMO) of both DnHPA and DcHPA reside mostly on the central anthracene unit and a bit on the two appended benzene units. The different substituted alkyl groups of n-hexyl and cylco-hexyl hardly affect the HOMO and LUMO energies. Thermal stability of DcHPA and DnHPA was measured by TGA (**Figure 1F**). The weight of both the materials was almost constant when the temperature was below 300°C, and the sublimation temperature (with 5% weight loss) of DcHPA and DnHPA was 360°C and 310°C under nitrogen atmosphere, respectively. According to results of TGA, DSC measurements were carried out simultaneously to investigate their thermal stability. No endothermic peak and exothermic peak of DcHPA was observed during heating and cooling process before the sublimation temperature, and DnHPA showed endothermic peaks around 226 and 249°C during heating and exothermic peaks around 216 and 245°C during cooling in the range of 20 to 300°C. The peaks around 250°C is caused by the melting and crystallization process of DnHPA which was confirmed by the measurement of the melting point, while peaks at around 226 and 216°C might related to a phase transition process.

DcHPA thin films were deposited on the OTS-treated Si/SiO_2 substrate with different T_{sub}, and the corresponding morphology of thin films were characterized by AFM as illustrated in **Figures 2A–C**. The films were quite rough and lots of rod-like domains could be observed when deposited on the substrate at room temperature. With the increasing T_{sub}, the morphology of DcHPA films gradually became smoother and the rod-like grains gradually evolved into layer-by-layer crystalline domains. Especially in **Figure 2C**, large and uniform grains with layer-by-layer growth were observed, which proved that increasing the T_{sub} was beneficial to the formation of uniform films. XRD measurements were performed to study the structural order of thin films. Strong and ordered diffraction peaks were obtained (**Figure 2D**) indicating high crystallinity. Similar diffraction peaks were observed for films deposited at different T_{sub}. A primary diffraction peaks appeared at $2\theta = 5.30°$, with third-order diffraction perks at $2\theta = 15.87°$. And the same 2θ detected for all these films, indicates the simple morphology change instead of phase transition for thin films deposited at different T_{sub} (He et al., 2015; Zhang et al., 2016). Moreover, the relative high diffraction intensity for films deposited at elevated temperatures indicates higher crystallinity of the films.

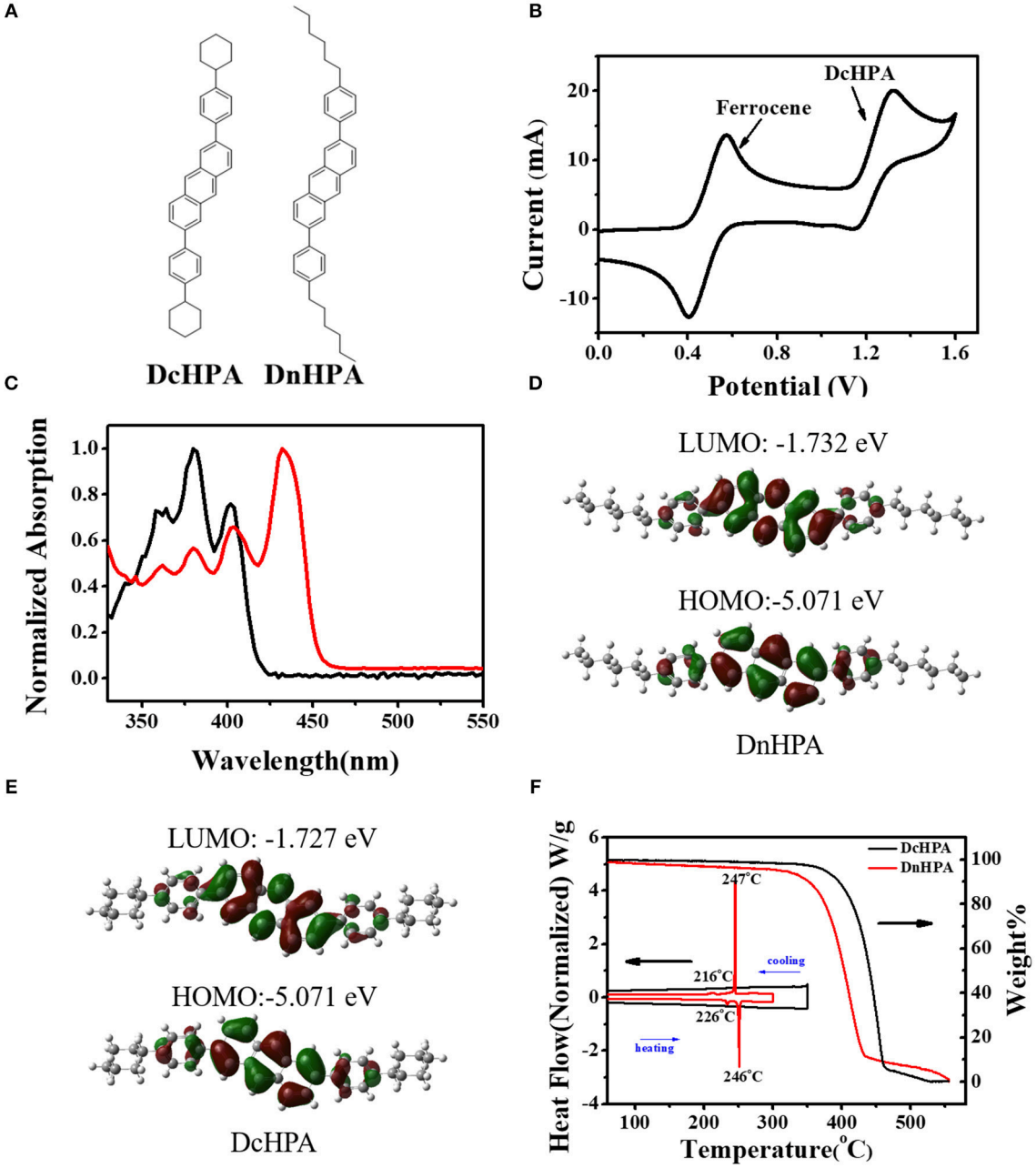

FIGURE 1 | (A) Molecular structure of DcHPA and DnHPA. **(B)** Cyclic voltammogram curves of DcHPA in CH_2Cl_2 with concentration of 10^{-3} M. **(C)** Uv-vis absorption of DcHPA in dilute CH_2Cl_2 solution (10^{-5} M, black) and in thin film state (red). Frontier molecular orbitals for DnHPA **(D)** and DcHPA **(E)**. **(F)** Thermogravimetric analysis (TGA) and differential scanning calorimetry (DSC) of DcHPA and DnHPA.

The d-spacing of DcHPA obtained from the first diffraction peak was 1.67 nm based on the equation of $2d \times \sin\theta = n\lambda$, which was consistent with the single layer thickness shown in **Figure 2C** inset. **Figures 2E,F** showed the typical transfer and output characteristics at room temperature with the T_{sub} of 20°C, and slight hysteresis was observed in transfer curves which might be deduced from the trap states in thin films which blocking carrier transport. The distribution of mobility and threshold voltage of 40 devices was shown in the **Figures 2G,H**, and most devices exhibit mobility in the range of 0.1–0.15 $cm^2V^{-1}s^{-1}$, with the threshold voltage in the range of −24∼-28 V. The larger grain size and better crystallinity of films deposited at elevated temperatures also exhibited higher mobility (**Table S1**), with typical transfer characteristics shown in **Figures S2A,B**. And the average mobility increased from 0.12 to 0.37 $cm^2V^{-1}s^{-1}$ and 0.52 $cm^2V^{-1}s^{-1}$ for films deposited at T_{sub} from 20 to 60°C and

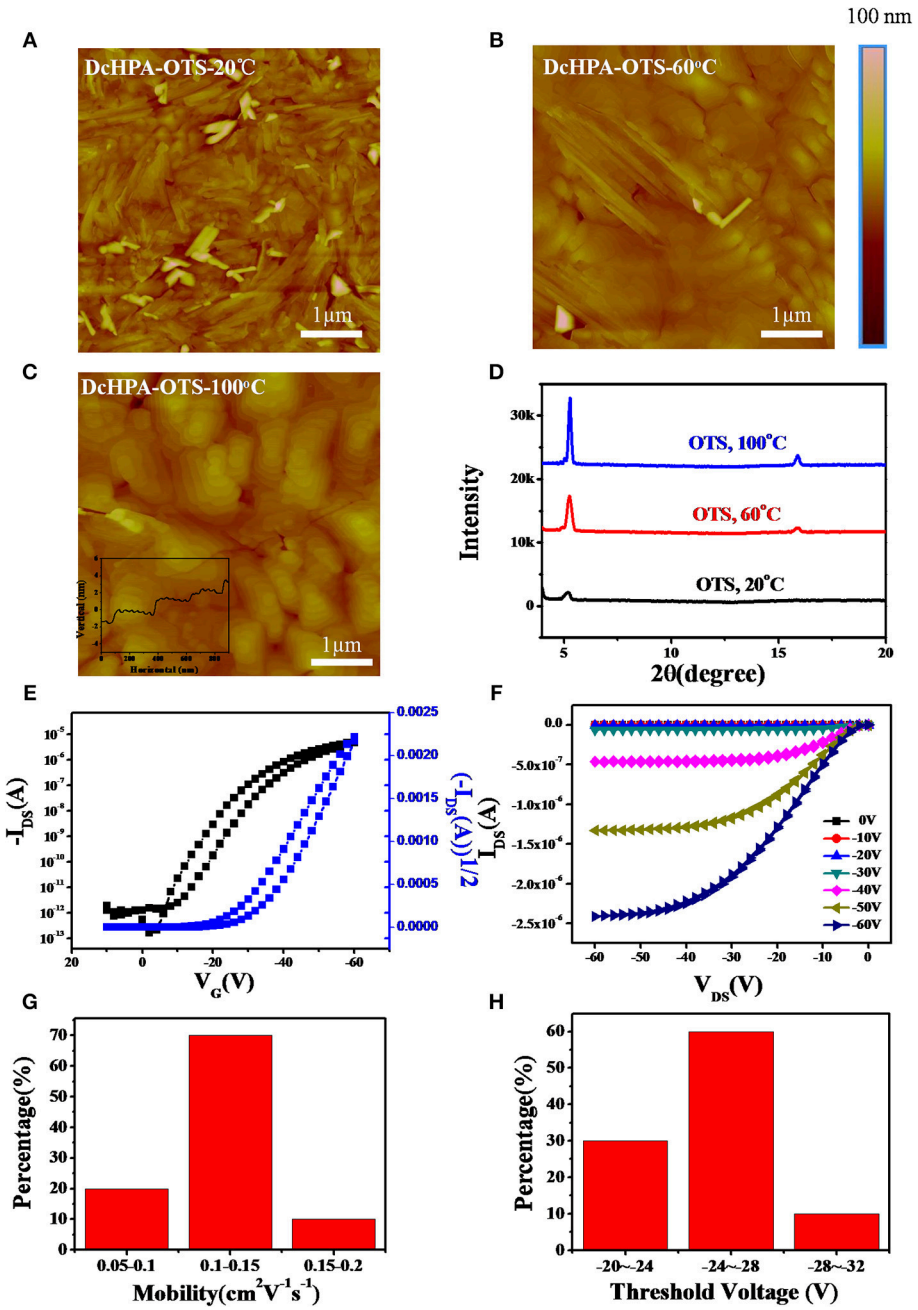

FIGURE 2 | AFM images of 50 nm thin films of DcHPA at **(A)** 20°C, **(B)** 60°C, and **(C)** 100°C, respectively. **(D)** Out of plane XRD results of DcHPA 50 nm films. **(E)** Typical transfer and **(F)** output characteristics of thin film transistors. The distribution of the mobility **(G)** and threshold voltage **(H)** of DcHPA thin film transistors.

100°C, respectively. Besides, OFETs studies were also conducted on DnHPA thin films (**Figures S3A,B**). Typical transfer and output curves were shown in **Figures S3C,D**, which exhibited mobility of about 0.47 $cm^2V^{-1}s^{-1}$, and thin films deposited at T_{sub} of 60°C showed mobility of 0.54 $cm^2V^{-1}s^{-1}$ (**Figure S4A**). However, lower mobility of 0.35 $cm^2V^{-1}s^{-1}$ (**Figure S4B**) was obtained for films deposited at T_{sub} of 100°C. The slightly higher mobility of DnHPA devices than DcHPA devices fabricated at T_{sub} of 20°C could be explained by the larger grain size of DnHPA films (**Figures S3A,B**) than that of DcHPA thin films (**Figure 2A**) at the T_{sub} of 20°C, which result in less grain boundaries in the conducting channel. The increased mobility of DcHPA indicated that, the elevated temperature benefited the growth of DcHPA in the whole temperature range. While DnHPA films were found with lots of cracks at T_{sub} of 100°C (**Figure S5**), which might be caused by the different coefficient of thermal expansion of the

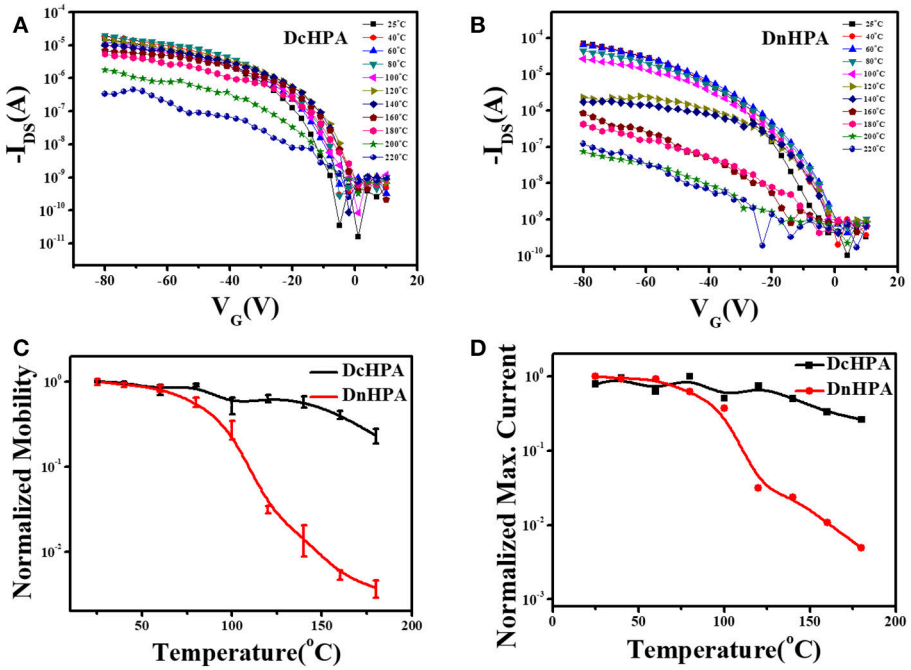

FIGURE 3 | Typical transfer characteristics of DcHPA **(A)** and DnHPA **(B)** at elevated temperature from 20 to 220°C in steps of 20°C. Field-effect mobility **(C)** and Maximum current **(D)** of DcHPA (black line) and DnHPA (red line) TFTs as a function of heating temperature.

semiconductor and the substrates, and these cracks act as traps in the conducting channel and result in the lower mobility.

To investigate the thermal stability, OFETs were tested at varied temperatures from 20 to 220°C in steps of 20°C (Okamoto et al., 2013) for films deposited at T_{sub} of 50°C. The AFM images of DcHPA and DnHPA at T_{sub} of 50°C were depicted in **Figures S6A,B**, respectively. The heating rate was 0.5°C/s and the tests were carried out in air during heating. **Figures 3A,B** showed the transfer characteristics of DcHPA and DnHPA, respectively. Slight performance degradation was observed from room temperature to about 180°C for DcHPA devices, and DnHPA devices degraded obviously when heated to 120°C. The results were further presented in **Figure 3C**. The mobility of DcHPA and DnHPA devices as a function of the temperature demonstrated that DcHPA TFTs are significantly more stable than DnHPA TFTs at elevated temperatures. The mobility of DnHPA devices decreased by 50% when heated to 80°C, and rapidly degraded thereafter and had almost lost field-effect performance when heated to 120°C. By contrast, the change in mobility of DcHPA devices was as small as 8% when heated to 80°C, and the devices still maintained half of its original value up to about 150°C. The morphology of thin films at pristine state and after heating were shown in **Figures S7A–D**, the morphology of DcHPA thin films was almost unchanged, indicating strong thermal stability of them. However, DnHPA thin films became discontinuous after heating and large domains were formed with abundance of cracks, which made poor connectivity of the conducting channel. The change of maximum current in this experiment in **Figure 3D** was similar to the change of mobility. Obviously, devices of DcHPA have better thermal stability than DnHPA. XRD measurements were also conducted for DcHPA and DnHPA thin films at elevated temperatures from 20 to 200°C in steps of 20°C, and the results were depicted in **Figures S8A,B**. It can be observed that, there is no significant change of DcHPA thin films in peak position except for slightly changes in intensity. However, the second-order diffraction peak of DnHPA thin films at $2\theta = 13.63°$ obviously disappeared and a shoulder peak emerged at diffraction $2\theta = 5.84°$ at 160°C, and further elevating the temperature resulted in the disappearance of the diffraction at $2\theta = 5.46°$ and intensified diffraction at $2\theta = 5.84°$, which indicates a phase transition of DnHPA thin films at elevated temperature. And this result correlates well to the DSC result where a phase transition occurs at 226°C. Instead of the phase transition (He et al., 2015; Zhang et al., 2016), quick performance degradation of DnHPA at around 80°C might be caused by the energetic disorder at high temperatures and the deterioration in electrical contacts (Fan et al., 2018).

Due to the poor uniformity and small grains of DcHPA thin films, many traps and defects exist in the conducting channel. To address this issue, we next fabricated single crystal transistors to investigate the intrinsic mobility of DcHPA semiconductor. Bottom-gate top-contact single crystal transistors based on DcHPA crystals with thickness of about 20 nm were fabricated using the "organic ribbon mask" technique. Ribbon-like DcHPA microcrystals were obtained by PVT method and AFM image (**Figure S9**) showed that the DcHPA microcrystals have smooth surfaces and clear edges, which promise HR-AFM characterization (**Figure 4B**). TEM and SAED were performed

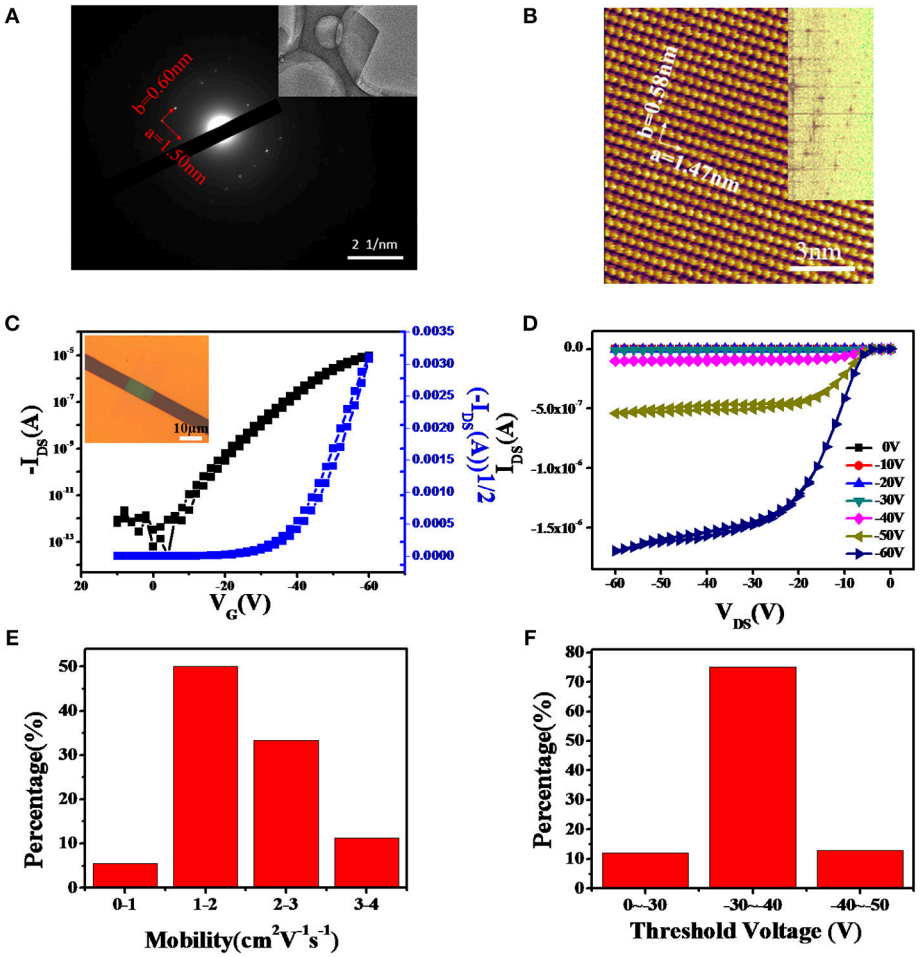

FIGURE 4 | TEM and SAED **(A)** and HR-AFM **(B)** images of DcHPA single crystal obtained by PVT method. **(C)** Typical transfer and **(D)** output characteristics of DcHPA single crystal transistors, and the insert of **(C)** was the optical image of single crystal device based on DcHPA. The distribution of the mobility **(E)** and threshold voltage **(F)** of DcHPA single crystal transistors.

for microcrystal grown on copper grid (**Figure 4A**). And lattice parameters of a-axis and b-axis were about 1.50 nm and 0.60 nm, respectively. HR-AFM image of DcHPA microcrystals was illustrated in **Figure 4B**. The results showed that the lattice type was rectangular and the lattice parameters of a-axis and b-axis were 1.47 and 0.58 nm, respectively, which were consistent with the SADE results. Combining the results from HR-AFM (**Figure 4B** and **Figure S10D**) and XRD (**Figure 2D** and **Figure S3E**), the lattice parameters of a = 1.47 nm and b = 0.58 nm with d-spacing of 1.67 nm could be obtained for DcHPA, and the values were 0.44, 0.52, and 1.62 nm for DnHPA, respectively. Since longer molecular length could be expected for the linear DnHPA compared with DcHPA, the comparable d-spacing observed for the two materials, indicating smaller tilt angle for DcHPA in the solid states, which might result in more efficient π-π interactions, and thus enhanced thermal stability and higher mobility. To gain insights into the different thermal stability, a theoretical simulation was carried out regarding 200 molecules in the solid states, however, the intermolecular interaction energy density is almost identical for the two compounds (Supplementary Material theoretical calculation and **Figure S11**), and further estimation based on the precise packing structure is needed to find the intrinsic origin of the higher thermal stability of DcHPA.

The typical transfer and output characteristics with little hysteresis were illustrated in **Figures 4C,D**, and the optical image of single crystal transistor structure was shown in the inset in **Figure 4C**. Mobility of the device was calculated to be 1.83 $cm^2V^{-1}s^{-1}$ by using the equation of $I_{DS} = (W/2L) \times C_i \times u \times (V_G - V_T)^2$ with the channel length of 5.82 μm and channel width of 12.3 μm. A total of 20 devices were measured, and 95% devices exhibited mobility above 1.0 $cm^2V^{-1}s^{-1}$ with the average mobility of 1.98 $cm^2V^{-1}s^{-1}$ as well as the maximum mobility up to 3.16 $cm^2V^{-1}s^{-1}$. The distribution of mobility was shown in **Figure 4E**. On the other hand, 75% single crystal devices had threshold voltage in the range of −30∼-40 V (**Figure 4F**).

And the output in **Figure 4D** indicated a relatively large contact resistance in the device, which may be highly related to the mismatch between the HOMO energy level of DcHPA (5.6 eV) and the work function of gold (5.1 eV), and the series resistance from the electrode to the conducting channel. Therefore, higher mobility could be expected by reducing the contact resistance (Li et al., 2013). In addition, DnHPA single crystals were obtained and corresponding DnHPA single crystal transistors were fabricated using the same method, which exhibited the average mobility of 1.30 $cm^2V^{-1}s^{-1}$ (**Figures S10A–D**).

CONCLUSIONS

In summary, we have synthesized a novel semiconductor material DcHPA by simply incorporating cyclohexyl-phenyl groups into the 2, 6-position of the molecular skeleton of anthracene. The effect of deposition temperature on film morphology was explored, showing that the morphology of DcHPA thin films were more uniform, smoother and tended to grow layer-by-layer with higher crystallinity at the elevated substrate temperature. More importantly, thin film devices of DcHPA exhibited apparently higher thermal stability than DnHPA. DcHPA OFETs could maintain half of the original mobility value up to 150°C, while the performance of DnHPA thin film devices decreased by 50% when heated to 80°C and degraded rapidly thereafter. Although DcHPA and DnHPA have similar molecular weight, DcHPA thin film devices were obviously more stable than DnHPA devices under high temperature. In addition, single crystal transistors were fabricated to investigate intrinsic mobility of DcHPA semiconductor, which exhibits highest mobility of 3.16 $cm^2V^{-1}s^{-1}$. All these results might provide guidelines for the development of materials with high thermal stability.

AUTHOR CONTRIBUTIONS

JL, TL, and LJ designed the experiments with help of WH. YD synthesized the compound with help of JL. XL, JL, YD, and HZ designed and performed the thin film and single crystal OFET experiments. JZ and YS helped to obtain TEM, AFM, and HR-AFM characterization. YG and YY helped to obtain theoretical calculation. YD, JL, TL, and LJ wrote the manuscript. All the authors participated in the result discussion.

FUNDING

This work was supported by the Ministry of Science and Technology of China (2017YFA0204704, 2016YFB0401100, 2017YFA0207500), National Natural Science Foundation of China (21805284, 21873108, 51673114, 91233205, 51503037), Shanghai Science and Technology Committee (17ZR1447300), and Chinese Academy of Sciences [Hundred Talents Plan, Youth Innovation Promotion Association and the Strategic Priority Research Program of Sciences (Grant No. XDB30000000 & XDB12030300)].

SUPPLEMENTARY MATERIAL

The Supplementary Material for this article can be found online at: https://www.frontiersin.org/articles/10.3389/fchem.2019.00011/full#supplementary-material

REFERENCES

Chen, M., Yan, L., Zhao, Y., Murtaza, I., Meng, H., and Huang, W. (2018). Anthracene-based semiconductors for organic field-effect transistors. *J. Mater. Chem. C* 6, 7416–7444. doi: 10.1039/c8tc01865k

Chen, M., Zhao Y., Yan, L., Yang, S., Zhu, Y., Murtaza, I., et al. (2017). A unique blend of 2-fluorenyl-2-anthracene and 2-anthryl-2-anthracence showing white emission and high charge mobility. *Angew. Chem. Int. Ed.* 56, 722–727. doi: 10.1002/anie.201608131

Dong, H., Wang, C., and Hu, W. (2010). High performance organic semiconductors for field-effect transistors. *Chem. Commun.* 46, 5211–5222. doi: 10.1039/c0cc00947d

Fan, Z.-P., Li, X.-Y., Purdum, G. E., Hu, C.-X., Fei, X., Shi, Z.-F., et al. (2018). Enhancing the thermal stability of organic field-effect transistors by electrostatically interlocked 2D molecular packing. *Chem. Mater.* 30, 3638–3642. doi: 10.1021/acs.chemmater.8b01579

Gumyusenge, A., Tran, D. T., Luo, X., Pitch, G. M., Zhao, Y., Kaelon, A., et al. (2018). Semiconducting polymer blends that exhibit stable charge transport at high temperatures. *Science* 362, 1131–1134. doi: 10.1126/science.aau0759

He, P., Tu, Z., Zhao, G., Zhen, Y., Geng, H., Yi, Y., et al. (2015). Tuning the crystal polymorphs of alkyl thienoacene via solution self-assembly toward air-stable and high-performance organic field-effect transistors. *Adv. Mater.* 27, 825–830. doi: 10.1002/adma.201404806

Huang, J., Sun, J., and Katz, H. E. (2008). Monolayer-Dimensional 5,5′-Bis(4-hexylphenyl)-2,2′-bithiophene transistors and chemically responsive heterostructures. *Adv. Mater.* 20, 2567–2572. doi: 10.1002/adma.200703212

Huang, J., Zhang, G., Zhao, X., Wu, X., Liu, D., Chu, Y., et al. (2017). Direct detection of dilute solid chemicals with responsive lateral organic diodes. *J. Am. Chem. Soc.* 139, 12366–12369. doi: 10.1021/jacs.7b06223

Jiang, L., Fu, Y., Li, H., and Hu, W. (2008a). Single-crystalline, size, and orientation controllable nanowires and ultralong microwires of organic semiconductor with strong photoswitching property. *J. Am. Chem. Soc.* 130, 3937–3941. doi: 10.1021/ja077600j

Jiang, L., Gao, J., Wang, E., Li, H., Wang, Z., Hu, W., et al. (2008b). Organic single-crystalline ribbons of a rigid "H"-type anthracene derivative and high-performance, short-channel field-effect transistors of individual micro/nanometer-sized ribbons fabricated by an "organic ribbon mask" technique. *Adv. Mater.* 20, 2735–2740. doi: 10.1002/adma.200800341

Jiang, L., Hu, W., Wei, Z., Xu, W., and Meng, H. (2009). High-performance organic single-crystal transistors and digital inverters of an anthracene derivative. *Adv. Mater.* 21, 3649–3653. doi: 10.1002/adma.200900503

Klauk, H., Zschieschang, U., Weitz, R. T., Meng, H., Sun, F., Nunes, G., et al. (2007). Organic transistors based on Di(phenylvinyl)anthracene: performance and stability. *Adv. Mater.* 19, 3882–3887. doi: 10.1002/adma.200701431

Knopfmacher, O., Hammock, M. L., Appleton, A. L., Schwartz, G., Mei, J., Lei, T., et al. (2014). Highly stable organic polymer field-effect transistor sensor for selective detection in the marine environment. *Nat. Commun.* 5:2954. doi: 10.1038/ncomms3954

Kuribara, K., Wang, H., Uchiyama, N., Fukuda, K., Yokota, T., Zschieschang, U., et al. (2012). Organic transistors with high thermal stability for medical applications. *Nat. Commun.* 3:723. doi: 10.1038/ncomms1721

Li, J., Liu, J., Zhen, Y., Meng, L., Wang, Y., Dong, H., et al. (2015). Naphthyl substituted anthracene combining charge transport with light emission. *J. Mater. Chem. C* 3, 10695–10698. doi: 10.1039/c5tc02254a

Li, T., Jevric, M., Hauptmann, J. R., Hviid, R., Wei, Z., Wang, R., et al. (2013). Ultrathin reduced graphene oxide films as transparent top-contacts for light switchable solid-state molecular junctions. *Adv. Mater.* 25, 4164–4170. doi: 10.1002/adma.201300607

Liu, J., Dong, H., Wang, Z., Ji, D., Cheng, C., Geng, H., et al. (2015a). Thin film field-effect transistors of 2,6-diphenyl anthracene (DPA). *Chem. Commun.* 51, 11777–11779. doi: 10.1039/c4cc10348c

Liu, J., Zhang, H., Dong, H., Meng, L., Jiang, L., et al. (2015b). High mobility emissive organic semiconductor. *Nat. Commun.* 6:10032. doi: 10.1038/ncomms10032

Liu, J., Zhu, W., Zhou, K., Wang, Z., Zou, Y., Meng, Q., et al. (2016). Pyridyl-substituted anthracene derivatives with solid-state emission and charge transport properties. *J. Mater. Chem. C* 4, 3621–3627. doi: 10.1039/c6tc00499g

Liu,. J., Jiang, L., and Hu, W. (2009). The application of anthracene and its derivatives in organic field-effect transistors. *Prog. Chem.* 21, 2568–2577.

Lu, J., Bao, D. L., Dong, H., Qian, K., Zhang, S., Liu, J., et al. (2017a). Construction of two-dimensional chiral networks through atomic bromine on surfaces. *J Phys Chem Lett.* 8, 326–331. doi: 10.1021/acs.jpclett.6b02680

Lu, J., Liu, D., Zhou, J., Chu, Y., Chen, Y., Wu, X., et al. (2017b). Porous organic field-effect transistors for enhanced chemical sensing performances. *Adv. Funct. Mater* 27:1700018. doi: 10.1002/adfm.201700018

Meng, H., Sun, F., Goldfinger, M. B., Feng, Gao, F., Londono, D. J., Marshal, W. J., et al. (2006). 2,6-Bis[2-(4-pentylphenyl)vinyl]anthracene: a stable and high charge mobility organic semiconductor with densely packed crystal structure. *J. Am. Chem. Soc.* 128, 9304–9305. doi: 10.1021/ja062683+

Mori, T., Nishimura, T., Yamamoto, T., Doi, I., Miyazaki, E., Osaka, I., et al. (2013). Consecutive thiophene-annulation approach to pi-extended thienoacene-based organic semiconductors with [1]benzothieno[3,2-b][1]benzothiophene (BTBT) substructure. *J. Am. Chem. Soc.* 135, 13900–13913. doi: 10.1021/ja406257u

Okamoto, T., Mitsui, C., Yamagishi, M., Nakahara, K., Soeda, J., Hirose, Y., et al. (2013). V-shaped organic semiconductors with solution processability, high mobility, and high thermal durability. *Adv. Mater.* 25, 6392–6397. doi: 10.1002/adma.201302086

Park, J. I., Chung, J. W., Kim, J. Y., Lee, J., Jung, J. Y., Koo, B., et al. (2015). Dibenzothiopheno[6,5-b:6',5'-f]thieno[3,2-b]thiophene (DBTTT): high-performance small-molecule organic semiconductor for field-effect transistors. *J. Am. Chem. Soc.* 137, 12175–12178. doi: 10.1021/jacs.5b01108

Seifrid, M., Ford, M. J., Li, M., Koh, K. M., Trefonas, P., and Bazan, G. C. (2017). Electrical performance of a molecular organic semiconductor under thermal stress. *Adv. Mater.* 29:5511. doi: 10.1002/adma.201605511

Sekitani, T., Iba, S., Kato, Y., and Someya, T. (2004). Pentacene field-effect transistors on plastic films operating at high temperature above 100°C. *Appl. Phys. Lett.* 85, 3902–3904. doi: 10.1063/1.1812374

Subramanian, V., Chang, P. C., Lee, J. B., Molesa, S. E., and Volkman, S. K. (2005). Printed organic transistors for ultra-low-cost RFID applications. *IEEE Trans. Compo. Pack. Tech.* 28, 742–747. doi: 10.1109/TCAPT.2005.859672

Tang, Q., Tong, Y., Hu, W., Wan, Q., and Bjørnholm, T. (2009). Assembly of nanoscale organic single-crystal Cro cyclohexyl-substituted anthracene derivatives for high thermally stable organic semiconductorsss-Wire Circuits. *Adv. Mater.* 21, 4234–4237. doi: 10.1002/adma.200901355

Wang, C., Dong, H., Jiang, L., and Hu, W. (2018). Organic semiconductor crystals. *Chem. Soc. Rev.* 47, 422–500. doi: 10.1039/c7cs00490g

Watanabe, M., Chang, Y. J., Liu, S. W., Chao, T. H., Goto, K., Islam, M. M., et al. (2012). The synthesis, crystal structure and charge-transport properties of hexacene. *Nat. Chem.* 4, 574–578. doi: 10.1038/nchem.1381

Xu, C., He, P., Liu, J., Cui, A., Dong, H., Zhen, Y., et al. (2016). A general method for growing two-dimensional crystals of organic semiconductors by "solution epitaxy". *Angew. Chem. Int. Ed.* 55, 9519–9523. doi: 10.1002/anie.201602781

Yi, H. T., Chen, Z., Facchetti, A., and Podzorov, V. (2016). Solution-processed crystalline n-type organic transistors stable against electrical stress and photooxidation. *Adv. Funct. Mater.* 26, 2365–2370. doi: 10.1002/adfm.201502423

Yokota, T., Kuribara, K., Tokuhara, T., Zschieschang, U., Klauk, H., Takimiya, K., et al. (2013). Flexible low-voltage organic transistors with high thermal stability at 250 degrees C. *Adv. Mater.* 25, 3639–3644. doi: 10.1002/adma.201300941

Zhang, Z., Jiang, L., Cheng, C., Zhen, Y., Zhao, G., Geng, H., et al. (2016). The impact of interlayer electronic coupling on charge transport in organic semiconductors: a case study on titanylphthalocyanine single crystals. *Angew. Chem. Int. Ed. Engl.* 55, 5206–5209. doi: 10.1002/anie.201601065

Conflict of Interest Statement: The authors declare that the research was conducted in the absence of any commercial or financial relationships that could be construed as a potential conflict of interest.

frontiers in Chemistry

ORIGINAL RESEARCH
published: 17 April 2019
doi: 10.3389/fchem.2019.00142

Nitrogen Doped Carbons Derived From Graphene Aerogel Templated Triazine-Based Conjugated Microporous Polymers for High-Performance Supercapacitors

Lan Peng[1,2], *Qianyin Guo*[1,2], *Zhaolin Ai*[1,2], *Yan Zhao*[2,3], *Yunqi Liu*[2,3] *and Dacheng Wei*[1,2]*

[1] State Key Laboratory of Molecular Engineering of Polymers, Department of Macromolecular Science, Fudan University, Shanghai, China, [2] Institute of Molecular Materials and Devices, Fudan University, Shanghai, China, [3] Department of Material Sciences, Fudan University, Shanghai, China

Conjugated microporous polymers (CMPs) have attracted intensive attention owing to their permanent nanoporosity, large surface area and possibility for functionalization, however their application in energy storage suffers from poor conductivity and low hetero-atom content. Here, we demonstrate a hybrid of conjugated microporous polymers and graphene aerogel with improved conductivity. After treating at 800°C in NH_3, the nitrogen content increases to 9.8%. The resulting microporous carbon exhibits a significant rise in supercapacitive performance up to 325 F g^{-1}, 55% higher than pristine triazine-based CMPs, with energy density up to 12.95 Wh kg^{-1}. Moreover, it has high stability with 99% retention after 10,000 cycles at 5 A g^{-1}. The synergy of hierarchical porous structure, graphene-based conduction path and high percentage of hybridization with nitrogen ensures effective ion/electron transport and diffusion, making NH_3-treated graphene aerogel/CMP hybrid a promising electrode material in high-performance supercapacitor.

Keywords: conjugated microporous polymer, graphene aerogel, supercapacitors, triazine-based electrode materials, nitrogen-doped carbon

OPEN ACCESS

Edited by:
Penglei Chen,
Institute of Chemistry (CAS), China

Reviewed by:
Xiaodong Zhuang,
Shanghai Jiao Tong University, China
Bao-Hang HAN,
National Center for Nanoscience and Technology (CAS), China
Huiqiao Li,
Huazhong University of Science and Technology, China

***Correspondence:**
Dacheng Wei
weidc@fudan.edu.cn

Specialty section:
This article was submitted to Supramolecular Chemistry, a section of the journal Frontiers in Chemistry

Received: *25 November 2018*
Accepted: *26 February 2019*
Published: *17 April 2019*

Citation:
Peng L, Guo Q, Ai Z, Zhao Y, Liu Y and Wei D (2019) Nitrogen Doped Carbons Derived From Graphene Aerogel Templated Triazine-Based Conjugated Microporous Polymers for High-Performance Supercapacitors. Front. Chem. 7:142. doi: 10.3389/fchem.2019.00142

INTRODUCTION

Conjugated microporous polymers (CMPs) are one kind of covalently linked organic porous materials which have attracted extensive interest in recent years due to their strong π-conjugated linkage, permanent nanoporosity, large surface area, possibility to modify functional groups as well as high stability compared with other porous organic materials (Xu et al., 2013). Until now, CMPs have been used in various fields, including gas adsorption and storage (Yuan et al., 2010; Reich et al., 2012), gas separation, heterogeneous catalysis, light harvesting devices, photoluminescence, electric energy conversion and storage, etc. Among them, supercapacitor, as one kind of electrochemical energy storage devices, shows great potential for daily appliances (Pang et al., 2015; Zhang et al., 2015, 2016; Xie and Zhang, 2016) owing to its fast charge-discharge rate, high power density, less environment pollution, etc. (Zhang and Zhao, 2009; Wang G. et al., 2012; Peng et al., 2014; Salunkhe et al., 2014; Wang Q. et al., 2014)Compared with traditional supercapacitor electrode materials, CMPs have high specific surface area and the possibility to tailor pore and channel structures. Recently, the CMPs are normally produced by solvothermal method, which is

suitable for carbon-carbon bond-forming reactions. However, CMPs produced by solvothermal method have relatively poor orbital overlap due to the twisted benzene rings, leading to low electrical conductivity (Lee et al., 2016). To improve the conductivity, CMPs with high carbon content are synthesized by coupling reactions, however it usually results in poor wettability of CMPs-based electrode.

To improve the performance of CMPs as electrode material, hybridization with other heteroatoms are widely used, which can increase both the wettability and the pseudocapacitance. With higher nitrogen content, the supercapacitive performance of a triazatruxene-functional CMP are remarkably improved, however the value only reaches 183 F g^{-1} (Li et al., 2017). Moreover, to increase the material conductivity, CMPs are usually carbonized under high temperature, which graphitizes the framework of carbon-based materials (Li et al., 2014; Wang L. et al., 2014). As an example, Cooper et al. improve the electrical conductivity and pseudocapacitive contributions of CMPs by combining molecular design and carbonization under an ammonia atmosphere, however the value only increased to about 260 F g^{-1} and the performance still restricts by the limited intrinsic conductivity of CMPs, which is also a common problem for other porous organic electrode materials (Lee et al., 2016).

Here, graphene aerogels (GA) are hybridized with CMPs, for the first time, to improve three-dimensional intrinsic conductivity of CMPs. After carbonization under ammonia atmosphere, the nitrogen content increases to 9.8%, while the ratio of pyridinic nitrogen increase from 15 to 25.5%. Owing to the improved electrical conductivity and higher nitrogen content, the resulting NH_3-treated GA/CMPs (N-GA /CMPs) has extraordinary specific capacitance up to 325 F g^{-1} at 0.5 A g^{-1} with excellent long-term cycling stability, showing its great potential in high performance supercapacitors.

MATERIALS AND METHODS

Preparation of CMP, GA/CMP, N-GA/CMP

CMPs were synthesized by the ionothermal method (Kuhn et al., 2008a). The proportional (1:20) monomer (m-phthalodinitrile) and $ZnCl_2$ were added to a Pyrex ampoule in an argon atmosphere, and then the ampoule was evacuated and sealed. With a 10°C min^{-1} heating rate, the ampoule was heated to 600°C for 40 h, and then was cooled down to room temperature. If the synthesis temperature was higher than 500°C, the ampule was under pressure and would be released during opening (Kuhn et al., 2008b). The product was subsequently grounded in an agate mortar to get powder, and washed by deionized water to remove $ZnCl_2$. After that, the sample was stirred in 5% HCl for 15 h to remove the residual $ZnCl_2$. After purification, the black powder was filtered and washed with deionized water and tetrahydrofuran. Finally, it was dried in vacuum at 150°C for 15 h. Graphene oxide was synthesized from natural graphite according to a modified Hummers method (Hummers Jr and Offeman, 1958). The prepared graphene oxide solution was purified by 5% HCl and deionized water for several times so that residual salts and acids can be washed completed. Graphene Aerogel was synthesized according to the literature (Xu et al., 2010). A 10 mL portion of 1.5 mg mL^{-1} homogeneous graphene oxide aqueous dispersion was sealed in a 20 mL Teflon-lined autoclave and maintained at 180°C for 12 h. The autoclave was naturally cooled to room temperature, and the as-prepared graphene aerogels were taken out and transferred to glass bottles. The graphene aerogels were obtained by putting the glass bottles into a freeze drying equipment for 24 h. The preparation of GA/CMPs followed the preparation of CMPs but different ratio of graphene aerogels, monomers and $ZnCl_2$ were grinded evenly in an agate mortar before adding to a Pyrex ampoule. The weight percentage of GA was 15%. To prepare N-GA/CMP, GA/CMPs (200 mg) was placed in a ceramic boat, which was located in the center of a tube furnace. The sample was exposed to a flow of N_2 for 30 min to remove the air from the tube, and then was treated by ammonia at 800°C for 2 h using nitrogen as the carrier gas. After ammonia treatment, the sample was cooled to room temperature and NH_3-treated GA/CMP was obtained.

Material Characterization

The samples were measured by scanning electron microscopy (SEM, Zeiss-Ultra 55), transmission electron microscopy (TEM, Tecnai G2F20S-Twin), X-ray diffraction (XRD, Rigaku D/Max 2400, CuKα radiation, 40 kV, 100 mA, λ = 1.5406 Å), and X-ray photoelectron spectroscopy (XPS, Axis Ultra Dld, Al Kα radiation, 15 kV, 30 mA). Elemental analyses were carried out using a vario EL cube analyzer. The pore structure was measured by N_2 sorption at 77 K, Brunauer–Emmett–Teller (BET) surface areas were calculated from the isotherm using the BET equation.

Fabrication of Electrodes and Supercapacitor

The active material (80 wt.%), carbon black (10 wt.%), and polytetrafluoroethylene (PTFE, 10 wt.% of a 60 wt.% dispersion in water) were dispersed in ethanol, and then thoroughly mixed in an agate mortar, adding ethanol several times. After that, the mixtures were rolled into a uniform thin film and dried at 80°C for 12 h in a vacuum oven, and then film was cut into 1 cm^2 electrode slice and coated on a slice of nickel foam current collector. Exerted 10 MPa pressure by a table press, the as-prepared electrodes were used as the working electrode. Pt foil and an Hg/HgO electrode were used as the counter electrode and reference electrode, respectively.

Electrochemical Measurement

Electrochemical measurement was performed by using an electrochemical station (CHI660E, CH Instruments, Shanghai) and a three-electrode system in 6 M KOH alkaline electrolyte. The specific capacitances of materials derived from galvanostatic discharge curves were calculated by Equation (1):

$$C_m = \frac{I_d \times \Delta t}{m \times \Delta V} \quad (1)$$

where Δt was the discharge time (s), I_d was the constant discharge current (mA), ΔV was the potential change (excluding ohmic drop IR), m was the mass of active materials in the working electrode when using three-electrode system. In two-electrode system, m was the mass of active material of whole device (mg).

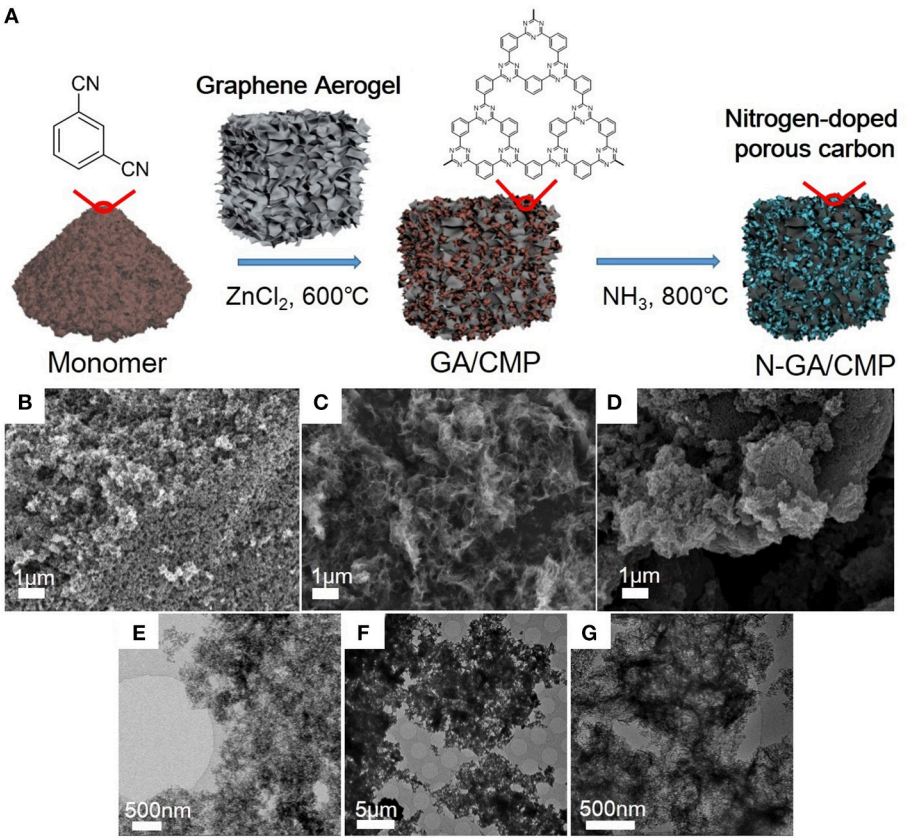

FIGURE 1 | (A) Illustration of synthesis of N-GA/CMPs. **(B–G)** FESEM and TEM images of the CMPs **(B,E)**, GA **(C,F),** and N-GA/CMPs **(D,G)**, respectively.

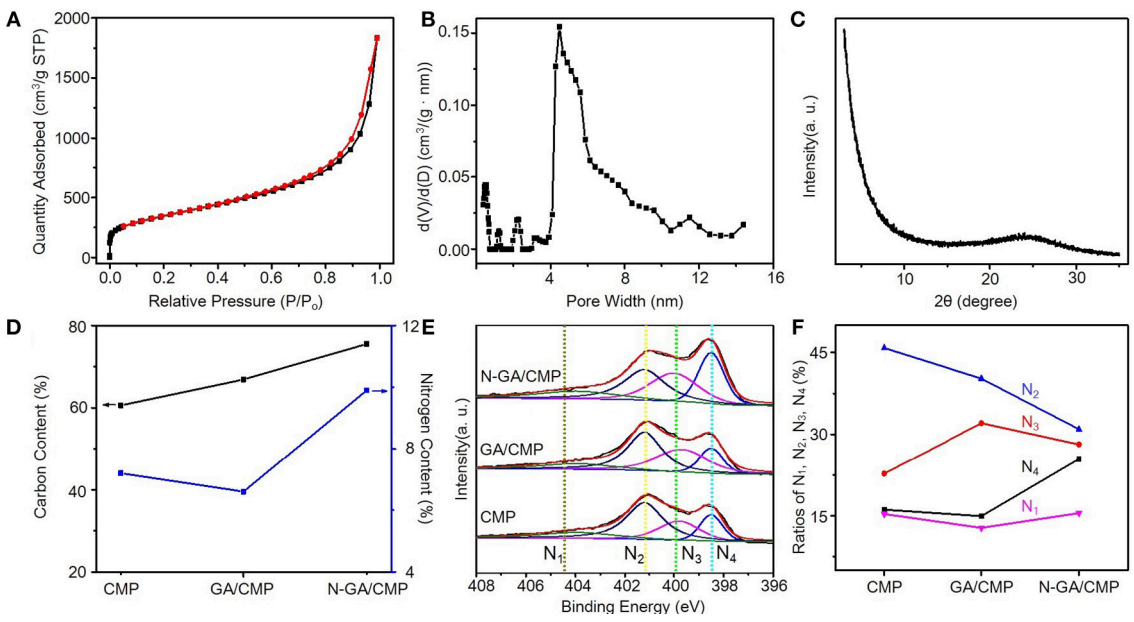

FIGURE 2 | (A) Nitrogen adsorption and desorption isotherms of CMPs (red) and N-GA/CMPs (blue). **(B)** Pore size distribution of CMPs and N-GA/CMPs. **(C)** XRD pattern of N-GA/CMPs. **(D)** EA of N-GA/CMPs for carbon (black) and nitrogen (blue). **(E)** XPS N 1s spectra of CMPs, GA/CMPs and N-GA/CMPs (N_1, oxide nitrogen; N_2, quaternary nitrogen; N_3, pyrrolic nitrogen; N_4, pyridinic nitrogen). **(F)** Ratios of different configurations of nitrogen in the materials.

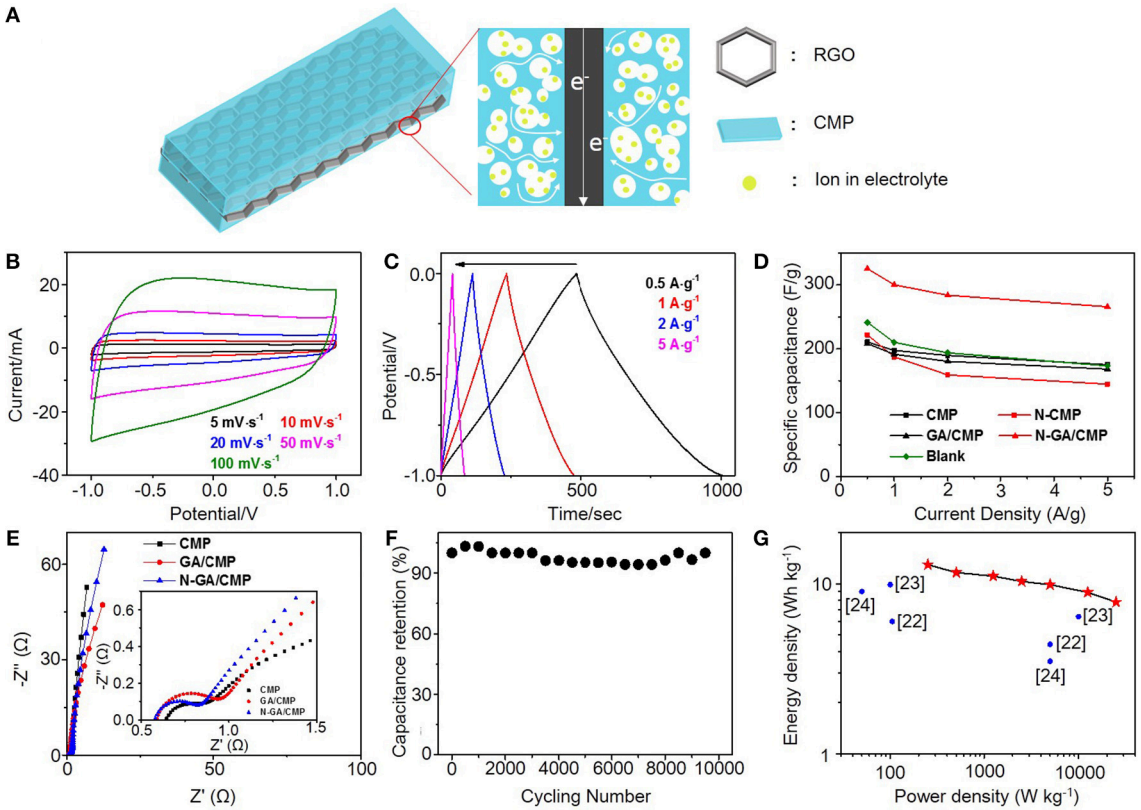

FIGURE 3 | (A) Illustration of the charge transfer in an N-GA/CMPs electrode. **(B)** CV curves and **(C)** GCD curves of the N-GA/CMPs. **(D)** Specific capacitances of CMPs, N-CMPs, GA/CMPs, N-GA/CMPs, GA and physical mixture of 85% CMP and 15% GA as blank. **(E)** Nyquist plots of the CMPs, GA/CMPs and N-GA/CMPs. The insert shows the plots in the high-frequency region. **(F)** Cycling performance of the N-GA/CMPs based supercapacitor. **(G)** Ragone plots of the N-GA/CMPs based two-electrode supercapacitor. The values reported by literatures are shown in the figure.

The energy density (E, W h kg^{-1}) and average power density (P, W kg^{-1}) of the whole two-electrode device were calculated separately by Equations (2, 3):

$$E = \frac{1}{2} \times \frac{C_m \times \Delta V^2}{m \times 3.6} \quad (2)$$

$$P = 3600 \times \frac{E}{\Delta t} \quad (3)$$

RESULTS AND DISCUSSION

After growth (**Figure 1A**), the morphologies of CMPs, GA, and N-GA/CMPs were studied by field emission SEM (FESEM, **Figures 1B–D**) and TEM (**Figures 1E–G**). The FESEM image shows that the CMPs have similar porous structures with the triazine-based CMPs reported in literature (Kuhn et al., 2008b). The TEM image of the N-GA/CMPs shows that the GA skeleton with layered structure is cross-linked and uniformly covered by porous CMPs. Nitrogen adsorption-desorption measurement (**Figures 2A,B**) has been performed to analyze the porous structure of the N-GA/CMPs. The isotherm of the N-GA/CMPs reveals a typical II type, which indicates the combination of micro-pores and meso-pores in the material. The surface area of N-GA/CMPs measured by BET is 1268.5 m^2 g^{-1}, and the powder XRD pattern shows that the N-GA/CMPs don't have any crystallization peaks, proving the amorphous nature (**Figure 2C**).

To further study the chemical structure and elemental composition, N-GA/CMPs were characterized by elemental analysis and XPS. The elemental analysis shows that the pristine GA/CMPs have a 6.3% nitrogen content (**Figure 2D**) (Hao et al., 2014). After carbonization at 800°C in ammonia, the nitrogen content of N-GA/CMPs increases to 9.8%. In order to analyze the nitrogen species in the material, we measured XPS spectra of CMPs, GA/CMPs and N-GA/CMP (**Figure 2E**). The XPS N 1s has four sub-peaks at 398.5, 399.8, 400.9, and 403.1 eV, which represent pyridinic nitrogen, pyrrolic nitrogen, quaternary nitrogen and oxidized nitrogen, respectively. Except quaternary nitrogen, other three types of nitrogen are located at the edges or defects of the CMPs or GA layers. All examples have low percentage of oxidized nitrogen, since the reactions were token place under an inert atmosphere. Notably, after treating at high temperature in ammonia atmosphere, no obvious changes happen on pyrrolic and oxidized nitrogen, while the ratio of quaternary nitrogen decreases and the ratio of pyridinic

nitrogen remarkably increases up to 25.5% (**Figure 2F**), which is of importance for achieving high supercapacitive performance.

To evaluate the supercapacitive performance, cyclic voltammetry (CV), galvanostatic charge–discharge (GCD) tests and electrochemical impedance spectroscopy (EIS) were carried out in a 6M KOH aqueous electrolyte in a conventional three-electrode system (**Figure 3A**). The CV curves for N-GA/CMPs at different scanning rates are shown in **Figure 3B**. All CV curves have quasi-rectangular shape without obvious reduction and oxidation peaks, indicating the N-GA/CMPs have good electroconductivity and stores energy mainly by double-layer energy storage mechanism despise higher content of pyridinic nitrogen. The GCD tests are performed at different current densities from 0.5 to 5 A g^{-1}. The GCD curves (**Figure 3C**) have a triangular shape, consistent with theoretical electrochemical double layer capacitors, and don't have obvious voltage drop, showing the good conductivity of materials. The N-GA/CMPs exhibit the highest specific capacitance of 325 F g^{-1} at the current density of 0.5 A g^{-1}. The calculated specific capacitance values of CMP, GA/CMP and N-GA/CMP (**Figure 3D**) show that the GA cannot greatly increase the specific capacitance, while the high-temperature annealing in ammonia atmosphere leads to a great enhancement. To understand the synergy effect of the GA and the CMPs in the hybrids, we physically mixed same content GA with CMPs and annealed at the same temperature in ammonia atmosphere (named as blank group). The specific capacitance of the physical mixture is nearly same with the CMPs (**Figure 3D**), implying that the increase of specific capacitance mainly results from the chemical combination of porous structure of CMPs and in-plane conductive structure of GA (**Figure 3A**). The CMPs cover on both sides of GA. The interconnected micro-pores and meso-pores of CMPs shorten the diffusion length between external electrolyte and the surface of electrode materials. At the same time, the GA acts as a conductive framework to increase the conductivity of the electrodes.

The Nuquist plot (**Figure 3E**) measured by EIS reveals the device resistance including the electrolyte resistance, the ionic resistance of ions moving through the separator, the intrinsic resistance of the active electrode, and the contact resistance at the interface between the active materials with the current collector. In the high-frequency region, the equivalent series resistance (ESR) of the N-GA/CMPs (0.58 Ω) is smaller than that of CMPs (0.65 Ω) after N-doping, which indicates lower charge transfer resistance at the electrode/electrolyte interface. The smaller radius of semicircular and the more vertical line in the low-frequency region indicate faster ion diffusion in the electrode of the N-GA/CMPs. This phenomenon is attributed to higher ratio of nitrogen in the N-GA/CMPs (Xiang et al., 2015), in agreement with the EA.

In order to test the stability in the application, the N-GA/CMPs were used in a conventional two-electrode system for cycling experiments. The capacitance (**Figure 3F**) remains above 95% after 10,000 charge-discharge cycles at a current density of 5 A g^{-1}. Therefore, the N-GA/CMPs produced by ionothermal synthesis possess not only high supercapacitive performance but also excellent cycling life. The energy density of the N-GA/CMPs supercapacitors (**Figure 3G**) is up to 12.95 Wh kg^{-1}, which is among the highest reported value of the CMP-based supercapacitors (Xu et al., 2017; Yuan et al., 2017; Zhao et al., 2017).

CONCLUSIONS

In summary, GA templated triazine-based CMPs are synthesized by ionothermal method followed by high temperature treatment in ammonia atmosphere. By using GA as the template, the inherent conductivity of triazine-based CMPs is improved. High temperature process in ammonia atmosphere results in higher pyridinic nitrogen content in the GA/CMPs, which introduces more edge sites and defects in the material. As a result, the specific capacitance of N-GA/CMPs electrode increases by 55% up to 325 F g^{-1}, and the energy density reaches 12.95 Wh kg^{-1}. Moreover, there is no significant degradation after 10,000 cycles at a current density of 5A g^{-1}. Considering the easy preparation and outstanding energy storage performance, the N-GA/CMPs show great potential for practical application in high-performance aqueous supercapacitors.

AUTHOR CONTRIBUTIONS

DW designed research. DW, YZ, and YL supervised the project. LP, QG, and ZA performed the experiments. DW and LP wrote the manuscript. All authors commented on the manuscript.

FUNDING

This work was supported by the National Natural Science Foundation of China (51773041, 21603038, 61890940, 21544001), Strategic Priority Research Program of the Chinese Academy of Sciences (XDB30000000), Shanghai Committee of Science and Technology in China (Grant No. 18ZR1404900) and Fudan University.

REFERENCES

Hao, L., Ning, J., Luo, B., Wang, B., Zhang, Y., Tang, Z., et al. (2014). Structural evolution of 2D microporous covalent triazine-based framework toward the study of high-performance supercapacitors. *J. Am. Chem. Soc.* 137, 219–225. doi: 10.1021/ja508693y

Hummers Jr, W. S., and Offeman, R. E. (1958). Preparation of graphitic oxide. *J. Am. Chem. Soc.* 80, 1339–1339. doi: 10.1021/ja01539a017

Kuhn, P., Antonietti, M., and Thomas, A. (2008a). Porous, covalent triazine-based frameworks prepared by ionothermal synthesis. *Angew. Chem. Int. Edn.* 47, 3450–3453. doi: 10.1002/anie.200705710

Kuhn, P., Thomas, A., and Antonietti, M. (2008b). Toward tailorable porous organic polymer networks: a high-temperature dynamic polymerization scheme based on aromatic nitriles. *Macromolecules* 42, 319–326. doi: 10.1021/ma802322j

Lee, J. S. M., Wu, T. H., Alston, B. M., Briggs, M. E., Hasell, T., Hu, C. C., et al. (2016). Porosity-engineered carbons for supercapacitive energy storage using conjugated microporous polymer precursors. *J. Mater. Chem. A*, 4, 7665–7673. doi: 10.1039/C6TA02319C

Li, X. C., Zhang, Y., Wang, C. Y., Wan, Y., Lai, W. Y., Pang, H., et al. (2017). Redox-active triazatruxene-based conjugated microporous polymers for high-performance supercapacitors. *Chem. Sci.* 8, 2959–2965. doi: 10.1039/C6SC05532J

Li, Y., Zhu, H., Shen, F., Wan, J., Han, X., Dai, J., et al. (2014). Highly conductive microfiber of graphene oxide templated carbonization of nanofibrillated cellulose. *Adv. Funct. Mater.* 24, 7366–7372. doi: 10.1002/adfm.201402129

Pang, H., Zhang, Y. Z., Run, Z., Lai, W. Y., and Huang, W. (2015). Amorphous nickel pyrophosphate microstructures for high-performance flexible solid-state electro-chemical energy storage devices. *Nano Energy* 17, 339–347. doi: 10.1016/j.nanoen.2015.07.030

Peng, Y. J., Wu, T. H., Hsu, C. T., Li, S. M., Chen, M. G., and Hu, C. C. (2014). Electrochemical characteristics of the reduced graphene oxide/carbon nanotube/polypyrrole composites for aqueous asymmetric supercapacitors. *J. Power Sourc.* 272, 970–978. doi: 10.1016/j.jpowsour.2014.09.022

Reich, T. E., Behera, S., Jackson, K. T., Jena, P., and El-Kaderi, H. M. (2012). Highly selective CO_2/CH_4 gas uptake by a halogen-decorated borazine-linked polymer. *J. Mater. Chem.* 22, 13524–13528. doi: 10.1039/C2JM31123B

Salunkhe, R. R., Kamachi, Y., Torad, N. L., Hwang, S. M., Sun, Z., Dou, S. X., et al. (2014). Fabrication of symmetric supercapacitors based on MOF-derived nanoporous carbons. *J. Mater. Chem. A*. 2, 19848–19854. doi: 10.1039/C4TA04277H

Wang, G., Zhang, L., and Zhang, J. (2012). A review of electrode materials for electrochemical supercapacitors. *Chem. Soc. Rev.* 41, 797–828. doi: 10.1039/C1CS15060J

Wang, L., Schütz, C., Salazar-Alvarez, G., and Titirici, M. M. (2014). Carbon aerogels from bacterial nanocellulose as anodes for lithium ion batteries. *Rsc Adv.* 4, 17549–17554. doi: 10.1039/C3RA47853J

Wang, Q., Yan, J., Wang, Y., Wei, T., Zhang, M., Jing, X., et al. (2014). Three-dimensional flower-like and hierarchical porous carbon materials as high-rate performance electrodes for supercapacitors. *Carbon* 67, 119–127. doi: 10.1016/j.carbon.2013.09.070

Xiang, Z., Wang, D., Xue, Y., Dai, L., Chen, J. F., and Cao, D. (2015). PAF-derived nitrogen-doped 3D carbon materials for efficient energy conversion and storage. *Sci. Rep.* 5:8307. doi: 10.1038/srep08307

Xie, J., and Zhang, Q. (2016). Recent progress in rechargeable lithium batteries with organic materials as promising electrodes. *J. Mater. Chem. A*. 4, 7091–7106. doi: 10.1039/C6TA01069E

Xu, Y., Jin, S., Xu, H., Nagai, A., and Jiang, D. (2013). Conjugated microporous polymers: design, synthesis and application. *Chem. Soc. Rev.* 42, 8012–8031. doi: 10.1039/C3CS60160A

Xu, Y., Sheng, K., Li, C., and Shi, G. (2010). Self-assembled graphene hydrogel via a one-step hydrothermal process. *ACS Nano* 4, 4324–4330. doi: 10.1021/nn101187z

Xu, Y., Wu, S., Ren, S., Ji, J., Yue, Y., and Shen, J. (2017). Nitrogen-doped porous carbon materials generated via conjugated microporous polymer precursors for CO 2 capture and energy storage. *RSC Adv.* 7, 32496–32501. doi: 10.1039/C7RA05551J

Yuan, K., Zhuang, X., Hu, T., Shi, L., Sfaelou, S., Polnick, U., et al. (2017). 2D Heterostructures derived from MoS2-Templated, cobalt-containing conjugated microporous polymer sandwiches for the oxygen reduction reaction and electrochemical energy storage. *Chem. Electro. Chem*. 4, 709–715. doi: 10.1002/celc.201600850

Yuan, S., Dorney, B., White, D., Kirklin, S., Zapol, P., Yu, L., et al. (2010). Microporous polyphenylenes with tunable pore size for hydrogen storage. *Chem. Commun.* 46, 4547–4549. doi: 10.1039/C0CC00235F

Zhang, L. L., and Zhao, X. S. (2009). Carbon-based materials as supercapacitor electrodes. *Chem. Soc. Rev.* 38, 2520–2531. doi: 10.1039/B813846J

Zhang, Y. Z., Cheng, T., Wang, Y., Lai, W. Y., Pang, H., and Huang, W. (2016). A simple approach to boost capacitance: flexible supercapacitors based on manganese oxides@MOFs via chemically induced *in situ* self-transformation. *Adv. Mater.* 28, 5242–5248. doi: 10.1002/adma.201600319

Zhang, Y. Z., Wang, Y., Cheng, T., Lai, W. Y., Pang, H., and Huang, W. (2015). Flexible supercapacitors based on paper substrates: a new paradigm for low-cost energy storage. *Chem. Soc. Rev.* 44, 5181–5199. doi: 10.1039/C5CS00174A

Zhao, Y., Xie, F., Zhang, C., Kong, R., Feng, S., and Jiang, J. X. (2017). Porous carbons derived from pyrene-based conjugated microporous polymer for supercapacitors. *Micropor. Mesopor. Mater.* 240, 73–79. doi: 10.1016/j.micromeso.2016.10.048

Conflict of Interest Statement: The authors declare that the research was conducted in the absence of any commercial or financial relationships that could be construed as a potential conflict of interest.

frontiers in Chemistry

REVIEW
published: 01 May 2019
doi: 10.3389/fchem.2019.00292

Phytotoxicity of Graphene Family Nanomaterials and Its Mechanisms: A Review

*Qinghai Wang[1], Cui Li[1], Yu Wang[2] and Xiaoe Que[3]**

[1] Beijing Research and Development Center for Grass and Environment, Beijing Academy of Agriculture and Forestry Sciences, Beijing, China, [2] State Key Laboratory of Multiphase Complex Systems, Institute of Process Engineering, Chinese Academy of Sciences, Beijing, China, [3] Institute of Desertification Studies, Chinese Academy of Forestry, Beijing, China

Graphene family nanomaterials (GFNs) have experienced significant development in recent years and have been used in many fields. Despite the benefits, they bring to society and the economy, their potential for posing environmental and health risks should also be considered. The increasing release of GFNs into the ecosystem is one of the key environmental problems that humanity is facing. Although most of these nanoparticles are present at low concentrations, many of them raise considerable toxicological concerns, particularly regarding their accumulation in plants and the consequent toxicity introduced at the bottom of the food chain. Here, we review the recent progress in the study of toxicity caused by GFNs to plants, as well as its influencing factors. The phytotoxicity of GFNs is mainly manifested as a delay in seed germination and a severe loss of morphology of the plant seedling. The potential mechanisms of phytotoxicity were summarized. Key mechanisms include physical effects (shading effect, mechanical injury, and physical blockage) and physiological and biochemical effects (enhancement of reactive oxygen species (ROS), generation and inhibition of antioxidant enzyme activities, metabolic disturbances, and inhibition of photosynthesis by reducing the biosynthesis of chlorophyll). In the future, it is necessary to establish a widely accepted phytotoxicity evaluation system for safe manufacture and use of GFNs.

Keywords: nanomaterials, plant, phytotoxicity, influencing factor, toxicity mechanisms

OPEN ACCESS

Edited by:
Bin Wu,
Institute of Chemistry (CAS), China

Reviewed by:
Mingzhi Huang,
South China Normal University, China
Zhengyi Hu,
University of Chinese Academy of Sciences (UCAS), China

****Correspondence:***
Xiaoe Que
xiaoeque@sina.com

Specialty section:
This article was submitted to Supramolecular Chemistry, a section of the journal Frontiers in Chemistry

Received: *26 February 2019*
Accepted: *10 April 2019*
Published: *01 May 2019*

Citation:
Wang Q, Li C, Wang Y and Que X (2019) Phytotoxicity of Graphene Family Nanomaterials and Its Mechanisms: A Review. Front. Chem. 7:292. doi: 10.3389/fchem.2019.00292

INTRODUCTION

Graphene family nanomaterials (GFNs), a typical representative of two-dimensional carbon nanomaterials (CNMs), have been widely used in various fields, including energy storage, nanoelectronic devices and batteries, biomedical applications, biosensors, cell imaging, drug delivery, and tissue engineering (Ou et al., 2016). GFNs include few-layer-graphene (FLG), ultrathin graphite, graphene oxide (GO), reduced graphene oxide (rGO), and graphene nanosheets (GNS) (Sanchez et al., 2012). Furthermore, GFNs can serve as an important building platform for constructing various supramolecular products that have several advantageous applications (Dreyer et al., 2010; Zhou et al., 2013). However, these carbon nanomaterials will inevitably be released into the environment during their production, transport, consumption, and disposal. Their environmental use for wastewater and drinking water treatment will likely lead to considerable release of the aforementioned materials (Zhao et al., 2014). There has been considerable research regarding the phytotoxicity of GFNs, but far less research on the realistic release amount and

concentration in the environmental media (air, water, and soil). Yan et al. (2019) reported that the maximum release amount of graphene was 1.6 mg/kg from graphene-polyethylene composite films applied in food packaging, confirming the release of GFNs. Miralles et al. (2012) summarized the release pathways of engineered nanomaterials into the natural environment as follows: their use in environment remediation, as delivery systems in agriculture, as biosensors, and as release from medical and cosmetic applications; as well as accidental release (e.g., atmospheric emissions, leaching from sewage sludge, etc.). This information is helpful in understanding the release pathways of GFNs. Early in 2005, researchers conducted an evaluation of nanomaterials regarding human health risks (Thomas and Sayre, 2005). Hereafter, considering its persistent and hydrophobic properties, and dramatically increasing production, (Arvidsson et al., 2013) proposed that the fate of graphene in the environment and its toxicity should be further studied. Many researchers have so far expressed concern about the potential human health and ecological risks resulting from the manufacture and use of GFNs (Gilbert, 2009; Suárez-Iglesias et al., 2017; Chen et al., 2018b; Naasz et al., 2018). Currently, most research is focused on the effects of GFMs on humans, small mammals, invertebrates, and aquatic organisms, and little research has investigated their effects on plants (Lee et al., 2016). As primary producers, plants play a major role in the ecosystem. They not only interact directly with the soil, water, and atmospheric compartments of the environment (Miralles et al., 2012), but also provide food for people and other animals. It is also the starting point for the bioaccumulation of toxic substances. Therefore, it is likely that nanoparticles are gradually enriched to higher levels of the food chain, leading to toxic effects in organisms further up the chain (Yang and Zhao, 2013). Understanding the hazards of nanomaterials (e.g., toxicity, mutagenicity, impacts on ecosystem services), and the underlying toxicity mechanisms, is a basis for the more focused study of the processes required to control their exposure (Wiesner et al., 2009). Therefore, we should pay more attention to the phytotoxicity of GFNs and its influencing factors, as well as its potential toxicity mechanisms. The purpose of this article is to critically review the existing literature on the phytotoxicity, toxic influencing factors, and toxicological mechanisms of GFNs. Some reviews have been written on the toxic effects of GFNs in several organs and cell models (Ou et al., 2016). In addition, toxicity, uptake, and translocation of engineered nanomaterials in vascular plants (Miralles et al., 2012). We believe that a comprehensive review is necessary to recognize emerging trends and to discuss existing knowledge gaps on the toxicity of GFNs to plants, especially crop plants.

PHYTOTOXICITY OF GFNS

Due to possible direct human exposure through the food chain, crop plants have been chosen as test subjects in most research on phytotoxicity of GFNs. The following review is mainly focused on the findings obtained regarding crop plants. The toxicity of GFNs to plants is summarized in **Figure 1**.

GFNs Fate in Plants

Graphene can be transferred from wheat roots to shoots and enter the cytoplasm and chloroplasts (Hu et al., 2014c); however, GO accumulation was not observed in the root cells of wheat (Chen et al., 2018a). Furthermore, GO did not accumulate in the seedlings of spinach and chive from if their seeds were treated with 50 mg/L GO (He et al., 2018). In another study, Zhao et al. (2015) found that GO in the range of μg/L accumulated in root hair and root parenchyma cells; however, it did not translocate into the stem or leaves of *Arabidopsis thaliana*. This finding was supported by Chen et al. (2017); GO was readily absorbed by the plant roots, but the absorbed GO showed limited upward translocation. Different quantitative and distributional trends between the two graphene materials in pea plants were observed by Chen et al. (2019). Their study showed that rGO was translocated into leaves after being absorbed by the roots. The uptake amount in the root tended to stabilize at 15-day exposure, and the cumulative amount in the leaves was higher than that in the roots at 20-day exposure, reaching accumulation amounts up to mg level. Conversely, GO mainly accumulated in the roots and low levels in leaves. Besides root accumulation and translocation from root to shoot, Huang et al. (2018) further discovered that ∼9% of the accumulated FLG was degraded to CO_2 in the rice plant, and that the hydroxyl radical in the leaf played an important role in degrading FLG. Earlier studies have demonstrated that CO_2 was the final product of the complete enzymatic catalyzed oxidation of GO (Kotchey et al., 2011), and H_2O_2 was a key component of this degradation process (Xing et al., 2014). In plants, H_2O_2 plays an important role in regulating biotic and abiotic stress responses (Sun et al., 2018). Thus, given the widespread presence of H_2O_2 in plants, they can potentially eliminate accumulated GFNs and could be used as phytoremediation agents for environmental clean-up.

Toxic Effects on Plant Germination

Generally, GFNs produce a delaying effect in plant germination. For example, in rice seeds treated with 50 mg/L of graphene, germination started 3 days after the control group (Nair et al., 2012). A later study confirmed that the increase in graphene stress (≤200 mg/L) induced a delay in the initiation of the germination process in rice, but had no negative effects on the final germination percentage (Liu et al., 2015). A similar delay occurred in the appearance of the cotyledons and the root system of tomato, cabbage, and red spinach seeds treated with graphene (Begurn et al., 2011). However, tomato seeds exposed to graphene at concentrations as low as 40 mg/L obtained rapid seed germination and higher germination rates, which was attributed to the penetration of the seed coat by the graphene, thus facilitating water uptake (Zhang et al., 2015b). GO also significantly stimulated plant germination at 50 mg/L because its hydrophobic sp^2 domains transported more water to the seed in the soil (He et al., 2018). GO at concentrations in the order of μg/L (10–1000 μg/L) had no obvious influence on the germination of *Arabidopsis* seeds (Zhao et al., 2015). When GO concentration was up to 100 mg/L, the rice germination percentage insignificantly decreased; the effect became significant at 500 mg/L GO

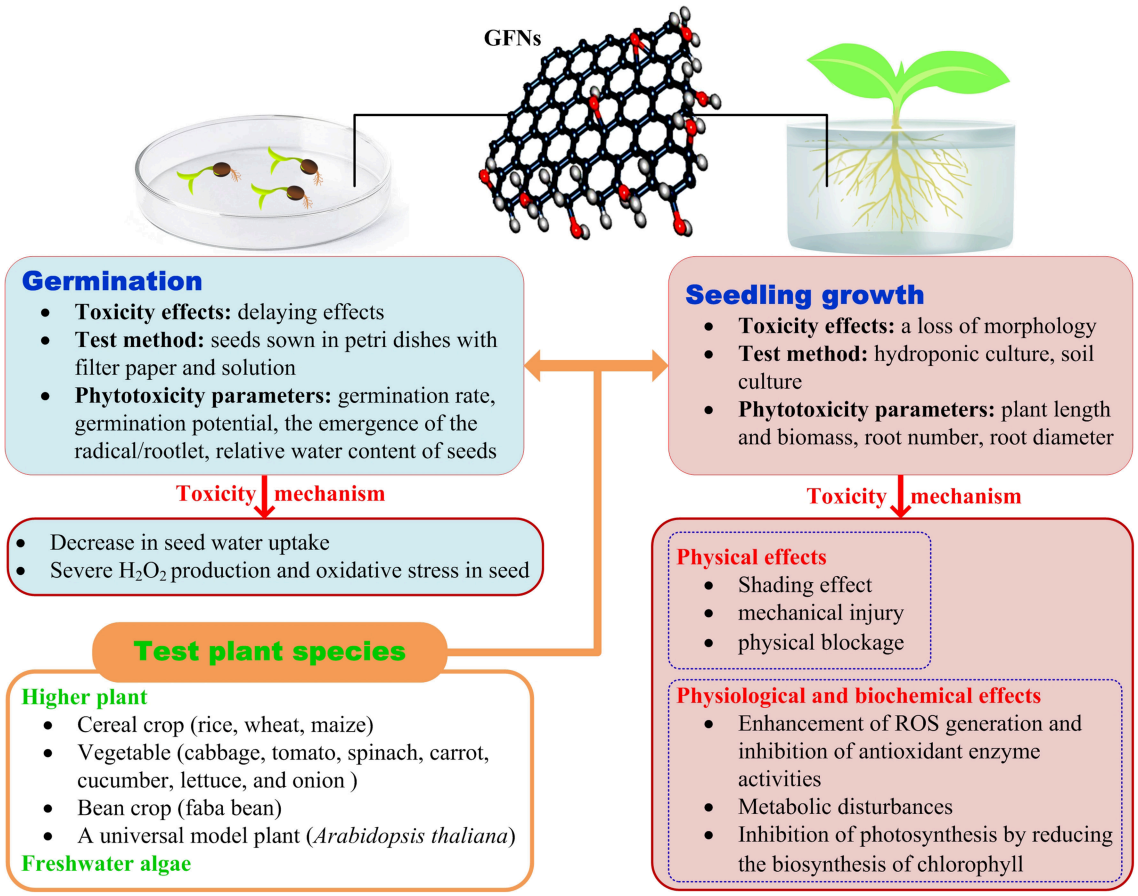

FIGURE 1 | Schematic diagram of the phytotoxicity and possible mechanisms of GFNs.

(Liu et al., 2015). Similar to rice, the germination of wheat seeds was inhibited owing to GO concentrations exceeding 400 mg/L (Chen et al., 2017).

Toxic Effects on Plant Growth

The common toxicity symptoms observed in plants exposed to GFNs are a severe loss of morphology and decreases in growth parameters, such as root and shoot length, root number, root diameter, and biomass production (**Table 1**). For instance, the morphology of rice seedlings was significantly inhibited if graphene concentration reached 100 mg/L (Liu et al., 2015). GO also adversely affected biomass accumulation and stem elongation in wheat seedlings (Chen et al., 2017). After exposure to 50 and 500 mg/kg rGO, negative effects on the shoot height and root length of rice seedlings were observed by Hao et al. (2018); in addition, the root diameter and the number of cells in the transverse section significantly decreased. However, GO in the range of μg/L did not cause significant changes in shoot and root development of *Arabidopsis* seedlings, or flowering time (Zhao et al., 2015). These apparently contrasting results suggest that the toxic effects of GFNs are associated with exposure concentrations.

FACTOR

The potential effects of GFNs depend on many factors, such as their physicochemical, the exposure concentration and time, and the plant species, which deserve further attention.

Physicochemical Properties of GFNs

The biological impacts of nanomaterials are dependent on their size, chemical composition, surface structure, solubility, shape, and aggregation. Of these properties, size and surface area are important characteristics from a toxicological perspective; a small size and a large surface area increase the uptake and interaction with biological tissues, thus increasing the probability of generating adverse biological effects in living cells (Nel et al., 2006).

Because the large size of GO sheets hinders its translocation from the roots to the stem and leaves, GO bioaccumulation was much lower than that of fullerenol in wheat roots (Chen et al., 2017). Using freshwater algae as a test plant, Zhao et al. (2017) investigated the toxicity of GFNs based on their different physicochemical properties and colloidal behaviors. They found that GO with abundant functional groups could adsorb more macronutrients (N, P, Mg, and Ca) from the culture

TABLE 1 | Toxic effects on the germination and growth of crop plants.

Plant species	GFNs	Exposure concentration	Exposure time	Toxic symptoms of growth	References
Rice (*Oryza sativa*)	Graphene	100 and 200 mg/L	16 days	Inhibition of root and stem length, adventitious root number, and root and stem fresh weight	Liu et al., 2015
	rGO	50, 500 mg/kg	30 days	Reduced shoot height and root length, decreased root diameter and number of cells in transverse section	Hao et al., 2018
wheat (*Triticum aestivum*)	GO	>1000 μg/mL	9 days	Decrease in root length, shoot length and relative biomass; obvious damage to plant tissue structures	Chen et al., 2018a
	Graphene	250, 500, 1000, and 1500 mg/L	30 days	Root hair reduction, oxidative burst, photosynthesis inhibition, and nutritional disorder	Zhang et al., 2016
		200 mg/L	5 days	Inhibition in the number of wheat roots	Hu et al., 2014c
Maize (*Zea mays*)	GO	100, 500, 1500 mg/L	15 days	Significant decrease of shoot and root weight	Yin et al., 2018
Brassica napus	GO	25–100 mg/L	15 days	Shorter seminal root length	Cheng et al., 2016
		50-100 mg/L		Decrease in fresh root weight	
Cabbage (*Brassica oleracea*), tomato (*Lycopersicon esculentum*), red spinach (*Amaranthus tricolor* and *A. lividus*)	Graphene	500–2000 mg/L	20 days	Significant inhibition of plant growth and biomass. Decrease in the number and size of leaves	Begurn et al., 2011

medium than rGO, thus leading to stronger nutrient depletion-induced indirect toxicity; rGO could directly penetrate into algal cells, but GO, with more flexible sheets, could not. In addition, GO had a significant shading effect on algal growth due to its good dispersibility and transformation. Compared to graphene and GO, hydrated graphene ribbon (HGR) not only promoted the germination rate of aged seed, but also increased root differentiation; the disordered layer structures of HGR played a key role in this process (Hu and Zhou, 2014). The observations of Chen et al. (2018a) showed that GO induced obvious toxic symptoms in wheat, while amine-functionalized GO was non-toxic and enhanced plant growth. They inferred that the introduction of amines could decrease the surface electrical resistivity of GO, creating higher electronic conductivity, and activating bioactivity in plant cells.

Exposure Concentration and Time

The general effect of GFNs on plant growth is dose-dependent. Graphene at 5 mg/L promoted the number of adventitious roots, and increased the root and shoot fresh weight of rice seedlings; however, at a concentration of 50 mg/L, it significantly inhibited the stem length and fresh shoot weight (Liu et al., 2015). Graphene at 500 mg/L resulted in only a slight decrease in root and shoot length of tomato, cabbage, and red spinach, whereas a marked inhibition was induced by graphene at concentrations up to 2,000 mg/L (Begurn et al., 2011). After a 10-day exposure to GO, the lower concentrations (5 and 10 mg/L) had no significant effect on root length and fresh weight, but the higher concentrations (50 and 100 mg/l) showed inhibited root growth (Cheng et al., 2016). However, this effect is not completely concentration-dependent. Anjum et al. (2014) found that GO at 1600, 200, and 100 mg/L significantly inhibited the germination rate and root length of the faba bean (*Vicia faba*), while the health status of the plant was improved with exposure to GO at 400 and 800 mg/L. Their previous study assessed the tolerance of faba bean to GO, in which the plant showed a significantly higher sensitivity to GO at 1,600, 200, and 100 mg/L, and its tolerance increased when exposed to 400 and 800 mg/L concentrations (Anjum et al., 2013). Their further investigations indicated that the sensitivity and/or tolerance of the plant to GO depended on the cellular GSH redox system. Additionally, the concentration-dependent toxicity of GFNs is also related to exposure time. Zhang et al. (2016) found that long-term graphene exposure (30 d) caused wheat leaf deformities and yellowing, whereas no distinct alterations in leaf elongation were found after short-term exposures (24 or 48 h). This exposure time-dependent toxicity was also observed by Zhao et al. (2017). In their investigation, the growth inhibition of GFNs to freshwater algae highly increased with increasing exposure times (24–96 h).

Plant Species

Heretofore, only a few studies have been designed to compare the toxicity of GFNs to different plants. The hydroponics experiments conducted by Begurn et al. (2011) indicated that graphene had little or no significant toxic effect on lettuce seedlings, but significantly inhibited the growth and biomass of tomato, cabbage, and red spinach seedlings under the same conditions. Among these selected vegetable species, tomato seedlings exhibited the highest sensitivity to graphene, according to the root and shoot weight data.

Interaction With Co-existing Pollutants

Compared with studies on the ecotoxicity of single nanomaterials, relatively little research has focused on the interaction of nanoparticles and other contaminants (Zhang et al., 2018). In general, GFNs coexist with other pollutants in the natural environment. Heavy metals and organic pollutants (OPs) are common in the water and soil environment. The interactive toxic effects are different when GFNs are combined with these pollutants; these are termed additive or antagonistic effects. The research of Hu et al. (2014a) found that GO amplified the phytotoxicity of As in wheat. It further revealed the main mechanisms of indirect toxicity of GO: (a) enhancing the uptake of GO and As by damaging cellular structures and electrolyte leakage, and (b) promoting the transformation of As^{5+} to high-toxicity As^{3+}. Conversely, another investigation found that GO alleviated the inhibitive effects of Cd^{2+} on the seminal root and bud growth of rice, which possibly resulted from Cd^{2+} adsorption in available contact sites or accumulation in the interlayer space of GO (Yin et al., 2018). Early researchers had already noticed the strong attractive forces between Cd^{2+} and GO, and had used GO as a sorbent for heavy metal removal from waste water (Tan et al., 2015). Lingamdinne et al. (2016) found that the adsorption occurred through physical and chemical interactions between heavy metal ions and oxygen-containing surface functional groups, and the π-π bond electrons of GO. Moreover, functionalized GO exhibited significantly higher adsorption capacity (Pirveysian and Ghiaci, 2018). However, once desorption occurs, high adsorption capacity implies the potential release, thus presenting a high risk to public health and the environment (Yang and Xing, 2007). GFNs have also been widely used to remove OPs from the environment (Chowdhury and Balasubramanian, 2014; Amaranatha et al., 2015; Zhang et al., 2015a). Although no direct data currently suggest that interaction of GFNs and OPs enhances phytotoxicity of either, it has been confirmed that GO can serve as an insecticide carrier to enhance contact toxicities (Wang et al., 2019). This synergistic mode of adsorption-delivery-release is most likely equally effective for plants. Moreover, previous research demonstrated that C_{60} fullerenes significantly increase the bioaccumulation of DDE (dichlorodiphenyldichloroethylene, DDT metabolite) into three selected food crops (De La Torre-Roche et al., 2012). These findings indicate that the carbon nanomaterials can affect the accumulation and bioavailability of co-existing pollutants, and thereby be regarded as a toxic alert to plants.

TOXICITY MECHANISM OF GFNS

The toxicity mechanism of GFNs to plants is summarized in **Figure 1**.

Physical Effects

The main physical mechanisms for the phytotoxicity of GFNs include the shading effect, mechanical injury, and physical blockage. Both shading effect and mechanical injury were observed by Zhao et al. (2017). They found that the dispersed and darkened GO reduced light transmittance, thus decreasing the available light required to support plant growth, resulting in approximately 16% of growth inhibition; and more interestingly, direct penetration into algal cells by graphene materials was discovered for the first time. The physical blockage is closely related to the size of GFNs. If nanoparticle diameter is larger than the diameter of root cell wall pores, particles will accumulate at the root surfaces and form surface layers, thus decreasing the hydraulic conductivity and uptake of nutrients (Asli and Neumann, 2009).

Physiological and Biochemical Effects

GFNs enhance the generation of reactive oxygen species (ROS) and inhibit antioxidant enzyme activities, resulting in oxidative stress, which has been recognized as one of the most important mechanisms in growth-limiting effects on plants (Hu et al., 2014b; Zhang et al., 2016; Chen et al., 2017). GO also caused metabolic disturbances linked to key biological processes, such as inhibiting carbohydrate and amino acid metabolisms, and increasing the ratios of unsaturated to saturated fatty acids, changing the flux of nitrogen metabolism (Hu et al., 2014b).

It is well-known that photosynthesis is critical for plant survival and growth. Graphene significantly inhibited the biosynthesis of chlorophyll and decreased chlorophyll content in plants, leading to impaired photosynthesis and reduced growth (Hu et al., 2014c; Zhang et al., 2016). Hu et al. (2014c) also found that glyconic acid and aconitic acid were upregulated by graphene, and these metabolites were negatively correlated with the biosynthesis of chlorophyll.

PROBLEMS AND PROSPECTS

Plant bioassay, the physicochemical properties of GFNs, and toxicity endpoints, are key factors in toxicity evaluation. At present, most research has focused on crop species (Miralles et al., 2012), and competitive toxicity assays between GFNs has only been conducted for lower plant forms. More risk assessments in a large range of plants must be systematically investigated. In order to develop GFNs for further use in various fields, many efforts have already been initiated on functionalization of GFNs by supramolecular approaches (Chen et al., 2015; Gobbi et al., 2017); such modifications create multiple and complex properties in GFNs (Xu et al., 2018). However, little is known about the relevance of phytotoxicity with the properties of GFNs, and a fundamental understanding of this relationship is essential to their applications. Additionally, functionalized, and non-functionalized nanomaterials exhibited significantly different toxicity to several crop species, thereby requiring future study to evaluate the potential toxicity of both forms Cañas et al. (2008). Currently, indicators of plant germination, growth, and physiology have been often used to evaluate the toxicity of GFNs in most existing studies. These visually identifiable and practical indicators are easy to obtain, but might not fully reflect the toxic effects and mechanisms of GFNs; in addition, they have a different sensitivity to GFNs. For instance, the number of roots was more sensitive to graphene than seed germination or fresh weight (Hu et al., 2014c). Therefore, endpoint selection in toxicity tests is very important, and studies at the molecular

level are needed to develop a deep understanding of the toxicity mechanisms of GFNs in plants.

Compared to assessing their toxicity, the uptake, transport, distribution, and degradation of GFNs within plants remains poorly understood (Huang et al., 2018). Their transformation pathways and fate in water/soil-plant systems requires additional research, which will contribute to prevention of environmental risks. It is possible that the phytotoxicity of GFNs could lead to crop yield reduction. However, the current research is mainly focused on responses of crop plants to GFNs at the seedling stage, there is no direct data to support this. Therefore, relevant researches should cover the whole of the growth period of each tested crop.

Taken together, although a large number of phytotoxicity assays for GFNs have been carried out, there is a big difference in terms of the selected plant species, the growth stages of the plants, the plant material culture methods (soil culture or hydroponics), and the exposure time between these toxicity tests; this leads to a lack of comparability of the assessment results. Moreover, the systematical assessment of GFNs phytotoxicity is hampered by this limited comparability. Therefore, it is necessary to establish a phytotoxicity evaluation system for GFNs, like the U.S. EPA or OECD guidelines for chemical testing.

Once GFNs are in use, release into the environment should be avoided to the largest extent possible by a rational scientific approach. For this purpose, the cooperation of chemists and biologists is crucial to implementing the proper preventive management strategies for safe manufacture and use.

AUTHOR CONTRIBUTIONS

All authors listed have made a substantial, direct and intellectual contribution to the work, and approved it for publication.

ACKNOWLEDGMENTS

This work was supported by Beijing Natural Science Foundation (5192004), and the National Natural Science Foundation of China (21473209 and 31370540).

REFERENCES

Amaranatha, R. D., Ma, R., Choi, M. Y., and Kim, T. K. (2015). Reduced graphene oxide wrapped ZnS-Ag_2S ternary composites synthesized via hydrothermal method: applications in photocatalyst degradation of organic pollutants. *Appl. Surf. Sci.* 324, 725–735. doi: 10.1016/j.apsusc.2014.11.026

Anjum, N. A., Singh, N., Singh, M. K., Sayeed, I., Duarte, A. C., Pereira, E., et al. (2014). Single-bilayer graphene oxide sheet impacts and underlying potential mechanism assessment in germinating faba bean (*Vicia faba* L.). *Sci. Total Environ.* 472, 834–841. doi: 10.1016/j.scitotenv.2013.11.018

Anjum, N. A., Singh, N., Singh, M. K., Shah, Z. A., Duarte, A. C., Pereira, E., et al. (2013). Single-bilayer graphene oxide sheet tolerance and glutathione redox system significance assessment in faba bean (*Vicia faba* L.). *J. Nanopart. Res.* 15, 1–12. doi: 10.1007/s11051-013-1770-7

Arvidsson, R., Molander, S., and Sandén, B. A. (2013). Review of potential environmental and health risks of the nanomaterial graphene. *Hum. Ecol. Risk Assess.* 19, 873–887. doi: 10.1080/10807039.2012.702039

Asli, S., and Neumann, P. M. (2009). Colloidal suspensions of clay or titanium dioxide nanoparticles can inhibit leaf growth and transpiration via physical effects on root water transport. *Plant Cell Environ.* 32, 577–584. doi: 10.1111/j.1365-3040.2009.01952.x

Begurn, P., Ikhtiari, R., and Fugetsu, B. (2011). Graphene phytotoxicity in the seedling stage of cabbage, tomato, red spinach, and lettuce. *Carbon* 49, 3907–3919. doi: 10.1016/j.carbon.2011.05.029

Cañas, J. E., Long, M., Nations, S., Vadan, R., Dai, L., Luo, M., et al. (2008). Effects of functionalized and nonfunctionalized single-walled carbon nanotubes on root elongation of select crop species. *Environ. Toxicol. Chem.* 27, 1922–1931. doi: 10.1897/08-117.1

Chen, J., Yang, L., Li, S., and Ding, W. (2018a). Various physiological response to graphene oxide and amine-functionalized graphene oxide in wheat (*Triticum aestivum*). *Molecules* 23, 1104. doi: 10.3390/molecules23051104

Chen, L., Wang, C., Li, H., Qu, X., Yang, S., and Chang, X. (2017). Bioaccumulation and toxicity of ^{13}C-skeleton labeled graphene oxide in wheat. *Environ. Sci. Technol.* 51, 10146–10153. doi: 10.1021/acs.est.7b00822

Chen, L., Wang, C., Yang, S., Guan, X., Zhang, Q., Shi, M., et al. (2019). Chemical reduction of graphene enhances *in vivo* translocation and photosynthetic inhibition in pea plants. *Environ. Sci-Nano.* 6, 1077–1088. doi: 10.1039/C8EN01426D

Chen, M., Zhou, S., Zhu, Y., Sun, Y., Zeng, G., Yang, C., et al. (2018b). Toxicity of carbon nanomaterials to plants, animals and microbes: recent progress from 2015-present. *Chemosphere* 206, 255–264. doi: 10.1016/j.chemosphere.2018.05.020

Chen, Z., Umar, A., Wang, S., Wang, Y., Tian, T., Shang, Y., et al. (2015). Supramolecular fabrication of multilevel graphene-based gas sensors with high NO_2 sensibility. *Nanoscale* 7, 10259–10266. doi: 10.1039/C5NR01770J

Cheng, F., Liu, Y., Lu, G., Zhang, X., Xie, L., Yuan, C., et al. (2016). Graphene oxide modulates root growth of *Brassica napus* L. and regulates ABA and IAA concentration. *J. Plant Physiol.* 193, 57–63. doi: 10.1016/j.jplph.2016.02.011

Chowdhury, S., and Balasubramanian, R. (2014). Recent advances in the use of graphene-family nanoadsorbents for removal of toxic pollutants from wastewater. *Adv. Colloid Interface* 204, 35–56. doi: 10.1016/j.cis.2013.12.005

De La Torre-Roche, R., Hawthorne, J., Deng, Y., Xing, B., Cai, W., and Newman, L. A., et al. (2012). Fullerene-enhanced accumulation of p,p′-DDE in agricultural crop species. *Environ. Sci. Technol.* 46, 9315–9323. doi: 10.1021/es301982w

Dreyer, D. R., Park, S., Bielawski, C. W., and Ruoff, R. S. (2010). The chemistry of graphene oxide. *Chem. Soc. Rev.* 39, 228–240. doi: 10.1039/B917103G

Gilbert, N. (2009). Nanoparticle safety in doubt. *Nature* 460:937. doi: 10.1038/460937a

Gobbi, M., Bonacchi, S., Lian, J. X., Liu, Y., Wang, X., and Stoeckel, M., et al. (2017). Periodic potentials in hybrid van der Waals heterostructures formed by supramolecular lattices on graphene. *Nat. Commun.* 8:14767. doi: 10.1038/ncomms14767

Hao, Y., Ma, C., Zhang, Z., Song, Y., Cao, W., Guo, J., et al. (2018). Carbon nanomaterials alter plant physiology and soil bacterial community composition in a rice-soil-bacterial ecosystem. *Environ. Pollut.* 232, 123–136. doi: 10.1016/j.envpol.2017.09.024

He, Y., Hu, R., Zhong, Y., Zhao, X., Chen, Q., and Zhu, H. (2018). Graphene oxide as a water transporter promoting germination of plants in soil. *Nano Res.* 11, 1928–1937. doi: 10.1007/s12274-017-1810-1

Hu, X., Kang, J., Lu, K., Zhou, R., Mu, L., and Zhou, Q. (2014a). Graphene oxide amplifies the phytotoxicity of arsenic in wheat. *Sci. Rep.* 4:6122. doi: 10.1038/srep06122

Hu, X., Lu, K., Mu, L., Kang, J., and Zhou, Q. (2014b). Interactions between graphene oxide and plant cells: Regulation of cell morphology, uptake, organelle damage, oxidative effects and metabolic disorders. *Carbon* 80, 665–676. doi: 10.1016/j.carbon.2014.09.010

Hu, X., Mu, L., Kang, J., Lu, K., Zhou, R., and Zhou, Q. (2014c). Humic acid acts as a natural antidote of graphene by regulating nanomaterial translocation and metabolic fluxes *in vivo*. *Environ. Sci. Technol.* 48, 6919–6927. doi: 10.1021/es5012548

Hu, X., and Zhou, Q. (2014). Novel hydrated graphene ribbon unexpectedly promotes aged seed germination and root differentiation. *Sci. Rep.* 4:3782. doi: 10.1038/srep03782

Huang, C., Xia, T., Niu, J., Yang, Y., Lin, S., Wang, X., et al. (2018). Transformation of ^{14}C-labeled graphene to $^{14}CO_2$ in the shoots of a rice plant. *Angew. Chem. Int. Edit*. 57, 9759–9763. doi: 10.1002/anie.201805099

Kotchey, G. P., Allen, B. L., Vedala, H., Yanamala, N., Kapralov, A. A., Tyurina, Y. Y., et al. (2011). The enzymatic oxidation of graphene oxide. *ACS Nano* 5, 2098–2108. doi: 10.1021/nn103265h

Lee, J. H., Han, J. H., Kim, J. H., Kim, B., Bello, D., Kim, J. K., et al. (2016). Exposure monitoring of graphene nanoplatelets manufacturing workplaces. *Inhal. Toxicol*. 28, 281–291. doi: 10.3109/08958378.2016.1163442

Lingamdinne, L. P., Koduru, J. R., Roh, H., Choi, Y., Chang, Y., and Yang, J. (2016). Adsorption removal of Co(II) from waste-water using graphene oxide. *Hydrometallurgy* 165, 90–96. doi: 10.1016/j.hydromet.2015.10.021

Liu, S., Wei, H., Li, Z., Li, S., Yan, H., He, Y., et al. (2015). Effects of graphene on germination and seedling morphology in rice. *J. Nanosci. Nanotechno*. 15, 2695–2701. doi: 10.1166/jnn.2015.9254

Miralles, P., Church, T. L., and Harris, A. T. (2012). Toxicity, uptake, and translocation of engineered nanomaterials in vascular plants. *Environ. Sci. Technol*. 46, 9224–9239. doi: 10.1021/es202995d

Naasz, S., Altenburger, R., and Kuehnel, D. (2018). Environmental mixtures of nanomaterials and chemicals: The Trojan-horse phenomenon and its relevance for ecotoxicity. *Sci. Total Environ*. 635, 1170–1181. doi: 10.1016/j.scitotenv.2018.04.180

Nair, R., Mohamed, M. S., Gao, W., Maekawa, T., Yoshida, Y., and Ajayan, P. M., et al. (2012). Effect of carbon nanomaterials on the germination and growth of rice plants. *J. Nanosci. Nanotechno*. 12, 2212–2220. doi: 10.1166/jnn.2012.5775

Nel, A., Xia, T., Mädler, L., and Li, N. (2006). Toxic potential of materials at the nanolevel. *Science* 311, 622. doi: 10.1126/science.1114397

Ou, L., Song, B., Liang, H., Liu, J., Feng, X., Deng, B., et al. (2016). Toxicity of graphene-family nanoparticles: a general review of the origins and mechanisms. *Part. Fibre Toxicol*. 13:57. doi: 10.1186/s12989-016-0168-y

Pirveysian, M., and Ghiaci, M. (2018). Synthesis and characterization of sulfur functionalized graphene oxide nanosheets as efficient sorbent for removal of Pb^{2+}, Cd^{2+}, Ni^{2+} and Zn^{2+} ions from aqueous solution: A combined thermodynamic and kinetic studies. *Appl. Surf. Sci*. 428, 98–109. doi: 10.1016/j.apsusc.2017.09.105

Sanchez, V. C., Jachak, A., Hurt, R. H., and Kane, A. B. (2012). Biological interactions of graphene-family nanomaterials: an interdisciplinary review. *Chem. Res. Toxicol*. 25, 15–34. doi: 10.1021/tx200339h

Suárez-Iglesias, O., Collado, S., Oulego, P., and Díaz, M. (2017). Graphene-family nanomaterials in wastewater treatment plants. *Chem. Eng. J*. 313, 121–135. doi: 10.1016/j.cej.2016.12.022

Sun, M., Jiang, F., Cen, B., Wen, J., Zhou, Y., and Wu, Z. (2018). Respiratory burst oxidase homologue-dependent H_2O_2 and chloroplast H_2O_2 are essential for the maintenance of acquired thermotolerance during recovery after acclimation. *Plant Cell Environ*. 41, 2373–2389. doi: 10.1111/pce.13351

Tan, P., Sun, J., Hu, Y., Fang, Z., Bi, Q., Chen, Y., et al. (2015). Adsorption of Cu^{2+}, Cd^{2+} and Ni^{2+} from aqueous single metal solutions on graphene oxide membranes. *J. Hazard. Mater*. 297, 251–260. doi: 10.1016/j.jhazmat.2015.04.068

Thomas, K., and Sayre, P. (2005). Research strategies for safety evaluation of nanomaterials, Part I: evaluating the human health implications of exposure to nanoscale materials. *Toxicol. Sci*. 87, 316–321. doi: 10.1093/toxsci/kfi270

Wang, X., Xie, H., Wang, Z., He, K., and Jing, D. (2019). Graphene oxide as a multifunctional synergist of insecticides against lepidopteran insect. *Environ. Sci. Nano* 6, 75–84. doi: 10.1039/C8EN00902C

Wiesner, M. R., Lowry, G. V., Jones, K. L., Hochella, J. M. F., Di Giulio, R. T., Casman, E., et al. (2009). Decreasing uncertainties in assessing environmental exposure, risk, and ecological implications of nanomaterials. *Environ. Sci. Technol*. 43, 6458–6462. doi: 10.1021/es803621k

Xing, W., Lalwani, G., Rusakova, I., and Sitharaman, B. (2014). Degradation of graphene by hydrogen peroxide. *Part. Part. Syst. Char*. 31, 745–750. doi: 10.1002/ppsc.201300318

Xu, J., Cao, Z., Zhang, Y., Yuan, Z., Lou, Z., Xu, X., et al. (2018). A review of functionalized carbon nanotubes and graphene for heavy metal adsorption from water: Preparation, application, and mechanism. *Chemosphere* 195, 351–364. doi: 10.1016/j.chemosphere.2017.12.061

Yan, J., Hu, C., Chen, K., and Lin, Q. (2019). Release of graphene from graphene-polyethylene composite films into food simulants. *Food Packaging Shelf* 20:100310. doi: 10.1016/j.fpsl.2019.100310

Yang, K., and Xing, B. (2007). Desorption of polycyclic aromatic hydrocarbons from carbon nanomaterials in water. *Environ. Pollut*. 145, 529–537. doi: 10.1016/j.envpol.2006.04.020

Yang, X. P., and Zhao, F. (2013). A review of uptake, translocation and phytotoxicity of engineered nanoparticles in plants. *Environ. Sci*. 34, 4495–4502 doi: 10.13227/j.hjkx.2013.11.005

Yin, L., Wang, Z., Wang, S., Xu, W., and Bao, H. (2018). Effects of graphene oxide and/or Cd^{2+} on seed germination, seedling growth, and uptake to Cd^{2+} in solution culture. *Water Air Soil Poll*. 229, 151. doi: 10.1007/s11270-018-3809-y

Zhang, C., Zhang, R. Z., Ma, Y. Q., Guan, W. B., Wu, X. L., and Liu, X., et al. (2015a). Preparation of cellulose/graphene composite and its applications for triazine pesticides adsorption from water. *ACS Sustain. Chem. Eng*. 3, 396–405. doi: 10.1021/sc500738k

Zhang, M., Gao, B., Chen, J., and Li, Y. (2015b). Effects of graphene on seed germination and seedling growth. *J. Nanopart. Res*. 17:78. doi: 10.1007/s11051-015-2885-9

Zhang, P., Zhang, R., Fang, X., Song, T., Cai, X., Liu, H., et al. (2016). Toxic effects of graphene on the growth and nutritional levels of wheat (*Triticum aestivum* L.): short- and long-term exposure studies. *J. Hazard. Mater*. 317, 543–551. doi: 10.1016/j.jhazmat.2016.06.019

Zhang, Z., Hu, J., Liu, S., Zhang, C., Liu, X., Ye, C., et al. (2018). Effect of nano-SiO_2 on the toxicity of Hg^{2+} to *Skeletonema costatum*. *Environ. Chem*. 37, 661–669 doi: 10.7524/j.issn.0254-6108.2017081506

Zhao, J., Cao, X., Wang, Z., Dai, Y., and Xing, B. (2017). Mechanistic understanding toward the toxicity of graphene-family materials to freshwater algae. *Water Res*. 111, 18–27. doi: 10.1016/j.watres.2016.12.037

Zhao, J., Wang, Z., White, J. C., and Xing, B. (2014). Graphene in the aquatic environment: Adsorption, dispersion, toxicity and transformation. *Environ. Sci. Technol*. 48, 9995–10009. doi: 10.1021/es5022679

Zhao, S., Wang, Q., Zhao, Y., Rui, Q., and Wang, D. (2015). Toxicity and translocation of graphene oxide in *Arabidopsis thaliana*. *Environ. Toxicol. Phar*. 39, 145–156. doi: 10.1016/j.etap.2014.11.014

Zhou, J., Chen, M., and Diao, G. (2013). Calix[4,6,8]arenesulfonates functionalized reduced graphene oxide with high supramolecular recognition capability: Fabrication and application for enhanced host-guest electrochemical recognition. *ACS Appl. Mater. Inter*. 5, 828–836. doi: 10.1021/am302289v

Conflict of Interest Statement: The authors declare that the research was conducted in the absence of any commercial or financial relationships that could be construed as a potential conflict of interest.

frontiers in Chemistry

ORIGINAL RESEARCH
published: 14 May 2019
doi: 10.3389/fchem.2019.00334

Assembly of Copper Phthalocyanine on TiO_2 Nanorod Arrays as Co-catalyst for Enhanced Photoelectrochemical Water Splitting

Yuangang Li[1,2], Mengru Yang[1], Zimin Tian[1], Ningdan Luo[1], Yan Li[3], Haohao Zhang[1], Anning Zhou[1,2] and Shanxin Xiong[1,2]**

[1] College of Chemistry and Chemical Engineering, Xi'an University of Science and Technology, Xi'an, China, [2] Key Laboratory of Coal Resources Exploration and Comprehensive Utilization, Xi'an, China, [3] Key Laboratory of Synthetic and Natural Functional Molecule Chemistry of the Ministry of Education, College of Chemistry and Materials Science, Northwest University, Xi'an, China

OPEN ACCESS

Edited by:
Penglei Chen,
Institute of Chemistry (CAS), China

Reviewed by:
Zhiyong Tang,
National Center for Nanoscience and Technology (CAS), China
Bin Chen,
Technical Institute of Physics and Chemistry (CAS), China
Jiahai Ma,
University of Chinese Academy of Sciences (UCAS), China

***Correspondence:**
Yuangang Li
liyuangang@xust.edu.cn
Shanxin Xiong
xiongsx@xust.edu.cn.

Specialty section:
This article was submitted to Supramolecular Chemistry, a section of the journal Frontiers in Chemistry

Received: 21 December 2018
Accepted: 24 April 2019
Published: 14 May 2019

Citation:
Li Y, Yang M, Tian Z, Luo N, Li Y, Zhang H, Zhou A and Xiong S (2019) Assembly of Copper Phthalocyanine on TiO_2 Nanorod Arrays as Co-catalyst for Enhanced Photoelectrochemical Water Splitting. Front. Chem. 7:334. doi: 10.3389/fchem.2019.00334

A photoelectrochemical device was achieved by interfacial self-assembly of macrocyclic π-conjugated copper phthalocyanine (CuPc) on surface of TiO_2 nanorod arrays (NRs). The photocurrent density of the elegant TiO_2@CuPc NRs photoanode reaches 2.40 mA/cm^2 at 1.23 V vs. RHE under the illumination of 100 mW/cm^2 from AM 1.5G sun simulator, which is 2.4 times higher than that of the pure TiO_2. At the same time, the photoelectrochemical device constructed through this strategy has good stability and the photocurrent density remain almost no decline after 8 h of continuous operation. The Mott-Schottky and LSV curves demonstrate that CuPc act as a co-catalyst for water oxidation and a possible mechanism is proposed for water oxidation based on careful analysis of the detailed results. The holes from VB of TiO_2 photogenerated by electrons exciting are consumed by a process in which Cu^{2+} is oxidized to Cu^{3+} and Cu^{4+}, and then oxidize water to produce oxygen. CuPc species is considered to be a fast redox mediator to reduce the activation energy of water oxidation in and effectively promote charge separation.

Keywords: self-assembly, copper phthalocyanine, TiO_2, water oxidation, surficial naostructutre

INTRODUCTION

Photoelectrochemical (PEC) water splitting is considered as one of the most promising technologies to address the challenges of impending worldwide energy consuming and associated climate change resulting from combustion of fossil fuels (Du and Eisenberg, 2012; Wang et al., 2016; Seh et al., 2017). Through this promising strategy, hydrogen could be produced as a clean fuel by sun light photolysis of water under the help of a bias potential (Ferreira et al., 2004; Gibson et al., 2017; Li et al., 2017). However, the sluggish kinetics of the two half-reactions of water splitting, especially the more sluggish four-electron oxygen evolution reaction, always leads to poor performance of the PEC device and relatively low energy efficiency (Haumann et al., 2005; Bessel et al., 2010; Fang et al., 2017). Therefore, many research works in the past have still focused on the design and improving the performance of photo anode on which water oxidation occurred, although the more desired hydrogen evolution reaction occurred on the photo cathode (Osterloh, 2013; Meyer et al., 2017). In order to achieve PEC device with relatively high performance, many

strategies have been employed. One of the effective strategies is adopting photo electrode of vertically aligned arrays (Lee and Chen, 2014) compositing of low dimensional nanostructures such as nanorods (Bin and Aydil, 2009; Liu B. et al., 2013; Li et al., 2016b; Tang et al., 2017), nanowires (Hang et al., 2001; Li et al., 2016a; Zhang et al., 2016; Jeong et al., 2018; Yao et al., 2018), and nanosheets (Zhu et al., 2011; Yang et al., 2012; Du et al., 2013; Zhang et al., 2014; Zhang R. et al., 2018; Shi et al., 2018; Zhao et al., 2018a) because this kind of interfacial nanostructures can decouple the length scales of charge diffusion and light absorption, at the same time offering sufficient surface area for the photogenerated electrons or holes to diffuse onto the interface of electrolyte and electrode (Xiao et al., 2015). TiO_2 nanorod arrays (Akira and Kenichi, 1972; Liu L. et al., 2013; Li et al., 2015, 2016c) had been applied extensively in PEC water splitting as for its low cost, non-toxic, and stable performance.

Another effective way is selecting a suitable co-catalyst to improve the photo electrochemical performance and water oxidation activity in the process of assembling photo electrochemical device (Ran et al., 2014; Ding et al., 2017; Zhang Y. et al., 2018). In the process of PEC water splitting, co-catalysts play three pivotal roles for improving the reliability and activity of semiconductor: (i) co-catalysts could reduce the over-potential (Artero et al., 2011) or activation energy for oxygen production reactions on the surface of semiconductors; (ii) co-catalysts are capable of slowing electron-hole recombination at the interface between co-catalyst and semiconductor; (iii) co-catalysts could improve the stability of semiconductor photo electrode and suppress the photo-corrosion. Over the past few years, the advances of electrode manufacturing technology and materials science have greatly expanded in O_2 evolution (Li et al., 2012; Nepal and Das, 2013; Lauinger et al., 2015; Gong et al., 2016). Many kinds of novel co-catalysts and interlayers were successfully loaded on various photoelectrodes (Long et al., 2018; Zhao et al., 2018b; Yin et al., 2019). Thus far, noble-metal oxides (IrO_2 or RuO_2) act as the best accepted O_2-evolution co-catalysts, which have lower over-potential for oxygen evolution in acidic conditions (Junya et al., 2005; Blakemore et al., 2010; Cherevko et al., 2015).

With the exception of rare and precious metals, some noble-metal-free and low-cost transitional metals, such as Co (Youn et al., 2015; Zhang et al., 2017), Ni (Yoon et al., 2015) and Fe (Youn et al., 2015) have also been used as co-catalysts in PEC O_2 production. Although copper (Zhou et al., 2015) based catalyst often has been applied for H_2 evolution (Kumar et al., 2016), hardly for O_2 production (Terao et al., 2016; Chauhan et al., 2017), in Lu group (Lu et al., 2016), Cu(II) aliphatic diamine complexes was immobilized on ITO as heterogeneous water oxidation catalysts. In Su (Su et al., 2015) and Zhang (Zhang et al., 2013) group, copper complexes were synthesized as homogeneous O_2 production catalysts. Copper phthalocyanine is a kind of organic heterocyclic compounds, containing large ring Π conjugated structure with good stability and effective property (Jiang et al., 2017).

It has been proven that supramolecular self-assembly of pi-conjugated molecules was a good strategy to fabricate various functional organic-based nanostructured materials, which aims to manufacturing sophisticated organized molecular aggregate, through various non-covalent interactions, including hydrophobic interactions, π-π interactions, electrostatic interactions, etc. (Chen et al., 2008; Zhang et al., 2009; Qiu et al., 2010; Guo et al., 2011, 2012). Although, supramolecular assembled nanostructures (Wang et al., 2014; Liu et al., 2015; Geng et al., 2018) based on pi-conjugated phthalocyanine derivatives have been reported to be effective in the field of laser printing, xerography, organic solar cells, etc., it is very rare to apply this kind of strategy for constructing PEC device. Herein, we adopted an electro-induced surficial assembly method to construct PEC device with enhanced performance. We employ copper phthalocyanine (CuPc) as an O_2 evolution co-catalyst and TiO_2 nanorod arrays (TNRAs) as semicondustor for light harvesting. The obtained surficial nanostructured assembly could be used as photo anode for efficient PEC water splitting. The photocurrent density of the elegant CuPc assembled TiO_2 nanorod arrays (CTNRAs) photoanode reaches 2.4 mA/cm^2 at 1.23 V vs. RHE, which is more than 2 folders higher than that of the pristine TNRAs and the stability of the PEC device is also very good. There have no obvious performance decline after 8 h continuous operation. A possible mechanism for PEC water oxidation on CTNRAs was proposed based on detailed experiments.

EXPERIMENTAL SECTION

Sample Preparation

Materials

All chemicals were analytical grade and used without further treatment. Fluorine-doped tin oxide (FTO) substrates (14 Ω/square) were obtained from Huanan Xiangcheng Technology Co., Ltd. Copper phthalocyanine ($C_{32}H_{16}CuN_8$), tetrabutyl titanate ($C_{16}H_{36}O_4Ti$), Trifluoroacetic acid (CF_3COOH), and methanol (CH_3OH) were purchased from Aladdin Chemical Reagent Co. Ltd. In addition, acetone (C_3H_6O), hydrochloric acid (HCl), and absolute ethanol (C_2H_5OH) were bought from Sinopharm Chemical Reagent Co. Ltd. Ultrapure water was used in the experiments.

Preparation of FTO@TiO_2 (TNRAs) and FTO@TiO_2@CuPc (CTNRAs)

Preparation of TNRAs TiO_2 nanorod arrays were prepared by hydrothermal method in autoclave (Bin and Aydil, 2009). Firstly, FTO were cleaned ultrasonically three times in solvents of acetone, ethanol and deionized water alternatively 15 min per step, and were dried in vacuum dryer at 60°C. Next, 0.4 mL tetrabutyl titanate were added drop wise into uniform mixed solution of 12 mL ultrapure water and 12 mL hydrochloric acid (mass fraction 36.5–38 %). When the mixture solution of precursor was clarified, we transferred it into 100 mL of Teflon-lined stainless steel autoclave. The conductive surface of FTO was put downwards at a slight angle with the inner wall of autoclave. Then, the autoclave was kept in an oven of 150°C for 15 h and cooled to 25°C. Then the FTO with nanorod arrays of TiO_2 were taken out and dried. Finally, the TiO_2 nanorod arrays were annealed at 450°C for 1 h.

Preparation of CTNRAs For synthesis of CTNRAs, 3 μmol CuPc were dissolved in 5 mmol trifluoroacetic acid, which mixed with 50 mL chloroform as electroplate solution (Ogunsipe and Nyokong, 2004). The mono-protonated $[CuPc{\cdot}H]^+$ (**Figure S1A**) and di-protonated $[CuPc{\cdot}H_2]^{2+}$ (**Figures S1B,C**) forms of copper phthalocyanine (CuPc) were obtained by TFA (Su et al., 2009). The CTNRAs was fabricated by the electrophoretic deposition (EPD) method from the protonated CuPc dissolved in chloroform containing TFA. Then The $CuPc^+$ ($[CuPc{\cdot}H]^+$ and $[CuPc{\cdot}H_2]^{2+}$) was loaded on TNRAs by electrodeposition of 30, 60, 90, 120, and 150 s. Next $CuPc^+$ were deprotonated by dipping the TNRAs substrate in 1 M ammonia for 1 h and drying for 1 h at 200°C and CuPc was successfully covered onto TiO_2 nanorod arrays (**Figure 1**). FTO@CuPc was prepared in the same way.

Materials Characterizations

XRD were characterized by a Shimadzu 7000S X-ray diffract meter with Cu-Kα radiation and operating in a 2θ range of 20–70° at a scan rate of 5° per minute. XPS patterns of the as-prepared samples were carried on a Kratos Axis Ultra DLD system with an Al Kα X-ray source ($h\nu = 1486.69$ eV). The morphologies, EDS mapping analyse and high-resolution images were studied by a field emission Tecnai G2 F20 transmission electron microscopy with an acceleration voltage of 200 kV. SEM images were achieved using a Hitachi S-4800 field-emission scanning electron microscopy. Raman spectra were investigated on a WITec Alpha 300 R Confocal Raman Spectrometer, which has an excitation wavelength of 532 nm at the room temperature. The UV-vis spectra were characterized by a Shimadzu UV-2550 UV-Vis spectrophotometer using $BaSO_4$ as the reference. The linear sweep voltammetry (LSV), electrochemical impedance spectroscopy (EIS) and cycle voltammetry (CV) were conducted using an electrochemical workstation (CHI 660E) in a three-electrode system. The incident photon-to-current conversion efficiency (IPCE) was measured by the same workstation and a Xenon lamp (300 W) coupled with a monochromator. Inductively coupled plasma (ICP) measurement was carried on Varian 715-ES.

PEC Measurements

PEC water oxidation was investigated using a three-electrode potential station (CHI 660 E, China) with a saturated Ag/AgCl (in 3 M KCl) as reference electrode and a platinum wire as counter electrode. The schematic illustration for the geometry and design of PEC reactor was shown in **Figure S16**. Under AM 1.5G simulated solar light illumination (100 mW/cm^2) from a Xe lamp (300 W), the as-prepared working electrodes exhibit photoelectron activity for water splitting. 0.1 M sodium sulfate solution (pH ≈ 6.8) was used as electrolyte with 30 min N_2 bubbling. LSV was conducted at a scan rate of 10 mV/s. The potential of the working electrodes (vs. Ag/AgCl) can be converted to the reversible hydrogen electrode (RHE) by the Nernst equation:

$$\mathbf{E_{RHE} = E_{Ag/AgCl} + 0.0591pH + 0.19742}$$

RESULT AND DISCUSSION

TNRAs on FTO were prepared in an autoclave by a hydrothermal method. The obtained TNRAs are almost vertically grown on the FTO substrate, with an average diameter and length of ∼500 nm and ∼3 μm, respectively (**Figure 2A** and **Figure S4A**). Each nanorod consisted of several smaller rods as shown in **Figure S1C**. Transmission electron microscopy picture from a single nanorod (**Figure 2C**, and **Figures S2A,B**) shown that the diameter observed is about 600∼800 nm which is in accordance with SEM observation. High-resolution transmission electron microscopy (HR-TEM) of TNRAs showed that two kinds of lattice fringes could be clearly observed and the distances between adjacent lattice fringes were about 0.325 and 0.249 nm (**Figure 2E**), respectively. After careful comparison with the results of literature we attribute them as lattice fringes from the crystal lattice of (110) and (101) of rutile TiO_2, respectively, illustrating that the obtained TNRAs is rutile TiO_2 and grow along with the direction of (001) lattice (Wang et al., 2011).

The CTNRAs were fabricated through a simple electrodeposition method, as illustrated in **Figure 1**. The SEM images of CTNRAs were almost the same as pure TNRAs (**Figure 2B** and **Figures S3C**, **S4B**), which indicate the process of the CuPc deposition does not damage the structure of the pristine TNRAs. But from **Figure 2D** and **Figure S3** we can observe that the surface of TiO_2 was more rough compared with that of TNRAs. The HR-TEM of CTNRAs reveals a single crystalline structure in **Figure 2F**. Lattice fringes of 0.147 nm (002), 0.167 nm (211), and 0.249 nm (101) belong to rutile TiO_2 and which is consistent with that of pure TNRAs. Although the lattice structure of CuPc was not found, the characteristic elements of nitrogen and copper of CuPc could be seen in energy dispersive X-ray elemental mapping (**Figures 2G,H**). From the elemental mapping images of CTNRAs as shown in **Figure 2G**, it is observed that the copper and nitrogen elements from CuPc distribute as uniformly as the elements of oxygen and titanium from TiO_2, which means that CuPc was successfully deposited on the surface of TNRAs and the deposited CuPc distribute uniformly on the whole surface of TiO_2 nanorod.

X-ray diffraction (XRD) curves (**Figure 3A**) indicate that both TNRAs and CTNRAs can be ascribed to the tetragonal TiO_2 with the rutile phase (JCPDS 21-1276). As for pristine TiO_2, the main distinct diffraction peaks at 36.3°, 54.5°, and 62.6° can be well attributed to (101), (211), and (002) crystal planes, respectively. The XRD spectra are consistent with HR-TEM patterns. The other distinct diffraction peaks from TNRAs located at 2θ values of 27.2°, 33.7°, 38.1°, 57.1°, and 66.2 ° are attributed to SnO_2 from FTO substrate. No apparent peaks of CuPc can be observed in CTNRAs samples due to the low loading of CuPc, or the amorphous state of CuPc from electrodeposition method.

Raman spectroscopy measurements were employed to further observe the existence of CuPc on the surface of CTNRAs. The data shown in **Figure 3B** clearly proved that CuPc was successfully deposited on TNRAs to form CTNRAs. The spectrum of pristine TNRAs show four characteristic peaks at 143, 448, 608, and 238 cm^{-1}, respectively, matching well with the B1g, Eg, A1g of rutile TiO_2 and lattice distortion or multi spectral

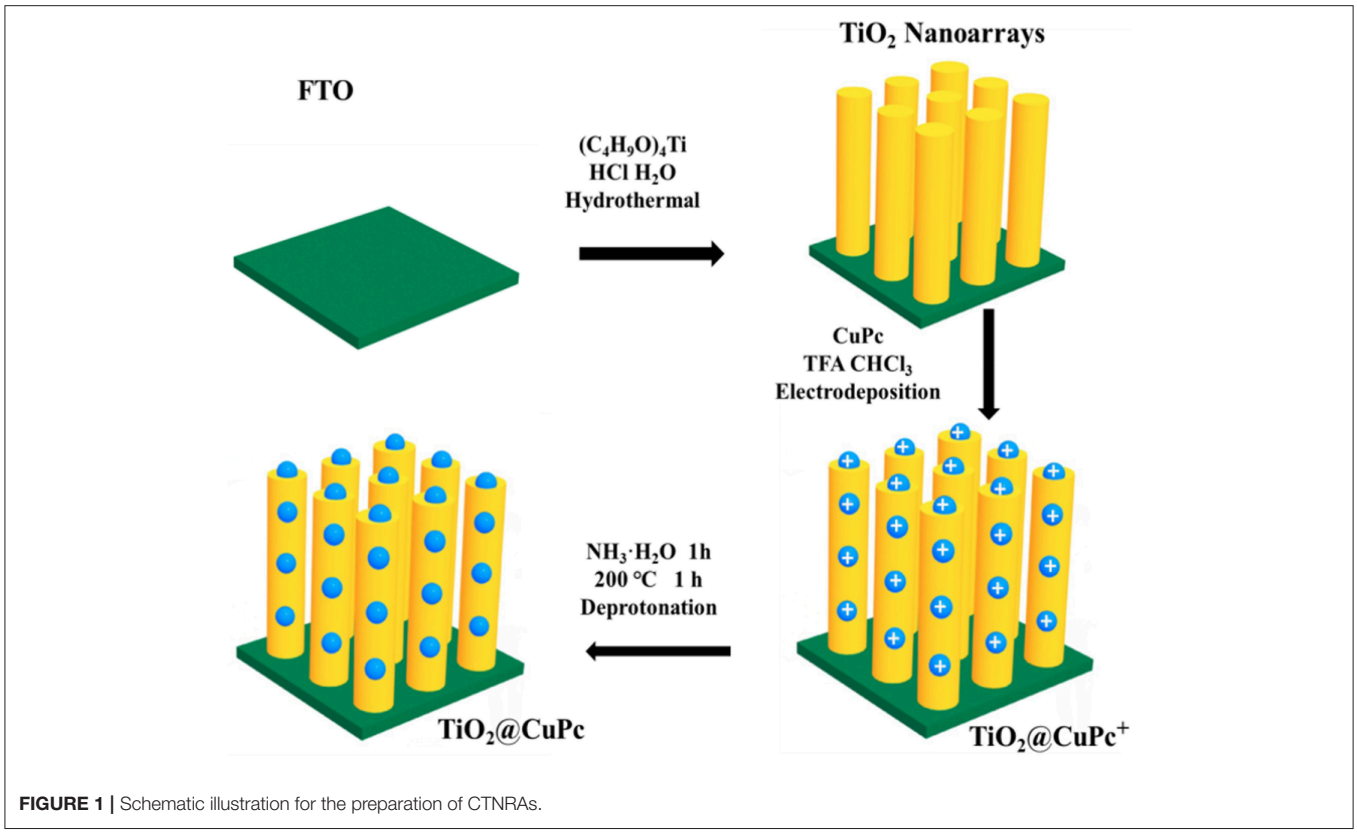

FIGURE 1 | Schematic illustration for the preparation of CTNRAs.

of rutile TiO_2. In contrast, the characteristic Raman peaks located at 1,535, 1,338, and 685 cm^{-1} are observed in the CuPc samples (Ludemann et al., 2011), which could be accordance with the C-N stretching vibration on pyrrole bonded to central copper ion, C-N stretching vibration peak on heterocyclic ring and vibration of large phthalocyanine ring, resprctively. As for the sample of CTNRAs all characteristic peaks of CuPc and rutile TiO_2 could be seen with a slightly shift, which further elucidate the existence of CuPc on CTNRAs. Optical properties of CTNRAs, CuPc, and TNRAs were measured by UV-Vis absorption measurement (**Figures S6, S7**). Owing to the broad band gap (3.0 eV), TiO_2 only reveal a strong absorption at wavelength shorter than 410 nm. CuPc display strong absorption bands in the range of 500–800 nm. In comparison, TiO_2@CuPc sample exhibit a strong absorption shorter than 410 nm, and two very weak absorption peaks at about 550 and 650 nm which results from CuPc due to the lower deposition amount.

In order to further confirm the existence of CuPc in TNRAs and understand the surface chemical state of the sample, we have employed the X-ray photoelectron spectroscopy (XPS) measurements. Obvious photoelectron peaks of C, N, Cu, O, and Ti elements are observed in the XPS survey spectrum (**Figure 3C**) of CTNRAs. In compare with pristine TNRAs, TCNRAs contain not only Ti, O and C elements from TNRAs, but also Cu and N elements from CuPc. The high resolution Ti 2p XPS spectrum (**Figure 3D**) shows two different peaks at 462.4 eV and 458.4 eV, which can be ascribed to the characteristic of Ti $2p_{1/2}$ and Ti $2p_{2/3}$ deriving from Ti^{4+}, respectively. Furthermore, the O 1s spectra (**Figure S8**) of TNRAs and CTNRAs can be factored into two peaks at about 529.6 and 530.1 eV. The peak 1 at about 530.1 eV is ascribed to surface Ti-OH species, while peak 2 is assigned to lattice oxygen in O-Ti^{4+}. Compared to pure TiO_2, the deposition of CuPc reduces the area ratio of peak 1 to peak 2, maybe indicating the surface of TiO_2 was covered by CuPc, so that it adsorb less amount of OH groups. It can be seen from **Figure 3E** that the high resolution XPS spectrum of Cu 2p in CTNRAs has two strong peaks at 954.3 and 934.5 eV, which are the Cu $2p_{1/2}$ and Cu $2p_{2/3}$, respectively. The binding energy of the Cu 2p2/3 is 934.5 eV, indicating that the Cu atom in the CTNRAs exists in the Cu (II) state (Zheng et al., 2004). This data can be explained by the chemical structure of the CuPc molecule, in which the copper exists in the bivalent form. In addition, the satellite peak of the Cu(II) state can be seen, which imply that the CuPc molecular plane contains $3dx^2$-y^2 orbitals. From the fine spectrum of N 1s (**Figure 3F**), we can see two peaks located at 400.1 eV and 398.6 eV. N atoms have two chemical environments in CuPc, one is C-N=C bond forming by 4 C atoms with 2 N atoms which located in 398.6 eV, the other is the 4 N atoms coordination bonding with the Cu atom, the signal of which located at 400.1 eV. As for high resolution XPS spectrum of C 1s (**Figure S9**), there are two types of carbon atoms in the CTNRAs 8 C atoms are bonded to 2 N atoms forming N-C=N bond at 289.4 eV; the remaining 24 C atoms have aromatic hydrocarbon properties which is located at 285.0 eV. With decided contrast, the XPS spectrum of pure TNRAs only have a C 1S signal at 284.8 eV, which can be attributed to the absorbed contaminants. Combined with the results of XRD analysis, Raman spectra and UV-Vis absorption, we concluded that CuPc indeed assembled

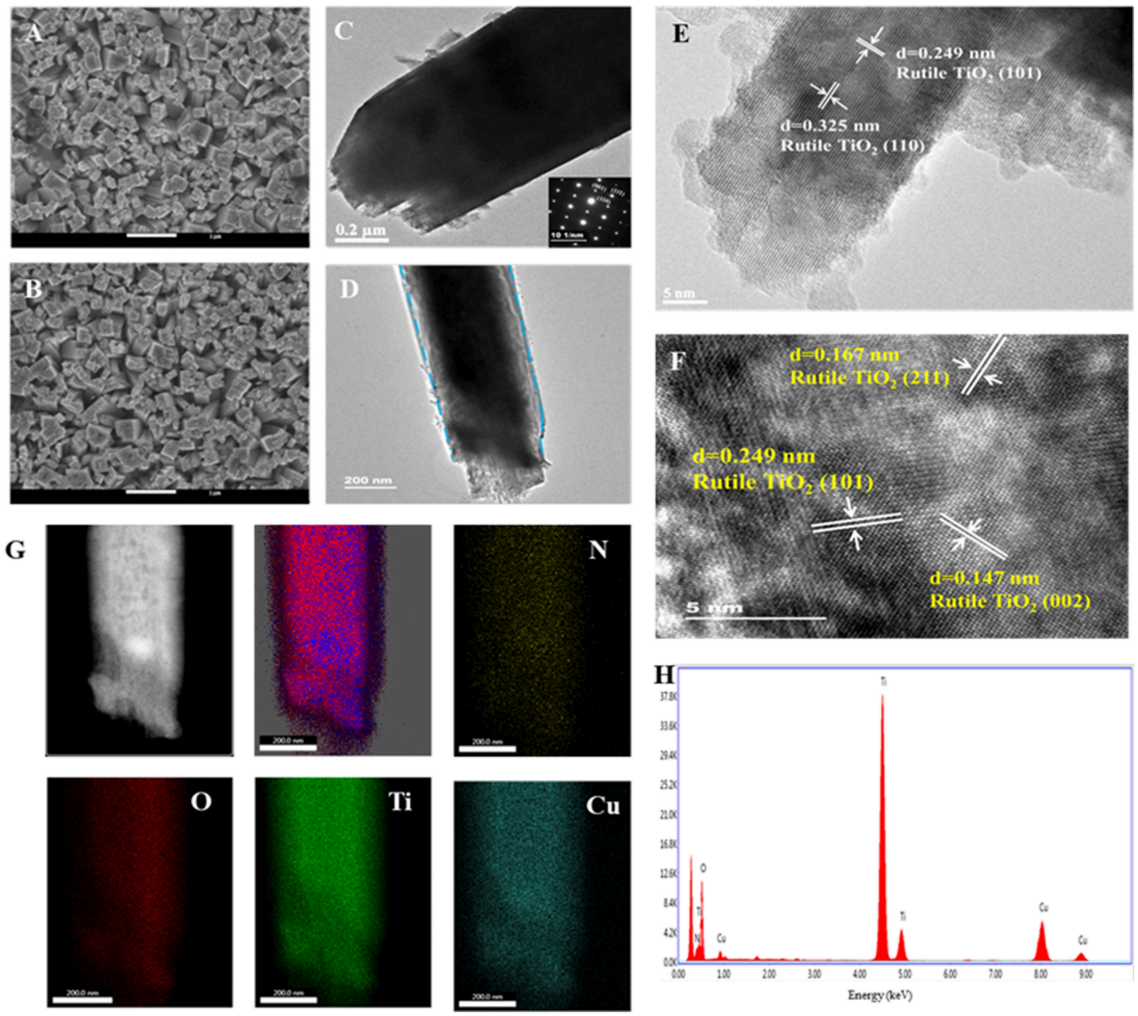

FIGURE 2 | Typical top-view SEM images of **(A)** pure TNRAs and **(B)** the CTNRAs; TEM images of **(C)** pure TNRAs and **(D)** the CTNRAs; HR-TEM images of **(E)** pure TNRAs and **(F)** the CTNRAs; **(G)** EDX elemental mapping of N, O, Ti, and Cu; **(H)** EDX spectrum of the CTNRAs.

onto the surface of TNRAs to form a uniform coverage through electro-induced assembly. As far as the assembled pattern of CuPc on the surface of TiO_2 nanord was concerned, we inferred that the plane CuPc molecules adopt a flattened pattern rather than a standing pattern on the surface of TiO_2 nanorod through electrostatic self-assembly because CuPc have a plane structure and the positive charge located near the center of the plane, so the flattened pattern is more stable than the standing pattern, which will be proved by the good stability of obtained device for PEC operation.

The linear sweep voltammetry (LSV) curves showed in **Figure 4A** reveals the photoelectrochemical (PEC) activities of the as-prepared samples. Under 100 mW/cm^2 irradiation by the simulated solar light (AM 1.5G), transient photocurrent responses of pristine TNRAs is 1.01 mA/cm^2 at 1.23 V (vs. RHE), while pure CuPc almost have no PEC response. After coating with CuPc, the photocurrent density of CTNRAs showed dramatically increase. With the electrodeposition time prolonged, the photocurrent density increased first and then decreased (**Figure S15**). The optimized electrodeposition time is 60 s, the photocurrent density reaches 2.40 mA/cm^2 at 1.23 V (vs. RHE), which was 2.40 times as that of pure TNRAs. Then, the photocurrent response was decrease when electrodeposition time longer than 60 s. The photocurrent density of CTNRAs was 1.80, 1.60, and 1.30 mA/cm^2, when the electrodeposition time was 90, 120, and 150 s, respectively.

To more intuitive observe the relationship between the photocurrent density enhancement and the deposition time of the CTNRAs, the curve of growth rate of photocurrent density vs. deposition time was ploted in **Figure 4B**. Growth rate can be expressed concretely as:

$$\textbf{Growth ratio} = \frac{I_{CTNRAs} - I_{TNRAs}}{I_{TNRAs}} \times 100\%$$

Where I_{CTNRAs} and I_{TNRAs} were the photocurret density of CTNRAs and TNRAs, respectively. The plot was shown as a

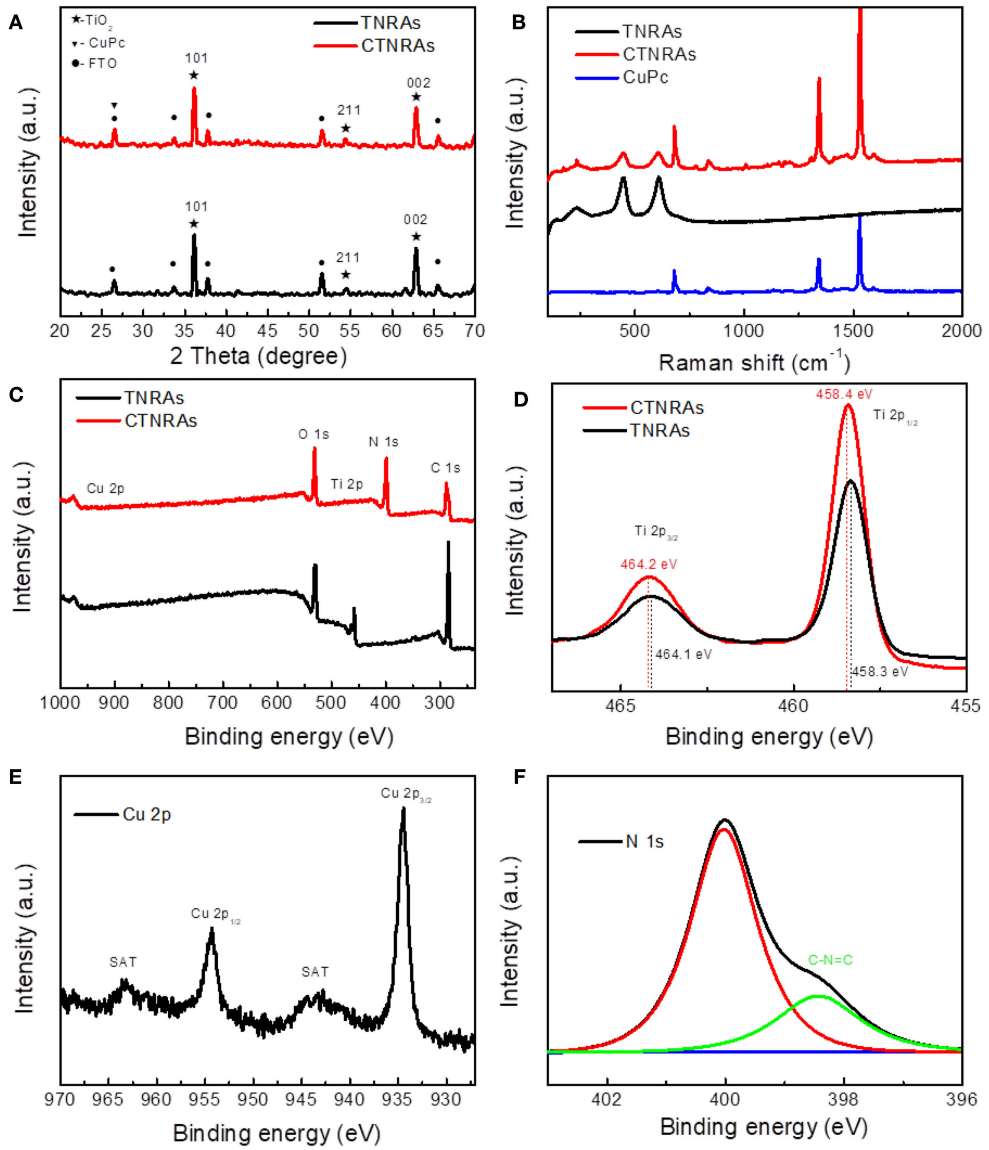

FIGURE 3 | XRD patterns **(A)**, Raman shift spectra **(B)** of pure TNRAs, CuPc and CTNRAs, XPS survey **(C)** of pristine TNRAs and CTNRAs; High resolution XPS spectra of Ti 2p **(D)**, Cu 2p **(E)**, and N 1s **(F)**.

single peak curve that the growth ratio increased rapidly as the deposition time <60 s and reaches the maximum average growth rate of about 120% at 60 s. When the time was prolonged further, the growth ratio declined with deposition time. ICP-MS measurements was carried out to estimate the loaded amount of CuPc on the surface of TNRAs, when the electrodeposition time was 30, 60, 90, 120, and 150 s, the anchoring mass of CuPc was 0.024, 0.047, 0.069, 0.089, and 0.112 μmol on per square centimeter TiO_2, respectively. With the amount of CuPc increased, the photocurrent density increased first and then decreased. And the fine XPS spectrum of Cu_{2p} and Ti_{2p} in the optimized CTNRAs sample was calculated carefully to estimate the surface atom ratio of Ti and Cu (**Figure S10**), the results illustrated that the surface atom ratio of Ti and Cu from the optimized sample was about 30:1.

The stability of the optimized CTNRAs was detected by photocurrent-time (I-t) measurement at 1.23 V vs. RHE under continuous illumination (100 mW/cm^2, AM 1.5G) for 8 h (**Figure 4C**). Starting without illumination, the photocurrent density is almost zero. When illumination was opened, the photocurrent density reached 2.40 mA/cm^2. The value of photocurrent density stays almost no decline in the long 8 h operation which means that CTNRAs have a good stability for PEC water oxidation. To observe the composition and morphology change of the device during the process of PEC operation, SEM, XPS and ICP-MS measurements were

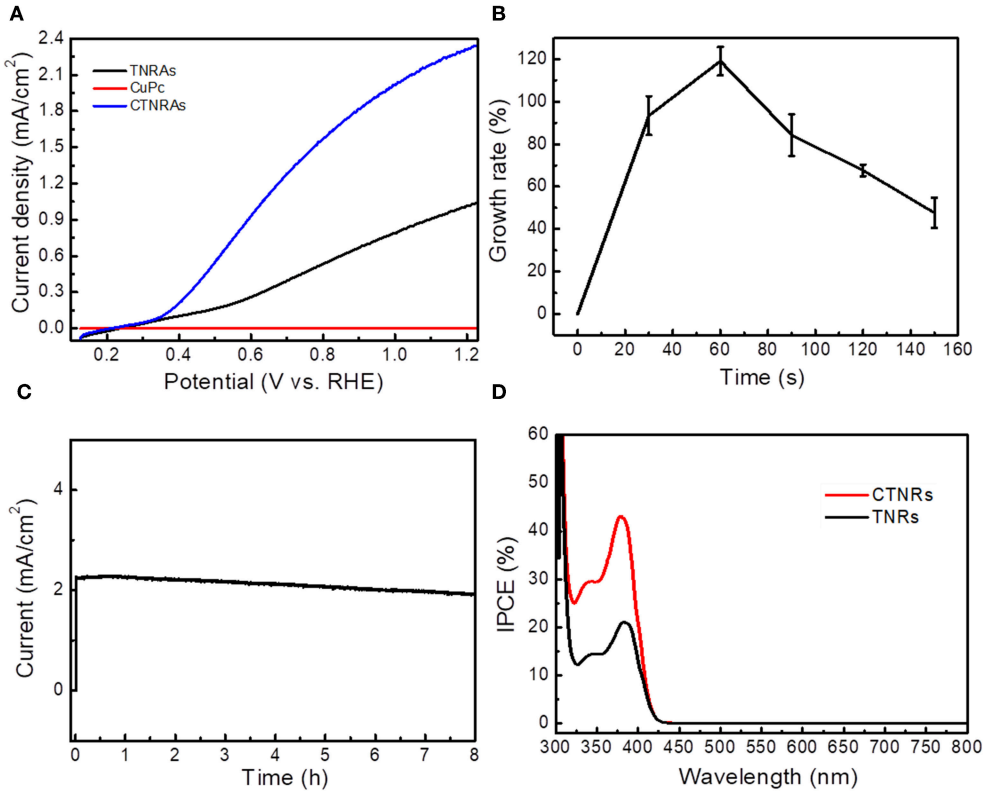

FIGURE 4 | (A) Photocurrent density vs. potential curves for the CTNRAs, pristine TNRAs, and CuPc under AM 1.5G (100 mW/cm^2); **(B)** Growth rate of photocurrent density-potential of CTNRAs with various deposition time; **(C)** Chronoamperometry (i-t) of CTNRAs with a three-electrode system at 1.23 V_{RHE} for 8 h. **(D)** IPCE pectrum of TNRAs and CTNRAs.

conducted. The results shown that: (1) the morphology of the electrode after operation is almost the same as that before operation (**Figure S5**); (2) XPS measurement (**Figures S11, S12**) confirmed the exist of CuPc on the sample after operation, but the ICP measurement show that the loaden amount of CuPc is declined compared to the sample before operation. This is probably due to the slight leakage of CuPC during the PEC process.

Incident photon-to-current conversion efficiency (IPCE) was measured at 1.23 V vs. RHE, to further elucidate the enhanced PEC oxygen production performance of CTNRAs. IPCE (Cho et al., 2011) can be calculate concretely as:

$$\mathbf{IPCE} = \frac{(\mathbf{1240} \times \mathbf{J})}{(\lambda \times \mathbf{I})} \times \mathbf{100\%}$$

Where λ and I are the incident light wavelength and the power density for each wavelength, respectively, and J is the photocurrent density produced by excited electrons. As shown in **Figure 4D**, the IPCE of CTNRAs is higher than that of pristine TNRAs in the whole spectrum, which indicates that the photogenerated electron-hole pairs are effectively separated in the CTNRAs. The IPCE value was reached 45% at 380 nm, but the IPCE of pure TNRAs is only 21%. The IPCE value can be improved by enhancing the charge injection efficiency, efficiency of light capture and charge collection efficiency. CTNRAs not only have TiO_2 nanorod arrays that are grown perpendicularly to the FTO substrate with a large surface area, in case to enhance the light harvesting efficiency, but also have CuPc layer which can provide a direct pathway for excited holes to improve the collection efficiency and water oxidation kinetics. Accordingly, the IPCE of CTNRAs can reach as high as 45%.

In order to further verify the proposed mechanism, Mott-Schottky measurements were used to obtain flat band potential and the charge carrier density of the interface between semiconductors. The positive slope of CTNRAs and pristine TNRAs (**Figure 5A**) suggests the expected n-type semiconductor of TiO_2 in the nanocomposites. For n-type semiconductor, flat band potential is consistent with the bottom of the conduction band. Pristine TNRAs and CTNRAs have the same flat band voltage, implying that the deposition of CuPc did not change the flat band position of TNRAs. From the results of Mott-Schottky measurements, we excluded the possibility of p-n junction formation between the interface of CuPc and TNRAs, which also confirmed by the IPCE measurements where no response was observed from the longer wavelength according to the absorption of CuPc.

In order to further understand the enhanced PEC performance, the inherent electronic properties of CTNRAs were characterized by measuring electrochemical impedance spectroscopy (EIS), the onset OER potential and linear Tafel plots. It is well-known that the larger over potential of TNRAs for water oxidation, presenting the sluggish kinetics, which can limits its wide application in PEC water splitting. The onset potential for OER of TNRAs and CTNRAs (**Figure 5C**) is 2.36,

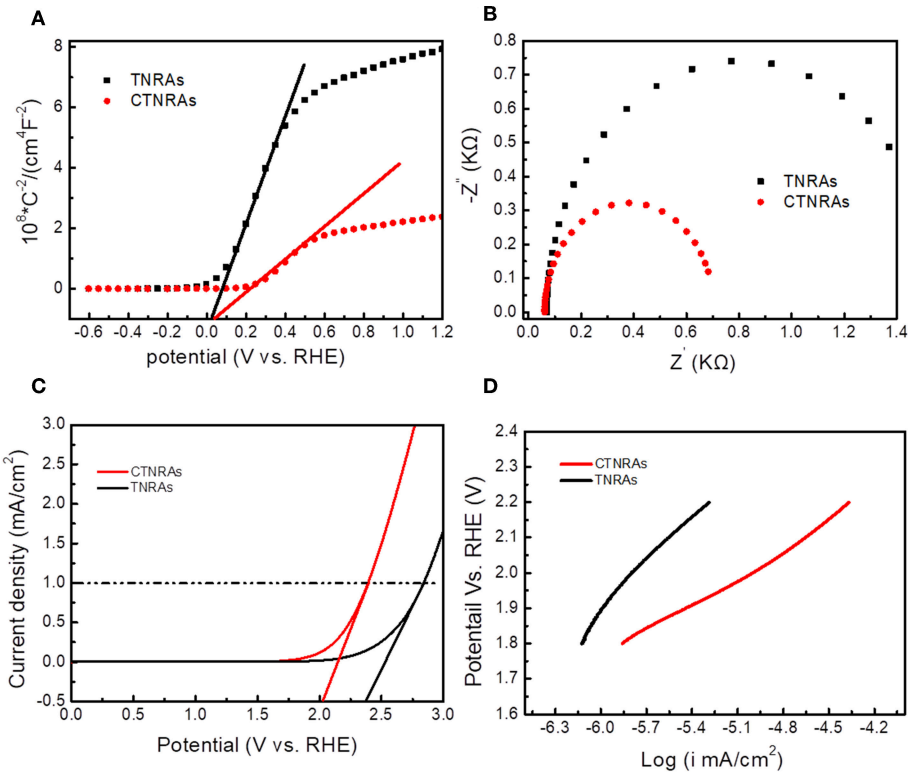

FIGURE 5 | Mott-Schottky curves **(A)**; electrochemical impedance specra **(B)**; Polarization curves **(C)**, and Tafel plots **(D)** of pristine TNRAs and the CTNRAs with 60 s deposition.

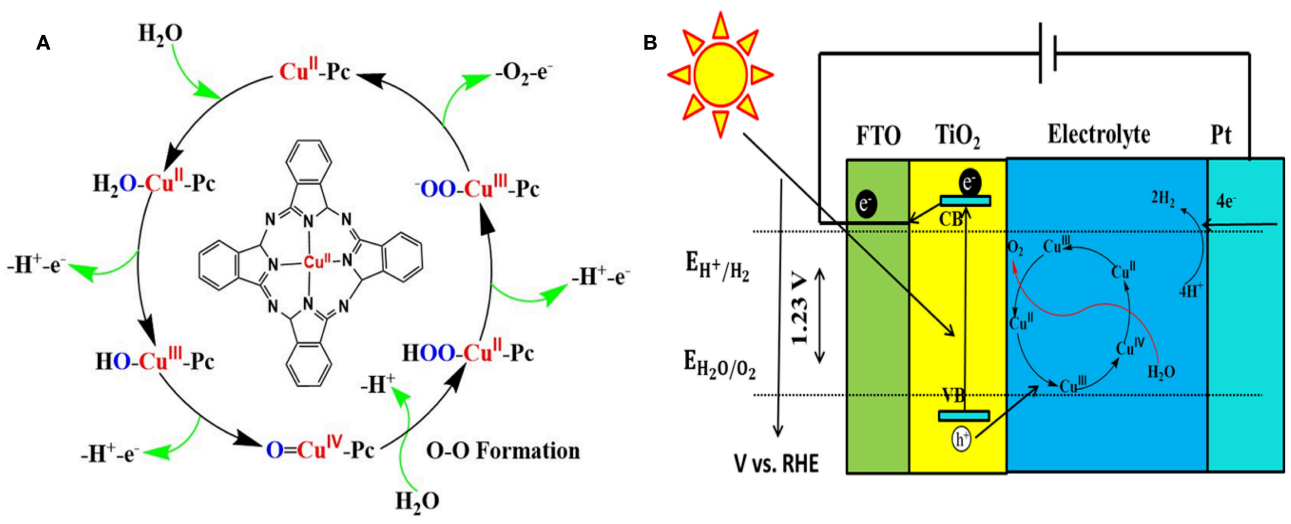

FIGURE 6 | (A) Proposed water-oxidation mechanism of CuPc catalysis, **(B)** Schematic diagram for transfer and separation of photogenerated charges and holes in the CTNRAs heterostructure.

and 2.04 V, respectively, which indicate electrocatalytical activity in CTNRAs was greatly enhanced by the deposition of CuPc. Electrochemical impedance is an effective method for assessing the kinetic of electron transfer at the electrode-electrolyte interface. From **Figure 5B**, electrochemical impedance spectra show that pristine TNRAs has higher resistance than CTNRAs, indicating the loading of CuPc effectively promote the separation of electron and hole and enable high-speed electron transport for water splitting.

The Tafel plot depicts the relationship between the logarithm of the current density (ik) and the over potential (η), which is an important parameter for water spiltting electrocatalysts and can provide important information about electronic enhancement of electrocatalysts activity (Tong et al., 2014). Generally, the decrease in the slope of the curve represents an increased kinetics for PEC oxygen revolution. As shown in **Figure 5D**, the slope of the Tafel curve for TNRAs and CTNRAs is about 405, and 256 mV per decade, respectively. The result show CTNRAs has lower slop value than TNRAs, which can indicate TNRAs has a more sluggish kinetics than CTNRAs.

To validate the mechanism of PEC performance enhancement by CuPc deposition, we compared the cyclic voltamn spectra of TNRAs and CTNRAs, there exist two unconspicuous oxidation peaks located at about 1.3 and 1.8 V vs. RHE in the CV curve of CTNRAs, while there are not any oxidation peaks in the same range in the CV curve of TNRAs (**Figure S13**). Then the LSV curve of CuPc deposited on FTO with that of blank FTO, as shown in **Figure S14A**, the onset potential of CuPc is about 2.01 V vs. RHE, while the onset potential of blank FTO anode is about 2.29 V vs. RHE under the same conditions. Obvious cathodic shift of onset potential about 280 mV is observed, indicating that CuPc has acted as a co-catalyst for electrochemical water oxidation which is coincident with the results of Mott-Schottky. In order to further clarify the detailed process of water oxidation catalyzed by CuPc, the cycle voltammetry (CV) curves were measured and the results was shown in **Figure S14B**. Compared with the CV curve of blank FTO, there appeared two more oxidation peaks located at 1.31 and 1.69 V vs. RHE in the CV curve of CuPc, which could be attributed to the oxidation process of Cu^{2+} to Cu^{3+} and Cu^{3+} to Cu^{4+}, respectively (Zhang et al., 2013). Based on the electrochemical analysis above, a possible mechanism for water-oxidation catalyzed by CuPc was proposed (**Figure 6A**). During the PEC process, a water molecule from solution firstly coordinated to Cu center of CuPc molecule anchored on the surface of the elelctrod to form hydrated copper phthalocyanine (Li et al., 2012). As follows, the resulting $H_2O{=}Cu^{II}$-Pc is oxidized through a PCET to yield a $HO{=}Cu^{III}$-Pc, which can be further oxidized to a $O{=}Cu^{IV}$-Pc by PCET. Next, $O{=}Cu^{IV}$-Pc is attacked by H_2O or OH^- from the electrolyte, correspondingly, and O-O bond can be generated. The process is in accordance with the water nucleophilic attack (WNA) mechanism. HOO-Cu^{II}-Pc is an important intermediate in the peroxide bridge structure, which can be further oxidized to a $^-OO{=}Cu^{IV}$-Pc by PCET, then releases oxygen molecules and the CuPc species restore to the initial state.

Based on the characterizations as mentioned earlier, a possible mechanism for the PEC performance improvement over CTNRAs is proposed as shown in **Figure 6B**. Under simulated sunlight irradiation, photo generated electrons are excited from the valence band (VB) of TiO_2 to its conduction band (CB), leaving holes in VB of TiO_2. Ultimately, electrons pass through the external circuit to the counter electrode and H^+ were reduced to produce H_2. Accordingly, the holes from VB of TiO_2 were consumed by the process in which Cu^{2+} is oxidized to Cu^{3+} and then to Cu^{4+}. In the process of water oxidation, the presence of CuPc derivated species is considered to be a fast redox mediator, which not only reduce the activation energy of PEC water oxidation, but promote effective charge separation as well.

CONCLUSION

In conclusion, through a simple electro-induced assembly method π-conjugated copper phthalocyanine was successfully deposited on the surface of TiO_2 nanorod arrays to form organic-inorganic hybrid nanostructures which were directly grown on the FTO substrate. The obtained hybrid nanostructures can be used as photoanode for PEC water splitting with enhanced performance and good stability. Electrodeposited copper phthalocyanine molecules were proved to act as a co-catalyst for PEC water oxidation rather than a p-type semiconductor to form p-n junction with TiO_2. Detailed mechanism was also proposed based on detailed experiments and analysis. This design establishes a cost-effective surficial assembly strategy to fabricate PEC device with enhanced performance using functional π-conjugated molecules in the field of PEC water splitting, carbon dioxide reduction and other related energy-storing reactions.

AUTHOR CONTRIBUTIONS

YL designed experiments. MY carried out experiments. ZT, NL, and HZ analyzed experimental results. YaL, AZ, and SX analyzed sequencing data and gave helpful discussions to the conclusions. MY and YL wrote the manuscript.

ACKNOWLEDGMENTS

We thank the National Natural Science Foundation of China (21103134, 21675124) and the financial support from Beijing National Laboratory for Molecular Sciences (BNLMS201825) and the ACS key lab of Colloids, interfaces, and Thermal Dynamics. We also thank Prof. Kaiqiang Liu and Mr. Xiangyang Yan (School of Chemistry and Chemical Engineering, Shaanxi Normal University) for their technical supports in TEM and XPS measurements.

SUPPLEMENTARY MATERIAL

The Supplementary Material for this article can be found online at: https://www.frontiersin.org/articles/10.3389/fchem.2019.00334/full#supplementary-material

REFERENCES

Akira, F., and Kenichi, H. (1972). Electrochemical photolysis of water at a semiconductor electrode. *Nature* 238, 37–38. doi: 10.1038/238037a0

Artero, V., Chavarot-Kerlidou, M., and Fontecave, M. (2011). Splitting water with cobalt. *Angew. Chem. Int. Ed. Engl.* 50, 7238–7266. doi: 10.1002/anie.201007987

Bessel, K., Borbush, F., and Mcgloin, M. (2010). Cooperation of charges in photosynthetic O_2 evolution-I. A linear four step mechanism. *Photochem. Photobiol.* 11, 457–475. doi: 10.1111/j.1751-1097.1970.tb06017.x

Bin, L., and Aydil, E. S. (2009). Growth of oriented single-crystalline rutile TiO_2 nanorods on transparent conducting substrates for dye-sensitized solar cells. *J.Am. Chem. Soc.* 131, 3985–3990. doi: 10.1021/ja8078972

Blakemore, J. D., Schley, N. D., David, B., Hull, J. F., Olack, G. W., Incarvito, C. D., et al. (2010). Half-sandwich iridium complexes for homogeneous water-oxidation catalysis. *J. Am. Chem. Soc.* 132, 16017–16029. doi: 10.1021/ja104775j

Chauhan, M., Reddy, K. P., Gopinath, C. S., and Deka, S. (2017). Copper cobalt sulphide nanosheets realizing promising electrocatalytic oxygen evolution reaction. *Acs Catal.* 7, 5871–5879. doi: 10.1021/acscatal.7b01831

Chen, P., Chen, Z., and Liu, M. (2008). Nanotapes formed through the air/water interfacial self-assembly of a bola-form pentanediamide derivative. *Colloid. Surface. A* 313, 666–669. doi: 10.1016/j.colsurfa.2007.04.142

Cherevko, S., Geiger, S., Kasian, O., Kulyk, N., Grote, J. P., Savan, A., et al. (2015). Oxygen and hydrogen evolution reactions on Ru, RuO_2 , Ir, and IrO_2 thin film electrodes in acidic and alkaline electrolytes: a comparative study on activity and stability. *Catal. Today* 262, 170–180. doi: 10.1016/j.cattod.2015.08.014

Cho, I. S., Chen, Z., Forman, A. J., Kim, D. R., Rao, P. M., Jaramillo, T. F., et al. (2011). Branched TiO_2 nanorods for photoelectrochemical hydrogen production. *Nano Lett.* 11, 4978–4984. doi: 10.1021/nl2029392

Ding, C., Shi, J., Wang, Z., and Li, C. (2017). Photoelectrocatalytic water splitting: significance of cocatalysts, electrolyte and interfaces. *Acs Catal.* 7, 675–688. doi: 10.1021/acscatal.6b03107

Du, J., Zhou, G., Zhang, H., Cheng, C., Ma, J., Wei, W., et al. (2013). Ultrathin porous $NiCo_2O_4$ nanosheet arrays on flexible carbon fabric for high-performance supercapacitors. *ACS Appl. Mater. Inter.* 5, 7405–7409. doi: 10.1021/am4017335

Du, P., and Eisenberg, R. (2012). Catalysts made of earth-abundant elements (Co, Ni, Fe) for water splitting: recent progress and future challenges. *Energy Environ. Sci.* 5, 6012–6021. doi: 10.1039/c2ee03250c

Fang, M., Dong, G., Wei, R., and Ho, J. C. (2017). Hierarchical nanostructures: design for sustainable water splitting. *Adv. Energy Mater.* 7:1700559. doi: 10.1002/aenm.201700559

Ferreira, K. N., Iverson, T. M., Maghlaoui, K., Barber, J., and Iwata, S. (2004). Architecture of the photosynthetic oxygen-evolving center. *Science* 303, 1831–1838. doi: 10.1126/science.1093087

Geng, G., Wang, Z., Chen, P., Guan, B., Yang, C., and Liu, M. (2018). Platinized spherical supramolecular nanoassemblies of a porphyrin: facile synthesis and excellent catalytic recyclability. *Phys. Chem. Chem. Phys.* 20, 8488–8497. doi: 10.1039/c8cp00173a

Gibson, L., Wilman, E. N., and Laurance, W. F. (2017). How green is 'green' energy? *Trends. Ecol. Evol.* 32, 922–935. doi: 10.1016/j.tree.2017.09.007

Gong, Y. N., Ouyang, T., He, C. T., and Lu, T. B. (2016). Photoinduced water oxidation by an organic ligand incorporated into the framework of a stable metal-organic framework. *Chem. Sci.* 7, 1070–1075. doi: 10.1039/c5sc02679b

Guo, P., Chen, P., and Liu, M. (2011). Shuttle-like supramolecular nanostructures formed by self-assembly of a porphyrin via an oil/water system. *Nanoscale Res. Lett.* 6, 529–538. doi: 10.1186/1556-276X-6-529

Guo, P., Chen, P., Ma, W., and Liu, M. (2012). Morphology-dependent supramolecular photocatalytic performance of porphyrin nanoassemblies: from molecule to artificial supramolecular nanoantenna. *J. Mater. Chem.* 22, 20243–20249. doi: 10.1039/c2jm33253a

Hang, M. H., Mao, S., Feick, H., Yan, H., Wu, Y., Kind, H., et al. (2001). Room-temperature ultraviolet nanowire nanolasers. *Cheminform* 32, 1897–1899. doi: 10.1126/science.1060367

Haumann, M., Liebisch, P., Muller, C., Barra, M., Grabolle, M., and Dau, H. (2005). Photosynthetic O_2 formation tracked by time-resolved x-ray experiments. *Science* 310, 1019–1021. doi: 10.1126/science.1117551

Jeong, K., Deshmukh, P. R., Park, J., Sohn, Y., and Shin, W. G. (2018). ZnO-TiO_2 core–shell nanowires: a sustainable photoanode for enhanced photoelectrochemical water splitting. *ACS Sustain. Chem. Eng.* 6, 6518–6526. doi: 10.1021/acssuschemeng.8b00324

Jiang, X., Yu, Z., Lai, J., Zhang, Y., Lei, N., Wang, D., et al. (2017). Efficient perovskite solar cells employing a solution-processable copper phthalocyanine as a hole-transporting material. *Sci. China Chem.* 60, 119–126. doi: 10.1007/s11426-016-0393-5

Junya, S., Nobuo, S., Yoko, Y., Kazuhiko, M., Tsuyoshi, T., Kondo, J. N., et al. (2005). RuO_2-loaded beta-Ge_3N_4 as a non-oxide photocatalyst for overall water splitting. *J. Am. Chem. Soc.* 127, 4150–4151. doi: 10.1021/ja042973v

Kumar, D. P., Reddy, N. L., Srinivas, B., Durgakumari, V., Roddatis, V., Bondarchuk, O., et al. (2016). Stable and active Cu_xO/TiO_2 nanostructured catalyst for proficient hydrogen production under solar light irradiation. *Sol. Energ. Mat. Sol. C* 146, 63–71. doi: 10.1016/j.solmat.2015.11.030

Lauinger, S. M., Sumliner, J. M., Yin, Q., Xu, Z., Liang, G., Glass, E. N., et al. (2015). High stability of immobilized polyoxometalates on tio_2 nanoparticles and nanoporous films for robust, light-induced water oxidation. *Chem. Mater.* 27, 5886–5891. doi: 10.1021/acs.chemmater.5b01248

Lee, P. S., and Chen, X. (2014). Nanomaterials for energy and water management. *Small* 10, 3432–3433. doi: 10.1002/smll.201402027

Li, B., Li, F., Bai, S., Wang, Z., Sun, L.i., Yang, Q., et al. (2012). Oxygen evolution from water oxidation on molecular catalysts confined in the nanocages of mesoporous silicas. *Energ. Environ. Sci.* 5, 8229–8233. doi: 10.1039/c2ee22059h

Li, H., Gao, Y., Zhou, Y., Fan, F., Han, Q., Xu, Q., et al. (2016a). Construction and nanoscale detection of interfacial charge transfer of elegant Z-scheme WO_3/Au/In_2S3 nanowire arrays. *Nano Lett.* 16, 5547–5552. doi: 10.1021/acs.nanolett.6b02094

Li, Q., Liu, Y., Guo, S., and Zhou, H. (2017). Solar energy storage in the rechargeable batteries. *Nano Today* 16, 46–60. doi: 10.1016/j.nantod.2017.08.007

Li, Y., Feng, J., Li, H., Wei, X., Wang, R., and Zhou, A. (2016b). Photoelectrochemical splitting of natural seawater withα-Fe_2O_3/WO_3 nanorod arrays. *Int. J. Hydrogen Energy* 41, 4096–4105. doi: 10.1016/j.ijhydene.2016.01.027

Li, Y., Wang, R., Li, H., Wei, X., Feng, J., Liu, K., et al. (2015). Efficient and stable photoelectrochemical seawater splitting with TiO_2@g-C_3N_4 nanorod arrays decorated by Co-Pi. *J. Phys. Chem. C* 119, 20283–20292. doi: 10.1021/acs.jpcc.5b05427

Li, Y., Wei, X., Zhu, B., Wang, H., Tang, Y., Sum, T. C., et al. (2016c). Hierarchically branched Fe_2O_3@TiO_2 nanorod arrays for photoelectrochemical water splitting: facile synthesis and enhanced photoelectrochemical performance. *Nanoscale* 8, 11284–11290. doi: 10.1039/c6nr02430k

Liu, B., Wang, D., Wang, L., Sun, Y., Lin, Y., Zhang, X., et al. (2013). Glutathione-assisted hydrothermal synthesis of CdS-decorated TiO_2 nanorod arrays for quantum dot-sensitized solar cells. *Electrochim. Acta* 113, 661–667. doi: 10.1016/j.electacta.2013.09.143

Liu, L., Ji, Z., Zou, W., Gu, X., Deng, Y., Gao, F., et al. (2013). *In situ* loading transition metal oxide clusters on TiO_2 nanosheets as co-catalysts for exceptional high photoactivity. *Acs Catal.* 3, 2052–2061. doi: 10.1021/cs4002755

Liu, M., Zhang, L., and Wang, T. (2015). supramolecular chirality in self-assembled systems. *Chem. Rev.* 115, 7304–7397. doi: 10.1021/cr500671p

Long, C., Li, X., Guo, J., Shi, Y., Liu, S., and Tang, Z. (2018). Electrochemical reduction of CO_2 over heterogeneous catalysts in aqueous solution: recent progress and perspectives. *Small Method.* 2018:1800369. doi: 10.1002/smtd.201800369

Lu, C., Du, J., Su, X. J., Zhang, M. T., Xu, X., Meyer, T. J., et al. (2016). Cu(II) aliphatic diamine complexes for both heterogeneous and homogeneous water oxidation catalysis in basic and neutral solutions. *Acs Catal.* 6, 77–83. doi: 10.1021/acscatal.5b02173

Ludemann, M., Brumboiu, I. E., Gordan, O. D., and Zahn, D. R. T. (2011). Surface-enhanced Raman effect in ultra-thin CuPc films employing periodic silver nanostructures. *J. Nanopart. Res.* 13, 5855–5861. doi: 10.1007/s11051-011-0564-z

Meyer, T. J., Sheridan, M. V., and Sherman, B. D. (2017). Mechanisms of molecular water oxidation in solution and on oxide surfaces. *Chem. Soc. Rev.* 46, 6148–6169. doi: 10.1039/c7cs00465f

Nepal, B., and Das, S. (2013). Sustained water oxidation by a catalyst cage-isolated in a metal-organic framework. *Angew. Chem. Int. Ed. Engl.* 52, 7224–7227. doi: 10.1002/anie.201301327

Ogunsipe, A., and Nyokong, T. (2004). Effects of substituents and solvents on the photochemical properties of zinc phthalocyanine complexes and their protonated derivatives. *J Mol Struct. J. Mol. Struct.* 689, 89–97. doi: 10.1016/j.molstruc.2003.10.024

Osterloh, F. E. (2013). Inorganic nanostructures for photoelectrochemical and photocatalytic water splitting. *Chem. Soc. Rev.* 42, 2294–2320. doi: 10.1039/c2cs35266d

Qiu, Y., Chen, P., and Liu, M. (2010). Evolution of various porphyrin nanostructures via an oil/aqueous medium: controlled self-assembly, further organization, and supramolecular chirality. *J. Am. Chem. Soc.* 132, 9644–9652. doi: 10.1021/ja1001967

Ran, J., Zhang, J., Yu, J., Jaroniec, M., and Qiao, S. Z. (2014). Earth-abundant cocatalysts for semiconductor-based photocatalytic water splitting. *Chem. Soc. Rev.* 43, 7787–7812. doi: 10.1039/c3cs60425j

Seh, Z. W., Kibsgaard, J., Dickens, C. F., Chorkendorff, I., Nørskov, J. K., and Jaramillo, T. F. (2017). Combining theory and experiment in electrocatalysis: insights into materials design. *Science* 355, 4998–5013. doi: 10.1126/science.aad4998

Shi, T., Duan, Y., Lv, K., Hu, Z., Li, Q., Li, M., et al. (2018). Photocatalytic oxidation of acetone over high thermally stable TiO_2 nanosheets with exposed (001) facets. *Front. Chem.* 6:175. doi: 10.3389/fchem.2018.00175

Su, J., Xue, M., Ma, N., Sheng, Q., Zhang, Q., and Liu, Y. (2009). Dissolution of copper phthalocyanine and fabrication of its nano-structure film. *Sci. China Ser. B* 52, 911–915. doi: 10.1007/s11426-009-0021-3

Su, X. J., Gao, M., Jiao, L., Liao, R. Z., Siegbahn, P. E., Cheng, J. P., et al. (2015). Electrocatalytic water oxidation by a dinuclear copper complex in a neutral aqueous solution. *Angew. Chem. Int. Ed. Engl.* 54, 4909–4914. doi: 10.1002/anie.201411625

Tang, R., Zhou, S., Yuan, Z., and Yin, L. (2017). Metal-organic framework derived Co_3O_4/TiO_2 /Si heterostructured nanorod array photoanodes for efficient photoelectrochemical water oxidation. *Adv. Funct. Mater.* 27:1701102. doi: 10.1002/adfm.201701102

Terao, R., Nakazono, T., Parent, A. R., and Sakai, K. (2016). Photochemical water oxidation catalysed by a water-soluble copper phthalocyanine. *Chempluschem* 81, 1064–1067. doi: 10.1002/cplu.201600263

Tong, X., Yang, P., Wang, Y., Qin, Y., and Guo, X. (2014). Enhanced photoelectrochemical water splitting performance of TiO_2 nanotube arrays coated with an ultrathin nitrogen-doped carbon film by molecular layer deposition. *Nanoscale* 6, 6692–6700. doi: 10.1039/c4nr00602j

Wang, H., Bai, Y., Wu, Q., Zhou, W., Zhang, H., Li, J., et al. (2011). Rutile TiO_2 nano-branched arrays on FTO for dye-sensitized solar cells. *Phys. Chem. Chem. Phys.* 13, 7008–7013. doi: 10.1039/c1cp20351g

Wang, H., Yang, Y., and Guo, L. (2016). Nature-inspired electrochemical energy-storage materials and devices. *Adv. Energy Mater.* 7:1601709. doi: 10.1002/aenm.201601709

Wang, X., Duan, P., and Liu, M. (2014). Self-assembly of pi-conjugated gelators into emissive chiral nanotubes: emission enhancement and chiral detection. *Chem. Asian. J.* 9, 770–778. doi: 10.1002/asia.201301518

Xiao, F. X., Miao, J., Tao, H. B., Hung, S. F., Wang, H. Y., Yang, H. B., et al. (2015). One-dimensional hybrid nanostructures for heterogeneous photocatalysis and photoelectrocatalysis. *Small* 11, 2115–2131. doi: 10.1002/smll.201402420

Yang, J., Li, W., Li, J., Sun, D., and Chen, Q. (2012). Hydrothermal synthesis and photoelectrochemical properties of vertically aligned tungsten trioxide (hydrate) plate-like arrays fabricated directly on FTO substrates. *J. Mater. Chem.* 22, 17744–17752. doi: 10.1039/c2jm33199c

Yao, L., Wang, W., Wang, L., Liang, Y., Fu, J., and Shi, H. (2018). Chemical bath deposition synthesis of TiO_2/Cu-$_2$O core/shell nanowire arrays with enhanced photoelectrochemical water splitting for H_2 evolution and photostability. *Sci. Direct* 43, 15907–15917. doi: 10.1016/j.ijhydene.2018.06.127

Yin, Y., Ma, N., Xue, J., Wang, G., Liu, S., Li, H., et al. (2019). Insights into the role of poly(vinylpyrrolidone) in the synthesis of palladium nanoparticles and their electrocatalytic properties. *Langmuir* 35, 787–795. doi: 10.1021/acs.langmuir.8b04032

Yoon, K. R., Ko, J. W., Youn, D.-Y., Park, C. B., and Kim, D. (2015). Synthesis of Ni-based co-catalyst functionalized W:$BiVO_4$ nanofibers for solar water oxidation. *Green Chem.* 18, 944–950. doi: 10.1039/C5GC01588J

Youn, D. H., Park, Y. B., Kim, J. Y., Magesh, G., Jang, Y. J., and Lee, J. S. (2015). One-pot synthesis of NiFe layered double hydroxide/reduced graphene oxide composite as an efficient electrocatalyst for electrochemical and photoelectrochemical water oxidation. *J. Power Sources* 294, 437–443. doi: 10.1016/j.jpowsour.2015.06.098

Zhang, K., Wang, L., Sheng, X., Ma, M., Jung, M. S., Kim, W., et al. (2016). Tunable bandgap energy and promotion of H_2O_2 oxidation for overall water splitting from carbon nitride nanowire bundles. *Adv. Energy Mater.* 6:1502352. doi: 10.1002/aenm.201502352

Zhang, L., Yang, C., Xie, Z., and Wang, X. (2017). Cobalt manganese spinel as an effective cocatalyst for photocatalytic water oxidation. *App. Catal. B Environ.* 224,886–894. doi: 10.1016/j.apcatb.2017.11.023

Zhang, M. T., Chen, Z., Kang, P., and Meyer, T. J. (2013). Electrocatalytic water oxidation with a copper(II) polypeptide complex. *J. Am. Chem. Soc.* 135, 2048–2051. doi: 10.1021/ja3097515

Zhang, P., Zhang, J., and Gong, J. (2014). Tantalum-based semiconductors for solar water splitting. *Chem. Soc. Rev.* 43, 4395–4422. doi: 10.1039/c3cs60438a

Zhang, R., Ren, X., Shi, X., Xie, F., Zheng, B., Guo, X., et al. (2018). Enabling effective electrocatalytic N_2 conversion to NH_3 by the TiO_2 nanosheets array under ambient conditions. *ACS Appl. Mater. Inter.* 10, 28251–28255. doi: 10.1021/acsami.8b06647

Zhang, Y., Chen, P., Ma, Y., He, S., and Liu, M. (2009). Acidification and assembly of porphyrin at an interface: counterion matching, selectivity, and supramolecular chirality. *ACS Appl. Mater. Inter.* 1, 2036–2043. doi: 10.1021/am900399w

Zhang, Y., Zhang, H., Liu, A., Chen, C., Song, W., and Zhao, J. (2018). Rate-limiting o-o bond formation pathways for water oxidation on hematite photoanode. *J. Am. Chem. Soc.* 140, 3264–3269. doi: 10.1021/jacs.7b10979

Zhao, H., Dai, Z., Xu, X., Pan, J., and Hu, J. (2018a). Integrating semiconducting catalyst of ReS_2 nanosheets into P-silicon photocathode for enhanced solar water reduction. *ACS Appl. Mater. Inter.* 10, 23074–23080. doi: 10.1021/acsami.8b04740

Zhao, H., Tang, Z., Sun, J., Lowe, S. E., Zhang, L., and Wang, Y. (2018b). Ultrathin nitrogen-doped holey carbon @ graphene bifunctional electrocatalyst for oxygen reduction and evolution reactions in alkaline and acidic media. *Angew. Chem.*130, 16749–16753. doi: 10.1002/anie.201811573

Zheng, D., Gao, Z., He, X., Zhang, F., and Liu, L. (2004). Surface and interface analysis for copper phthalocyanine (CuPc) and indium-tin-oxide (ITO) using X-ray photoelectron spectroscopy (XPS). *Spectrosc. Spect. Anal.* 211, 24–30. doi: 10.1016/S0169-4332(02)01333-8

Zhou, L. L., Fang, T., Cao, J. P., Zhu, Z. H., Su, X. T., and Zhan, S. Z. (2015). A dinuclear copper(II) electrocatalyst both water reduction and oxidation. *J. Power Sources* 273, 298–304. doi: 10.1016/j.jpowsour.2014.09.075

Zhu, M., Chen, P., and Liu, M. (2011). Graphene oxide enwrapped Ag/AgX (X = Br, Cl) nanocomposite as a highly efficient visible-light plasmonic photocatalyst. *ACS Nano* 5, 4529–4536. doi: 10.1021/nn200088x

Conflict of Interest Statement: The authors declare that the research was conducted in the absence of any commercial or financial relationships that could be construed as a potential conflict of interest.

frontiers in Chemistry

REVIEW
published: 15 May 2019
doi: 10.3389/fchem.2019.00336

Functional Supramolecular Gels Based on the Hierarchical Assembly of Porphyrins and Phthalocyanines

Xuenan Feng, Chenxi Liu, Xiqian Wang, Yuying Jiang, Gengxiang Yang, Rong Wang, Kaishun Zheng, Weixiao Zhang, Tianyu Wang and Jianzhuang Jiang**

Beijing Key Laboratory for Science and Application of Functional Molecular and Crystalline Materials, Department of Chemistry, University of Science and Technology Beijing, Beijing, China

Supramolecular gels containing porphyrins and phthalocyanines motifs are attracting increased interests in a wide range of research areas. Based on the supramolecular gels systems, porphyrin or phthalocyanines can form assemblies with plentiful nanostructures, dynamic, and stimuli-responsive properties. And these π-conjugated molecular building blocks also afford supramolecular gels with many new features, depending on their photochemical and electrochemical characteristics. As one of the most characteristic models, the supramolecular chirality of these soft matters was investigated. Notably, the application of supramolecular gels containing porphyrins and phthalocyanines has been developed in the field of catalysis, molecular sensing, biological imaging, drug delivery and photodynamic therapy. And some photoelectric devices were also fabricated depending on the gelation of porphyrins or phthalocyanines. This paper presents an overview of the progress achieved in this issue along with some perspectives for further advances.

Keywords: supramolecular assembly, supramolecular gels, porphyrins, phthalocyanine, π-conjugated systems, functional soft matters

OPEN ACCESS

Edited by:
Penglei Chen,
Institute of Chemistry (CAS), China

Reviewed by:
Shuo Bai,
Institute of Process Engineering (CAS), China
Kaiqiang Liu,
Shaanxi Normal University, China
Weihua Zhu,
Jiangsu University, China

****Correspondence:***
Tianyu Wang
twang@ustb.edu.cn
Jianzhuang Jiang
jianzhuang@ustb.edu.cn

Specialty section:
This article was submitted to Supramolecular Chemistry, a section of the journal Frontiers in Chemistry

Received: *14 February 2019*
Accepted: *25 April 2019*
Published: *15 May 2019*

Citation:
Feng X, Liu C, Wang X, Jiang Y, Yang G, Wang R, Zheng K, Zhang W, Wang T and Jiang J (2019) Functional Supramolecular Gels Based on the Hierarchical Assembly of Porphyrins and Phthalocyanines. Front. Chem. 7:336. doi: 10.3389/fchem.2019.00336

INTRODUCTION

Supramolecular gels (Steed, 2010; Buerkle and Rowan, 2012; Smith, 2012; Yu et al., 2013), in which organic molecules self-assemble into nano/microstructures and immobilize the solvents (**Figure 1A**), are attracting increased interests in different fields (Edwards and Smith, 2014; Shen et al., 2015; Kaufmann et al., 2016). Depending on the solvent included into the gels systems, the supramolecular gels can be either hydrogels or organogels. As the soft matters depending on non-covalent interactions, supramolecular gels not only show very nice dynamic, reversible and stimuli-responsive nature (Foster et al., 2010; Zhao et al., 2013; Wang et al., 2015a, 2018), but also have versatile applications in the field of life and materials sciences (Bhattacharya and Samanta, 2016; Goujon et al., 2017; Yang et al., 2017; Das et al., 2018). Based on the self-assembly of various molecular systems, supramolecular gels with delicate structures have been designed and developed (Yu et al., 2014; Silverman et al., 2017; Mallia and Weiss, 2018). One of the most important advantages of supramolecular gels can be their capability of incorporating different functional motifs via varied, sometimes very simple processes (Buerkle and Rowan, 2012). For example, the fabrication of supramolecular gels containing π-conjugated systems can be either from the synthesis and subsequent self-assembly of π-conjugated gelators or the co-assembly

within carefully designed multicomponent gelating systems, wherein π-conjugated functional groups can be included by using simple molecular building blocks (Bhattacharya and Samanta, 2016).

Tetrapyrrole macrocycle based π-conjugated systems, such as porphyrin and phthalocyanine derivatives (**Figure 1B**), are very famous rigid and aromatic molecular building blocks with special electronic structures (Buchler and Ng, 2000; Mack and Stillman, 2003). Porphyrin is one of the most important natural pigments, which sets up the basis of hemoglobin and chloroplasts, realizes many significant functions, from carrying oxygen to photosynthesis (Drain et al., 2009; Severance and Hamza, 2009; Kundu and Patra, 2017). Both porphyrin and phthalocyanine derivatives have distinctive photophysical, photochemical and electrochemical properties (Bian et al., 2011; Lauceri et al., 2011; Hasobe, 2014). And the application of these tetrapyrrole macrocycle based π-conjugated systems have been developed in the field of catalysis (Feiters et al., 2000; Zhang et al., 2017), molecular sensing (Paolesse et al., 2017), organic semiconductor (Jiang et al., 2018), solar cells (Urbani et al., 2014), and photodynamic therapy (Liu et al., 2013; Giuntini et al., 2014; Moylan et al., 2015; Chen et al., 2017; Li et al., 2018a; Zhu et al., 2018). It is conceivable that these different functions should be dependent on both the molecular structures and supramolecular architectures of porphyrin and phthalocyanine derivatives. Especially, the systems derived from the hierarchical assembly of porphyrins and phthalocyanines are becoming more and more important. For the achievement of so many applications, the cooperative organization of molecular building blocks plays very important role (Guo et al., 2014; Zhao et al., 2014; Zhang et al., 2015; Geng et al., 2017, 2018; Yang et al., 2018c; Chang et al., 2019; Li et al., 2019b). And supramolecular gels with plentiful nanostructures and properties can be good carriers for the fabrication of porphyrin and phthalocyanine assemblies. Moreover, based on supramolecular gels, the porphyrin and phthalocyanine assemblies with stimuli-responsive and dynamic properties can also be expected. Most importantly, the good biocompatible nature of supramolecular gels has been demonstrated, which guarantee the biomedical applications of porphyrin and phthalocyanine assemblies.

Although the advantages of supramolecular gels based on the assembly of porphyrins and phthalocyanines are distinct, building these systems has been demonstrated to be not easy. This situation is partly due to the difficulty of the synthesis of gelators containing porphyrin or phthalocyanine motifs (Ishi-i and Shinkai, 2005). Especially, the modification of phthalocyanine rings with typical functional groups for gelation, for example cholesterol, sugar and amino acids (Weiss and Terech, 2006; Weiss, 2018), is difficult. And the synthesis of porphyrin derivatives may also be confronted with some serious barriers, such as low yield, limitations on preparative scale, and difficulties in purification. On the other hand, even though introducing porphyrin or phthalocyanine motifs into supramolecular gels can be totally dependent on the hierarchical self-assembly, the network of complex non-covalent interactions and possible phase separation (Tanaka et al., 2012; Helmich and Meijer, 2013) within multicomponent supramolecular gels still should be considered. This strategy also requires carefully molecular designing to form delicate supramolecular assemblies.

In this manuscript, we will focus on the works about the construction and functions of supramolecular gels containing porphyrin and phthalocyanine derivatives. And the functions and typical applications of these systems depict a very good prospect for the further development. The supramolecular gels containing π-conjugated systems have many common characters like that of general low-molecular-weight gels. Certainly, porphyrin or phthalocyanine derivatives also can afford supramolecular gels with many new features, which expand the application of these soft matters. The gelation usually needs chiral component to be included (Weiss and Terech, 2006). However, the supramolecular gels containing only achiral molecules were also developed (Shen et al., 2015). Therefore, the supramolecular chirality of these gels systems was addressed in the paper. The mechanical properties of supramolecular gels can be changed upon the variation of gelator substituents, which were investigated in the gels systems containing porphyrin and phthalocyanines. In addition to supramolecular gels containing porphyrin and phthalocyanine derivatives, some interesting works on the polymer gels (**Figure 3G**) related with porphyrin or phthalocyanine assemblies were also included in this review. Comparing with supramolecular gels, polymer gels can be much more stable but may lack of some dynamic features. However, the polymer gels have been widely applicated in many fields, which also plays a leading role for the further development of supramolecular gels. Nonetheless, polymer gels containing porphyrin and phthalocyanine molecules also show some distinctive features.

CONSTRUCTING SUPRAMOLECULAR GELS CONTAINING PORPHYRIN OR PHTHALOCYANINE MOLECULES

In principle, there are two strategies for introducing porphyrin and phthalocyanine derivatives into supramolecular gels. The fundamental method can be the synthesis of gelators containing porphyrin and phthalocyanine motifs. In this case, the self-assembly of these π-conjugated systems can form supramolecular gels. Another process for constructing porphyrin/phthalocyanine based supramolecular gels is not dependent on the porphyrin and phthalocyanine based gelators. Thus, even though porphyrin and phthalocyanine molecules themselves cannot form supramolecular gels, these π-conjugated molecules still can be included into the supramolecular gels via the hierarchical co-assembly of different components or just by simple mixing. The realization of this approach depends on the unique characteristics of supramolecular gels.

Porphyrin or Phthalocyanine Gelators

The systematic research on the synthesis of porphyrin-based gelators is from Shinkai group. They have developed several types of gelators by introducing cholesterol, chiral urea groups or sugar substituents onto the phenyl groups of tetraphenylporphyrins (TPP) derivatives.

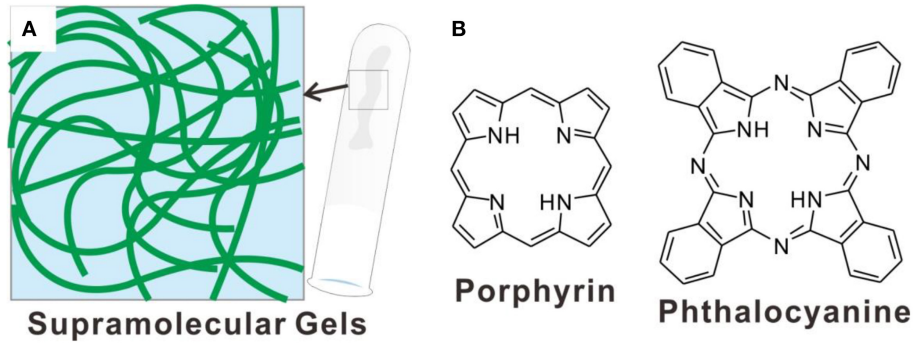

FIGURE 1 | (A) Schematic illustration showing nanostructures of typical supramolecular gels; **(B)** molecular structures of porphyrin and phthalocyanine.

For example, they have synthesized zinc porphyrin appended cholesterol derivatives (**1**) (**Figure 2A**), and found that the gelation of these porphyrins are dependent on the odd or even carbon numbers in the spacer $(CH_2)_n$, which connects the porphyrin moiety with the cholesterol groups. After adding fullerene C_{60} into the systems, the intermolecular Zn(II) porphyrin-fullerene interaction can enhance the gelation abilities of the corresponding porphyrin gelators (**Figure 2A**) (Ishi-i et al., 2001). Many chiral substituents associated with natural molecules have been introduced onto the porphyrin rings to synthesize porphyrin-based gelators. For instance, some brucine-appended porphyrins have been demonstrated to be nice gelators (Setnicka et al., 2002). Porphyrin gelators based on sugar substituents, which could be amphiphilic porphyrin bearing four β-D-galactopyranoside groups at its periphery (**2**) (**Figure 2B**), have been synthesized and studied (Tamaru et al., 2001). Compound **2** assembles into very stable organogels in DMF/alcohol mixture. The SEM and TEM measurements on the corresponding gels suggest that the self-assembly of this sugar-based porphyrin could form helical nanofibers (**Figure 2C**), wherein the π-π interactions between porphyrin rings and the hydrogen-bonding among sugar moieties could operate cooperatively.

Notably, for the study of porphyrin-based gelators, the co-assembly with fullerene C_{60} has attracted a lot of attention. Shinkai et al. have synthesized porphyrin bearing eight amide moieties (**3**) (**Figure 2D**). The cooperative non-covalent interactions including π-π interaction between porphyrin rings and the hydrogen-bonding between amide groups result in the gelation. While adding fullerene C_{60} into the systems could create one-dimensional multicapsular structures, which can be supramolecular polymer showing fibrous structures (**Figures 2E,F**). Both porphyrin-C_{60} interaction and hydrogen-bonding play very important role (Shirakawa et al., 2003a).

The hydrogen-bonding interactions always plays very important role for the gelation of different porphyrin-based gelators. By changing the position of amide groups around porphyrin rings, the aggregation of porphyrin building blocks can be changed from J-aggregation into H-aggregation (Shirakawa et al., 2003b). Depending on the strong hydrogen-bonding interactions from several amide groups close to each other, the porphyrins without distinct hydrophilic substituents can also form organogels. Ihara and his co-workers have synthesized porphyrins (**4**, **5**) substituted by didodecyl L-glutamic acid. These porphyrin molecules can be either derived from protoporphyrin IX (**4**) or TPP based porphyrin (**5**) (**Figure 2G**). These L-glutamide-functionalized porphyrin derivatives self-assemble into organogels with fibrous nanostructures. Interestingly, the packing modes of porphyrin molecules can be modulated from H-aggregation to J-aggregation with the variation of handedness of supramolecular chirality upon changing the solvent, concentration and temperature (**Figure 2H**) (Sagawa et al., 2002; Jintoku et al., 2008).

The asymmetric porphyrin containing both carboxylic acid and pyridine substituents (**6**) shows much better gelation properties in different organic solvents, compared with that of symmetrical reference porphyrins bearing two pyridyl substituents (**8**) or two carboxylic acid groups (**7**) (**Figure 2I**). In cyclohexane, the π-π interactions between porphyrin rings and the carboxylic acid-pyridine hydrogen bonding work cooperatively and render porphyrin **6** self-assemble into two-dimensional sheet-like structures (Tanaka et al., 2005).

Moreover, the porphyrin containing both host and guest motifs can form oganogels based on host-guest interactions. Stoddart and his co-workers have synthesized porphyrin derivative with pillar[5]arene and viologen at its 5- and 15-meso positions (**9**). The host-guest interactions between pillar[5]arenes and viologen could render the porphyrin to assemble into linear supramolecular polymer with head-to-tail manner (**Figure 3A**), which further form organogels at relatively higher concentrations (Fathalla et al., 2015).

Some porphyrin dimmers were also developed as supramolecular gelators. For example, the porphyrin-azulene-porphyrin conjugate (**10**) can form organogels in different organic solvents, while the corresponding monomer (**11**) self-assemble into vesicles in chloroform/methanol mixture (**Figure 3B**). For the self-assembly of porphyrin dimmer and monomer, the intermolecular dipole–dipole interaction of the azulene units plays very important role (**Figure 3C**) (Xiao et al., 2009).

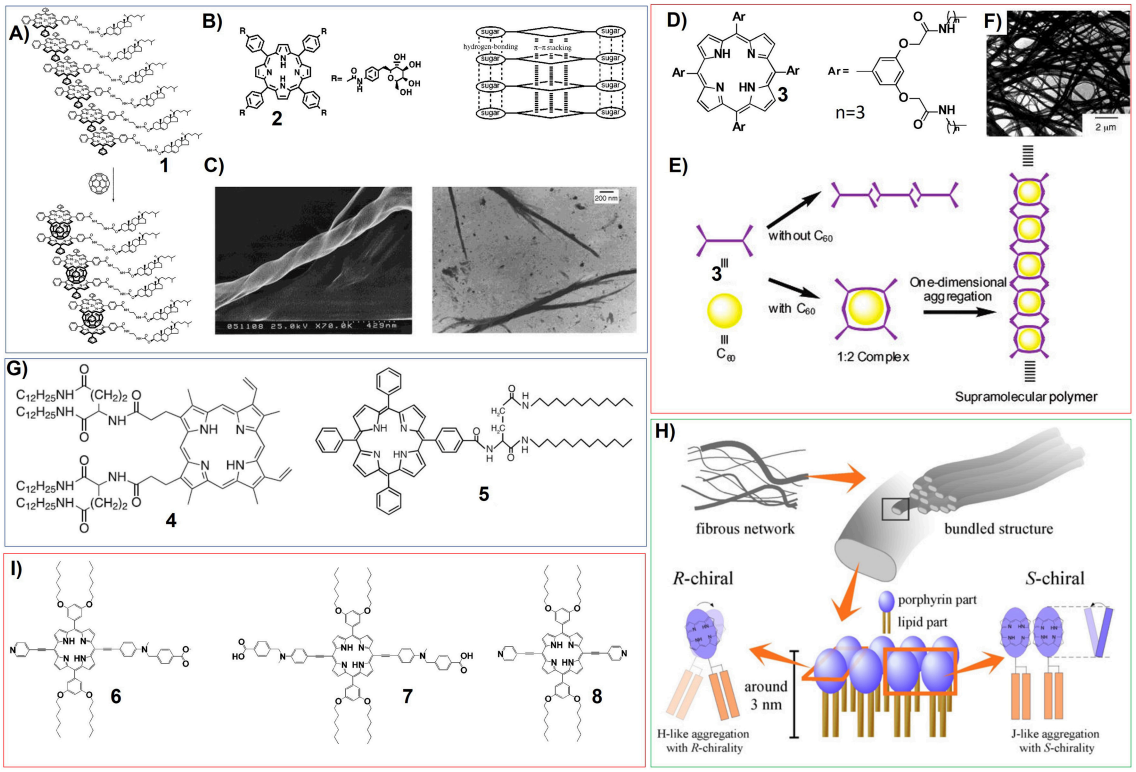

FIGURE 2 | (A) Porphyrin appended cholesterol derivatives (1) can interact with fullerene C_{60} to form a 2:1 Zn(II) porphyrin/C_{60} sandwich complex; Reprinted with permission from Ishi-i et al. (2001). Copyright 2001 American Chemical Society. **(B)** Molecular structures of porphyrin bearing four β-D-galactopyranoside groups (2), and schematic illustration showing the molecular packing mode; Reprinted with permission from Tamaru et al. (2001). Copyright 2001 American Chemical Society. **(C)** SEM (left) and TEM (right) pictures of the xerogel of porphyrin 2; Reprinted with permission from Tamaru et al. (2001). Copyright 2001 American Chemical Society. **(D)** Molecular structures of porphyrin bearing eight amide moieties (3); Reprinted with permission from Shirakawa et al. (2003a). Copyright 2003 American Chemical Society. **(E)** Schematic illustration showing the self-assembly of porphyrin 3 as well as the co-assembly of porphyrin 3 with C_{60}; Reprinted with permission from Shirakawa et al. (2003a). Copyright 2003 American Chemical Society. **(F)** TEM image of porphyrin 3 co-assembly with 0.50 equiv of C_{60}; Reprinted with permission from Shirakawa et al. (2003a). Copyright 2003 American Chemical Society. **(G)** Molecular structures of porphyrin bearing didodecyl L-glutamic acid; **(H)** Schematic proposal on the ordered structure in the 5 aggregates; Reprinted with permission from Jintoku et al. (2008). Copyright 2008 Elsevier Ltd. **(I)** Molecular structures of porphyrin containing carboxylic acid and pyridine substituents.

Different from porphyrin-based molecular building blocks, phthalocyanine molecules usually have better planarity, which introduces stronger π-π interactions and serious aggregation (Chen et al., 2009; Gao et al., 2009). And the modification of the periphery of phthalocyanine rings is more difficult, compared with that of porphyrin derivatives. Nevertheless, some intelligent molecular design was also performed on the phthalocyanine gelators, which show some interesting characteristics.

Nolte and his co-workers have synthesized phthalocyanine containing crown ethers substituents and eight hydrophobic chiral tails (**12**) (**Figure 3D**). This phthalocyanine can form gels in chloroform upon self-assembly into helical fibers. The further investigations show that the molecular packing mode of phthalocyanine **12** containing (S)-chiral centers could follow a typical hierarchical process. Firstly, the stacking of phthalocyanine 12 along clockwise orientation forms the fibers with right-handed helicity. And then, coiled-coil interactions between different right-handed helical fibers could form large aggregates with left-handed helicity (**Figure 3D**) (Engelkamp et al., 1999).

Due to the strong π-π interactions between phthalocyanine molecules, some very simple phthalocyanine molecules were also found to form organogels. For example, tetra-n-butyl peripheral substituted copper(II) phthalocyanine (**13**) can form organogels in 1,2-dichlorobenzene upon ultrasonication (**Figure 14C**) (Xu et al., 2016).

For the fabrication of phthalocyanine-based soft matters, polymer gels have been employed. And the polymers containing phthalocyanine motifs have been developed. For example, the reaction between zinc phthalocyanine conjugated poly(ethylene glycol) (PEG) and ε-caprolactone produces a type of copolymer (**14**), which could form hydrogels (Dong et al., 2016a). And the zinc phthalocyanine conjugated poly(ethylene glycol) (PEG) with hydroxyl groups at the end can also be connected with alginate (**15**). Copolymer **15** can form hydrogels, which show near infrared fluorescence (Liang et al., 2017a; **Figure 3E**). Actually, poly(ethylene glycol) (PEG) substituents were often utilized for

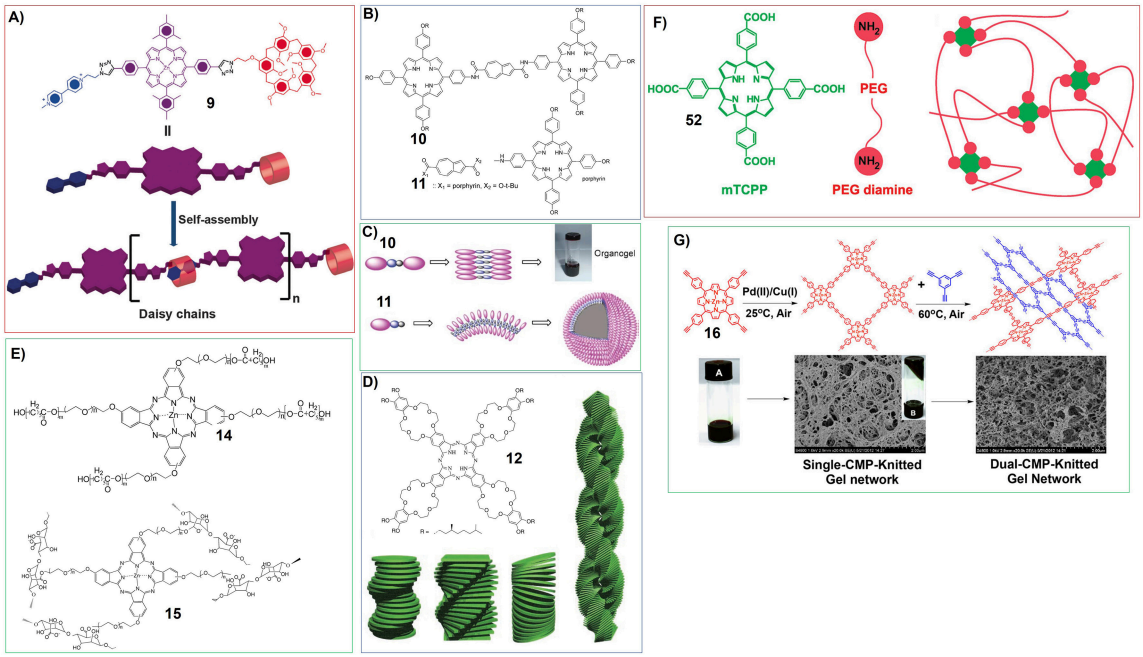

FIGURE 3 | (A) Molecular structure and proposed self-assembly of porphyrin 9 to form linear supramolecular polymers; Reprinted with permission from Fathalla et al. (2015). Copyright 2015 Royal Society of Chemistry. **(B)** Molecular structures of porphyrin-azulene-porphyrin conjugate (10) and porphyrin-azulene conjugate (11); **(C)** Proposed mode for the formation of nanowire from 10 and vesicles from 11; Reprinted with permission from Xiao et al. (2009). Copyright 2009 Royal Society of Chemistry. **(D)** Molecular structures of phthalocyanine gelator containing crown ethers substituents and eight hydrophobic chiral tails (12) and schematic illustration showing helical aggregation formed by 12, the coiled-coil interactions introduce right-handed helical fibers form large aggregates with left-handed helicity; Reprinted with permission from Engelkamp et al. (1999). Copyright 1999 American Association for the Advancement of Science. **(E)** Molecular structures of zinc phthalocyanine polymeric gelator (14, 15); **(F)** Schematic illustration showing the reaction between PEG diamine and meso-tetrakis(4-carboxyphenyl) porphine (mTCPP) form polymer hydrogels; Reprinted with permission from Lovell et al. (2011). Copyright 2011 American Chemical Society. **(G)** Porphyrin based mesoporous polymers can uptake organic solvents to form organogels (Wu et al., 2014). Reprinted with permission from Wu et al. (2014). Copyright 2014 American Chemical Society.

building porphyrins and phthalocyanines polymeric hydrogels. For instance, the reaction between PEG diamine and meso-tetrakis(4-carboxyphenyl) porphine (mTCPP) could form stable polymer hydrogels (Lovell et al., 2011; **Figure 3F**).

Multicomponent Supramolecular Gels Containing Porphyrin or Phthalocyanine Molecules

The supramolecular gels containing porphyrin or phthalocyanine building blocks were also fabricated by using multicomponent systems (Cornwell et al., 2015; Draper et al., 2015; Kar and Ghosh, 2015; Versluis et al., 2016). In general, these multicomponent supramolecular gels can be divided into two types. One is the special supramolecular gels in which the gelators can be some co-assemblies including porphyrin/phthalocyanine molecular building blocks. While another type of supramolecular gels is not dependent on the assembly of porphyrin/phthalocyanine molecules. These π-conjugated molecules can be mixed into supramolecular gels formed by other different gelators. Certainly, this simple "mixing" strategy requests relatively stable supramolecular gels with tolerant features. Otherwise adding additional porphyrin/phthalocyanine molecules into the systems could destroy the supramolecular gels. And the interactions between mixed porphyrin/phthalocyanine molecules and gelators should be considered. Depending on the solvents included into the supramolecular gels, these mixed porphyrin/phthalocyanine molecules either can be dissolved into the liquid phase or form aggregations within the gels systems. Even though the solubility of porphyrin/phthalocyanine components and complex non-covalent interactions should be considered, the advantage of this simple "mixing" approach is still obvious. Thus, porphyrin and phthalocyanine with different molecular structures can be included into the supramolecular gels.

Only little works were performed on the development of porphyrin or phthalocyanine molecules as the complementary ingredient for the formation of gelators. Considering the difficulty involved in the synthesis processes, sometimes synthesis of porphyrin/phthalocyanine based gelators should be easier than that of developing complementary molecular pairs. What is worth noticing is α-cyclodextrin (α-CD), which help the amphiphilic porphyrin-cored, star-shaped poly (e-caprolactone)-b-poly (ethylene glycol) (SPPCL-b-PEG) copolymer (**17**) form thixotropic and reversible supramolecular hydrogels (**Figure 9A**; Jin et al., 2015). Moreover, hydrogel nanocomposites systems were also fabricated by using the co-assembly of α-cyclodextrin, PEG-conjugated porphyrin, and multi-walled carbon nanotubes

(**Figure 7C**; Liang et al., 2017b). By connecting α-cyclodextrin with photothermal dyes and further co-assemble with PEG-conjugated porphyrins, photothermally controllable, visible, dual fluorescent thermosensitive hydrogels were developed (Yang et al., 2018a). Except for porphyrin derivatives, cyclodextrin was also applied for the gelation of phthalocyanine systems. For example, multi-photoresponsive supramolecular hydrogels have been developed by mixing poly-β-cyclodextrin polymer, hydrophobically modified dextran, zinc phthalocyanine, and a tailored nitric oxide photodonor (**Figure 10A**; Fraix et al., 2014).

For another type of supramolecular gel based on complementary phthalocyanine, both the phthalocyanine molecules and their complemental molecular systems have gelation substituents. The thermoreversible organogels were prepared by using combination of low-molecular-weight organogelators (**18**, **19**) and zinc phthalocyanine moieties

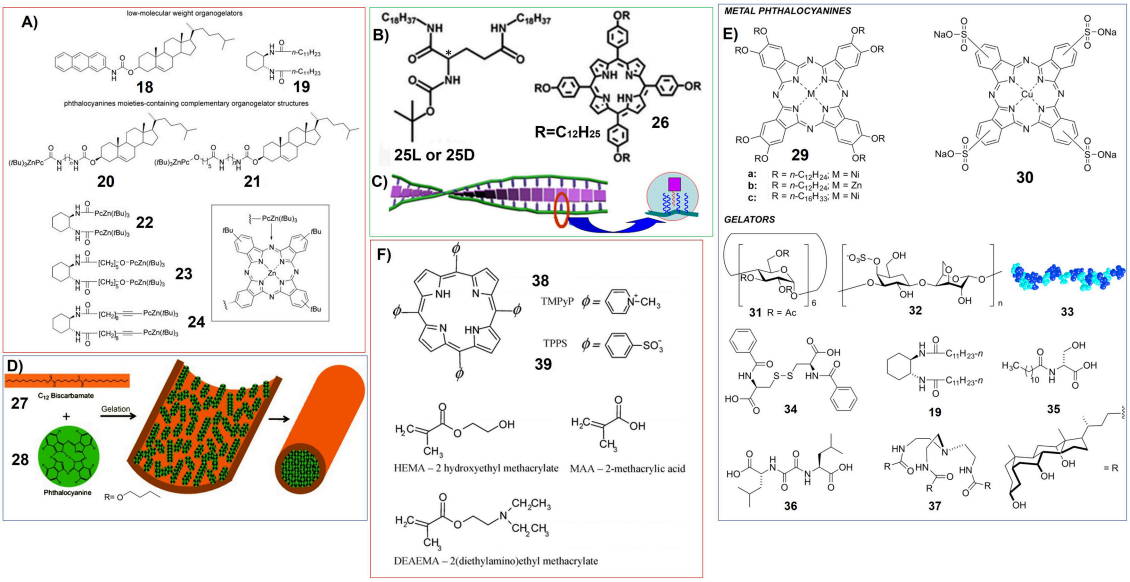

FIGURE 4 | (A) Molecular structures of organogelators (18, 19) and zinc phthalocyanine containing complementary organogelators (20-24); Reprinted with permission from Díaz et al. (2008). Copyright 2008 John Wiley and Sons. **(B)** Molecular structures of glutamic acid-based gelators (25) and achiral porphyrin with long alkyl chains (26); **(C)** Schematic illustration showing the formation of induced supramolecular chirality of 26 upon the gelation with 25; Reprinted with permission from Li et al. (2007). Copyright 2007 Royal Society of Chemistry. **(D)** Schematic illustration showing the encapsulation of phthalocyanine (28) in the hollow tubes of biscarbamate (27) gels.; Reprinted with permission from Khan and Sundararajan (2011). Copyright 2011 John Wiley and Sons. **(E)** Structures of metallo-phthalocyanines and gelator molecules. 33 is the schematic structure of a protein which can form hydrogels.; **(F)** Molecular structures of charged porphyrins (38, 39) and monomers used for making polymer hydrogels.

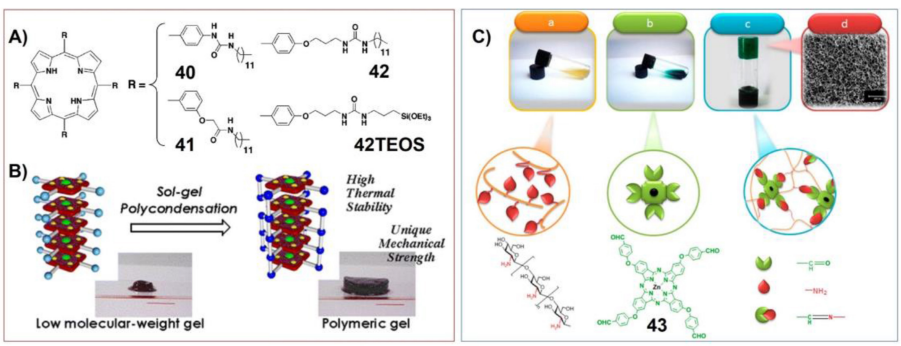

FIGURE 5 | (A) Molecular structures of porphyrin gelators containing triethoxysilyl substituents; **(B)** schematic illustration showing the sol-gel polycondensation of the peripheral triethoxysilyl groups of porphyrin-based gelators, which change supramolecular gels into organic/inorganic hybrid materials with unique mechanical strength; Reprinted with permission from Kishida et al. (2005b). Copyright 2005 American Chemical Society. **(C)** Photograph and chemical structure of (a) chitosan and (b) zinc phthalocyanine containing tetra-aldehyde substituents (43) before gelation. (c) Photograph and schematic of a proposed structure of the phthalocyanine/chitosan hydrogel through Schiff-based reaction. (d) Pore size of 3D porous nanostructure phthalocyanine/chitosan hydrogel. Reprinted with permission from Karimi and Khodadadi (2016). Copyright 2016 American Chemical Society.

containing complementary organogelator (**20**-**24**). And further *in situ* cross-linking could enhance the strength of the gels (**Figure 4A**; Díaz et al., 2008).

On the other hand, "mixing" strategy has been used more widely for the fabrication of multicomponent supramolecular gels containing porphyrin or phthalocyanine molecules. Certainly, the careful molecular design for the good gelators is necessary for this strategy. The most representative gelator can be some glutamic acid derivatives, for example N,N'-bis(octadecyl)-L-Boc-glutamic diamide (**25**-**L**) and N,N'-bis(octadecyl)-D-Boc-glutamic diamide (**25**-**D**) (**Figure 4B**). **25** can form supramolecular gel in nearly all kinds of organic solvents. And the achiral porphyrin with long alkyl chains (**26**) has been included upon mixing without damaging the mechanical strength of the corresponding gels formed in DMSO. Most interestingly, these glutamic acid-based gelators can induce achiral porphyrin form supramolecular chiral assemblies (Li et al., 2007).

Except for glutamic acid-based gels, the hydrogels formed by aromatic short peptide Fluorenylmethoxycarbonyl-Leucine-Leucine-Leucine-OMe (Fmoc-L3-OMe) can also be doped with zinc porphyrin. And enhanced photocurrent generation was investigated from this hydrogel system (**Figure 13A**) (Feng et al., 2018).

A similar approach was developed by using organogel fabricated by (1R,2R)-trans-1,2-bis(dodecanoylamino)cyclohexane. When octakis(alkyloxy)-substituted Zn(II)-phthalocyanines were incorporated into the gels, unique brush-like nanostructures can be detected (Diaz Diaz et al., 2007). A non-chiral organogelator (**27**) was also found to form gels with hollow fibrous nanostructures, which can encapsulate phthalocyanine molecules (**28**). And phthalocyanine

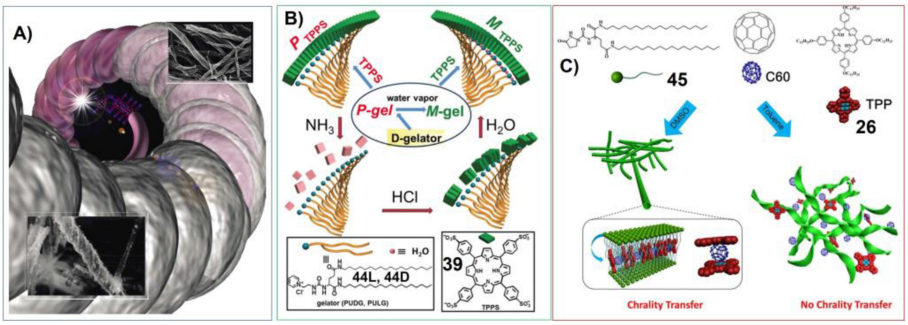

FIGURE 6 | (A) Porphyrin-based hydrogels working as template to manufacture helical silica; Reprinted with permission from Kawano et al. (2004). Copyright 2004 John Wiley and Sons. **(B)** Molecular structure of gelator and porphyrin. 44D can form gel with P-chirality, which changes into M-chiral gel upon water vapor. Porphyrin 39 co-assemble with 44D into J aggregates with P helical packing. NH_3 can destroy porphyrin assemblies, while subsequent treatment with HCl and water vapor can reassemble 39 into M-chirality; Reprinted with permission from Wang et al. (2016). Copyright 2016 Royal Society of Chemistry. **(C)** Molecular structures of the glutamic acid-based gelator containing two chiral centers (45) and achiral C60 and porphyrin (26), and a schematic illustration of the self-assembly of the two achiral molecules with the gelators. Chirality transfer occurred in the DMSO gel but not in the toluene gel. Reprinted with permission from Li et al. (2017b). Copyright 2017 John Wiley and Sons.

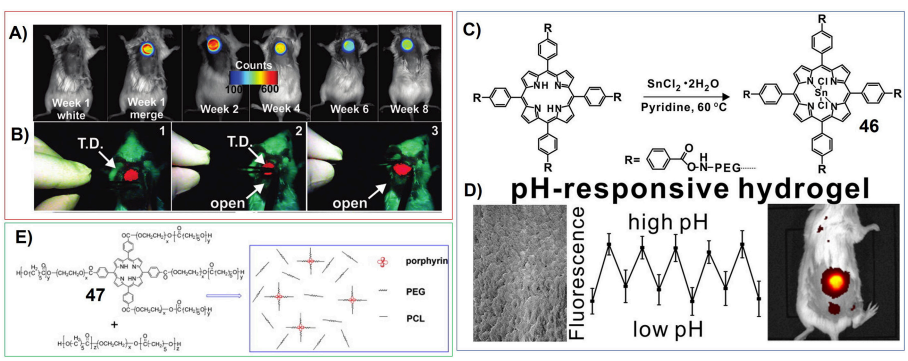

FIGURE 7 | (A) Fluorescence images of a mouse with the hydrogel implanted subcutaneously and monitored noninvasively; Reprinted with permission from Lovell et al. (2011). Copyright 2011 American Chemical Society. **(B)** Screen captures from a fluorescence camera used to guide fluorescently the surgical removal of the hydrogel in real time; Reprinted with permission from Lovell et al. (2011). Copyright 2011 American Chemical Society. **(C)** Synthesis of tin-porphyrin-PEG hydrogels; Reprinted with permission from Huang et al. (2017). Copyright 2017 American Chemical Society. **(D)** Implantable tin porphyrin-PEG hydrogels with pH-responsive fluorescence *in vivo*; Reprinted with permission from Huang et al. (2017). Copyright 2017 American Chemical Society. **(E)** Molecular structures of porphyrin conjugated poly(ethylene glycol) (PEG) and ε-caprolactone (47). Reprinted with permission from Lv et al. (2014). Copyright 2014 John Wiley and Sons.

molecules (**28**) form crystal within the gels (**Figure 4D**; Khan and Sundararajan, 2011). In another sample, hydrogels based on the mixture of sodium deoxycholate and lysine hydrochloride were included with magnesium phthalocyaninate containing crown ether substituents (Goldshleger et al., 2018).

Recently, non-covalent inclusion of different metallo-phthalocyanines into different gel networks have been thoroughly investigated (**Figure 4E**; Keseberg et al., 2016). The results show that adding metallo-phthalocyanines could change the thermal, morphological, and mechanical properties of supramolecular gels.

Polymer gels always play very important roles for including porphyrin and phthalocyanine molecules. For example, charged porphyrins TMPyP (tetrakis(4-N-methylpyridyl)porphyrin) (**38**) and TPPS (tetrakis(4-sulfonatophenyl)porphyrin) (**39**) have been doped into the polymer hydrogels fabricated by copolymers of HEMA (2-hydroxyethyl methacrylate) with either MAA (methacrylic acid) or DEAEMA (2-(diethylamino)ethyl methacrylate) (**Figure 4F**). Upon photoirradiation, the porphyrin molecules (**38**, **39**) included in the hydrogels can generate singlet oxygen (Brady et al., 2007).

Doping with different functional molecules is one of the distinctive features of polymer gels. And different polymer gels systems, which can be fabricated by polypyrrole (Wang et al., 2015b), chitosan (Karimi and Khodadadi, 2016; Xia et al., 2017) or cellulose derivatives (Yang et al., 2018b) have been doped with porphyrin and phthalocyanine molecules. And the applications of these functional systems will be discussed in the following of this article.

FUNCTIONS OF SUPRAMOLECULAR GELS CONTAINING PORPHYRIN AND PHTHALOCYANINE

As a type of characteristic soft matter, porphyrin/phthalocyanine based supramolecular gels have great potential for different applications, from biomedical systems to optoelectronic devices. Even though we cannot address every aspect of these functions in this manuscript, we still want to show some typical new advances of these issues. Since attentions have been focused on the mechanical properties of supramolecular gels,

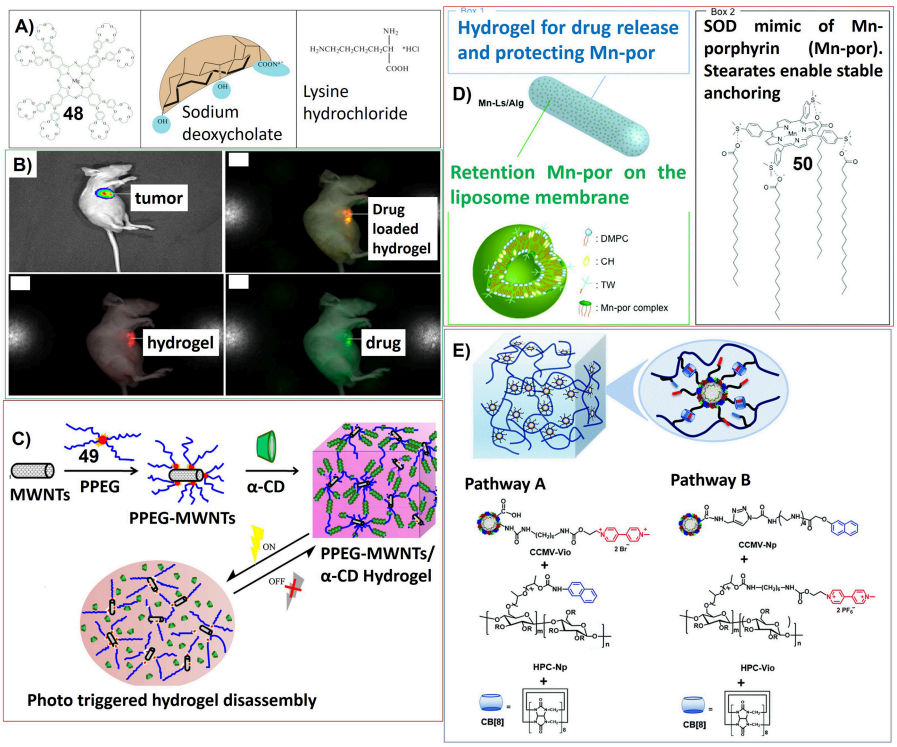

FIGURE 8 | (A) Molecular structures of crown-containing phthalocyanines, sodium deoxycholate, and lysine hydrochloride; Reprinted with permission from Goldshleger et al. (2018). Copyright 2018 Pleiades Publishing, Ltd. **(B)** Bioluminescence imaging and multispectral fluorescence imaging for the drug (doxorubicin) loaded hydrogel of mixed fluorescence of the drug and the hydrogel with green and red, representing one of three in each group; Reprinted with permission from Dong et al. (2016a). Copyright 2016 American Chemical Society. **(C)** Schematic of the thermosensitive porphyrin-poly(ethylene glycol) (49)/α-cyclodextrin hydrogel loaded with carbon nanotubes for photo controlled disassembly; Reprinted with permission from Liang et al. (2017b). Copyright 2017 Elsevier Ltd. **(D)** Drug formulation for oral administration of the SOD mimic (50); Reprinted with permission from Aikawa et al. (2015). Copyright 2015 Royal Society of Chemistry. **(E)** Two pathways to prepare compartmentalized supramolecular hydrogels based on virus nanoparticles. Polymeric material HPC and CCMV nanoparticles were cross-linked through a ternary hos-guest interaction, which involved methyl viologen and naphthyl moieties and CB[8]. Reprinted with permission from Yang et al. (2018b). Copyright 2018 Royal Society of Chemistry.

tuning mechanical properties of supramolecular gels containing porphyrin and phthalocyanine molecules will be discussed. Moreover, the concerns on the supramolecular chirality of porphyrin/phthalocyanine based supramolecular gels also will be addressed in this review.

The photophysical, photochemical and electrochemical properties of porphyrin/phthalocyanine based supramolecular gels will be discussed. And the applications of these soft matters could be found in the fields of photodynamic therapy, molecular sensing, luminescence and cell imaging, photocurrents and semiconducting. Moreover, the catalytic properties of gels containing porphyrin and phthalocyanine molecules are also very interesting. These gels-based catalysts have been used for photocatalytic hydrogen production, some organic reactions, and even mimicking enzymes *in vivo*.

Mechanical Properties of Porphyrin/Phthalocyanine Based Supramolecular Gels

One of the important characteristics of supramolecular gels is their mechanical properties, which can be the tunable strength, self-healing properties and so on. The mechanical properties of porphyrin/phthalocyanine based supramolecular gels have been investigated by scientists for a long time. The original idea could be developing robust materials containing porphyrin. For example, Shinkai and his co-workers have synthesized the porphyrin gelators containing triethoxysilyl substituents (**42TEOS**) (**Figure 5A**). The interactions between porphyrin and copper ions could form supramolecular gels with H-aggregated one-dimensional molecular assemblies, which can be further immobilized by sol-gel polycondensation of the peripheral triethoxysilyl groups. Therefore, by using porphyrin-based supramolecular gels as the template, novel functional organic/inorganic hybrid materials with very high thermal stability as well as a unique mechanical strength can be prepared (**Figure 5B**; Kishida et al., 2005a,b).

Moreover, when phthalocyanine molecules were integrated into the polymer hydrogels, the materials with mechanically robust 3D nanostructure and self-healing properties can be fabricated. Karimi and his co-workers have synthesized zinc phthalocyanine containing tetra-aldehyde substituents (**43**), which can crosslink covalently with chitosan containing amino groups to form dynamic schiff-base linkage (**Figure 5C**). The corresponding phthalocyanine/chitosan frameworks are hydrogels with 3D porous nanostructure and self-healing ability. Moreover, further including carbon nanotubes (CNTs) could modulate the mechanical properties and electrical conductivity of the hydrogels (Karimi and Khodadadi, 2016).

Supramolecular Chirality of Porphyrin/Phthalocyanine Based Supramolecular Gels

Chirality is the basic characteristics of nature. And the origin and evolution of life is closely related to the molecular chirality and supramolecular chirality (Michaeli et al., 2016; Pizzarello, 2016). The research on chirality is significant for understanding many of the secrets of nature. Notably, chiral information can be expressed within different scales, from molecules to supramolecular assemblies until macroscopic scales. Constructing assemblies with supramolecular chirality is very useful for producing novel soft matters with different potential applications (Liu et al., 2015). For supramolecular gels containing porphyrin/phthalocyanine, the research works on chirality transfer and amplification are very important.

These situations are manifested in the transcription of helical assemblies into helical-silica structures. Shinkai et al have synthesized the porphyrin-based gelators containing carbohydrate substituents. And the self-assembly of these sugar-appended porphyrins can form different helical structures depending on the molecular structure and chirality of carbohydrate groups. Upon Sol-Gel polycondensation of tetraethyl orthosilicate (TEOS), the organic helical nanostructures can be transcripted into helical-silica structures, which nicely inherit the organic morphology (**Figure 6A**; Kawano et al., 2004).

For the chiral-related application of porphyrin/phthalocyanine based supramolecular gels, understanding the chirality transfer within these systems could be significant. Sometimes, when the chiral gelators self-assemble into helical nanostructures, the handedness of their molecular chirality and the corresponding supramolecular chirality could be different. In this context, the optical activity of doped porphyrin assemblies could be interesting. Liu et al. have designed cationic gelators bearing pyridinium and glutamide moieties (**44D** or **44L**). And the co-assembly of these cationic chiral gelators with dianionic tetrakis(4-sulfonatophenyl)porphyrin (**39**) could form J-aggregates. Interestingly, the chiral signs of porphyrin assemblies were found to follow the supramolecular chirality of **44** assemblies instead of the molecular chirality of **44** (**Figure 6B**; Wang et al., 2016).

The chirality transfer, inversion and amplification within more complex supramolecular gels were further investigated by Liu et al. The glutamic acid-based gelator containing two chiral centers (**45**) was found to form chiral nanotwists and nanotubes in toluene and DMSO, respectively. While the co-assembly of **45** with achiral porphyrin containing long alkyl chains (**26**) and C60 can also form gel in DMSO by keeping the tubular nanostructures. Both porphyrin and C60 were included in confined nanotubes. Chirality transfer occurred from the host chiral gel matrixes to guest achiral porphyrin in DMSO. Remarkably, the addition of C60 to the porphyrin/gelator gel could invert and further amplify the induced chirality of the porphyrin due to the formation of donor-acceptor pairs. However, in the case of multicomponent toluene gel, **26** and C60 only dissolve in the liquid phase. And no chirality transfer was observed in the toluene gel (**Figure 6C**; Li et al., 2017b).

Porphyrin/Phthalocyanine Based Hydrogels for Biological Imaging

Porphyrin molecules usually show strong fluorescence, which has great potential for biological imaging. On the other hand, hydrogels have been widely used in the field of biology and

medicine. Therefore, when porphyrin molecules were doped into hydrogels, the first application to be developed can be biological imaging.

For example, Zheng et al. have developed the hydrogels based on the reaction between PEG diamine and tetracarboxylic acid porphyrins (Lovell et al., 2011; **Figure 3F**). Within the network of corresponding hydrogels, porphyrin molecules were well separated to prevent fluorescence self-quenching. The near-infrared properties of the fluorescence of porphyrin enabled low background, non-invasive fluorescence monitoring of the implanted hydrogel in a mouse *in vivo*, as well as its image-guided surgical removal in real time (**Figures 7A,B**).

Moreover, the porphyrin-PEG-diamines polymer can be further chelated with tin ions (**46**) (**Figure 7C**). Interestingly, the fluorescence emission of Tin porphyrin hydrogel is strongly reversible and pH responsive in the physiological range between pH 6 and pH 8. This pH-sensitive emission was detected via non-invasive transdermal fluorescence imaging *in vivo* following subcutaneous implantation in mice (**Figure 7D**; Huang et al., 2017).

Lv et al. have synthesized zinc phthalocyanine-PEG-alginate copolymer (**15**). And the hydrogels formed by **15** can be further included with another dye molecule (rhodamine). These dual fluorescent hydrogels can be used for *in vivo* near infrared fluorescence imaging (Liang et al., 2017a). In another work, Lv et al. have synthesized porphyrin conjugated poly (ethylene glycol) (PEG) and ε-caprolactone (**47**) (**Figure 7E**). And the fluorescent nanogel fabricated by **47** can be used for *in vivo* imaging, which targets tumor tissues in hepatoma tumor-bearing mice (Lv et al., 2014; Dong et al., 2016b).

Hydrogels Containing Porphyrin/Phthalocyanine for Drug Delivery

The stimuli-responsive, dynamic properties as well as the biocompatible nature of supramolecular gels render their potential application in the field of drug delivery. For example, the hydrogels based on biodegradable sodium deoxycholate (SDC) and lysine hydrochloride (lys×HCl) can be included with magnesium crown-containing phthalocyanines (**48**), which can be released dependent on thermoreversible of hydrogels (**Figure 8A**; Goldshleger et al., 2018).

For the gels containing porphyrin and phthalocyanine molecules, sometimes the drug delivery can be related with biological imaging. For example, by using porphyrin-PEG-ε-caprolactone conjugates (**47**) as gelator, the doxorubicin-loaded hydrogel has been developed as dual fluorescent anti-tumor drug delivery system. Using nude mice bearing luciferase expressed hepatic tumor as models, the whole process from the drug delivery to the tumor therapeutic effects were real time visualized simultaneously after administration at interval from 0 to 18 days (Dong et al., 2017). A similar dual fluorescent drug delivery system, which also enables the tracking of a drug delivery process and the degradation of the carrier, was developed by using doxorubicin loaded zinc phthalocyanine (**14**) incorporated hydrogel (**Figure 8B**; Dong et al., 2016a).

Based on the hydrogel nanocomposites upon co-assembly of α-cyclodextrin, PEG-conjugated porphyrin (**49**) and multi-walled carbon nanotubes, the drug delivery systems with photo response, fluorescence imaging tracking and photothermal remote controlling properties can be achieved (**Figure 8C**). The controlled disassembly of the hydrogel, which can be efficiently accelerated under laser irradiation, was monitored in real time by *in vivo* fluorescence imaging after subcutaneous injection using mice as models (Liang et al., 2017b). By connecting α-cyclodextrin with photothermal dyes and further co-assemble with PEG-conjugated porphyrins, photothermally controllable, visible, dual fluorescent thermosensitive hydrogels were developed (Yang et al., 2018a). The hydrogel disassembly with drug delivery can be achieved by the photothermal effect of dye molecules. And the dual fluorescence imaging visualization of hydrogels revealed the disassembly process by tracking each component.

For the recently developed drug delivery systems based on porphyrin containing hydrogels, porphyrin molecules can be used as mimic of superoxide dismutase (SOD) inhibiting tumor growth. Yuasa et al. have designed encapsulating

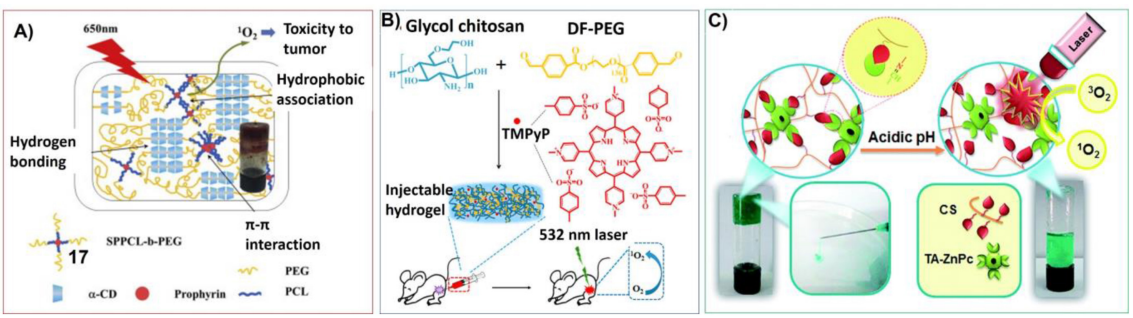

FIGURE 9 | (A) Schematic illustration of intermolecular multi-interactions of hydrogels fabricated by 51 and a-cyclodextrin; Reprinted with permission from Jin et al. (2015). Copyright 2015 Elsevier Ltd. **(B)** The synthetic route of the TMPyP(38)-loaded injectable hydrogel and *in vivo* anticancer application; Reprinted with permission from Xia et al. (2017). Copyright 2017 American Chemical Society. **(C)** pH-sensitive and injectable covalently cross-linked hydrogel for *in situ* tetra-aldehyde functionalized zinc phthalocyanine (43) delivery for PDT. Reprinted with permission from Karimi et al. (2016). Copyright 2016 American Chemical Society.

liposomal drugs by using an alginate hydrogel as carrier. The liposomal drug was composed of manganese porphyrin (**50**), which has been developed as a mimic of superoxide dismutase (SOD). A cytochrome c assay revealed that the $O_2^{\bullet-}$ inhibitory activity of **50** could be maintained even after treatment with simulated gastric and intestinal fluids due to the protection of hydrogels and liposomal aggregations (**Figure 8D**). The oral administration of the formulated drug significantly inhibited the growth of transplanted tumors in mice (Aikawa et al., 2015).

The most elaborate drug delivery systems based on hydrogels could be the complex of cowpea chlorotic mottle virus (CCMV) particles and guest-modified hydroxylpropyl cellulose (HPC), which were non-covalently crosslinked through the formation of ternary host-guest complexes with cucurbit[8]uril (CB[8]) (**Figure 8E**). When tetrasulfonated zinc phthalocyanine molecules were loaded in CCMV particles within these hydrogel complex, they showed nice water solubility without undesired aggregation. Moreover, the particles together with phthalocyanine cargo can be released in a controlled way without an initial burst release (Yang et al., 2018b).

Porphyrin/Phthalocyanine Based Supramolecular Gels for Photodynamic Therapy

When photosensitizers were irradiated with light in the presence of oxygen, free radicals or singlet oxygen could be generated. And photodynamic therapy (PDT) can be achieved by using these active substances for killing tumor cells, bacteria or viruses (Liu et al., 2013; Giuntini et al., 2014; Moylan et al., 2015; Chen et al., 2017; Li et al., 2018a; Zhu et al., 2018). The effects of PDT can be dependent on the photochemical properties of photosensitizers, metabolic characteristic of PDT molecules and accumulation of photosensitizers in the diseased tissue. In this context, both the molecular structure and supramolecular assembly (Li et al., 2018b, 2019a; Zhang et al., 2018) of photosensitizers are important.

Many porphyrins or phthalocyanine molecules have been developed for the photodynamic therapy (PDT) of different illnesses (Singh et al., 2015; Martinez De Pinillos Bayona et al., 2017). On the other hand, porphyrin/phthalocyanine based supramolecular gels for photodynamic therapy not only provides the possibility of controllable photosensitizer delivery, but also help photosensitizer molecules form useful supramolecular nanostructures. The networks of supramolecular gels segment the space within microscopic scale, which brings many unique features for photodynamic therapy. For polymer hydrogels containing porphyrin photosensitizers, the porphyrin molecules can either be included in solid phase or liquid phase. And both the self-assembly of porphyrin and interaction between porphyrin and gelators could affect the corresponding photochemical properties and yield of singlet oxygen (Brady et al., 2007).

Nevertheless, the applications of hydrogels for the delivery and release of porphyrin for photodynamic therapy are receiving increasing attention. For example, one derivative of α-cyclodextrin, PEG-conjugated porphyrin (**17**) was used for constructing supramolecular hydrogels upon host-guest interaction with a-cyclodextrin (a-CD). The corresponding supramolecular hydrogels have good biodegradable and biocompatible properties, which can be used as carrier for doxorubicin (DOX) delivery systems. Considering the generation of singlet oxygen upon photoirradiation on porphyrin, the hydrogels for both sustained-release drug delivery and photodynamic therapy (PDT) can be achieved (**Figure 9A**; Jin et al., 2015).

Wu et al. have developed porphyrin included injectable hydrogel by using glycol chitosan and dibenzaldehyde-terminated telechelic poly(ethylene glycol) as well as water soluble porphyrin (TMPyP) (**38**). Comparing to the solution, the hydrogel containing porphyrin shows enhanced fluorescence intensity with much more singlet oxygen generation upon the same laser irradiation. Moreover, much longer tumor retention can be observed due to the low fluidity of the hydrogel (**Figure 9B**; Xia et al., 2017).

Another injectable hydrogel containing phthalocyanines photosensitizers was developed by Karimi et al. By connecting tetra-aldehyde functionalized zinc phthalocyanine (**43**) with NH_2 groups on chitosan through a dynamic covalent Schiff-base linkage, pH sensitive photosensitizer delivery hydrogels for localized cancer therapy can be prepared. The hydrogel can release **43** in the acidic environment of tumors directly by evading the circulation system. And the viability of cancer cells incubated with the hydrogel was decreased significantly at acidic pH after laser irradiation (**Figure 9C**; Karimi et al., 2016).

Taking advantages of the inclusiveness of hydrogel systems, multicomponent architectures with more complex functionality can be fabricated for photodynamic therapy. For example, Sortino et al. have developed engineered supramolecular hydrogel containing four different components: poly-b-cyclodextrin polymer, hydrophobically modified dextran, zinc phthalocyanine (**51**) and tailored nitric oxide photodonor (**52**). Upon visible light irradiation, both singlet oxygen and nitric oxide can be generated for photodynamic cancer and bacterial therapies (**Figure 10A**; Fraix et al., 2014).

In another system, Lin et al. have synthesized poly(ethylene glycol) diacrylate (PEGDA) hydrogels containing rare earth-doped nanophosphors (UCNPs) and zinc(II) phthalocyanine. Upon 980 nm irradiation, the multicolor upconversion luminescence of UCNPs not only can trigger the polymerization of PEGDA, but also can excite photosensitizer zinc(II) phthalocyanine to produce singlet oxygen (**Figure 10B**; Xiao et al., 2013).

In another approach, the hydrogel containing poly (ethylene glycol) double acrylates (PEGDA), polyethylene glycol 400 (PEG400), zinc phthalocyanine (ZnPc), and phosphotungstic acid (PTA) was prepared. The polymer hydrogel not only prevents diffusion of the photosensitizer, but also maintains a high zinc phthalocyanine concentration around tumor cells for more effective PDT. And phosphotungstic acid also can help the acceleration of singlet oxygen generation (**Figure 10C**; Wang et al., 2013).

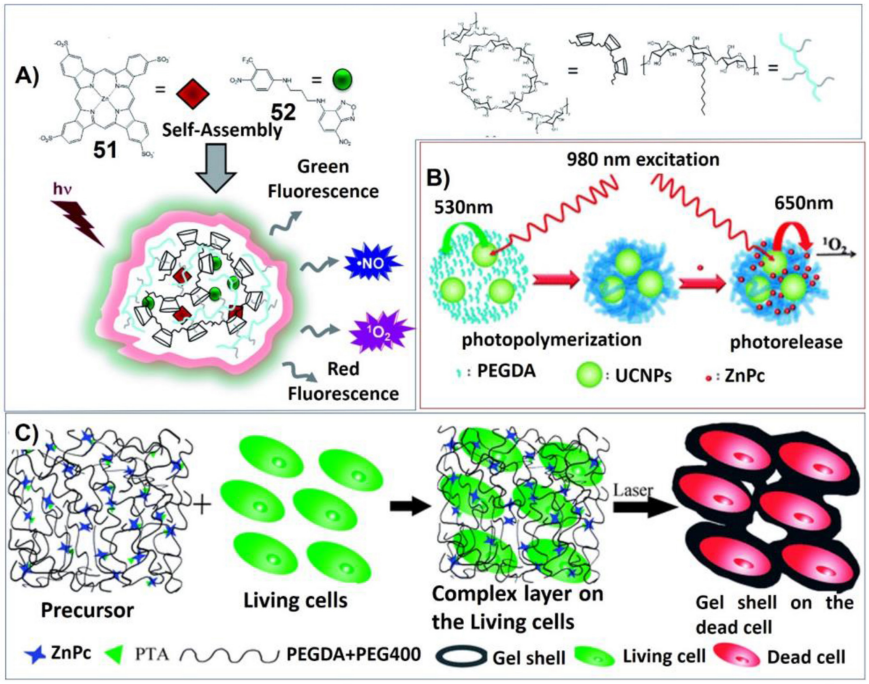

FIGURE 10 | (A) The multi-photoresponsive supramolecular hydrogel containing four different components can generate both singlet oxygen and nitric oxide upon visible light irradiation; Reprinted with permission from Fraix et al. (2014). Copyright 2014 Royal Society of Chemistry. **(B)** PEGDA hydrogels containing rare earth-doped nanophosphors (UCNPs) and zinc(II) phthalocyanine. Upon 980 nm irradiation, the multicolor upconversion luminescence of UCNPs can excite photosensitizer zinc(II) phthalocyanine to produce singlet oxygen; Reprinted with permission from Xiao et al. (2013). Copyright 2013 Royal Society of Chemistry. **(C)** Illustrations of the formation process and anti-tumor mechanism of the hydrogel containing poly (ethylene glycol) double acrylates (PEGDA), polyethylene glycol 400 (PEG400), zinc phthalocyanine (ZnPc), and phosphotungstic acid (PTA). Reprinted with permission from Wang et al. (2013). Copyright 2013 Royal Society of Chemistry.

Porphyrin/Phthalocyanine Based Gels for Molecular Sensing

Some supramolecular assemblies can be used for sensing ions, gas or small organic molecules. For these applications, the interactions between sensors and target molecules could produce some special signals, such as electrical signals or fluorescence (Che et al., 2010; Wong et al., 2010; Saha et al., 2016; Chen et al., 2018). And the molecular sensing can be achieved by analyzing the changes of these signals. Notably, such sensing is dependent on both the molecular structures and the supramolecular properties of the sensors.

The supramolecular gels containing porphyrin or phthalocyanine have been investigated for molecular sensing. For example, Zheng et al. have fabricated polymeric hydrogels included with porphyrin by connecting 4-arm poly (ethylene glycol) (PEG), 5,10,15,20-tetrakis(4-hydroxyphenyl) porphyrin and hexamethylene diisocyanate (**Figure 11A**). The corresponding hydrogels show strong fluorescent, which can be further changed upon interaction with heavy metal ions, such as Cu^{2+}, Zn^{2+}, Pb^{2+}, Co^{2+}, Hg^{2+}, and Ni^{2+}. Based on this characteristic, the hydrogel exhibits rapid, significant and visual sensitivity to low concentrations of heavy metal ions (**Figure 11B**). Moreover, the uptake and release of heavy metal ions can be recycled conveniently (Jia et al., 2015).

Another polymer hydrogel containing porphyrin derivative (**54**) has been prepared into complex devices for real-time and indicator-free detection of aqueous nitric oxide. The polymer hydrogel can be photoluminescence, which is sensing specific to NO. And the changes of photoluminescence can be further transformed into electric signal by the photodetector (**Figure 11C**; Chao et al., 2011).

Hassan et al. have prepared multifunctional conducting polyacrylic acid (PAA) hydrogel (MFH) integrated with reduced grapheme oxide (rGO), vinyl substituted polyaniline (VS-PANI), double-deck lutetium Phthalocyanine (LuPc2), and glucose oxidase (GOx). This complex system can be used for electrochemical detection of glucose with high sensitivity (15.31 $\mu A\ mM^{-1}\ cm^{-2}$), large concentration range of (2–12 mM) and low detection limit (25 μm). This biosensor based on polymer hydrogel has very fast response time (1 s) and high storage stability (**Figure 11D**; Al-Sagur et al., 2017).

Different polymer gels systems containing porphyrins have been developed for gas sensing. For example, McShane et al. have prepared ratiometric oxygen sensor by incorporating two luminophores into polymer hydrogels. In this case, near-infrared emitting quantum dots can be employed as reference luminophores; while long-lifetime platinum (II) porphyrin phosphor was used as oxygen indicator (**Figure 12A**).

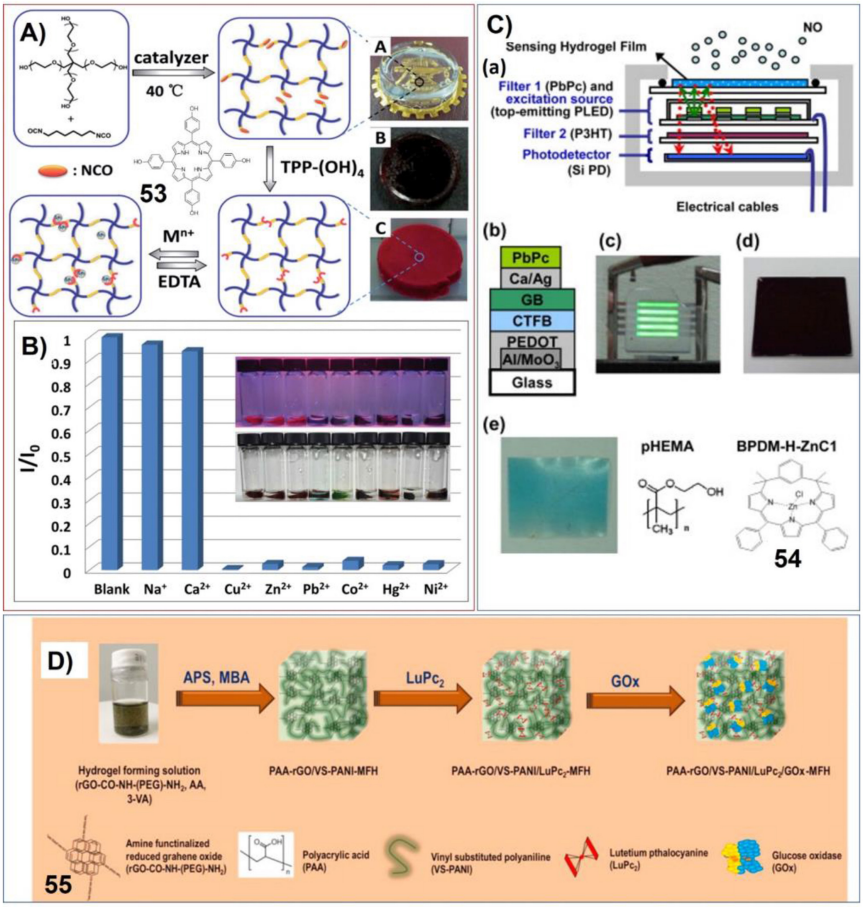

FIGURE 11 | (A) Preparation procedure of the PEG-diisocyanate-porphyrin hydrogel; Reprinted with permission from Jia et al. (2015). Copyright 2015 Royal Society of Chemistry. **(B)** Fluorescent intensity of PEG-diisocyanate-porphyrin hydrogels in different metal ion aqueous solutions (0.25 M) at 420 nm. Insert: respective photographs of hydrogels at 365 nm irradiation and visible light (from left to right: blank, Na^+, Ca^{2+}, Cu^{2+}, Zn^{2+}, Pb^{2+}, Co^{2+}, Hg^{2+}, Ni^{2+}); Reprinted with permission from Jia et al. (2015). Copyright 2015 Royal Society of Chemistry. **(C)** Integrated semiconductor optoelectronic devices based on hydrogels for real-time and indicator-free detection of aqueous nitric oxide; Reprinted with permission from Chao et al. (2011). Copyright 2011 Royal Society of Chemistry. **(D)** Schematic representation of the formation of hydrogel (MFH) integrated with reduced grapheme oxide (rGO), vinyl substituted polyaniline (VS-PANI), double-deck lutetium Phthalocyanine (LuPc2), and glucose oxidase (GOx). Reprinted with permission from Al-Sagur et al. (2017). Copyright 2017 Elsevier.

This sensing system possess excellent sensitivity ($K_{SV} = 0.00826\ \mu M^{-1}$) at oxygen concentrations below 300 mM and is resistant to photobleaching (Collier et al., 2011). The hydrogel containing porphyrins for *in vivo* oxygen sensing has been developed by Lovell et al (Huang et al., 2014). The reaction between PEG diamine and Pd substituted meso-tetrakis(4-carboxyphenyl) porphine can generate hydrogels with extreme porphyrin density ($\approx 5 \times 10^{-3}$ M) and very weak molecular aggregation. This hydrogel exhibits oxygen-responsive phosphorescence (**Figure 12B**) and can be stably implanted subcutaneously in mice for weeks without degradation, bleaching, or host rejection. When the matrix containing lots of identical dots included with different luminescent molecules, the fluorescent sensor membrane can be fabricated for sensing both pH value and O_2 at different emission wavelengths. Wolfbeis et al. have prepared the sensing chips by including platinum(II)-5,10,15,20-tetrakis-(2,3,4,5,6-pentafluorophenyl) porphyrin (**56**), fluorescein isothiocyanate (**57**) (**Figure 12C**), and the reference fluorophore diphenylanthracene into each dot (Meier et al., 2011). In this case, oxygen can be detected by Pt-porphyrin, while fluorescein isothiocyanate was used to sense pH. The dual sensing can be achieved via RGB (red-green-blue) method, wherein the fluorescence intensities can be imaged with a digital camera (**Figure 12D**). Nevertheless, sensing cellular oxygen is attracting increased interests recently. By using porphyrin-based hydrogels, more versatile, flexible, and simple oxygen sensors can be fabricated. Papkovsky et al. have developed cell-penetrating phosphorescent nanosensor MM2 by including porphyrin (**56**), fluorescent antennae dyes (**58**) and Förster resonance energy transfer (FRET) donor poly(9,9-dioctylfluorene) (**59**) into cationic hydrogel (Kondrashina et al., 2012). This system provides efficient delivery into the cell and subsequent sensing and high-resolution imaging of cellular oxygen in different detection modalities, including ratiometric intensity and phosphorescence lifetime (**Figure 12E**).

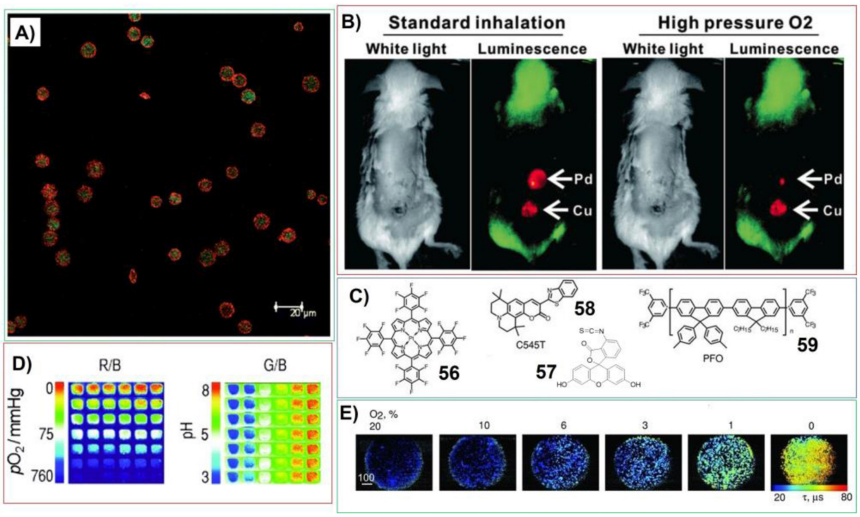

FIGURE 12 | (A) Confocal images of microparticle-based ratiometric oxygen sensors (green represents PtP emission; red represents QD emission); Reprinted with permission from Collier et al. (2011). Copyright 2011 Royal Society of Chemistry. **(B)** Transdermal luminescence imaging of dual-implanted Pd-mTCPP and 15% free base-Cu-mTCPP hydrogels. Left images were taken following anesthetization and right ones taken following high-pressure oxygen administration; Reprinted with permission from Huang et al. (2014). Copyright 2014 John Wiley and Sons. **(C)** Molecular structures of components within fluorescent sensor membrane for sensing both pH value and O_2; **(D)** Sensing process for both O2 and pH. the ratio of red to blue channel pictures (R/B; displayed in pseudo colors) represents the oxygen response and shows the lack of cross-reactivity to pH. The ratio of green to blue channel pictures (G/B; also displayed in pseudo colors) reflects the response to pH and also demonstrates the lack of cross reactivity to oxygen; Reprinted with permission from Meier et al. (2011). Copyright 2011 John Wiley and Sons. **(E)** Widefield fluorescence/phosphorescence lifetime imaging microscopy images of MEF cells stained with MM2 measured at different levels of atmospheric oxygen. Scale bar unit is in μ m. Reprinted with permission from Kondrashina et al. (2012). Copyright 2012 John Wiley and Sons.

Porphyrin/Phthalocyanine Based Gels for Catalyzing

Metal porphyrins or phthalocyanines are good catalysts for different reactions. Many related systems, such as P450, have been thoroughly investigated (Feiters et al., 2000). On the other hand, catalyzing based on gels systems belong to supramolecular catalysis (Feng et al., 2017). When molecules with catalytic properties were self-assembled into ordered nanostructures, their catalytic active centers can also form ordering aggregations. Moreover, the confinement effect derives from self-assembled nanostructures could be very useful for improving the yields and stereoselectivity of chemical reactions. Importantly, the catalytic properties of supramolecular assemblies can be modulated upon changing the solvents and molecular building blocks. In principle, the gels containing porphyrin or phthalocyanine components can be used for catalyzing. And the nature of gel systems should give the advantages for different applications. Although there is still small amount of corresponding results can be found in the literature, the ongoing works already cover different fields. The gels systems containing porphyrin and phthalocyanine have been proved to be able to catalyze some special organic reactions. The photocatalyzing for degradation of contaminants and hydrogen production was also investigated. Moreover, the *in vivo* catalyzing strongly highlights the advantages of the gels.

For catalyzing aerobic oxidation of olefins, Ghorbanloo et al. have developed the hydrogels based on cationic cross-linked polymeric ionic liquid (poly[(3-acrylamidopropyl) trimethylammonium chloride]) embedded with anionic [Mn(tetrakis(4-sulfonatophenyl)porphyrin)(OAc)] (**39a**) (**Figure 13A**). The activity for catalyzing aerobic oxidation of olefins was found to be dependent on substituent effect of reactants, temperature and the amount of catalysts. And this catalytic hydrogel can be easily recovered from the reaction medium and could be reused for another seven runs without significant loss of activity (Yazdely et al., 2018).

Chen et al. have developed poly(ethylene glycol)-based nanocomposite hydrogels containing Fe-octacarboxylic acid phthalocyanine (FeOCAP)/magnetic attapulgite (**Figure 13B**). This system has excellent photocatalytic activity for rhodamine B photodegradation. And the hydrogels could be reused more than five times without losing any photodegradation ability (Yuan and Chen, 2017).

An excellent gel system showing enhanced visible light photocatalytic hydrogen production has been developed by Zhang et al. These porphyrin-based imine gels offer chemical variety and hierarchically porous structures. And the properties of these catalysts can be easily medicated by changing porphyrin metal centers. The Pd gel enables efficient photocatalytic H_2 evolution via photoinjection of electrons from the light-harvesting gel network into the Pt nanoparticles. Upon visible light irradiation, the Pd-porphyrin gels doped with Pt nanoparticles show very high efficiency for hydrogen production in aqueous sodium ascorbate solution (1.0744×10^5 μmol g^{-1} for 120 h totally) without significant degradation during four runs (**Figure 13C**; Liao et al., 2018).

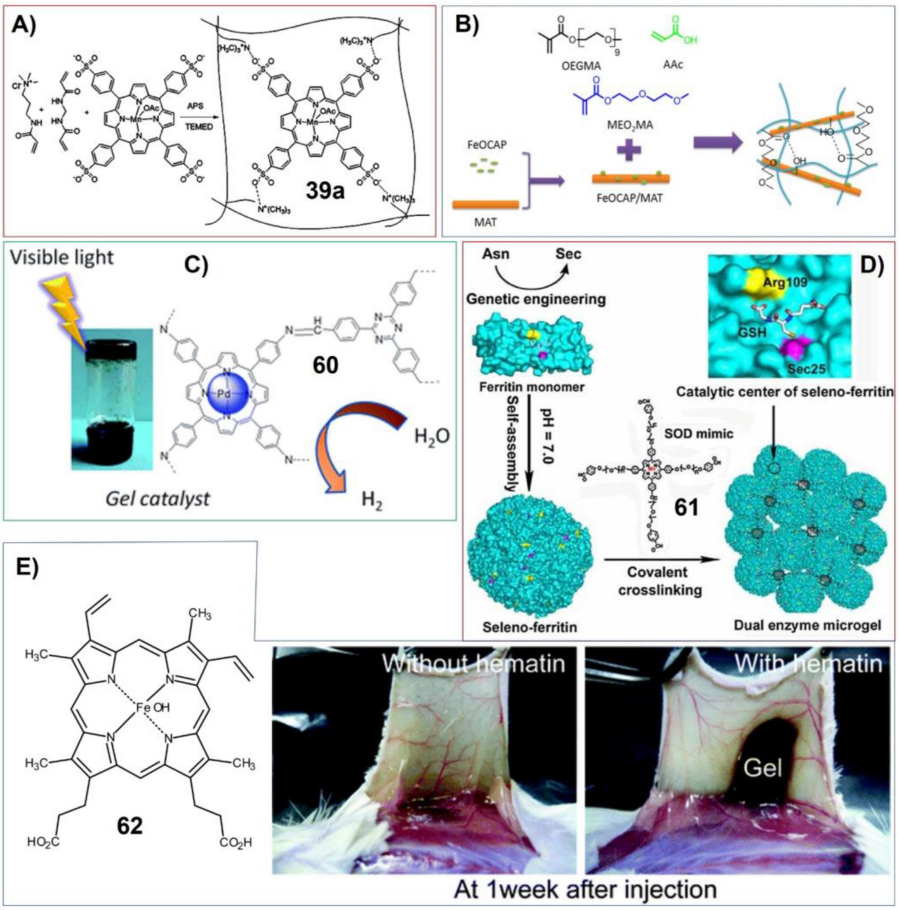

FIGURE 13 | (A) Catalyst system comprised of anionic [Mn(tetrakis(4-sulfonatophenyl)porphyrin)(OAc)] ([Mn(TPPS)(OAc)]) embedded within cationic cross-linked polymeric ionic liquid (poly[(3-acrylamidopropyl)trimethylammonium chloride]); Reprinted with permission from Yazdely et al. (2018). Copyright 2018 John Wiley and Sons. **(B)** Poly(ethylene glycol)-based nanocomposite hydrogels containing Fe-octacarboxylic acid phthalocyanine (FeOCAP)/magnetic attapulgite; Reprinted with permission from Yuan and Chen (2017). Copyright 2017 John Wiley and Sons. **(C)** Porphyrin-based imine gels for enhanced visible-light photocatalytic hydrogen production; Reprinted with permission from Liao et al. (2018). Copyright 2018 Royal Society of Chemistry. **(D)** Dual enzyme gel with high antioxidant ability based on engineered seleno-ferritin and artificial superoxide dismutase; Reprinted with permission from Gao et al. (2013). Copyright 2013 John Wiley and Sons. **(E)** Molecular structure of hematin (62), and subcutaneous *in situ* gelation catalyzed by hematin (right). Reprinted with permission from Sakai et al. (2010). Copyright 2010 American Chemical Society.

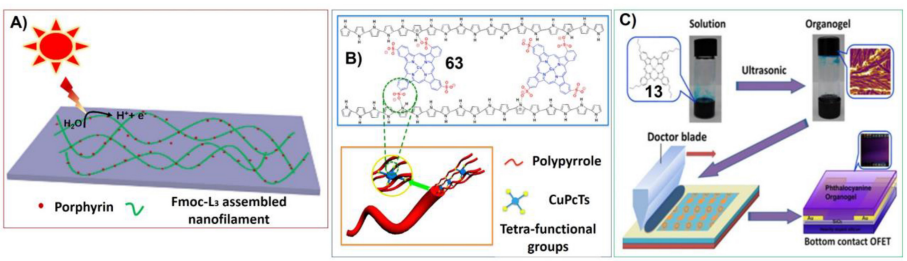

FIGURE 14 | (A) Self-assembled peptide hydrogel with porphyrin as a dopant for enhanced photocurrent generation; Reprinted with permission from Feng et al. (2018). Copyright 2018 Elsevier. **(B)** Dopant-enabled supramolecular approach for controlled synthesis of nanostructured conductive polymer hydrogels; Reprinted with permission from Wang et al. (2015b). Copyright 2015 American Chemical Society. **(C)** Ultrasound-induced formation of phthalocyanine organogel for field-effect transistor applications. Reprinted with permission from Xu et al. (2016). Copyright 2016 American Chemical Society.

The catalytic properties of porphyrin-based gels have been utilized for tissue engineering depending on enzyme mimicking. Sakai et al. found that iron-containing porphyrin hematin can act as alternative catalyst to horseradish peroxidase (HRP) for *in situ* gelation of polymers with phenolic hydroxyl (Ph) moieties *in vivo* (**Figure 13E**). The gelatin derivative with phenolic hydroxyl moieties can form gel in the presence of both hematin and H_2O_2 (Sakai et al., 2010).

By making gels containing porphyrin molecules, more complex catalytic systems with delicate nanostructures and functions can be achieved. Liu et al. have fabricated antioxidant microgel with both glutathione peroxidase (GPx) and superoxide dismutase (SOD) activities. In this case, the main catalytic components of glutathione peroxidase were put onto the surface of ferritin. The resulting seleno-ferritin (Se-Fn) monomers can self-assemble into nanocomposites that exhibit remarkable GPx activity due to the well-organized multi-GPx catalytic centers. On the other hand, since some metal porphyrin molecules are good superoxide dismutase mimic, the gel system mimicking synergistic dual enzyme can be prepared by crosslinking seleno-ferritin nanocomposites with porphyrin (**Figure 13D**; Gao et al., 2013).

Photoelectric Device Based on Porphyrin or Phthalocyanine Gels

The supramolecular gels containing porphyrin or phthalocyanine building blocks could provide the porphyrin assemblies or phthalocyanine aggregates with nice nanostructures and tailored molecular packing modes. For example, the tetrapyrrole macrocycle based π-conjugated systems can form either J-aggregation or H-aggregation. Different molecular packing modes could render the assemblies with varied spectral characteristics, special energy transfer or electron transfer properties. Therefore, some unusual photophysical, photochemical or electrochemical properties of these assemblies can be expected.

For example, Bai et al. have fabricated the hydrogels upon the co-assembly of 5,10,15,20-Tetraphenyl-21H,23H-porphine zinc (TPP-Zn) and aromatic short peptide Fluorenylmethoxycarbonyl-Leucine-Leucine-Leucine-OMe (Fmoc-L_3-OMe). These assemblies show great light response properties. In this case, the long-range order assembly of aromatic peptide can act as photoelectron acceptor and conductor to promote the production of photoelectrons by the light antenna porphyrin molecules. And porphyrin can effectively reduce the resistance, facilitating the transfer of photoelectrons (**Figure 14A**; Feng et al., 2018).

On the other hand, when porphyrin or phthalocyanine molecules were doped into the supramolecular systems, they can also change the aggregation properties of other molecular building blocks. Polypyrrole is a type of conducting polymer. While doping copper phthalocyanine-3,4′,4″,4‴-tetrasulfonic acid tetrasodium salt (**63**) could cross-link polypyrrole to form hydrogels with three-dimensional network. Phthalocyanine favors the formation of polypyrrole nanofibers. And the enhanced interchain charge transport of polypyrrole/**63** hydrogels resulted in greatly enhanced conductivity and pseudocapacitance compared with pristine polypyrrole (**Figure 14B**; Wang et al., 2015b).

The gels containing metal phthalocyanines not only can be good electric conductor, but also can be nice semiconductor. Xu et al. synthesized tetra-n-butyl peripheral substituted copper(II) phthalocyanine, which can form supramolecular gels upon ultrasonic irradiation. The corresponding gels can be further fabricated into field-effect transistor (**Figure 14C**). Due to the stronger π-π interactions within the assemblies, organogel exhibits significant increase in charge carrier mobility in comparison with other solution process techniques (Xu et al., 2016).

CONCLUSION AND OUTLOOK

Fabrication of supramolecular gels containing porphyrins or phthalocyanines molecules represents the efforts to build novel functional soft matters. In this case, functional molecular building blocks could organize into hierarchical nanostructures in a controlled manner. Many interesting features and subsequently novel applications of these materials could be developed depending on ordered nanostructures. Notably, the dynamic and stimuli-responsive nature of supramolecular gels has greatly expanded the application of included π-conjugated systems.

In principle, gels especially hydrogels can be considered as matter of life, due to many similarities between their nature and that of the organisms (Li et al., 2017a). However, making the supramolecular assemblies as complex as the nanostructures of some cell organelles is still very difficult. It is necessary to further understand the complex non-covalent interactions within various materials. Although there are still big challenges to both controlling the nanostructures and improving performance of functional soft matters, the development of gels systems has provided unlimited expectation and possibility (Weiss, 2014). And the fabrication of different gels systems should be more dependent on the principles and methods of biomimetic. Nevertheless, considering the infinite constructing possibilities of supramolecular gels, functional gels containing the hierarchical assembly of porphyrins or phthalocyanines will be further developed in the field of chemistry, nanoscience, and biological applications.

AUTHOR CONTRIBUTIONS

All authors listed have made a substantial, direct and intellectual contribution to the work, and approved it for publication.

ACKNOWLEDGMENTS

The financial support from Natural Science Foundation of China (nos. 21631003, 21471015, 21671017, 21474118, and 21773006), Major Science and Technology Program for Water Pollution Control and Treatment (2017ZX07402001), Beijing Municipal Commission of Education, and University of Science and Technology Beijing (no. FRF-BR-16-008A) is gratefully acknowledged.

REFERENCES

Aikawa, T., Ito, S., Shinohara, M., Kaneko, M., Kondo, T., and Yuasa, M. (2015). A drug formulation using an alginate hydrogel matrix for efficient oral delivery of the manganese porphyrin-based superoxide dismutase mimic. *Biomater. Sci.* 3, 861–869. doi: 10.1039/C5BM00056D

Al-Sagur, H., Komathi, S., Khan, M. A., Gurek, A. G., and Hassan, A. (2017). A novel glucose sensor using lutetium phthalocyanine as redox mediator in reduced graphene oxide conducting polymer multifunctional hydrogel. *Biosens. Bioelectron.* 92, 638–645. doi: 10.1016/j.bios.2016.10.038

Bhattacharya, S., and Samanta, S. K. (2016). Soft-nanocomposites of nanoparticles and nanocarbons with supramolecular and polymer gels and their applications. *Chem. Rev.* 116, 11967–12028. doi: 10.1021/acs.chemrev.6b00221

Bian, Y., Zhang, Y., Ou, Z., and Jiang, J. (2011). "Chemistry of sandwich tetrapyrrole rare earth complexes," in *Handbook of Porphyrin Science*, eds K. M. Kadish, K. M. Smith, and R. Guilard (Singapore: World Scientific Publishing Co. Pte. Ltd.), 249–460.

Brady, C., Bell, S. E. J., Parsons, C., Gorman, S. P., Jones, D. S., and Mccoy, C. P. (2007). Novel porphyrin-incorporated hydrogels for photoactive intraocular lens biomaterials. *J. Phys. Chem. B* 111, 527–534. doi: 10.1021/jp066217i

Buchler, J. W., and Ng, D. K. P. (2000). *Metal Tetrapyrrole Double- and Triple-Deckers With Special Emphasis on Porphyrin Systems*. New York, NY: Academic Press.

Buerkle, L. E., and Rowan, S. J. (2012). Supramolecular gels formed from multi-component low molecular weight species. *Chem. Soc. Rev.* 41, 6089–6102. doi: 10.1039/c2cs35106d

Chang, Y., Jiao, Y., Symons, H. E., Xu, J.-F., Faul, C. F. J., and Zhang, X. (2019). Molecular engineering of polymeric supra-amphiphiles. *Chem. Soc. Rev.* 48, 989–1003. doi: 10.1039/C8CS00806J

Chao, Y.-C., Yeh, S.-D., Zan, H.-W., Chang, G.-F., Meng, H.-F., Hung, C.-H., et al. (2011). Integrated semiconductor optoelectronic devices for real-time and indicator-free detection of aqueous nitric oxide. *Org. Electron.* 12, 751–755. doi: 10.1016/j.orgel.2011.02.003

Che, Y., Yang, X., Liu, G., Yu, C., Ji, H., Zuo, J., et al. (2010). Ultrathin n-type organic nanoribbons with high photoconductivity and application in optoelectronic vapor sensing of explosives. *J. Am. Chem. Soc.* 132, 5743–5750. doi: 10.1021/ja909797q

Chen, L., Bai, H., Xu, J.-F., Wang, S., and Zhang, X. (2017). Supramolecular porphyrin photosensitizers: controllable disguise and photoinduced activation of antibacterial behavior. *ACS Appl. Mater. Interfaces* 9, 13950–13957. doi: 10.1021/acsami.7b02611

Chen, Z., Lohr, A., Saha-Moeller, C. R., and Wuerthner, F. (2009). Self-assembled π-stacks of functional dyes in solution: structural and thermodynamic features. *Chem. Soc. Rev.* 38, 564–584. doi: 10.1039/B809359H

Chen, Z., Wang, J., Pan, D., Wang, Y., Noetzel, R., Li, H., et al. (2018). Mimicking a dog's nose: scrolling graphene nanosheets. *ACS Nano* 12, 2521–2530. doi: 10.1021/acsnano.7b08294

Collier, B. B., Singh, S., and Mcshane, M. (2011). Microparticle ratiometric oxygen sensors utilizing near-infrared emitting quantum dots. *Analyst* 136, 962–967. doi: 10.1039/C0AN00661K

Cornwell, D. J., Daubney, O. J., and Smith, D. K. (2015). Photopatterned multidomain gels: multi-component self-assembled hydrogels based on partially self-sorting 1,3:2,4-dibenzylidene-D-sorbitol derivatives. *J. Am. Chem. Soc.* 137, 15486–15492. doi: 10.1021/jacs.5b09691

Das, T., Häring, M., Haldar, D., and Díaz Díaz, D. (2018). Phenylalanine and derivatives as versatile low-molecular-weight gelators: design, structure and tailored function. *Biomater. Sci.* 6, 38–59. doi: 10.1039/C7BM00882A

Diaz Diaz, D., Torres, T., Zentel, R., Davis, R., and Brehmer, M. (2007). Physicochemical characterization of octakis(alkyloxy)-substituted Zn(II)-phthalocyanines non-covalently incorporated into an organogel and their remarkable morphological effect on the nanoscale-fibers. *Chem. Commun.* 2369–2371. doi: 10.1039/B703685J

Díaz, D. D., Cid, J. J., Vázquez, P., and Torres, T. (2008). Strength enhancement of nanostructured organogels through inclusion of phthalocyanine-containing complementary organogelator structures and *in situ* cross-linking by click chemistry. *Chem. Eur. J.* 14, 9261–9273. doi: 10.1002/chem.200800714

Dong, X., Chen, H., Qin, J., Wei, C., Liang, J., Liu, T., et al. (2017). Thermosensitive porphyrin-incorporated hydrogel with four-arm PEG-PCL copolymer (II): doxorubicin loaded hydrogel as a dual fluorescent drug delivery system for simultaneous imaging tracking *in vivo*. *Drug Deliv.* 24, 641–650. doi: 10.1080/10717544.2017.1289570

Dong, X., Wei, C., Chen, H., Qin, J., Liang, J., Kong, D., et al. (2016a). Real-time imaging tracking of a dual fluorescent drug delivery system based on zinc phthalocyanine-incorporated hydrogel. *ACS Biomater. Sci. Eng.* 2, 2001–2010. doi: 10.1021/acsbiomaterials.6b00403

Dong, X., Wei, C., Lu, L., Liu, T., and Lv, F. (2016b). Fluorescent nanogel based on four-arm PEG-PCL copolymer with porphyrin core for bioimaging. *Mater. Sci. Eng. C* 61, 214–219. doi: 10.1016/j.msec.2015.12.037

Drain, C. M., Varotto, A., and Radivojevic, I. (2009). Self-organized porphyrinic materials. *Chem. Rev.* 109, 1630–1658. doi: 10.1021/cr8002483

Draper, E. R., Eden, E. G. B., Mcdonald, T. O., and Adams, D. J. (2015). Spatially resolved multicomponent gels. *Nat. Chem.* 7, 848–852. doi: 10.1038/nchem.2347

Edwards, W., and Smith, D. K. (2014). Enantioselective component selection in multicomponent supramolecular gels. *J. Am. Chem. Soc.* 136, 1116–1124. doi: 10.1021/ja411724r

Engelkamp, H., Middelbeek, S., and Nolte, R. J. (1999). Self-assembly of disk-shaped molecules to coiled-coil aggregates with tunable helicity. *Science* 284, 785–788. doi: 10.1126/science.284.5415.785

Fathalla, M., Strutt, N. L., Sampath, S., Katsiev, K., Hartlieb, K. J., Bakr, O. M., et al. (2015). Porphyrinic supramolecular daisy chains incorporating pillar[5]arene-viologen host-guest interactions. *Chem. Commun.* 51, 10455–10458. doi: 10.1039/C5CC03717D

Feiters, M. C., Rowan, A. E., and Nolte, R. J. M. (2000). From simple to supramolecular cytochrome P450 mimics. *Chem. Soc. Rev.* 29, 375–384. doi: 10.1039/a804252g

Feng, L., Wang, A., Ren, P., Wang, M., Dong, Q., Li, J., et al. (2018). Self-assembled peptide hydrogel with porphyrin as a dopant for enhanced photocurrent generation. *Colloid Interface Sci. Commun.* 23, 29–33. doi: 10.1016/j.colcom.2018.01.006

Feng, Z., Zhang, T., Wang, H., and Xu, B. (2017). Supramolecular catalysis and dynamic assemblies for medicine. *Chem. Soc. Rev.* 46, 6470–6479. doi: 10.1039/C7CS00472A

Foster, J. A., Piepenbrock, M.-O., Lloyd, G. O., Clarke, N., Howard, J. A., et al. (2010). Anion-switchable supramolecular gels for controlling pharmaceutical crystal growth. *Nat. Chem.* 2, 1037–1043. doi: 10.1038/nchem.859

Fraix, A., Gref, R., and Sortino, S. (2014). A multi-photoresponsive supramolecular hydrogel with dual-color fluorescence and dual-modal photodynamic action. *J. Mater. Chem. B* 2, 3443–3449. doi: 10.1039/C4TB00257A

Gao, Y., Chen, Y., Li, R., Bian, Y., Li, X., and Jiang, J. (2009). Nonperipherally octa(butyloxy)-substituted phthalocyanine derivatives with good crystallinity: effects of metal-ligand coordination on the molecular structure, internal structure, and dimensions of self-assembled nanostructures. *Chem. Eur. J.* 15, 13241–13252. doi: 10.1002/chem.200901722

Gao, Y., Hou, C., Zhou, L., Zhang, D., Zhang, C., Miao, L., et al. (2013). A dual enzyme microgel with high antioxidant ability based on engineered seleno-ferritin and artificial superoxide dismutase. *Macromol. Biosci.* 13, 808–816. doi: 10.1002/mabi.201300019

Geng, G., Chen, P., Guan, B., Jiang, L., Xu, Z., Di, D., et al. (2017). Shape-controlled metal-free catalysts: facet-sensitive catalytic activity induced by the arrangement pattern of noncovalent supramolecular chains. *ACS Nano* 11, 4866–4876. doi: 10.1021/acsnano.7b01427

Geng, G., Wang, Z., Chen, P., Guan, B., Yang, C., and Liu, M. (2018). Platinized spherical supramolecular nanoassemblies of a porphyrin: facile synthesis and excellent catalytic recyclability. *Phys. Chem. Chem. Phys.* 20, 8488–8497. doi: 10.1039/C8CP00173A

Giuntini, F., Boyle, R., Sibrian-Vazquez, M., and Vicente, M. G. H. (2014). "Porphyrin conjugates for cancer therapy," in *Handbook of Porphyrin Science*, eds K. M. Kadish, K. M. Smith, and R. Guilard (Singapore: World Scientific Publishing Co. Pte. Ltd.), 303–416.

Goldshleger, N. F., Gak, V. Y., Lobach, A. S., Kalashnikova, I. P., Baulin, V. E., and Tsivadze, A. Y. (2018). Magnesium octa[(4'-benzo-15-crown-5)-oxy]phthalocyaninate in low-molecular hydrogels: spectral properties and release under stimulation. *Prot. Met. Phys. Chem. Surf.* 54, 174–184. doi: 10.1134/S2070205118020053

Goujon, A., Mariani, G., Lang, T., Moulin, E., Rawiso, M., Buhler, E., et al. (2017). Controlled sol-gel transitions by actuating molecular machine based supramolecular polymers. *J. Am. Chem. Soc.* 139, 4923–4928. doi: 10.1021/jacs.7b00983

Guo, P., Zhao, G., Chen, P., Lei, B., Jiang, L., Zhang, H., et al. (2014). Porphyrin nanoassemblies via surfactant-assisted assembly and single nanofiber nanoelectronic sensors for high-performance H2O2 vapor sensing. *ACS Nano* 8, 3402–3411. doi: 10.1021/nn406071f

Hasobe, T. (2014). "Supramolecular assemblies of porphyrin and phthalocyanine derivatives for solar energy conversion and molecular electronics," in *Handbook of Porphyrin Science*, eds K. M. Kadish, K. M. Smith, and R. Guilard (Singapore: World Scientific Publishing Co. Pte. Ltd.), 147–194.

Helmich, F., and Meijer, E. W. (2013). Controlled perturbation of the thermodynamic equilibrium by microfluidic separation of porphyrin-based aggregates in a multi-component self-assembling system. *Chem. Commun.* 49, 1796–1798. doi: 10.1039/C2CC36887K

Huang, H., Chauhan, S., Geng, J., Qin, Y., Watson, D. F., and Lovell, J. F. (2017). Implantable tin porphyrin-PEG hydrogels with pH-responsive fluorescence. *Biomacromolecules* 18, 562–567. doi: 10.1021/acs.biomac.6b01715

Huang, H., Song, W., Chen, G., Reynard, J. M., Ohulchanskyy, T. Y., Prasad, P. N., et al. (2014). Pd-porphyrin-cross-linked implantable hydrogels with oxygen-responsive phosphorescence. *Adv. Healthcare Mater.* 3, 891–896. doi: 10.1002/adhm.201300483

Ishi-i, T., Iguchi, R., Snip, E., Ikeda, M., and Shinkai, S. (2001). [60]Fullerene can reinforce the organogel structure of porphyrin-appended cholesterol derivatives: novel odd–even effect of the (CH2)n spacer on the organogel stability. *Langmuir* 17, 5825–5833. doi: 10.1021/la0107749

Ishi-i, T., and Shinkai, S. (2005). Dye-based organogels: stimuli-responsive soft materials based on one-dimensional self-assembling aromatic dyes. *Top. Curr. Chem.* 258, 119–160. doi: 10.1007/b135554

Jia, H., Li, Z., Wang, X., and Zheng, Z. (2015). Facile functionalization of a tetrahedron-like PEG macromonomer-based fluorescent hydrogel with high strength and its heavy metal ion detection. *J. Mater. Chem. A* 3, 1158–1163. doi: 10.1039/C4TA05736H

Jiang, H., Hu, P., Ye, J., Ganguly, R., Li, Y., Long, Y., et al. (2018). Hole mobility modulation in single-crystal metal phthalocyanines by changing the metal-π/π-π interactions. *Angew. Chem. Int. Ed.* 57, 10112–10117. doi: 10.1002/anie.201803363

Jin, H., Dai, X.-H., Wu, C., Pan, J.-M., Wang, X.-H., Yan, Y.-S., et al. (2015). Rational design of shear-thinning supramolecular hydrogels with porphyrin for controlled chemotherapeutics release and photodynamic therapy. *Eur. Polym. J.* 66, 149–159. doi: 10.1016/j.eurpolymj.2015.01.047

Jintoku, H., Sagawa, T., Sawada, T., Takafuji, M., Hachisako, H., and Ihara, H. (2008). Molecular organogel-forming porphyrin derivative with hydrophobic L-glutamide. *Tetrahedron Lett.* 49, 3987–3990. doi: 10.1016/j.tetlet.2008.04.103

Kar, H., and Ghosh, S. (2015). Multicomponent gels remote control for self-assembly. *Nat. Chem.* 7, 765–767. doi: 10.1038/nchem.2351

Karimi, A. R., and Khodadadi, A. (2016). Mechanically robust 3D nanostructure chitosan-based hydrogels with autonomic self-healing properties. *ACS Appl. Mater. Interfaces* 8, 27254–27263. doi: 10.1021/acsami.6b10375

Karimi, A. R., Khodadadi, A., and Hadizadeh, M. (2016). A nanoporous photosensitizing hydrogel based on chitosan cross-linked by zinc phthalocyanine: an injectable and pH-stimuli responsive system for effective cancer therapy. *RSC Adv.* 6, 91445–91452. doi: 10.1039/C6RA17064A

Kaufmann, L., Kennedy, S. R., Jones, C. D., and Steed, J. W. (2016). Cavity-containing supramolecular gels as a crystallization tool for hydrophobic pharmaceuticals. *Chem. Commun.* 52, 10113–10116. doi: 10.1039/C6CC04037C

Kawano, S.-I., Tamaru, S.-I., Fujita, N., and Shinkai, S. (2004). Sol-gel polycondensation of tetraethyl orthosilicate (TEOS) in sugar-based porphyrin organo-gels: inorganic conversion of a sugar-directed porphyrinic fiber library through sol-gel transcription processes. *Chem. Eur. J.* 10, 343–351. doi: 10.1002/chem.200305042

Keseberg, P., Bachl, J., and Diaz, D. D. (2016). Non-covalent incorporation of some substituted metal phthalocyanines into different gel networks and the effects on the gel properties. *J. Porphyrins Phthalocyanines* 20, 1390–1400. doi: 10.1142/S1088424616501145

Khan, M. K., and Sundararajan, P. (2011). Encapsulation of dye molecules and nanoparticles in hollow organogel fibers of a nonchiral polyurethane model compound. *Chem. Eur. J.* 17, 1184–1192. doi: 10.1002/chem.201001850

Kishida, T., Fujita, N., Sada, K., and Shinkai, S. (2005a). Porphyrin gels reinforced by sol-gel reaction via the organogel phase. *Langmuir* 21, 9432–9439. doi: 10.1021/la0515569

Kishida, T., Fujita, N., Sada, K., and Shinkai, S. (2005b). Sol-gel reaction of porphyrin-based superstructures in the organogel phase: creation of mechanically reinforced porphyrin hybrids. *J. Am. Chem. Soc.* 127, 7298–7299. doi: 10.1021/ja050563g

Kondrashina, A. V., Dmitriev, R. I., Borisov, S. M., Klimant, I., O'brien, I., Nolan, Y. M., et al. (2012). A Phosphorescent nanoparticle-based probe for sensing and imaging of (Intra)cellular oxygen in multiple detection modalities. *Adv. Funct. Mater.* 22, 4931–4939. doi: 10.1002/adfm.201201387

Kundu, S., and Patra, A. (2017). Nanoscale strategies for light harvesting. *Chem. Rev.* 117, 712–757. doi: 10.1021/acs.chemrev.6b00036

Lauceri, R., D'urso, A., and Purrello, R. (2011). "Preparation of transition metal complexes with multiporphyrin species in aqueous solutionm," in *Handbook of Porphyrin Science*, eds K. M. Kadish, K. M. Smith, and R. Guilard (Singapore: World Scientific Publishing Co. Pte. Ltd.), 151–196.

Li, J., Celiz, A. D., Yang, J., Yang, Q., Wamala, I., Whyte, W., et al. (2017a). Tough adhesives for diverse wet surfaces. *Science* 357, 378–381. doi: 10.1126/science.aah6362

Li, J., Wang, A., Ren, P., Yan, X., and Bai, S. (2019a). One-step co-assembly method to fabricate photosensitive peptide nanoparticles for two-photon photodynamic therapy. *Chem. Commun.* 55, 3191–3194. doi: 10.1039/C9CC00025A

Li, J., Wang, A., Zhao, L., Dong, Q., Wang, M., Xu, H., et al. (2018a). Self-assembly of monomeric hydrophobic photosensitizers with short peptides forming photodynamic nanoparticles with real-time tracking property and without the need of release *in vivo*. *ACS Appl. Mater. Interfaces* 10, 28420–28427. doi: 10.1021/acsami.8b09933

Li, J., Xing, R., Bai, S., and Yan, X. (2019b). Recent advances of self-assembling peptide-based hydrogels for biomedical applications. *Soft Matter* 15, 1704–1715. doi: 10.1039/C8SM02573H

Li, S., Zou, Q., Li, Y., Yuan, C., Xing, R., and Yan, X. (2018b). Smart peptide-based supramolecular photodynamic metallo-nanodrugs designed by multicomponent coordination self-assembly. *J. Am. Chem. Soc.* 140, 10794–10802. doi: 10.1021/jacs.8b04912

Li, Y., Duan, P., and Liu, M. (2017b). Solvent-regulated self-assembly of an achiral donor-acceptor complex in confined chiral nanotubes: chirality transfer, inversion and amplification. *Chem. Eur. J.* 23, 8225–8231. doi: 10.1002/chem.201700613

Li, Y., Wang, T., and Liu, M. (2007). Gelating-induced supramolecular chirality of achiral porphyrins: chiroptical switch between achiral molecules and chiral assemblies. *Soft Matter* 3, 1312–1317. doi: 10.1039/b710165a

Liang, J., Dong, X., Wei, C., Kong, D., Liu, T., and Lv, F. (2017a). Phthalocyanine incorporated alginate hydrogel with near infrared fluorescence for non-invasive imaging monitoring *in vivo*. *RSC Adv.* 7, 6501–6510. doi: 10.1039/C6RA27756J

Liang, J., Dong, X., Wei, C., Ma, G., Liu, T., Kong, D., et al. (2017b). A visible and controllable porphyrin-poly(ethylene glycol)/α-cyclodextrin hydrogel nanocomposites system for photo response. *Carbohydr. Polym.* 175, 440–449. doi: 10.1016/j.carbpol.2017.08.023

Liao, P., Hu, Y., Liang, Z., Zhang, J., Yang, H., He, L.-Q., et al. (2018). Porphyrin-based imine gels for enhanced visible-light photocatalytic hydrogen production. *J. Mater. Chem. A* 6, 3195–3201. doi: 10.1039/C7TA09785A

Liu, K., Liu, Y., Yao, Y., Yuan, H., Wang, S., Wang, Z., et al. (2013). Supramolecular photosensitizers with enhanced antibacterial efficiency. *Angew. Chem. Int. Ed.* 52, 8285–8289. doi: 10.1002/anie.201303387

Liu, M., Zhang, L., and Wang, T. (2015). Supramolecular chirality in self-assembled systems. *Chem. Rev.* 115, 7304–7397. doi: 10.1021/cr500671p

Lovell, J. F., Roxin, A., Ng, K. K., Qi, Q., Mcmullen, J. D., Da Costa, R. S., et al. (2011). Porphyrin-cross-linked hydrogel for fluorescence-guided monitoring and surgical resection. *Biomacromolecules* 12, 3115–3118. doi: 10.1021/bm200784s

Lv, F., Mao, L., and Liu, T. (2014). Thermosensitive porphyrin-incorporated hydrogel with four-arm PEG-PCL copolymer: preparation, characterization

and fluorescence imaging *in vivo*. *Mater. Sci. Eng. C* 43, 221–230. doi: 10.1016/j.msec.2014.07.019

Mack, J., and Stillman, M. J. (2003). "Electronic structures of metal phthalocyanine and porphyrin complexes from analysis of the UV-visible absorption and magnetic circular dichroism spectra and molecular orbital calculations," in *The Porphyrin Handbook*, eds K. Kadish, K. Smith, and R. Guilard (London: Elsevier Science), 43–116.

Mallia, V. A., and Weiss, R. G. (2018). Structure-property comparison and self-assembly studies of molecular gels derived from (R)-12-hydroxystearic acid derivatives as low molecular mass gelators. *ACS Symp. Ser.* 1296, 227–243. doi: 10.1021/bk-2018-1296.ch012

Martinez De Pinillos Bayona, A., Mroz, P., Thunshelle, C., and Hamblin, M. R. (2017). Design features for optimization of tetrapyrrole macrocycles as antimicrobial and anticancer photosensitizers. *Chem. Biol. Drug Des.* 89, 192–206. doi: 10.1111/cbdd.12792

Meier, R. J., Schreml, S., Wang, X.-D., Landthaler, M., Babilas, P., and Wolfbeis, O. S. (2011). Simultaneous photographing of oxygen and pH *in vivo* using sensor films. *Angew. Chem. Int. Ed.* 50, 10893–10896. doi: 10.1002/anie.201104530

Michaeli, K., Kantor-Uriel, N., Naaman, R., and Waldeck, D. H. (2016). The electron's spin and molecular chirality - how are they related and how do they affect life processes? *Chem. Soc. Rev.* 45, 6478–6487. doi: 10.1039/C6CS00369A

Moylan, C., Scanlan, E. M., and Senge, M. O. (2015). Chemical synthesis and medicinal applications of glycoporphyrins. *Curr. Med. Chem.* 22, 2238–2348. doi: 10.2174/0929867322666150429113104

Paolesse, R., Nardis, S., Monti, D., Stefanelli, M., and Di Natale, C. (2017). Porphyrinoids for chemical sensor applications. *Chem. Rev.* 117, 2517–2583. doi: 10.1021/acs.chemrev.6b00361

Pizzarello, S. (2016). Molecular asymmetry in prebiotic chemistry: an account from meteorites. *Life* 6, 18/11–18/19. doi: 10.3390/life6020018

Sagawa, T., Fukugawa, S., Yamada, T., and Ihara, H. (2002). Self-assembled fibrillar networks through highly oriented aggregates of porphyrin and pyrene substituted by dialkyl l-glutamine in organic media. *Langmuir* 18, 7223–7228. doi: 10.1021/la0255267

Saha, M. L., Yan, X., and Stang, P. J. (2016). Photophysical Properties of organoplatinum(II) compounds and derived self-assembled metallacycles and metallacages: fluorescence and its applications. *Acc. Chem. Res.* 49, 2527–2539. doi: 10.1021/acs.accounts.6b00416

Sakai, S., Moriyama, K., Taguchi, K., and Kawakami, K. (2010). Hematin is an alternative catalyst to horseradish peroxidase for *in situ* hydrogelation of polymers with phenolic hydroxyl groups *in vivo*. *Biomacromolecules* 11, 2179–2183. doi: 10.1021/bm100623k

Setnicka, V., Urbanova, M., Pataridis, S., Kral, V., and Volka, K. (2002). Sol-gel phase transition of brucine-appended porphyrin gelator: a study by vibrational circular dichroism spectroscopy. *Tetrahedron* 13, 2661–2666. doi: 10.1016/S0957-4166(02)00740-1

Severance, S., and Hamza, I. (2009). Trafficking of heme and porphyrins in metazoa. *Chem. Rev.* 109, 4596–4616. doi: 10.1021/cr9001116

Shen, Z., Jiang, Y., Wang, T., and Liu, M. (2015). Symmetry breaking in the supramolecular gels of an achiral gelator exclusively driven by π-π stacking. *J. Am. Chem. Soc.* 137, 16109–16115. doi: 10.1021/jacs.5b10496

Shirakawa, M., Fujita, N., and Shinkai, S. (2003a). [60]Fullerene-motivated organogel formation in a porphyrin derivative bearing programmed hydrogen-bonding sites. *J. Am. Chem. Soc.* 125, 9902–9903. doi: 10.1021/ja035933k

Shirakawa, M., Kawano, S., Fujita, N., Sada, K., and Shinkai, S. (2003b). Hydrogen-bond-assisted control of h versus j aggregation mode of porphyrins stacks in an organogel system. *J. Org. Chem.* 68, 5037–5044. doi: 10.1021/jo03 41822

Silverman, J. R., Zhang, Q., Pramanik, N. B., Samateh, M., Shaffer, T. M., Sagiri, S. S., et al. (2017). Radiation-responsive esculin-derived molecular gels as signal enhancers for optical imaging. *ACS Appl. Mater. Interfaces* 9, 43197–43204. doi: 10.1021/acsami.7b15548

Singh, S., Aggarwal, A., Bhupathiraju, N. V., Arianna, G., Tiwari, K., and Drain, C. M. (2015). Glycosylated porphyrins, phthalocyanines, and other porphyrinoids for diagnostics and therapeutics. *Chem. Rev.* 115, 10261–10306. doi: 10.1021/acs.chemrev.5b00244

Smith, D. K. (2012). "Self-assembling fibrillar networks-supramolecular gels," in *Soft Matter,* eds J. W. Steed and P. A. Gale. (Weinheim: John Wiley and Sons Ltd.), 3355–3376.

Steed, J. W. (2010). Anion-tuned supramolecular gels: a natural evolution from urea supramolecular chemistry. *Chem. Soc. Rev.* 39, 3686–3699. doi: 10.1039/b926219a

Tamaru, S., Nakamura, M., Takeuchi, M., and Shinkai, S. (2001). Rational design of a sugar-appended porphyrin gelator that is forced to assemble into a one-dimensional aggregate. *Org. Lett.* 3, 3631–3634. doi: 10.1021/ol0165544

Tanaka, S., Sakurai, T., Honsho, Y., Saeki, A., Seki, S., Kato, K., et al. (2012). Toward ultralow-band gap liquid crystalline semiconductors: use of triply fused metalloporphyrin trimer-pentamer as extra-large π-extended mesogenic motifs. *Chem. Eur. J.* 18, 10554–10561. doi: 10.1002/chem.201201101

Tanaka, S., Shirakawa, M., Kaneko, K., Takeuchi, M., and Shinkai, S. (2005). Porphyrin-based organogels: control of the aggregation mode by a pyridine–carboxylic acid interaction. *Langmuir* 21, 2163–2172. doi: 10.1021/la0 47070u

Urbani, M., Grätzel, M., Nazeeruddin, M. K., and Torres, T. (2014). Meso-substituted porphyrins for dye-sensitized solar cells. *Chem. Rev.* 114, 12330–12396. doi: 10.1021/cr5001964

Versluis, F., Van Elsland, D. M., Mytnyk, S., Perrier, D. L., Trausel, F., Poolman, J. M., et al. (2016). Negatively charged lipid membranes catalyze supramolecular hydrogel formation. *J. Am. Chem. Soc.* 138, 8670–8673. doi: 10.1021/jacs.6b03853

Wang, H., Wang, H., Yang, X., Wang, Q., and Yang, Y. (2015a). Ion-Unquenchable and thermally "on-off" reversible room temperature phosphorescence of 3-bromoquinoline induced by supramolecular gels. *Langmuir* 31, 486–491. doi: 10.1021/la5040323

Wang, Q., Zhang, L., Yang, D., Li, T., and Liu, M. (2016). Chiral signs of TPPS co-assemblies with chiral gelators: role of molecular and supramolecular chirality. *Chem. Commun.* 52, 12434–12437. doi: 10.1039/C6CC05668G

Wang, Y., Han, B., Shi, R., Pan, L., Zhang, H., Shen, Y., et al. (2013). Preparation and characterization of a novel hybrid hydrogel shell for localized photodynamic therapy. *J. Mater. Chem. B* 1, 6411–6417. doi: 10.1039/c3tb20779j

Wang, Y., Lovrak, M., Liu, Q., Maity, C., Le Sage, V. A. A., Guo X., et al. (2018). Hierarchically compartmentalized supramolecular gels through multilevel self-sorting. *J. Am. Chem. Soc.* 141, 2847–2851. doi: 10.1021/jacs.8b09596

Wang, Y., Shi, Y., Pan, L., Ding, Y., Zhao, Y., Li, Y., et al. (2015b). Dopant-enabled supramolecular approach for controlled synthesis of nanostructured conductive polymer hydrogels. *Nano Lett.* 15, 7736–7741. doi: 10.1021/acs.nanolett.5b03891

Weiss, R.G., and Terech, P. (eds.). (2006). "Materials with self-assembled fibrillar networks," in *Molecular Gels* (Dordrecht: Springer), 978.

Weiss, R. G. (2014). The past, present, and future of molecular gels. What is the status of the field, and where is it going? *J. Am. Chem. Soc.* 136, 7519–7530. doi: 10.1021/ja503363v

Weiss, R. G. (2018). Controlling variables in molecular gel science: how can we improve the state of the art? *Gels* 4:25. doi: 10.3390/gels4020025

Wong, W.-Y., Leung, K. C., and Stoddart, J. F. (2010). Self-assembly, stability quantification, controlled molecular switching, and sensing properties of an anthracene-containing dynamic [2]rotaxane. *Org. Biomol. Chem.* 8, 2332–2343. doi: 10.1039/b926568f

Wu, K., Guo, J., and Wang, C. (2014). Gelation of Metalloporphyrin-based conjugated microporous polymers by oxidative homocoupling of terminal alkynes. *Chem. Mater.* 26, 6241–6250. doi: 10.1021/cm503086w

Xia, L.-Y., Zhang, X., Cao, M., Chen, Z., and Wu, F.-G. (2017). Enhanced fluorescence emission and singlet oxygen generation of photosensitizers embedded in injectable hydrogels for imaging-guided photodynamic cancer therapy. *Biomacromolecules* 18, 3073–3081. doi: 10.1021/acs.biomac.7b00725

Xiao, Q., Ji, Y., Xiao, Z., Zhang, Y., Lin, H., and Wang, Q. (2013). Novel multifunctional NaYF4:Er3+,Yb3+/PEGDA hybrid microspheres: NIR-light-activated photopolymerization and drug delivery. *Chem. Commun.* 49, 1527–1529. doi: 10.1039/c2cc37620b

Xiao, Z.-Y., Zhao, X., Jiang, X.-K., and Li, Z.-T. (2009). Self-assembly of porphyrin-azulene-porphyrin and porphyrin-azulene conjugates. *Org. Biomol. Chem.* 7, 2540–2547. doi: 10.1039/b904009a

Xu, J., Wang, Y., Shan, H., Lin, Y., Chen, Q., Roy, V., et al. (2016). Ultrasound-induced organogel formation followed by thin film fabrication via simple doctor blading technique for field-effect transistor applications. *ACS Appl. Mater. Interfaces* 8, 18991–18997. doi: 10.1021/acsami.6b04817

Yang, A., Dong, X., Liang, J., Zhang, Y., Yang, W., Liu, T., et al. (2018a). Photothermally triggered disassembly of a visible dual fluorescent poly(ethylene glycol)/α-cyclodextrin hydrogel. *Soft Matter* 14, 4495–4504. doi: 10.1039/C8SM00626A

Yang, L., Liu, A., De Ruiter, M. V., Hommersom, C. A., Katsonis, N., Jonkheijm, P., et al. (2018b). Compartmentalized supramolecular hydrogels based on viral nanocages towards sophisticated cargo administration. *Nanoscale* 10, 4123–4129. doi: 10.1039/C7NR07718A

Yang, X.-Y., Chen, L.-H., Li, Y., Rooke, J. C., Sanchez, C., and Su, B.-L. (2017). Hierarchically porous materials: synthesis strategies and structure design. *Chem. Soc. Rev.* 46, 481–558. doi: 10.1039/C6CS00829A

Yang, Y., Liu, Z., Chen, J., Cai, Z., Wang, Z., Chen, W., et al. (2018c). A facile approach to improve interchain packing order and charge mobilities by self-assembly of conjugated polymers on water. *Adv. Sci.* 5:1801497. doi: 10.1002/advs.201801497

Yazdely, T. M., Ghorbanloo, M., and Hosseini-Monfared, H. (2018). Polymeric ionic liquid material-anchored Mn–porphyrin anion: heterogeneous catalyst for aerobic oxidation of olefins. *Appl. Organometallic Chem.* 32:e4388. doi: 10.1002/aoc.4388

Yu, G., Yan, X., Han, C., and Huang, F. (2013). Characterization of supramolecular gels. *Chem. Soc. Rev.* 42, 6697–6722. doi: 10.1039/c3cs60080g

Yu, H., Lü, Y., Chen, X., Liu, K., and Fang, Y. (2014). Functionality-oriented molecular gels: synthesis and properties of nitrobenzoxadiazole (NBD)-containing low-molecular mass gelators. *Soft Matter* 10, 9159–9166. doi: 10.1039/C4SM01869A

Yuan, Z., and Chen, D. (2017). Fabrication and photocatalytic behavior of a novel nanocomposite hydrogels containing Fe-octacarboxylic acid phthalocyanine. *J. Appl. Polym. Sci.* 134, n/a. doi: 10.1002/app.45428

Zhang, C., Chen, P., Dong, H., Zhen, Y., Liu, M., and Hu, W. (2015). Porphyrin supramolecular 1D structures via surfactant-assisted self-assembly. *Adv. Mater.* 27, 5379–5387. doi: 10.1002/adma.201501273

Zhang, H., Liu, K., Li, S., Xin, X., Yuan, S., Ma, G., et al. (2018). Self-assembled minimalist multifunctional theranostic nanoplatform for magnetic resonance imaging-guided tumor photodynamic therapy. *ACS Nano* 12, 8266–8276. doi: 10.1021/acsnano.8b03529

Zhang, W., Lai, W., and Cao, R. (2017). Energy-related small molecule activation reactions: oxygen reduction and hydrogen and oxygen evolution reactions catalyzed by porphyrin- and corrole-based systems. *Chem. Rev.* 117, 3717–3797. doi: 10.1021/acs.chemrev.6b00299

Zhao, G.-Z., Chen, L.-J., Wang, W., Zhang, J., Yang, G., Wang, D.-X., et al. (2013). Stimuli-responsive supramolecular gels through hierarchical self-assembly of discrete rhomboidal metallacycles. *Chem. Eur. J.* 19, 10094–10100. doi: 10.1002/chem.201301385

Zhao, Q., Wang, Y., Yan, Y., and Huang, J. (2014). Smart nanocarrier: self-assembly of bacteria-like vesicles with photoswitchable cilia. *ACS Nano* 8, 11341–11349. doi: 10.1021/nn5042366

Zhu, W., Yang, Y., Jin, Q., Chao, Y., Tian, L., Liu, J., et al. (2018). Two-dimensional metal-organic-framework as a unique theranostic nano-platform for nuclear imaging and chemo-photodynamic cancer therapy. *Nano Res.* 1–6. doi: 10.1007/s12274-018-2242-2

Conflict of Interest Statement: The authors declare that the research was conducted in the absence of any commercial or financial relationships that could be construed as a potential conflict of interest.

frontiers in Chemistry

ORIGINAL RESEARCH
published: 15 May 2019
doi: 10.3389/fchem.2019.00333

Fluoro-Modulated Molecular Geometry in Diketopyrrolopyrrole-Based Low-Bandgap Copolymers for Tuning the Photovoltaic Performance

Cai'e Zhang†, Yahui Liu†, Jia Tu, Shouli Ming, Xinjun Xu and Zhishan Bo**

Beijing Key Laboratory of Energy Conversion and Storage Materials, College of Chemistry, Beijing Normal University, Beijing, China

OPEN ACCESS

Edited by:
Penglei Chen,
Institute of Chemistry (CAS), China

Reviewed by:
Yingping Zou,
Central South University, China
Zuo-Quan Jiang,
Soochow University, China
Lu Kun,
National Center for Nanoscience and Technology (CAS), China

***Correspondence:**
Xinjun Xu
xuxj@bnu.edu.cn
Zhishan Bo
zsbo@bnu.edu.cn

†These authors have contributed equally to this work

Specialty section:
This article was submitted to Supramolecular Chemistry, a section of the journal Frontiers in Chemistry

Received: *27 February 2019*
Accepted: *24 April 2019*
Published: *15 May 2019*

Citation:
Zhang C, Liu Y, Tu J, Ming S, Xu X and Bo Z (2019) Fluoro-Modulated Molecular Geometry in Diketopyrrolopyrrole-Based Low-Bandgap Copolymers for Tuning the Photovoltaic Performance. Front. Chem. 7:333. doi: 10.3389/fchem.2019.00333

Fluorination of conjugated polymers is an effective strategy to tune the energy levels for obtaining high power conversion efficiency (PCE) in organic solar cells. In this work, we have developed fluoro-modulated molecular geometries in diketopyrrolopyrrole based low-bandgap copolymers. In these polymers, planar conformation can be locked by intramolecular non-covalent interaction (intramolecular supramolecular interaction) between the sulfur atoms and the introduced F atoms (F···S interaction). By varying the fluorinated moieties, such a planarity can be disturbed and the molecular geometry is tuned. As a result, the polymer' properties can be modulated, including the ultraviolet-visible absorption spectrum to become broaden, charge mobility to be enhanced, open-circuit voltage (V_{OC}) and short-circuited current (J_{SC}) to be elevated, and thus photovoltaic performance to be improved. The photovoltaic device based on PCFB, one of the fluorinated terpolymers, exhibited a high PCE near 8.5% with simultaneously enhanced V_{OC} and J_{SC} relative to the non-fluorinated one (PCB).

Keywords: diketopyrrolopyrrole, fluorination, supramolecular interaction, polymer solar cell, photovoltaic performance

INTRODUCTION

Low-band gap (LBG) polymers have attracted lots of research attention due to their possibility to extend the absorption of solar spectrum from ultraviolet-visible (UV-vis) to near-infrared (NIR) region to make a good utilization of solar energy when used in organic solar cells (OSCs). They have the merits of enhancing the light absorption, realizing high-efficiency tandem solar cells with a wide bandgap polymer (Dou et al., 2012; You et al., 2013), and achieving semitransparent photovoltaic devices that strongly absorb light in the NIR region while allowing most of the visible light to get through (Dou et al., 2013). Among these LBG polymers, conjugated polymers employing diketopyrrolopyrrole (DPP) unit were frequently reported in the areas of organic field-effect transistors (OFETs) and OSCs in recent years (Hendriks et al., 2014a; Li et al., 2014b, 2018; Li C. et al., 2016; Yu et al., 2016). The DPP moiety usually has strong intermolecular interactions in the solid state including hydrogen bonding and π-π interactions and its polar nature enhances the tendency of DPP-based polymers to crystallize (Sonar et al., 2010). As a result, DPP-based conjugated polymers often exhibit an advantageously tunable and broad optical absorption, high

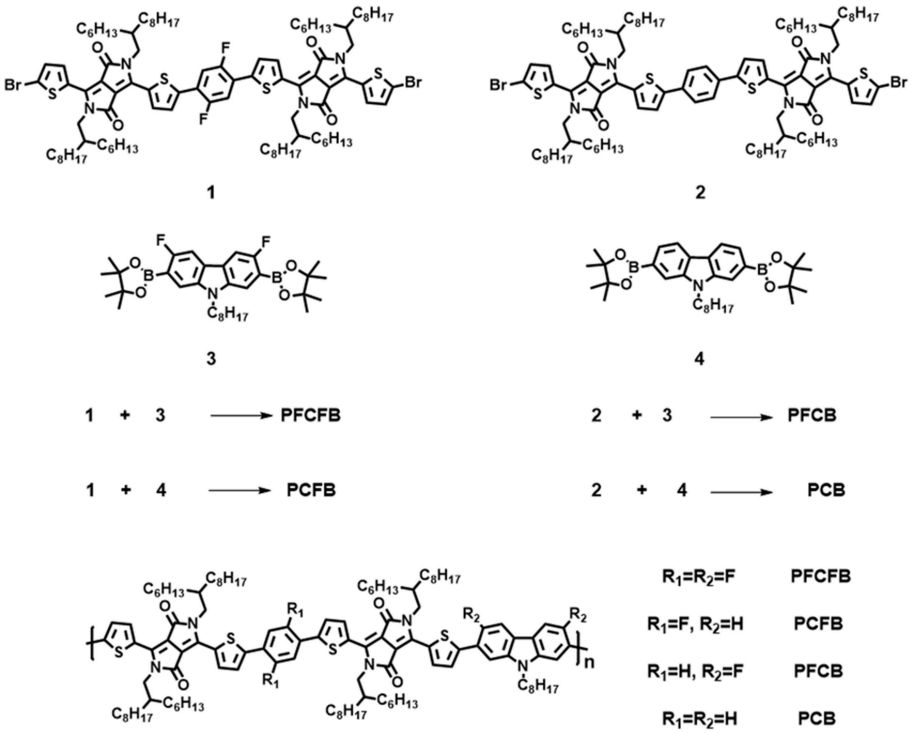

SCHEME 1 | Molecular structures and synthetic methods of the polymers.

charge carrier mobilities, and good nanoscale morphologies (Nielsen et al., 2013; Li et al., 2015; Wang et al., 2016), which can result in high photocurrents and good fill factors (FF) in OSCs. For instance, the optical absorption of the DPP based polymers can extend much farther into the NIR region (Hendriks et al., 2014b; Li et al., 2015), which provides wide photo-response in a long wavelength range to give a high short-circuit current (J_{sc}) in OSCs and can be applied in NIR organic photodetectors (Ashraf et al., 2015).

However, there are also some drawbacks in DPP based OSCs. Their open circuit voltage (V_{oc}) was usually <0.7 V due to their shallow highest occupied molecular orbital (HOMO) energy levels. Therefore, there are only several reports showed a power conversion efficiency (PCE) over 8% in single-junction OSCs based on DPP polymers (Hendriks et al., 2013; Choi et al., 2015; Zheng et al., 2016). There are several ways to adjust the energy level of polymers. One approach is to introduce electron-withdrawing groups in the backbone of the polymers. For example, poly (2,5-bis(2-decyltetradecyl)-pyrrolo[3,4-c]pyrrole-1,4(2H,5H)-dione-3,6-diyl-alt-3″,4′ -difluoro-2,2′:5′,2″:5″,2‴-quaterthiophene-5,5‴-diyl (PDPP4T-2F) was successfully designed by introducing two fluorine atoms to the 2,2′-bithiophene monomer which gave deeper energy level and higher V_{oc} (Zheng et al., 2016). Introducing F atom is also important in tailoring the chemical and physical properties of the resulting polymers (Albrecht et al., 2012; Li et al., 2014a). The non-covalent interaction of F atom not only exists in copolymers, but also can be observed in non-fullerene small molecule acceptors (Zhao et al., 2017; Liu et al., 2018). Because fluorine is the most electronegative element in the periodic table, the F atom is a powerful functional group for donor/acceptor materials. It has a quite strong electron-withdrawing nature, so the introduction of fluorine into the polymer/acceptor backbone can lower the HOMO and the lowest unoccupied molecular orbital (LUMO) energy level, resulting in the increase of V_{oc}. It is also believed that the fluorine atom offers non-covalent attractive interactions in a molecule (i.e., intramolecular supramolecular interaction) between the hydrogen or sulfur atoms, which may contribute to enhancing the coplanarity of the polymer backbone which would be favorable for the self-assembly and the crystallinity of the polymer (Li et al., 2014a; Kawashima et al., 2016; Zhang Q. et al., 2017). Another way to adjust the energy levels of polymers is to fabricate copolymers with different units. Recently, terpolymers which comprise three various components in the backbone have emerged as a new design strategy for donor polymers (Qin et al., 2014; Duan et al., 2016; Wang X. et al., 2017; Wang Y. et al., 2017; Huo et al., 2018). Among these copolymers, regioregular ones provide natural advantages, such as well-defined molecular structure, highly reproducibility and better molecular packing (Qin et al., 2014; Kim et al., 2015; Lee et al., 2015). Based on the above thinking, DPP based regioregular terpolymer with difluorobenzene and difluorocarbazole units was successfully fabricated and applied as donor material for OSCs in our previous work with a high V_{oc} of 0.86 V and PCE over 8% (Liu et al., 2016).

Despite such advantages of F substitutions to the properties of donor polymers, some reports demonstrated that excessive F atoms would reduce the photovoltaic performance due to the significantly aggravated aggregation of polymer chains and enhanced trap-assisted charge recombinations (Jo et al., 2015; Kawashima et al., 2016; Lee et al., 2016). It should be noted that such results were all obtained based on donor-acceptor (D-A) alternating binary copolymers. However, investigations of the effect of fluorine substitutions on both LBG terpolymers and DPP based copolymers are all currently absent. How the F atoms will affect the properties of such copolymers and their photovoltaic performance? With these questions in mind, here we expect to investigate the photovoltaic performance of DPP-based terpolymers by introducing fluorine atoms into different moieties of the polymer backbone and adjusting the number of fluorine atoms so as to modulate their properties. In this work, four polymers (**PFCFB, PCFB, PFCB,** and **PCB**) were designed by altering F atoms in the monomers. They were synthesized with Suzuki coupling and exhibited similar molecular weight. Their HOMO energy levels were significantly reduced with the introduction of F atoms which gave higher V_{oc} in the photovoltaic device. F atoms was able to flatten the adjacent aromatic units because of the F· · ·S and F· · ·H interactions. The F· · ·S and F· · ·H interactions are ultimately electrostatic interaction. In the previous literature (Fei et al., 2015), according to density functional theory (DFT) calculations, positively charged sulfur atom (+0.308) and negatively charged fluorine atom (−0.281) tend to form strong electrostatic interaction. However, hydrogen atom (+0.148) is less positively charged than sulfur atom, so F···S rather than F···H intramolecular interaction is preferred in our polymer backbone. Besides, Yan et al obtained single crystal structure of the model compounds (Li Z. et al., 2016). The observations of F· · ·S interactions dominate the conformation or geometry. Therefore, we think the backbone of our polymer tend to form F· · ·S intramolecular interaction. In addition, the FF was decreased with the diminution of F atom. The photovoltaic device based on PFCFB exhibited the highest PCE of 8.48% with a highest V_{oc} of 0.86 V and the device based on PCFB displayed a similar PCE of 8.46% with the highest J_{sc} of 17.20 mA cm^{-2}, which are all improved relative to that of devices based on the non-fluorinated polymer (**PCB**).

RESULTS AND DISCUSSION

The synthetic route of polymers **PFCFB, PCFB, PFCB,** and **PCB** was shown in **Scheme 1** (see **Table S1**). The original monomers **1**, **2**, **3**, and **4** were synthesized as reported (Du et al., 2013; Park et al., 2013; Liu et al., 2016). These polymers can be acquired by Suzuki coupling using $Pd(PPh_3)_4$ as the catalyst. The molecular weights of these polymers via gel permeation chromatography (GPC) measurements are listed in **Table 1**. It is worth noting that high number-average molecular weight over 250 kg/mol can be acquired with facile Suzuki polymerization for these polymers.

UV-vis spectra of polymers were investigated in thin films (**Figure 1A**). These polymers show similar absorption in visible light region with two absorption bands. The one located at shorter wavelength can be attributed to the localized π-π* transition and the strong peaks located at longer wavelength originate from the intramolecular charge transfer (ICT) (Tanaka et al., 2013). The absorption edges of these polymers are not the same. Optical bandgaps (E_g) calculated from the absorption edges of these polymers are listed in **Table 1**. It shows that fluorination of the polymer backbone reduces the optical bandgap. In addition, the dominant absorption peak of **PCFB** (∼740 nm) is slightly red-shifted compared with that of other polymers. This result can be explained by the shorter lamellar distance existing in **PCFB** film as validated from X-ray diffraction (XRD) data (*vide infra*, see **Figure S1**, **Table S2**), which indicates that the polymer chains were packed more tightly (Wang Y. et al., 2017). The electrochemical properties were also investigated by cyclic voltammetry (CV). Based on the CV results, energy levels of these polymers can be calculated according to the equations: $E_{HOMO} = -e[E_{ox,onset} - E_{(Fc/Fc+)} + 4.8]$ (Li G. et al., 2016; Zhang C. E. et al., 2017), and $E_{LUMO} = E_{HOMO} + E_{g,opt}$, where $E_{g,opt}$ is the optical bandgap of the polymer. The detailed information is shown in **Figure 1B**, **Table 1**. As expected, the HOMO energy level was tunable and lowered in an observable scale with the introduction of F atoms, which is consistent with literature (Liu et al., 2018). Inevitably, the V_{oc} of corresponding devices is affected, which will be discussed further below. The thermostability was investigated with thermogravimetric analysis (TGA) shown in **Figure S2** which indicates good thermal stability with a decomposition temperature over 350°C with a weight loss of 5% under nitrogen atmosphere. The packing behaviors of **PFCFB**, **PCFB**, **PFCB,** and **PCB** in films was surveyed by XRD measurements. All of these polymers exhibit two diffraction peaks. As displayed in **Figure S1**, **Table S2**, one set of the diffraction peaks in **PFCFB**, **PCFB**, **PFCB,** and **PCB** films are located at 2θ of 4.76°, 4.84°, 4.75°, and 4.79°, corresponding to lamellar distances of 18.58, 18.26, 18.61, and 18.44 Å, respectively. Diffraction peaks arising from the π-π stacking of backbones appeared at 2θ of 24.03°, 23.85°, 23.92°, and 23.63°, corresponding to distances of 3.70, 3.73, 3.72, and 3.77 Å for **PFCFB**, **PCFB**, **PFCB** and

TABLE 1 | The physical, optical, and electrical properties of polymers.

Polymer	M_n (kg/mol)	M_w (kg/mol)	PDI	λ_{max} (nm) in film	$E_{g,opt}$ (eV)	HOMO (eV)	LUMO (eV)
PFCFB	264	728	2.8	403, 677, 738	1.57	−5.31	−3.74
PCFB	284	1,006	3.5	393, 678, 742	1.55	−5.29	−3.74
PFCB	285	886	3.1	403, 670, 733	1.57	−5.28	−3.71
PCB	278	923	3.3	387, 667, 728	1.60	−5.25	−3.65

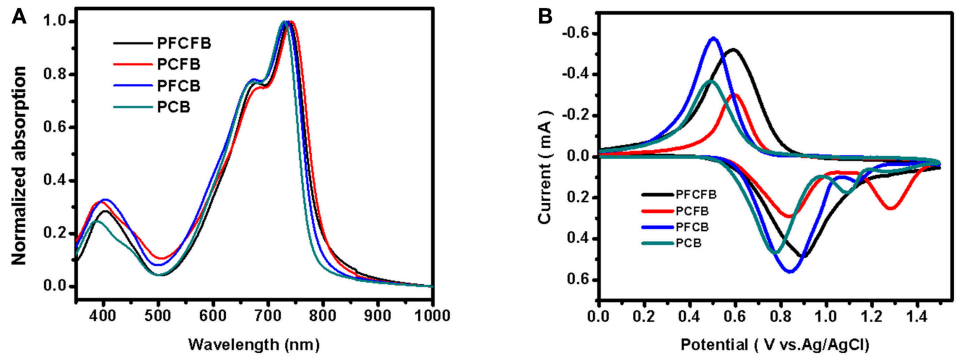

FIGURE 1 | UV-vis spectra of polymers as thin films **(A)**, and CV curves of polymer films on a Pt electrode measured in 0.1 M Bu_4NPF_6 acetonitrile solutions for oxidation at a scan rate of 100 mV/s **(B)**.

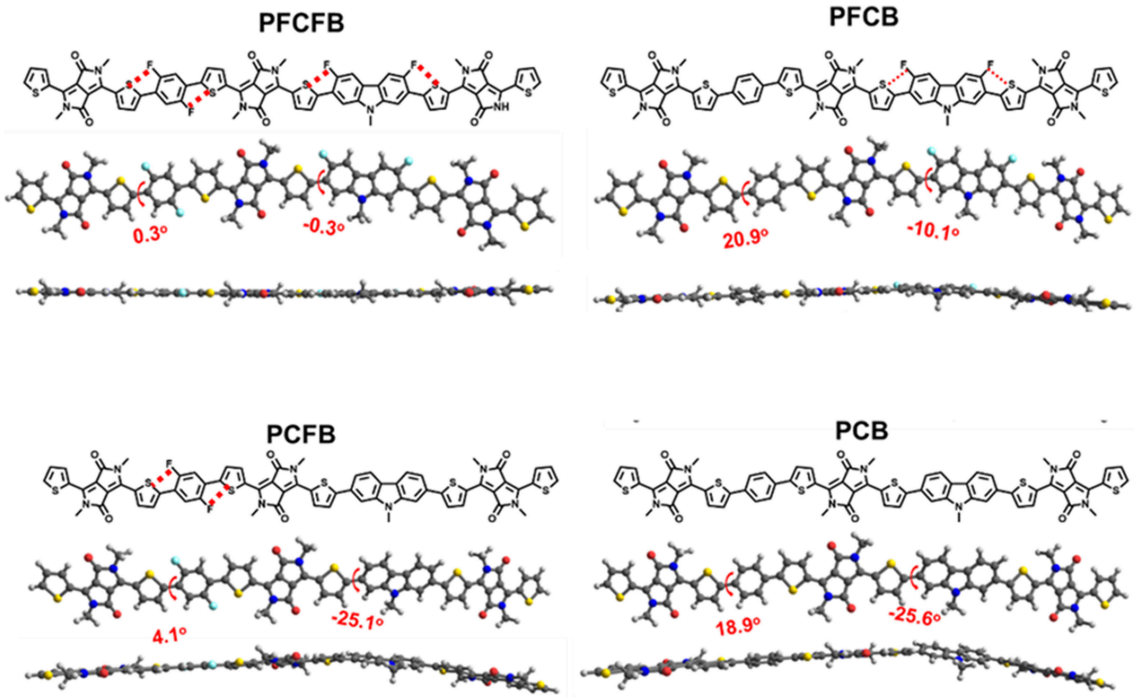

FIGURE 2 | Optimized chemical geometries of the simplified repeating units using DFT at the B3LYP/6-31G(d) level.

PCB, respectively. The consequence indicates that **PCFB** with fluorinated benzene but non-fluorinated carbazole moieties in the polymer chain possesses the minimum lamellar distance, while **PFCFB** with both fluorinated benzene and fluorinated carbazole moieties shows the minimum π-π stacking distance. Since the long-wavelength absorption peak (700∼750 nm) is susceptible to the aggregation of polymer chains and the short-wavelength one (around 400 nm) is influenced by the π-π stacking of aromatic units, the XRD results are thus in line with the UV-vis absorption spectra of the polymers, where **PCFB** shows the most bathochromic-shifted peak in the long-wavelength region but **PFCFB** does so in the short-wavelength one.

DENSITY FUNCTIONAL THEORY CALCULATIONS

Density functional theory (DFT) calculations at the B3LYP/6-31G(d) level was used to investigate the chemical geometry and electronic structures of the simplified repeating units. As shown in **Figure 2**, the two important dihedral angles in the repeating units are marked. The one formed by benzene and thiophene is significantly reduced from about 20° to only several degrees after fluorine substitution. However, the other one formed by carbazole and thiophene is quite large about 25° and only decreased to 10° after fluorine substitution. It is worth noting that these dihedral angles were approaching to zero degree after

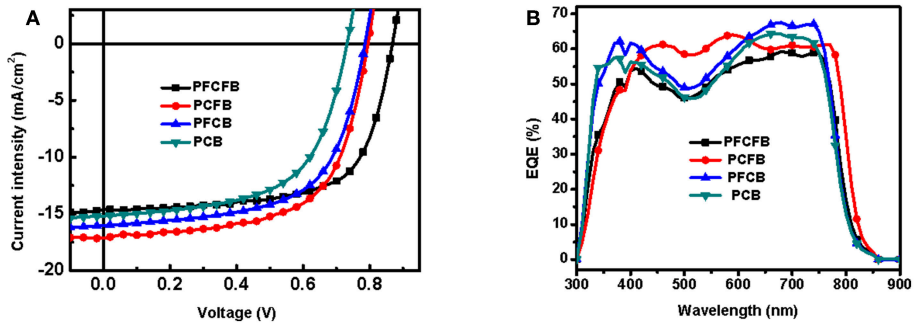

FIGURE 3 | *J-V* **(A)** and EQE **(B)** curves of OSCs based on **PFCFB, PCFB, PFCB,** and **PCB**.

TABLE 2 | Photovoltaic parameters of devices based on **PFCFC, PCFB, PFCB,** and **PCB**.

Polymer	DIO	V_{oc}(V)	J_{sc}(mA/cm^2)	FF	PCE (%)
PFCFB	1%	0.86	14.60 (14.34)[a]	0.66	8.48
PCFB	0.8%	0.79	17.20 (16.56)[a]	0.62	8.46
PFCB	1%	0.78	16.21 (15.71)[a]	0.61	7.73
PCB	1%	0.73	15.19 (14.91)[a]	0.59	6.64

[a]*Calculated by EQE measurements.*

fluorination of both the carbazole and the benzene units, which endows excellent planarity of the repeating unit based on **PFCFB**. This planarity guarantees the outstanding transport mobility of the polymers which may give the high FF of the devices. **PCFB** is the other one who possesses a moderate planarity with two dihedral angles of 4.1° and 25.1°, which may give a reason why it has both a short lamellar and π-π stacking distance. Such an enhanced planarity of the aromatic fragments in fluorinated polymer chains arises from the intramolecular F· · ·S interaction, which lock their planar conformations in the solid states (Jackson et al., 2013; Cheng et al., 2016). It is worth noting that the result of the calculations is consistent with the X-ray diffractions. As shown in **Table S2**, polymer film based on **PFCFB** exhibit the lowest d-spacing distance about 3.70 Å, the one based on **PCB** own a d-spacing distance of 3.76 Å, and the d-spacing distance of the **PFCB** and **PCFB** was between **PFCFB** and **PCB**. This phenomenon arises from the different planarity of the polymers caused by the differences in intramolecular non-covalent interactions. The electronic properties are also investigated *via* DFT calculations (see **Figure S3**). The tendency was consistent with CV measurements. The HOMO energy level moved downwards after the introduction of F atoms, which will be helpful to enhance V_{oc} of the devices based on fluorinated polymers.

PHOTOVOLTAIC PROPERTIES

The photovoltaic properties of the polymers was investigated using conventional device with a structure of ITO/PEDOT:PSS/polymer:$PC_{71}BM$/LiF/Al in which ITO and PEDOT:PSS mean indium tin oxide, poly(3,4-ethylenedioxythiophene):poly(styrenesulfonate), phenyl-C_{71}-butyric acid methyl, respectively. Various conditions were employed to optimize the photovoltaic performance, such as different ratios of donor/acceptor, solvent additives and spin-coating rates. The optimized current-voltage (*J-V*) curves is shown in **Figure 3**. The active layer was spin-coated on the substrate with a solution of $CHCl_3$ (with DIO as the additive). The optimized donor to acceptor weight ratio is 1:2 (w/w), and the optimized thickness is 100 nm by a spin-coating rate about 1,100 r/min with dilute polymer concentration of 3 mg/mL. The optimized photovoltaic parameters were summarized in **Table 2**. Devices based on **PFCFB** and **PCFB** gave the high PCE of 8.48 and 8.46%, respectively. It should be noted that PFCFB shows a different photovoltaic performance with PCDPP (Liu et al., 2016), which has a similar molecular structure as PFCFB. The difference comes from two aspects. First, PFCFB has a straight alkyl chain (n-octyl) on the carbazole unit; however, PCDPP has a branched one (2-ethylhexyl). Second, the processing solvents for depositing the active layer are different. The active layer was deposited from chlorobenzene solutions for PCDPP based device (Liu et al., 2016). In contrast, the active layer was deposited from a solution of $CHCl_3$ for PFCFB. Here, the reason for using a solution of $CHCl_3$ is that **PCFB** dissolves better in $CHCl_3$ than in chlorobenzene. In order to make a comparison with the other three compounds, we thus chose chloroform as the processing solvent. The optimized **PFCB** and **PCB** based devices gave a relatively low PCE of 7.73 and 6.64%, respectively. Moreover, the V_{oc} of these devices was decreased with the reduction of F atoms due to the increase of HOMO energy level of polymers. Typically, the V_{oc} of PFCFB based device was 0.86 V which is among the highest V_{oc} of DPP-based polymers (Liu et al., 2016). The V_{oc} of **PCB** based device was decreased about 15% with a value of 0.73 V. The elevated J_{sc} of **PFCB** and **PCFB** based devices relative to that of **PCB** based one can be attributed to the reduced π-π stacking distance which facilitates the charge transport (vide infra). Although **PFCFB** demonstrated the highest V_{oc} among the four polymers, it shows the lowest J_{sc} value which arises from its low photoresponse in the wavelength range of 600–800 nm. External quantum efficiency (EQE) measurements were performed under monochromatic irradiation to investigate the spectral photoresponse and to verify the J_{sc} obtained from *J-V* curves. The photo-electron response region was contributed by both the two components of the blend film. In addition, the edge of EQE curves were mainly decided by the UV-vis absorption of the polymers due to the narrow absorption of the

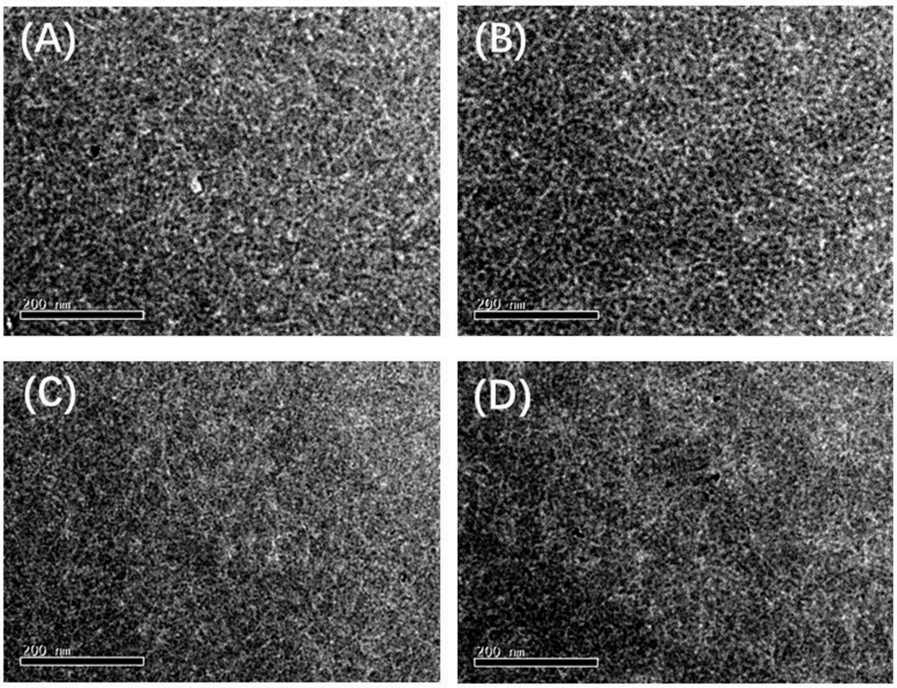

FIGURE 4 | TEM images of the blend films based on the polymer **(A) PFCFB, (B) PCFB, (C) PFCB,** and **(D) PCB**.

$PC_{71}BM$. Therefore, devices based on **PCFB** exhibit the broadest photo-electron response region, while **PCB** based devices possess the narrowest one. It is worth noting that the J_{sc} obtained from EQE curves is within 5% deviation to that of *J-V* curves.

CHARGE TRANSPORT PROPERTIES

The charge transport properties were characterized to further expose the differences in the four polymers. Hole and electron mobilities were measured by the space-charge-limited-current (SCLC) method with a structure of ITO/PEDOT:PSS/active layer/Au and ITO/ZnO/active layer/Al, respectively (shown in **Figure S4**). The hole and electron mobilities were listed in **Table S3**. The hole and electron mobility of **PCFB** was the highest one with a value of 4.63×10^{-4} and 2.40×10^{-4} cm^2 V^{-1} s^{-1}, respectively, which leads to the high J_{sc} of optimized device based on **PCFB**.

FILM MORPHOLOGIES

In order to better understand the fluorine effect on the photovoltaic performance, the morphologies of the blend films were investigated by atomic force microscope (AFM) and transmission electron microscope (TEM). As shown in **Figure S5**, the corresponding root-mean-square (RMS) roughness (R_q) values of **PFCFB**, **PCFB**, **PFCB,** and **PCB** based films are 1.51, 1.77, 1.41, and 1.26 nm, respectively. Networks of polymer fibrils can be found in the blended films (see **Figure 4**), which facilitate the charge separation and transport. Specially, proper aggregation was observed in **Figure S5B** based on **PCFB** which may explain why its hole and electron mobility is the highest and give the highest J_{sc}.

CONCLUSION

In summary, regioregular terpolymers by changing F atoms in the various moieties in the polymer chain were carefully designed and synthesized by Suzuki coupling. These polymers showed broad absorption in the visible region and exhibited a low bandgap <1.6 eV. From DFT calculations we know that the introduction of F atoms can flatten the molecular geometry between adjacent aromatic units due to the intramolecular supramolecular interaction. By introduction of F atoms to the benzene or carbazole segments or both of them, the molecular geometry can be modulated. Among the four terpolymers, **PFCFB** exhibited an excellent planarity with low dihedral angles. **PCFB** and **PFCB** showed a less good planarity than **PFCFB** but they are still much better than the unfluorinated one (**PCB**). Their molecular geometries thus influence the corresponding UV-vis spectra and charge transport properties. The introduction of F atom into the polymer chains can also significantly affect their energy levels. We demonstrate that **PFCFB** based devices have the highest V_{oc} of 0.86 V which seriously reduce to 0.73 V after the remove of F atoms (the **PCB** case), while **PCFB** based ones give the highest J_{sc} of 17.20 mA/cm^2. For these two polymers (**PFCFB** and **PCFB**), the highest PCE of ∼8.5% was achieved. Our results give a clear explanation that how F atoms take effect on the regioregular terpolymers and modulate their photovoltaic performances. We show that selecting proper donor units with F atom to fabricate

copolymers is an effective way to realizing high-efficiency polymer solar cells based on DPP units by enhancing in both V_{oc} and J_{sc}.

DATA AVAILABILITY

The raw data supporting the conclusions of this manuscript will be made available by the authors, without undue reservation, to any qualified researcher.

AUTHOR CONTRIBUTIONS

All authors listed have made a substantial, direct and intellectual contribution to the work, and approved it for publication.

ACKNOWLEDGMENTS

Financial support from the NSF of China (21574013, 51673028, 51003006, 21734009, 21421003), the Program for Changjiang Scholars and Innovative Research Team in University are gratefully acknowledged.

SUPPLEMENTARY MATERIAL

The Supplementary Material for this article can be found online at: https://www.frontiersin.org/articles/10.3389/fchem.2019.00333/full#supplementary-material

Experimental details, instruments, OPV fabrication and measurements. XRD, TGA, SCLC measurements, DFT calculations, and AFM images.

REFERENCES

Albrecht, S., Janietz, S., Schindler, W., Frisch, J., Kurpiers, J., Kniepert, J., et al. (2012). Fluorinated copolymer PCPDTBT with enhanced open-circuit voltage and reduced recombination for highly efficient polymer solar cells. *J. Am. Chem. Soc.* 134, 14932–14944. doi: 10.1021/ja305039j

Ashraf, R. S., Meager, I., Nikolka, M., Kirkus, M., Planells, M., Schroeder, B. C., et al. (2015). Chalcogenophene comonomer comparison in small band gap diketopyrrolopyrrole-based conjugated polymers for high-performing field-effect transistors and organic solar cells. *J. Am. Chem. Soc.* 137, 1314–1321. doi: 10.1021/ja511984q

Cheng, Y., Qi, Y., Tang, Y., Zheng, C., Wan, Y., Huang, W., et al. (2016). Controlling intramolecular conformation through nonbonding interaction for soft-conjugated materials: molecular design and optoelectronic properties. *J. Phys. Chem. Lett.* 7, 3609–3615. doi: 10.1021/acs.jpclett.6b01695

Choi, H., Ko, S.-J., Kim, T., Morin, P.-O., Walker, B., Lee, B. H., et al. (2015). Small-bandgap polymer solar cells with unprecedented short-circuit current density and high fill factor. *Adv. Mater.* 27, 3318–3324. doi: 10.1002/adma.201501132

Dou, L., Chang, W. H., Gao, J., Chen, C. C., You, J., and Yang, Y. (2013). A selenium-substituted low-bandgap polymer with versatile photovoltaic applications. *Adv. Mater.* 25, 825–831. doi: 10.1002/adma.201203827

Dou, L., You, J., Yang, J., Chen, C.-C., He, Y., Murase, S., et al. (2012). Tandem polymer solar cells featuring a spectrally matched low-bandgap polymer. *Nat. Photon.* 6, 180–185. doi: 10.1038/nphoton.2011.356

Du, C., Li, W., Duan, Y., Li, C., Dong, H., Zhu, J., et al. (2013). Conjugated polymers with 2,7-linked 3,6-difluorocarbazole as donor unit for high efficiency polymer solar cells. *Polym. Chem.* 4:2773. doi: 10.1039/c3py00177f

Duan, C., Gao, K., van Franeker, J. J., Liu, F., Wienk, M. M., and Janssen, R. A. (2016). Toward practical useful polymers for highly efficient solar cells via a random copolymer approach. *J. Am. Chem. Soc.* 138, 10782–10785. doi: 10.1021/jacs.6b06418

Fei, Z., Boufflet, P., Wood, S., Wade, J., Moriarty, J., Gann, E., et al. (2015). Influence of backbone fluorination in regioregular poly(3-alkyl-4-fluoro)thiophenes. *J. Am. Chem. Soc.* 137, 6866–6879. doi: 10.1021/jacs.5b02785

Hendriks, K. H., Heintges, G. H. L., Gevaerts, V. S., Wienk, M. M., and Janssen, R. A. J. (2013). High-molecular-weight regular alternating diketopyrrolopyrrole-based terpolymers for efficient organic solar cells. *Angew. Chem. Int. Ed.* 52, 8341–8344. doi: 10.1002/anie.201302319

Hendriks, K. H., Li, W., Heintges, G. H., van Pruissen, G. W., Wienk, M. M., and Janssen, R. A (2014a). Homocoupling defects in diketopyrrolopyrrole-based copolymers and their effect on photovoltaic performance. *J. Am. Chem. Soc.* 136, 11128–11133. doi: 10.1021/ja505574a

Hendriks, K. H., Li, W., Wienk, M. M., and Janssen, R.A. J. (2014b). Small-bandgap semiconducting polymers with high near-infrared photoresponse. *J. Am. Chem. Soc.* 136, 12130–12136. doi: 10.1021/ja506265h

Huo, L., Xue, X., Liu, T., Xiong, W., Qi, F., Fan, B., et al. (2018). Subtle side-chain engineering of random terpolymers for high-performance organic solar cells. *Chem. Mater.* 30, 3294–3300. doi: 10.1021/acs.chemmater.8b00510

Jackson, N. E., Savoie, B. M., Kohlstedt, K. L., Olvera de la Cruz, M., Schatz, G. C., Chen, L. X., et al. (2013). Controlling conformations of conjugated polymers and small molecules: the role of nonbonding interactions. *J. Am. Chem. Soc.* 135, 10475–10483. doi: 10.1021/ja403667s

Jo, J. W., Jung, J. W., Jung, E. H., Ahn, H., Shin, T. J., and Jo, W. H. (2015). Fluorination on both D and A units in D–A type conjugated copolymers based on difluorobithiophene and benzothiadiazole for highly efficient polymer solar cells. *Energy Environ. Sci.* 8, 2427–2434. doi: 10.1039/c5ee00855g

Kawashima, K., Fukuhara, T., Suda, Y., Suzuki, Y., Koganezawa, T., Yoshida, H., et al. (2016). Implication of fluorine atom on electronic properties, ordering structures, and photovoltaic performance in naphthobisthiadiazole-based semiconducting polymers. *J. Am. Chem. Soc.* 138, 10265–10275. doi: 10.1021/jacs.6b05418

Kim, H., Lee, H., Seo, D., Jeong, Y., Cho, K., Lee, J., et al. (2015). Regioregular low bandgap polymer with controlled thieno[3,4-b]thiophene orientation for high-efficiency polymer solar cells. *Chem. Mater.* 27, 3102–3107. doi: 10.1021/acs.chemmater.5b00632

Lee, J. W., Ahn, H., and Jo, W. H. (2015). Conjugated random copolymers consisting of pyridine- and thiophene-capped diketopyrrolopyrrole as co-electron accepting units to enhance both JSC and VOC of polymer solar cells. *Macromolecules* 48, 7836–7842. doi: 10.1021/acs.macromol.5b01826

Lee, W., Lee, H. D., Bae, J. H., and Jung, J. W. (2016). Fluoro-substituted low band gap polymers based on isoindigo for air-stable polymer solar cells with high open circuit voltages. *Org. Electron.* 39, 85–90. doi: 10.1016/j.orgel.2016.09.026

Li, C., Yu, C., Lai, W., Liang, S., Jiang, X., Feng, G., et al. (2018). Multifunctional diketopyrrolopyrrole-based conjugated polymers with perylene bisimide side chains. *Macromol. Rapid. Commun.* 39:e1700611. doi: 10.1002/marc.201700611

Li, C., Zhang, A., Wang, Z., Liu, F., Zhou, Y., Russell, T. P., et al. (2016). All polymer solar cells with diketopyrrolopyrrole-polymers as electron donor and a naphthalenediimide-polymer as electron acceptor. *RSC Adv.* 6, 35677–35683. doi: 10.1039/c6ra03681c

Li, G., Gong, X., Zhang, J., Liu, Y., Feng, S., Li, C., et al. (2016). 4-Alkyl-3,5-difluorophenyl-Substituted Benzodithiophene-Based Wide Band Gap Polymers for High-Efficiency Polymer Solar Cells. *ACS Appl. Mater. Interfaces* 8, 3686–3692. doi: 10.1021/acsami.5b08769

Li, W., Albrecht, S., Yang, L., Roland, S., Tumbleston, J. R., McAfee, T., et al. (2014a). Mobility-controlled performance of thick solar cells based on fluorinated copolymers. *J. Am. Chem. Soc.* 136, 15566–15576. doi: 10.1021/ja5067724

Li, W., Hendriks, K. H., Furlan, A., Roelofs, W. S., Meskers, S. C., Wienk, M. M., et al. (2014b). Effect of the fibrillar microstructure on the efficiency of high molecular weight diketopyrrolopyrrole-based polymer solar cells. *Adv. Mater.* 26, 1565–1570. doi: 10.1002/adma.201304360

Li, W., Hendriks, K. H., Wienk, M. M., and Janssen, R. A. J. (2015). Diketopyrrolopyrrole polymers for organic solar cells. *Acc. Chem. Res.* 49, 78–85. doi: 10.1021/acs.accounts.5b00334

Li, Z., Jiang, K., Yang, G., Lai, J. Y., Ma, T., Zhao, J., et al. (2016). Donor polymer design enables efficient non-fullerene organic solar cells. *Nat. Commun.* 7:13094. doi: 10.1038/ncomms13094

Liu, Y., Li, G., Zhang, Z., Wu, L., Chen, J., Xu, X., et al. (2016). An effective way to reduce energy loss and enhance open-circuit voltage in polymer solar cells based on a diketopyrrolopyrrole polymer containing three regular alternating units. *J. Mater. Chem. A* 4, 13265–13270. doi: 10.1039/c6ta05471d

Liu, Y., Zhang, C. E., Hao, D., Zhang, Z., Wu, L., Li, M., et al. (2018). Enhancing the performance of organic solar cells by hierarchically supramolecular self-assembly of fused-ring electron acceptors. *Chem. Mater.* 30, 4307–4312. doi: 10.1021/acs.chemmater.8b01319

Nielsen, C. B., Turbiez, M., and McCulloch, I. (2013). Recent advances in the development of semiconducting DPP-containing polymers for transistor applications. *Adv. Mater.* 25, 1859–1880. doi: 10.1002/adma.201201795

Park, J. H., Jung, E. H., Jung, J. W., and Jo, W. H. (2013). A fluorinated phenylene unit as a building block for high-performance n-type semiconducting polymer. *Adv. Mater.* 25, 2583–2588. doi: 10.1002/adma.201205320

Qin, T., Zajaczkowski, W., Pisula, W., Baumgarten, M., Chen, M., Gao, M., et al. (2014). Tailored Donor–Acceptor Polymers with an A–D1–A–D2 Structure: controlling intermolecular interactions to enable enhanced polymer photovoltaic devices. *J. Am. Chem. Soc.* 136, 6049–6055. doi: 10.1021/ja500935d

Sonar, P., Singh, S. P., Li, Y., Soh, M. S., and Dodabalapur, A. (2010). A Low-bandgap diketopyrrolopyrrole-benzothiadiazole-based copolymer for high-mobility ambipolar organic thin-film transistors. *Adv. Mater.* 22, 5409–5413. doi: 10.1002/adma.201002973

Tanaka, H., Shizu, K., Nakanotani, H., and Adachi, C. (2013). Twisted intramolecular charge transfer state for long-wavelength thermally activated delayed fluorescence. *Chem. Mater.* 25, 3766–3771. doi: 10.1021/cm402428a

Wang, B., Huynh, T. -P., Wu, W., Hayek, N., Do, T. T., Cancilla, J. C., et al. (2016). A highly sensitive diketopyrrolopyrrole-based ambipolar transistor for selective detection and discrimination of xylene isomers. *Adv. Mater.* 8, 4012–4018. doi: 10.1002/adma.201505641

Wang, X., Deng, W., Chen, Y., Wang, X., Ye, P., Wu, X., et al. (2017). Fine-tuning solid state packing and significantly improving photovoltaic performance of conjugated polymers through side chain engineering via random polymerization. *J. Mater. Chem. A* 5, 5585–5593. doi: 10.1039/c6ta10864d.

Wang, Y., Hasegawa, T., Matsumoto, H., Mori, T., and Michinobu, T. (2017). D-A1-D-A2 Backbone strategy for benzobisthiadiazole based n-channel organic transistors: clarifying the selenium-substitution effect on the molecular packing and charge transport properties in electron-deficient polymers. *Adv. Fun. Mater.* 27:1701486. doi: 10.1002/adfm.201701486

You, J., Dou, L., Yoshimura, K., Kato, T., Ohya, K., Moriarty, T., et al. (2013). A polymer tandem solar cell with 10.6% power conversion efficiency. *Nat. Commun.* 4:1446. doi: 10.1038/ncomms2411

Yu, Y., Wu, Y., Zhang, A., Li, C., Tang, Z., Ma, W., et al. (2016). Diketopyrrolopyrrole polymers with thienyl and thiazolyl linkers for application in field-effect transistors and polymer solar cells. *ACS Appl. Mater. Interfaces.* 8, 30328–30335. doi: 10.1021/acsami.6b06967

Zhang, C. E., Feng, S., Liu, Y., Hou, R., Zhang, Z., Xu, X., et al. (2017). Effect of non-fullerene acceptors' side chains on the morphology and photovoltaic performance of organic solar cells. *ACS Appl. Mater. Interfaces.* 9, 33906–33912. doi: 10.1021/acsami.7b09915

Zhang, Q., Kelly, M. A., Bauer, N., and You, W. (2017). The curious case of fluorination of conjugated polymers for solar cells. *Acc. Chem. Res.* 50, 2401–2409. doi: 10.1021/acs.accounts.7b00326

Zhao, W., Li, S., Yao, H., Zhang, S., Zhang, Y., Yang, B., et al. (2017). Molecular optimization enables over 13% efficiency in organic solar cells. *J. Am. Chem. Soc.* 139, 7148–7151. doi: 10.1021/jacs.7b02677

Zheng, Z., Zhang, S., Zhang, J., Qin, Y., Li, W., Yu, R., et al. (2016). Over 11% Efficiency in tandem polymer solar cells featured by a low-band-gap polymer with fine-tuned properties. *Adv. Mater.* 8, 5133–5138. doi: 10.1002/adma.201600373

Conflict of Interest Statement: The authors declare that the research was conducted in the absence of any commercial or financial relationships that could be construed as a potential conflict of interest.

frontiers in Chemistry

ORIGINAL RESEARCH
published: 16 May 2019
doi: 10.3389/fchem.2019.00351

Photoresponsive Porphyrin Nanotubes of *Meso*-tetra(4-Sulfonatophenyl)Porphyrin and Sn(IV) *meso*-tetra(4-pyridyl)porphyrin

Ekaterina A. Koposova[1,2], *Andreas Offenhäusser*[1], *Yuri E. Ermolenko*[2] and *Yulia G. Mourzina*[1]*

[1] Forschungszentrum Jülich, Institute of Complex Systems-8 (Bioelectronics), Jülich, Germany, [2] Institute of Chemistry, Saint-Petersburg State University, Saint-Petersburg, Russia

Porphyrin macrocycles and their supramolecular nanoassemblies are being widely explored in energy harvesting, sensor development, catalysis, and medicine because of a good tunability of their light-induced charge separation and electron/energy transfer properties. In the present work, we prepared and studied photoresponsive porphyrin nanotubes formed by the self-assembly of *meso*-tetrakis(4-sulfonatophenyl)porphyrin and Sn(IV) *meso*-tetra(4-pyridyl)porphyrin. Scanning electron microscopy and transmission electron microscopy showed that these tubular nanostructures were hollow with open ends and their length was 0.4–0.8 μm, the inner diameter was 7–15 nm, and the outer diameter was 30–70 nm. Porphyrin tectons, $H_4TPPS_4^{2-}$: Sn(IV)$TPyP^{4+}$, self-assemble into the nanotubes in a ratio of 2:1, respectively, as determined by the elemental analysis. The photoconductivity of the porphyrin nanotubes was determined to be as high as 3.1×10^{-4} S m^{-1}, and the dependence of the photoconductance on distance and temperature was investigated. Excitation of the Q-band region with a Q-band of $SnTPyP^{4+}$ (550–552 nm) and the band at 714 nm, which is associated with J-aggregation, was responsible for about 34 % of the photoconductive activity of the $H_4TPPS_4^{2-}$-Sn(IV)$TPyP^{4+}$ porphyrin nanotubes. The sensor properties of the $H_4TPPS_4^{2-}$- Sn(IV)$TPyP^{4+}$ nanotubes in the presence of iodine vapor and salicylate anions down to millimolar range were examined in a chemiresistor sensing mode. We have shown that the porphyrin nanotubes advantageously combine the characteristics of a sensor and a transducer, thus demonstrating their great potential as efficient functional layers for sensing devices and biomimetic nanoarchitectures.

Keywords: porphyrin nanotubes, Sn(IV) porphyrin, *meso*-tetra(4-sulfonatophenyl)porphyrin, π-tecton, supramolecular nanoassembly, photoconductivity, chemiresistor, salicylate

OPEN ACCESS

Edited by:
Penglei Chen,
Institute of Chemistry (CAS), China

Reviewed by:
Feng Bai,
Henan University, China
Tianyu Wang,
University of Science and Technology Beijing, China

***Correspondence:**
Yulia G. Mourzina
y.mourzina@fz-juelich.de

Specialty section:
This article was submitted to Supramolecular Chemistry, a section of the journal Frontiers in Chemistry

Received: *18 February 2019*
Accepted: *29 April 2019*
Published: *16 May 2019*

Citation:
Koposova EA, Offenhäusser A, Ermolenko YE and Mourzina YG (2019) Photoresponsive Porphyrin Nanotubes of Meso-tetra(4-Sulfonatophenyl)Porphyrin and Sn(IV) meso-tetra(4-pyridyl)porphyrin. Front. Chem. 7:351. doi: 10.3389/fchem.2019.00351

INTRODUCTION

The self-organization of tetrapyrroles in the form of molecular aggregates is known in biological systems for its role in light harvesting, energy transformation, and electron transport. The properties and functions of natural chlorophyll pigments, which in the composition of the chloroplasts carry out the photosynthesis, and hemes, which in the composition of hemoglobin carry out oxygen transport, in the composition of myoglobin—its storage, and in the composition of cytochromes—catalysis of biological redox reactions, inspired wide use of porphyrins and their

molecular assemblies as biomimetic materials in systems replicating photosynthesis, electron transport, and enzymatic catalysis. Therefore, the self-assembly of porphyrin macrocycles, whose nanostructures have interesting electronic and optical properties, is being used in search for new nanoscale materials in the field of reversible binding and (photo)catalysis, biomimetic sensors, solar energy conversion, and electrically active components in various nanodevices (Fukuzumi and Imahori, 2008; El-Khouly et al., 2014; Fuhrhop, 2014; Guo et al., 2014; Ou et al., 2014; Zhang et al., 2015; Chen et al., 2016; Koposova et al., 2016a; Mirkovic et al., 2017; Paolesse et al., 2017).

Particular attention has been given in the past to the water-soluble porphyrins. The synthesis of the first J-aggregates of a water-soluble porphyrin, 5,10,15,20-tetra(4-sulphonatophenyl) porphyrin, formed in acidified aqueous solutions, provided the stimulus for the investigations of the self-assembled porphyrin nanostructures (Pasternack et al., 1972; Ohno et al., 1993; Mchale, 2012). Fine-tuning the properties of a metallo-porphyrin complex by varying its different components, such as the molecular skeleton, peripheral substituents, coordinated metal as well as pH and ionic strength of the solutions, allows the creation of self-assembled nanostructures of various shapes with different properties. Self-assembly of porphyrin tectons into nanostructures is controlled by a multiplicity of non-covalent interactions such as hydrogen bonds, electrostatic and π-π interactions, axial coordination, and van der Waals forces (Guldi and Imahori, 2004; Martin et al., 2010, 2013;Würthner et al., 2011).

The electrical and photoconductivity properties of aromatic π-conjugated porphyrin macrocycles and their nanoarchitectures are intensively studied. The π-conjugated porphyrin macrocycles absorb the visible light energy, which may lead to the intermolecular transfer or delocalization of the excitation energy in porphyrin aggregates and arrays making them photoconductive under application of electric field (Weigl, 1957; Golubchikov and Berezin, 1986; Kobayashi et al., 1993; Chou et al., 2000; Drain, 2002; Schwab et al., 2004; Yeats et al., 2008; Kocherzhenko et al., 2009; Friesen et al., 2010; Martin et al., 2010; Riley et al., 2010; Cai et al., 2014; Adinehnia et al., 2016; Koposova et al., 2016b, 2018; Borders et al., 2017). So far, electrical properties of porphyrin nanostructures and the mechanisms of charge transport in their aggregates have not been investigated and explained in details. Photoconductivity was reported in J-aggregates of free-base porphyrins (Schwab et al., 2004; Yeats et al., 2008; Friesen et al., 2010; Riley et al., 2010), whereby most studies so far have dealt with the self-assembled nanorods of 5,10,15,20-tetra(4-sulphonatophenyl) porphyrin. Later on, Adinehnia et al. (2016) and Borders et al. (2017) studied photoconductive properties of porphyrin nanostructures composed of oppositely charged free-base porphyrins: 5,10,15,20-tetra(4-sulfonatophenyl)porphyrin with 5,10,15,20-tetra(N-methyl-4-pyridyl)porphyrin, $TPPS_4$:TMPyP, (Adinehnia et al., 2016) or 5,10,15,20-tetra(4-pyridyl)porphyrin, $TPPS_4$:TPyP, (Borders et al., 2017).

Martin et al. (2010) described photoconductive microscale clover-shaped structures self-assembled from the water-soluble metalloporphyrins Zn(II)$TPPS^{4-}$ as a donor and Sn(IV)T(N-EtOH-4-Py)P^{4+} as an acceptor. The authors discussed the observed photoconductivity of the nanostructures in terms of exciton delocalization and charge-transfer exciton theory based on a model of the electron-donor-acceptor charge-transfer complex tetrathiafulvalene-tetracyanoquinodimethane (TTF-TCNQ) (Ferraris et al., 1973). By analogy with TTF-TCNQ, the authors proposed an arrangement of individual electron donor, Zn(II)$TPPS^{4-}$, and acceptor, Sn(IV)T(N-EtOH-4-Py)P^{4+}, porphyrin molecules in segregated stacks, whereby the charge carriers produced by photoexcitation can move along the stacks, when an electric potential is applied in the direction of the stacks. Formation of heteroaggregates with charge-transfer interactions was also found earlier in the assembly of electron-attracting Au(III) porphyrin and electron-releasing Zn(II) porphyrin (Segawa et al., 1989). Segawa et al. (1992b) reported photoinduced electron-transfer reactions in porphyrin heteroaggregates of the water-soluble Au(III) and Zn(II) porphyrins and formation of the contact radical ion pair as a result of photoexcitation. Recently, photoinduced charge separation has been observed for the ion-pairs obtained from water-soluble cationic and anionic porphyrins $ZnTMePyP^{4+}$ or $H_2TMePyP^{4+}$ and $ZnTPPS^{4-}$ or H_2TPPS^{4-} (Natali and Scandola, 2016). In this system, the porphyrins of cationic character were reduced, while the porphyrins of anionic character were oxidized. Collman et al. (2000) reported a series of bis(metalloporphyrin) sandwich complexes as charge-transfer materials and their conductivities. Porphyrins as molecular acceptors form donor-acceptor systems with other molecular donors (Segawa et al., 1992a; Jana et al., 2017). The above studies give an evidence for the electron-donor-acceptor charge-transfer complex mechanism of the photoconductivity of the porphyrin dimers, aggregates, arrays, and nanostructures. However, a better knowledge of the supramolecular non-covalently bonded porphyrin nanoaggregates and their properties is required to understand natural macrocycles assemblies, evaluate their utility as electrical components in nanodevices, and advance the exploitation of their properties, such as excited state delocalization, energy and electron transfer, and photoconductivity in bio-mimicking materials in the fields of photodetectors, solar energy applications, catalysis, and sensors. Earlier, we reported on the self-assembly and photoconductivity of the porphyrin nanostructures in systems of *meso*-substituted Co(III) and Sn(IV) porphyrins as well as *meso*-substituted Co(III) and free-base porphyrins. In this report, we present the morphological, spectral, electrochemical properties, and photoconductivity phenomenon of self-assembled porphyrin nanostructures of m*eso*-tetra(4-sulfonatophenyl)porphyrin and Sn(IV) *meso*-tetra(4-pyridyl)porphyrin, which shows the highest photoconductivity of the last systems.

MATERIALS AND METHODS

Chemicals

Sn(IV) *meso*-tetra(4-pyridyl)porphyrin dichloride and *meso*-tetra(4-sulfonatophenyl)porphyrin dihydrochloride were

obtained from Frontier Scientific (>95% purity) and used as received, (**Figure 1**). All other chemicals were from Sigma-Aldrich. Diamond (1 μm) and alumina (0.05 μm) polishing suspensions and the corresponding polishing pads were from ALS Co. All solutions were prepared using distilled water. Sodium hydroxide and hydrochloric acid solutions were used to adjust the pH.

Nanotube Synthesis

The porphyrin nanotubes were prepared using equal volumes of the 10 μM stock solutions of individual porphyrins (an equimolar, 1:1 concentration ratio) and adjusting the pH of the mixture to pH 2, 6, and 10.5. The formation of colloids started immediately at pH 2, while at pH 6 and 10.5 no nanostructure formation was observed. The nanostructures were also prepared using 1:5 and 5:1 concentration ratios of $Sn(IV)TPyP^{4+}$: $H_4TPPS_4^{2-}$ in solutions at pH 2. The colloidal solutions remained in the dark for 5 days. To prepare the stock solutions, $Sn(IV)TPyP^{4+}$ was dissolved in 0.02 M HCl, while $H_2TPPS_4^{4-}$/$H_4TPPS_4^{2-}$ ($TPPS_4$) was dissolved in water.

Characterization of the Structure and Composition

The nanostructures were characterized by scanning electron microscopy using a Gemini 1550 VP SEM (Carl Zeiss, Jena, Germany). To prepare the samples for SEM, 50 μL of the nanostructures solutions were dropped on the Si substrates, and the samples were left to dry for 12 h. After that, the samples were washed with 0.01 M HCl, water, and left to dry. The transmission electron microscopy (TEM) images were obtained using a FEI Tecnai G2 F20 microscope operated at 200 kV. EDX analysis was performed using a JEOL 840 A. The samples of the nanostructures for the EDX analysis were concentrated in a 0.02 M HCl by centrifugation (10,000 rpm 7 min) and washing several times until a transparent supernatant solution was obtained to remove not self-assembled porphyrins. Fifty microliter of the nanostructures solutions were dropped on the Si/SiO_2 substrates, and the samples were left to dry. This procedure was repeated four times. After that, the samples were washed with 0.01 M HCl, water, and left to dry. The AFM measurements of the nanostructures on the Si/SiO_2 substrates were performed using a MultiMode scanning probe system (Bruker) in a tapping mode. The samples were prepared as described above for the SEM samples.

The optical spectra were obtained on a PerkinElmer Lambda 900 spectrometer. Quartz cuvettes with a path length of 10 and 5 mm were used. Individual porphyrin solutions for spectra measurements were prepared by dissolving $Sn(IV)TPyP^{4+}$ in acidified water (pH = 2.0) and $H_4TPPS_4^{2-}$ in water. The samples of the nanostructures for the UV-vis spectrometry were concentrated in a 0.02 M HCl by centrifugation (10,000 rpm 7 min) and washing several times until a transparent supernatant solution was obtained to remove not self-assembled porphyrins.

The ratio of S:N atoms was found using an elemental analysis, which determines the absolute element content. The samples of the nanorods for the elemental analysis were prepared by centrifugation (10,000 rpm 7 min) and washing of the nanorods solutions with subsequent drying of the collected sediments and analyzed by the "vario El cube" (Elementar) with a thermal conductivity detector.

Electrochemical Methods

Electrochemical experiments were performed with a potentiostat (Autolab PGSTAT100, The Netherlands) controlled by the Nova 2.1 software. The experimental setup for recording the cyclic voltammograms included a three-electrode electrochemical cell. A coiled platinum wire was used as a counter electrode. A glassy carbon electrode (BASi Inc.) with a diameter of 3 mm was used as a working electrode. The potentials were controlled relative to a double junction Ag/AgCl, Metrohm, Ag | AgCl | KCl 3 M::0.5 M KCl reference electrode. The solution in the bridge of the reference electrode was replaced after each measurement to avoid contaminations of the electrochemical cell. Measurements were carried out under Ar in the dark at room temperature (21 ± 1°C). Glassy carbon electrodes were cleaned before each electrochemical measurement as described below: the electrodes were polished with diamond (1 μm) and then alumina (0.05 μm) slurry on the respective polishing cloths. Immediately after polishing, the electrodes were rinsed with distilled water and sonicated in a mixture of water and ethanol for about 10 s to remove polishing residues from the electrode surface. The electrodes were then thoroughly rinsed with distilled water and dried with nitrogen.

Electrophotoresponse Measurements

To measure the (photo)conductance of the porphyrin nanorods, two types of thin-film gold electrodes were used: gold electrode pairs with an electrode gap of 400 nm, (**Figure S1**), and interdigitated electrode arrays with a 2 μm spacing between the electrode lines and an electrode line thickness of 2 μm. The electrodes were produced on a Si substrate with a silicon dioxide layer of 1,000 nm thickness using electron beam lithography, lift-off process, and thin-film technologies in an ISO 5 cleanroom as described in detail in Muratova et al. (2016). Thin metal layers of titanium for adhesion (10 nm) and gold (50 nm) were deposited by means of an electron beam evaporation using a Pfeiffer PLS 500 equipment. After fabrication, the electrodes were cleaned in acetone and isopropanol. After that, the electrodes were treated with oxygen plasma (≪Plasma system FEMTO≫). Finally, the electrodes were rinsed with ethanol and distilled water. Two microliter of the porphyrin nanostructures solution was pipetted onto the electrodes and the samples were allowed to dry in the dark for 2 h. The samples were then rinsed with 0.01 M HCl, water, and allowed to dry for 24 h. The measurements were also performed using an equimolar solution of $TPPS_4$ and $Sn(IV)TPyP^{4+}$ of pH 6 instead of the nanostructure solution. The device was prepared in a similar way as for the nanostructures, namely, 2 μL of the solution of porphyrins was pipetted onto the electrodes and the device was allowed to dry in the dark for 2 h. The device was then rinsed with water and allowed to dry for 24 h.

The (photo)conductance was recorded with a Keithley 4200 SCS semiconductor analyzer using a two-probe configuration. Applied potential was 0.5 V. The gold electrodes were connected to the external circuit by contacting the bond pads with tungsten

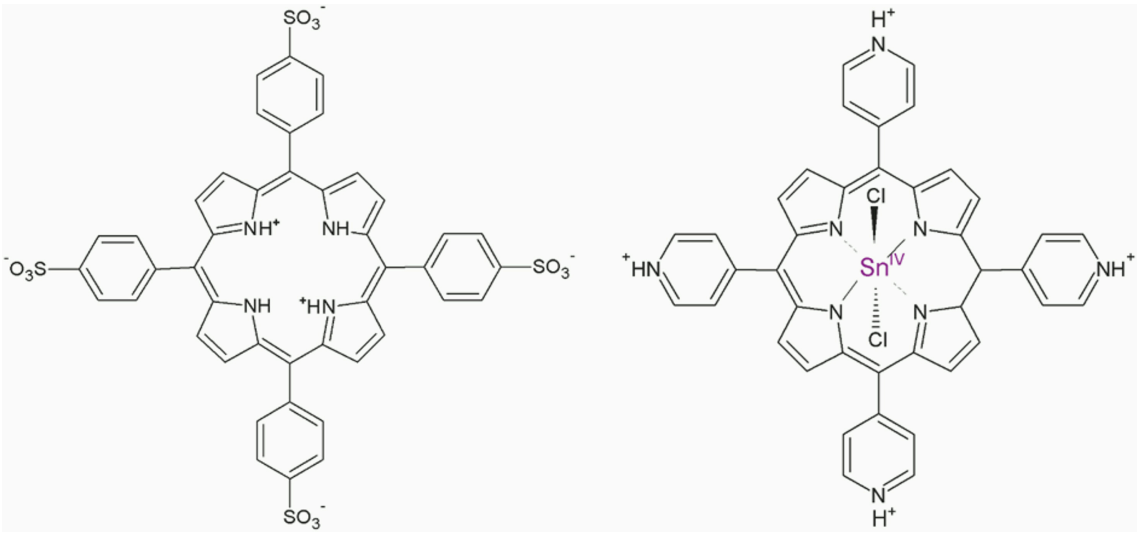

FIGURE 1 | Structures of the porphyrin diacid $H_4TPPS_4^{2-}$ and Sn(IV)TPyP^{4+} (pyridyl groups are shown in the protonated state).

needles. A 150 W xenon arc lamp assembled with an AM1.5 filter (Oriel Instruments, Model No. 6255) and a visible light filter (390–630 nm) was used for photoexitation. The light intensity of the beam focused on the sample during experiments was measured using a photodetector (CAS140CT-154 Kompakt-Array-Spektrometer model UV-vis-NIR, Instrument Systems) and equaled 29 mW cm^{-2}.

RESULTS AND DISCUSSION

Nanotube Morphology

Sn(IV)TPyP^{4+} and $H_4TPPS_4^{2-}$ solutions produced brown precipitates in a self-assembly reaction at pH 2. It should be noted that that for a concentration ratio of 5:1 (Sn(IV)TPyP^{4+} : $H_4TPPS_4^{2-}$), a very small amount of the nanostructures is formed in a self-assembly reaction, which makes them not very suitable for practical use. SEM, TEM, and AFM analyses revealed that these two porphyrins form the tubular nanostructures, (**Figures 2**–**4**) and (**Figures S2, S3**).

TEM images show that the tubular nanostructures are hollow with open ends. These structural details are clearer at the edges of the round formed conglomerates, because the material layers overlap at the places with a higher density of nanotubes. Additionally, the open ends of the nanotubes can be seen in some of the SEM images, e.g., (**Figure S2B**). The nanotubes have a length of 0.4–0.8 μm, an inner diameter of 7–15 nm, and an outer diameter of 30–70 nm, (**Figures 2**–**4**) and (**Figures S2, S3**).

Interestingly, SEM and AFM investigations indicated a presence of two types of the nanostructures in a system, where the porphyrins were taken in a 1:5 (Sn(IV)TPyP^{4+}: $H_4TPPS_4^{2-}$) concentration ratio, (**Figures 2C,D**, **4C,D**) and (**Figures S2**, **S4**). One kind of the nanostructures is similar to the nanostructures in the systems, where the porphyrins were taken in 1:1 and 5:1 (Sn(IV)TPyP^{4+} and $H_4TPPS_4^{2-}$) concentration ratios, while the presence of much thinner nanorods of about 10 nm diameter and patches (unrolled pieces of nanorods) of about 6 nm thickness is observed in a 1:5 (Sn(IV)TPyP^{4+} : $H_4TPPS_4^{2-}$) system, (**Figures 2C,D**) and (**Figures S2, S4**). We assume that these thinner and segregated nanostructures are $H_4TPPS_4^{2-}$ self-assembled nanorods formed due to the excess of this porphyrin because of the structural and optical absorption similarity (see below). The thin nanorods and patches were observed to be located under the thicker Sn(IV)TPyP^{4+}-$H_4TPPS_4^{2-}$ nanotubes and on the edges of the layers formed by the thick Sn(IV)TPyP^{4+}-$H_4TPPS_4^{2-}$ nanotubes, (**Figures 2C,D**) and (**Figure S2**). One may conclude that the excess of $H_4TPPS_4^{2-}$ results in a larger dispersion of the nanostructures, which is also supported by the AFM investigation below, producing at least two types of the nanostructures. These segregated thin nanorods and patches do not form, however, continuous layers like the thick Sn(IV)TPyP^{4+}-$H_4TPPS_4^{2-}$ nanotubes form.

An interesting feature of the nanostructures self-assembled in a system, where the porphyrins were taken in a 5:1 (Sn(IV)TPyP^{4+} : $H_4TPPS_4^{2-}$) concentration ratio, in comparison with other two systems at pH 2 was a transparency of the nanotubes, (**Figures 2E,F**) which is probably related to their thickness or non-dense structure.

AFM analysis showed that the nanostructures self-assembled from equimolar solutions of two porphyrins produced smoother layers, (**Figures 4A,B**), while the nanostructures obtained from 1:5 (Sn(IV)TPyP^{4+} : $H_4TPPS_4^{2-}$) solutions formed more rough layers, (**Figures 4C,D**), which might be explained by the presence of the nanostructures of two types. Additionally, AFM showed a different morphology of the nanotube surfaces formed in a system, where the porphyrins were taken in a 5:1 (Sn(IV)TPyP^{4+} : $H_4TPPS_4^{2-}$) concentration ratios. One can observe a nodular or twisted surfaces of the

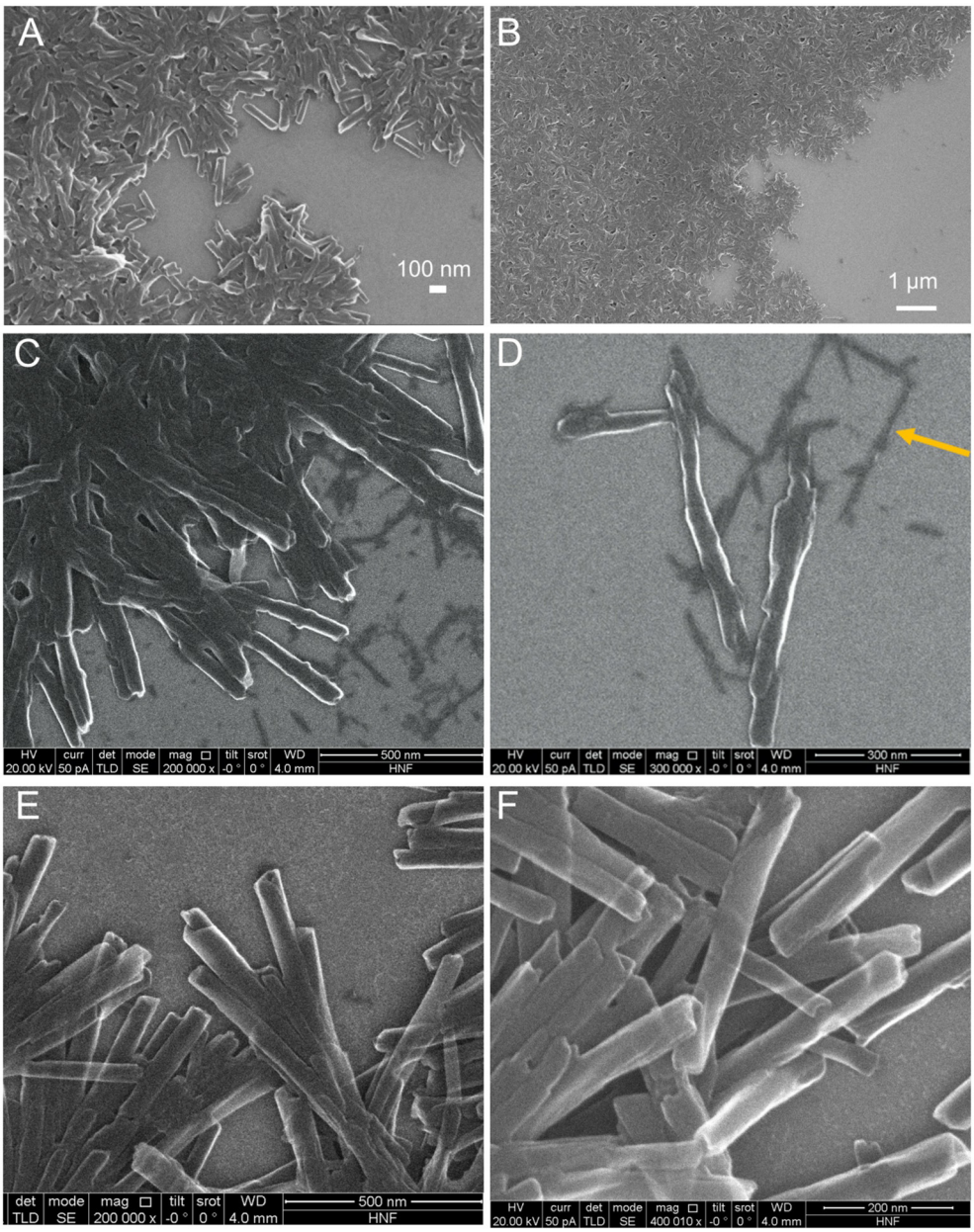

FIGURE 2 | SEM images of the $H_4TPPS_4^{2-}$-Sn(IV)TPyP^{4+} porphyrin nanostructures formed by the self-assembly in solutions at pH = 2.0 and Sn(IV)TPyP^{4+} and $H_4TPPS_4^{2-}$ taken in a 1:1 concentration ratio **(A,B),** Sn(IV)TPyP^{4+} and $H_4TPPS_4^{2-}$ taken in a 1:5 concentration ratio **(C,D)**, the arrow shows the second type of nanostructures formed in this system, which are thinner nanorods, also visible in image **(C)**, and Sn(IV)TPyP^{4+} and $H_4TPPS_4^{2-}$ taken in a 5:1 concentration ratio **(E,F)**.

nanotubes, (**Figures 4E,F**). This feature requires, however, further investigations.

The nanotubes in the TEM images appear in round formed agglomerates, being connected together by one edge and diverging in different directions from one place. The appearance of the round nanostructure conglomerates may emerge either in the solution during synthesis after the formation of individual nanotubes which then stick together or after deposition of the nanotubes on a solid substrate and subsequent water evaporation. Thus, SEM, TEM, and AFM analyses show that the structural features of the $H_4TPPS_4^{2-}$ –Sn(IV)TPyP^{4+} binary nanotubes differ essentially from those of the self-assembled $H_4TPPS_4^{2-}$ nanorods. The latter are well-segregated nanorods with an essentially smaller outer diameter of about 10–15 nm, as it is shown in **Figure S5**. The smaller nanostructures in the system, where the porphyrins in the solution were taken in a concentration ratio of 1:5 (Sn(IV)TPyP^{4+} : $H_4TPPS_4^{2-}$), were probably the result of self-assembly mainly $H_4TPPS_4^{2-}$ because of its excess. A synergy of various intermolecular interactions and structural features of individual porphyrin tectons (Agranovich

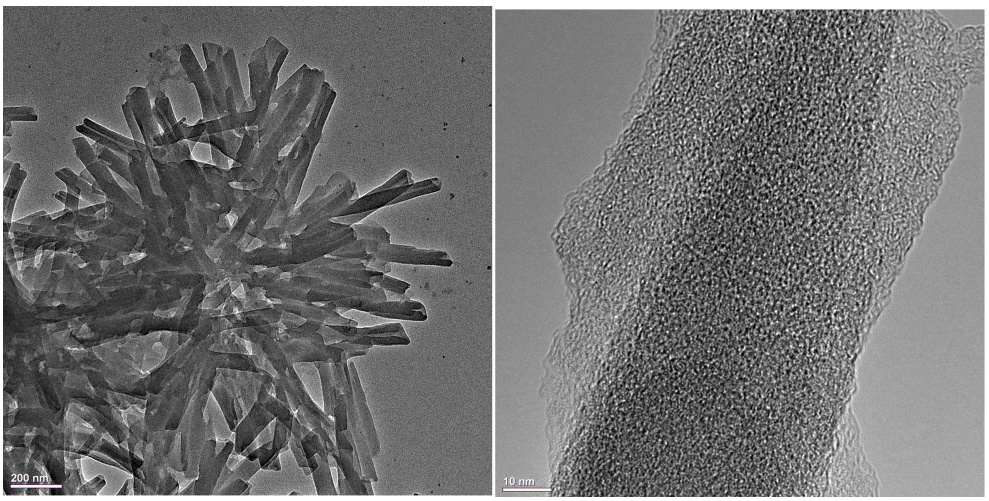

FIGURE 3 | TEM images of the $H_4TPPS_4^{2-}$ –Sn(IV)TPyP^{4+} porphyrin nanostructures formed in equimolar porphyrin solutions at pH = 2.0 by the self-assembly reaction.

and Bassani, 2003; Guldi and Imahori, 2004; Medforth et al., 2009; Koposova et al., 2016b, 2018) are responsible for a great multiplicity of the observed 1D to 3D geometries of porphyrin molecular aggregates formed by self-assembly.

The self-assembly of the $H_4TPPS_4^{2-}$: SnTPyP^{4+} porphyrin nanotube (2.4:1 mol mol^{-1}) was first shown by Shelnutt and co-workers (Wang et al., 2004). The self-assembly was highly pH dependent, since the protonation states of the porphyrin molecules determined the balance of molecule charges for the assembly (Wang et al., 2004; Franco et al., 2010). At pH = 2.0, partially dissociated sulfonato-groups (pK_a = 2.6 for benzenesulfonic acid), a protonated center of $H_4TPPS_4^{2-}$ (pK_a = 4.9), and protonated pyridyl groups of Sn(IV)TPyP^{4+} (pK_a = 5.2 for pyridine) participate in the molecular assembly. Influence of the pH on the porphyrin molecular assembly was also documented in the study of the Sn(IV)$TPPS_4$-Co(III)TPyP nanostructures, where the Sn:Co atomic ratio was found to be 1:1.15 at pH 2.7 and 1:3 at pH 4.8 (Koposova et al., 2016b). These molecule ratios were due to the neutralization of anionic and cationic porphyrin species at different pH. Accordingly, pH plays an important role in the self-assembly, since it determines the electrostatic interactions of the porphyrin tectons.

In our study, $TPPS_4$ and Sn(IV)TPyP^{4+} taken in a 1:1 concentration ratio did not self-assembly into the nanostructures at pH 6 and 10.5, where $TPPS_4$ is predominantly in its deprotonated $H_2TPPS_4^{4-}$ form. This indicates that the presence of the protonated center of $H_4TPPS_4^{2-}$ and its assembly into the slipped face-to-face configuration is a driving force for the self-assembly process, while the Sn(IV)TPyP^{4+} tectons, which do not produce the nanostructures by its own, co-assembly in this self-assembly process. In these cases, the optical absorption spectra, (**Figure 5**), of Sn(IV)TPyP^{4+} and $TPPS_4$ taken in 1:1 concentration ratio at pH 6 and 10.5 are practically overlap of the optical absorption spectra of the individual porphyrins at the same pH and are not indicative for the formation of new species. In addition, as it was mentioned earlier, a very small amount of nanostructures was formed if the initial molar ratio of $H_4TPPS_4^{2-}$: SnTPyP^{4+} in solution was 1:5, pH 2. Altogether, these observations indicate that $H_4TPPS_4^{2-}$ represents the driving force for self-assembly in this porphyrin couple, while SnTPyP^{4+} is rather included due to its cationic nature.

The UV-visible absorption spectrum of the $H_4TPPS_4^{2-}$ nanorods demonstrates a sharp J-band at 491 nm red-shifted from the monomer absorption and distinguished by its narrowness and high extinction coefficient together with a band at 706 nm in a Q-region typical for the J-aggregates of $H_4TPPS_4^{2-}$, (**Figure 5**).

Absorption spectrum of the $H_4TPPS_4^{2-}$-SnTPyP^{4+} nanotubes prepared using different molar ratios of the porphyrins in the solutions at pH 2 in our study, **Figures 5A,C**, indicates presence of the J-aggregates in the Sn(IV)TPyP^{4+}-$H_4TPPS_4^{2-}$ self-assembly according to the characteristic absorption bands at λ = 500–516 nm and λ = 714–726 nm. The bands are red-shifted and broadened compared to the absorption bands of the $H_4TPPS_4^{2-}$ nanorods (dark yellow line), (**Figures 5A,C**). Interestingly, that in the case of a system, where SnTPyP^{4+} and $H_4TPPS_4^{2-}$ porphyrins were taken in a concentration ratio of 1:5 (green line), (**Figure 5C**), the J-band at about 500–516 nm is splitted, which may support existence of two types of nanostructures in this system, as it was discussed above. The presence of J-aggregate bands indicates that excitons may be delocalized over multiple molecules (Torres and Bottari, 2013). Thin nanotubes formed by self-assembly of the metal-free porphyrin $H_4TPPS_4^{2-}$ into slipped face-to-face columnar arrangements as well as the mechanism of their formation have been presented and discussed in a series of studies (Ohno et al., 1993; Maiti et al., 1995; Würthner et al., 2011; Mchale, 2012). Inclusion of the hexacoordinated Sn(IV)TPyP^{4+} metalloporphyrin with a heavy metal results in thicker nanotubes with larger sizes saving stack configuration in the assembly and interrupting the usual dipole coupling that

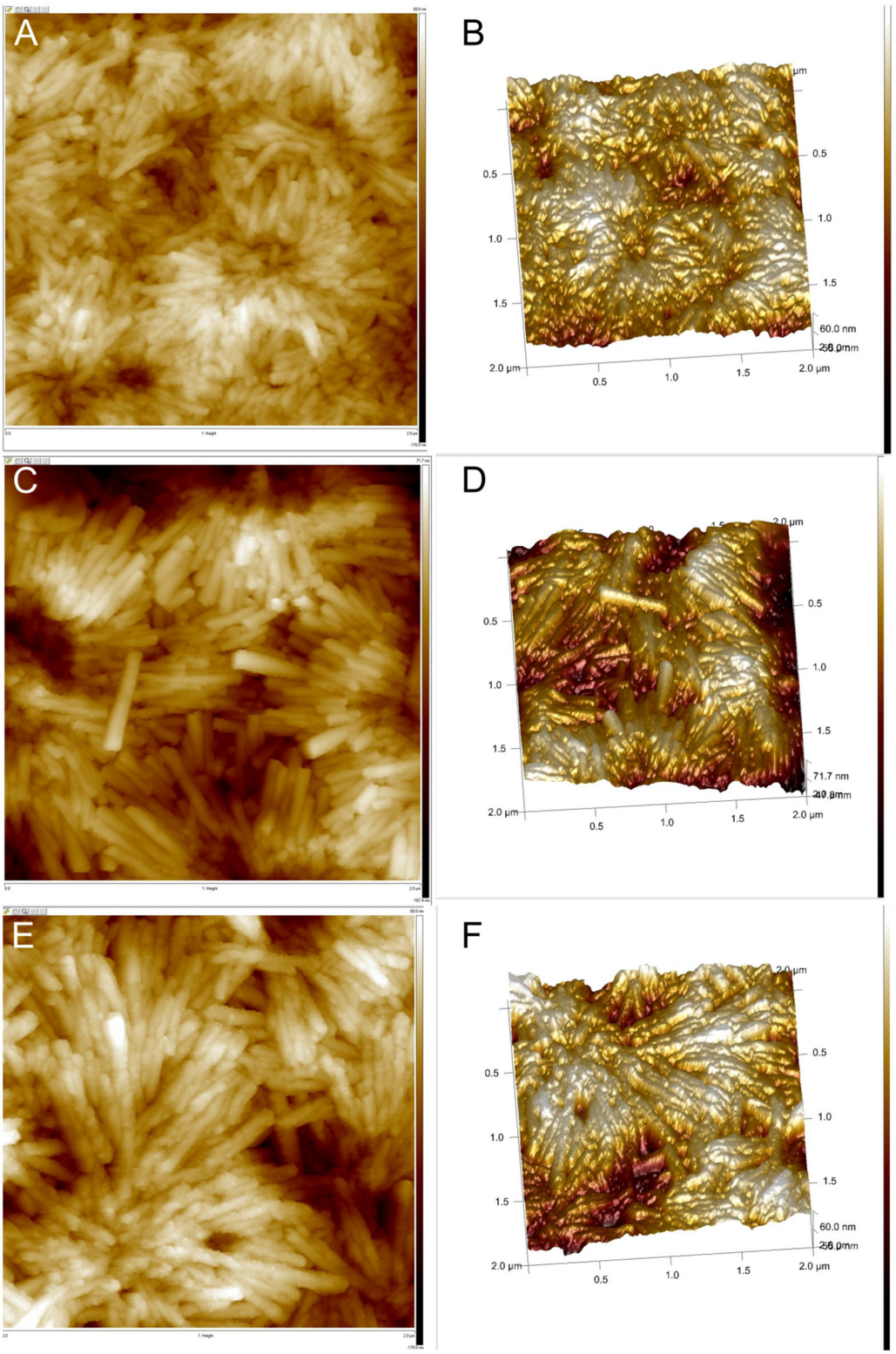

FIGURE 4 | AFM images of the $H_4TPPS_4^{2-}$-Sn(IV)TPyP^{4+} porphyrin nanostructures formed by the self-assembly in solutions at pH = 2.0 and Sn(IV)TPyP^{4+} and $H_4TPPS_4^{2-}$ taken in a 1:1 concentration ratio **(A,B),** Sn(IV)TPyP^{4+} and $H_4TPPS_4^{2-}$ taken in a 1:5 concentration ratio **(C,D)**, and Sn(IV)TPyP^{4+} and $H_4TPPS_4^{2-}$ taken in a 5:1 concentration ratio **(E,F)**.

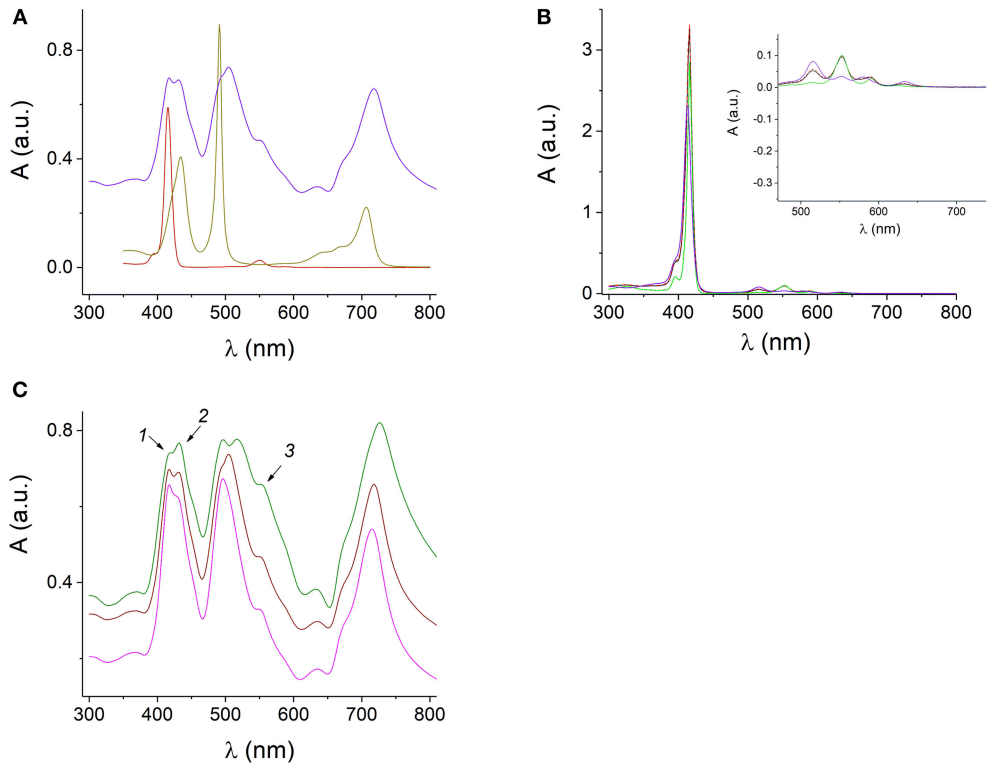

FIGURE 5 | UV-visible absorption spectra of the protonated $H_4TPPS_4^{2-}$ and $H_4TPPS_4^{2-}$ J-aggregates at pH 0.94 (dark yellow), 1 μM $SnTPyP^{4+}$ (dark red), and $H_4TPPS_4^{2-}$-$SnTPyP^{4+}$ nanotubes (blue) at pH 2 **(A)**. Spectra of the mixed equimolar solutions of $TPPS_4$ and $SnTPyP^{4+}$ porphyrins at pH 6 (red dashed line) and pH 10.5 (black line) and the spectra of the corresponding porphyrins at pH 10.5: SnTPyP at pH 10.5 (green) and deprotonated $TPPS_4$ at pH 10.5 (violet). The formation of nanostructures is not observed. The insert in **(B)** shows an enlarged long-wavelength region **(B).** Spectra of the $SnTPyP^{4+}$-$H_4TPPS_4^{2-}$ nanotubes self-assembled in solutions at pH 2 and $SnTPyP^{4+}$ and $H_4TPPS_4^{2-}$ taken in concentration ratios of 1:5 (green line), 1:1 (brown), and 5:1 (pink). The arrows indicate the spectral features characteristic for the absorption of individual porphyrins **(C)**.

lead to broadening of J-bands (Franco et al., 2010). Unlike $H_4TPPS_4^{2-}$, Sn(IV)TMPyP^{4+} does not form homoaggregates on its own (George et al., 2010). This may be explained by the presence of the obligate axial ligands of the Sn(IV) porphyrin, which is expected to inhibit macrocycle stacking due to the lack of a cationic center (Ohno et al., 1993; Franco et al., 2010). The Sn^{4+} ion with the axially coordinated Cl^- ions hinder the face-to-face geometry, preventing its own J-aggregates but allowing electrostatic interaction between $H_4TPPS_4^{2-}$ and $SnTPyP^{4+}$ via the cationic and anionic peripheral groups (Rosaria et al., 2008), which is another force of the assembly process. In Koposova et al. (2016b), a cationic center of the $H_4TPPS_4^{2-}$ dianion was replaced with a metal cation, which resulted in a network-like nanostructures prepared by self-assembly of two metalloporphyrins, Sn(IV)$TPPS_4$-Co(III)TPyP, instead of well-formed nanorods characteristic for the $H_4TPPS_4^{2-}$ self-assembly. Thus, the central metal affects the assembly dimension (Rosaria et al., 2008), which is useful for modulating the aggregate size and properties. Based on previous literature and our experiments above, we assume that the main driving force of self-assembly in this porphyrins pair is assembly of the $TPPS_4$ dianion, $H_4TPPS_4^{2-}$, with a slipped face-to-face stacking with inclusion of a six-coordinated tin porphyrin, which do not form aggregates by its own. However, exact relative molecular arrangement of both porphyrins in these nanostructures remains under discussion (Wang et al., 2004; Franco et al., 2010).

In the present study, EDX spectroscopy showed a presence of both porphyrins (according to the presence of both sulfur and tin elements) in the self-assembled nanotubes, (**Figure 6** and **Figure S6**). Because of the poor accuracy of quantitative EDX analysis, we used chemical elemental analysis to estimate the presence of both porphyrins in the nanotubes. Since a very small amount of the nanostructures is formed in a 5:1 (Sn(IV)TPyP^{4+} : $H_4TPPS_4^{2-}$) solution, and system 1:5 (Sn(IV)TPyP^{4+} : $H_4TPPS_4^{2-}$) produced at least two different kinds of nanostructures, we performed an elemental analysis of the nanostructures self-assembled from the equimolar porphyrin solutions at pH 2, **Figure S7**, which indicated a $H_4TPPS_4^{2-}$: $SnTPyP^{4+}$ molar ratio in the nanostructures of 2:1.

Photoconductivity

The electrophotoresponse of the $H_4TPPS_4^{2-}$-$SnTPyP^{4+}$ porphyrin nanotubes was measured in the dark (dark current) and after photoexcitation with visible light, (**Figure 7**).

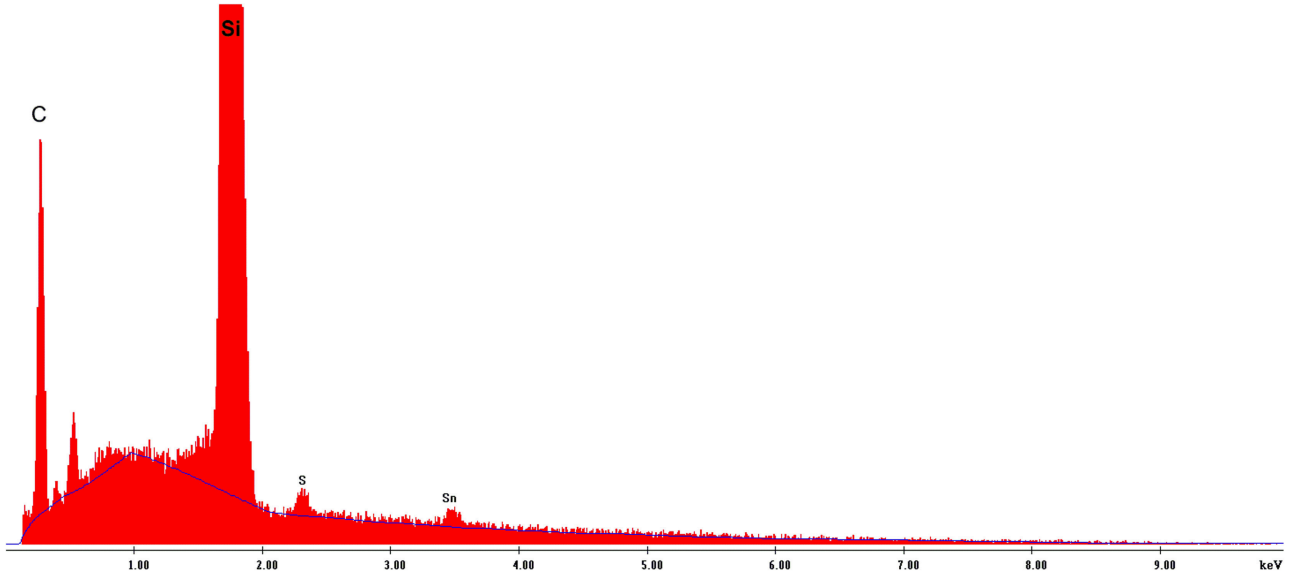

FIGURE 6 | EDS analysis of the $H_4TPPS_4^{2-}$-Sn(IV)TPPyP^{4+} nanotubes formed in an equimolar solution at pH = 2.0.

Photoexcitation resulted in a photocurrent in case of the $H_4TPPS_4^{2-}$-SnTPyP^{4+} porphyrin nanotubes as one can see in **Figure 7**. Photoresponse of a device, where an equimolar solution of $TPPS_4$ and SnTPyP^{4+} porphyrins (pH 6) was dropcasted onto the device and prepared for the measurements in the same way as for the nanostructures (see section Electrophotoresponse Measurements) is also shown. However, no photocurrent was observed in this case probably due to the absence of a permanent layer of porphyrins in the gap between the contact electrodes in the conditions of experiments and a lower photoconductivity of the individual porphyrin molecular layers.

After subtracting the dark current, the apparent photoconductivity of the $H_4TPPS_4^{2-}$ –Sn(IV)TPyP^{4+} nanotubes at 23 °C was estimated as $(3.1 \pm 0.9)\times10^{-4}$ S m^{-1} ($n = 5$). Slightly lower and less reproducible value, $(2.2 \pm 1.0) \times 10^{-4}$ S m^{-1}, was found for the nanostructures prepared in a solution with a Sn(IV)TPyP^{4+} : $H_4TPPS_4^{2-}$ concentration ratio of 1:5. We assume that this might be due to the presence of several types of the smaller nanostructures formed by $H_4TPPS_4^{2-}$, which do not form a continuous layer over hundreds of nm distances, (**Figures 2C,D** and **Figure S5**), and contact area with the metal electrodes. The latter value is thus not a characteristic of one type of nanostructures, but rather characterizes a nonhomogeneous mixture of the nanostructures obtained in this system. Amounts of the nanostructures prepared in a solution with a Sn(IV)TPyP^{4+} : $H_4TPPS_4^{2-}$ concentration ratio of 5:1 was practically very small for the accurate measurements of photoconductivity, giving a similar approximate value of $(1.8 \pm 0.8) \times 10^{-4}$ S m^{-1} ($n = 2$). Identical spectral features of the nanostructures prepared at pH 2, (**Figure 5C**), are in agreement with similar values of photoconductivities in these systems.

The value of the apparent photoconductivity of the $H_4TPPS_4^{2-}$-Sn(IV)TPyP^{4+} nanotubes is lower than for the

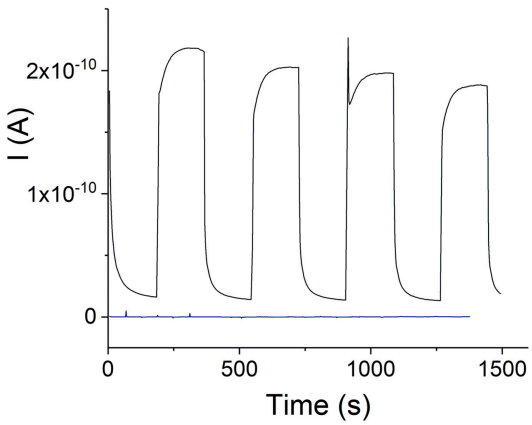

FIGURE 7 | Visible light photoresponse of the $H_4TPPS_4^{2-}$-SnTPyP^{4+} nanotubes prepared in an equimolar solution at pH 2, electrode gap 400 nm, $V_{app} = 0.5$ V. A dark blue curve shows a visible light photoresponse of a device with no nanostructures. The device was prepared by dropcasting an equimolar solution of $TPPS_4$ and SnTPyP^{4+} (pH 6) onto the chip as described in experimental section Electrophotoresponse Measurements.

porphyrin-acetylene-thiophene polymer wires synthesized in Li et al. (2004), which, had, however, covalent nature, (**Table 1**). On the other hand, the apparent photoconductivity of the $H_4TPPS_4^{2-}$-Sn(IV)TPyP^{4+} nanotubes is higher by several orders of magnitude than for similar systems, (**Table 1**), and corresponds to the conductivity region of semiconductors (Kobayashi et al., 1993; Naarman, 2012). As can be seen in **Table 1**, the photoconductivities of the porphyrin films and porphyrin self-assembled nanostructures were demonstrated in a range of 10^{-10}-10^{-3} S m^{-1} (Golubchikov and Berezin, 1986).

TABLE 1 | Conductivity and photoconductivity of different self-assembled and covalently bonded porphyrin systems.

Porphyrin system	σ, S m^{-1}	References
Tetraphenylporphine (TPP) film[a]	1.5×10^{-9}	Weigl, 1957
Oxygen-doped (air) ZnTPP thin film[b]	$<10^{-9}$	Kobayashi et al., 1993
Charge-transfer complexes of Lanthanide(III) bis(porphyrin) sandwich complexes of Gd and Lu and Zr(IV) bis(porphyrin) sandwiches[b]	10^{-5}-8×10^{-3}	Collman et al., 2000
Cu-porphyrin Langmuir-Blodgett film[b]	2.54×10^{-5} (x axis) and 4.71×10^{-7} (y axis)	Zhang et al., 1995
Porphyrin-acetylene-thiophene polymer wires[b]	6×10^{-1}	Li et al., 2004
P(V)-porphyrin(electron acceptor)-oligothiophene(electron donor) polymers[b,c]	1.2×10^{-7}-5.1×10^{-6}	Segawa et al., 1992a
Porphyrin polymer with oligophenylenevinylene		Jiang et al., 1997
bridge undoped[b]	$<10^{-10}$	
after doping[b]	10^{-4}	
Nanofilaments of tetra-*meso*-amidophenyl substituted porphyrin[a,d] 90–400 W m^{-2}, bias 1 V	up to 100×10^{-12} m Ω^{-1} W^{-1}	Schall et al., 2015
meso-tri(4-sulfonatophenyl)monophenylporphine, $TPPS_3$, nanotapes [a,d]	5×10^{-8} m Ω^{-1} W^{-1}	Yeats et al., 2008
Chlorophyll-a[a,e]	$(0.2–1.0) \times 10^{-8}$	Jones et al., 1983
Protoporphyrin IX dimethyl ester	1.5×10^{-5}	
TPyP:TSPP crystalline rods[a,f]	9.3×10^{-8}	Borders et al., 2017
TMPyP:TSPP crystalline rods [a,g]	4.0×10^{-10}	Adinehnia et al., 2016
H_2TMPyP:Cu(II)TSPP[a,h]	7.7×10^{-8}	Borders et al., 2018
Cu(II)TMPyP:H_2TSPP	1.1×10^{-8}	
H_2TMPyP:Ni(II)TSPP	7.7×10^{-9}	
Ni(II)TMPyP: H_2TSPP	6.3×10^{-9}	
Sn(IV)$TPPS_4$-Co(III)TPyP nanostructures[a,i]	6×10^{-7}	Koposova et al., 2016b
Co(III)TPyP-$H_4TPPS_4^{2-}$ porphyrin nanostructures[a,i]	5×10^{-5}	Koposova et al., 2018
Sn(IV)TPyP-$H_4TPPS_4^{2-}$ porphyrin nanotubes[a,i]	3.1×10^{-4}	This work

[a] *Photoconductivity.*
[b] *Conductivity.*
[c] *In polymers the conductivity was enhanced by the photoirradiation. In the case of photoirradiation by 500 W Xe lamp through UV and IR cut-off filters, the enhancement was > 3 fold (Segawa et al., 1992a).*
[d] *The photoconductivity in this study is defined as the conductivity divided by the light intensity.*
[e] *Photoconductivity parallel to the plane of the multilayer, in-plane photoconductivity, 50 W m^{-2} of white light, 5 V bias.*
[f] *At 405 nm excitation, 10 kW m^{-2}, 2 V bias.*
[g] *At 445 nm excitation, 10 kW m^{-2}, 2 V bias.*
[h] *At 445 nm excitation, 1.0 W cm^{-2}, 5 V bias.*
[i] *Visible light, Xe lamp, 0.25 kW m^{-2}, bias 0.5 V.*

Figure 6A shows that the photocurrent of the self-assembled $H_4TPPS_4^{2-}$-Sn(IV)$TPyP^{4+}$ nanotubes decreases over the μm distances. The dependence of the photroconductance of the $H_4TPPS_4^{2-}$ –Sn$TPyP^{4+}$ nanostructures on temperature was investigated in the range from 23 to 70°C, (**Figure 6B**). Increasing the temperature resulted in a decrease in the photocurrent, dσ/dT<0. At the highest temperature, 70 °C, a decrease in the dark current was also observed. The metal-like character of the dependence of the photoconductivity of the $H_4TPPS_4^{2-}$ –Sn$TPyP^{4+}$ nanotubes on temperature was also observed earlier for the $H_4TPPS_4^{2-}$ –Co(III)T(4-Py)P self-assembled nanostructures (Koposova et al., 2018). Furthermore, the photoconductivity of the Sn(IV)$TPPS_4$-CoTPyP nanostructures was characterized by the decrease in both photocurrent and dark current at the elevated temperature (Koposova et al., 2016b). The observed dependence may be explained by overcoming the energy of intermolecular interactions with increased disorder, as well as the recombination of electrons and holes at elevated temperatures. A similar metal-like character of the conductance was also observed in a TTF-TCNQ complex in a narrow range of temperature (Ferraris et al., 1973) and arrayed iodine-doped metallo-macrocycles (Schramm et al., 1980; Hoffman and Ibers, 1983; Golubchikov and Berezin, 1986). After cooling down to the initial temperature, the conductance properties recovered and photoconductance even increased slightly, (**Figure 6B**) (dotted line). This indicates that the destruction of the nanostructure assembly does not occur during heating.

Photoinduced charge transfer in self-assembled porphyrin nanomaterials can be described in terms of charge-transfer exciton theory, where two neighboring porphyrin molecules with different electronic characteristics form an electron-donor-acceptor charge-transfer complex (Segawa et al., 1989, 1992b; Knoester and Agranovich, 2003; Scholes and Rumbles, 2006; Zhu et al., 2009; Martin et al., 2010; Natali and Scandola, 2016). This theory assumes that the charge-transfer excitons in the electron-donor-acceptor complexes are generated by absorption of light, and that these are essential for the creation of free

carriers (Knoester and Agranovich, 2003). The locations of the hole and electron on different porphyrin molecules due to their different electron donating and electron accepting properties (Knoester and Agranovich, 2003; Martin et al., 2010; Natali and Scandola, 2016) increases the electron and hole separation distance and the probability of a free charge-carrier formation. An applied electric field may favor the charge separation (Scholes and Rumbles, 2006) and result in a photocurrent. Exciton theory has been applied to biomolecular aggregates in the light-harvesting systems of plants and several types of green bacteria, which absorb sunlight and transport the excitation energy to the reaction centers (Knoester and Agranovich, 2003).

As it was mentioned in the introduction section, Martin et al. (2010) described the photoconductance of the microscale clover-shaped assemblies of two metalloporphyrins Zn(II)TPPS^{4-} and Sn(IV)T(N-EtOH-4-Py)P^{4+} in terms of the charge-transfer excitons produced in the photoexcited nanostrucutres. ZnPs were considered donors and Sn(IV)Ps were considered acceptors because of the redox potentials estimations based on the literature data for the Zn and Sn(IV)OEPs. The segregated stacking of molecules similar to that in a classical donor-acceptor organic solid TTF-TCNQ was supposed. In this configuration, the excitation with light resulted in electrons on acceptor porphyrin in columns of positive charges of the pyridinium groups, and the holes remained on porphyrin with a donor character with channels formed by the negative charges of the sulfonate groups.

The donor and acceptor character of the nanorod tectons can be estimated from the energy levels of each component. This can be approached using cyclic voltammetry, which reveals the first oxidation and reduction potentials and, as a result, the relative location of the porphyrin energy levels (Mairanovsky, 1987; Bouvet and Simon, 1990; Rieger, 1994; Kadish and Van Caemelbecke, 2003; Martin et al., 2010). Under defined conditions (Delahay, 1954; Rieger, 1994), the half-wave potentials of the compounds can be taken as an approximation to the standard potentials and it is expected that their values correlate with the electron affinity of the compounds. The electron affinity is expected to be related to the energy of the lowest unoccupied molecular orbital. We carried out cyclic voltammetry of $TPPS_4$ and Sn(IV)TPyP^{4+}, (**Figure 7** and **Table 2**). Measurements were performed at pH=2.0 and 3.5 for SnTPyP^{4+}, and at pH = 4.0 for $H_4TPPS_4^{2-}$ (dimerization, self-assembly) and pH = 6.9 for $H_2TPPS_4^{4-}$, respectively. On the one hand, the measurements at higher pH were impeded by a poor solubility of Sn(IV)TPyP^{4+}. On the other hand, $H_4TPPS_4^{2-}$ forms dimers, J-aggregates, and nanotubes in neutral and acidic media (pH < 4.8), respectively, and the redox peaks were very sluggish and poorly defined. In general, adsorption also complicates the electrochemical measurements of $TPPS_4$ and Sn(IV)TPyP compounds. Therefore, we used a negative shift of 0.030 V pH^{-1} for the first reduction of SnTPyP (found from the values taken at pH 2.0 and 3.5) to estimate $E_{1/2}^{red}$ of about −0.534 V for SnTPyP at pH 6.9. It is lower in energy than that found for $H_2TPPS_4^{4-}$ at this pH. The oxidation peak could be resolved only for $H_2TTPS_4^{4-}$ at pH 6.9. The oxidation peak of Sn(IV)TPyP is at more positive potentials interfering with the decomposition of the aqueous solutions. The CV of the NS adsorbed overnight on a GCE (washed thoroughly with water before measurements) revealed a broad feature corresponding presumably to the reduction of the Sn(IV)TPyP species at a lower potential window of about −0.6 to −0.4 V (Ag/AgCl). It also revealed a reduction process at a higher energy of about −0.7 V (Ag/AgCl), (**Figure 7**), presumably corresponding to the reduction processes of the $TPPS_4$ species. However, it was shown that the redox potentials of the porphyrins may be shifted due to their interactions, e.g., as shown for the porphyrin ion-paired porphyrin dimers (Natali and Scandola, 2016). Altogether, the data suggest that Sn(IV)TPyP can be considered as a molecule with more acceptor properties and $TPPS_4$ as a molecule with more donor properties in this couple. Indeed, this is in agreement with the fact that the Sn(IV) complex is considered one of the most electropositive metalloporphyrins (Fuhrhop et al., 1973; Koposova et al., 2016a). While it is stable against electrophilic attack, it is very reactive with reducing agents (Fuhrhop et al., 1973). Moreover, the Py substituents of the porphyrin ring have more electron-withdrawing properties than 4-sulfonatophenyl substituents, contributing to lowering the reduction potential of Sn(IV) porphyrins with Py substituents of the macrocycle and the stability of a π-radical anion of Sn(IV)P (Jahan et al., 2012; Koposova et al., 2016a). It is worth mentioning that the CV of the adsorbed nanostructures indicates that the energy levels of individual molecules may be changed in the nanostrucutres, as shown for the porphyrin ion pairs (Natali and Scandola, 2016).

Thus, applying this principle to the couple under investigation and based on the cyclic voltammetry data we can assume that photoirradiation may lead to exciton delocalization in the $H_4TPPS_4^{2-}$ –Sn(IV)TPyP^{4+} porphyrin nanotubes, where Sn(IV)TPyP porphyrin possesses an acceptor character and $H_4TPPS_4^{2-}$ porphyrin possesses a donor character in this couple, although, the positions of LUMO and HOMO for Sn(IV)TPyP^{4+} and $H_4TPPS_4^{2-}$ are difficult to define at the same conditions. However, donor-acceptor interactions and charge-transfer exciton may appear not only in systems with two types of molecules but for one type of molecules such as chlorophyll (Katz, 1979), in the case of separation and transportation of the photogenerated electron-hole pairs in the 5,10,15,20-tetraphenylporphyrin nanospheres (Zhang et al., 2015), or molecule crystals such as anthracene, naphthalene, etc. (Knoester and Agranovich, 2003). In the latter case, any molecule in the crystal can play the role of donor or acceptor.

TABLE 2 | Half-wave reduction ($E_{1/2}^{red}$) and oxidation E_p^{ox} potentials of $TPPS_4$ and Sn(IV)TPyP^{4+} at different pH in aqueous solution.

Porphyrin	$E_{1/2}$ ^{red}, E_p^{ox}, V			
	pH = 2.0	pH = 3.5	pH = 4.0	pH = 6.9
$TPPS_4$			(−0.434)[a]	−0.703
			–	+0.868
Sn(IV)TPyP	−0.384	−0.429	–	(−0.534)[b]
	>1.40	>1.40		–

[a] *Possible formation of dimers or larger aggregates.*
[b] *Calculated assuming ca. 30 mV pH^{-1} for Sn(IV)TPyP.*

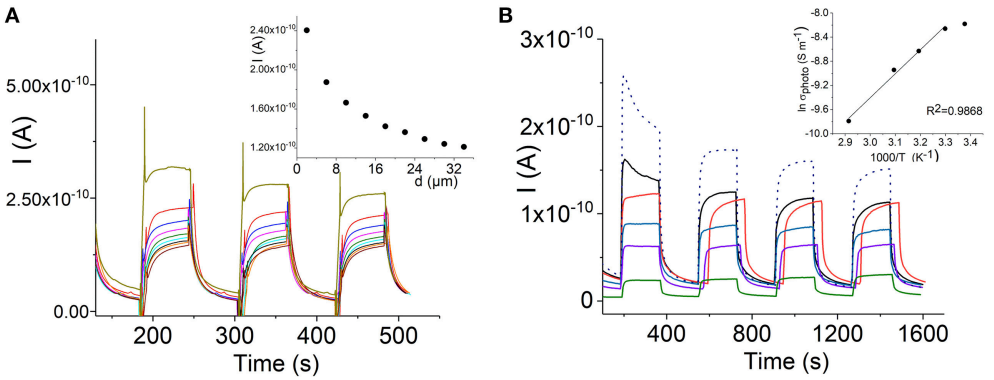

FIGURE 8 | Dependence of the photocurrent of the $H_4TPPS_4^{2-}$-Sn(IV)TPyP^{4+} porphyrin nanotubes on the path length, interdigitated electrode array (see experimental section), V_{app} = 0.5 V **(A)**. Temperature dependence of the photocurrent of the $H_4TPPS_4^{2-}$ - Sn(IV)TPyP^{4+} nanotubes: 23°C–black line, 30°C– red line, 40°C–blue line, 50°C– violet line,70°C– green line, after cooling down to 23°C–dotted line. Insert shows a dependence of lnσ_{photo} on 1,000/*T*, 400 nm electrode gap, V_{app} = 0.5 V **(B)**.

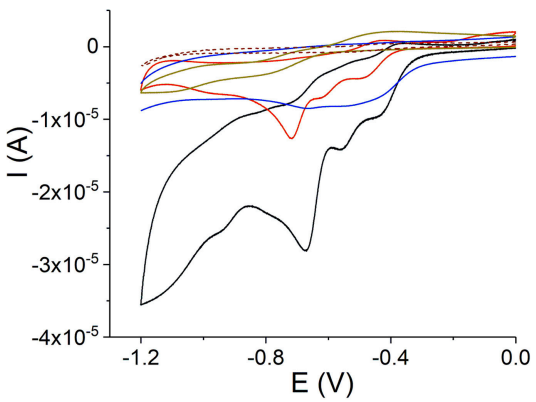

FIGURE 9 | Cyclic voltammograms on a GCE: Sn(IV)TPyP^{4+} at pH 2 (black line) and 3.5 (red line), $H_2TPPS_4^{4-}$ at pH 6.9 (dark yellow line), $H_4TPPS_4^{2-}$ and aggregates at pH 4 (brown dashed line), and $H_4TPPS_4^{2-}$-Sn(IV)TPyP^{4+} adsorbed overnight (blue line), 0.1 M KNO_3, scan rate 50 mV s^{-1}.

Additionally, it was supposed in the above-mentioned works (Franco et al., 2010; Martin et al., 2010) that the location of the hole on the positively charged porphyrins (Sn(IV)TPyP^{4+}) and the electrons on the negatively charged porphyrins ($H_4TPPS_4^{2-}$) might be energetically unfavorable and result in electron-hole recombination not favoring the conductivity (Martin et al., 2010). These data also support the charge-transfer mechanism in the $H_4TPPS_4^{2-}$-Sn(IV)TPyP^{4+} system with Sn(IV)TPyP^{4+} as an electron acceptor and $H_4TPPS_4^{2-}$ as a donor.

It is interesting to compare the apparent photoconductivity of the $H_4TPPS_4^{2-}$-Sn(IV)TPyP^{4+} nanotubes with that of the $H_4TPPS_4^{2-}$-Co(III)T(4-Py)P self-assembled nanotubes (Koposova et al., 2018) and Sn(IV)TPPS$_4$-Co(III)T(4-Py)P nanostructures (Koposova et al., 2016b), which we studied recently. In the first two systems, the optical UV-visible spectra of the self-assembled nanostructures exhibit J-aggregate absorbance bands at about 500 nm, 716 nm and 494 nm, 709 nm, respectively, while the absorption spectrum of the Sn(IV)TPPS$_4$ - Co(III)T(4-Py)P nanostructures lacks these bands, probably because of the longer intermolecular distances, weaker intermolecular interactions, and a weaker electronic coupling in the latter system. As a result, the apparent conductivities of the $H_4TPPS_4^{2-}$-Sn(IV)TPyP^{4+} and $H_4TPPS_4^{2-}$-Co(III)T(4-Py)P self-assembled nanotubes are higher due to a higher probability of the exciton delocalization. Additional factors, which may contribute to the higher photoconductivity of the $H_4TPPS_4^{2-}$-Sn(IV)TPyP^{4+} system is closeness of the energies of unoccupied molecular orbitals and electron affinity of the porphyrins in this system as follows from the above mentioned experiments so that no completed redox processes between two porphyrins takes place, which would stop a directed electron flow. Further studies on elucidation of exact relative arrangement and packing of different porphyrin molecules in the nanostructures may be useful to explain influence of the structural features on photoconductivity in the porphyrin nanotubes.

Porphyrin and porphyrin nanostructures are important compounds for the development of sensors (Malinski, 2000; Guo et al., 2014; Paolesse et al., 2017; Skripnikova et al., 2017). In particular, Sn(IV)Ps are responsible for the selectivity to salicylate anions in ion-selective electrodes due to axial salicylate ligand binding to the metal center (Malinski, 2000; Skripnikova et al., 2017). In this study, we also examined the sensing properties of the $H_4TPPS_4^{2-}$ –Sn(IV)TPyP^{4+} nanorods based on their photoconductivity in a chemiresistor sensor mode (Muratova et al., 2016, **Figure 8A**). **Figure 8B** illustrates the change in the photocurrent of the nanostructures after exposure to Sal^--ions at room temperature. All samples were dried before the measurements. Insert in **Figure 8B** demonstrates a corresponding dependence of the photoconductivity of the $H_4TPPS_4^{2-}$-Sn(IV)TPyP^{4+} nanorod chemiresistor on the concentration of salicylate ions. We suppose that a relatively large error of measurements is due to a poor reproducibility

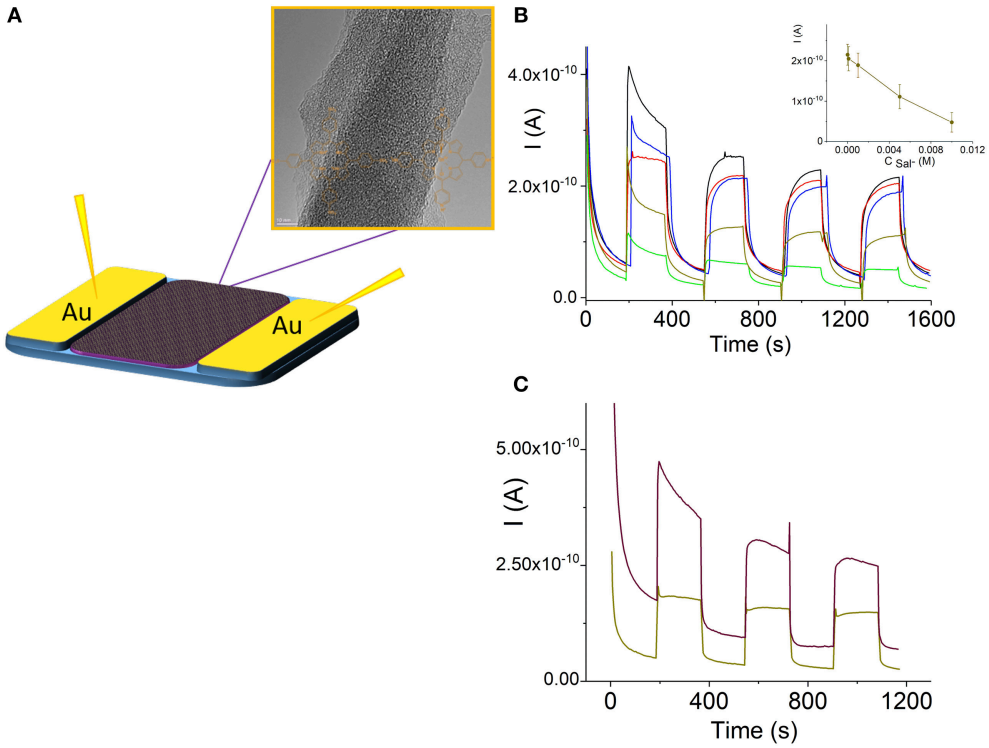

FIGURE 10 | Schematic illustration of a porphyrin nanorod chemiresistor **(A)**. (Photo)current response curves of the $H_4TPPS_4^{2-}$-Sn(IV)$TPyP^{4+}$ porphyrin nanorods in a chemoresistor sensor mode before (black line) and after exposure to salicylate 10^{-4} M (red line), 10^{-3} M (blue line), $5{\cdot}10^{-2}$ (dark yellow line), and 10^{-2} M (green line) **(B)**, insert in **(B)** shows a corresponding dependence of the photocurrent of the $H_4TPPS_4^{2-}$-Sn(IV)$TPyP^{4+}$ nanorod chemiresistor on the concentration of salicylate ion, $n = 3$, $p = 0.95$. (Photo)current of the $H_4TPPS_4^{2-}$-$SnTPyP^{4+}$ porphyrin nanorods before (dark yellow line) and after (brown line) exposure to iodine vapor for 60 min, $V_{app} = 0.5$ V **(C)**.

of the interface between porphyrin nanorods and the contact metal electrodes, (**Figure 8A**). However, these experiments show a potential utility of the self-assembled porphyrin nanorods as functional layers for the sensor devices.

Both the dark current and photoconductance of the $H_4TPPS_4^{2-}$-$SnTPyP^{4+}$ nanorods increased in case of exposure to iodine vapor, **Figure 10C**. The photocurrents of porphyrin films pretreated with iodine or oxygen electron acceptors were found to be higher than those without pretreatment (Yamashita and Maenobe, 1980; Hoffman and Ibers, 1983; Zhang et al., 1995; Savenije and Goossens, 2001). The contribution of acceptor impurities, e.g., O_2 or iodine, should be taken into account in the exciton mechanism of the photoconductance of porphyrins, where a charge-transfer complex formation with an acceptor such as iodine (Hoffman and Ibers, 1983) or oxygen (Kobayashi et al., 1993) was proposed. Recently, a nanoelectronic chemosensor was proposed for the detection of vapor-phase H_2O_2 based on the self-assembled Ti porphyrin (Guo et al., 2014). It can be assumed that hydrogen peroxide influences the number of charge carriers in the porphyrin nanostructure-based channel, which would be responsible for the sensor sensitivity.

The absorption spectrum of $SnTPyP^{4+}$-$H_4TPPS_4^{2-}$ porphyrin nanotubes has a series of absorption bands in 400–750 nm region, (**Figure 4**). Previous studies have shown that the photoconductivity is observed at a laser illumination of 488 nm (close to the absorption wavelength of J-aggregates) in the $TPPS_4$ and $TPPS_3$ nanorods (Schwab et al., 2004; Yeats et al., 2008), any wavelength of absorption in TTP (Weigl, 1957), and at different wavelengths with different intensity according to the absorption spectra of the nanorods assembled from TSPP and TMPyP or TPyP (Adinehnia et al., 2016; Borders et al., 2017). In this study, we found that the Q-band region with a Q-band of Sn(IV)$TPyP^{4+}$ (550–552 nm) and the J-band of nanostructures at 714 nm are responsible for about 34% of photoconductance of the self-assembled $H_4TPPS_4^{2-}$-Sn(IV)$TPyP^{4+}$ porphyrin nanotubes by exposure to visible light irradiation with an additional 550 nm longpass filter.

CONCLUSIONS

We investigated morphological, spectral, and electrical properties of the self-assembled $H_4TPPS_4^{2-}$-Sn(IV)$TPyP^{4+}$ tubular nanostructures formed by monomers at pH = 2.0. The formation of hollow tubes can include a series of mechanisms of self-assembly assuming a combination of a series of intermolecular interactions. The $H_4TPPS_4^{2-}$ –Sn(IV)$TPyP^{4+}$ nanotube network demonstrates a photoconductivity under

visible light in a semiconductor range of $(3.1 \pm 0.9) \times 10^{-4}$ S m^{-1}. The temperature dependence of the photoconductance of the nanotubes showed a metal-like character of decreasing current with increasing temperature. The photocurrent decreased over the μm distances. It was found that excitation of the Q-band region with a Q-band of Sn(IV)TPyP^{4+} (550–552 nm) and the J-band of the nanostructures at 714 nm is responsible for about 34% of the photoconductance activity of the $H_4TPPS_4^{2-}$ –Sn(IV)TPyP^{4+}- porphyrin nanotubes. The sensor properties of the nanotubes in a chemiresistor mode were tested to demonstrate a perspective of the self-assembled porphyrin nanorods as functional layers for the sensor devices and biomimetic nanoarchitectures.

DATA AVAILABILITY

All datasets generated for this study are included in the manuscript and/or the **Supplementary Files**.

AUTHOR CONTRIBUTIONS

EK made substantial contributions to design, acquisition, analysis, and interpretation of data, and participated in drafting the article. AO and YE made substantial contributions to conception, analysis, and interpretation of data, and participated in drafting the article. YM made substantial contributions to conception, design, acquisition, analysis, and interpretation of data, and participated in drafting the article. All authors gave final approval of the submitted manuscript.

FUNDING

This research did not receive any specific grant from funding agencies in the public, commercial, or not-for-profit sectors.

ACKNOWLEDGMENTS

The authors thank Dr. D. Mayer (ICS-8) for the AFM analysis and discussion, Dr. S. Willbold (Central Institute of Chemical Analysis) for the elemental analysis, Dr. M. Heggen (Ernst Ruska-Center) for the TEM investigations, W. Sybertz and E. Brauweiller-Reuters for the SEM and EDX studies, Dr. V. Schöps and Dr. I. Muratova for the thin-film gold electrodes.

SUPPLEMENTARY MATERIAL

The Supplementary Material for this article can be found online at: https://www.frontiersin.org/articles/10.3389/fchem.2019.00351/full#supplementary-material

REFERENCES

Adinehnia, M., Borders, B., Ruf, M., Chilukuri, B., Hipps, K. W., and Mazur, U. (2016). Comprehensive structure–function correlation of photoactive ionic π-conjugated supermolecular assemblies: an experimental and computational study. *J. Mater. Chem. C* 4, 10223–10239. doi: 10.1039/C6TC03957J

Agranovich, E. V. M., and Bassani, G. F. (2003). *Electronic Excitations in Organic Based Nanostructures*. Oxford, UK: Elsevier Academic Press.

Borders, B., Adinehnia, M., Chilukuri, B., Ruf, M., Hipps, K. W., and Mazur, U. (2018). Tuning the optoelectronic characteristics of ionic organic crystalline assemblies. *J. Mater. Chem. C* 6, 4041–4056. doi: 10.1039/C8TC00416A

Borders, B., Adinehnia, M., Rosenkrantz, N., Van Zijll, M., Hipps, K. W., and Mazur, U. (2017). Photoconductive behavior of binary porphyrin crystalline assemblies. *J. Porphyrins Phthalocyan.* 21, 569–580. doi: 10.1142/S1088424617500638

Bouvet, M., and Simon, J. (1990). Electrical properties of rare earth bisphthalocyanine and bisnaphthalocyanine complexes. *Chem. Phys. Lett.* 172, 299–302. doi: 10.1016/0009-2614(90)85407-4

Cai, J., Chen, H., Huang, J., Wang, J., Tian, D., Dong, H., et al. (2014). Controlled self-assembly and photovoltaic characteristics of porphyrin derivatives on a silicon surface at solid-liquid interfaces. *Soft Matter* 10, 2612–2618. doi: 10.1039/c3sm53061b

Chen, Y., Li, A., Huang, Z.-H., Wang, L.-N., and Kang, F. (2016). Porphyrin-based nanostructures for photocatalytic applications. *Nanomaterials* 6:51. doi: 10.3390/nano6030051

Chou, J. H., Kosal, M. E., Nalwa, H. S., Rakow, N. A., and Suslick, K. S. (2000). "Application of porphyrins and metalloporphyrins of materials chemistry," in *The Porphyrin Handbook*, eds K. M. Kadish, K. M. Smith, and R. Guilard (San Diego, CA: Academic Press), 346.

Collman, J. P., Kendall, J. L., Chen, J. L., Collins, K. A., and Marchon, J.-C. (2000). Formation of charge-transfer complexes from neutral bis(porphyrin) sandwiches. *Inorg. Chem.* 39, 1661–1667. doi: 10.1021/ic9907516

Delahay, P. (1954). *New Instrumental Methods in Electrochemistry*. New York, NY: Interscience Publ. Inc.

Drain, C. M. (2002). Self-organization of self-assembled photonic materials into functional devices: photo-switched conductors. *Proc. Natl. Acad. Sci. U.S.A.* 99, 5178–5182. doi: 10.1073/pnas.062635099

El-Khouly, M. E., Fukuzumi, S., and D'souza, F. (2014). Photosynthetic antenna–reaction center mimicry by using boron dipyrromethene sensitizers. *ChemPhysChem* 15, 30–47. doi: 10.1002/cphc.201300715

Ferraris, J., Walatka, V., Perlstein, J., and Cowan, D. O. (1973). Electron-transfer in a new highly conducting donor-acceptor complex. *J. Am. Chem. Soc.* 95, 948–949. doi: 10.1021/ja00784a066

Franco, R., Jacobsen, J. L., Wang, H., Wang, Z., Istvan, K., Schore, N. E., et al. (2010). Molecular organization in self-assembled binary porphyrin nanotubes revealed by resonance raman spectroscopy. *Phys. Chem. Chem. Phys.* 12, 4072–4077. doi: 10.1039/b926068d

Friesen, B. A., Wiggins, B., Mchale, J. L., Mazur, U., and Hipps, K. W. (2010). Differing HOMO and LUMO mediated conduction in a porphyrin nanorod. *J. Am. Chem. Soc.* 132, 8554–8556. doi: 10.1021/ja103078q

Fuhrhop, J. H. (2014). Porphyrin assemblies and their scaffolds. *Langmuir* 30, 1–12. doi: 10.1021/la402228g

Fuhrhop, J. H., Kadish, K. M., and Davis, D. G. (1973). The redox behavior of metallooctaethylporphyrins. *J. Am. Chem. Soc.* 95, 5140–5147. doi: 10.1021/ja00797a008

Fukuzumi, S., and Imahori, H. (2008). "Biomimetic electron-transfer chemistry of porphyrins and metalloporphyrins," in *Electron Transfer in Chemistry*, ed V. Balzani (Weinheim: Wiley-VCH Verlag GmbHGmbH), 927–975. doi: 10.1002/9783527618248.ch31

George, R. C., Egharevba, G. O., and Nyokong, T. (2010). Spectroscopic studies of nanostructures of negatively charged free base porphyrin and positively charged tin porphyrins. *Polyhedron* 29, 1469–1474. doi: 10.1016/j.poly.2010.01.028

Golubchikov, O. A., and Berezin, B. D. (1986). Applied aspects of the chemistry of porphyrins. *Uspehi Chimii* 8, 1361–1389. doi: 10.1070/RC1986v055n08ABEH003221

Guldi, D. M., and Imahori, H. (2004). Supramolecular assemblies for electron transfer. *J. Porphyrins Phthalocyanines* 8, 976–983. doi: 10.1142/S1088424604000337

Guo, P., Zhao, G., Chen, P., Lei, B., Jiang, L., Zhang, H., et al. (2014). Porphyrin nanoassemblies via surfactant-assisted assembly and single nanofiber nanoelectronic sensors for high-performance H_2O_2 vapor sensing. *ACS Nano* 8, 3402–3411. doi: 10.1021/nn406071f

Hoffman, B. M., and Ibers, J. A. (1983). Porphyrinic molecular metals. *Acc. Chem. Res.* 16, 15–21. doi: 10.1021/ar00085a003

Jahan, M., Bao, Q., and Loh, K. P. (2012). Electrocatalytically active graphene–porphyrin MOF composite for oxygen reduction reaction. *J. Am. Chem. Soc.* 134, 6707–6713. doi: 10.1021/ja211433h

Jana, A., Ishida, M., Park, J. S., Bähring, S., Jeppesen, J. O., and Sessler, J. L. (2017). Tetrathiafulvalene- (TTF-) derived oligopyrrolic macrocycles. *Chem. Rev.* 117, 2641–2710. doi: 10.1021/acs.chemrev.6b00375

Jiang, B., Yang, S.-W., and Jones, W. E. (1997). Conjugated porphyrin cpolymers: control of chromophore separation by oligophenylenevinylene bridges. *Chem. Mat.* 9, 2031–2034. doi: 10.1021/cm970225h

Jones, R., Tredgold, R. H., and Hodge, P. (1983). Langmuir-Blodgett films of simple esterified porphyrins. *Thin Solid Films* 99, 25–32. doi: 10.1016/0040-6090(83)90355-3

Kadish, K. M., and Van Caemelbecke, E. (2003). Electrochemistry of porphyrins and related macrocycles. *J. Solid State Electrochem.* 7, 254–258. doi: 10.1007/s10008-002-0306-3

Katz, J. J. (1979). "Charge separation in synthetic photoreaction centers," in *Light-Induced Charge Separation in Biology and Chemistry*, eds H. Gerischer and J. J. Katz (Weinheim: Chemie), 331–359.

Knoester, J., and Agranovich, V. M. (2003). "Frenkel and charge-transfer excitons in organic solids," in *Electronic Excitations in Organic Based Nanostructures,* eds V. M. Agranovich and G. F. Bassani (Oxford, UK: Elsevier Academic Press), 508. doi: 10.1016/S1079-4050(03)31001-4

Kobayashi, N., Andrew Nevin, W., Mizunuma, S., Awaji, H., and Yamaguchi, M. (1993). Ring-expanded porphyrins as an approach towards highly conductive molecular semiconductors. *Chem. Phys. Lett.* 205, 51–54. doi: 10.1016/0009-2614(93)85165-K

Kocherzhenko, A. A., Patwardhan, S., Grozema, F. C., Anderson, H. L., and Siebbeles, L. D. A. (2009). Mechanism of charge transport along zinc porphyrin-based molecular wires. *J. Am. Chem. Soc.* 131, 5522–5529. doi: 10.1021/ja809174y

Koposova, E., Liu, X., Pendin, A., Thiele, B., Shumilova, G., Ermolenko, Y., et al. (2016a). Influence of meso-substitution of the porphyrin ring on enhanced hydrogen evolution in a photochemical system. *J. Phys. Chem. C* 120, 13873–13890. doi: 10.1021/acs.jpcc.6b01467

Koposova, E. A., Ermolenko, Y. E., Offenhäusser, A., and Mourzina, Y. G. (2018). Self-assembly and photoconductivity of binary porphyrin nanostructures of meso-tetrakis(4-sulfonatophenyl)porphine and Co(III) meso-tetra(4-pyridyl)porphine chloride. *Colloid Surf. A Physicochem. Eng. Asp.* 548, 172–178. doi: 10.1016/j.colsurfa.2018.03.053

Koposova, E. A., Pendin, A. A., Ermolenko, Y. E., Shumilova, G. I., Starikova, A. A., and Mourzina, Y. G. (2016b). Morphological properties and photoconductivity of self-assembled Sn/Co porphyrin nnostructures. *Rev. Adv. Mater. Sci.* 45, 15–19. Available online at: http://www.ipme.ru/e-journals/RAMS/no_14516/03_14516_koposova.pdf

Li, G., Wang, T., Schulz, A., Bhosale, S., Lauer, M., Espindola, P., et al. (2004). Porphyrin-acetylene-thiophene polymer wires. *Chem. Commun.* 2004, 552–553. doi: 10.1039/B313415F

Mairanovsky, V. G. (1987). "Electrochemistry of porphyrins," in *Porphyrins: Spectroscopy, Electrochemistry, Application*, ed N. Enikolopyan (Moscow: Nauka), 127–181.

Maiti, N. C., Ravikanth, M., Mazumdar, S., and Periasamy, N. (1995). Fluorescence dynamics of non-covalently linked porphyrin dimers and aggregates. *J. Phys. Chem.* 99, 17192–17197. doi: 10.1021/j100047a024

Malinski, T. (2000). "Porphyrin-based electrochemical sensors," in *The Porphyrin Handbook*, eds K. M. Kadish, K. M. Smith, and R. Guilard (San Diego, CA: Academic Press), 232–256.

Martin, K. E., Tian, Y., Busani, T., Medforth, C. J., Franco, R., Van Swol, F., et al. (2013). Charge effects on the structure and composition of porphyrin binary ionic solids: ZnTPPS/SnTMePyP nanomaterials. *Chem. Mat.* 25, 441–447. doi: 10.1021/cm303595s

Martin, K. E., Wang, Z., Busani, T., Garcia, R. M., Chen, Z., Jiang, Y., et al. (2010). Donor–acceptor biomorphs from the ionic self-assembly of porphyrins. *J. Am. Chem. Soc.* 132, 8194–8201. doi: 10.1021/ja102194x

Mchale, J. L. (2012). "Hierarchal structure of light-harvesting porphyrin aggregates," in *J-Aggregates,* ed T. Kobayashi (Singapore: World Scientific), 77–118. doi: 10.1142/9789814365796_0003

Medforth, C. J., Wang, Z., Martin, K. E., Song, Y., Jacobsen, J. L., and Shelnutt, J. A. (2009). Self-assembled porphyrin nanostructures. *Chem. Commun.* 2009, 7261–7277. doi: 10.1039/b914432c

Mirkovic, T., Ostroumov, E. E., Anna, J. M., Van Grondelle, R., Govindjee, and Scholes, G. D. (2017). Light absorption and energy transfer in the antenna complexes of photosynthetic organisms. *Chem. Rev.* 117, 249–293. doi: 10.1021/acs.chemrev.6b00002

Muratova, I. S., Mikhelson, K. N., Ermolenko, Y. E., Offenhäusser, A., and Mourzina, Y. (2016). Chemiresistors based on ultrathin gold nanowires for sensing halides, pyridine and dopamine. *Sens. Actuator B Chem.* 232, 420–427. doi: 10.1016/j.snb.2016.03.151

Naarman, H. (2012). "Polymers, electrically conducting," in *Ullmann's Encyclopedia of Industrial Chemistry*, ed B. Elvers (Weinheim: Wiley-VCH Verlag GmbH), 295–314.

Natali, M., and Scandola, F. (2016). Photoinduced charge separation in porphyrin ion pairs. *J. Phys. Chem. A* 120, 1588–1600. doi: 10.1021/acs.jpca.6b00960

Ohno, O., Kaizu, Y., and Kobayashi, H. (1993). J-aggregate formation of a water-soluble porphyrin in acidic aqueous media. *J. Chem. Phys.* 99, 4128–4139. doi: 10.1063/1.466109

Ou, X., Chen, P., Jiang, L., Shen, Y., Hu, W., and Liu, M. (2014). π-Conjugated molecules crosslinked graphene-based ultrathin films and their tunable performances in organic nanoelectronics. *Adv. Funct. Mater.* 24, 543–554. doi: 10.1002/adfm.201302153

Paolesse, R., Nardis, S., Monti, D., Stefanelli, M., and Di Natale, C. (2017). Porphyrinoids for chemical sensor applications. *Chem. Rev.* 117, 2517–2583. doi: 10.1021/acs.chemrev.6b00361

Pasternack, R. F., Huber, P. R., Boyd, P., Engasser, G., Francesconi, L., Gibbs, E., et al. (1972). Aggregation of meso-substituted water-soluble porphyrins. *J. Am. Chem. Soc.* 94, 4511–4517. doi: 10.1021/ja00768a016

Rieger, P. H. (1994). *Electrochemistry*. New York, NY: Chapman & Hall Inc. doi: 10.1007/978-94-011-0691-7

Riley, C. K., Muller, E. A., Feldman, B. E., Cross, C. M., Aken, K. L. V., Johnston, D. E., et al. (2010). Effects of O_2, Xe, and gating on the photoconductivity and persistent photoconductivity of porphyrin nanorods. *J. Phys. Chem. C* 114, 19227–19233. doi: 10.1021/jp1068494

Rosaria, L., D'urso, A., Mammana, A., and Purrello, R. (2008). Chiral memory: induction, amplification, and switching in porphyrin assemblies. *Chirality* 20, 411–419. doi: 10.1002/chir.20464

Savenije, T. J., and Goossens, A. (2001). Hole transport in porphyrin thin films. *Phys. Rev. B* 64:115323. doi: 10.1103/PhysRevB.64.115323

Schall, A. P., Iavicoli, P., Qi, Z. J., Menko, J., Lu, Y., Linares, M., et al. (2015). Photoconductivity of nanofilaments that are self-assembled from a porphyrin with long alkyl-chain substituents. *J. Phys. Chem. C* 119, 26154–26163. doi: 10.1021/acs.jpcc.5b07902

Scholes, G. D., and Rumbles, G. (2006). Excitons in nanoscale systems. *Nat. Mater.* 5, 683–697. doi: 10.1038/nmat1710

Schramm, C. J., Scaringe, R. P., Stojakovic, D. R., Hoffman, B. M., Ibers, J. A., and Marks, T. J. (1980). Chemical, spectral, structural, and charge transport properties of the "molecular metals" produced by iodination of nickel phthalocyanine. *J. Am. Chem. Soc.* 102, 6702–6713. doi: 10.1021/ja00542a008

Schwab, A. D., Smith, D. E., Bond-Watts, B., Johnston, D. E., Hone, J., Johnson, A. T., et al. (2004). Photoconductivity of self-assembled porphyrin nanorods. *Nano Lett.* 4, 1261–1265. doi: 10.1021/nl049421v

Segawa, H., Nakayama, N., and Shimidzu, T. (1992a). Electrochemical synthesis of one-dimensional donor–acceptor polymers containing oligothiophenes and phosphorus porphyrins. *J. Chem. Soc. Chem. Commun.* 1992, 784–786. doi: 10.1039/C39920000784

Segawa, H., Nishino, H., Kamikawa, T., Honda, K., and Shimidzu, T. (1989). Hetero-aggregation between gold porphyrins and zinc porphyrins

through charge transfer interaction. *Chem. Lett.* 18, 1917–1920. doi: 10.1246/cl.1989.1917

Segawa, H., Takehara, C., Honda, K., Shimidzu, T., Asahi, T., and Mataga, N. (1992b). Photoinduced electron-transfer reactions of porphyrin heteroaggregates: energy gap dependence of an intradimer charge recombination process. *J. Phys. Chem.* 96, 503–506. doi: 10.1021/j100181a001

Skripnikova, T. A., Starikova, A. A., Shumilova, G. I., Ermolenko, Y. E., Pendin, A. A., and Mourzina, Y. G. (2017). Towards stabilization of the potential response of Mn(III) tetraphenylporphyrin-based solid-state electrodes with selectivity for salicylate ions. *J. Solid State Electrochem.* 21, 2269–2279. doi: 10.1007/s10008-017-3575-6

Torres, T., and Bottari, G. (2013). *Organic Nanomaterials: Synthesis, Characterization, and Device Applications.* Hoboken, NJ: John Wiley & Sons Inc. doi: 10.1002/9781118354377

Wang, Z., Medforth, C. J., and Shelnutt, J. A. (2004). Porphyrin nanotubes by ionic self-assembly. *J. Am. Chem. Soc.* 126, 15954–15955. doi: 10.1021/ja045068j

Weigl, J. W. (1957). Spectroscopic properties of organic photoconductors. Part IV. TetraphenyIporphine. *J. Mol. Spectrosc.* 1, 216–222. doi: 10.1016/0022-2852(57)90024-3

Würthner, F., Kaiser, T. E., and Saha-Möller, C. R. (2011). J-Aggregates: from serendipitous discovery to supramolecular engineering of functional dye materials. *Angew. Chem. Int. Edit.* 50, 3376–3410. doi: 10.1002/anie.201002307

Yamashita, K., and Maenobe, K. (1980). Extrinsic photoconduction in metalloporphyrin films. *Chem. Lett.* 1980, 307–310. doi: 10.1246/cl.1980.307

Yeats, A. L., Schwab, A. D., Massare, B., Johnston, D. E., Johnson, A. T., De Paula, J. C., et al. (2008). Photoconductivity of self-assembled nanotapes made from meso-Tri(4-sulfonatophenyl)monophenylporphine. *J. Phys. Chem. C* 112, 2170–2176. doi: 10.1021/jp0765695

Zhang, X., Wang, Y., Chen, P., Guo, P., and Liu, M. (2015). A general protocol for π-conjugated molecule-based micro/nanospheres: artificial supramolecular antenna in terms of heterogeneous photocatalysis. *RSC Adv.* 5, 78427–78435. doi: 10.1039/C5RA13283E

Zhang, X. Q., Wu, H. M., Wu, X. J., Cheng, Z. P., and Wei, Y. (1995). Synthesis, orientation and conductivity investigation of a new porphyrin Langmuir-Blodgett film. *J. Mater. Chem.* 5, 401–404. doi: 10.1039/jm9950500401

Zhu, X. Y., Yang, Q., and Muntwiler, M. (2009). Charge-transfer excitons at organic semiconductor surfaces and interfaces. *Acc. Chem. Res.* 42, 1779–1787. doi: 10.1021/ar800269u

Conflict of Interest Statement: The authors declare that the research was conducted in the absence of any commercial or financial relationships that could be construed as a potential conflict of interest.

frontiers in Chemistry

ORIGINAL RESEARCH
published: 21 May 2019
doi: 10.3389/fchem.2019.00359

Aza-Based Donor-Acceptor Conjugated Polymer Nanoparticles for Near-Infrared Modulated Photothermal Conversion

Guobing Zhang[1,2], Suxiang Ma[1], Weiwei Wang[1], Yao Zhao[1], Jiufu Ruan[1], Longxiang Tang[2], Hongbo Lu[1,2], Longzhen Qiu[1,2]* and Yunsheng Ding[2]*

[1] National Engineering Laboratory of Special Display Technology, State Key Laboratory of Advanced Display Technology, Academy of Photoelectronic Technology, Hefei University of Technology, Hefei, China, [2] Key Laboratory of Advanced Functional Materials and Devices of Anhui Province (HFUT), Department of Polymer Science and Engineering, School of Chemistry and Chemical Engineering, Hefei University of Technology, Hefei, China

It is highly desired that synthesis of photothermal agents with near-infrared (NIR) absorption, excellent photostability, and high photothermal conversion efficiency are essential for potential applications. In this work, three (D-A) conjugated polymers (**PBABDF-BDTT, PBABDF-BT,** and **PBABDF-TVT**) based on aza-heterocycle, bis(2-oxo-7-azaindolin-3-ylidene)benzodifurandione (BABDF) as the strong acceptor, and benzodithiophene-thiophene (BDTT), bithiophene (BT), and thiophene-vinylene-thiophene (TVT) as the donors, were designed and synthesized. The conjugated polymers showed significant absorption in the NIR region and a maximum absorption peak at 808 nm by adjusting the donor and acceptor units. Their photothermal properties were also investigated by using poly(ethylene glycol)-block-poly(hexyl ethylene phosphate) (mPEG-b-PHEP) to stabilize the conjugated polymers. Photoexcited conjugated polymer (**PBABDF-TVT**) nanoparticles underwent non-radiative decay when subjected to single-wavelength NIR light irradiation, leading to an excellent photothermal conversion efficiency of 40.7%. This work indicated the aza-heterocycle BABDF can be a useful building block for constructing D-A conjugated polymer with high conversion efficiency.

Keywords: conjugated polymer, aza-heterocycle acceptor, near-infrared absorption, nanoparticles, photothermal conversion

OPEN ACCESS

Edited by:
Bin Wu,
Institute of Chemistry (CAS), China

Reviewed by:
Amparo Ruiz Carretero,
Centre National de la Recherche Scientifique (CNRS), France
Masashi Mamada,
Kyushu University, Japan

****Correspondence:***
Guobing Zhang
gbzhang@hfut.edu.cn
Longzhen Qiu
lzhqiu@hfut.edu.cn

Specialty section:
This article was submitted to Supramolecular Chemistry, a section of the journal Frontiers in Chemistry

Received: *14 February 2019*
Accepted: *30 April 2019*
Published: *21 May 2019*

Citation:
Zhang G, Ma S, Wang W, Zhao Y, Ruan J, Tang L, Lu H, Qiu L and Ding Y (2019) Aza-Based Donor-Acceptor Conjugated Polymer Nanoparticles for Near-Infrared Modulated Photothermal Conversion. Front. Chem. 7:359. doi: 10.3389/fchem.2019.00359

INTRODUCTION

Near-infrared (NIR) light has been widely used in sensing, imaging, and biotherapy fields (Qian et al., 2013; Yang et al., 2013; He et al., 2015; Antaris et al., 2016; Song et al., 2016; Zhang et al., 2016), owing to its superior advantages in remote sensing operations, microinvasion, and biological window. Photothermal conversion is the result of the non-radiative transition of excited electrons back to the ground state. (Huschka et al., 2011; Geng et al., 2015). Therefore, photothermal agents with NIR absorption are very important as they can convert NIR light into thermal energy. To date, various photothermal conversion reagents with various NIR absorbance have been explored. Among them, precious metals (such as Au, Ag, and Pt) (Shi et al., 2014; Kim et al., 2015; Marta et al., 2015; Luo et al., 2016), carbon nanomaterials (Yang et al., 2010; Guo et al., 2015),

inorganic compounds (Tian et al., 2013), and other materials have shown excellent photothermal properties. However, these materials are not biodegradable and may cause potential long-term toxicity in biological applications (Li et al., 2016a; Zhou et al., 2016). Compared with inorganic materials, organic NIR dyes have attracted considerable attention because of their good biocompatibility and biodegradability (Chen et al., 2013; Zheng et al., 2013). However, severe photobleaching and low photothermal conversion efficiency has hindered their further application. Therefore, organic photothermal agents with a high photothermal conversion efficiency and excellent photostability should be developed. The conjugated polymers showed a sharp and broad absorption peak in the NIR region by adjusting the donor and acceptor units and they have been widely used in organic photovoltaics and field-effect transistors (Günes et al., 2007; Liang and Yu, 2010). As reported, the conjugated polymers displayed excellent photostability, high photothermal conversion efficiency, and good biocompatibility (Pu et al., 2014; Lyu et al., 2017). They also exhibited strong donor–acceptor (D-A) interaction between the nearest neighbor intermolecular overlapping regions and ordered close packing of polymer chains. The D-A structure facilitated strong intramolecular charge transfer (ICT), resulting in efficient fluorescence quenching and high photothermal performance (Guo et al., 2017). Therefore, conjugated polymers are a promising photothermal agent which can effectively utilize the NIR light for photothermal application. For example, Lee and co-workers used the D-A strategy to synthesize a semiconductor nanoparticle with a low bandgap to harvest infrared light. Furthermore, they introduced a porphyrin as a light-harvesting side chain into the backbone, resulting in a record-high photothermal conversion efficiency of 62.3% (Zhang et al., 2017b). Huang and co-workers achieved good planar backbone structure through turning the acceptor unit; it exhibited higher photothermal conversion efficiency of 74% and this is the highest one so far for conjugated polymers (Dong et al., 2018). Within the building block library for conjugated polymer, isoindigo (IIG) is one of the most popular acceptors to construct high-performance semiconductors (Mei et al., 2013; Holliday et al., 2014; Chang et al., 2018). The advantages of IIG as an acceptor unit for D-A conjugated polymers arise from low energy levels, large local dipole, and excellent solubility after N-alkylation (Deng and Zhang, 2014). However, IIG-based conjugated polymers exhibited relatively narrow absorption, the edges of the film absorption bands only extend to about 800 nm. Consequently, the maximum absorption of IID-based polymer showed bad overlap with the NIR window, which has an irradiation at about 808nm. Thus, the exploration of IIG-based conjugated polymers with maximum absorption located in the NIR region is highly desired.

In our previous work, an IIG derivative unit and its D-A conjugated polymer were designed by incorporating benzodifurandione into the π-conjugated backbone. The introduction of an electron-deficient moiety not only results in strongly electron-deficient characteristics but also extends the conjugation and enhances the intramolecular and intermolecular interactions of the polymers. Therefore, the D-A conjugated polymer (PBIBDF-BT) had the absorption extend to the NIR region and exhibited excellent photothermal conversion efficiency (34.7%) (Yang et al., 2017). Herein, we currently introduce another isoindigo derivative (BABDF) by replacing the outer benzene rings of BIBDF with aza rings (**Figure 1**), an obvious next step, synthesize three BABDF-based conjugated polymers (PBABDF-BDTT, PBABDF-BT, and PBABDF-TVT) and study their photothermal properties. On the one hand, the introduction of electronegative N atom could further enhance the electron-withdrawing power of acceptor which result in strong push-pull interaction and significant red-shifts of absorption (Zhang et al., 2017a). On the other hand, the N-substitution on backbone can produce non-covalent interaction (S…N and CH....N) and endows the polymer with improved planar structure, which can also lead the redshift of absorption (Jackson et al., 2013; Zhang et al., 2019). Because of the hydrophobic conjugated polymers, it is difficult to further apply to living organisms, conjugated polymer-based NPs were prepared by using amphiphilic diblock copolymer poly(ethylene glycol)-block-poly(hexyl ethylene phosphate) (mPEG-b-PHEP) as the stabilizer using the single emulsion method. As a result, the polymer based on TVT as donor and BABDF as acceptor exhibited an excellent extinction coefficient of 55 $cm^{-1}{\cdot}mg^{-1}{\cdot}mL$ and a high photothermal conversion efficiency of 40.7%. These demonstrate that the aza-heterocyclic BABDF unit may be promising in development of D-A conjugated polymer with high photothermal conversion efficiency.

EXPERIMENTAL SECTION

Materials

Three conjugated polymers were synthesized. And a diblock copolymer mPEG-b-PHEP reported previously (Sun et al., 2014). bis(6-bromo-1-(4-decyltetradecyl)-2-oxo-7-azaindolin-3-ylidene)benzo[1,2-b:4,5-b′]-difuran-2,6(3H,7H)-dione (2Br-BABDF), (3,3′-didodecyl-[2,2′-bithiophene]-5,5′-diyl)bis(trimethylstannane) (2tin-BT), ((4,8-bis(5-(2-ethylhexyl)thiophen-2-yl)-6-(trimethylstannyl)benzo[1,2-b:4,5-b']dithiophen-2-yl)dimethylstannyl)methylium (2tin-BDTT), and (E)-1,2-bis(3-dodecyl-5-(trimethylstannyl)thiophen-2-yl)ethene (2tin-TVT) were synthesized according to the methods that reported in documents (Li et al., 2016b; Zhang et al., 2017a). Tris(dibenzylideneacetone)dipalladium ($Pd_2(dba)_3$), tri(o-tolyl)phosphine ($P(o\text{-}tol)_3$), and other chemicals were purchased from Sigma-Aldrich Chemical Company, Alfa Aeasar Chemical Company, and Sinopharm Chemical Reagent Co. Ltd., China. Chemical regents were purchased and used as received. 3-(4,5-Dimethylthiazol-2-yl)-2,5-diphenyl tetrazolium bromide (MTT) was purchased from Sigma-Aldrich (St. Louis, MO, United States).

Synthesis of the Polymer PBABDF-BDTT

Tris(dibenzylideneacetone)dipalladium ($Pd_2(dba)_3$, 0.004 g, 0.0044 mmol) and tri(o-tolyl)phosphine ($P(o\text{-}tol)_3$, 0.0055 g, 0.018 mmol) were added to a solution of 2Br-BABDF (0.15 g, 0.11 mmol) and 2tin-BDTT (0.10 g, 0.11 mmol) in toluene (15 mL) under nitrogen. The solution was subjected to three cycles of evacuation and nitrogen filling. The mixture was then

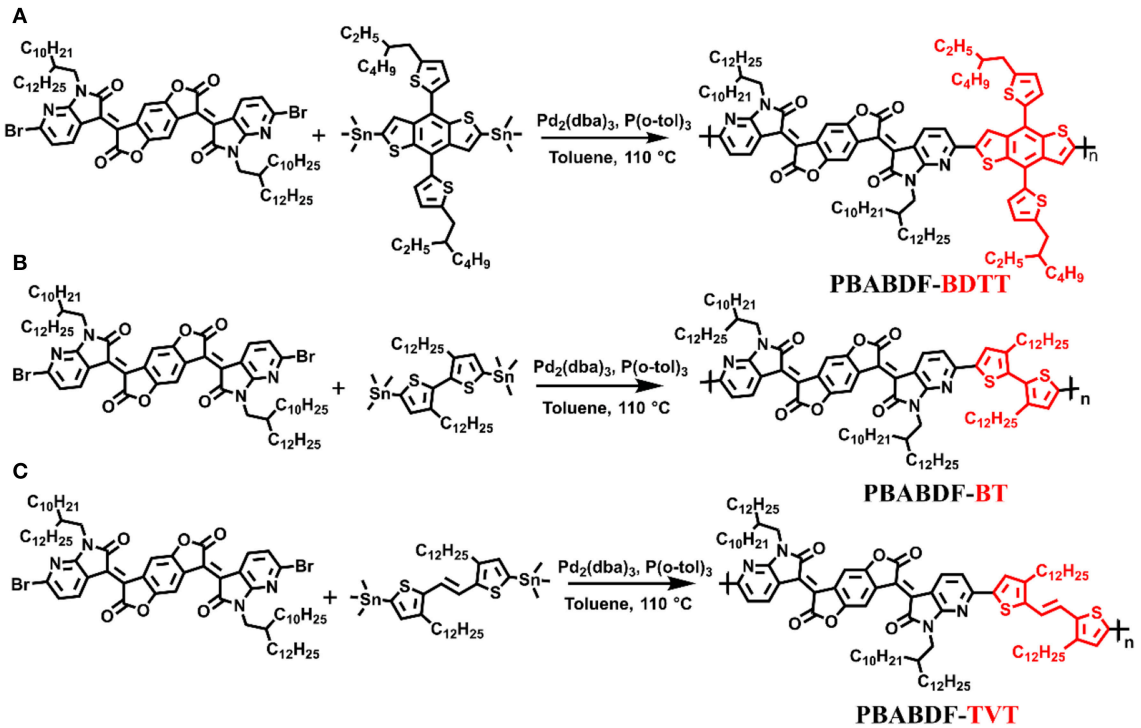

FIGURE 1 | Synthesis pathways for the CPs: PBABDF-BDTT **(A)**, PBABDF-BT **(B)**, and PBABDF-TVT **(C)**.

heated to 110°C for 48 h. After cooling to room temperature, the mixture was poured into methanol and stirred for 12 h. A black precipitate was collected by filtration. The product was purified by Soxhlet extractor using methanol and dichloromethane. The residue was extracted with hot chloroform in an extractor for 24 h. After removing the solvent, a black solid was collected (0.14 g, 70.5%). GPC: Mn = 42.5 *kDa*, *PDI* = 2.47. Elemental analysis: calcd for $C_{104}H_{144}N_4O_6S_4$ (%): C, 74.60, H, 8.67, N, 3.35, S, 7.66. Found (%): C, 74.75, H, 8.73, N, 3.30, S, 7.58.

Synthesis of the Polymer PBABDF-BT

The same procedure was used as PBABDF-BDTT. The compounds used were $Pd_2(dba)_3$, (0.004 g, 0.0044 mmol), P(o-tol)$_3$ (0.055 g, 0.018 mmol), 2Br-BABDF (0.15 g, 0.11 mmol) and 2tin-BT (0.09 g, 0.11 mmol). After the workup, a black solid was collected (0.14 g, 72.0%). GPC: Mn = 40.6 *kDa*, *PDI* = 2.30. Elemental analysis: calcd for $C_{104}H_{156}N_4O_6S_2$ (%): C, 76.99, H, 9.69, N, 3.45, S, 3.95. Found (%): C, 77.02, H, 9.87, N, 3.22, S, 3.90.

Synthesis of the Polymer PBABDF-TVT

The same procedure was used as PBABDF-TVT. The compounds used were $Pd_2(dba)_3$, (0.004 g, 0.0044 mmol), P(o-tol)$_3$ (0.055 g, 0.018 mmol), 2Br-BABDF (0.15 g, 0.11 mmol) and 2tin-TVT (0.094 g, 0.11 mmol). After the workup, a black solid was collected (0.14 g, 73.1%). GPC: Mn = 44.2 *kDa*, *PDI* = 2.12. Elemental analysis: calcd for $C_{106}H_{158}N_4O_6S_2$ (%): C, 77.23, H, 9.66, N, 3.40, S, 3.89. Found (%): C, 77.70, H, 9.57, N, 3.23, S, 3.72.

Fabrication and Characterization of Nanoparticles

A $CHCl_3$ solution (200 μL) containing mPEG-b-PHEP (10.0 mg), PBABDF-BT (1.0 mg), and ultrapurified water (1.0 mL) was emulsified by ultrasound for 2 min (work 5 s and rest 2 s) at a 325 W output using a microtip probe sonicator (JY92-IIN, Scientz Biotechnology, Ningbo, China). The solution was vortexed for 30 min to remove the organic solvent and centrifuged at a speed of 3,500 for 5 min. No precipitation occurred in this way. It was then further purified by being passed through a 0.45 μm filter (Millipore). Also, the above steps were repeated s to obtain the NP_{TVT} and NP_{BDTT}. The size distribution of conjugated polymer nanoparticles in aqueous solution was measured by dynamic light scattering (DLS) that conducted with a NanoBrook-90 Plus instrument (Brookhaven Instrument Corporation, Holtsville, NY, United States). The transmission electron microscope (TEM, JEOL-2010, Japan) measurements were implemented with an acceleration voltage of 200 kV.

Measurement of Photothermal Conversion Efficiency

In order to evaluate the photothermal ability, the aqueous solution of these conjugated polymer nanoparticles (40.0 μg/mL) was placed in centrifuge tube and then illuminated with 808 nm irradiation at 2.0 W/cm^2 (New Industries Optoelectronics, Changchun, China) for 15 min. In this process, the temperature of the solution and the infrared thermal images was recorded

using an infrared camera (ICI7320, Infrared Camera Inc., Beaumont, TX, United States).

According to the reported method by Roper et al. the total energy balance for the system can be indicated by Equation 1:

$$\eta = \frac{hS\,(T_{Max} - T_{Surr}) - Q_{Dis}}{I(1 - 10^{-A_{808}})} \quad (1)$$

In which, h is heat transfer coefficient, S is the surface area of the container, T_{Max} (unit: °C) and T_{Surr} (unit: °C) are the balance temperature and ambient temperature of the surroundings, respectively, Q_{Dis} is the heat induced by the light absorbance of water solvent without nanoparticle, and I (unit: mW) is the incident laser power. A_{808} is the absorbance of nanoparticle solution at 808 nm.

Photostability

The NPs (40.0 μg/mL) were irradiated by 808 nm NIR laser (2.0 W/cm^2, 15 min, laser on). Subsequently, the NIR laser was closed for 15 min, and then the solution was naturally cooled to room temperature. The laser on and laser off cycles were repeated three times to monitor temperature changes as described above.

In vitro Cytotoxicity of NP_{TVT}

Breast cancer MDA-MB-231 cells (American Type Culture Collection, Rockefeller, Maryland, United States), were seeded in a 96-well plate (1×10^4 cells per well) at 37°C with 5% CO_2 overnight. The medium was substituted by fresh medium containing NP_{TVT} at different concentrations. After incubation for 4 h, and then the cell viability was analyzed by MTT assay.

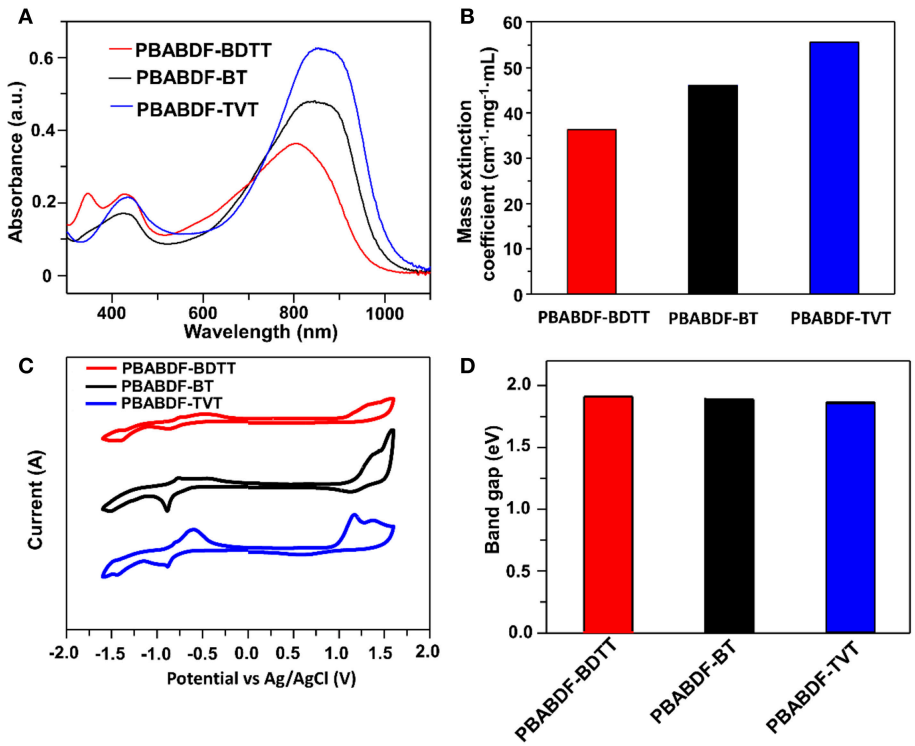

FIGURE 2 | (A) Absorption spectra of these conjugated polymers with different D units (10.0 μg/mL). **(B)** Mass extinction coefficients at 808 nm. **(C)** Cyclic voltammetry. **(D)** The band gaps of these conjugated polymers.

TABLE 1 | Molecular Weight, optical and electrochemical properties of polymers.

Polymer	(λ_{max}^{abs}) nm solution	M_n	PDI(kDa)	λ_{onset}(nm)	E_g^{opt} [a](eV)	HOMO[b] (eV)	LOMO[c] (eV)	E_g^{ec} [d] (eV)
PBABDF-BDTT	804	42.5	2.47	969	1.28	−5.80	−4.08	1.72
PBABDF-BT	846	40.6	2.30	998	1.24	−5.81	−4.11	1.70
PBABDF-TVT	853	44.2	2.12	1019	1.22	−5.70	−4.02	1.68

[a] $E_g^{opt} = 1240/\lambda_{onset}$.
[b] $HOMO = -(4.75 + E_{onset}^{ox})$.
[c] $LUMO = -(4.75 + E_{onset}^{red})$.
[d] $E_g^{ec} = -(HOMO - LUMO)$.

Measurements and Characterization

Nuclear magnetic resonance (NMR) spectra were recorded on a Mercury plus 600 MHz machine. Elemental analysis was performed using a Vario EL instrument. Molecular weights were characterized by gel permeation chromatography (GPC) using a Waters Series 1525 binary HPLC pump and 1,2,4-trichlorobenznen as the eluent and polystyrene as the standard. Thermogravimetric analysis (TGA) analyses were conducted with a TA instrument QS000IR at a heating rate of 20°C min^{-1} under nitrogen gas flow. Differential scanning calorimetry (DSC) was performed on a TA instrument Q2000 under nitrogen. The sample was first cooled down to −65°C, then heated up to 250°C and held for 2 min to remove thermal history, followed by cooling at a rate of 10°C min^{-1} to −65°C and then heating at a rate of 10°C min^{-1} to 250°C in all cases. UV-vis-NIR spectra were detected using a UV-3802 (UNICO, Shanghai, China) spectrophotometer. The absorption spectra were recorded on polymer solutions in chloroform and nanoparticle solutions in water. Electrochemical measurements were conducted on a CHI 660D electrochemical analyzer under nitrogen in a deoxygenated anhydrous acetonitrile solution of tetra-n-butylammonium hexafluorophosphate (0.1 M) with a scan rate of 0.1 V/s. A platinum electrode was used as both working and auxiliary electrodes, and an Ag/Ag^{+} electrode was used as a reference electrode.

RESULTS AND DISCUSSION

Synthesis and Characterization

The synthetic route of three polymers (**PBABDF-BDTT, PBABDF-BT,** and **PBABDF-TVT**) are shown in **Figure 1**. The three polymers were synthesized by Stille cross-coupling polymerization in the presence of tris(dibenzylideneacetone)dipalladium ($Pd_2(dba)_3$) as the

TABLE 2 | Optical and fluorescence quantum yield of NPs.

Nanoparticle	λ_{max}^{abs} (nm) Solution	ε^{808} ($cm^{-1}.mg^{-1}.mL$)	Quantum yield, QY(%)
NP_{BDTT}	799	35.1	0.012
NP_{BT}	821	45.2	0.015
NP_{TVT}	819	57.2	0.010

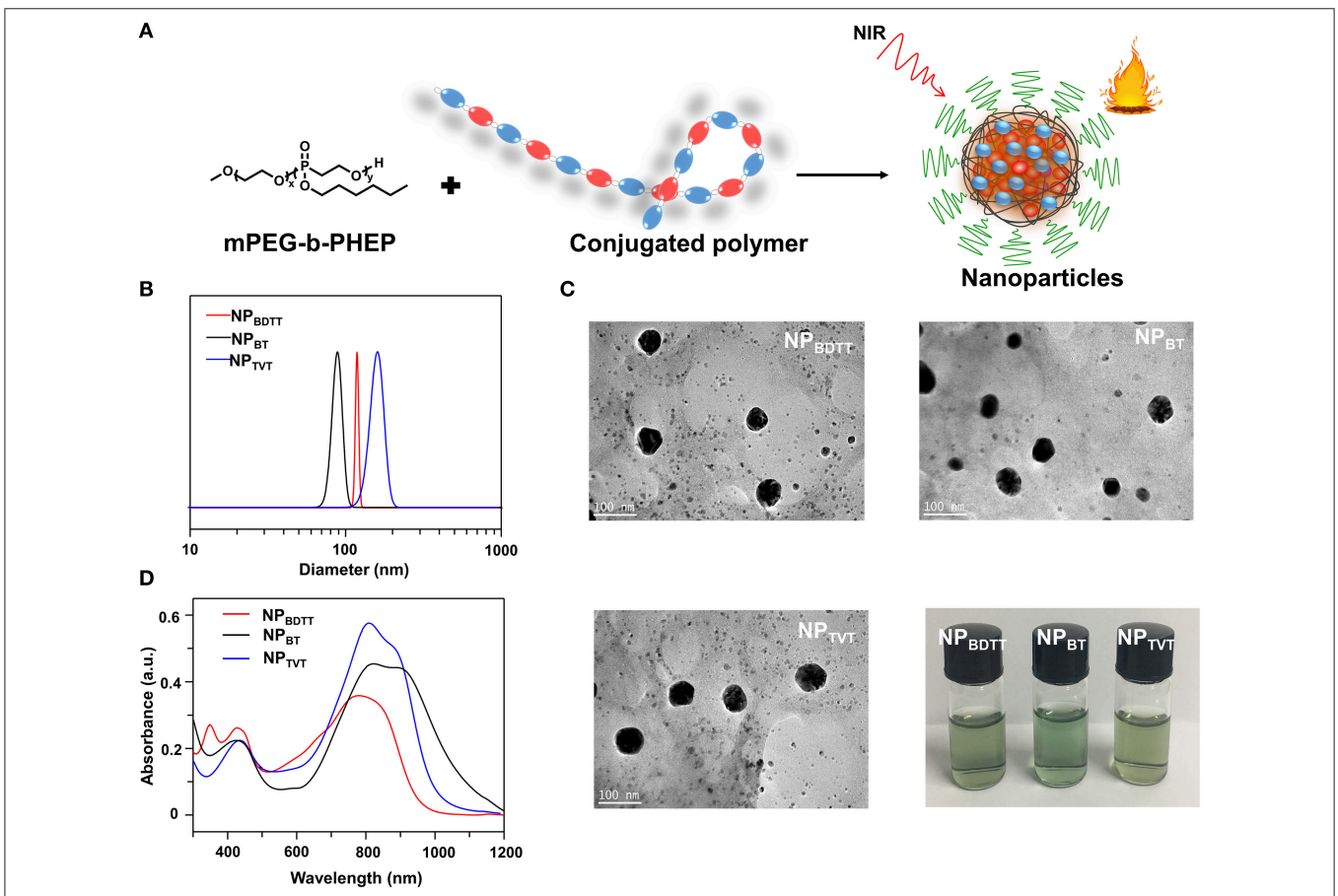

FIGURE 3 | (A) Scheme illustration of the nanoparticles prepared. **(B)** Size distributions. **(C)** TEM images and Photographic images. **(D)** Absorption spectra of NPs (10.0 μg/mL).

catalyst and tri(o-tolyl)phosphine (P(o-tolyl)$_3$) as the ligand. The three polymers were purified by precipitating from methanol and washing with methanol and hexane by Soxhlet extraction for 24 h to eliminate the oligomers. Then, the residue was extracted with chloroform. After concentrating the chloroform solvent under vacuum distillation, the three polymers were obtained by precipitating from methanol. The structures were characterized by nuclear magnetic resonance (NMR) (**Figures S5–S7**). And the molecular weights of three polymers were determined by gel permeation chromatography (GPC), using trichlorobenzene as the eluent. The number average molecular weights (M_n) of **PBABDF-BDTT, PBABDF-BT,** and **PBABDF-TVT** were 42.5, 40.6, and 44.2 kDa, respectively, and the polydispersity indexes (PDI) were 2.47, 2.30, and 2.12, respectively.

As shown in **Figure S1**, the thermal properties of three polymers were evaluated by thermogravimetric analysis (TGA) and differential scanning calorimetry (DSC) under nitrogen atmosphere. The decomposition temperature (Td) at 5% weight loss for polymers was above 350°C, high enough for photothermal study. The DSC results did not provide any information about the glass transition temperature of polymers in the temperature range of our study.

Optical and Electrochemical Properties

The UV-vis-NIR absorption spectra of the polymers characterized in chloroform solution (10 μg/mL with 2 mL) were shown in **Figure 2A**. All the polymers showed typical dual-band absorption in the solution, and the absorption band-edge (λ_{onset}) extend to ∼1000 nm. The maximum absorption peaks were 804, 846, 853 nm for **PBABDF-BDTT, PBABDF-BT, PBABDF-TVT**, respectively. The low-energy band ranged from 600 nm to 1000 nm; this can be attributed to intramolecular charge transfer (ICT) from the donor to the acceptor core. The high-energy band ranged from 310 nm to 500 nm that can be assigned to the π-π* transition of polymer backbone (Pierre et al., 2010; Kim et al., 2014). Moreover, the corresponding mass extinction coefficients at 808 nm (**Figure 2B**) were calculated to be 36.3, 46.1, and 55.7 $cm^{-1}\cdot mg^{-1}\cdot mL$ for **PBABDF-BDTT, PBABDF-BT, PBABDF-TVT**, respectively. The absorption intensity gradually increased with increasing concentrations (**Figures S2A–C**), and all CPs displayed a linear relationship between absorbance and concentration at 808 nm (**Figure S2D**). In addition, the **PBABDF-TVT** showed a slightly red shift and strong NIR absorption compared with the other two materials. This is most probably attributed to the more planar structure of PBABDF-TVT (Lei et al., 2012). The corresponding optical bandgaps of **PBABDF-BDTT**, **PBABDF-BT**, and

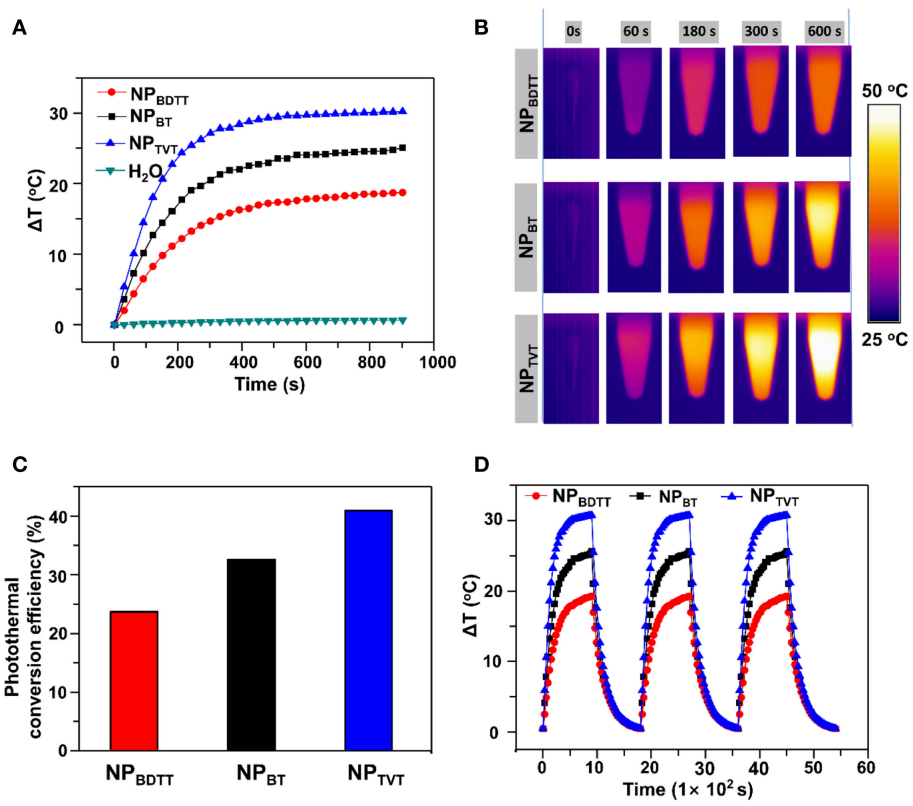

FIGURE 4 | (A) Temperature change curves of the nanoparticles upon exposure to NIR laser (808 nm, 2.0 W/cm^2, 15 min). **(B)** Thermal images of NPs upon exposure to the NIR laser (808 nm, 2.0 W/cm^2). **(C)** Photothermal conversion efficiency. **(D)** Temperature elevation of NPs (40.0 μg/mL) over three laser on/off cycles of NIR irradiation (808 nm, 2.0 W/cm^2, 15 min).

PBABDF-TVT were 1.28, 1.24, and 1.22 eV, respectively. The narrow bandgaps were due to the extended π-conjugation along the polymer backbone and may be beneficial to their photothermal conversion in NIR region (Lei et al., 2012).

The electrochemical properties of three polymers were investigated by cyclic voltammetry (CV) (**Figure 2C**). And the corresponding data was summarized in **Table 1**. Three polymers showed deep lowest unoccupied molecular orbital (LUMO) and highest occupied molecular orbital (HOMO) energy levels due to the presence of strong electron-withdrawing BABDF group. The LUMO/HOMO energy levels were −4.08/−5.80 eV, −4.11/−5.81 eV and −4.02/−5.70 eV for **PBABDF-BDTT**, **PBABDF-BT**, and **PBABDF-TVT**, respectively. As shown in **Figure 2D**, the bandgaps were 1.72 eV, 1.70 eV, and 1.68 eV, respectively, which are 0.4 eV higher than their optical bandgaps calculated from the absorption of their solutions. These differences may be caused by large exciton binding energy (Bredas, 2014, Zhu et al., 2016).

Preparation and Characterization of NPs

To endow these polymers with good stability for subsequent applications, an amphipathic carrier mPEG-b-PHEP was used to package the D-A conjugated polymer through self-assembly and to provide a relatively inert particle surface (**Figure 3A**). This is the hydrophobic conjugated polymer and the hydrophobic part of the amphiphilic block copolymer gradually tangled during the evaporation of organic solvents from oil/water emulsion, which is result of the intermolecular interactions, mainly involving the hydrophilic and hydrophobic interactions. The obtained NPs were denoted as NP_{BDTT}, NP_{BT}, and NP_{TVT}, respectively. The average size of all the obtained NPs determined by dynamic light Scattering (DLS) was about 100 nm (**Figure 3B**). Additionally, the transmission electron microscopy (TEM) images of NPs showed a classic spherical structure (**Figure 3C**). No sediment was observed for the NPs after storage at 4°C for three months (**Figure 3C**). These results indicated that all the NPs have good stability. The UV-vis-NIR absorption spectra of the polymer nanoparticles in water obtained at the same concentration (10 μg/mL with 2 mL) were shown in **Figure 3D**. NP_{BDTT}, NP_{BT}, and NP_{TVT} exhibited absorption peaks at 799 nm, 821 nm and 819 nm, respectively, which are blue-shifted by about 5 nm, 25 nm and 32 nm compared to the absorption peaks from these conjugated polymers. Moreover, the corresponding mass extinction coefficients of NPs at 808 nm were calculated to be 35.1, 45.2, and 57.5 $cm^{-1}{\cdot}mg^{-1}{\cdot}mL$, respectively. The results showed that the extinction coefficient of NPs was similar to those of conjugated polymers. The corresponding data was summarized in **Table 2**.

Photothermal Performance of NPs

To demonstrate the photothermal conversion ability of NPs, the temperature change was monitored under 808-nm irradiation at 2.0 W/cm^2. NPs with a concentration of 40.0 μg/mL were irradiated for 15 min, the infrared thermal images of nanoparticle aqueous solution were recorded. As the irradiation time increased, the temperature of particle solution gradually increased in the following order: NP_{BDTT} < NP_{BT} < NP_{TVT} (**Figure 4A**). After the irradiation for 15 min, the temperature

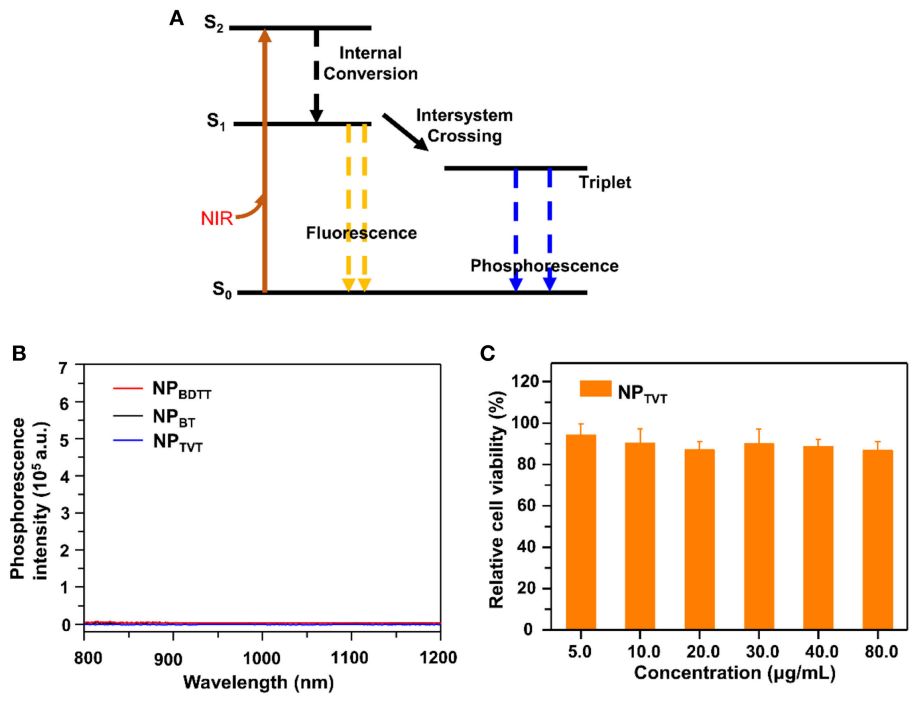

FIGURE 5 | (A) Energy level diagram. **(B)** Phosphorescence spectra of NP_{BDTT}, NP_{BT}, NP_{TVT} upon excitation at 808 nm. **(C)** Cell viability of 231 cells in the presence of NPs treated with different concentrations.

changes of NP_{BDTT}, NP_{BT}, and NP_{TVT} increased by 18.78, 25.16, and 30.27°C, respectively. In addition, the temperature of all the NPs monotonically increased with increasing concentration, and the temperature increased of NPs at each concentration followed this order (**Figure S3**). The infrared imaging color also showed the temperature difference between these NPs. As shown in **Figure 4B**, the color of photothermal images changed from violet (low temperature) to bright yellow (high temperature). According to the method developed by Roper et al. (2007), the photothermal conversion efficiencies (η value) of NPs were calculated (see calculation details in **Supporting Information**). As shown in **Figure 4C** and **Figure S4**, the η values of NP_{BDTT}, NP_{BT}, and NP_{TVT} were calculated to be 23.5, 32.4, and 40.7%, respectively. Further, the photostability of these NPs was studied. Three cycles of laser on/off (time: 15 min) with NIR irradiation (808 nm, 2.0 W/cm^2) were performed. Compared to the temperature change after the first laser irradiation, the temperature showed no significant reduction for all these NPs for another two cycles (**Figure 4D**). Moreover, the NPs were exposed to the 808-nm NIR laser of 2.0 W/cm^2 for 15 min until steady-state temperature was reached. **Figure 4D** showed that all the NPs reached a certain temperature and remained unchanged, indicating that they had excellent NIR photostability. The excellent photostability of NPs can be attributed to the thermal properties of semiconducting polymers. As mentioned before, their decomposition temperatures were above 350°C (**Figure S1**), which was enough for the photothermal effect.

Interpretation of Photothermal Performance

The abovementioned results indicated that the photothermal effect of NPs decreased in the following order: $NP_{TVT} > NP_{BT} > NP_{BDTT}$. When nanoparticle solutions are irradiated by a beam of light, it produces a range of possible physical phenomena, such as scattering (including the result of multiple refractions and reflections), absorption, and luminescence. We set the intensity of the incident light to $I_{incident}$, the intensity of the scattered light to I_{scat}, and the intensity of the absorbed light to I_{abs}, then $I_{incident} = I_{scat} + I_{abs}$, and the absorbance of light can be calculated as: $Q_{abs} = I_{abs}/I_{incident}$. As shown in **Figure 5A**, the absorbed light energy usually undergoes (i) fluorescence emission, (ii) non-radiation (thermal energy loss), and (iii) intersystem conversion to long-lived species (e.g., phosphorescence) (Silvia and George, 1992). If nanoparticle solutions are not chemiluminescent or negligible, then the absorbed light energy could be eventually converted into almost all heat. To prove the photothermal effect of these NPs in such an order, the photothermal conversion efficiency, absorption spectrum, fluorescence quantum yield, phosphorescence, and mass extinction coefficient were tested. All NPs showed almost no fluorescence emission (**Table 2**). And phosphorescence spectra of NPs upon excitation at 808 nm were shown in **Figure 5B**. It can be seen that their absorption was negligible. Therefore, the generation of heat may be the main way to eliminate the absorption of energy after NIR irradiation. The mass extinction coefficient of NPs was calculated from its absorption spectrum, which are 35.1, 45.2, and 57.5 $cm^{-1}\cdot mg^{-1}\cdot mL$, respectively. NP_{TVT} absorbed more light energy at the same concentration compared to NP_{BDTT}. Therefore, the photothermal performance of NP_{TVT} was significantly higher than that of NP_{BDTT}. These results showed that photothermal effect was related to the mass extinction coefficient. The strongest absorbance at 808 nm ensured the highest photothermal effect of NP_{TVT}, followed by NP_{BT} and NP_{BDTT}.

In vitro Cytotoxicity of NP_{TVT}

To achieve the full potential of NP_{TVT} in biomedical fields, 3-(4,5-Dimethylthiazol-2-yl)-2,5-diphenyl tetrazolium bromide (MTT) assay was used to detect the cytotoxicity of NP_{TVT}. MDA-MB-231 cells were selected as cancer cell model. MDA-MB-231 cells were incubated with NP_{TVT} at different PBABDF-TVT concentrations. As shown in **Figure 5C**, with the increase in concentration, no obvious cytotoxicity and proliferation inhibition of 231 cells were observed. Notably, incubation with NP_{TVT} nanoparticles, even at the highest concentration, also did not exhibit obvious toxicity to MDA-MB-231 cells without NIR light illumination. This indicated that the NP_{TVT} nanoparticle is biocompatible, and because of its high photothermal conversion efficiency, it can be further applied to organisms for cancer photothermal therapy.

CONCLUSION

Here, a series of polymers with different chemical structures were synthesized by varying the donor moieties. A systematic study showed that the chemical structure of a strong acceptor and suitable donor unit has a significant effect on the absorption spectrum, extinction coefficient, and photothermal conversion efficiency of polymers. This study demonstrated that high extinction coefficient, excellent photothermal conversion efficiency, good biocompatibility, and high stability of conjugated polymers can be obtained through rational molecular design by introducing a strong electron-withdrawing electron acceptor.

DATA AVAILABILITY

All datasets generated for this study are included in the manuscript and/or the **Supplementary Files**.

AUTHOR CONTRIBUTIONS

GZ, LQ, and YD conceived and designed the experiments. LQ supervised the project. SM performed the experiments. JR, LT, HL, WW, and YZ assisted in the preparation of the manuscript. GZ and SM wrote the paper. All authors analyzed the data.

FUNDING

This work was supported by the National Natural Science Foundation of China (NSFC, Grant Nos. 51573036 and

51703047), the Distinguished Youth Foundation of Anhui Province (No. 1808085J03), the Fundamental Research Funds for the Central Universities (Grant No. JZ2018HGPB0276), the Open Foundation of Key Laboratory of Advanced Functional Materials and Devices of Anhui Province.

SUPPLEMENTARY MATERIAL

The Supplementary Material for this article can be found online at: https://www.frontiersin.org/articles/10.3389/fchem.2019.00359/full#supplementary-material

REFERENCES

Antaris, A. L., Chen, H., Cheng, K., Sun, Y., Hong, G., Qu, C., et al. (2016). A small-molecule dye for NIR-II imaging. *Nat. Mater.* 15, 235–242. doi: 10.1038/NMAT4476

Bredas, J. (2014). Mind the gap! *Mater. Horiz.* 1, 17–19. doi: 10.1039/C3MH00098B

Chang, K., Liu, Y., Hu, D., Qi, Q., Gao, D., Wang, Y., et al. (2018). Highly stable conjugated polymer dots as multifunctional agents for photoacoustic imaging-guided photothermal therapy. *ACS Appl. Mater. Inter.* 10, 7012–7021. doi: 10.1021/acsami.8b00759

Chen, R., Wang, X., Yao, X., Zheng, X., Wang, J., and Jiang, X. (2013). Near-IR-triggered photothermal/photodynamic dual-modality therapy system via chitosan hybrid nanospheres. *Biomaterials* 34, 8314–8322. doi: 10.1016/j.biomaterials.2013.07.034

Deng, P., and Zhang, Q. (2014). Recent developments on isoindigo-based conjugated polymers. *Polym. Chem.* 5, 3298–3305. doi: 10.1039/C3PY01598J

Dong, T., Wen, K., Chen, J., Xie, J., Fan, W., Ma, H., et al. (2018). Signifcant enhancement of photothermal and photoacoustic effciencies for semiconducting polymer nanoparticles through simply molecular engineering. *Adv. Funct. Mater.* 28, 1800135. doi: 10.1002/adfm.201800135

Geng, J., Sun, C., Liu, J., Liao, L. D., Yuan, Y., Thakor, N., et al. (2015). Biocompatible conjugated polymer nanoparticles for efficient photothermal tumor therapy. *Small* 11, 1603–1610. doi: 10.1002/smll.201402092

Günes, S., Neugebauer H., and Sariciftci, N. S. (2007). Conjugated polymer-based organic solar cells. *Chem. Rev.* 107, 1324–1338. doi: 10.1021/cr050149z

Guo, B., Sheng, Z., Hu, D., Li, A., Xu, S., Manghnani, P. N., et al. (2017). Molecular engineering of conjugated polymers for biocompatible organic nanoparticles with highly efficient photoacoustic and photothermal performance in cancer theranostics. *ACS Nano* 11, 10124–10134. doi: 10.1021/acsnano.7b04685

Guo, M., Huang, J., Deng, Y., Shen, H., Ma, Y., Zhang, M., et al. (2015). PH-responsive cyanine-grafted graphene oxide for fluorescence resonance energy tansfer-enhanced photothermal therapy. *Adv. Funct. Mater.* 25, 59–67. doi: 10.1002/adfm.201402762

He, Y., Liao, S., Jia, H., Cao, Y., Wang, Z., and Wang, Y. (2015). A self-healing electronic sensor based on thermal-sensitive fluids. *Adv. Mater.* 27, 4622–4627. doi: 10.1002/adma.201501436

Holliday, S., Donaghey, J., and McCulloch, I. (2014). Advances in charge carrier mobilities of semiconducting polymers used in organic transistors. *Chem. Mater.* 26, 647–663. doi: 10.1021/cm402421p

Huschka, R., Zuloaga, J., Knight, M. W., Brown, L. V., Nordlander, P., and Halas, N. J. (2011). Light-induced release of DNA from gold nanoparticles: nanoshells and nanorods. *J. Am. Chem. Soc.* 133, 12247–12255. doi: 10.1021/ja204578e

Jackson, N. E., Savoie, B. M., Kohlstedt, K. L., Olvera de la Cruz, M., Schatz, G. C., Chen, L. X., et al. (2013). Controlling conformations of conjugated polymers and small molecules: the role of nonbonding interactions. *J. Am. Chem. Soc.* 135, 10475–10483. doi: 10.1021/ja403667s

Kim, J., Han, A. R., Hong, J., Kim, G., Lee, J., Shin, T. J., et al. (2014). Ambipolar semiconducting polymers with π-spacer linked bis-benzothiadiazole blocks as strong accepting units. *Chem. Mater.* 26, 4933–4942. doi: 10.1021/cm500800u

Kim, Y. K., Na, H. K, Kim, S., Jang, H., Chang, S. J., and Min, D. H. (2015). One-pot synthesis of multifunctional Au@Graphene oxide nanocolloid core@shell nanoparticles for raman bioimaging, photothermal, and photodynamic therapy. *Small* 11, 2527–2535. doi: 10.1002/smll.201402269

Lei, T., Dou, J. H., and Pei, J. (2012). Influence of alkyl chain branching positions on the hole mobilities of polymer thin-film transistors. *Adv. Mater.* 24, 6457–6461. doi: 10.1002/adma.201202689

Li, D., Wang, J., Ma, Y., Qian, H., Wang, D., Wang, L., et al. (2016a). A donor-acceptor conjugated polymer with alternating isoindigo derivative and bithiophene units for near-infrared modulated cancer thermo-chemotherapy. *ACS Appl. Mater. Interf.* 8, 19312–19320. doi: 10.1021/acsami.6b05495

Li, S., Ye, L., Zhao, W., Zhang, S., Mukherjee, S., Ade, H., et al. (2016b). Energy-level modulation of small-molecule electron acceptors to achieve over 12% efficiency in polymer solar cells. *Adv. Mater.* 28, 9423–9429. doi: 10.1002/adma.201602776

Liang, Y., and Yu, L. (2010). A new class of semiconducting polymers for bulk heterojunction solar cells with exceptionally high performance. *Accounts Chem. Res.* 43, 1227–1236. doi: 10.1021/ar1000296

Luo, G., Chen, W., Lei, Q., Qiu, W., Liu, Y., Cheng, Y., et al. (2016). A triple-collaborative strategy for high-performance tumor therapy by multifunctional mesoporous silica-coated gold nanorods. *Adv. Funct. Mater.* 26, 4339–4350. doi: 10.1002/adfm.201505175

Lyu, Y., Zhen, X., Miao, Y., and Pu, K. (2017). Reaction-based semiconducting polymer nanoprobes for photoacoustic imaging of protein sulfenic acids. *ACS Nano* 11, 358–367. doi: 10.1021/acsnano.6b05949

Marta, P., Pablo, P., Scott, G. M., Mar,i, M., Grazyna, S., Beatriz, P., et al. (2015). Dissecting the molecular mechanism of apoptosis during photothermal therapy using gold nanoprisms. *ACS Nano* 9, 52–61. doi: 10.1021/nn505468v

Mei, J., Diao, Y., Appleton, A., Fang, L., and Bao, Z. (2013). Integrated materials design of organic semiconductors for field-effect transistors. *J. Am. Chem. Soc.* 135, 6724–6746. doi: 10.1021/ja400881n

Pierre, M., Chad, M., and John, R. (2010). Spectral engineering in π-conjugated polymers with intramolecular donor-acceptor interactions. *Accounts Chem. Res.* 43, 1396–1407. doi: 10.1021/ar100043u

Pu, K., Shuhendler, A. J., Jokerst, J. V., Mei, J., Gambhir, S. S., Bao, Z., et al. (2014). Semiconducting polymer nanoparticles as photoacoustic molecular imaging probes in living mice. *Nat. Nanotechnol* 9, 233–239. doi: 10.1038/NNANO.2013.302

Qian, Q., Huang, X., Zhang, X., Xie, Z., and Wang, Y. (2013). One-step preparation of macroporous polymer particles with multiple interconnected chambers: a candidate for trapping biomacromolecules. *Angew. Chem. Int. Ed.* 52, 10625–10629. doi: 10.1002/ange.201305003

Roper, D. K., Ahn, W., and Hoepfner, M (2007). Microscale heat transfer transduced by surface plasmon resonant gold nanoparticles. *J. Phys. Chem. C.* 111, 3636–3641. doi: 10.1021/jp064341w

Shi, J., Wang, L., Zhang, J., Ma, R., Gao, J., Liu, Y., et al. (2014). A tumor-targeting near-infrared laser-triggered drug delivery system based on GO@Ag nanoparticles for chemo-photothermal therapy and X-ray imaging. *Biomaterials* 35, 5847–5861. doi: 10.1016/j.biomaterials.2014.03.042

Silvia, E., and George, E. (1992). Time-resolved photothermal and photoacoustic methods applied to photoinduced processes in solution. *Chem. Rev.* 92, 1381–1410.

Song, J., Wang, F., Yang, X., Ning, B., Harp, M. G., Culp, S. H., et al. (2016). Gold nanoparticle coated carbon nanotube ring with enhanced raman scattering and photothermal conversion property for theranostic applications. *J. Am. Chem. Soc.* 138, 7005–7015. doi: 10.1021/jacs.5b13475

Sun, C., Ma, Y., Cao, Z., Li, D., Fan, F., Wang, J., et al. (2014). Effect of hydrophobicity of core on the anticancer efficiency of micelles as drug delivery carriers. *ACS Appl. Mater. Inter.* 6, 22709–22718. doi: 10.1021/am5068723

Tian, Q., Hu, J., Zhu, Y., Zou, R., Chen, Z., Yang, S., et al. (2013). Sub-10 nm Fe_3O_4@$Cu_{2-x}S$ core-shell nanoparticles for dual-modal imaging and photothermal therapy. *J. Am. Chem. Soc.* 135, 8571–8577. doi: 10.1021/ja4013497

Yang, J., Shen, D., Zhou, L., Li, W., Li, X., Yao, C., et al. (2013). Spatially confined fabrication of core-shell gold nanocages@mesoporous silica for near-infrared controlled photothermal drug release. *Chem. Mater.* 25, 3030–3037. doi: 10.1021/cm401115b

Yang, K., Zhang, S., Zhang, G., Sun, X., Lee, S. T., and Liu, Z. (2010). Graphene in mice: ultrahigh in vivo tumor uptake and efficient photothermal therapy. *Nano Letters* 10: 3318–3323. doi: 10.1021/nl100996u

Yang, T., Liu, L., Deng, Y., Guo, Z., Zhang, G., Ge, Z., et al. (2017). Ultrastable near-infrared conjugated-polymer nanoparticles for dually photoactive tumor inhibition. *Adv. Mater.* 1700487. doi: 10.1002/adma.201700487

Zhang, G., Dai, Y., Song, K., Lee, H., Ge, F., Qiu, L., et al. (2017a). Bis(2-oxo-7-azaindolin-3-ylidene)benzodifuran-dione-based donor-acceptor polymers for high-performance n-type field-effect transistors. *Polym. Chem.* 8, 2381–2389. doi: 10.1039/C7PY00295E

Zhang, G., Zhao, Y., Kang, B., Park, S., Ruan, J., Lu, H., et al. (2019). Fused heptacyclic-based acceptor-donor-acceptor small molecules: N-substitution toward high-performance solution-processable field-effect transistors. *Chem. Mater.* 2019, 31, 2027–2035. doi: 10.1021/acs.chemmater.8b05054

Zhang, J., Yang, C., Zhang, R., Chen, R., Zhang, Z., Zhang, W., et al. (2017b). Biocompatible D–A semiconducting polymer nanoparticle with light-harvesting unit for highly effective photoacoustic imaging guided photothermal therapy. *Adv. Funct. Mater.* 27, 1605094. doi: 10.1002/adfm.201605094

Zhang, Y., Teh, C., Li, M., Ang, C. Y., Tan, S. Y., Qu, Q., et al. (2016). Acid-responsive polymeric doxorubicin prodrug nanoparticles encapsulating a near-infrared dye for combined photothermal-chemotherapy. *Chem. Mater.* 28, 7039–7050. doi: 10.1021/acs.chemmater.6b02896

Zheng, M., Yue, C., Ma, Y., Gong, P., Zhao, P., Zheng, C., et al. (2013). Single-step assembly of DOX/ICG loaded lipid-polymer nanoparticles for highly effective chemo-photothermal combination therapy. *ACS Nano*, 7, 2056–2067. doi: 10.1021/nn400334y

Zhou, B., Li, Y., Niu, G., Lan, M., Jia, Q., and Liang, Q. (2016). Near-infrared organic dye-based nanoagent for the photothermal therapy of cancer. *ACS Appl. Mater. Interfaces* 8, 29899–29905. doi: 10.1021/acsami.6b07838

Zhu, Y., Champion, R., and Jenekhe, S. (2016). Conjugated donor–acceptor copolymer semiconductors with large intramolecular charge transfer: synthesis, optical properties, electrochemistry, and field effect carrier mobility of thienopyrazine-based copolymers. *Macromolecules* 39, 8712–8719. doi: 10.1021/ma061861g

Conflict of Interest Statement: The authors declare that the research was conducted in the absence of any commercial or financial relationships that could be construed as a potential conflict of interest.

frontiers in Chemistry

ORIGINAL RESEARCH
published: 29 May 2019
doi: 10.3389/fchem.2019.00362

Low Bandgap Donor-Acceptor π-Conjugated Polymers From Diarylcyclopentadienone-Fused Naphthalimides

Xiaolin Li[1], Jing Guo[2], Longfei Yang[3], Minghao Chao[3], Liping Zheng[1], Zhongyun Ma[1], Yuanyuan Hu[2], Yan Zhao[3]*, Huajie Chen[1]* and Yunqi Liu[3]*

[1] Key Laboratory for Green Organic Synthesis and Application of Hunan Province, and Key Laboratory of Environmentally Friendly Chemistry and Applications of Ministry of Education, College of Chemistry, Xiangtan University, Xiangtan, China, [2] Key Laboratory for Micro/Nano Optoelectronic Devices of Ministry of Education & Hunan Provincial Key Laboratory of Low-Dimensional Structural Physics and Devices, School of Physics and Electronics, Hunan University, Changsha, China, [3] Department of Materials Science, Institute of Molecular Materials and Devices, Fudan University, Shanghai, China

Two novel aromatic imides, diarylcyclopentadienone-fused naphthalimides (BCPONI-2Br and TCPONI-2Br), are designed and synthesized by condensation coupling cyclopentadienone derivatives at the lateral position of naphthalimide skeleton. It has been found that BCPONI-2Br and TCPONI-2Br are highly electron-withdrawing acceptor moieties, which possess broad absorption bands and very low-lying LUMO energy levels, as low as −4.02 eV. On the basis of both building blocks, six low bandgap D-A copolymers (P1–P6) are prepared via Suzuki or Stille coupling reactions. The optical and electrochemical properties of the polymers are fine-tuned by the variations of donors (carbazole, benzodithiophene, and dithienopyrrole) and π-conjugation linkers (thiophene and benzene). All polymers exhibit several attractive photophysical and electrochemical properties, i.e., broad near-infrared (NIR) absorption, deep-lying LUMO levels (between −3.88 and −3.76 eV), and a very small optical bandgap (E_g^{opt}) as low as 0.81 eV, which represents the first aromatic diimide-based polymer with an E_g^{opt} of <1.0 eV. An investigation of charge carrier transport properties shows that P5 exhibits a moderately high hole mobility of 0.02 $cm^2\ V^{-1}\ s^{-1}$ in bottom-gate field-effect transistors (FETs) and a typical ambipolar transport behavior in top-gate FETs. The findings suggest that BCPONI-2Br, TCPONI-2Br, and the other similar acceptor units are promising building blocks for novel organic semiconductors with outstanding NIR activity, high electron affinity, and low bandgap, which can be extended to various next-generation optoelectronic devices.

Keywords: diarylcyclopentadienone-fused naphthalimides, D-A conjugated polymers, optical band gap, electron-transporting materials, charge carrier transport

OPEN ACCESS

Edited by:
Bin Wu,
Institute of Chemistry (CAS), China

Reviewed by:
Zhengxu Cai,
Beijing Institute of Technology, China
Zhuping Fei,
Tianjin University, China

***Correspondence:**
Yuanyuan Hu
yhu@hnu.edu.cn
Yan Zhao
zhaoy@fudan.edu.cn
Huajie Chen
chenhjoe@163.com

Specialty section:
This article was submitted to Supramolecular Chemistry, a section of the journal Frontiers in Chemistry

Received: *25 March 2019*
Accepted: *02 May 2019*
Published: *29 May 2019*

Citation:
Li X, Guo J, Yang L, Chao M, Zheng L, Ma Z, Hu Y, Zhao Y, Chen H and Liu Y (2019) Low Bandgap Donor-Acceptor π-Conjugated Polymers From Diarylcyclopentadienone-Fused Naphthalimides. Front. Chem. 7:362. doi: 10.3389/fchem.2019.00362

INTRODUCTION

Soluble donor–acceptor (D–A) conjugated polymers can offer a flexible and tunable electronic structure and optoelectronic properties (Guo et al., 2014; Dou et al., 2015), which encourage the incessant exploration of multiple potential applications in next-generation optoelectronic devices, including organic light-emitting diodes (OLEDs) (Grimsdale et al., 2009), organic photovoltaics

(OPVs) (Cheng et al., 2009), organic field-effect transistors (OFETs) (Hu et al., 2018; Yang et al., 2018), and organic photodetectors (OPDs) (Gong et al., 2009). By independently selecting or modifying D/A segments, one can readily regulate optical properties, electronic structures (bandgap and HOMO/LUMO energy levels), and charge carrier transport of the target D-A polymers (Hwang et al., 2012; Cui and Wudl, 2013; Zhao et al., 2015; Chen et al., 2016; Fei et al., 2016; Li et al., 2016). Such a D-A strategy has led to the rapid development of numerous D-A conjugated polymers and makes a great contribution to promote device performance in organic electronics (Guo et al., 2014; Dou et al., 2015; Yang et al., 2018). In recent years, some classical organic dyes, such as diketopyrrolopyrrole (DPP) (Zou et al., 2009; Li et al., 2011, 2013c) and isoindigo (IDG) (Stalder et al., 2010; Lei et al., 2011; Mei et al., 2011; Gao et al., 2017), have been successfully used as the acceptor building blocks to construct low bandgap D-A conjugated polymers for various optoelectronic devices, especially in OPVs and OFETs. Hole or electron mobilities higher than 5.0 $cm^2\ V^{-1}\ s^{-1}$ (Chen et al., 2012; Gao et al., 2015) and a power conversion efficiency (PCE) of above 8.0% (Hendriks et al., 2013) have been reported for the DPP-containing D-A polymers.

In view of the urgent need for electron-transporting materials, aromatic imides like rylene diimides have been widely studied (Zhan et al., 2011). Moreover, they have also become attractive acceptor building blocks for *n*-type conjugated polymers due to the strong electron-deficient feature, high electron mobility, tunable solubility supported by *N*-alkylation, and excellent chemical and photochemical stability (Zhan et al., 2011). So far, the most studied rylene diimides are perylene diimide (PDI, **1**) and naphthalene diimide (NDI, **4**) (**Figure 1**). Zhan and co-workers reported the synthesis of the first soluble PDI-dithienothiophene copolymers (Zhan et al., 2007), which yielded a moderately high electron mobility of 0.013 $cm^2\ V^{-1}\ s^{-1}$ and a PCE value of 1.5% when used as the active layers in top-gate OFETs and all-polymer OPVs, respectively. Since then, great efforts have been made to structurally modify PDI acceptor units, thereby generating a sets of core-extended PDI analogs (Choi et al., 2011; Usta et al., 2012; Cai et al., 2017, 2018), such as dithienocoronene diimides (DTCDI, **2**) (Choi et al., 2011; Zhou et al., 2012) and naphthodiperylenetetraimide (NTDPI, **3**) (Guo et al., 2017) (**Figure 1**). Compared with PDIs, both DTCDI and NTDPI acceptor building blocks possess larger conjugation backbones than PDI, which could facilitate strong intermolecular interactions and charge carriers transport of the polymers (Zhou et al., 2012). Facchetti and co-workers reported the synthesis of soluble D-A polymers containing DTCDI and thiophene units (Usta et al., 2012), which exhibited good hole and electron mobilities of 0.04 and 0.3 $cm^2\ V^{-1}\ s^{-1}$, respectively. Zhao and co-workers synthesized the NTDPI and vinylene-linked *n*-type polymer and afforded an excellent PCE value of 8.59% in the inverted all-polymer OPVs (Guo et al., 2017).

Naphthalene diimide (NDI, **4**, **Figure 1**) is the other strongly electron-deficient building block for the development of polymer electron-transporting materials. Watson and co-workers. pioneered the use of NDI as an acceptor building block in D-A copolymers with a tunable optical bandgap (E_g^{opt}) ranging from 1.7 to 1.1 eV (Guo and Watson, 2008). Later, Facchetti and co-workers reported the synthesis and OFETs properties of an NDI-bithiophene polymer (N2200), which exhibited an impressive electron mobility up to 0.85 $cm^2\ V^{-1}\ s^{-1}$ under ambient conditions (Yan et al., 2009). Thanks to structural optimization and device engineering, copolymers-based NDI units have also very recently provided near state-of-the-art electron mobilities >7.0 $cm^2\ V^{-1}\ s^{-1}$ (Zhao et al., 2017; Wang et al., 2019). An all-polymer OPV device, reported by Huang and co-workers has been further developed to a benchmark PCE value of 11% (Li et al., 2019), which fabricated from an N2200 acceptor and polymer donor (PTzBI-Si). Recently, a core-extended strategy has been successfully utilized to prepare various heteroaromatic-fused NDI derivatives, such as thiophene-fused NDI (NDTI, **5**) (Fukutomi et al., 2013), thiazole-fused NDI (NDTZ, **6**) (Chen et al., 2013), and pyrazine-fused NDI (BFI, **7**) (**Figure 1**) (Li et al., 2013b). These core-extended NDI units can afford a rigid π-conjugation backbone with distinct electronic structures as relative-to-simple core-linked NDIs, which has been developed as the promising building blocks for polymer electron-transporting materials (Chen et al., 2013; Fukutomi et al., 2013; Li et al., 2013a). A typical example of the core-extended NDI is tetraazabenzodifluoranthene diimide (BFI, **7**) reported by Jenekhe and co-workers; moreover, it was found that a BFI-containing copolymer has a large lateral extension (2.0 nm) of π-conjugation and perfect lamellar ordering, thereby achieving high electron mobilities of 0.3 $cm^2\ V^{-1}\ s^{-1}$ (Li et al., 2013a).

Diarylcyclopentadienone-fused naphthalimide (CPONI, **Figure 2**) is a novel family of aromatic imide building blocks that originally derived from naphthalimide and cyclopentadienone units and is similar in structure to cyclopentadieneones. Wudl and co-workers reported the synthesis and OFET properties of cyclopentadieneones-containing oligomers (Walker et al., 2008; Yang et al., 2008), which demonstrated very small bandgaps as low as 0.9 eV and a moderate hole mobility of 2.26×10^{-2} $cm^2\ V^{-1}\ s^{-1}$ (Yang et al., 2008). Compared with cyclopentadieneone analogs, the combined advantages of both NDI and cyclopentadienone units endow CPONI acceptors with extended π-conjugation backbone, enhanced electron-withdrawing capacity, as well as tunable solubility that supported by *N*-alkylation. The imide nitrogens in the CPONI units allow attachment of solublizing side chains in the polymer backbone in order to tune solubility and self-organization without disrupting backbone's coplanarity. Thus, CPONI derivatives are of great interest to construct low band-gap D-A conjugated polymers with promising electronic structure and optoelectronic properties. Nevertheless, literature reports on the synthesis, reactivity, and optoelectronic properties of diarylcyclopentadienone-fused naphthalimide derivatives are rarely seen (Ding et al., 2015; Ishikawa et al., 2018). To our knowledge, the CPONI-based polymers have not been reported.

In this article, two novel CPONI-derived acceptor building-blocks, diphenylcyclopentadienone- fused naphthalimide (BCPONI-2Br) and dithienylcyclopentadienone-fused naphthalimide (TCPONI-2Br) (**Figure 2**), were designed and synthesized for low bandgap D-A polymers. Herein,

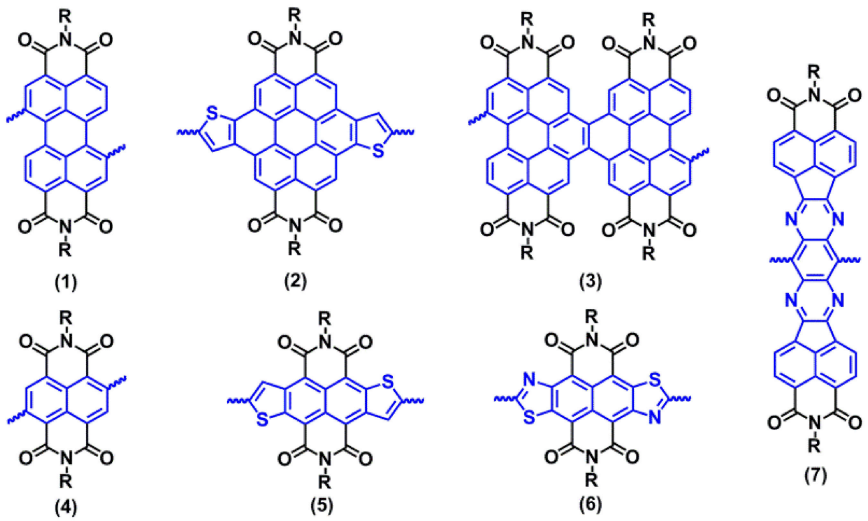

FIGURE 1 | Some perylene diimide and naphthalene diimide building blocks in conjugated polymers.

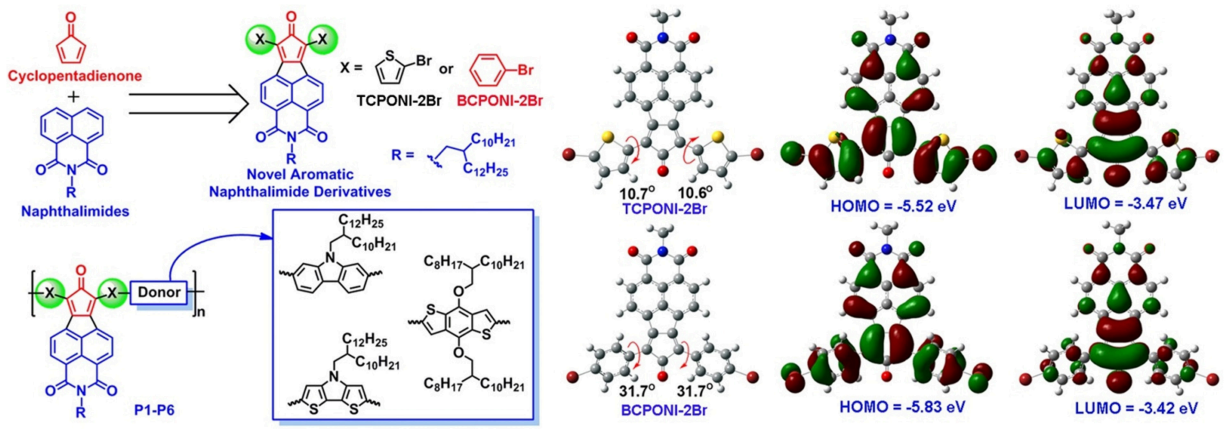

FIGURE 2 | Molecular design and chemical structures of the two monomers (BCPONI-2Br and TCPONI-2Br) and their D-A copolymers (P1–P6). The optimized structures, molecular orbitals, and HOMO/LUMO energy levels of the two monomers as obtained from density functional theory (DFT) calculations.

thiophene and benzene rings were selected as the π-linker units of TCPONI-2Br and BCPONI-2Br, respectively, in order to manipulate backbone coplanarity, energy levels, and absorption of the target polymers. As revealed by theoretical calculations, the dihedral angles of thiophene-flanked TCPONI-2Br (ca. 10.6 and 10.7°) are smaller than those of benzene-flanked BCPONI-2Br (ca. 31.7°), indicating better backbone coplanarity for TCPONI-2Br. Interestingly, the attachment of electron-rich thiophene units endows TCPONI-2Br with a slightly reduced LUMO value (ca. −3.47 eV) but sharply improved the HOMO value (ca. −5.52 eV) relative to BCPONI-2Br. Such deep-lying LUMO values indicate that TCPONI-2Br (ca. −3.47 eV) and BCPONI-2Br (ca. −3.42 eV) are promising strong acceptor units for electron-transporting polymers. By using both building blocks as the electron acceptors, six novel D-A conjugated polymers with different electron-donating capability donor units (carbazole, benzodithiophene, and dithienopyrrole) were prepared by Suzuki or Stille coupling reactions. The polymers exhibit very attractive photophysical and electrochemical properties, i.e., broad near-infrared (NIR) absorption extended to 1,600 nm and adjustable E_g^{opt} values from 0.81 to 1.55 eV, which was realized by employing different donor units and π-conjugation linkers. To our satisfaction, an ultralow E_g^{opt} of 0.81 eV was achieved for TCPONI-containing polymer (P6), which represents the first aromatic diimide-based polymer with the E_g^{opt} <1.0 eV.

EXPERIMENTAL SECTION

General Measurements

Nuclear magnetic resonance spectra (^{1}H NMR and ^{13}C NMR) were collected on a Bruker AVANCE 400 spectrometer. Mass

spectrometry (MALDI-TOF-MS) was performed on a Bruker AutoflexTM III instrument. Molecular weight was determined by high temperature gel permeation chromatography (150°C in 1,2,4-trichlorobenzene) on a Polymer Labs PL 220 system. UV–vis–NIR absorption spectroscopy was measured using a Perkin-Elmer Lamada 750 UV/vis spectrometer. Thermogravimetric analysis (TGA) was recorded on a Perkin-Elmer TGA-7 Analyzer with a heating rate of 10°C min^{-1}. Differential scanning calorimetry (DSC) was measured on a DSC Q10 instrument with the heating/cooling rates of 10°C min^{-1}. Cyclic voltammetry (CV) was performed on an electrochemistry workstation (CHI660E, Chenhua Shanghai) using a three-electrode cell. For the characterization of small molecules, three-electrode cell with a Pt wire counter electrode, a Ag/AgCl (KCl, Sat'd) reference electrode, and a glassy carbon working electrode was utilized. For the measurement of polymers, a Pt wire, a Ag/AgCl (KCl, Sat'd) electrode and a Pt disk drop-coated with polymer film were used as the counter, reference electrode, and working electrode, respectively. The electrolytes were anhydrous and N_2-saturated tetrabutylammonium hexafluorophosphate (TBAPF6, 0.1 M) solutions in dichloromethane or acetonitrile. A Fourier-transform infrared spectroscopy (FT-IR) was carried out on a Nicolet 6700 FT-IR spectrometer in a scan range from 4,000 to 600 cm^{-1}. The film surface morphology was characterized by atomic force microscopy (AFM, Bruker Multi-Mode 8 microscope) using a tapping mode. Grazing incidence X-ray diffraction (GIXRD) experiments were performed to characterize film organization. The polymer film samples were illuminated at a constant incidence angle of 0.2°.

Materials and Synthesis

Tetrahydrofuran (THF) and chlorobenzene were dried and distilled prior to use. All the reagents and chemicals were purchased from Chem Greatwall, Derthon, and Alfa Aesar. Some important intermediates, including 1,3-dithiophenyl-2-propanone (1) (Walker et al., 2008), 1,3-bis(4-bromophenyl)-2-propanone (3) (Walker et al., 2008), 2-(2-decyltetradecyl)-1*H*-indeno[6,7,1-*def*]isoquinoline-1,3,6,7(2*H*)-tetraone (4) (Li et al., 2013b), *N*-(2-decyltetradecyl)-2,7-bis-(4,4,5,5-tetramethyl-1,3,2-dioxaborolane-2-yl)carbazole (Kim et al., 2011), 2,6-bis(trimethyltin)-4,8-di(2-hexyl)decyloxybenzo[1,2-*b*;3,4-*b*′]dithiophene (Mei et al., 2013), and 2,6-bis(trimethylstannyl)-*N*-(2-decyltetradecyl)dithieno[3,2-*b*:2′,3′-*d*]pyrrole (Zhang et al., 2010), were synthesized according to literature procedures, respectively.

Synthesis of Compound 2

Under nitrogen, a mixture of 1,3-dithiophenyl-2-propanone (1.2 g, 5.40 mmol) and $CHCl_3$ (25 mL) was stirred at 0°C. Next, 2.11 g of *N*-bromobutanimide (NBS) (11.88 mmol) was slowly added to the reaction mixture. After stirring for 5 h at room temperature, the reaction was quenched with water. The organic layer was extracted by CH_2Cl_2 and dried over anhydrous $MgSO_4$. After removal of the solvent, the crude product was purified by column chromatography on silica gel using a mixed eluent of petroleum ether and CH_2Cl_2 (3:1, v/v) to afford a yellow solid (1.05 g, 51%). ^{1}H NMR (400 MHz, $CDCl_3$), δ (ppm): 6.93–6.92 (d, $J = 3.7$ Hz, 2H), 6.65–6.64 (d, $J = 3.7$ Hz, 2H), 3.91 (s, 4H). ^{13}C NMR (100 MHz, $CDCl_3$), δ (ppm): 201.47, 135.94, 129.78, 127.53, 111.81, 42.74. FT-IR spectra data: $\upsilon_{C=O}$: 1,698 and 1,663 cm^{-1}.

Synthesis of BCPONI-2Br

Under nitrogen, to a mixture of compound 4 (500 mg, 0.85 mmol), 1,3-bis(4-bromophenyl)-2-propanone (313 mg, 0.85 mmol), and ethanol (25 mL), 24 mg of KOH (0.42 mmol) in 5 mL of ethanol were added slowly. The solution changed to red immediately and then precipitates formed gradually. The mixture was refluxed for 30 min and then cooled down to room temperature. The organic layer was extracted by CH_2Cl_2 and dried with anhydrous $MgSO_4$. After removal of the solvent, the crude product was purified by column chromatography on silica gel using a mixed eluent of petroleum ether and CH_2Cl_2 (1:2, v/v) to yield a brown solid (470 mg, 60%). ^{1}H NMR (400 MHz, $CDCl_3$), δ (ppm): 8.60–8.58 (d, $J = 7.6$ Hz, 2H), 8.22–8.20 (d, $J = 7.6$ Hz, 2H), 7.73 (br, 8H), 4.13–4.12 (d, $J = 4.0$ Hz, 2H), 1.98 (br, 1H), 1.21 (m, 40H), 0.86 (m, 6H). ^{13}C NMR (100 MHz, $CDCl_3$), δ (ppm): 199.52, 163.35, 151.73, 142.55, 135.34, 132.61, 132.23, 130.53, 128.95, 126.73, 124.58, 124.08, 122.56, 121.34, 44.76, 36.67, 31.95, 31.77, 30.07, 29.69, 29.38, 26.54, 22.71, 14.14. FT-IR spectra data: $\upsilon_{C=O}$: 1,698 and 1,663 cm^{-1}. HRMS (MALDI–TOF): m/z $[M]^+$ calcd for ($C_{53}H_{62}Br_2NO_3$): 918.3090; found: 918.3090.

Synthesis of TCPONI-2Br

Under nitrogen, to a mixture of compound 4 (500 mg, 0.85 mmol), 1,3-bis(5-bromothiophenyl)-2-propanone (324 mg, 0.85 mmol), and ethanol (25 mL), 24 mg of KOH (0.42 mmol) in 5 mL of ethanol were added slowly. The red mixture was then refluxed for 30 min. The organic layer was extracted by CH_2Cl_2 and dried with anhydrous $MgSO_4$. After filtration and removal of the solvent, the crude product was purified by column chromatography on silica gel using a mixed eluent of petroleum ether and CH_2Cl_2 (1:2, v/v) to yield a brown solid (476 mg, 60%). ^{1}H NMR (400 MHz, $CDCl_3$), δ (ppm): 8.43–8.41 (d, $J = 7.6$ Hz, 2H), 8.05–8.03 (d, $J = 7.7$ Hz, 2H), 7.37–7.36 (d, $J = 4.0$ Hz, 2H), 6.99–6.98 (d, $J = 4.0$ Hz, 2H), 4.10–4.08 (d, $J = 7.1$ Hz, 2H), 1.98 (br, 1H), 1.38–1.20 (m, 40H), 0.86 (m, 6H). ^{13}C NMR (100 MHz, $CDCl_3$), δ (ppm): 197.23, 163.02, 146.76, 141.29, 133.36, 133.24, 131.87, 130.60, 130.04, 125.93, 122.08, 121.80, 118.18, 117.01, 36.93, 31.98, 31.74, 30.25, 29.76, 29.73, 29.42, 26.50, 22.73, 14.16. FT-IR spectra data: $\upsilon_{C=O}$: 1,698 and 1,660 cm^{-1}. HRMS (MALDI–TOF): m/z $[M]^+$ calcd for ($C_{49}H_{58}Br_2NO_3S_2$): 930.2219; found: 930.2226.

Synthesis of P1

Under nitrogen, a mixture of BCPONI-2Br (147 mg, 0.16 mmol), *N*-(2-decyltetradecyl)-2,7-bis-(4,4,5,5-tetramethyl-1,3,2-dioxaborolane-2-yl)carbazole (124 mg, 0.16 mmol), $Pd(PPh_3)_2Cl_2$ (15 mg), chlorobenzene (5 mL), 2 mL of Na_2CO_3 aqueous solution (2M), and a drop of aliquat 336 was added into a 25 mL Schlenk tube. The tube was charged with nitrogen through a freeze-pump-thaw cycle for three times. The mixture was stirred at 100°C for 5 h in the absence of light. After cooling to room temperature, the mixture was dropped into a mixed

solution of methanol (200 mL) and concentrated hydrochloric acid (5 mL) and stirred for another 0.5 h. The dark solid was collected and Soxhlet-extracted with ethanol, acetone, hexane, and chlorobenzene. After removal of chlorobenzene, a black solid was obtained (170 mg, 84%). ^{1}H NMR (500 MHz, $C_2D_2Cl_4$, 373 K), δ (ppm): 8.70–7.31 (br, 18H), 4.50–4.00 (br, 4H), 2.31 (br, 1H), 2.12 (br, 1H), 1.60–0.70 (m, 92H). FT-IR spectra data: $\upsilon_{C=O}$: 1,699 and 1,664 cm^{-1}. GPC: M_n = 7.47 kDa, M_w = 24.12 kDa, PDI = 3.23.

Synthesis of P2

Under nitrogen, a mixture of BCPONI-2Br (147 mg, 0.16 mmol), 2,6-bis(trimethyltin)-4,8-di(2-hexyl)decyloxybenzo[1,2-*b*;3,4-*b*′]dithiophene (177 mg, 0.16 mmol), $Pd_2(dba)_3$ (9 mg), P(o-tol)$_3$ (15 mg), and anhydrous chlorobenzene (5 mL) was added into a 25 mL Schlenk tube. The tube was subsequently charged with nitrogen through a freeze-pump-thaw cycle for three times. The mixture was heated to 120°C and stirred for 60 h in the absence of light. After cooling to room temperature, the mixture was dropped into a mixed solution of methanol (200 mL) and concentrated hydrochloric acid (5 mL) and stirred for another 0.5 h. The black solid was collected and further Soxhlet-extracted with ethanol, acetone, hexane, and chlorobenzene. After removal of chlorobenzene, P2 was obtained as a black solid (227 mg, 92%). ^{1}H NMR (500 MHz, $C_2D_2Cl_4$, 373 K), δ (ppm): 8.70–7.50 (br, 14H), 4.50–4.00 (br, 6H), 2.20–2.00 (m, 3H), 2.00–0.70 (m, 122H). FT-IR spectra data: $\upsilon_{C=O}$: 1,700 and 1,666 cm^{-1}. GPC: M_n = 55.31 kDa, M_w = 75.67 kDa, PDI = 1.37.

Synthesis of P3

A mixture of BCPONI-2Br (147 mg, 0.16 mmol), 2,6-bis(trimethylstannyl)-*N*-(2-decyltetradecyl)-dithieno[3,2-*b*:2′,3′-*d*]pyrrole (135 mg, 0.16 mmol), $Pd_2(dba)_3$ (9 mg), P(*o*-tol)$_3$ (15 mg), and anhydrous chlorobenzene (5 mL) was added to a 25 mL Schlenk tube. The tube was then charged with nitrogen through a freeze-pump-thaw cycle for three times. The mixture was heated to 115°C and stirred for 72 h under nitrogen atmosphere. After cooling to room temperature, the mixture was dropped into a mixed solution of methanol (200 mL) and concentrated hydrochloric acid (5 mL) and stirred for another 0.5 h. The solid product was collected and Soxhlet-extracted with ethanol, acetone, hexane, and chlorobenzene. After removal of chlorobenzene, a black solid was obtained (188 mg, 92%). ^{1}H NMR (500 MHz, $C_2D_2Cl_4$, 373 K), δ (ppm): 8.70–7.00 (br, 14H), 4.50–3.70 (br, 4H), 2.18–2.04 (br, 2H), 1.70–0.70 (m, 92H). FT-IR spectra data: $\upsilon_{C=O}$: 1,697 and 1,662 cm^{-1}. GPC: M_n = 23.50 kDa, M_w = 45.82 kDa, PDI = 1.95.

Synthesis of P4

A mixture of TCPONI-2Br (149 mg, 0.16 mmol), *N*-(2-decyltetradecyl)-2,7-bis-(4,4,5,5-tetramethyl-1,3,2-dioxaborolane-2-yl)carbazole (124 mg, 0.16 mmol), $Pd(PPh_3)_2Cl_2$ (15 mg), chlorobenzene (5 mL), 2 mL of Na_2CO_3 aqueous solution (2 M), and a drop of aliquat 336 was added to a 25 mL Schlenk tube. The tube was then charged with nitrogen through a freeze-pump-thaw cycle for three times. The mixture was stirred at 100°C for 5 h under nitrogen atmosphere. After cooling to room temperature, the mixture was dropped into a mixed solution of methanol (200 mL) and concentrated hydrochloric acid (5 mL) and stirred for another 0.5 h. The crude product was collected and Soxhlet-extracted with ethanol, acetone, hexane, and chlorobenzene. After removal of chlorobenzene, P4 was obtained as a black solid (171 mg, 84%). ^{1}H NMR (500 MHz, $C_2D_2Cl_4$, 373 K), δ (ppm): 9.00–6.50 (br, 14H), 4.50–3.80 (br, 4H), 2.00–0.60 (m, 94H). FT-IR spectra data: $\upsilon_{C=O}$: 1,697 and 1,660 cm^{-1}. GPC: M_n = 20.10 kDa, M_w = 40.41 kDa, PDI = 2.01.

Synthesis of P5

A mixture of TCPONI-2Br (149 mg, 0.16 mmol), 2,6-bis(trimethyltin)-4,8-di(2-hexyl)decyloxybenzo[1,2-*b*;3,4-*b*′]dithiophene (177 mg, 0.16 mmol), $Pd_2(dba)_3$ (9 mg), P(o-tol)$_3$ (15 mg), and anhydrous chlorobenzene (5 mL) was added to a 25 mL Schlenk tube. The mixture was charged with nitrogen through a freeze-pump-thaw cycle for three times and then stirred at 110°C for 3 h in the absence of light. After cooling to room temperature, the mixture was dropped into a mixed solution of methanol (200 mL) and concentrated hydrochloric acid (5 mL) and stirred for another 0.5 h. The solid product was collected and Soxhlet-extracted with ethanol, acetone, hexane, and chlorobenzene. After removal of chlorobenzene, a black solid was obtained (239 mg, 96%). ^{1}H NMR (500 MHz, $C_2D_2Cl_4$, 373 K), δ (ppm): 9.00–6.50 (br, 10H), 4.60–3.80 (br, 6H), 2.50–0.60 (m, 125H). FT-IR spectra data: $\upsilon_{C=O}$: 1,698 and 1,662 cm^{-1}. GPC: M_n = 32.21 kDa, M_w = 77.10 kDa, PDI = 2.40.

Synthesis of P6

A mixture of TCPONI-2Br (149 mg, 0.16 mmol), 2,6-bis(trimethylstannyl)-*N*-(2-decyltetradecyl)-dithieno[3,2-*b*:2′,3′-*d*]pyrrole (135 mg, 0.16 mmol), $Pd_2(dba)_3$ (9 mg), P(*o*-tol)$_3$ (15 mg), and anhydrous chlorobenzene (5 mL) was added to a 25 mL Schlenk tube. The mixture was charged with nitrogen through a freeze-pump-thaw cycle for three times and then stirred at 115°C for 24 h in the absence of light. After cooling to room temperature, the mixture was dropped into a mixed solution of methanol (200 mL) and concentrated hydrochloric acid (5 mL) and stirred for another 0.5 h. The solid product was collected and Soxhlet-extracted with ethanol, acetone, hexane, and chlorobenzene. After removal of chlorobenzene, a black solid was obtained (196 mg, 95%). ^{1}H NMR (500 MHz, $C_2D_2Cl_4$, 373 K), δ (ppm): 8.00–6.40 (br, 10H), 4.50–3.60 (br, 4H), 2.40–0.50 (m, 94H). FT-IR spectra data: $\upsilon_{C=O}$: 1,696 and 1,660 cm^{-1}. GPC: M_n = 7.06 kDa, M_w = 16.49 kDa, PDI = 2.34.

RESULTS AND DISCUSSION

Synthesis

Figure 3 describes the synthetic routes of the two CPONI-containing monomers and their D–A copolymers. Two important intermediates, 1,3-dithiophenyl-2-propanone (1) (Walker et al., 2008) and 1,3-bis(4-bromophenyl)-2-propanone (3) (Walker et al., 2008), were synthesized according to the reported procedures, respectively. The synthesis of both

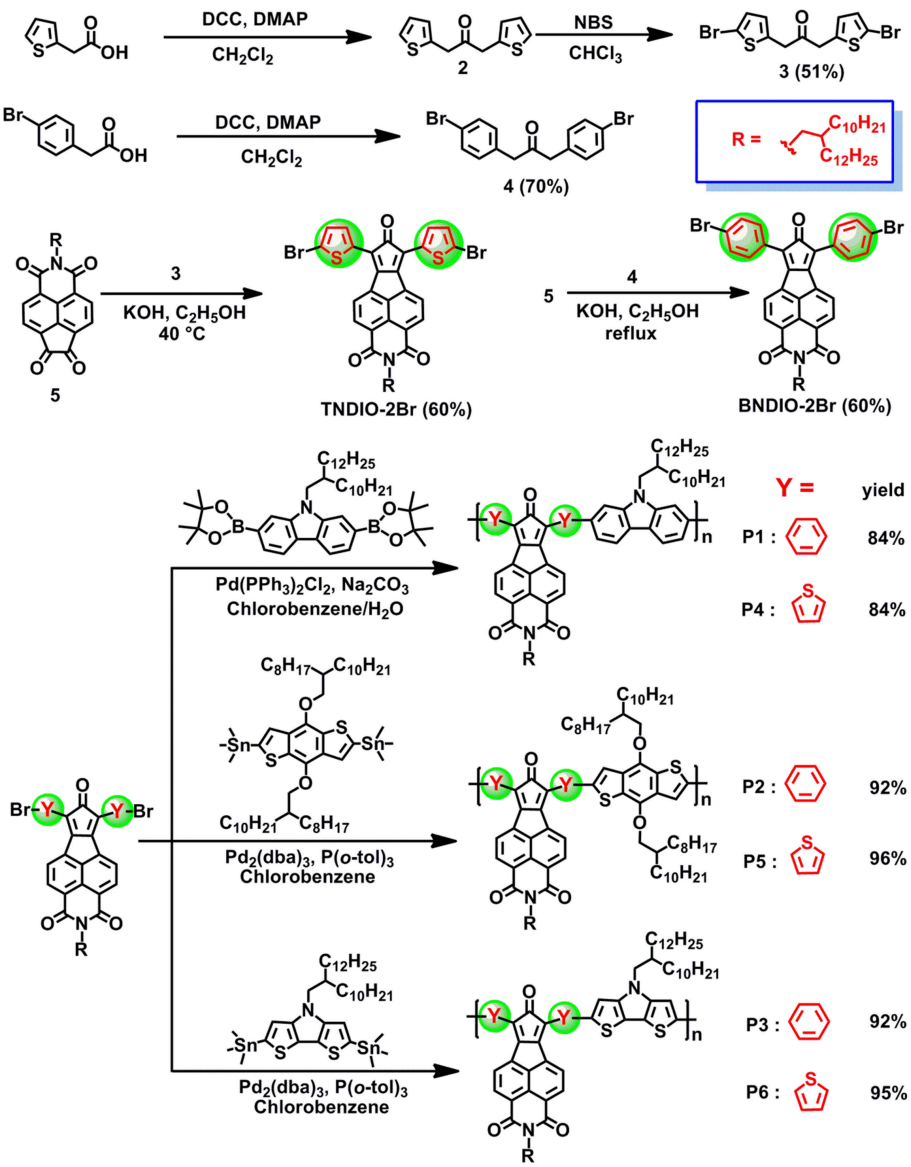

FIGURE 3 | Synthetic route for the CPONI-based monomers and their copolymers.

monomers started from the self-condensation reactions of thiopheneacetic acid or 4-bromobenzeneacetic acid to give compounds 1 and 3, respectively. Then, bromination of compound 1 with NBS afforded 1,3-bis(5-bromothiophenyl)-2-propanone (2) in 51% yields. Finally, double Knoevenagel condensation reactions were readily performed between diketone-containing 5 and compounds 1 or 3 to produce two black solids, BCPONI-2Br and TCPONI-2Br, respectively. The chemical structures of all the intermediates and dibrominated monomers were confirmed by ^{1}H NMR and ^{13}C NMR (**Figures S11–S16**). In addition, the diboronicester reagent of carbazole (Kim et al., 2011), as well as distannyl derivatives of benzodithiophene (Mei et al., 2013) and dithienopyrrole (Zhang et al., 2010), were prepared according to similar literature procedures, and their ^{1}H NMR data are provided in **Figures S17–S19**.

The target copolymers were synthesized via the standard palladium-catalyzed Suzuki or Stille coupling reaction between the dibrominated monomers (BCPONI-2Br and TCPONI-2Br) and electron-donated monomers (carbazole, benzodithiophene, and dithienopyrrole). For benzodithiophene- and dithienopyrrole-containing polymers (P2, P3, P5, and P6), Stille polymerization was conducted using $Pd_2(dba)_3$/P(*o*-tol)$_3$ as the catalyst, while P1 and P4 was synthesized by $Pd(PPh)_2Cl_2$-catalyzed Suzuki polymerization. In fact, when we chose $Pd_2(dba)_3$/P(*o*-tol)$_3$ as the catalyst, all the resulted P1 and P4 samples were insoluble due to "over-polymerization." Fortunately, we obtained all the solution-processable polymer

TABLE 1 | Molecular weight, yield, and decomposition temperature of the polymers.

Polymer	Yield	M_n	M_w	PDI	T_d
	(%)	(kDa)	(kDa)		(°C)
P1	84	7.47	24.12	3.23	405
P2	92	55.31	75.67	1.37	344
P3	92	23.50	45.82	1.95	412
P4	84	20.10	40.41	2.01	429
P5	96	32.21	77.10	2.40	351
P6	95	7.06	16.49	2.34	413

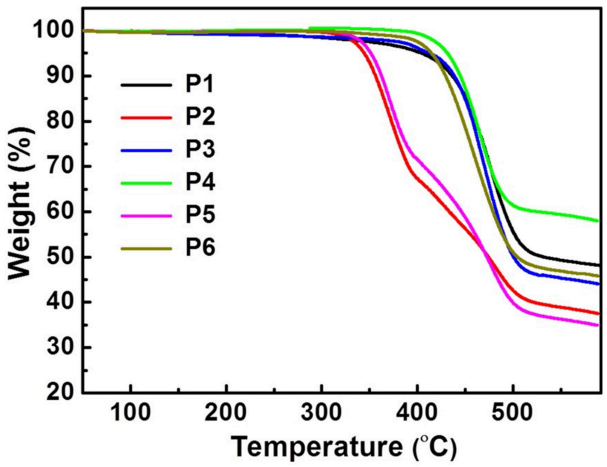

FIGURE 4 | TGA curves of the CPONI-based polymers.

samples (P1–P6) that can be dissolved in warm organic solvents (chloroform, chlorobenzene, and xylene).

Molecular weight of the polymers was measured by high-temperature (150°C) GPC and calibrated by monodisperse polystyrene. The observed number-average molecular weights (M_n) are 7.06–55.31 kDa, and the polydispersity indices are 1.37–3.23 (**Table 1** and **Figures S1–S6**). The thermal properties of the polymers were investigated by TGA and DSC instruments under nitrogen. As seen from **Figure 4**, all the polymers display excellent thermal stability. For the carbazole- and dithienopyrrole-containing polymers (P1, P3, P4, and P6), the thermal decomposition temperature (T_d) at 5% weight loss are above 398°C, while the benzodithiophene-containing P2 and P5 exhibit much lower T_d (ca. 350°C). Additionally, no obvious phase transition was detected from the DSC measurements during the heating/cooling scan between room temperature and 280°C (**Figure S7**). FT-IR spectroscopy of the polymers displays typical characteristic bands ($\upsilon_{C=O}$) at ca. 1,697 and 1,660 cm^{-1}, thereby providing direct evidence for the carbonyl groups in the polymers (**Figures S8, S9**). Although ^1H NMR spectroscopy of the polymers were collected at a high temperature of 373 K, only broad and featureless signals were detected at aromatic (δ = 7.0–9.0 ppm) and alkyl bands (δ = 3.5–4.5 and 0.5–2.5 ppm) (**Figures S20–S25**). The results suggest that a common phenomenon, i.e., strong interchain aggregation (Guo and Watson, 2011), also exists in the newly-developed CPONI-containing polymers and cannot be broken even at high temperature of 373 K.

Optical Properties

UV-vis-NIR absorption spectra of the CPONI-containing monomers and their D-A polymers were recorded in chloroform (ca. 10^{-5} M) and in spin-coated thin films (**Table 2** and **Table S1**). As seen from **Figure 5A**, the absorption spectrum of the BCPONI-2Br solution covers the whole UV-vis band, while the one of TCPONI-2Br is further extended to the NIR band, as far as 850 nm. The maximum absorption peak of the TCPONI-2Br solution is 532 nm, which exhibits a 46 nm red-shift compared with BCPONI-2Br (**Figures 5A** and **Table S1**). This bathochromic shift can be ascribed to the enhanced coplanarity and stronger D-A intramolecular interaction between rich-electron thipohene and CPONI moieties. Interestingly, the overwhelmingly electron-deficient feature of the central CPONI acceptor unit endows BCPONI-2Br and TCPONI-2Br with remarkably extended absorption onsets when compared with the well-known acceptor building blocks, such as DPPT-2Br (Gao et al., 2015) and NDIT-2Br (Senkovskyy et al., 2011) (**Figures 5A,B**). In comparison with solution spectra, both BCPONI-2Br and TCPONI-2Br thin films exhibit much broader absorption bands, with the maximum absorption onsets of ca. 750 and 950 nm, respectively. All these results indicate a strong solid-state aggregation or interchain organization, generally associated with high-mobility charge carrier transport (Zhu et al., 2017).

Due to the strong D-A intramolecular interactions (Zhu et al., 2017), all polymers achieve ultra-broadband absorption from UV to NIR (**Figures 5C,D**). Moreover, three typical absorption bands, corresponding to π-π* transition (ca. 350–500 nm) and charge transfer (ca. 500–1,600 nm), were clearly observed in both solution and thin-film spectra. For TCPONI-based polymers, the maximum absorption peaks were 408 nm for P4, 440 nm for P5, and 475 nm for P6 (**Table 2**). Compared with TCPONI-containing analogs, three BCPONI-based polymers exhibit relatively narrower light-capturing bands and sharply blue-shifted π-π* transition peaks, which could be explained by the strong backbone twisting and weak electron-donating ability of benzene moieties. In thin film, the π-π* transition peaks for all polymers display a slight (ca. 2–6 nm) red-shift, while the maximum absorption edges were blue-shifted by ca. 4–56 nm (**Table 2**), indicative of a more planar conformation in their solid-state films (Zhu et al., 2017). Accordingly, all these observations reveal that the absorption and E_g^{opt} of the BCPONI- and TCPONI-containing polymers can be fine-tuned by choosing different donors and π-conjugation linkers. Moreover, the absorption wavelength can be extended easily by increasing the electron-donating ability of the donor units. On the basis of the absorption onsets of polymer films, the E_g^{opt} values were determined to be 1.55 eV for P1, 1.44 eV for P2, 1.20 eV for P3, 1.07 eV for P4, 1.06 eV for P5, and 0.81 for P6. Notably, such ultralow $E_g^{opt} \approx 0.81$ observed here suggests that P6 has a highly

TABLE 2 | Photophysical and electrochemical properties of the Polymers.

Polymer	λ_{max}^{sol}	λ_{onset}^{sol}	λ_{max}^{film}	λ_{onset}^{film}	$\Delta E_g^{opt\ a}$	E_{HOMO}	$E_{onset}^{ox\ b}$	E_{LUMO}	$E_{onset}^{red\ b}$	ΔE_g^{cv}
	(nm)	(nm)	(nm)	(nm)	(eV)	(eV)	(V)	(eV)	(V)	(eV)
P1	330	762	338	798	1.55	−5.78	1.36	−3.79	−0.63	1.99
P2	389	863	390	860	1.44	−5.34	0.92	−3.77	−0.65	1.57
P3	408	1,088	410	1,032	1.20	−5.12	0.70	−3.76	−0.66	1.36
P4	408	1,174	414	1,152	1.07	−5.43	1.01	−3.88	−0.54	1.55
P5	440	1,196	444	1,164	1.06	−5.40	0.98	−3.88	−0.54	1.52
P6	475	1,534	481	1,530	0.81	−4.96	0.54	−3.86	−0.56	1.10

[a]*Optical bandgaps estimated from the onset of film absorption and calculated from* $\Delta E_g^{opt}(eV) = 1,240/\lambda_{onset}^{film}$; [b] E_{onset}^{ox} *and* E_{onset}^{red} *determined from the first onset of oxidation and reduction potentials, respectively.*

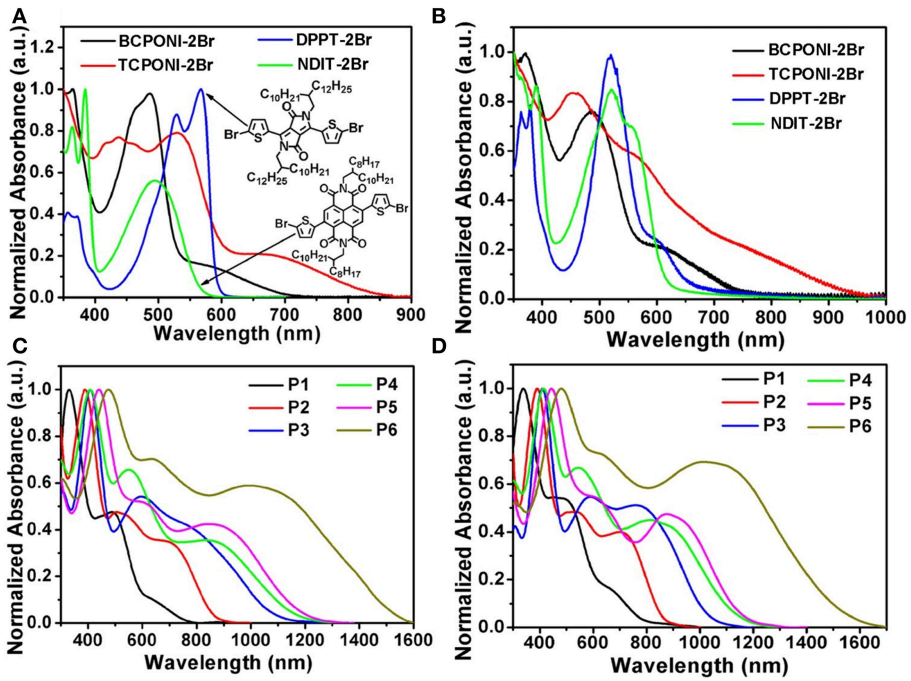

FIGURE 5 | Absorption spectra of the monomers (BCPONI-2Br and TCPONI-2Br), their analogs (DPPT-2Br and NDIT-2Br), and as-synthesized polymers that measured in chloroform solution **(A,C)** and in thin film **(B,D)**.

delocalization of the π-electrons, which can be associated with good backbone coplanarity, large π-conjugation, and strong D-A interaction between donor and CPONI acceptor moieties (Chen et al., 2012; Zhu et al., 2017).

Electrochemical Properties

To evaluate the electrochemical properties of the CPONI-containing monomers and their D-A polymers, CV measurements were performed in both dichloromethane solution and thin film. Detailed CV data are provided in **Table 2**, **Table S1**, and **Figure 6**. The E_{HOMO} and E_{LUMO} levels are calculated from the onset oxidation (E_{onset}^{ox}) and reduction (E_{onset}^{red}) potentials using the following equations: $E_{HOMO} = -(E_{onset}^{ox} + 4.42)$ (eV) and $E_{LUMO} = -(E_{onset}^{red} + 4.42)$ (eV), which is calibrated by ferrocene/ferrocenium (Fc/Fc^+) couple (0.38 V vs. Ag/AgCl) (Chen et al., 2012; Zhu et al., 2017). During positive and negative scans, reversible oxidation, and reduction processes were observed for TCPONI-2Br, while only reduction processes show a reversible feature for BCPONI-2Br (**Figure 6A**). The calculated LUMO and HOMO energy levels of BCPONI-2Br are −3.87 and −5.79 eV, respectively. In comparison with benzene-flanked BCPONI-2Br, thiophene-flanked TCPONI-2Br exhibits a reduced LUMO energy level (−4.02 eV) but an elevated HOMO energy level (−5.63 eV), owing to enhanced molecular coplanarity as well as improved electron-donating ability of thiophene units (Cui and Wudl, 2013). Surprisingly, much deeper LUMO energy levels for both monomers are observed than that of the previously reported acceptor unit DPPT-2Br (LUMO = −3.34 eV) (Gao et al., 2015), and are even comparable to the classical *n*-type

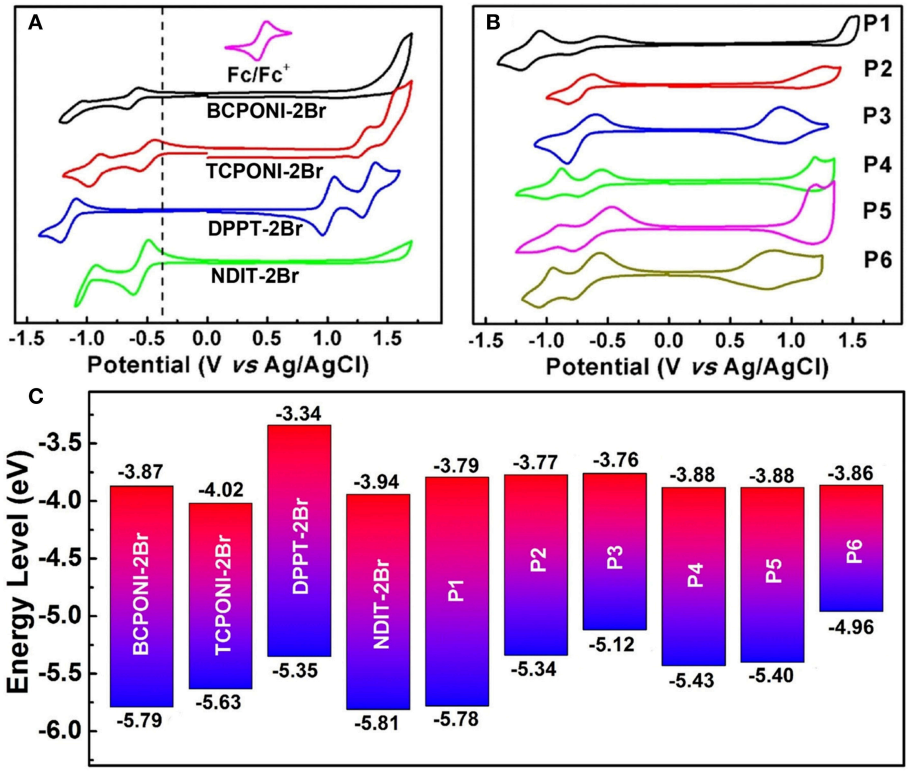

FIGURE 6 | (A) CV curves of the monomers (BCPONI-2Br and TCPONI-2Br), their analogs (DPPT-2Br and NDIT-2Br). **(B)** CV curves of the polymers. **(C)** Comparative diagram for the HOMO and LUMO energy levels.

building block NDIT-2Br (LUMO = −3.94 eV) (Senkovskyy et al., 2011). These results suggest that BCPONI-2Br and TCPONI-2Br are very strong acceptor units, which exhibits great potential in construction of various organic/polymeric electron-transporting materials.

All the polymers P1–P6 exhibit strong and reversible oxidation and reduction processes (**Figure 6B**). The LUMO energy levels of P1–P6, estimated from E_{onset}^{red}, are −3.79 eV for P1, −3.77 eV for P2, −3.76 eV for P3, −3.88 eV for P4, −3.88 eV for P5, and −3.86 eV for P6. As to two type of polymers, their LUMO energy levels show a negligible change with the enhancement of the electron-donating capability of the donor units, while they can be directly influenced by the π-conjugation linkers of both BCPONI-2Br and TCPONI-2Br monomers; therefore, the thiophene-flanked P4–P6 show slightly reduced LUMO energy levels relative to the benzene-flanked analogs (P1–P3). It was found that the HOMO energy levels and band gaps of the polymers can be readily tuned by the selection of different donors. With increasing donor strength, the HOMO energy levels of the polymers will be upshifted, which caused a reduced band gap. Additionally, the electrochemical band gaps (E_g^{cv}) determined here are ca. 0.13–0.48 eV higher than those of their E_g^{opt}. Such a small difference between E_g^{cv} and E_g^{opt} has been reported in many studies (Cui and Wudl, 2013 and Chen et al., 2016) and can be explained by the exciton binding energy of the π-conjugated polymers (Sariciftci, 1997).

OFET Performance and Film Organization

To demonstrate the application potential of the CPONI-based polymers in OFETs, P5 was chosen as an example to fabricate polymer FET devices due to its good backbone coplanarity, proper HOMO/LUMO energy levels, good solubility, and high molecular weight. For the optimization of charge carrier transport performance, both bottom-gate/bottom-contact (BG/BC) and top-gate/bottom-contact (TG/BC) device configurations were used to fabricate polymeric FETs. The detailed device fabrication procedures can be found in the supporting information. Under ambient conditions, P5-based BG/BC OFETs exhibited a typical *p*-type transport characteristic with a moderately high hole mobility of 0.02 $cm^2\ V^{-1}\ s^{-1}$ and current on/off ratio $>10^4$, while only weak electron transport can be observed in both transfer and output curves (**Figures 7A,B**). Considering that the LUMO value (−3.88 eV) of P5 is far from the requirement of thermodynamic stabile electron transport, electrons can be readily captured by H_2O/O_2 in air (Zhan et al., 2011 and Chen et al., 2013). Therefore, only strong hole transport were observed in the P5-based BG/BC OFETs. Due to an effective encapsulation effect of the dielectric layer in TG/BC OFET devices, P5 exhibited an obvious ambipolar transport behavior with both *p*- and *n*-type operation modes for negative and positive gate voltages, respectively. The saturation mobilities were determined to be $4.11\times10^{-3}\ cm^2\ V^{-1}\ s^{-1}$ for holes and $5.15\times10^{-4}\ cm^2\ V^{-1}\ s^{-1}$ for electrons (**Figures 7C–F**).

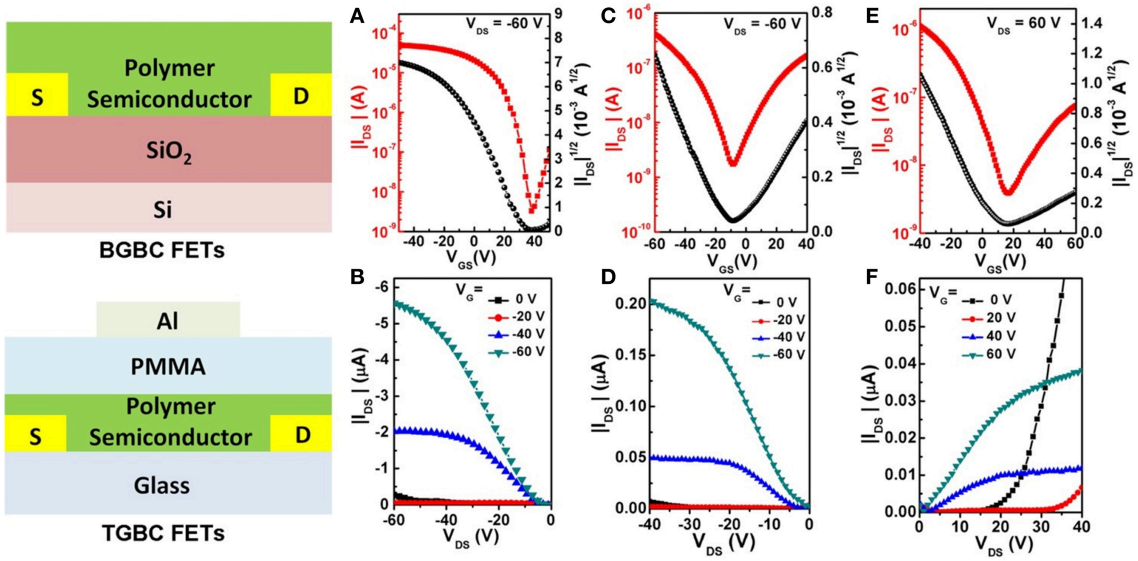

FIGURE 7 | (A) Transfer and **(B)** output curves of the BGBC OFET devices. **(C,E)** Transfer and **(D,F)** output curves of the TGBC OFET devices.

The observed hole and electron mobilities are sufficient for charge carrier transport in potential OPV devices, especially in all-polymer OPVs (Cui and Wudl, 2013). The findings presented above suggest that BCPONI-2Br and TCPONI-2Br are promising building blocks for the construction of polymer electron-transporting materials with attractive electronic properties. To further characterize film organization and surface morphology, AFM and GIXRD measurements were conducted. As seen from **Figure S10A**, the π-π stacking reflection (010) are clearly observed in the q_z direction, indicative of a primarily face-on model packing for the P5 film. This type of stacking model is consistent with the classical NDI-based polymers such as N2200 (Yan et al., 2009). The calculated lamellar stacking distance and π-π stacking distance are around 29.11 and 3.79 Å, which were determined from the (100) and (010) peaks, respectively. Furthermore, P5 film shows a smooth surface microscopy and a very small root-mean-square surface roughness of 0.82 nm (**Figure S10B**), which is helpful for good interface contact between polymer film and dielectric layer (Zhu et al., 2017).

CONCLUSIONS

We have designed and synthesized two novel aromatic imides, diarylcyclopentadienone-fused naphthalimides (BCPONI-2Br and TCPONI-2Br), in which a five-membered cyclopentadienone unit is fused at the lateral position of the naphthalimide skeleton. Compared with both well-known DPPT-2Br and NDIT-2Br building blocks, BCPONI-2Br and TCPONI-2Br exhibit extended absorption bands, narrower band gaps, and even lower LUMO levels, as low as −4.02 eV. Such deep-lying LUMO values enable them to function as the strong acceptors. Furthermore, Stille and Suzuki polycondensation between both novel acceptors and different donors (carbazole, benzodithiophene, and dithienopyrrole) was performed to afford six novel D–A polymers (P1–P6). It was found that optical and electrochemical properties of the polymers are fine-tuned by the variations of donors and π-conjugation linkers. Compared with the BCPONI-containing analogs (P1–P3), the TCPONI-containing P4–P6 exhibit extended absorption bands and deeper LUMO energy levels due to more electron-rich thiophene and more planar π-conjugation skeleton. With an increasing electron-donating ability of the donor units, an extended NIR absorption and an upshifted HOMO levels were observed clearly, while LUMO levels were almost unaffected. The estimated LUMO levels were as low as −3.88 eV, indicating very strong electron affinities for these polymers. Preliminary OFETs results show that P5 exhibits a moderately high hole mobility of 0.02 $cm^2\ V^{-1}\ s^{-1}$ in BGBC OFETs and a typical ambipolar transport behavior in TGBC OFETs. All these observed results suggest that BCPONI-2Br and TCPONI-2Br units are very strong and interesting acceptor building blocks for the creation of various low bandgap π-conjugated materials, especially for electron-transporting polymers. These polymers could be functioned as the electron acceptor materials in all-polymer solar cells or other optoelectronic devices.

DATA AVAILABILITY

All datasets generated for this study are included in the manuscript and/or the **Supplementary Files**.

AUTHOR CONTRIBUTIONS

HC and XL designed, synthesized, and characterized polymeric semiconductors. JG, LY, YH, and YZ measured OFET devices. LZ conducted the CV experiments. ZM performed DFT calculations. All authors were responsible for discussing the results. HC designed experiments and wrote the manuscript.

FUNDING

National Natural Science Foundation of China (21875202, 61804051, 61890941), the Hunan Provincial Natural Science Foundation of China (2018JJ1024), the Science and Technology Planning Project of Hunan Province (2017RS3048), and the Research Foundation of Education Bureau of Hunan Province (17B253).

ACKNOWLEDGMENTS

The authors acknowledge Prof. Zebing Zeng (Hunan University) for his assistance in UV-Vis-NIR absorption measurements. This work was financially supported by the National Natural Science Foundation of China (21875202, 61804051, 61890941), the Hunan Provincial Natural Science Foundation of China (2018JJ1024), the Science and Technology Planning Project of Hunan Province (2017RS3048), and the Research Foundation of Education Bureau of Hunan Province (17B253).

SUPPLEMENTARY MATERIAL

The Supplementary Material for this article can be found online at: https://www.frontiersin.org/articles/10.3389/fchem.2019.00362/full#supplementary-material

REFERENCES

Cai, Z., Zhao, D., Sharapov, V., Awais, M. A., Zhang, N., Chen, W., et al. (2018). Enhancement in open-circuit voltage in organic solar cells by using ladder-type nonfullerene acceptors. *ACS Appl. Mater. Interfaces* 10, 13528–13533. doi: 10.1021/acsami.8b01308

Cai, Z. X., Vázquez, R. J., Zhao, D. L., Li, L. W., Lo, W., Zhang, N., et al. (2017). Two photon absorption study of low-bandgap, fully conjugated perylene diimide-thienoacene-perylene diimide ladder-type molecules. *Chem. Mater.* 29, 6726–6732. doi: 10.1021/acs.chemmater.7b01512

Chen, H., Liu, Z., Zhao, Z., Zheng, L., Tan, S., and Yin, Z. (2016). Synthesis, structural characterization, and field-effect transistor properties of n-channel semiconducting polymers containing five-membered heterocyclic acceptors: superiority of thiadiazole compared with oxadiazole. *ACS Appl. Mater. Interfaces* 8, 33051–33059. doi: 10.1021/acsami.6b12540

Chen, H. J., Guo, Y. L., Yu, G., Zhao, Y., Zhang, J., and Gao, D. (2012). Highly π-extended copolymers with diketopyrrolopyrrole moieties for high-performance field-effect transistors. *Adv. Mater. Weinheim.* 24, 4618–4622. doi: 10.1002/adma.201201318

Chen, X., Guo, Y. L., Tan, L. X., Yang, G., Li, Y. H., Zhang, G. X., et al. (2013). Dithiazole-fused naphthalene diimides toward new n-type semiconductors. *J. Mater. Chem. C* 1, 1087–1092. doi: 10.1039/C2TC00308B

Cheng, Y.-J., Yang, S.-H., and Hsu, C.-S. (2009). Synthesis of conjugated polymers for organic solar cell applications. *Chem. Rev.* 109, 5868–5923. doi: 10.1021/cr900182s

Choi, H., Paek, S., Song, J., Kim, C., Cho, N., and Ko, J. (2011). Synthesis of annulated thiophene perylene bisimide analogues: their applications to bulk heterojunction organic solar cells. *Chem. Commun.* 47, 5509–5511. doi: 10.1039/c0cc05448h

Cui, W. B., and Wudl, F. (2013). Dithienylbenzodipyrrolidone: new acceptor for donor–acceptor low band gap polymers. *Macromolecules* 46, 7232–7238. doi: 10.1021/ma400008h

Ding, L., Yang, C. Y., Su, Z. M., and Pei, J. (2015). Synthesis, crystal structure, and application of an acenaphtho[1,2-*k*]fluoranthene diimide derivative. *Sci. China Chem.* 58, 364–369. doi: 10.1007/s11426-014-5282-9

Dou, L., Liu, Y., Hong, Z., Li, G., and Yang, Y. (2015). Low-bandgap near-IR conjugated polymers/molecules for organic electronics. *Chem. Rev.* 115, 12633–12665. doi: 10.1021/acs.chemrev.5b00165

Fei, Z. P., Han, Y., Martin, J., Scholes, F. H., Al-Hashimi, M., AlQaradawi, S. Y., et al. (2016). Conjugated copolymers of vinylene flanked naphthalene diimide. *Macromolecules* 49, 6384–6393. doi: 10.1021/acs.macromol.6b01423

Fukutomi, Y., Nakano, M., Hu, J. Y., Osaka, I., and Takimiya, K. (2013). Naphthodithiophenediimide (NDTI): synthesis, structure, and applications. *J. Am. Chem. Soc.* 135, 11445–11448. doi: 10.1021/ja404753r

Gao, Y., Deng, Y. F., Tian, H., Zhang, J., Yan, D., and Geng, Y. (2017). Multifluorination toward high-mobility ambipolar and unipolar n-type donor-acceptor conjugated polymers based on isoindigo. *Adv. Mater. Weinheim.* 29:1606217. doi: 10.1002/adma.201606217

Gao, Y., Zhang, X., Tian, H., Zhang, J., Yan, D., and Geng, Y. (2015). High mobility ambipolar diketopyrrolopyrrole-based conjugated polymer synthesized via direct arylation polycondensation. *Adv. Mater. Weinheim.* 27, 6753–6759. doi: 10.1002/adma.201502896

Gong, X., Tong, M., Xia, Y., Cai, W., Moon, J. S., Cao, Y., et al. (2009). High-detectivity polymer photodetectors with spectral response from 300 nm to 1450 nm. *Science* 325, 1665–1667. doi: 10.1126/science.1176706

Grimsdale, A. C., Chan, K. L., Martin, R. E., Jokisz, P. G., and Homlmes, A. B. (2009). Synthesis of light-emitting conjugated polymers for applications in electroluminescent devices. *Chem. Rev.* 109, 897–1091. doi: 10.1021/cr000013v

Guo, X. G., Facchetti, A., and Marks, T. J. (2014). Imide- and amide-functionalized polymer semiconductors. *Chem. Rev.* 114, 8943–9021. doi: 10.1021/cr500225d

Guo, X. G., and Watson, M. D. (2008). Conjugated polymers from naphthalene bisimide. *Org. Lett.* 10, 5333–5336. doi: 10.1021/ol801918y

Guo, X. G., and Watson, M. D. (2011). Pyromellitic diimide-based donor-acceptor poly(phenyleneethynylene)s. *Macromolecules* 44, 6711–6716. doi: 10.1021/ma2009063

Guo, Y. K., Awartani, O., Han, H., Zhao, J. B., Ade, H., Yan, H., et al. (2017). Improved performance of all-polymer solar cells enabled by naphthodiperylenetetraimide-based polymer acceptor. *Adv. Mater. Weinheim.* 29:1700309. doi: 10.1002/adma.201700309

Hendriks, K. H., Heintges, G. H. L., Gevaerts, V. S., Wienk, M. W., and Janssen, R. A. J. (2013). High-molecular-weight regular alternating diketopyrrolopyrrole-based terpolymers for efficient organic solar cells. *Angew. Chem. Int. Ed.* 52, 8341–8344. doi: 10.1002/anie.201302319

Hu, Y. Y., Jiang, L., Chen, Q. J., Guo, J., and Chen, Z. J. (2018). Direct observation of the dipole-induced energetic disorder in rubrene single-crystal transistors by scanning kelvin probe microscopy. *J. Phys. Chem. Lett.* 9, 2869–2873. doi: 10.1021/acs.jpclett.8b01274

Hwang, Y. J., Kim, F. S., Xin, H., and Jenekhe, S. A. (2012). New thienothiadiazole-based conjugated copolymers for electronics and optoelectronics. *Macromolecules* 45, 3732–3739. doi: 10.1021/ma3000797

Ishikawa, H., Katayama, K., Nishida, J., Kitamura, C., and Kawase, T. (2018). Fluoranthene and its π-extended diimides: construction of new electron acceptors. *Tetrahedron Lett.* 59, 3782–3786. doi: 10.1016/j.tetlet.2018.09.012

Kim, J., Yun, M., Anant, P., Cho, S., Jacob, J., Kim, J. Y., et al. (2011). Copolymers comprising 2,7-carbazole and bis-benzothiadiazole units for bulk-heterojunction solar cells. *Chem. Eur. J.* 17, 14681–14688. doi: 10.1002/chem.201101258

Lei, T., Fan, Y. L., Liu, C. J., Yuan, S. C., and Pei, J. (2011). High-performance air-stable organic field-effect transistors: isoindigo-based conjugated polymers. *J. Am. Chem. Soc.* 133, 6099–6101. doi: 10.1021/ja111066r

Li, H. Y., Kim, F. S., Ren, G. Q., Hollenbeck, E. C., Subramaniyan, S., and Jenekhe, S. A. (2013b). Tetraazabenzodifluoranthene diimides: building blocks for solution-processable n-type organic semiconductors. *Angew. Chem. Int. Ed.* 52, 5513–5517. doi: 10.1002/anie.201210085

Li, H. Y., Kim, F. S., Ren, G. Q., and Jenekhe, S. A. (2013a). High-mobility n-type conjugated polymers based on electron-deficient tetraazabenzodifluoranthene

diimide for organic electronics. *J. Am. Chem. Soc.* 135, 14920–14923. doi: 10.1021/ja407471b

Li, W. W., Hendriks, K. H., Furlan, A., Roelofs, C., Wienk, M. M., and Janssen, R. A. J. (2013c). Universal correlation between fibril width and quantum efficiency in diketopyrrolopyrrole-based polymer solar cells. *J. Am. Chem. Soc.* 135, 18942–18948. doi: 10.1021/ja4101003

Li, Y. N., Sonar, P., Singh, S. P., Soh, M. S., van Meurs, M., and Tan, J. (2011). Annealing-free high-mobility diketopyrrolopyrrole-quaterthiophene copolymer for solution-processed organic thin film transistors. *J. Am. Chem. Soc.* 133, 2198–2204. doi: 10.1021/ja1085996

Li, Z. J., Xu, X. F., Zhang, W., Meng, X. Y., Ma, W., Yartsev, A., et al. (2016). High performance all-polymer solar cells by synergistic effects of fine-tuned crystallinity and solvent annealing. *J. Am. Chem. Soc.* 138, 10935–10944. doi: 10.1021/jacs.6b04822

Li, Z. Y., Ying, L., Zhu, P., Zhong, W. K., Li, N., Liu, F., et al. (2019). A generic green solvent concept boosting the power conversion efficiency of all-polymer solar cells to 11%. *Energy Environ. Sci.* 12, 157–163. doi: 10.1039/C8EE02863J

Mei, C. Y., Liang, L., Zhao, F. G., Wang, J. T., Yu, L. F., Li, Y. X., et al. (2013). A family of donor-acceptor photovoltaic polymers with fused 4,7-dithienyl-2,1,3-benzothiadiazole units: effect of structural fusion and side chains. *Macromolecules* 46, 7920–7931. doi: 10.1021/ma401298g

Mei, J. G., Kim, D. H., Ayzner, A. L., Toney, M. F., and Bao, Z. N. (2011). Siloxane-terminated solubilizing side chains: bringing conjugated polymer backbones closer and boosting hole mobilities in thin-film transistors. *J. Am. Chem. Soc.* 133, 20130–20133. doi: 10.1021/ja209328m

Sariciftci, N. S. (1997). *Primary Photoexcitations in Conjugated Polymers: Molecular Excitons vs Semiconductor Band Model*. Singapore: World Scientific. doi: 10.1142/3299

Senkovskyy, V., Tkachov, R., Komber, H., Sommer, M., Heuken, M., Voit, B., et al. (2011). Chain-growth polymerization of unusual anion-radical monomers based on naphthalene diimide: a new route to well-defined n-type conjugated copolymers. *J. Am. Chem. Soc.* 133, 19966–19970. doi: 10.1021/ja208710x

Stalder, R., Mei, J. G., and Reynolds, J. R. (2010). Isoindigo-based donor–acceptor conjugated polymers. *Macromolecules* 43, 8348–8352. doi: 10.1021/ma1018445

Usta, H., Newman, C., Chen, Z. H., and Facchetti, A. (2012). Dithienocoronenediimide-based copolymers as novel ambipolar semiconductors for organic thin-film transistors. *Adv. Mater. Weinheim.* 24, 3678–3684. doi: 10.1002/adma.201201014

Walker, W., Veldman, B., Chiechi, R., Patil, S., Bendikov, M., and Wudl, F. (2008). Visible and near-infrared absorbing, low band gap conjugated oligomers based on cyclopentadieneones. *Macromolecules* 41, 7278–7280. doi: 10.1021/ma8004873

Wang, Y., Hasegawa, T., Matsumoto, H., and Michinobu, T. (2019). Significant improvement of unipolar n-type transistor performances by manipulating the coplanar backbone conformation of electron-deficient polymers via hydrogen bonding. *J. Am. Chem. Soc.* 141, 3566–3575. doi: 10.1021/jacs.8b12499

Yan, H., Chen, Z. H., Zheng, Y., Newman, C., Quinn, J. R., Dotz, F., et al. (2009). A high-mobility electron-transporting polymer for printed transistors. *Nature* 457, 679–686. doi: 10.1038/nature07727

Yang, C. D., Cho, S., Chiechi, R. C., Walker, W., Coates, N. E., Moses, D., et al. (2008). Visible-near infrared absorbing dithienylcyclopentadienone-thiophene copolymers for organic thin-film transistors. *J. Am. Chem. Soc.* 130, 16524–16526. doi: 10.1021/ja806784e

Yang, J., Zhao, Z. Y., Wang, S., Guo, Y. L., and Liu, Y. Q. (2018). Insight into high-performance conjugated polymers for organic field-effect transistors. *Chem* 4, 2748–2785. doi: 10.1016/j.chempr.2018.08.005

Zhan, X. W., Facchetti, A., Barlow, S., Marks, T. J., Ratner, M. A., Wasielewski, M. R., et al. (2011). Rylene and related diimides for organic electronics. *Adv. Mater. Weinheim.* 23, 268–284. doi: 10.1002/adma.201001402

Zhan, X. W., Tan, Z. A., Domercq, B., An, Z. S., Zhang, X., Barlow, S., et al. (2007). A high-mobility electron-transport polymer with broad absorption and its use in field-effect transistors and all-polymer solar cells. *J. Am. Chem. Soc.* 129, 7246–7247. doi: 10.1021/ja071760d

Zhang, X., Steckler, T. T., Dasari, R. R., Ohira, S., Potscavage, W. J., Tiwari, J. S. P., et al. (2010). Dithienopyrrole-based donor–acceptor copolymers: low band-gap materials for charge transport, photovoltaics and electrochromism. *J. Mater. Chem.* 20, 123–134. doi: 10.1039/B915940A

Zhao, Y., Zhao, X. K., Zang, Y. P., Di, C. A., Diao, Y., and Mei, J. G. (2015). Conjugation-break spacers in semiconducting polymers: impact on polymer processability and charge transport properties. *Macromolecules* 48, 2048–2053. doi: 10.1021/acs.macromol.5b00194

Zhao, Z. Y., Yin, Z. H., Chen, H. J., Zheng, L. P., Zhu, C. G., Zhang, L., et al. (2017). High-performance, sir-stable field-effect transistors based on heteroatom-substituted naphthalenediimide-benzothiadiazole copolymers exhibiting ultrahigh electron mobility up to 8.5 cm^2 V^{-1} s^{-1}. *Adv. Mater. Weinheim.* 29:1602410. doi: 10.1002/adma.201602410

Zhou, W. Y., Jin, F., Huang, X. B., Duan, X. M., and Zhan, X. W. (2012). A low-bandgap conjugated copolymer based on porphyrin and dithienocoronene diimide with strong two-photon absorption. *Macromolecules* 45, 7823–7828. doi: 10.1021/ma3015257

Zhu, C. G., Zhao, Z. Y., Chen, H. J., Zheng, L. P., Li, X. L., Chen, J. Y., et al. (2017). Regioregular bis-pyridal[2,1,3]thiadiazole-based semiconducting polymer for high-performance ambipolar transistors. *J. Am. Chem. Soc.* 139, 17735–17738. doi: 10.1021/jacs.7b10256

Zou, Y. P., Gendron, D., Neagu-Plesu, R., and Leclerc, M. (2009). Synthesis and characterization of new low-bandgap diketopyrrolopyrrole-based copolymers. *Macromolecules* 42, 6361–6365. doi: 10.1021/ma901114j

Conflict of Interest Statement: The authors declare that the research was conducted in the absence of any commercial or financial relationships that could be construed as a potential conflict of interest.

frontiers in Chemistry

ORIGINAL RESEARCH
published: 31 May 2019
doi: 10.3389/fchem.2019.00383

N-Centered Chiral Self-Sorting and Supramolecular Helix of Tröger's Base-Based Dimeric Macrocycles in Crystalline State

Yuan Chen[1], *Ming Cheng*[1], *Benkun Hong*[1], *Qian Zhao*[1], *Cheng Qian*[1], *Juli Jiang*[1]*, *Shuhua Li*[1], *Chen Lin*[1]* and *Leyong Wang*[1,2]

[1] Key Laboratory of Mesoscopic Chemistry of MOE, Jiangsu Key Laboratory of Advanced Organic Materials, School of Chemistry and Chemical Engineering, Nanjing University, Nanjing, China, [2] School of Petrochemical Engineering, Changzhou University, Changzhou, China

Three stereoisomers of Tröger's Base-based dimeric macrocycles Trögerophane **1** (**T1**) including one pair of enantiomers (***rac*-T1**) and one meso isomer (***R*$_{2N}$*S*$_{2N}$-T1**) were obtained and fully characterized by X-ray analysis. In the crystalline stacking state ***R*$_{2N}$*S*$_{2N}$-T1** showed heterochiral self-sorting behavior along *a* axis with cofacial π-π stacking interactions, while ***rac*-T1** showed heterochiral self-sorting behavior along *c* axis with slipped π-π stacking interactions, respectively. Meanwhile both of them showed homochiral self-sorting behavior along *b* axis as well as one pair of supramolecular helixes were formed in both cases. All the self-sorting behaviors are controlled by two chiral Tröger's Base units from neighboring molecules. To the best of our knowledge, such chiral self-sorting and supramolecular helixes of *N*-centered chiral superstructures is a rare example. In addition, ***R*$_{2N}$*S*$_{2N}$-T1** and ***rac*-T1** demonstrated different adsorption capacities toward the vapor of dichloromethane and acetone, respectively.

Keywords: tröger's base, chiral self-sorting, supramolecular helix, gas adsorption, *N*-centered chirality

OPEN ACCESS

Edited by:
Penglei Chen,
Institute of Chemistry (CAS), China

Reviewed by:
Chunju Li,
Tianjin Normal University, China
Jean-Claude Chambron,
Centre National de la Recherche Scientifique (CNRS), France
Remi Chauvin,
Université de Toulouse, France

***Correspondence:**
Juli Jiang
jjl@nju.edu.cn
Chen Lin
linchen@nju.edu.cn

Specialty section:
This article was submitted to Supramolecular Chemistry, a section of the journal Frontiers in Chemistry

Received: *27 February 2019*
Accepted: *13 May 2019*
Published: *31 May 2019*

Citation:
Chen Y, Cheng M, Hong B, Zhao Q, Qian C, Jiang J, Li S, Lin C and Wang L (2019) N-Centered Chiral Self-Sorting and Supramolecular Helix of Tröger's Base-Based Dimeric Macrocycles in Crystalline State. Front. Chem. 7:383. doi: 10.3389/fchem.2019.00383

INTRODUCTION

Chirality is ubiquitous in the abundant forms of fundamental and crucial processes to create well-order functional structures (Liu et al., 2015; Xing and Zhao, 2018) from natural chiral products amino acid, carbohydrate, nucleic acids, to biomacromolecules of proteins, DNA double helix, to macroscopic systems of chiral crystals, and even to the spiral nebulae of the macroscopic universe.

Chiral self-sorting (Jedrzejewska and Szumna, 2017; Shang et al., 2018) is known as one of self-sorting (Safont-Sempere et al., 2011; Imai et al., 2019) behaviors, in which chirality is one of key differentiating factors for the selectivity of self-assembly. In general, chiral self-sorting is classified as chiral self-recognition or chiral self-discrimination based on the chiral recognization (Chen et al., 2015) by itself or the mirror image of enantiomer, resulting in the formation of homochiral (Makiguchi et al., 2015) or heterochiral species (Yao et al., 2016), respectively. Homochiral self-sorting commonly occurs during the breaking of the symmetry in racemic mixtures, and it is mainly found in (i) conglomerates during crystallization from solution to generate homochirality at the single-crystal scale, (ii) self-assembly on solid surfaces, and (iii) other higher-order functional structures. Compared with homochiral self-sorting, heterochiral systems are mostly relied on the mixture of enantiomers.

Currently, most of chiral self-sorting behaviors occured in the simple molecular system and even in the supramolecular self-assembly (Yashima et al., 2016) were based on *carbon stereogenic factor*. To the best of our knowledge, few studies have been attempted to elucidate chiral self-sorting properties based on *nitrogen stereogenic factor* so far, although *nitrogen stereogenic factor*, particularly *nitrogen stereogenic center* was one of the important sources of chirality (Slater et al., 2016; Feng et al., 2018). In order to understand broadly and deeply chiral behaviors: chiral recognition, chiral amplification, and chiral transmission, it was significant to fabricate chiral system possessing *nitrogen stereogenic factors*.

Along this line of consideration, Tröger's Base (TB) fell in our sights as the candidate. In 1887, Tröger first discovered the reaction of *p*-toluidine with formaldehyde in hydrochloric acid, and the product base was characterized as a white solid with the formula $C_{17}H_{18}N_2$. After research by Spielman, Reed, and other researchers, this base was identified as TB (Dolenský et al., 2012). In TB structure, its V-shaped structure and rigid conformation make it be a useful building block to construct various functional architectures in diverse areas such as catalysis (Du et al., 2010), molecular recognition (Shanmugaraju et al., 2017), optical materials (Neogi et al., 2015), and polymer membranes (Yang et al., 2016). In particular, TB unit is an inherently C_2-symmetric chiral compound as a classical example of *nitrogen stereogenic centers* with two *N*-centered chiral units due to the bridged methylene groups of diazocine nitrogen atoms, which prevents the inversion of the configuration around the stereogenic nitrogen atoms.

Since the birth of supramolecular chemistry, a large number of macrocycles (Cantrill et al., 1999; Ogoshi et al., 2016; Liu et al., 2017; Wu et al., 2017; Li et al., 2019) have been constructed and widely used in molecular machines (Erbas-Cakmak et al., 2015), interlocked structures (Akae et al., 2018), supramolecular catalysis (Blanco et al., 2015; Palma et al., 2017), gas adsorption (Li et al., 2018), adsorptive separation (Jie et al., 2018), and smart materials (Qu et al., 2015; Guo et al., 2018). However, the majority of synthetic macrocycles are bridged from repeating achiral functional units, which limit their applications in the chiral fields. Therefore, the efficient and convenient synthesis of covalent organic macrocycles bearing chiral units, typically with *N*-centered chiral TB units, is needed urgently (Weilandt et al., 2009).

TB-based dimeric macrocycles Trögerophane **1** (**T1**) with bridged oligoethylene glycol (OEG) between two TB units was reported in this work. The rectangular-like **T1** possessed four chiral nitrogen centers, and theoretically, should be a mixture of three stereoisomers: one pair of enantiomers and one meso isomer due to the fixed chirality of TB units ($\boldsymbol{R}_N$, $\boldsymbol{R}_N$ and $\boldsymbol{S}_N$, $\boldsymbol{S}_N$) in the macrocycle. In 1998, Inazu (Brahim et al., 1998) reported the synthesis of **T1** with very low yield (< 3.0%) in more than 10 days and stereoisomers of **T1** were not recognized correctly. In our research, three stereoisomers of **T1**: one pair of enantiomers ($\boldsymbol{R}_N$, $\boldsymbol{R}_N$, $\boldsymbol{R}_N$, $\boldsymbol{R}_N$)-**T1**(denoted as $\boldsymbol{R}_{4N}$-**T1**) or ($\boldsymbol{S}_N$, $\boldsymbol{S}_N$, $\boldsymbol{S}_N$, $\boldsymbol{S}_N$)-T1 (denoted as $\boldsymbol{S}_{4N}$-***T1***) and one meso isomer ($\boldsymbol{R}_N$, $\boldsymbol{R}_N$, $\boldsymbol{S}_N$, $\boldsymbol{S}_N$)-**T1**(denoted as $\boldsymbol{R}_{2N}\boldsymbol{S}_{2N}$-**T1**) were successfully synthesized, separated and characterized by X-ray analysis undoubtedly for the first time.

More interestingly, the obtained racemate crystals ***rac*-T1** showed the heterochiral self-sorting along *c* axis with slipped π-π stacking interactions and the homochiral self-sorting along *b* axis forming supramolecular *P*/*M* helix by each single enantiomer, respectively. However, either pure enantiomer $\boldsymbol{R}_{4N}$-**T1** or $\boldsymbol{S}_{4N}$-**T1** could not form supramolecular *P*/*M* helix in crystal state. Surprisingly, **T1** meso isomer, $\boldsymbol{R}_{2N}\boldsymbol{S}_{2N}$-**T1**, also showed heterochiral self-sorting behavior along *a* axis with cofacial π-π stacking interactions in crystal state, while homochiral self-sorting behavior was observed along *b* axis and supramolecular *P*/*M* helixes were formed although **T1** meso isomer itself is an achiral molecule. All the self-sorting behaviors occurred between two TB units from neighboring molecules and were controlled by the chirality of Tröger's Base units involved.

EXPERIMENTAL

Synthesis and Compound Characterization

As shown in (**Scheme 1**), **T1** was synthesized from nitroaromatic compound **3**, which was reduced to amine **2**. Then, amine **2** was reacted with 1.5 *equiv*. of paraformaldehyde and trifluoroacetic acid as the solvent under an inert atmosphere over 48 h at the ambient temperature. The resulting reaction mixture was basified (pH >10) using *aq*. NH_3 and then extracted by dichloromethane, which gave the target dimeric macrocycle **T1** in 13% yield. A combination of ^{1}H and ^{13}C nuclear magnetic resonance spectroscopy (NMR) and high-resolution mass spectrometry (HRMS) confirmed (**Figures S1–S3**) the formation of **T1**. The other isolated by-products could be some oligomers or polymers due to the broad peaks observed in the ^{1}H NMR spectra.

Isomer Separation and Circular Dichroism Spectrum

The investigation of the stereoisomer structures of **T1** was conducted further by injecting **T1** solution into a chiral

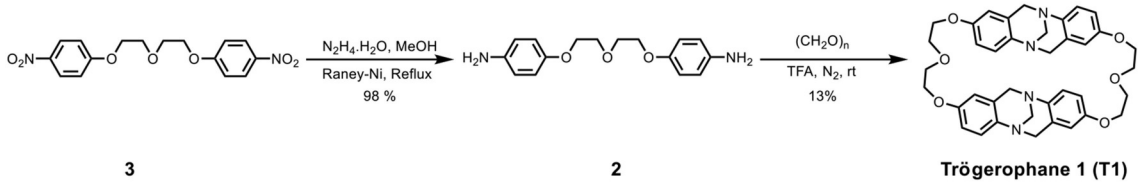

SCHEME 1 | Synthetic route to Trögerophane **1 (T1).**

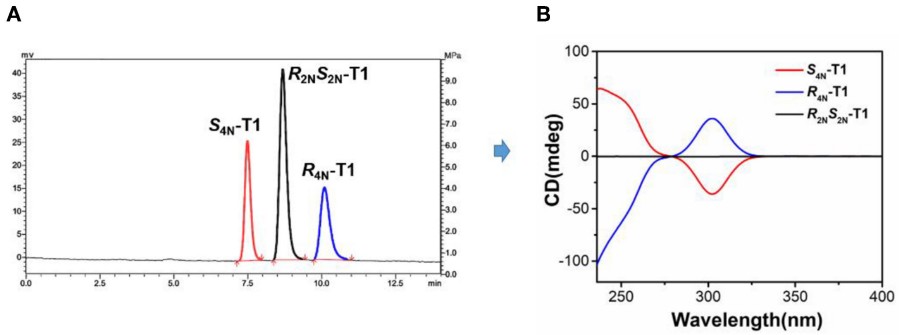

FIGURE 1 | (A) Resolution of stereoisomers of **T1** by a chiral HPLC (fractions of S_{4N}**-T1**, $R_{2N}S_{2N}$**-T1**, and R_{4N}**-T1** from *left* to *right*). **(B)** CD spectra of S_{4N}**-T1** (0.01 mM, *red*), $R_{2N}S_{2N}$**-T1** (0.01 mM, *black*), and R_{4N}**-T1** (0.01 mM, *blue*) in CH_2Cl_2.

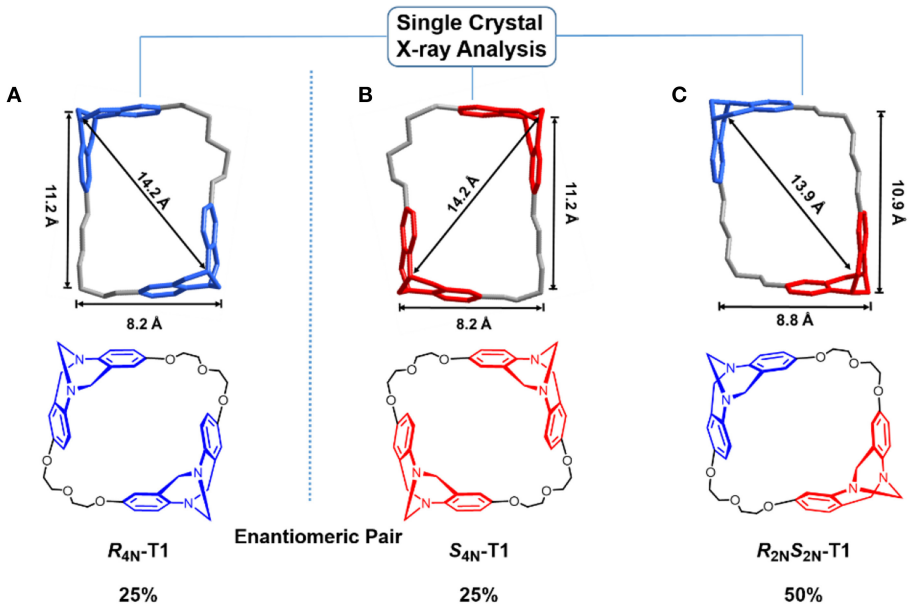

FIGURE 2 | Crystal structures of enantiopure R_{4N}**-T1 (A)**, enantiopure S_{4N}**-T1 (B)**, and $R_{2N}S_{2N}$-T1 **(C)** assigned to corresponding chemical structures of stereoisomers. TB units with $S_NS_N$is depicted in red, while TB units with R_NR_N is shown in blue.

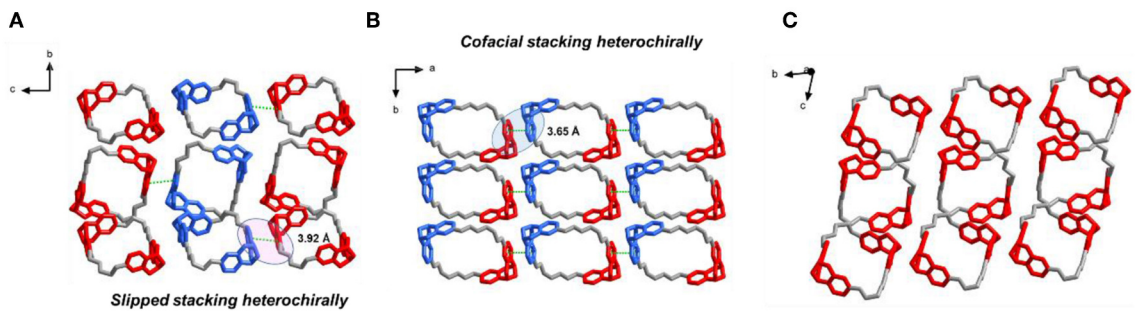

FIGURE 3 | Solid-state (super)structures of $R_{2N}S_{2N}$**-T1**, ***rac*-T1**, and S_{4N}**-T1** obtained from single-crystal X-ray crystallography. **(A)** Slipped π-π stacking between R_{4N}**-T1** and S_{4N}**-T1** molecules observed in ***rac*-T1** crystal packing (*left*). **(B)** Cofacial π-π stacking between two $R_{2N}S_{2N}$**-T1** molecules observed in crystal packing (*middle*). **(C)** Solid-state (super)structures of S_{4N}**-T1** molecules observed in crystal packing (*right*). TB units with S_NS_N are depicted in red, while TB units with R_NR_N are shown in blue.

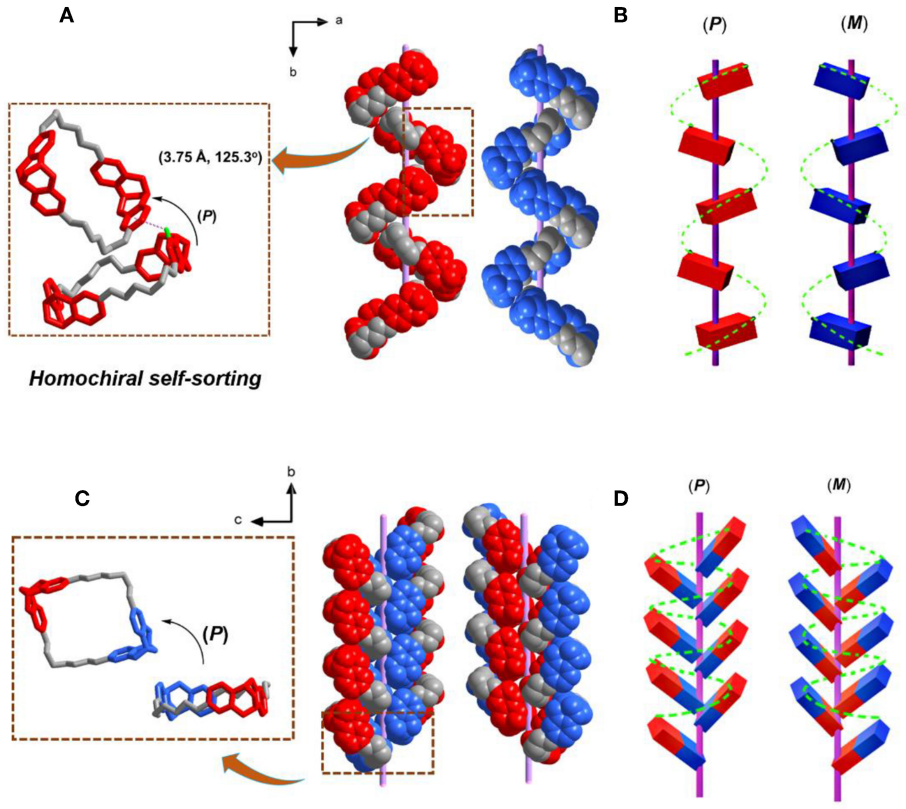

FIGURE 4 | Single-crystal (super)structure of the single helix formed on crystallization of ***rac*-T1** and $\boldsymbol{R_{2N}S_{2N}}$**-T1**, respectively. **(A)** Solid-state superstructure of the complementary (*P*) and (*M*)-single helixes formed separately from the enantiomeric $\boldsymbol{S_{4N}}$**-T1** and $\boldsymbol{R_{4N}}$**-T1**, respectively. **(B)** The corresponding single helixes of $\boldsymbol{S_{4N}}$**-T1** are depicted in red, while the corresponding single helixes of $\boldsymbol{R_{4N}}$**-T1** are shown in blue. **(C)** Solid-state superstructure of the complementary (*P*) and *M*-single helixes formed separately from the enantiomeric $\boldsymbol{R_{2N}S_{2N}}$**-T1**, **(D)** the corresponding single helixes of $\boldsymbol{R_{2N}S_{2N}}$**-T1**. Note: TB units with $\boldsymbol{S_NS_N}$ is depicted in red, while TB units with $\boldsymbol{R_NR_N}$ is shown in blue. For clarity, the solvent molecules inside were also omitted.

HPLC column, and three isolated peaks were observed clearly (**Figure 1A**). The HPLC spectrum exhibited three single peaks with the mole ratio of 1:2:1, which was well in accord with three types of stereoisomers of **T1**, one pair of enantiomers $\boldsymbol{R_{4N}}$**-T1**, $\boldsymbol{S_{4N}}$**-T1**, and one meso isomer $\boldsymbol{R_{2N}S_{2N}}$**-T1**. Then, these three fractions were collected separately as the single isolated pure stereoisomer for the study of circular dichroism (CD) spectroscopy. The CD spectrum of one of stereoisomers corresponding to the first fraction of HPLC spectrum exhibited a strong negative CD signal at 304 nm, and one of stereoisomers corresponding to the third fraction of HPLC spectrum exhibited a mirror spectrum with positive CD signals at the same wavelength, while another stereoisomer corresponding to the second fraction of HPLC spectrum showed no active Cotton effects in CD spectrum. Experimental results given by HPLC and CD indicated that the second fraction should be assigned to the meso structure (**Figure 1B**). As a result, **T1** can be confirmed experimentally as the mixture of three stereoisomers with the mole ratio of 1:1:2 of a pair of enantiomers of $\boldsymbol{R_{4N}}$**-T1**, $\boldsymbol{S_{4N}}$**-T1**, and one meso isomer $\boldsymbol{R_{2N}S_{2N}}$**-T1**, respectively.

Crystal Structure Analysis

Single crystals of $\boldsymbol{S_{4N}}$**-T1**, $\boldsymbol{R_{2N}S_{2N}}$**-T1**, and $\boldsymbol{R_{4N}}$**-T1** suitable for X-ray diffraction were obtained from each isolated pure fraction of the preparative chiral HPLC colunm fortunately (For details see **Tables S1–S4**). In the crystal of $\boldsymbol{R_{2N}S_{2N}}$**-T1**, the cavity size as defined by the distance between two bridged methylene carbons is 13.9 Å in diagonal length, and the distance from the centroid of the benzene rings to the opposite bridged methylene carbon is 10.9 Å and 8.8 Å, respectively. For each crystal of enantiopure $\boldsymbol{S_{4N}}$**-T1** or enantiopure $\boldsymbol{R_{4N}}$**-T1**, the distance between two bridged methylene carbons is 14.2 Å, with average dimensions of 11.2 × 8.2 $Å^2$. As shown in (**Figure 2**), all the three stereoisomers have rare rectangle-like shapes with four *nitrogen stereogenic centers* and relatively big cavities (>1 nm).

Slow evaporation of a solution of T1 in acetone/diisopropyl ether 1:1 afforded X-ray quality crystals of the racemate. Analysis of the packing of the enantiomers of T1 allowed us to understand how enantiomer segregation takes place. In the crystal of ***rac*-T1**, two neighboring enantiomers stacked *via* a slipped π-π interaction along *c* axis with the distance 3.92 Å, and showed heterochiral self-sorting behaviors ($\boldsymbol{R_NR_N}$-*to*-$\boldsymbol{S_NS_N}$) between two TB units from neighboring molecules (**Figure 3A**). Compared

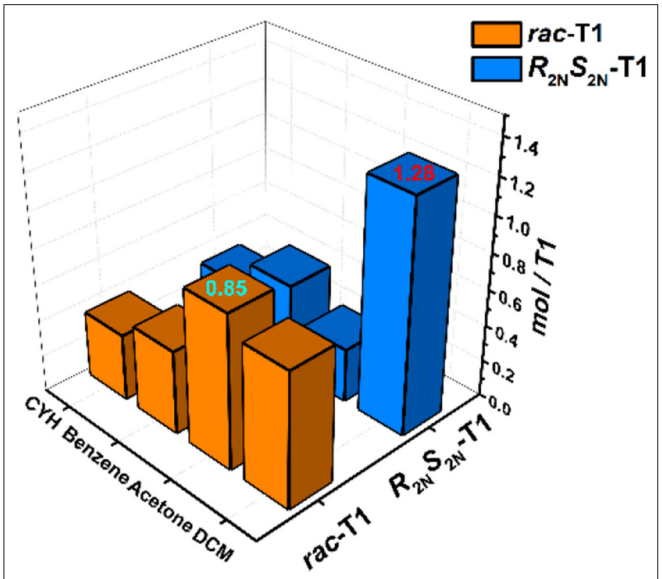

FIGURE 5 | Gas adsorption experiments in ***rac*-T1** or $R_{2N}S_{2N}$-T1 with dichloromethane (DCM), acetone, cyclohexane, benzene, respectively.

with the crystal of ***rac*-T1**, in the crystal of the meso isomer achiral $R_{2N}S_{2N}$-**T1** molecules are arranged in such a way that cofacial π-π stacking interactions between neighboring molecules in the *a* direction involve TB subunits of opposite chirality (**Figure 3B**).

Besides the heterochiral self-sorting in the racemate crystal of ***rac*-T1** along *c* axis, the helical chirality was also observed along *b* axis due to the homochiral self-sorting behavior of TB units. In the racemate crystal of ***rac*-T1**, two S_{4N}-**T1** molecules stacked together by C-H···π interactions ($d_{Cg\cdots C}$ = 3.75 Å and $\theta_{C-H\cdots O}$ = 125.3°) between H atom on one of the outwardly tilted phenylene ring and the centroid of another phenylene ring along the *b* axis. The vertical binding energy between two neighboring macrocycles is calculated to be −37.2 kJ/mol (For computational details see **Table S5**). Then, all S_{4N}-**T1** molecules stacked homochirally (S_NS_N-to-S_NS_N) along the *b* axis with a rotation of 180°, resulting in a right-handed (*P*) supramolecular single helix. Meanwhile, by the similar self-assembly behaviors, all R_{4N}-**T1** stacked homochirally (R_NR_N-*to*-R_NR_N) along the *b* axis, forming a left-handed (*M*)-single helix. It demonstated that the hands of the single helixes formed in ***rac*-T1** along *b* axis were controlled by homochiral self-sorting behaviors between two chiral TB units (**Figures 4A,B**). By comparison, in each enantiopure crystal R_{4N}-**T1** or S_{4N}-**T1** from the isolated enantiopure solution, no such supramolecular helix was observed (**Figure 3C**).

In the crystal of $R_{2N}S_{2N}$-**T1**, the left/right (M/P)-handed helix along *b* axis was found as well (**Figures 4C,D**). The chiral two TB units from neighboring molecules along the *b* axis in the case of (R_NR_N-*to*-R_NR_N) formed right-handed (*P*) helix and in the case of (S_NS_N-to-S_NS_N) formed left-handed (*M*) helix, and the interaction of Van der Waals forces was suggested as the main driving force. The vertical binding energy between two neighboring macrocycles is calculated to be −13.0 kJ/mol (**For computational details see SI**). Remarkably, the achiral meso isomer also shows segregation phenomena in the crystal state, as molecular packing results from interactions between homochiral TB subunits of neighboring achiral macrocycles. Therefore, in both cases, racemic and meso isomer, the supramolecular helical arrangements of the TB macrocycles in the solid state result from preferred intermolecular interactions between homochiral TB subunits.

Gas Absorption

As shown in **Figure 2**, three stereoisomers of **T1** have rare rectangle-like shapes and relatively big cavities (>1 nm), so solid-vapor adsorption experiments were carried out to investigate fundamental properties of special cavities of **T1**. The solid powder of $R_{2N}S_{2N}$-**T1** or ***rac*-T1** was desolvated at 80°C under vacuum, generating the activated solid powder of $R_{2N}S_{2N}$-**T1** or ***rac*-T1** (**For details, see SI**). The common solvents dichloromethane (DCM), acetone, benzene, and cyclohexane (CYH) were chosen as vapor sources, and adsorption results were monitored by ^{1}H NMR spectroscopy (For details see **Figures S4–S11**). It was found that the activated powder $R_{2N}S_{2N}$-**T1** could selectively adsorb DCM over acetone, benzene, and cyclohexane, and the mole ratio of adsorbed guest molecule: $R_{2N}S_{2N}$-**T1** is 1.28, 0.30, 0.48, and 0.33, respectively, where the activated powder ***rac*-T1** could slightly better adsorb acetone over DCM, benzene, and cyclohexane. The mole ratio of adsorbed guest molecule: ***rac*-T1** is 0.85, 0.75, 0.46, and 0.37, respectively (**Figure 5**).

Although many efforts to get all crystals with different solvents captured inside the cavity failed, the obtained crystal of 2DCM@$R_{2N}S_{2N}$-**T1** and 2acetone@***rac*-T1** could help us understand the properties of the cavities of $R_{2N}S_{2N}$-**T1** and ***rac*-T1** much more. In the crystal of 2DCM@$R_{2N}S_{2N}$-**T1** (**Figure 6A**), a 1:2 host-guest complex was formed *via* the favorable C-H···π interaction between DCM and phenylene ring of $R_{2N}S_{2N}$-**T1**. Interestingly, an inversion center (*i*) was found inside the crystal of 2DCM@$R_{2N}S_{2N}$-**T1**. In the racemate crystal of ***rac*-T1**, one acetone molecule was placed in each cavity of R_{4N}-**T1** or S_{4N}-**T1** respectively, which was stabilized by C-H···π interactions between acetone and phenylene ring of ***rac*-T1**, forming two 1:1 host-guest complexes. An inversion center was also found in the crystal of 2acetone@***rac*-T1** if 2acetone@***rac*-T1** was treated as a group (**Figure 6B**). Although the crystal structures were basically in accord with the corresponding selectivity of gas adsorption, further research still need to be conducted to elucidate the intrinsic relation between the formation of the inversion center and the selectivity of vapor adsorption.

CONCLUSION

In conclusion, we have synthesized three stereoisomers of Tröger's Base-based dimeric macrocycles **T1** with *four nitrogen stereogenic centers*, which exhibited interesting heterochiral and homochiral self-sorting behaviors between chiral TB units from neighboring molecules along different axis. In the crystal of ***rac*-T1**, two enantiomers stacked *via* a slipped π-π interaction

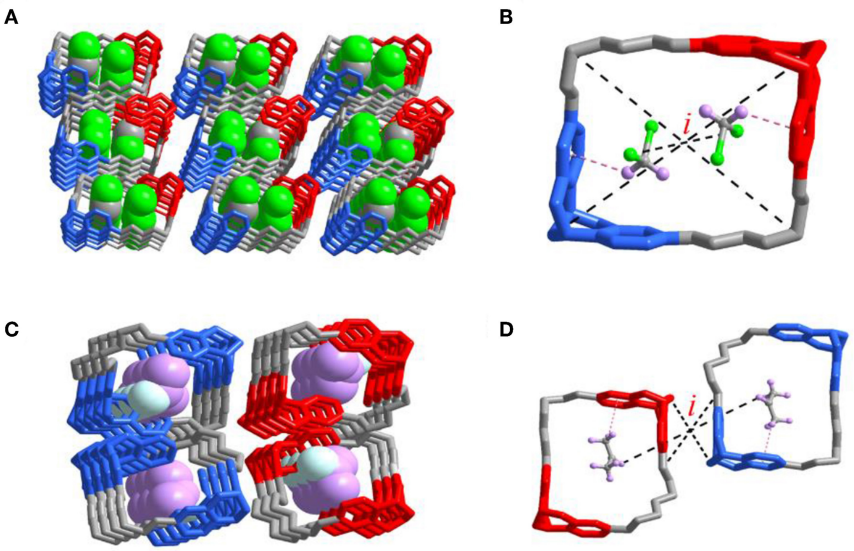

FIGURE 6 | Single-crystal X-ray structures of the complexes **(A)** ***2DCM@R***$_{2N}$***S***$_{2N}$**-T1**, two dichloromethane molecules were bound within the cavity. **(B)** Pink dashed lines indicate the [C-H···π] interactions and ***R***$_{2N}$***S***$_{2N}$**-T1** encapsulated two dichloromethane molecules. Corresponding guest molecule structural formulas: C, gray; H, pink; Cl, green. **(C)** *2**acetone**@**rac***-**T1**, two acetone molecules are bound within the cavity of ***S***$_{4N}$**-T1** and ***R***$_{4N}$**-T1**, respectively. **(D)** Pink dashed lines indicate the [C-H···π] interactions and ***rac***-**T1** encapsulated two acetone molecules. Corresponding guest molecule structural formulas: C, gray; H, pink; O, turquoise. *i:* inversion center.

along *c* axis, and showed heterochiral self-sorting behaviors. In the crystal of ***R***$_{2N}$***S***$_{2N}$-**T1**, neighboring molecules stacked *via* a cofacial π-π stacking along *a* axis, and showed heterochiral self-sorting behaviors as well. In the crystal state, both ***rac***-**T1** and ***R***$_{2N}$***S***$_{2N}$-**T1** showed homochiral self-sorting behaviors and as a consequence, the corresponding (*P*)- and (*M*)- single helixes were formed.

As mentioned above, most of the existing chiral self-sorting behavior was based on *carbon stereogenic factors*. *N*-centered chiral self-sorting example has been rarely reported so far. As the complementary of *carbon stereogenic factors*, our research extends the span and scope of chiral self-sorting behaviors, and paves a way to understand broadly the chirality between different chiral species in different scales.

DATA AVAILABILITY

CCDC 1888534 (S4N-T1), 1888548 (R4N-T1), 1888547 (R2NS2N-T1) and 1822570 (rac-T1) contain the supplementary crystallographic data for this paper. These data can be obtained free of charge from The Cambridge Crystallographic Data Centre.

AUTHOR CONTRIBUTIONS

JJ and CL conceived and designed the study. YC conducted the synthetic experiments, and BH, SL conducted the DFT calculations. All of authors analyzed and interpreted the data. JJ, CL, and LW wrote and revised the manuscript.

ACKNOWLEDGMENTS

This work was supported by the National Natural Science Foundation of China (Nos. 21672102, 21871135, 21871136). Most of the calculations in this work were performed using computational resources on an IBM Blade cluster system from the High-Performance Computing Center (HPCC) of Nanjing University.

SUPPLEMENTARY MATERIAL

The Supplementary Material for this article can be found online at: https://www.frontiersin.org/articles/10.3389/fchem.2019.00383/full#supplementary-material

REFERENCES

Akae, Y., Sogawa, H., and Takata, T. (2018). Cyclodextrin-based [3]rotaxane-crosslinked fluorescent polymer: synthesis and de-crosslinking using size complementarity. *Angew. Chem. Int. Ed.* 57, 14832–14836. doi: 10.1002/anie.201809171

Blanco, V., Leigh, D. A., and Marcos, V. (2015). Artificial switchable catalysts. *Chem. Soc. Rev.* 44, 5341–5370. doi: 10.1039/C5CS00096C

Brahim, A. A., Matsumoto, M., Miyahara, Y., Izumi, K., Suenaga, M., Shimizu, N., et al. (1998). Synthesis and properties of a new series of trögerophanes. *J. Heterocycl. Chem.* 35, 209–213. doi: 10.1002/jhet.5570350139

Cantrill, S. J., Fyfe, M. C. T., Heiss, A. M., Stoddart, J. F., White, A. J. P., and Williams, D. J. (1999). Rotaxane construction with a binaphthol-derived crown ether. *Chem. Commun.* 1251–1252. doi: 10.1039/a902096i

Chen, Z., Wang, Q., Wu, X., Li, Z., and Jiang, Y.-B. (2015). Optical chirality sensing using macrocycles, synthetic and supramolecular oligomers/polymers, and nanoparticle based sensors. *Chem. Soc. Rev.* 44, 4249–4263. doi: 10.1039/C4CS00531G

Dolenský, B., Havlík, M., and Král, V. (2012). Oligo Tröger's bases-new molecular scaffolds. *Chem. Soc. Rev.* 41, 3839–3858. doi: 10.1039/c2cs15307f

Du, X., Sun, Y., Tan, B., Teng, Q., Yao, X., Su, C., et al. (2010). Tröger's base-functionalised organic nanoporous polymer for heterogeneous catalysis. *Chem. Commun.* 46, 970–972. doi: 10.1039/B920113K

Erbas-Cakmak, S., Leigh, D. A., McTernan, C. T., and Nussbaumer, A. L. (2015). Artificial molecular machines. *Chem. Rev.* 115, 10081–10206. doi: 10.1021/acs.chemrev.5b00146

Feng, G., Xu, H., Li, W., and Zhang, J. (2018). Resolution of chiral nitrogen atoms in 1D helical coordination polymers. *Inorg. Chem. Commun.* 96, 81–85. doi: 10.1016/j.inoche.2018.08.011

Guo, S., Song, Y., He, Y., Hu, X.-Y., and Wang, L. (2018). Highly efficient artificial light-harvesting systems constructed in aqueous solution based on supramolecular self-assembly. *Angew. Chem. Int. Ed.* 57, 3163–3167. doi: 10.1002/anie.201800175

Imai, S., Takenaka, M., Sawamoto, M., and Terashima, T. (2019). Self-sorting of amphiphilic copolymers for self-assembled materials in water: polymers can recognize themselves. *J. Am. Chem. Soc.* 141, 511–519. doi: 10.1021/jacs.8b11364

Jedrzejewska, H., and Szumna, A. (2017). Making a right or left choice: chiral self-sorting as a tool for the formation of discrete complex structures. *Chem. Rev.* 117, 4863–4899. doi: 10.1021/acs.chemrev.6b00745

Jie, K., Zhou, Y., Li, E., Zhao, R., Liu, M., and Huang, F. (2018). Linear positional isomer sorting in nonporous adaptive crystals of a pillar[5]arene. *J. Am. Chem. Soc.* 140, 3190–3193. doi: 10.1021/jacs.7b13156

Li, B., Wang, B., Huang, X., Dai, L., Cui, L., Li, J., et al. (2019). Terphen[*n*]arenes and quaterphen[*n*]arenes (*n*=3–6): one-pot synthesis, self-assembly into supramolecular gels, and iodine capture. *Angew. Chem. Int. Ed.* 58, 3885–3889. doi: 10.1002/anie.201813972

Li, E., Jie, K., Zhou, Y., Zhao, R., and Huang, F. (2018). Post-synthetic modification of nonporous adaptive crystals of pillar[4]arene[1]quinone by capturing vaporized amines. *J. Am. Chem. Soc.* 140, 15070–15079. doi: 10.1021/jacs.8b10192

Liu, M., Zhang, L., and Wang, T. (2015). Supramolecular chirality in self-assembled systems. *Chem. Rev.* 115, 7304–7397. doi: 10.1021/cr500671p

Liu, Z., Nalluri, S. K. M., and Stoddart, J. F. (2017). Surveying macrocyclic chemistry: from flexible crown ethers to rigid cyclophanes. *Chem. Soc. Rev.* 46, 2459–2478. doi: 10.1039/C7CS00185A

Makiguchi, W., Tanabe, J., Yamada, H., Iida, H., Taura, D., Ousaka, N., et al. (2015). Chirality- and sequence-selective successive self-sorting via specific homo- and complementary-duplex formations. *Nat. Commun.* 6:7236. doi: 10.1038/ncomms8236

Neogi, I., Jhulki, S., Ghosh, A., Chow, T. J., and Moorthy, J. N. (2015). Amorphous host materials based on Tröger's base scaffold for application in phosphorescent organic light-emitting diodes. *ACS Appl. Mater. Inter.* 7, 3298–3305. doi: 10.1021/am508004n

Ogoshi, T., Yamagishi, T. A., and Nakamoto, Y. (2016). Pillar-shaped macrocyclic hosts pillar[n]arenes: new key players for supramolecular chemistry. *Chem. Rev.* 116, 7937–8002. doi: 10.1021/acs.chemrev.5b00765

Palma, A., Artelsmair, M., Wu, G., Lu, X., Barrow, S. J., Uddin, N., et al. (2017). Cucurbit[7]uril as a supramolecular artificial enzyme for Diels–Alder reactions. *Angew. Chem. Int. Ed.* 56, 1–6. doi: 10.1002/anie.201706487

Qu, D.-H., Wang, Q.-C., Zhang, Q.-W., Ma, X., and Tian, H. (2015). Photoresponsive host-guest functional systems. *Chem. Rev.* 115, 7543–7588. doi: 10.1021/cr5006342

Safont-Sempere, M. M., Fernández, G., and Würthner, F. (2011). Self-sorting phenomena in complex supramolecular systems. *Chem. Rev.* 111, 5784–5814. doi: 10.1021/cr100357h

Shang, X., Song, I., Jung, G. Y., Choi, W., Ohtsu, H., Lee, J. H., et al. (2018). Chiral self-sorted multifunctional supramolecular biocoordination polymers and their applications in sensors. *Nat. Commun.* 9:3933. doi: 10.1038/s41467-018-06147-8

Shanmugaraju, S., Dabadie, C., Byrne, K., Savyasachi, A. J., Umadevi, D., Schmitt, W., et al. (2017). A supramolecular Tröger's base derived coordination zinc polymer for fluorescent sensing of phenolic-nitroaromatic explosives in water. *Chem. Sci.* 8, 1535–1546. doi: 10.1039/C6SC04367D

Slater, N. H., Buckley, B. R., Elsegood, M. R. J., Teat, S. J., and Kimber, M. C. (2016). Controlling the assembly of C_2-symmetric molecular tectons using a thiocarbamate appended carbocyclic cleft molecule analogous to Tröger's base. *Cryst. Growth Des.* 16, 3846–3852. doi: 10.1021/acs.cgd.6b00388

Weilandt, T., Kiehne, U., Schnakenburgb, G., and Lützen, A. (2009). Diastereoselective self-assembly of dinuclear heterochiral metallosupramolecular rhombs in a self-discriminating process. *Chem. Commun.* 2320–2322. doi: 10.1039/b819335e

Wu, Z. W., Guo, Q. H., and Wang, M. X. (2017). Corona[5]arenes accessed by a macrocycle-to-macrocycle transformation route and a one-pot three-component reaction. *Angew. Chem. Int. Ed.* 56, 7151–7155. doi: 10.1002/anie.201703008

Xing, P., and Zhao, Y. (2018). Controlling supramolecular chirality in multicomponent selfAssembled systems. *Acc. Chem. Res.* 51, 2324–2334. doi: 10.1021/acs.accounts.8b00312

Yang, Z., Guo, R., Malpass-Evans, R., Carta, M., McKeown, N. B., Guiver, M. D., et al. (2016). Highly conductive anion-exchange membranes from microporous Tröger's base polymers. *Angew. Chem. Int. Ed.* 55, 11499–11502. doi: 10.1002/anie.201605916

Yao, L. Y., Lee, T. K. M., and Yam, V. W. W. (2016). Thermodynamic-driven self-assembly: heterochiral self-sorting and structural reconfiguration in gold(I)-sulfido cluster system. *J. Am. Chem. Soc.* 138, 7260–7263. doi: 10.1021/jacs.6b03844

Yashima, E., Ousaka, N., Taura, D., Shimomura, K., Ikai, T., and Maeda, K. (2016). Supramolecular helical systems: helical assemblies of small molecules, foldamers, and polymers with chiral amplification and their functions. *Chem. Rev.* 116, 13752–13990. doi: 10.1021/acs.chemrev.6b00354

Conflict of Interest Statement: The authors declare that the research was conducted in the absence of any commercial or financial relationships that could be constructed as a potential conflict of interest.

frontiers in Chemistry

ORIGINAL RESEARCH
published: 18 June 2019
doi: 10.3389/fchem.2019.00372

Short-Axis Methyl Substitution Approach on Indacenodithiophene: A New Multi-Fused Ladder-Type Arene for Organic Solar Cells

Yun Li[1], Menghan Wang[2], Fupeng Wu[1], Xuyu Gao[2], Sven Huettner[3], Youtian Tao[2] and Zuo-Quan Jiang[1]**

[1] Jiangsu Key Laboratory for Carbon-Based Functional Materials and Devices, Joint International Research Laboratory of Carbon-Based Functional Materials and Devices, Institute of Functional Nano and Soft Materials, Soochow University, Suzhou, China, [2] Key Lab for Flexible Electronics, Institute of Advanced Materials, Nanjing Tech University, Nanjing, China, [3] Macromolecular Chemistry I, Universität Bayreuth, Bayreuth, Germany

Indacenodithiophene (IDT) is a promising building block for designing organic semiconductors. In this work, a new pentacyclic ladder-type arene IDMe was designed and synthesized by introducing methyl substitution on the short-axis of IDT. Two non-fullerene electron acceptors (IDIC and ID-MeIC) without and with methyl substitution were designed and synthesized for further study. Compared with IDIC, ID-MeIC with methyl substitution on the short-axis of IDT shows smaller bandgap, stronger extinction coefficient, and better crystallinity. Besides, PBDB-T: ID-MeIC blend film shows more efficient exciton generation and dissociation and more balanced charge transport mobility. Therefore, polymer solar cells based on PBDB-T: ID-MeIC can achieve better photovoltaic performance with a PCE of 6.46% and substantial increase in J_{SC} to 14.13 mA cm^{-2} compared to 4.94% and 9.10 mA cm^{-2} of PBDB-T: IDIC. These results suggest that short-axis substitution on multi-fused ladder-type arenes, such as IDT is an effective way to change the optical and electronic properties of the organic semiconductors for high-performance OPVs.

Keywords: indacenodithiophene, methyl group, short-axis substitution, non-fullerene electron acceptors, polymer solar cells

OPEN ACCESS

Edited by:
Penglei Chen,
Institute of Chemistry (CAS), China

Reviewed by:
Bin Yang,
Hunan University, China
Linna Zhu,
Southwest University, China
Tian Xin Wei,
Beijing Institute of Technology, China

****Correspondence:***
Youtian Tao
iamyttao@njtech.edu.cn
Zuo-Quan Jiang
zqjiang@suda.edu.cn

Specialty section:
This article was submitted to Supramolecular Chemistry, a section of the journal Frontiers in Chemistry

Received: *26 February 2019*
Accepted: *06 May 2019*
Published: *18 June 2019*

Citation:
Li Y, Wang M, Wu F, Gao X, Huettner S, Tao Y and Jiang Z-Q (2019) Short-Axis Methyl Substitution Approach on Indacenodithiophene: A New Multi-Fused Ladder-Type Arene for Organic Solar Cells. Front. Chem. 7:372. doi: 10.3389/fchem.2019.00372

INTRODUCTION

Organic solar cell (OSC) is one of the most promising new energy technologies due to their advantages such as low cost, lightweight, enable roll-to-roll fabrication (Hiramoto et al., 1995; Halls et al., 1996). Generally, OSCs have a bulk hetero-junction (BHC) consist of an electron donor (D) and an electron acceptor (A) (Halls et al., 1995). In the past few years, fullerene and its derivatives such as ($PC_{61}BM$) are widely applied as the electron acceptor (Chen et al., 2015). Although the PCE of fullerene-based OSCs can above 11% (Zhao et al., 2016), it is hard to achieve a further development because of its complicated synthesis, low light absorption coefficient, and poor tunability in energy levels (He et al., 2010). In the past 3 years, non-fullerene electron acceptors (NFAs) as alternatives for fullerene-base electron acceptors have achieved great developments. Now, the maximum PCEs have surpassed 15% (Yuan et al., 2019) for single-junction cells and 17% for double-junction tandem cells (Meng et al., 2018). Among all kinds of NFAs, A-D-A type

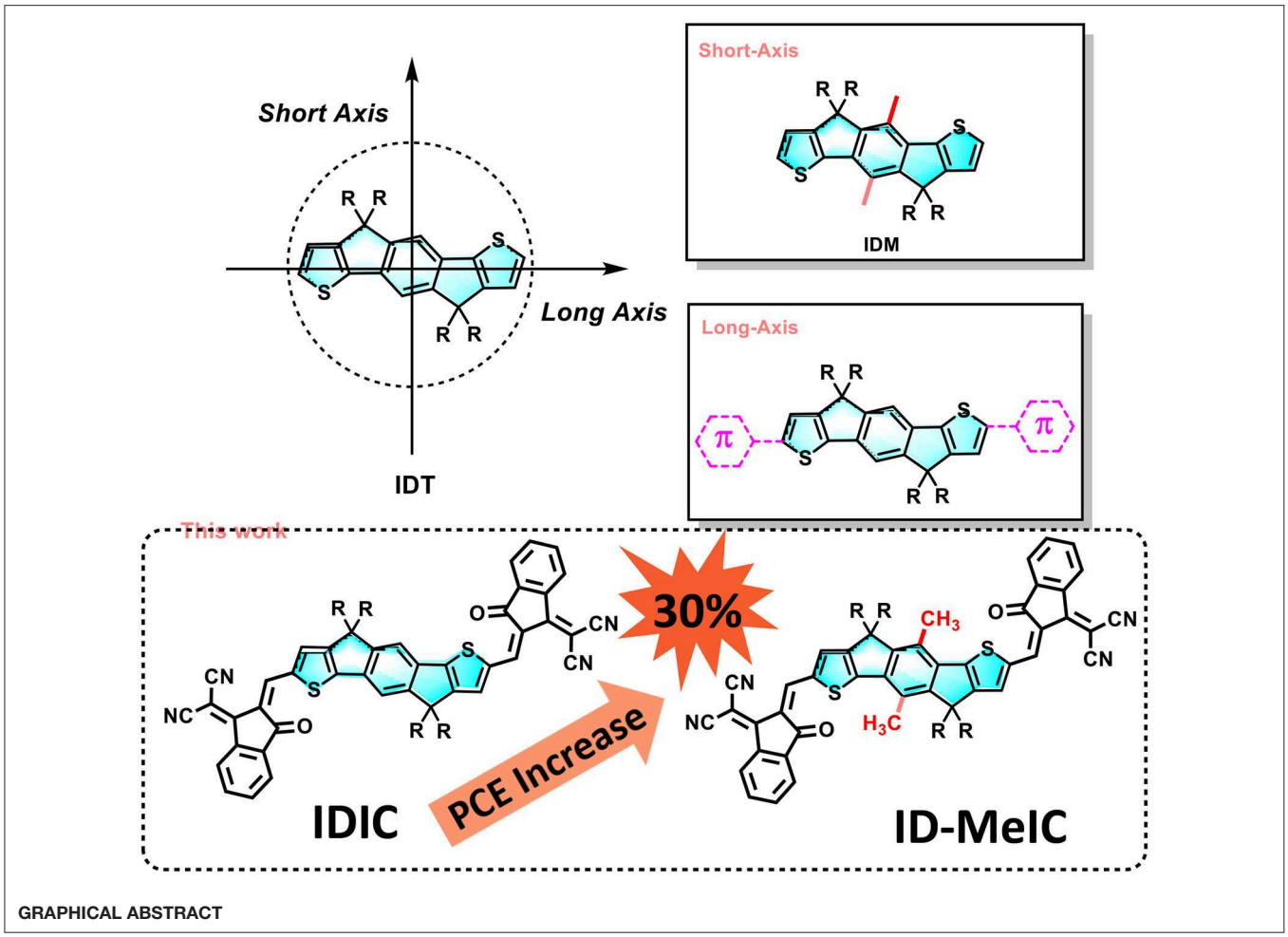

GRAPHICAL ABSTRACT

NFAs is one of the most successful design strategies (Kang et al., 2016; Li S. et al., 2016; Li Z. et al., 2016; Li et al., 2018; Xie et al., 2018a,b). What is particularly exciting is the chemistry that has allowed the synthesis of novel multi-fused ladder-type arenes with tunable energy levels and highly desirable optical or electronic properties for A-D-A NFAs (Lin et al., 2015a; Wu et al., 2015; Dai et al., 2017; Yang et al., 2018).

Indacenodithiophene (IDT), a pentacyclic ladder-type arene (Bai et al., 2015; Lin et al., 2015b), has a coplanar fused-ring aromatic structure with a low degree of energetic disorder and high carrier mobility (Würfel et al., 2015; Jia et al., 2017). Thus, IDT has been widely applied as a donor (D) unit and combined with an acceptor (A) unit to construct a variety of D-A conjugated polymers, which become one of the major families of polymers for organic solar cells (OSCs) (Li et al., 2017a; Zhang et al., 2017). In these 2 years, various non-fullerene electron acceptors based on IDT- and its derivatives have also been developed for OSCs (Yan et al., 2017; Jiang et al., 2018). These facts are enough to prove that IDT is a promising building block to design organic semiconductors for organic electronics. Thus, it is valuable to tailor the IDT's structure for selectively optimizing electrical properties of IDT-based organic semiconductors.

In the past 3 years, the structural diversity of IDT is flourishing (Liu et al., 2017). However, as shown in **Figure 1**, most of IDT-derivatives focus on the long-axis substitution approach such as through extension conjugated length along the long axis (Li et al., 2017b; Wang et al., 2017). Many researchers may notice that there are possible substituted positions on the central benzene of IDT core (Li et al., 2019). However, few related reports are available in this short-axis substitution approach probably due to synthesis difficulty. Dithienyl[1,2-b:4,5-b′] benzodithiophene (BDCPDT), another kind of core, can easily make this modification by using different side-chains in the precursors (Kan et al., 2018). Recently, our group designed and synthesized two new non-fullerene electron acceptors (CBT-IC and SBT-IC) by the short-axis substitution modification of non-fullerene acceptors based on the BDCPDT-system. This work shows that the short-axis substitution is also an effective way to optimize the optical and electronic properties of the organic semiconductors for organic photovoltaics (OPVs) (Lin et al., 2018). Besides, unlike the side-chains on the sp^3 hybridized carbon that make them point out of the backbone planes; short-axis substitution can provide another kind of side-chains appended to the conjugated backbone; thus, they can directly affect energy levels especially the HOMO(Yang

et al., 2016; Bin et al., 2017). This impact is quite similar to that of end-capping groups which are placed along the IDT's long-axis.

Herein, a new IDT-derivative core, denoted as IDMe, was design and synthesized through the short-axis methyl substitution approach (introducing the methyl on the central benzene of IDT core, **Figure 1**). Then, a new non-fullerene acceptor (ID-MeIC) based on IDMe was design and synthesized. For comparison, IDIC without methyl-substitution was also synthesized. Compared with IDIC, ID-MeIC with methyl substitution on short-axis of IDT shows a smaller bandgap, stronger extinction coefficient and better crystallinity. Besides, PBDB-T: ID-MeIC blend film shows more efficient exciton generation and dissociation a balanced charge transport mobility. Therefore, polymer solar cells based on PBDB-T: ID-MeIC can achieve better photovoltaic performance with a PCE of 6.46%, a substantial increase in J_{SC} (14.13 mA cm^{-2}) and a higher V_{OC} of 0.90 V while a smaller *FF* of 0.50. The value of PCE is 30% higher than that of PBDB-T: IDIC based PSCs.

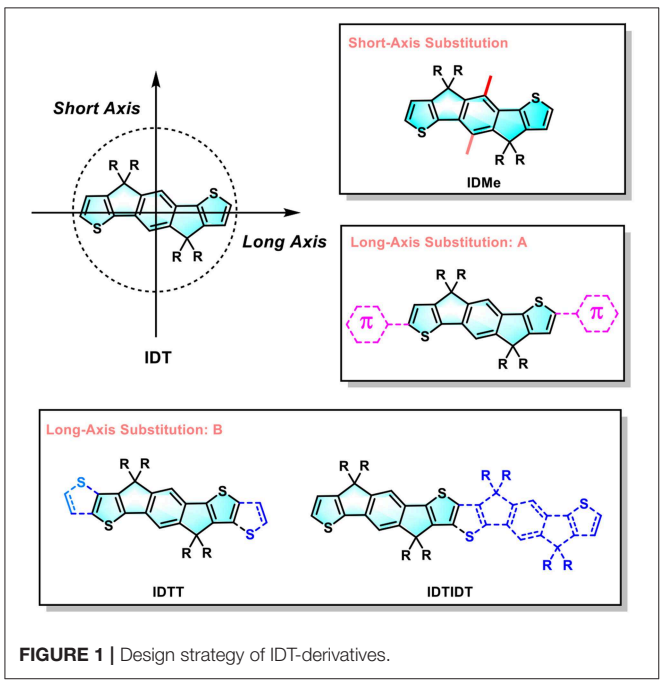

FIGURE 1 | Design strategy of IDT-derivatives.

RESULTS AND DISCUSSION

Material Synthesis and Characterization

Chemical structures of polymer donor (PBDB-T) and two non-fullerene electron acceptors (IDIC and ID-MeIC) are shown in **Figure 2**. The detail synthetic routes of compound ID-MeIC are illustrated in **Scheme 1**. The key intermediate compound 2 was obtained via Suzuki coupling reaction with 92% yield. Then 4-hexylphenyl was introduced into compound 2 via nucleophilic reaction, followed by intramolecular Friedel-Crafts cyclization under acidic conditions to afford the new building block (IDMe) with 68% yield in two steps. Compound 5 (IDMe-CHO) was obtained by Vilsmeier-Haack reaction using dimethylformamide (DMF) and phosphorus oxychloride ($POCl_3$) with 80% yield. Finally, ID-MeIC was synthesized by the Knoevenagel reaction of IDMe-CHO and 1,1-Dicyanomethylene-3-indanone (IC) in chloroform with 80% yield. For comparison, IDIC was also synthesized according to the literature report (Lin et al., 2017). All the chemically synthesized compounds were fully characterized by ^{1}H NMR and MALDI-TOF with their spectra described in the **Supporting Information**. Thermogravimetric analysis (TGA) was performed to study the thermal stability of ID-MeIC. As shown in **Figure S1**, ID-MeIC shows decomposition temperature

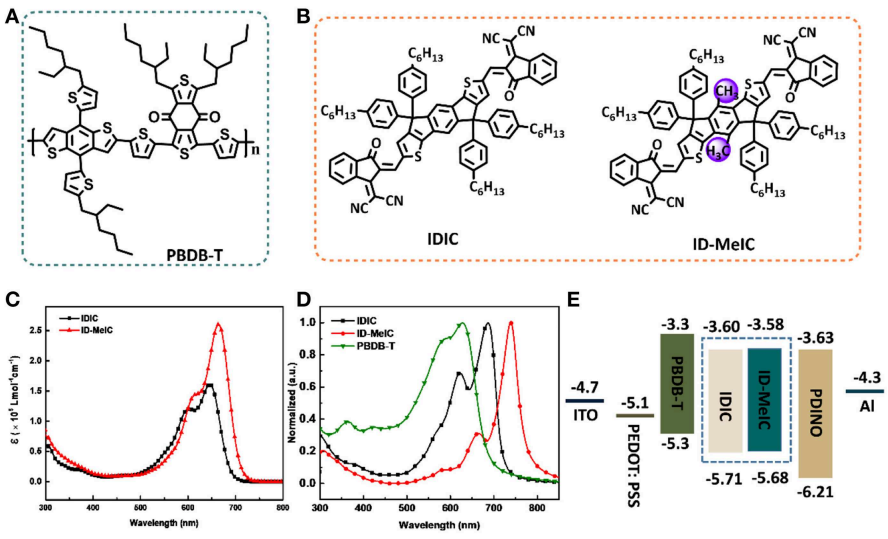

FIGURE 2 | Chemical structures of **(A)** donor PBDB-T and **(B)** acceptor IDIC and ID-MeIC; **(C)** The molar extinction coefficients of IDIC and ID-MeIC in chloroform (10^{-5} M); **(D)** Normalized absorption spectra of IDIC and ID-MeIC in thin film; **(E)** Energy diagram of materials used in the PSC.

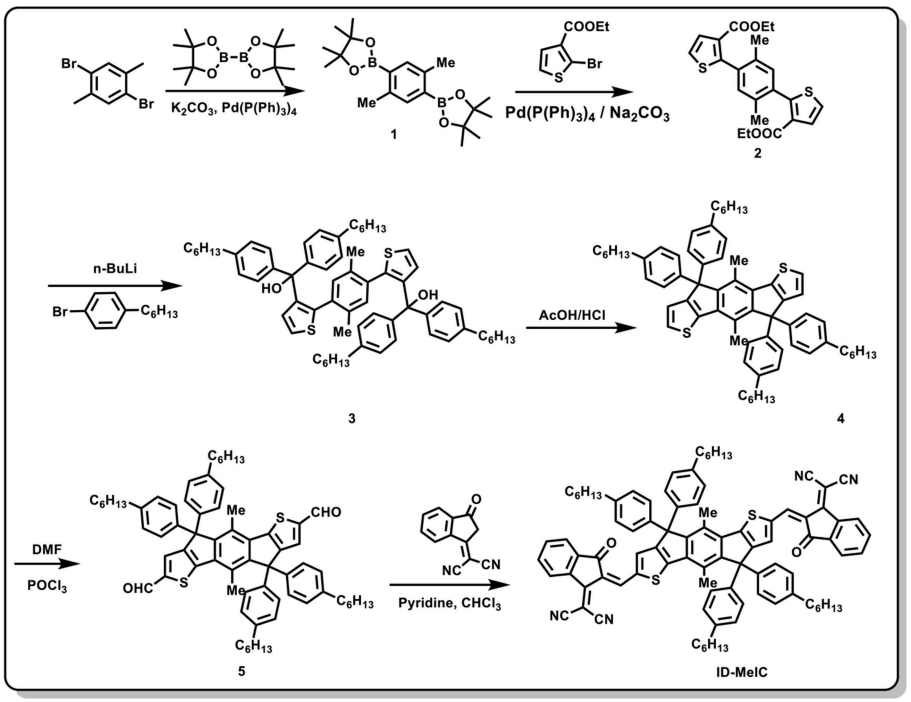

SCHEME 1 | Synthetic routes of ID-MeIC.

TABLE 1 | Optical and electrochemical properties of IDIC and ID-MeIC.

Acceptor	λ_{max}^{sol} (a) (nm)	λ_{max}^{film} (b) (nm)	λ_{onset}^{film} (c) (nm)	E_g^{opt} (d) (eV)	E_{HOMO} (e) (eV)	E_{LUMO} (e) (eV)	E_g^{cv} (f) (eV)
IDIC	646	689	741	1.67	−5.71	−3.60	2.11
ID-MeIC	665	741	819	1.51	−5.68	−3.58	2.10

(a)Maximum absorption in chloroform solution; (b)Maximum absorption at thin film; (c)Absorption onset at thin film; (d)Optical band gap calculated by the absorption onset of thin film state; (e)HOMO/LUMO value calculated from the onset oxidation/reduction potential; (f)HOMO-LUMO gap estimated from CV.

(T_d, 5% weight-loss) of 353°C, which indicated that ID-MeIC has good thermal stability.

As shown in **Figure 2C**, with the detail spectra data provided in **Table 1**. IDIC show absorption band in 500–700 nm with a maximum absorption wavelength at 646 nm. However, ID-MeIC has the maximum absorption wavelength red-shifting to 665 nm with an extinction coefficient of 2.61×10^5 L mol^{-1} cm^{-1}, which is larger than that of IDIC (1.63×10^5 L mol^{-1} cm^{-1}). In thin film, the maximum absorption wavelength of IDIC and ID-MeIC red-shift to 689 nm, 741 nm, respectively (**Figure 2D**). Interestingly, ID-MeIC shows larger bathochromic (about 76 nm) and stronger relative intensity of absorption peak in the long wavelength. This may due to the stronger intermolecular aggregation interaction by introducing the methyl substitution on the short-axis of IDT. The optical band gaps (E_g^{opt}) of IDIC and ID-MeIC calculated from their absorption edge are 1.67 and 1.51 eV, respectively. Meanwhile, the energy-level alignment of IDIC and ID-MeIC are calculated by the cyclic voltammetry measurements and the potentials are calibrated using Fc/Fc$^+$ redox couple (**Figure S2**). The corresponding highest occupied molecular orbital (HOMO) and lowest unoccupied molecular orbital (LUMO) energy levels are calculated from the onset oxidation and reduction potentials ($\phi_{ox/red}$), according to the equations: $E_{HOMO/LUMO}$ = -e ($\phi_{ox/red}$ + 4.8–$\phi_{Fc/Fc}^{+}$) (eV). The $E_{HOMO/LUMO}$ are calculated to be −5.68/−3.58 eV and −5.71/−3.60 eV for IDIC and ID-MeIC, respectively. The higher E_{HOMO} and deeper E_{LUMO} of ID-MeIC indicate that methyl substitution on the short-axis of IDT can directly affect the energy levels.

To investigate the geometric structure and electronic properties of IDIC and ID-MeIC, density functional theory (DFT) calculations at the B3LYP/6-31G (d) level were performed. As shown in **Figure S3**, IDIC and ID-MeIC both have highly coplanar structure. And the HOMO/LUMO wave functions of compound IDIC and ID-MeIC are well delocalized over their backbone, which is beneficial for their charge transport mobilities. In addition, the calculated HOMO/LUMO of IDIC and ID-MeIC are −5.63/−3.39 eV and −5.54/−3.34 eV, respectively, which are consistent with values estimated from CV experiments. These results suggest that methyl substitution

on short-axis of IDT methyl can increase the electron-donating ability of IDT core and directly affect its energy levels.

The methyl group has a tremendous impact on the crystallinity and molecular packing in the thin films, which be evidenced by grazing-incidence wide-angle X-ray scattering (GIWAXS) as shown in **Figures 3a–c**. For IDIC, both the lamellar (100) reflections and π-π stacking (010) reflections can be observed, which suggested that face-on and edge-on crystallites coexisted in the corresponding film. However, ID-MeIC with methyl substituents on the central benzene ring along the short-axis of IDT, displayed a predominant face-on crystalline orientation. Interestingly, ID-MeIC exhibited stronger π-π stacking (010) reflection with a new strong reflection peak appear in the out-of-plane direction. These results suggest methyl substituents on the short-axis can enhance the crystallinity of IDT.

Photovoltaic Performances

To investigate the photovoltaic performance of these NF-SMAs, polymer solar cells were fabricated with the device structure of indium tin oxide(ITO)/poly(3,4-ethylene dioxythiophene): poly(styrene sulfonate)(PEDOT: PSS)/Active Layer/3,3′-(1,3,8,10-Tetraoxoanthra[2,1,9-def: 6,5,10-d'e'f']diisoquinoline-2,9(1H,3H,8H,10H)-iyl)bis(N,N-dimethylpropan-1-amine oxide)(PDINO)/aluminum (Al), where PEDOT:PSS and PDINO served as the anode and cathode interlayers; a wide bandgap polymer donor named PBDB-T blending with these two NF-SMAs served as the active layer. The devices were optimized with different donor/acceptor (D/A) weight ratios, thermal annealing conditions, and active layer thickness. The detailed of optimization process are shown in ESI† **Tables S1–S4**.

The current density-voltage (*J-V*) curves are shown in **Figure 4A** with the detail photovoltaic performance parameters provided in **Table 2**. For IDIC without methyl substitution, the optimized PBDB-T: IDIC -based device shows a maximum PCE of 4.94% with a V_{OC} of 0.89 V, a J_{SC} of 9.10 mA cm^{-2} and an *FF* of 0.61. In contrast, for ID-MeIC, the PBDB-T: ID-MeIC -based device show the highest PCE of 6.46% with a substantial increase in J_{SC} (14.13 mA cm^{-2}) and a slightly higher V_{OC} of 0.90 V whereas a decrease of *FF* (0.50). This higher J_{SC} and V_{OC} of PBDB-T: IDIC-Me -based device is due to the methyl substitution on the short-axis of IDT which can elevate the E_{HOMO} and decrease the E_g of ID-MeIC acceptor. **Figure 4B** depicts the external quantum efficiency (EQE) curve of this device. It is obvious that device based on PBDB-T: ID-MeIC demonstrates has a strong solar spectral response at the range of 700–800 nm, which is in consistency with the UV-vis spectra and is accounted for its higher J_{SC}. The integrated current density J_{SC} of PBDB-T: IDIC and PBDB-T: ID-MeIC-based devices are calculated of 10.47, 13.03, mA cm^{-2}, respectively.

Charge Generation, Transport, and Recombination

The photocurrent density (J_{ph}) vs. effective voltage (V_{eff}) of the devices based on PBDB-T: acceptors were also plotted to

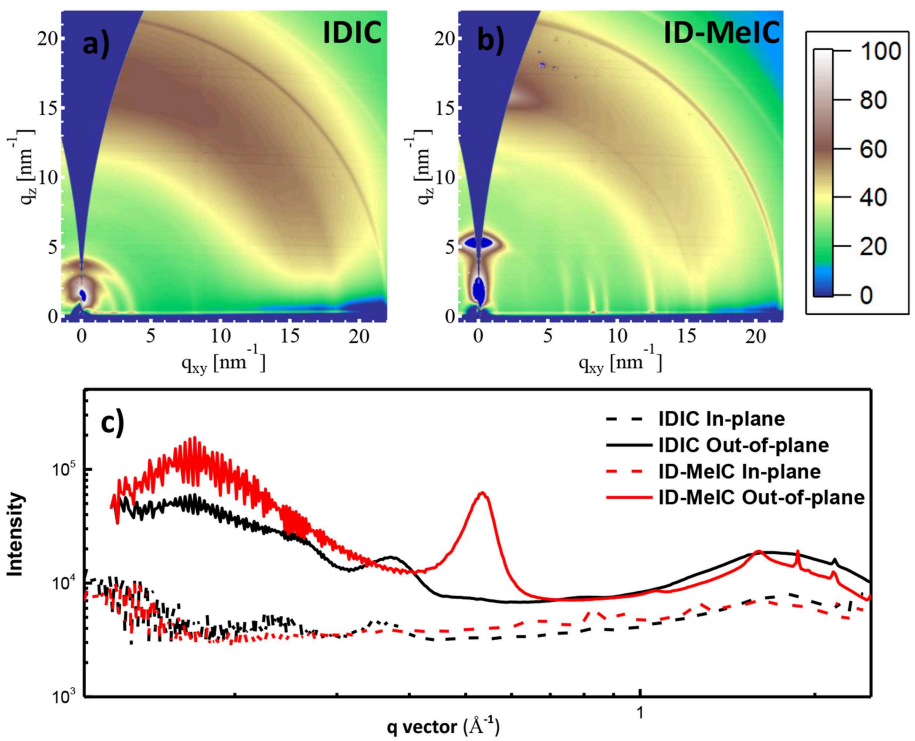

FIGURE 3 | 2D GIWAXS patterns of **(a)** IDIC film and **(b)** ID-MeIC film; **(c)** Sector average line outs of the GIWAXS images of IDIC and ID-MeIC neat film.

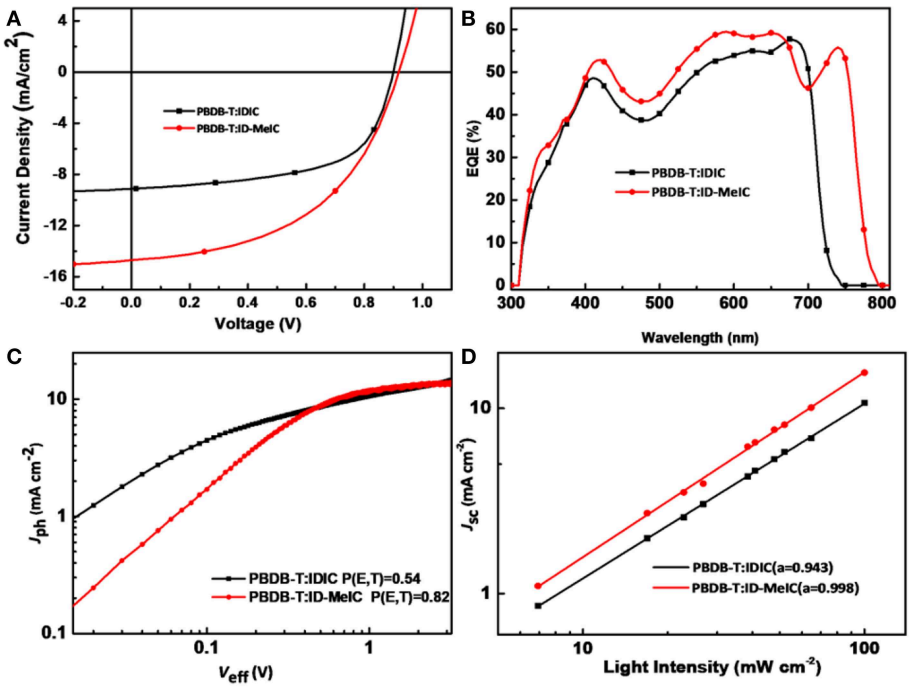

FIGURE 4 | IDIC and ID-MeIC-based devices **(A)** *J–V* curves; **(B)** EQE curves; **(C)** Photocurrent vs. effective voltage; **(D)** Light-intensity dependence of J_{SC}.

TABLE 2 | Comparison photovoltaic parameters of PSCs based on IDIC and ID-MeIC.

Active layer	V_{OC} (V)	J_{SC} (mA cm^{-2})	J_{SC} (mA cm^{-2}) [a]	*FF*	PCE_{max}/PCE [b]$_{avr}$ (%)
PBDB-T: IDIC	0.89 ± 0.00 (0.89)	8.67 ± 0.43 (9.10)	10.47	0.60 ± 0.01 (0.61)	4.94/4.67
PBDB-T: ID-MeIC	0.90 ± 0.00 (0.90)	13.67 ± 0.46 (14.13)	13.03	0.50 ± 0.01 (0.50)	6.46/6.28

[a]*Integrated current density calculated from EQE curves;* [b]*Average values were obtained from 10 devices.*

study the exciton dissociation and charge collection properties in the OSCs (**Figure 4C**). J_{ph} were measured as a function of the effective voltage (V_{eff} is defined as V_0-V_{bias}), from which we can calculate the exciton dissociation probability (P_{diss} defines as the ratio of J_{ph}/J_{sat}, and J_{sat} is the saturation current density at high V_{eff}). In this way, under short-circuit conditions, the values of P_{diss} were determined to be 54% and 82% for the PBDB-T: IDIC and PBDB-T: ID-MeIC–based devices, respectively. These results indicate that PBDB-T: ID-MeIC–based device has more efficient exciton generation and dissociation, which is contributed to its high J_{SC}.

To study the charge recombination kinetics properties in the devices we measured the dependence of J_{SC} on light intensity (P_{light}); There the power-law equation $J_{SC} \propto P^{\alpha}$ can be described the relationship between J_{SC} and P_{light}. As we know, if the value of α is close to 1, it means that all the charges are swept out and collected by the electrode without recombination in the device. As shown in **Figure 4D**, the value of α for PBDB-T: IDIC and PBDB-T: ID-MeIC–based devices are 0.943 and 0.998, respectively. These results imply that methyl substitution on the short-axis of IDT help prevent the bimolecular recombination.

The charge transport properties of IDIC and ID-MeIC were measured by space charge limited current (SCLC) measurements (**Figure S4**). The electron mobility (μ_e) of IDIC and ID-MeIC are 6.6 × 10^{-6} and 1.0 × 10^{-6} cm^2 V^{-1} s^{-1}, respectively. The hole (μ_h) and electron mobilities of the blend films also measured to investigate the charge-transport behavior in the active layer. As shown in **Figure S4**, the μ_h/ μ_e of PBDB-T: IDIC and PBDB-T: ID-MeIC–based devices were evaluated to be 2.1 × 10^{-4}/7.8 × 10^{-6} and 9.1 × 10^{-5}/3.4 × 10^{-6} $cm^2V^{-1}S^{-1}$ with a μ_h/μ_e ratio of 27 and 26, respectively. The slightly balanced charge transport proprieties of PBDB-T: ID-MeIC-based devices also contribute to its high J_{SC}.

Morphology Characterization

The morphologies of PBDB-T: IDIC and PBDB-T: ID-MeIC blend films were firstly investigated by GIWAXS (**Figure 5**). Similarly, both the lamellar (100) reflections and π-π stacking

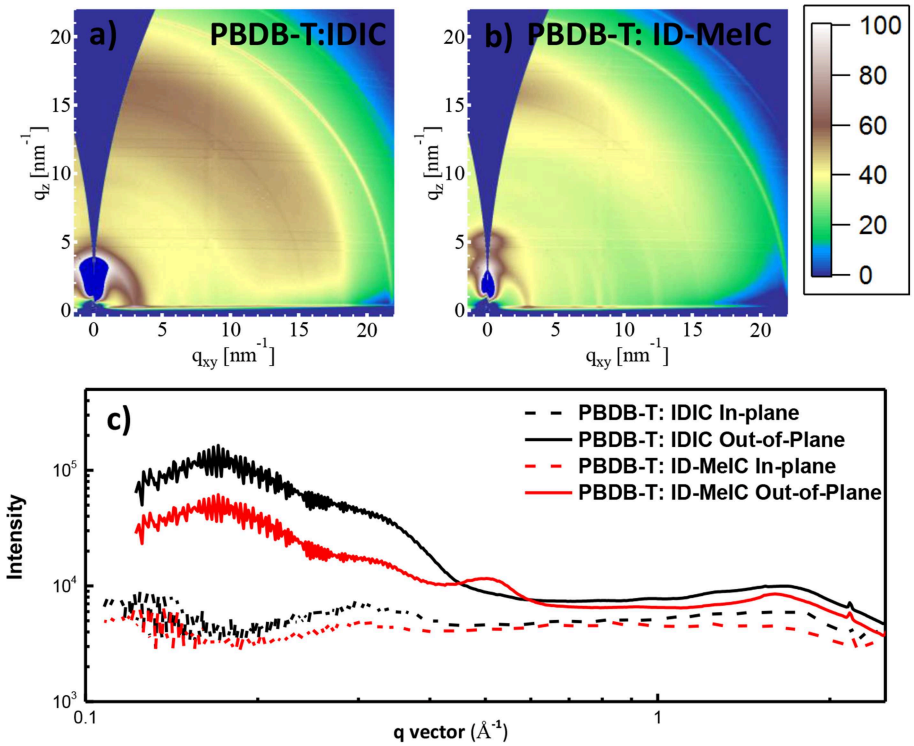

FIGURE 5 | 2D GIWAXS patterns of **(a)** PBDB-T: IDIC, **(b)** PBDB-T: ID-MeIC blend film; **(c)** Sector average line outs of the GIWAXS images of PBDB-T: IDIC and PBDB-T: ID-MeIC blend film.

(010) reflections were competitively observed for PBDB-T: IDIC blend film, confirming that face-on and edge-on crystallites coexisted. From **Figure 5b**, it is obvious that PBDB-T: ID-MeIC blend film has a predominant face-on crystalline orientation. This face-on crystalline orientation is beneficial for the charge transport in the solar cells. On the other hand, for PBDB-T: ID-MeIC blend film, polymer PBDB-T shifts too much lower q in the (010) direction corresponding to larger π-π distance and a smaller coherence length (CL) than that of PBDB-T: IDIC and PBDB-T: IDIC-Me blend film. These results indicate that PBDB-T has not good compact molecular packing when blending with ID-Me IC, which also accounts for the lower FF based on PBDB-T: ID-MeIC–based device.

The morphologies of the blend films PBDB-T: IDIC and PBDB-T: ID-MeIC were also investigated by atomic force microscopy (AFM). As shown in **Figure 6**. The excessive crystalline feature of ID-MeIC in the thin film is revealed by its larger root-mean-square (RMS) roughness of 8.20 nm over that of the IDIC film (3.84 nm). This larger RMS roughness of ID-MeIC is another factor that causes the low FF of the device based on PBTB-T: ID-MeIC blend films.

CONCLUSION

In summary, a new pentacyclic ladder-type arene ID-MeIC has been design and synthesized by methyl substitution on the short-axis of IDT core. ID-MeIC was functionalized as non-fullerene electron acceptors for comparison with previously reported IDIC without the methyl substitution. Compared with IDIC, ID-MeIC with methyl substitutionon on short-axis of IDT showed smaller bandgap, stronger extinction coefficient, better crystallinity. Besides, PBDB-T: ID-MeIC blended film exhibited more efficient exciton generation and dissociation as well as more balanced charge transport ability. Therefore, polymer solar cells based on PBDB-T: ID-MeIC demonstrated better photovoltaic performance with higher PCE of 6.46% and a substantial increase of J_{SC} to 14.13 mA cm^{-2}. The value of PCE is 30% higher than that of the PBDB-T: IDIC based PSC. Our results suggested that IDMe is a promising multi-fused ladder-type building block for designing efficient non-fullerene electron acceptors. And short-axis substitution on multi-fused ladder-type arenes, such as IDT and IDTT is an effective way to tune the optical and electronic properties of the organic semiconductors for high-performance OPVs.

DATA AVAILABILITY

The raw data supporting the conclusions of this manuscript will be made available by the authors, without undue reservation, to any qualified researcher.

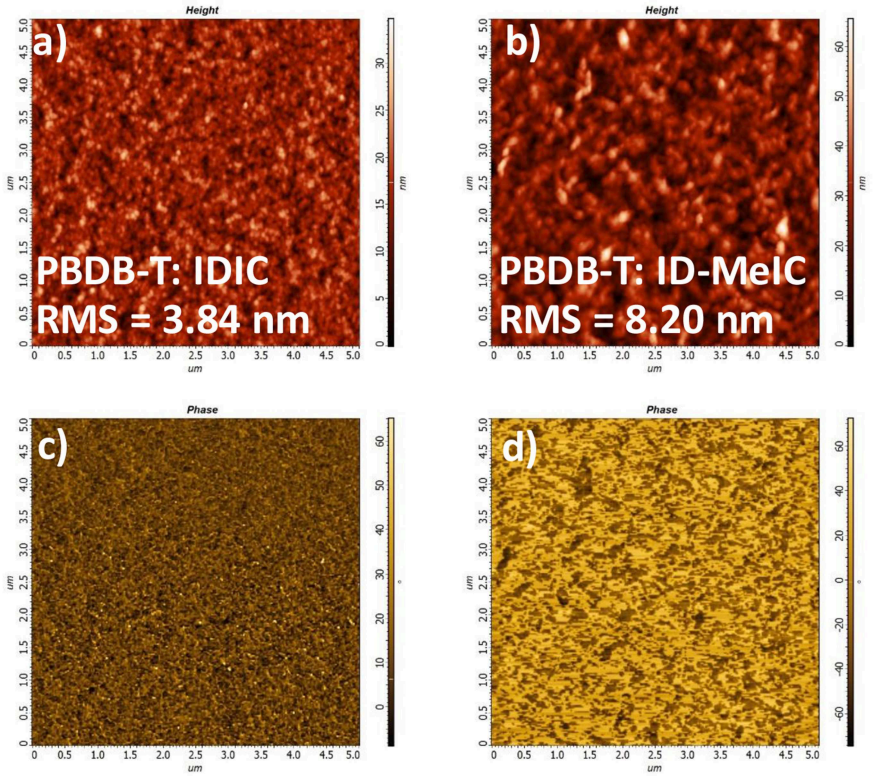

FIGURE 6 | AFM height images and phase images of **(a,c)** PBDB-T: IDIC, **(b,d)** PBDB-T: ID-MeIC.

AUTHOR CONTRIBUTIONS

YL: preparation and characterization of materials. MW: device preparation and characterization. FW: synthesis of materials. XG: morphology characterization. SH: morphology characterization. YT: guide device preparation. Z-QJ: guide material synthesis.

ACKNOWLEDGMENTS

The authors acknowledge financial support from the National Natural Science Foundation of China (Grant No. 21572152; 51873139 and 61761136013). This project is also funded by the Collaborative Innovation Center of Suzhou Nano Science and Technology (Nano-CIC), by the Priority Academic Program Development of Jiangsu Higher Education Institutions (PAPD), by the 111 Project of the State Administration of Foreign Experts Affairs of China. Natural Science Foundation of Jiangsu Province (BK20160042) for financial support. SH is thankful to the DFG project (Nr. 392306670) and Australian Synchrotron.

SUPPLEMENTARY MATERIAL

The Supplementary Material for this article can be found online at: https://www.frontiersin.org/articles/10.3389/fchem.2019.00372/full#supplementary-material

REFERENCES

Bai, H., Wang, Y., Cheng, P., Wang, J., Wu, Y., Hou, J., et al. (2015). An electron acceptor based on indacenodithiophene and 1,1-dicyanomethylene-3-indanone for fullerene-free organic solar cells. *J. Mater. Chem. A* 3, 1910–1914. doi: 10.1039/C4TA06004K

Bin, H., Zhong, L., Yang, Y., Gao, L., Huang, H., Sun, C., et al. (2017). Medium bandgap polymer donor based on Bi(trialkylsilylthienyl-benzo[1,2-b:4,5-b′]-difuran) for high performance nonfullerene polymer solar cells. *Adv. Energy Mater.* 7:1700746. doi: 10.1002/aenm.201700746

Chen, J.-D., Cui, C., Li, Y.-Q., Zhou, L., Ou, Q.-D., Li, C., et al. (2015). Single-junction polymer solar cells exceeding 10% power conversion efficiency. *Adv. Mater.* 27, 1035–1041. doi: 10.1002/adma.201404535

Dai, S., Zhao, F., Zhang, Q., Lau, T.-K., Li, T., Liu, K., et al. (2017). Fused nonacyclic electron acceptors for efficient polymer solar cells. *J. Am. Chem. Soc.* 139, 1336–1343. doi: 10.1021/jacs.6b12755

Halls, J. J. M., Pichler, K., Friend, R. H., Moratti, S. C., and Holmes, A. B. (1996). Exciton diffusion and dissociation in a poly(p-phenylenevinylene)/C_{60} heterojunction photovoltaic cell. *Appl. Phys. Lett.* 68, 3120–3122. doi: 10.1063/1.115797

Halls, J. J. M., Walsh, C. A., Greenham, N. C., Marseglia, E. A., Friend, R. H., Moratti, S. C., et al. (1995). Efficient photodiodes from interpenetrating polymer networks. *Nature* 376, 498–500. doi: 10.1038/376498a0

He, Y., Chen, H.-Y., Hou, J., and Li, Y. (2010). Indene–C_{60} bisadduct: a new acceptor for high-performance polymer solar cells. *J. Am. Chem. Soc.* 132, 1377–1382. doi: 10.1021/ja908602j

Hiramoto, M., Ihara, K., Fukusumi, H., and Yokoyama, M. (1995). Conduction type control from n to p type for organic pigment films purified by reactive sublimation. *J. Appl. Phys.* 78**,** 7153–7157. doi: 10.1063/1.360423

Jia, B., Wu, Y., Zhao, F., Yan, C., Zhu, S., Cheng, P., et al. (2017). Rhodanine flanked indacenodithiophene as non-fullerene acceptor for efficient polymer solar cells. *Sci. China Chem.* 60, 257–263. doi: 10.1007/s11426-016-0336-6

Jiang, Z.-Q., Wang, T.-T., Wu, F.-P., Lin, J.-D., and Liao, L.-S. (2018). Recent advances in electron acceptors with ladder-type backbone for organic solar cells. *J. Mater. Chem. A* 6, 17256–17287. doi: 10.1039/C8TA05440A

Kan, B., Zhang, J., Liu, F., Wan, X., Li, C., Ke, X., et al. (2018). Fine-tuning the energy levels of a nonfullerene small-molecule acceptor to achieve a high short-circuit current and a power conversion efficiency over 12% in organic solar cells. *Adv. Mater.* 30:1704904. doi: 10.1002/adma.201704904

Kang, H., Kim, G., Kim, J., Kwon, S., Kim, H., and Lee, K. (2016). Bulk-heterojunction organic solar cells: five core technologies for their commercialization. *Adv. Mater.* 28, 7821–7861. doi: 10.1002/adma.201601197

Li, S., Ye, L., Zhao, W., Yan, H., Yang, B., Liu, D., et al. (2018). A wide band gap polymer with a deep highest occupied molecular orbital level enables 14.2% efficiency in polymer solar cells. *J. Am. Chem. Soc.* 140, 7159–7167. doi: 10.1021/jacs.8b02695

Li, S., Ye, L., Zhao, W., Zhang, S., Mukherjee, S., Ade, H., et al. (2016). Energy-level modulation of small-molecule electron acceptors to achieve over 12% efficiency in polymer solar cells. *Adv. Mater.* 28, 9423–9429. doi: 10.1002/adma.201602776

Li, X., Pan, F., Sun, C., Zhang, M., Wang, Z., Du, J., et al. (2019). Simplified synthetic routes for low cost and high photovoltaic performance n-type organic semiconductor acceptors. *Nat. Commun.* 10:519. doi: 10.1038/s41467-019-08508-3

Li, Y., Gu, M., Pan, Z., Zhang, B., Yang, X., Gu, J., et al. (2017a). Indacenodithiophene: a promising building block for high performance polymer solar cells. *J. Mater. Chem. A* 5, 10798–10814. doi: 10.1039/C7TA02562A

Li, Y., Zhong, L., Gautam, B., Bin, H.-J., Lin, J.-D., Wu, F.-P., et al. (2017b). A near-infrared non-fullerene electron acceptor for high performance polymer solar cells. *Energy Environ. Sci.* 10, 1610–1620. doi: 10.1039/C7EE00844A

Li, Z., Jiang, K., Yang, G., Lai, J. Y. L., Ma, T., Zhao, J., et al. (2016). Donor polymer design enables efficient non-fullerene organic solar cells. *Nat. Commun.* 7:13094. doi: 10.1038/ncomms13094

Lin, J.-D., Zhong, L., Wu, F.-P., Li, Y., Yuan, Y., Bin, H., et al. (2018). Short-axis substitution approach on ladder-type benzodithiophene-based electron acceptor toward highly efficient organic solar cells. *Sci. China Chem.* 61, 1405–1412. doi: 10.1007/s11426-018-9275-6

Lin, Y., Wang, J., Zhang, Z.-G., Bai, H., Li, Y., Zhu, D., et al. (2015a). An electron acceptor challenging fullerenes for efficient polymer solar cells. *Adv. Mater.* 27, 1170–1174. doi: 10.1002/adma.201404317

Lin, Y., Zhang, Z.-G., Bai, H., Wang, J., Yao, Y., Li, Y., et al. (2015b). High-performance fullerene-free polymer solar cells with 6.31% efficiency. *Energy Environ. Sci.* 8, 610–616. doi: 10.1039/C4EE03424D

Lin, Y., Zhao, F., Wu, Y., Chen, K., Xia, Y., Li, G., et al. (2017). Mapping polymer donors toward high-efficiency fullerene free organic solar cells. *Adv. Mater.* 29:1604155. doi: 10.1002/adma.201604155

Liu, Y., Zhang, Z., Feng, S., Li, M., Wu, L., Hou, R., et al. (2017). Exploiting noncovalently conformational locking as a design strategy for high performance fused-ring electron acceptor used in polymer solar cells. *J. Am. Chem. Soc.* 139, 3356–3359. doi: 10.1021/jacs.7b00566

Meng, L., Zhang, Y., Wan, X., Li, C., Zhang, X., Wang, Y., et al. (2018). Organic and solution-processed tandem solar cells with 17.3% efficiency. *Science* 361, 1094–1098. doi: 10.1126/science.aat2612

Wang, J., Wang, W., Wang, X., Wu, Y., Zhang, Q., Yan, C., et al. (2017). Enhancing performance of nonfullerene acceptors via side-chain conjugation strategy. *Adv. Mater.* 29:1702125. doi: 10.1002/adma.201702125

Wu, Y., Bai, H., Wang, Z., Cheng, P., Zhu, S., Wang, Y., et al. (2015). A planar electron acceptor for efficient polymer solar cells. *Energy Environ. Sci.* 8, 3215–3221. doi: 10.1039/C5EE02477C

Würfel, U., Neher, D., Spies, A., and Albrecht, S. (2015). Impact of charge transport on current–voltage characteristics and power-conversion efficiency of organic solar cells. *Nat. Commun.* 6:6951. doi: 10.1038/ncomms7951

Xie, Y., Huo, L., Fan, B., Fu, H., Cai, Y., Zhang, L., et al. (2018a). High-performance semitransparent ternary organic solar cells. *Adv. Funct. Mater.* 28:1800627. doi: 10.1002/adfm.201800627

Xie, Y., Yang, F., Li, Y., Uddin, M. A., Bi, P., Fan, B., et al. (2018b). Morphology Control Enables Efficient Ternary Organic Solar Cells. *Adv. Mater.* 30:1803045. doi: 10.1002/adma.201803045

Yan, C., Wu, Y., Wang, J., Li, R., Cheng, P., Bai, H., et al. (2017). Enhancing performance of non-fullerene organic solar cells via side chain engineering of fused-ring electron acceptors. *Dyes and Pigments* 139, 627–634. doi: 10.1016/j.dyepig.2016.12.065

Yang, B., Li, J., Wu, C., Zhang, H., Pan, A., and Chen, J. (2018). Non-fullerene acceptors for large-open-circuit-voltage and high-efficiency organic solar cells. *Mater. Today Nano* 1, 47–59. doi: 10.1016/j.mtnano.2018.04.005

Yang, Y., Zhang, Z.-G., Bin, H., Chen, S., Gao, L., Xue, L., et al. (2016). Side-chain isomerization on an n-type organic semiconductor ITIC acceptor makes 11.77% high efficiency polymer solar cells. *J. Am. Chem. Soc.* 138, 15011–15018. doi: 10.1021/jacs.6b09110

Yuan, J., Zhang, Y., Zhou, L., Zhang, G., Yip, H.-L., Lau, T.-K., et al. (2019). Single-junction organic solar cell with over 15% efficiency using fused-ring acceptor with electron-deficient core. *Joule.* 3, 1140–1151. doi: 10.1016/j.joule.2019.01.004

Zhang, Z.-G., Yang, Y., Yao, J., Xue, L., Chen, S., Li, X., et al. (2017). Constructing a strongly absorbing low-bandgap polymer acceptor for high-performance all-polymer solar cells. *Angew. Chem. Int. Ed.* 56, 13503–13507. doi: 10.1002/anie.201707678

Zhao, J., Li, Y., Yang, G., Jiang, K., Lin, H., Ade, H., et al. (2016). Efficient organic solar cells processed from hydrocarbon solvents. *Nat. Energy* 1:15027. doi: 10.1038/nenergy.2015.27

Conflict of Interest Statement: The authors declare that the research was conducted in the absence of any commercial or financial relationships that could be construed as a potential conflict of interest.

frontiers in Chemistry

REVIEW
published: 18 June 2019
doi: 10.3389/fchem.2019.00428

Spin Transport in Organic Molecules

Lidan Guo[1,2,3†], *Yang Qin*[1,2†], *Xianrong Gu*[1,2], *Xiangwei Zhu*[1,2*], *Qiong Zhou*[3] and *Xiangnan Sun*[1,2*]

[1] Key Laboratory of Nanosystem and Hierarchical Fabrication, National Center for Nanoscience and Technology, CAS (Chinese Academy of Sciences) Center for Excellence in Nanoscience, Beijing, China, [2] Center of Materials Science and Optoelectronics Engineering, University of Chinese Academy of Sciences, Beijing, China, [3] Department of Materials Science and Engineering, College of New Energy and Materials, China University of Petroleum Beijing, Beijing, China

Because of the considerable advantages of functional molecules as well as supramolecules, such as the low cost, light weight, flexibility, and large area preparation via the solution method, molecular electronics has grown into an active and rapidly developing research field over the past few decades. Beyond those well-known advantages, a very long spin relaxation time of π-conjugated molecules, due to the weak spin-orbit coupling, facilitates a pioneering but fast-growing research field, known as molecular spintronics. Recently, a series of sustained progresses have been achieved with various π-conjugated molecular matrixes where spin transport is undoubtedly an important point for the spin physical process and multifunctional applications. Currently, most studies on spin transport are carried out with a molecule-based spin valve, which shows a typical geometry with a thin-film molecular layer sandwiched between two ferromagnetic electrodes. In such a device, the spin transport process has been demonstrated to have a close correlation with spin relaxation time and charge carrier mobility of π-conjugated molecules. In this review, the recent advances of spin transport in these two aspects have been systematically summarized. Particularly, spin transport in π-conjugated molecular materials, considered as promising for spintronics development, have also been highlighted, including molecular single crystal, cocrystal, solid solution as well as other highly ordered supramolecular structures.

Keywords: molecular spintronics, molecular spin valve, spin transport, functional molecules, supramolecules

OPEN ACCESS

Edited by:
Ronald K. Castellano, University of Florida, United States

Reviewed by:
Patrizio Graziosi, University of Warwick, United Kingdom
Shaomin Ji, Guangdong University of Technology, China

***Correspondence:**
Xiangwei Zhu
zhuxw@nanoctr.cn
Xiangnan Sun
sunxn@nanoctr.cn

[†]These authors have contributed equally to this work

Specialty section:
This article was submitted to Supramolecular Chemistry, a section of the journal Frontiers in Chemistry

Received: *28 February 2019*
Accepted: *27 May 2019*
Published: *18 June 2019*

Citation:
Guo L, Qin Y, Gu X, Zhu X, Zhou Q and Sun X (2019) Spin Transport in Organic Molecules. Front. Chem. 7:428. doi: 10.3389/fchem.2019.00428

INTRODUCTION

The spin degree of freedom of electrons exhibits particular potential on information non-volatile memory, transport, and processing (Wolf et al., 2001). The π-conjugated molecules, usually composed of elements with low atomic numbers, theoretically possess extremely long spin relaxation times and thus excellent spin transport properties. Organic spintronics has thus attracted extensive attention in the past decade (Dediu et al., 2009; Sanvito, 2011) after the successful spin injection in molecular materials was first reported (Dediu et al., 2002). Additionally, abundant chemical tailorability, functionality, and mechanical flexibility of organic semiconductors (OSCs) give organic spintronic devices various accessional functionalities except for a spin valve effect, such as a light embittering, photovoltaic effect, or a photoresponse, etc (Guo et al., 2019). Undoubtedly, spin transport, an important and basic topic of organic spintronics, plays a crucial role in understanding the mechanism of spin-related phenomena and in developing novel multipurpose spintronic devices (Sun X. et al., 2016; Sun et al., 2017).

In a molecule-based spintronic device, spin-polarized carriers are normally injected from a magnetic electrode, and transported in the OSC, and are finally detected by another magnetic electrode before their spin polarization becomes totally relaxed (Jang and Richter, 2017). Thus, the spin injection efficiency and the spin transport process co-determines the spin transport distance, wherein, an efficient spin-polarized injection is a prerequisite of spin transporting in the molecular layer (Shim et al., 2008; Raman et al., 2009). In order to enhance the spin injection efficiency, ferromagnetic (FM) electrodes with high spin polarization and Curie temperature are preferably used. In particular, LSMO possesses 100% spin polarization but can only be realized at 4.2 K (Bowen et al., 2003), which greatly reduces its application potential. In contrast, Fe_3O_4 (Zhang et al., 2014), NiFe (Sun X. et al., 2016), Ni (Starko-Bowes et al., 2013), and Co (Sun et al., 2013) with high Curie temperature is more inclined to be used in the devices in room-temperature operations. In addition, a thin buffer layer is normally inserted at the FM/molecule interface to relieve the Schottky barrier or energy level mismatch, which has been demonstrated as a very efficient method to enhance spin injection. Layer materials include metallic oxides or fluorides [e.g., AlO_x (Sun et al., 2013; Zhang X. et al., 2013), MgO (Szulczewski et al., 2009), LiF (Schulz et al., 2011; Nguyen et al., 2012)], molecules (Prieto-Ruiz et al., 2019), self-assembled monolayers (Pookpanratana et al., 2015), etc. The spin-polarized carriers tunnel across such an interface and thus the problem of energy level mismatch can be ignored. It is also worth noting that the inserted interfacial layer on the top of molecular layer can also reduce the penetration from the top electrode, which will efficiently protect the molecular layer and facilitate the formation of spin valves rather than tunnel junctions (whose spin transport mode is tunneling due to very thin molecular materials). Furthermore, novel spin injection methods via a spin pumping process (Ando et al., 2013; Jiang et al., 2015; Sun D. et al., 2016) or via hot spin electron emitting (Appelbaum et al., 2007; Gobbi et al., 2012) are also being actively explored. Indeed, a few recent reviews have made a relatively detailed introduction to spin injection and spinterface (Cinchetti et al., 2017; Jang and Richter, 2017; Sun and Mi, 2018), which can be referenced as well.

The influence factors of spin transport performance in OSC can be found in Einstein's relationship, $\lambda_s = \sqrt{(D_{hop} + D_{ex})\ \tau_s}$, where D_{hop}, D_{ex}, τ_s, are the spin diffusion constants based on the hopping spin transport mode and exchange coupling mode, spin relaxation time of molecules, respectively. It is worth noting that, only with a high carrier concentration in the molecular layer, generally induced via the impurity band (Yu, 2014; Bergenti et al., 2018; Riminucci et al., 2019) or doped molecular semiconductors (Wang et al., 2019), is D_{ex} a prominent value and should therefore be seriously considered. An exchange coupling model provides a particularly fast speed compared to hopping transport since the spin transport process can decouple with charge transport. Moreover, the absence of the Hanle effect (Grünewald et al., 2013; Riminucci et al., 2019) and the low operating voltage (Barraud et al., 2010; Grünewald et al., 2014) in a device based on a molecular layer with an impurity band can also be explained. For the hopping transport mode, $D_{hop}=k_BT\mu/e$, where k_B, μ are the Boltzmann constant, and charge carrier transport mobility, respectively. Therefore, from the Einstein relationship, a long spin relaxation time and high carrier concentration or mobility of OSC appears to improve the spin transport distance. The spin relaxation time therefore determines the duration of the spin polarization in OSC, which is mainly influenced by elemental compositions, molecular structure sand morphologies of OSC. The mobility of the semiconductor determines the transport rapid of spin-polarized carriers and is influenced by the molecular structures, packing mode, aggregation structure, as well as defects (Dong et al., 2013) (**Figure 1**).

One main purpose of this review is to provide guidelines for key points toward pursuing longer spin transport distances in OSCs, while the relationship between the characteristic of π-conjugated molecules and the spin transport process will be the focal point. First, by introducing two typical spin relaxation mechanisms, spin-orbit coupling (SOC) and hyperfine interaction (HFI), a systematic illustration on how the elementary composition and molecular structure affects the spin relaxation time will be provided. Second, has been found that the aggregation structure has dual effects on both the spin relaxation time and mobility. Thus, spin transport properties of OSCs, with three different aggregation structures including polycrystalline/amorphous thin films, single crystals as well as supramolecular assembly structures, are discussed and prospected, respectively. Additionally, a conclusion and outlook section has also been provided at the end in order to summarize the current achievements and outline challenges for obtaining longer spin transport distances.

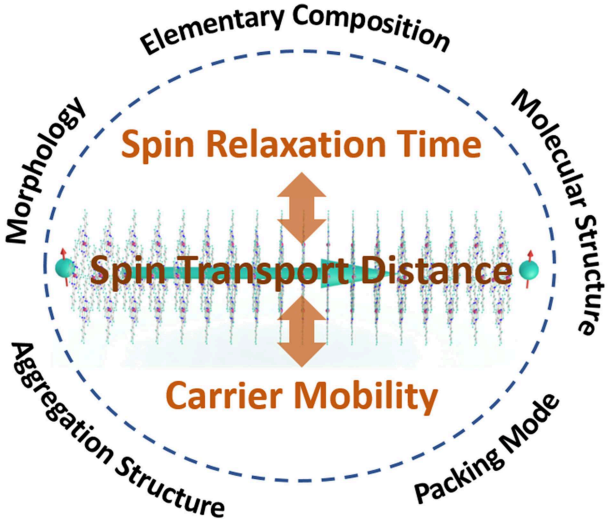

FIGURE 1 | An overview of this review, with the key points of achieving long spin transport distances in OSCs, where spin relaxation time and mobility are the direct impacts affected by elementary composition, molecular structure, packing mode, aggregation structure, and morphology of OSCs.

SPIN RELAXATION MECHANISM IN π-CONJUGATED MOLECULES

The SOC and HFI are considered to be the principal factors that cause spin relaxation in OSCs. So far, few studies have revealed that the modification of the elementary composition and chemical structure of molecules are feasible ways to weaken the SOC or HFI effects, therefore prolonging the spin relaxation time.

Spin-Orbit Coupling

The SOC is the interaction between the spin and charge's orbital angular momentum, which has a double impact on spin devices: it contributes to the spin-charge conversion and also causes spin relaxation (Schott et al., 2017). Generally, the SOC strength is proportional to the fourth power of the atomic number, and the light-weight-element composition (such as C, H, O, N) of OSCs just leads to a very weak SOC strength and therefore extremely long spin relaxation time up to a millisecond level experimentally and even second level in theory (Pramanik et al., 2007; Watanabe et al., 2014).

By comparing the SOC strength of tris-(8-hydroxyquinoline) aluminum (Alq_3) and tris(2-phenylpyridine) ($Ir(ppy)_3$) whose chemical structures are similar, Wohlgenannt's group demonstrated that heavier atoms of Ir leads to a stronger SOC in the $Ir(ppy)_3$ molecule (**Figure 2**) (Nguyen et al., 2007; Sheng et al., 2007). Furthermore, a series of molecules resembling such a molecular structure, Xq_3 (X = Al, Ga, In, Bi) and triethylsilylethynyl (TES) series molecules, are studied through muon spin resonance (μSR) and intersystem crossing rates, where a similar dependence on the atom number has been observed (Nuccio et al., 2013). In addition to attributing the SOC strength to different elements, benefiting from the chemical designability of OSCs, the SOC strength can be modulated by synthesizing molecules containing different concentrations of heavy metal atoms. With an increased Pt concentration in three synthetic Pt-containing polymers, the SOC strength obviously increased, which can be found, on one hand, in the molecular structure (Pt concentration, Pt-1<Pt-3<Pt-Q, **Figure 2**). The distance between two adjacent Pt-atoms shrunk gradually with an increased Pt-atom concentration, and the intersystem-crossing (ISC) between the singlet and triplet states enhanced due to the localized Metal-to-Ligand Charge Transfer (MLCT), finally leading to an increased ratio of phosphorescence(Ph)/fluorescence(FL) (Sheng et al., 2013). On the other hand, from the measured results of inverse spin Hall voltage (V_{ISHE}), the observation of the measured stronger SOC strength, corresponding to larger $V_{ISHE,}$ is consistent with the detected ratio of Ph/FL (Sun D. et al., 2016), which suggests the effect of atomic numbers.

Particularly, though theoretical calculations, Yu found that the SOC strength in sexythiophene (T6) and copper phthalocyanine (CuPc) was obviously lower than that in Alq_3 molecule, although the atom weight of sulfur (S) and copper (Cu) elements were higher than the aluminum (Al) element. It was found that, T6 and CuPc are planar structures, whereas Alq_3 is mainly a spatial stereostructure with three ligands arranged orthogonally, which enhances the spin mixing and thus leads to a stronger SOC (Yu, 2011, 2012). This report reveals that the SOC strength is not only related to the atomic number of materials but is also strongly affected by the molecular structure. The influence of the torsion angles of adjacent planar units in P3HT has also been researched through experiments and calculations, wherein, the large thiophene-thiophene dihedral angle corresponded to a larger spin admixture parameter which reflects the SOC strength, and thus a shorter spin diffusion length (Wang et al., 2019). Similarly, has also been found that the C_{60} expresses a large SOC even if it is purely composed by carbon atoms. Experimentally, through a more direct SOC measuring method of inverse spin Hall effect (ISHE), Sun et al. found that the SOC strength of C_{60} is even larger than the Pt-containing polymers. For such unusual observations, Sun et al. and Yu proved that the strong curvature of 60 carbon atoms on a spherical π orbitals results in the mixing of π and σ electrons (Yu, 2012; Sun D. et al., 2016). Moreover, with respect to the effect of curvature degree on the strength of SOC in fullerene-based materials, the effective SOC of C_{60} and C_{70} were estimated indirectly by obtaining the spin diffusion length in C_{60} film and C_{70} film by fitting the thickness dependence of magnetoresistance (MR) in OSVs using the modified Jullière equation, as well as the effective spin polarization at the interface of Co/C_{60} and Co/C_{70} using a first principle calculation. Stronger SOC in C_{60} and a higher spin polarization at Co/C_{60} interface, but shorter spin diffusion length, have been demonstrated, which reveals that the apparently larger SOC in C_{60} is derived from the lager curvature of the molecular structure (Liang et al., 2016).

Hyperfine Interaction

HFI is another main intrinsic effect that can cause spin relaxation in OSCs, which primarily originates from the half-integer nuclear spins of atoms, for example, ^{1}H, ^{19}F, ^{27}Al, ^{63}Cu, etc. The half-integer nuclear spins leads to random magnetic fields which can indirectly couple to the spins of the carbon π electrons through the exchange interaction of carbon s electrons. Such interactions leads to the precession of the π electron spin, and consequently gives rise to spin relaxation (Bobbert, 2010; Yu et al., 2013).

Quantitative research, for HFI fields in a few molecules frequently employed in studies of spintronics, has already been implemented via first-principle calculations or ab initio calculations (Filidou et al., 2012; Giro et al., 2013; Yu et al., 2013). An effective HFI field for electron and hole polarons in molecular materials with H and deuterium(D)-substituted, have been shown in Yu's research (Yu et al., 2013). It has been found that substituting a given nucleus with its isotope, is an effective method to modify the HFI strength. And by replacing H by D via deuteration, the effective HFI field is expected to be reduced by a quarter in poly(dioctyloxy)phenylenevinylene (DOO-PPV) (Yu et al., 2013). Furthermore, relevant experimental evidence has also been reported by Vardeny's group (Nguyen et al., 2010b). The important role that HFI plays in spin transport has been demonstrated in a designed D-polymeric semiconductor where all ^{1}H near the backbone carbon atoms on the polymer chains have been exchanged to ^{2}H (D) atoms, from which the electronic properties are reserved but the nuclear magnetic moment becomes smaller. All devices based on the D-polymer

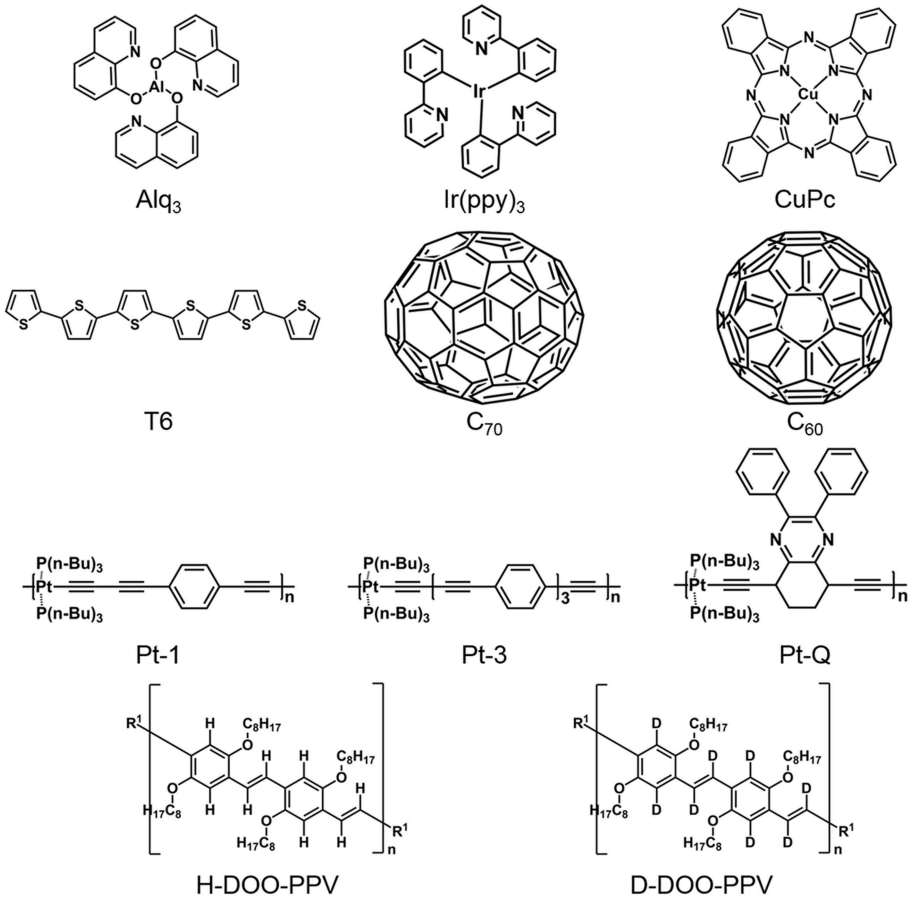

FIGURE 2 | Chemical structures of molecules that have been employed in recent studies regarding spin transport.

have a larger spin valve effect and longer spin diffusion length than those based on the H-polymer, which is in agreement with the increase of the spin-relaxation time they measured. Besides deuteration, the substitution of ^{12}C atoms with ^{13}C atoms in the chemical backbone of the DOO-PPV polymers has also been studied, and the HFI increases with the half-integer nuclear spins of ^{13}C, as expected (Nguyen et al., 2010a, 2011). Fullerene (C_{60}) is considered to be a particularly unique molecule that only contains ^{12}C and thus is considered to contain no HFI field. The HFI in C_{60} is estimated via organic magnetoresistance (OMAR) whose intrinsic mechanism can supposedly, according to some researchers, be interpreted by HFI (Kalinowski et al., 2003; Bobbert et al., 2007; Nguyen et al., 2007; Koopmans et al., 2011). Experimentally, no measurable OMAR effect is observed in C_{60}-based devices, therefore, they note that the absence of hydrogen in most inorganic materials may be the reason why the OMAR effect cannot be found in inorganic spin devices. From the research of spin transport and OMAR (Bobbert, 2010), on one hand, HFI should be as small as possible to achieve a long spin lifetime and transport distance. On the other hand, HFI is considered to be larger due to its effect on OMAR (Sheng et al., 2006; McCamey et al., 2010; Nguyen et al., 2010a) and the manipulation of spins in molecular spintronics (Bobbert, 2014).

EFFECT OF MOBILITY ON SPIN TRANSPORT

Charge carrier mobility is another important factor that determines the spin transport process in OSCs. At the initial research stage, thin-film semiconductors with low mobility are usually used as the spin transport layer, which is normally prepared via thermal evaporation (Xiong et al., 2004; Nguyen et al., 2012). So far, although many significant contributions have already been made based on such thin films (Nguyen et al., 2012; Sun et al., 2017), the low mobility is clearly a bottleneck for further enhancing the spin transport performance. Thanks to the great development in the field of organic electronics, especially the prosperous research on organic field effect transistors (OFETs) in the past decades, many high-mobility organic semiconductor materials have been developed (Dong et al., 2013; Gao and Zhao, 2015), which provides strong material support for the current research of spin transport. For instance, the high mobility n-type semiconductor, poly[N,N′-bis(2-octyldodecyl)-1,4,5,8-naphthalenedicarboximide)-2,6-diyl]-alt-5,5′-(2,2′-bithio-phene) [P(NDI2OD-T2)] with the electron mobility of 0.2∼0.85 cm^2/Vs, has been employed to build OSVs and a very long spin transport distance of 64 nm

has been observed at 4.2 K (Li et al., 2015). The OSC single crystal has long been considered to be the ideal material for spin transport, since it possesses both a long spin relaxation time and very high mobility due to the relatively pure matrix and thus weak scattering during the transport process of spin/charge carriers (Wang et al., 2018; Zhang et al., 2018). Additionally, supramolecular semiconductors, especially the cocrystals, have also exhibited significant advantages in terms of high conductivity, photoelectric property and non-linear optics, etc (Zhu et al., 2015; Wang et al., 2016). With the target of both high mobility for long spin transport distance and multifunctional applications, single crystal, and supramolecules are very promising for the future development of organic spintronics, however related research is currently still in its infancy.

OSC Thin Films

Since the first observation of giant magnetoresistance (GMR) in 8-hydroxy-quinoline aluminum (Alq_3) (Xiong et al., 2004), a variety of OSC thin films have been applied as the spacer in spin valves. **Table 1** shows a summary of the spin transport distances and corresponding mobilities of few OSCs that have been widely employed in previous studies of spintronics. Although the experimentally measured spin transport distance is comprehensively affected by magnetic electrodes, spin injection efficiency, device fabrication, etc (Dediu et al., 2009), a clear relationship that can be found is that the spin transport distance has obviously been enhanced in OSCs with higher mobility. Additionally, it worth noting from **Table 1** that a high-mobility polymer, known as P(NDI2OD-T2), corresponds to a relatively short spin transport distance of 42 nm at 300 K, which can be attributed to the vacancy or solvent residue in P(NDI2OD-T2) film prepared via the solution method (Li et al., 2015), whereas other organic semiconductors in **Table 1** are prepared via thermal evaporation. In fact, the defects in organic molecules will lead to strong spin scattering centers which are much more sensitive to defects in contrast to the carrier mobility of thin films. With regard to defects induced via the solution method, Mei's group have developed a novel melt-processing method which can clearly decrease the defect density and thus achieve an excellent charge carrier transport in thin films (Zhao et al., 2017, 2018).

A number of novel high-mobility OSCs (>5 cm^2/Vs) and feasible methods for achieving high-performance charge carrier transport have also been summarized in recent reviews (Tsao and Mullen, 2010; Dong et al., 2013; Gao and Zhao, 2015), and herein, several important points for selecting high-mobility semiconductors used in organic spintronic field were extracted. First, the condensed π-π stacking and little tilt angle of adjacent molecules will help increase the charge transfer integrals and thus the mobility, which can be realized via appropriate molecular design engineering, such as maximizing the intermolecular π-conjugated and by introducing intermolecular hydrogen-bonding or dipole-dipole interaction, and by increasing the intrachain conjugated length, etc. Second, morphology control is another key point for obtaining high mobility, and an accepted fact is that polycrystalline or ordered OSCs possess a higher mobility than a disordered structure. A grain boundary separating the packed crystalline domains is the main obstacle for pursing high mobility, and it can be highly reduced by controlling the chemical structure and molecular weight design, solvent or thermal annealing, etc. For simply fabricating an ordered thin film, a novel method of using Chinese brushes to control liquid transfer can make the molecules more ordered along the brushing direction and thus leading to an enhanced electrical property (Lin et al., 2017).

In previous studies it has been found that the grain boundaries can also work as the spin scattering centers in polycrystalline OSC thin films. The correlation between grain boundary density and spin transport performance has been investigated in polycrystalline C_{60} thin films whose carrier mobility can be changed from 2 to 5 cm^2/Vs according to the controllable grain size (Kwiatkowski et al., 2009). Recently, Nguyen et al. prepared C_{60} thin films with grain sizes between 8.8 and 10.5 nm by simply controlling the grown thicknesses of the films (**Figures 3A,B**) (Nguyen et al., 2013). It was found that the spin transport performance decreases with the increased thickness of the molecular layer, nevertheless, a variation of GMR has been measured and the highest MR is measured at the thickness of 45 nm (**Figure 3C**). Thus, it is clear that the dominant effect on spin transport distance has been changed from the mobility to morphology effect enhanced by spin scattering along with the increased thickness, which means the gradually increased grain boundary density in the film enhances the surface spin-flip probability and therefore weakens the spin transport distance. Similar morphology effects on carrier/spin transport performance have also been observed in other studies (Shim et al., 2008; Bobbert et al., 2009). Recently, Sun et al. demonstrated that the homogeneous amorphous OSC thin films may possess much better spin transport performance by excluding the negative effect of grain boundary density in thin-film spin valves (**Table 1**) (Sun X. et al., 2016). In that study, polycrystalline F_{16}CuPc has shown distinctive grain boundaries and much larger root-mean-square (RMS) roughness than the amorphous one (**Figures 3D,E**). Although the amorphous F_{16}CuPc deposited at low temperature (LT) merely shows a mobility of 0.9×10^{-3} cm^2/Vs, much lower than the polycrystalline one (4.2×10^{-3} cm^2/Vs), a large spin diffusion length up to 180 nm has been observed at room temperature (RT) which, to our knowledge, is the best recorded molecular matrix so far. According to the above studies, OSC materials with high mobility and weak spin scattering factors are very promising for spin transport applications. In fact, a long spin transport distance up to hundreds of nanometers or even at the millimeter level in single-crystal rubrene has been predicted in a theoretical study (Yu, 2012), whereas the amorphous rubrene thin film has shown a spin diffusion length of merely 13.3 nm (Shim et al., 2008).

Single Crystals

Organic semiconductor single crystals, with a perfect crystal texture, minimal density of defects, and an absence of grain boundaries have exhibited very high mobility (>5 cm^2/Vs) and unique physicochemical properties, which have developed rapidly in recent years (Briseno et al., 2006; Fan et al., 2013; Wang et al., 2018; Zhang et al., 2018). Different from the hopping

TABLE 1 | Mobility of thin-film OSCs and the corresponding spin transport distance in spintronic devices.

Organic semiconductor	Mobility of thin film (cm^2/Vs)	Device structure (bottom to top)	Spin transport distance
Alq_3	2×10^{-8}~2×10^{-10} (Chen et al., 1999)	Co/Al_2O_3/**Alq_3**/$Ni_{80}Fe_{20}$	1.6 nm @ 300 K (Santos et al., 2007)
		Ni/**Alq_3**/Co	4.25 nm @ 50 K (Pramanik et al., 2007)
		LSMO/**Alq_3**/Co/Al	45 nm @ 11 K (Xiong et al., 2004)
Rubrene (Amorphous)	~10^{-6} (Seo et al., 2006)	Fe_3O_4/AlO/**Rubrene**/Co	20 nm @ 300 K (Zhang et al., 2015)
		Fe/**Rubrene**/V[TCNE]$_X$/Al	10 nm @ 300 K (Li et al., 2011)
		Fe/Al_2O_3/**Rubrene**/Co/SiO	13.3 nm @ 0.45 K(Shim et al., 2008)
BCP	5×10^{-6} (Liu et al., 2011)	Co/leaky AlOx/**BCP**/$Ni_{80}Fe_{20}$	60 nm @ 300 K (Sun et al., 2013)
C_{60} (Amorphous)	1.4×10^{-5} (Im et al., 2011)	MgO/Fe_3O_4/Al-O/**C_{60}**/Co/Al	110 nm @ 300 K (Zhang J. et al., 2013)
		LSMO/**C_{60}**/AlOx/Co	36 nm @ 300 K (Li et al., 2014)
		LSMO/**C_{60}**/Co/Al	12 nm @ 10 K (Nguyen et al., 2013)
$F_{16}CuPc$	9×10^{-4} (Sun X. et al., 2016)	Co/AlOx/**$F_{16}CuPc$**/$Ni_{80}Fe_{20}$	180 nm @ 300 K (Sun X. et al., 2016)
P(NDI2OD-T2)	0.2~0.85 (Yan et al., 2009)	LSMO/**P(NDI2OD-T2)**/AlOx/Co	42 nm @ 300 K (Li et al., 2015)
			64 nm @ 4.2 K (Li et al., 2015)

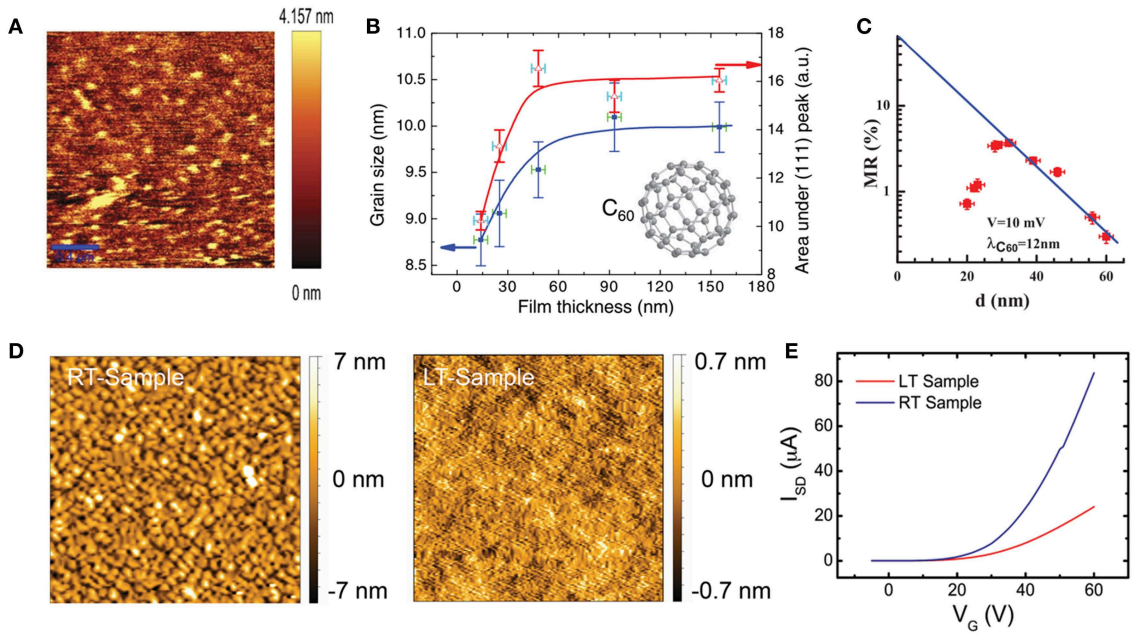

FIGURE 3 | The effect of morphology on carrier mobility and spin transport distance. AFM image of C_{60} thin film **(A)**. The relationship between grain size and film thickness, and the area of (111) Bragg scattering peak and film thickness **(B)**. C_{60} thickness dependence of MR with bias of 10 mV **(C)**. [A&B&C reproduced from (Nguyen et al., 2013), with permission of American Physical Society] AFM images of $F_{16}CuPc$ fabricated at RT and LT **(D)**. Transfer curves of $F_{16}CuPc$-based OFET at RT and LT **(E)**. [D&E reproduced from (Sun X. et al., 2016), with permission of John Wiley and Sons].

transport mode of carriers in thin-film OSCs, delocalized band-like charge transport is presented in organic single crystals, which possesses a negative temperature coefficient of mobility (Krupskaya et al., 2015; Xu et al., 2016). The long range ordered arrangement of the molecules leads to anisotropic charge-transport properties and carrier mobility. Generally, large π-stacking and strong transfer integrals will lead to an efficient charge transport along the π-π stacking direction (Zhang et al., 2018), and if the current direction is perpendicular to the strong interlayer electronic couplings, the charge transport will be diminished remarkably (Zhang Z. P. et al., 2016), which means that the called "face on" stacking style will be beneficial for the vertical spin devices and the "edge on" style will be more beneficial for lateral spintronic devices. However, the effect of stacking style on spin transport performance has not been systematically studied so far, and more research efforts still need to be devoted on this point. In a recent report, Tsurumi et al. studied the spin transport process and relaxation mechanism in a lateral-structured device based on C_{10}-DNBDT-NW single crystals, where the Hall mobility reached 16.5 cm^2/Vs

at the in-plane direction, while the experimental measured spin relaxation time reached 16.6 ns at RT. According to the Einstein relationship, the corresponding spin transport distance is estimated to be 840 nm at RT and up to 1.6 μm at 50 K, which shows the great potential of single crystals in the application of spintronic devices (Tsurumi et al., 2017). However, this experimental lateral device does not have a real spin injection process, which means it is not a true sense of the spintronic device and also implies a big challenge in using single crystals within the research field of spintronics.

As for using single crystals to fabricate spintronic devices and research spin transport properties, several challenges need to be addressed or paid attention to. With regard to spintronic device preparation, the fabrication of the top magnetic electrode is a serious issue, since the organic single crystal tends to be damaged by the very high temperature during the process (Sun et al., 2014). So far, the buffer layer assisted deposition (BLAG) (Sun et al., 2010) and the liquid nitrogen cooling method (Sun et al., 2013) are demonstrated to be very promising in avoiding metal penetration in organic spintronic devices during top electrode deposition on OSC thin films. However, such methods have not yet been applied to fabricate electrical devices based on a single crystal. For fabricating single-crystal-based electronic devices such as OFETs, thermal evaporation at a high vacuum and stamping Au layer are usually employed to pattern the source and drain electrodes on OSC crystals (Zhang et al., 2010; Kikuchi et al., 2017). Similar methods may possibly also be introduced for fabricating single crystal based spintronic devices by replacing the Au with magnetic metals, however, there are of course many technical challenges that still need to be overcome. Particularly, with regard to lateral single-crystal spintronic devices (**Figure 4A**), the limitation of existing spin transport distance will be an issue, since the longest spin transport distance is merely 180 nm currently (Sun X. et al., 2016; Tsurumi et al., 2017). In addition, spin injection, a key point for successfully detecting spin signals, may suffer from the influence of bad contact between the magnetic electrode and single crystal, which is limited by both the dedicated device structure and the current level of lab-scale fabrication techniques. Indeed, spintronic devices based on an organic single crystal is a novel research field and shows abundant possibilities due to its unique properties, however, various issues need to be addressed in the exploration of this new direction.

Supramolecules

The π-conjugated supramolecular materials are normally assembled by two or more kinds molecules that held together by non-covalent intramolecular interactions, such as π-π stacking, hydrogen-bonding and dipole-dipole interactions etc (Ghosh et al., 2017; Ikeda and Haino, 2017), which generally exhibit a special functionality compared to homogeneous OSC and have shown great potential in functional spintronic devices. Based on supramolecular material, Urdampilleta et al. fabricate a lateral spintronic device, in which the source and drain electrodes are palladium and the charge transport layer is composed of a single-walled carbon nanotube (SWCNT) coupled with modified $TbPc_2$ single-molecule magnets (Pc = phthalocyanine)

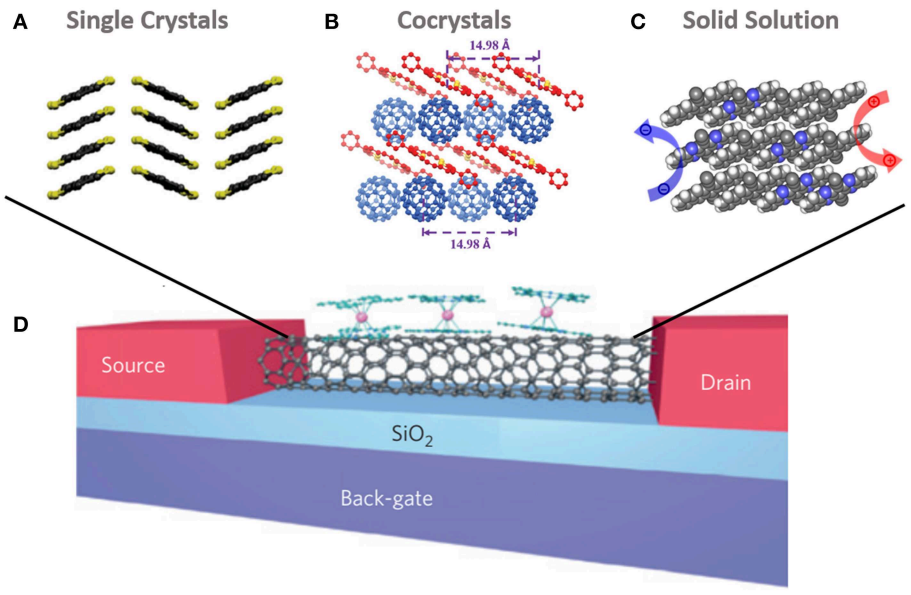

FIGURE 4 | Schematic diagram of lateral spintronic devices based on single crystals [Reproduced from Zhang et al., 2016, with permission of John Wiley and Sons] **(A)**, cocrystals [Reproduced from Zhang et al., 2016, with permission of John Wiley and Sons] **(B)** and solid solutions [Reproduced from (Xu et al., 2015), with permission of American Chemical Society] **(C)**. Schematic diagram of a supramolecular spin valve based on SWCNT, coupled with modified $TbPc_2$ single-molecule magnets [Reproduced from (Urdampilleta et al., 2011), with permission of Springer Nature] **(D)**, where the supramolecules of SWCNT coupled with modified $TbPc_2$ can be substituted by single crystals, cocrystals, and solid solutions.

through supramolecular π-π interaction (**Figure 4D**). When non-spin-polarized carriers transport in SWCNT, the localized magnetic moments from $TbPc_2$ will lead to obvious magnetic field dependence of conductance, where a magnetoresistance up to 300% can be observed below 1 K (Urdampilleta et al., 2011). Although this supramolecular spin valve has not shown a classical spin transport process in the molecular matrix, it still presents a very promising future of supramolecular assemblies for spintronic applications.

More functional supramolecular semiconductor materials are eagerly expected to be applied in the study of spin transport and functional spintronic devices, especially after the success of the first molecular spin photovoltaic (MSP) device, in which the spin transport, coupled with a photovoltaic effect, has been firstly achieved in molecule-based devices (Sun et al., 2017). However, in this study, the MSP device just shows an extremely low power conversion efficiency (PCE) since the active layer consists of only one component C_{60}, which is clearly a large limitation for further enhancing the spin performance of this device. As known in the organic photovoltaic (OPV) field, bulk heterojunction structured devices hold much higher PCE than single layer devices, where the supramolecular interaction and assembly of donor and accepter materials plays a crucial role (Wurthner, 2016; Ghosh et al., 2017). The purpose of studying supramolecular assembly in OPV is mainly to obtain a high charge transfer rate and low charge recombination in the perpendicular direction, which is partially consistent with the demand of vertical spintronic devices. However, the interface induced by a two-phase structure may enhance the spin scattering, which is similar to the impact of grain boundaries. Therefore, how to utilize the supramolecular Nano assembly to modulate the microphase separation, and thus to reduce spin scattering and enhance PCE, will be a very interesting research direction in the future.

Organic cocrystals, composed of two or more components through supramolecular interaction, is a single-phase semiconductor and appears to exhibit more benefits for spin transport (Zhu et al., 2015; Wang et al., 2016), in which the defect induced charge/spin carrier scattering can be minimized (**Figure 4B**). Hydrogen-bonded, halogen-bonded, π-π stacking and charge transfer are the four typical supramolecular interactions in organic cocrystals. The charge transfer interaction is an especially important type, showing high conductivity (Hiraoka et al., 2007; Zheng et al., 2018), while the π-π stacking interaction tends to make a contribution to the photoelectronic properties of cocrystals (Zhang J. et al., 2013). At present, organic cocrystals have already been preliminarily used in lateral OPV devices. Even though a PCE of only 0.27% has been obtained based on C_{60}-DPTTA with the electron and hole mobility of 0.01 and 0.3 cm^2/Vs, respectively, it distinctly demonstrates the possibility for applying cocrystal in MSP devices (Zhang et al., 2016b). In addition, solid solutions and doped crystals are two novel types of supramolecular crystals which also present unique photoelectric properties and high conductivity (**Figure 4C**). The different two-phase proportions in cocrystals, solid solutions and doped crystals may lead to different spin scattering strengths and spin transport performances, certainly it needs sufficient investigations in the future. Once the supramolecular semiconductors are successfully applied in spintronics, both the interesting functions and attractive transport properties in supramolecules should enrich the theoretical and experimental research of this field.

CONCLUSION AND OUTLOOK

Spin transport greatly depends on the spin relaxation time and carrier mobility of OSCs, where elementary composition, molecular structure, packing mode, aggregation structure, and morphology play crucial roles. In this review, correlations between the above parameters and spin transport performance are systemically discussed, and some primary guidelines for enhancing spin transport performances in π-conjugated molecular materials are provided. SOC and HFI, as two principle spin relaxation mechanisms, are closely related to elementary composition and molecular structure, which can be distinctly weakened by modifications on the molecular structure. In addition, on the basis of effectively controlling the spin scattering which originates from grain boundaries and other structure defects, the high mobility of π-conjugated molecular materials is demonstrated to be very promising for long-distance spin transport. Particularly, the ordered stacked aggregation of molecules with both high mobility and weak spin scattering factors possess great potential in high-performance spin transport, including single crystals and supramolecular Nano assembled structures (especially organic cocrystals). In terms of current developments in organic electronics and spintronics, spintronic devices based on single crystals or cocrystals can only be applied through lateral device structures, and many restrictions at the technical level still need to be overcome, while reliable device fabrication and efficient spin injection should receive more attention in the future.

AUTHOR CONTRIBUTIONS

LG and YQ co-wrote the paper. XG completed the spelling and grammar check, and copyright section. XZ and XS supervised this review and completed all the submissions. All authors joined the discussion and revision of this paper.

ACKNOWLEDGMENTS

We thank the financial support of the Ministry of Science and Technology of China (2016YFA0200700, 2017YFA0206600), the National Natural Science Foundation of China (51822301, 21673059, and 51803040), the CAS Instrument Development Project (YJKYYQ20170037) and the CAS Pioneer Hundred Talents Program.

REFERENCES

Ando, K., Watanabe, S., Mooser, S., Saitoh, E., and Sirringhaus, H. (2013). Solution-processed organic spin-charge converter. *Nat. Mater.* 12, 622–627. doi: 10.1038/nmat3634

Appelbaum, I., Huang, B., and Monsma, D. J. (2007). Electronic measurement and control of spin transport in silicon. *Nature* 447, 295–298. doi: 10.1038/nature05803

Barraud, C., Seneor, P., Mattana, R., Fusil, S., Bouzehouane, K., Deranlot, C., et al. (2010). Unravelling the role of the interface for spin injection into organic semiconductors. *Nat. Phys.* 6, 615–620. doi: 10.1038/nphys1688

Bergenti, I., Borgatti, F., Calbucci, M., Riminucci, A., Cecchini, R., Graziosi, P., et al. (2018). Oxygen impurities link bistability and magnetoresistance in organic spin valves. *ACS Appl. Mater. Interfaces* 10, 8132–8140. doi: 10.1021/acsami.7b16068

Bobbert, P. A. (2010). Organic semiconductors: what makes the spin relax? *Nat. Mater.* 9, 288–290. doi: 10.1038/nmat2718

Bobbert, P. A. (2014). Manipulating spin in organic spintronics. *Science* 345, 1450–1451. doi: 10.1126/science.1259655

Bobbert, P. A., Nguyen, T. D., van Oost, F. W., Koopmans, B., and Wohlgenannt, M. (2007). Bipolaron mechanism for organic magnetoresistance. *Phys. Rev. Lett.* 99:216801. doi: 10.1103/PhysRevLett.99.216801

Bobbert, P. A., Wagemans, W., van Oost, F. W., Koopmans, B., and Wohlgenannt, M. (2009). Theory for spin diffusion in disordered organic semiconductors. *Phys. Rev. Lett.* 102:156604. doi: 10.1103/PhysRevLett.102.156604

Bowen, M., Bibes, M., Barthélémy, A., Contour, J. P., Anane, A., Lemaitre, Y., et al. (2003). Nearly total spin polarization in La2/3Sr1/3MnO3 from tunneling experiments. *Appl. Phys. Lett.* 82, 233–235. doi: 10.1063/1.1534619

Briseno, A. L., Mannsfeld, S. C., Ling, M. M., Liu, S., Tseng, R. J., Reese, C., et al. (2006). Patterning organic single-crystal transistor arrays. *Nature* 444, 913–917. doi: 10.1038/nature05427

Chen, B. J., Lai, W. Y., Gao, Z. Q., Lee, C. S., Lee, S. T., and Gambling, W. A. (1999). Electron drift mobility and electroluminescent efficiency of tris(8-hydroxyquinolinolato) aluminum. *Appl. Phys. Lett.* 75, 4010–4012. doi: 10.1063/1.125521

Cinchetti, M., Dediu, V. A., and Hueso, L. E. (2017). Activating the molecular spinterface. *Nat. Mater.* 16, 507–515. doi: 10.1038/nmat4902

Dediu, V., Murgia, M., Matacatta, F. C., Taliani, C., and Barbanera, S. (2002). Room temperature spin polarized injection in organic semiconductor. *Solid State Commun.* 122, 181–184. doi: 10.1016/S0038-1098(02)00090-X

Dediu, V. A., Hueso, L. E., Bergenti, I., and Taliani, C. (2009). Spin routes in organic semiconductors. *Nat. Mater.* 8, 707–716. doi: 10.1038/nmat2510

Dong, H., Fu, X., Liu, J., Wang, Z., and Hu, W. (2013). 25th anniversary article: key points for high-mobility organic field-effect transistors. *Adv. Mater.* 25, 6158–6183. doi: 10.1002/adma.201302514

Fan, C., Zoombelt, A. P., Jiang, H., Fu, W., Wu, J., Yuan, W., et al. (2013). Solution-grown organic single-crystalline p-n junctions with ambipolar charge transport. *Adv. Mater.* 25, 5762–5766. doi: 10.1002/adma.201302605

Filidou, V., Ceresoli, D., Morton, J. J. L., and Giustino, F. (2012). First-principles investigation of hyperfine interactions for nuclear spin entanglement in photoexcited fullerenes. *Phys. Rev. B* 85:115430. doi: 10.1103/PhysRevB.85.115430

Gao, X., and Zhao, Z. (2015). High mobility organic semiconductors for field-effect transistors. *Sci. Chi. Chem.* 58, 947–968. doi: 10.1007/s11426-015-5399-5

Ghosh, T., Panicker, J., and Nair, V. (2017). Self-assembled organic materials for photovoltaic application. *Polymers* 9:112. doi: 10.3390/polym9030112

Giro, R., Rosselli, F. P., dos Santos Carvalho, R., Capaz, R. B., Cremona, M., and Achete, C. A. (2013). Molecular hyperfine fields in organic magnetoresistance devices. *Phys. Rev. B* 87:125204. doi: 10.1103/PhysRevB.87.125204

Gobbi, M., Bedoya-Pinto, A., Golmar, F., Llopis, R., Casanova, F., and Hueso, L. E. (2012). C60-based hot-electron magnetic tunnel transistor. *Appl. Phys. Lett.* 101:102404. doi: 10.1063/1.4751030

Grünewald, M., Göckeritz, R., Homonnay, N., Würthner, F., Molenkamp, L. W., and Schmidt, G. (2013). Vertical organic spin valves in perpendicular magnetic fields. *Phys. Rev. B* 88:085319. doi: 10.1103/PhysRevB.88.085319

Grünewald, M., Homonnay, N., Kleinlein, J., and Schmidt, G. (2014). Voltage-controlled oxide barriers in organic/hybrid spin valves based on tunneling anisotropic magnetoresistance. *Phys. Rev. B* 90:205208. doi: 10.1103/PhysRevB.90.205208

Guo, L., Gu, X., Zhu, X., and Sun, X. (2019). Recent advances in molecular spintronics: multifunctional spintronic devices. *Adv. Mater.* doi: 10.1002/adma.201805355

Hiraoka, M., Hasegawa, T., Yamada, T., Takahashi, Y., Horiuchi, S., and Tokura, Y. (2007). On-substrate synthesis of molecular conductor films and circuits. *Adv. Mater.* 19, 3248–3251. doi: 10.1002/adma.200701162

Ikeda, T., and Haino, T. (2017). Supramolecular polymeric assemblies of π-conjugated molecules possessing phenylisoxazoles. *Polymers* 128, 243–256. doi: 10.1016/j.polymer.2017.02.059

Im, D., Moon, H., Shin, M., Kim, J., and Yoo, S. (2011). Towards gigahertz operation: ultrafast low turn-on organic diodes and rectifiers based on C60 and tungsten oxide. *Adv. Mater.* 23, 644–648. doi: 10.1002/adma.201002246

Jang, H. J., and Richter, C. A. (2017). Organic spin-valves and beyond: spin injection and transport in organic semiconductors and the effect of interfacial engineering. *Adv. Mater.* 29:1602739. doi: 10.1002/adma.201602739

Jiang, S. W., Liu, S., Wang, P., Luan, Z. Z., Tao, X. D., Ding, H. F., et al. (2015). Exchange-dominated pure spin current transport in Alq3 molecules. *Phys. Rev. Lett.* 115:086601. doi: 10.1103/PhysRevLett.115.086601

Kalinowski, J., Cocchi, M., Virgili, D., Di Marco, P., and Fattori, V. (2003). Magnetic field effects on emission and current in Alq3-based electroluminescent diodes. *Chem. Phys. Lett.* 380, 710–715. doi: 10.1016/j.cplett.2003.09.086

Kikuchi, M., Takagi, K., Naito, H., and Hiramoto, M. (2017). Single crystal organic photovoltaic cells using lateral electron transport. *Org. Electron.* 41, 118–121. doi: 10.1016/j.orgel.2016.12.001

Koopmans, B., Wagemans, W., Bloom, F. L., Bobbert, P. A., Kemerink, M., and Wohlgenannt, M. (2011). Spin in organics: a new route to spintronics. *Philos. Trans. R. Soc. A* 369, 3602–3616. doi: 10.1098/rsta.2011.0172

Krupskaya, Y., Gibertini, M., Marzari, N., and Morpurgo, A. F. (2015). Band-like electron transport with record-high mobility in the TCNQ family. *Adv. Mater.* 27, 2453–2458. doi: 10.1002/adma.201405699

Kwiatkowski, J. J., Frost, J. M., and Nelson, J. (2009). The effect of morphology on electron field-effect mobility in disordered C60 thin films. *Nano Lett.* 9, 1085–1090. doi: 10.1021/nl803504q

Li, B., Kao, C.-Y., Lu, Y., Yoo, J.-W., Prigodin, V. N., and Epstein, A. J. (2011). Room-temperature organic-based spin polarizer. *Appl. Phys. Lett.* 99:153503. doi: 10.1063/1.3651329

Li, F., Li, T., Chen, F., and Zhang, F. (2014). Spin injection and transport in organic spin-valves based on fullerene C60. *Org. Electron.* 15, 1657–1663. doi: 10.1016/j.orgel.2014.03.016

Li, F., Li, T., Chen, F., and Zhang, F. (2015). Excellent spin transport in spin valves based on the conjugated polymer with high carrier mobility. *Sci. Rep.* 5:9355. doi: 10.1038/srep09355

Liang, S., Geng, R., Yang, B., Zhao, W., Chandra Subedi, R., Li, X., et al. (2016). Curvature-enhanced spin-orbit coupling and spinterface effect in fullerene-based spin valves. *Sci. Rep.* 6:19461. doi: 10.1038/srep19461

Lin, F. J., Guo, C., Chuang, W. T., Wang, C. L., Wang, Q., Liu, H., et al. (2017). Directional solution coating by the chinese brush: a facile approach to improving molecular alignment for high-performance polymer TFTs. *Adv. Mater.* 29:1606987. doi: 10.1002/adma.201606987

Liu, X. D., Zhao, S. L., Xu, Z., Zhang, F. J., Zhang, T. H., Gong, W., et al. (2011). Performance improvement of MEH-PPV:PCBM solar cells using bathocuproine and bathophenanthroline as the buffer layers. *Chin. Phys. B* 20:068801. doi: 10.1088/1674-1056/20/6/068801

McCamey, D. R., van Schooten, K. J., Baker, W. J., Lee, S. Y., Paik, S. Y., Lupton, J. M., et al. (2010). Hyperfine-field-mediated spin beating in electrostatically bound charge carrier pairs. *Phys. Rev. Lett.* 104:017601. doi: 10.1103/PhysRevLett.104.017601

Nguyen, T. D., Ehrenfreund, E., and Vardeny, Z. V. (2012). Spin-polarized light-emitting diode based on an organic bipolar spin valve. *Science* 337, 204–209. doi: 10.1126/science.1223444

Nguyen, T. D., Gautam, B. R., Ehrenfreund, E., and Vardeny, Z. V. (2010a). Magnetoconductance response in unipolar and bipolar organic diodes at ultrasmall fields. *Phys. Rev. Lett.* 105:166804. doi: 10.1103/PhysRevLett.105.166804

Nguyen, T. D., Hukic-Markosian, G., Wang, F., Wojcik, L., Li, X.-G., Ehrenfreund, E., et al. (2011). The hyperfine interaction role in the spin response of π-conjugated polymer films and spin valve devices. *Synth. Met.* 161, 598–603. doi: 10.1016/j.synthmet.2010.12.013

Nguyen, T. D., Hukic-Markosian, G., Wang, F., Wojcik, L., Li, X. G., Ehrenfreund, E., et al. (2010b). Isotope effect in spin response of pi-conjugated polymer films and devices. *Nat. Mater.* 9, 345–352. doi: 10.1038/nmat2633

Nguyen, T. D., Sheng, Y., Rybicki, J., Veeraraghavan, G., and Wohlgenannt, M. (2007). Magnetoresistance in π-conjugated organic sandwich devices with varying hyperfine and spin–orbit coupling strengths, and varying dopant concentrations. *J. Mater. Chem.* 17, 1995–2001. doi: 10.1039/B617541D

Nguyen, T. D., Wang, F., Li, X.-G., Ehrenfreund, E., and Vardeny, Z. V. (2013). Spin diffusion in fullerene-based devices: morphology effect. *Phys. Rev. B* 87:075205. doi: 10.1103/PhysRevB.87.075205

Nuccio, L., Willis, M., Schulz, L., Fratini, S., Messina, F., D'Amico, M., et al. (2013). Importance of spin-orbit interaction for the electron spin relaxation in organic semiconductors. *Phys. Rev. Lett.* 110:216602. doi: 10.1103/PhysRevLett.110.216602

Pookpanratana, S., Lydecker, L. K., Richter, C. A., and Hacker, C. A. (2015). Self-assembled monolayers impact cobalt interfacial structure in nanoelectronic junctions. *J. Phys. Chem. C* 119, 6687–6695. doi: 10.1021/acs.jpcc.5b00816

Pramanik, S., Stefanita, C. G., Patibandla, S., Bandyopadhyay, S., Garre, K., Harth, N., et al. (2007). Observation of extremely long spin relaxation times in an organic nanowire spin valve. *Nat. Nanotech.* 2, 216–219. doi: 10.1038/nnano.2007.64

Prieto-Ruiz, J. P., Miralles, S. G., Prima-Garcia, H., Lopez-Munoz, A., Riminucci, A., Graziosi, P., et al. (2019). Enhancing light emission in interface engineered spin-OLEDs through spin-polarized injection at high voltages. *Adv. Mater.* 31:1806817. doi: 10.1002/adma.201806817

Raman, K. V., Watson, S. M., Shim, J. H., Borchers, J. A., Chang, J., and Moodera, J. S. (2009). Effect of molecular ordering on spin and charge injection in rubrene. *Phys. Rev. B* 80:195212. doi: 10.1103/PhysRevB.80.195212

Riminucci, A., Yu, Z. G., Prezioso, M., Cecchini, R., Bergenti, I., Graziosi, P., et al. (2019). Controlling magnetoresistance by oxygen impurities in Mq3-based molecular spin valves. *ACS Appl. Mater. Interfaces* 11, 8319–8326. doi: 10.1021/acsami.8b20423

Santos, T. S., Lee, J. S., Migdal, P., Lekshmi, I. C., Satpati, B., and Moodera, J. S. (2007). Room-temperature tunnel magnetoresistance and spin-polarized tunneling through an organic semiconductor barrier. *Phys. Rev. Lett.* 98:016601. doi: 10.1103/PhysRevLett.98.016601

Sanvito, S. (2011). Molecular spintronics. *Chem. Soc. Rev.* 40, 3336–3355. doi: 10.1039/c1cs15047b

Schott, S., McNellis, E. R., Nielsen, C. B., Chen, H. Y., Watanabe, S., Tanaka, H., et al. (2017). Tuning the effective spin-orbit coupling in molecular semiconductors. *Nat. Commun.* 8:15200. doi: 10.1038/ncomms15200

Schulz, L., Nuccio, L., Willis, M., Desai, P., Shakya, P., Kreouzis, T., et al. (2011). Engineering spin propagation across a hybrid organic/inorganic interface using a polar layer. *Nat. Mater.* 10, 39–44. doi: 10.1038/nmat2912

Seo, S., Park, B.-N., and Evans, P. G. (2006). Ambipolar rubrene thin film transistors. *Appl. Phys. Lett.* 88:232114. doi: 10.1063/1.2210294

Sheng, C. X., Singh, S., Gambetta, A., Drori, T., Tong, M., Tretiak, S., et al. (2013). Ultrafast intersystem-crossing in platinum containing pi-conjugated polymers with tunable spin-orbit coupling. *Sci. Rep.* 3:2653. doi: 10.1038/srep02653

Sheng, Y., Nguyen, T. D., Veeraraghavan, G., Mermer, Ö., and Wohlgenannt, M. (2007). Effect of spin-orbit coupling on magnetoresistance in organic semiconductors. *Phys. Rev. B* 75:035202. doi: 10.1103/PhysRevB.75.035202

Sheng, Y., Nguyen, T. D., Veeraraghavan, G., Mermer, Ö., Wohlgenannt, M., Qiu, S., et al. (2006). Hyperfine interaction and magnetoresistance in organic semiconductors. *Phys. Rev. B* 74:045213. doi: 10.1103/PhysRevB.74.045213

Shim, J. H., Raman, K. V., Park, Y. J., Santos, T. S., Miao, G. X., Satpati, B., et al. (2008). Large spin diffusion length in an amorphous organic semiconductor. *Phys. Rev. Lett.* 100:226603. doi: 10.1103/PhysRevLett.100.226603

Starko-Bowes, R., Bodepudi, S. C., Alam, K. M., Singh, A. P., and Pramanik, S. (2013). Room temperature spin valve effect in highly ordered array of methanofullerene nanotubes. *J. Appl. Phys.* 114:044316. doi: 10.1063/1.4816330

Sun, D., Ehrenfreund, E., and Vardeny, Z. V. (2014). The first decade of organic spintronics research. *Chem. Commun.* 50, 1781–1793. doi: 10.1039/C3CC47126H

Sun, D., van Schooten, K. J., Kavand, M., Malissa, H., Zhang, C., Groesbeck, M., et al. (2016). Inverse spin hall effect from pulsed spin current in organic semiconductors with tunable spin-orbit coupling. *Nat. Mater.* 15, 863–869. doi: 10.1038/nmat4618

Sun, D., Yin, L., Sun, C., Guo, H., Gai, Z., Zhang, X. G., et al. (2010). Giant magnetoresistance in organic spin valves. *Phys. Rev. Lett.* 104:236602. doi: 10.1103/PhysRevLett.104.236602

Sun, M., and Mi, W. (2018). Progress in organic molecular/ferromagnet spinterfaces: towards molecular spintronics. *J. Mater. Chem. C* 6, 6619–6636. doi: 10.1039/C8TC01399C

Sun, X., Bedoya-Pinto, A., Mao, Z., Gobbi, M., Yan, W., Guo, Y., et al. (2016). Active morphology control for concomitant long distance spin transport and photoresponse in a single organic device. *Adv. Mater.* 28, 2609–2615. doi: 10.1002/adma.201503831

Sun, X., Gobbi, M., Bedoya-Pinto, A., Txoperena, O., Golmar, F., Llopis, R., et al. (2013). Room-temperature air-stable spin transport in bathocuproine-based spin valves. *Nat. Commun.* 4:2794. doi: 10.1038/ncomms3794

Sun, X., Vélez, S., Atxabal, A., Bedoya-Pinto, A., Parui, S., Zhu, X., et al. (2017). A molecular spin-photovoltaic device. *Science* 357, 677–680. doi: 10.1126/science.aan5348

Szulczewski, G., Tokuc, H., Oguz, K., and Coey, J. M. D. (2009). Magnetoresistance in magnetic tunnel junctions with an organic barrier and an MgO spin filter. *Appl. Phys. Lett.* 95:202506. doi: 10.1063/1.3264968

Tsao, H. N., and Mullen, K. (2010). Improving polymer transistor performance via morphology control. *Chem. Soc. Rev.* 39, 2372–2386. doi: 10.1039/b918151m

Tsurumi, J., Matsui, H., Kubo, T., Häusermann, R., Mitsui, C., Okamoto, T., et al. (2017). Coexistence of ultra-long spin relaxation time and coherent charge transport in organic single-crystal semiconductors. *Nat. Phys.* 13, 994–998. doi: 10.1038/nphys4217

Urdampilleta, M., Klyatskaya, S., Cleuziou, J. P., Ruben, M., and Wernsdorfer, W. (2011). Supramolecular spin valves. *Nat. Mater.* 10, 502–506. doi: 10.1038/nmat3050

Wang, C., Dong, H., Jiang, L., and Hu, W. (2018). Organic semiconductor crystals. *Chem. Soc. Rev.* 47, 422–500. doi: 10.1039/C7CS00490G

Wang, S.-J., Venkateshvaran, D., Mahani, M. R., Chopra, U., McNellis, E. R., Di Pietro, R., et al. (2019). Long spin diffusion lengths in doped conjugated polymers due to enhanced exchange coupling. *Nat. Electron.* 2, 98–107. doi: 10.1038/s41928-019-0222-5

Wang, Y., Zhu, W., Dong, H., Zhang, X., Li, R., and Hu, W. (2016). Organic cocrystals: new strategy for molecular collaborative innovation. *Top. Curr. Chem.* 374:83. doi: 10.1007/s41061-016-0081-8

Watanabe, S., Ando, K., Kang, K., Mooser, S., Vaynzof, Y., Kurebayashi, H., et al. (2014). Polaron spin current transport in organic semiconductors. *Nat. Phys.* 10, 308–313. doi: 10.1038/nphys2901

Wolf, S. A., Awschalom, D. D., Buhrman, R. A., Daughton, J. M., von Molnar, S., Roukes, M. L., et al. (2001). Spintronics: a spin-based electronics vision for the future. *Science* 294, 1488–1495. doi: 10.1126/science.1065389

Wurthner, F. (2016). Dipole-dipole interaction driven self-assembly of merocyanine dyes: from dimers to nanoscale objects and supramolecular materials. *Acc. Chem. Res.* 49, 868–876. doi: 10.1021/acs.accounts.6b00042

Xiong, Z. H., Wu, D., Vardeny, Z. V., and Shi, J. (2004). Giant magnetoresistance in organic spin-valves. *Nature* 427, 821–824. doi: 10.1038/nature02325

Xu, X., Xiao, T., Gu, X., Yang, X., Kershaw, S. V., Zhao, N., et al. (2015). Solution-processed ambipolar organic thin-film transistors by blending p- and n-type semiconductors: solid solution versus microphase separation. *ACS Appl. Mater. Interfaces* 7, 28019–28026. doi: 10.1021/acsami.5b01172

Xu, X. M., Yao, Y. F., Shan, B. W., Gu, X., Liu, D. Q., Liu, J. Y., et al. (2016). Electron mobility exceeding 10 cm(2) V-1 s(-1) and band-like charge transport in solution-processed n-channel organic thin-film transistors. *Adv. Mater.* 28, 5276–5283. doi: 10.1002/adma.201601171

Yan, H., Chen, Z., Zheng, Y., Newman, C., Quinn, J. R., Dotz, F., et al. (2009). A high-mobility electron-transporting polymer for printed transistors. *Nature* 457, 679–686. doi: 10.1038/nature07727

Yu, Z. G. (2011). Spin-orbit coupling, spin relaxation, and spin diffusion in organic solids. *Phys. Rev. Lett.* 106:106602. doi: 10.1103/PhysRevLett.106.106602

Yu, Z. G. (2012). Spin-orbit coupling and its effects in organic solids. *Phys. Rev. B* 85, 115201–115218. doi: 10.1103/PhysRevB.85.115201

Yu, Z. G. (2014). Impurity-band transport in organic spin valves. *Nat. Commun.* 5:4842. doi: 10.1038/ncomms5842

Yu, Z. G., Ding, F., and Wang, H. (2013). Hyperfine interaction and its effects on spin dynamics in organic solids. *Phys. Rev. B* 87:205446. doi: 10.1103/PhysRevB.87.205446

Zhang, H., Dong, H., Li, Y., Jiang, W., Zhen, Y., Jiang, L., et al. (2016). Novel air stable organic radical semiconductor of dimers of dithienothiophene, single crystals, and field-effect transistors. *Adv. Mater.* 28, 7466–7471. doi: 10.1002/adma.201601502

Zhang, H., Jiang, L., Zhen, Y., Zhang, J., Han, G., Zhang, X., et al. (2016). Organic cocrystal photovoltaic behavior: a model system to study charge recombination of C60 and C70 at the molecular level. *Adv. Electron. Mater.* 2:1500423. doi: 10.1002/aelm.201500423

Zhang, J., Tan, J., Ma, Z., Xu, W., Zhao, G., Geng, H., et al. (2013). Fullerene/sulfur-bridged annulene cocrystals: two-dimensional segregated heterojunctions with ambipolar transport properties and photoresponsivity. *J. Am. Chem. Soc.* 135, 558–561. doi: 10.1021/ja310098k

Zhang, X., Dong, H., and Hu, W. (2018). Organic semiconductor single crystals for electronics and photonics. *Adv. Mater.* 30:1801048. doi: 10.1002/adma.201801048

Zhang, X., Ma, Q., Suzuki, K., Sugihara, A., Qin, G., Miyazaki, T., et al. (2015). Magnetoresistance effect in rubrene-based spin valves at room temperature. *ACS Appl. Mater. Interfaces* 7, 4685–4692. doi: 10.1021/am508173j

Zhang, X., Mizukami, S., Kubota, T., Ma, Q., Oogane, M., Naganuma, H., et al. (2013). Observation of a large spin-dependent transport length in organic spin valves at room temperature. *Nat. Commun.* 4:1392. doi: 10.1038/ncomms2423

Zhang, X., Mizukami, S., Ma, Q., Kubota, T., Oogane, M., Naganuma, H., et al. (2014). Spin-dependent transport behavior in C60 and Alq3 based spin valves with a magnetite electrode (invited). *J. Appl. Phys.* 115:172608. doi: 10.1063/1.4870154

Zhang, Y. J., Dong, H. L., Tang, Q. X., He, Y. D., and Hu, W. P. (2010). Mobility dependence on the conducting channel dimension of organicfield-effect transistors based on single-crystalline nanoribbons. *J. Mater. Chem.* 20, 7029–7033. doi: 10.1039/c0jm01196g

Zhang, Z. P., Jiang, L., Cheng, C. L., Zhen, Y. G., Zhao, G. Y., Geng, H., et al. (2016). The impact of interlayer electronic coupling on charge transport in organic semiconductors: a case study on titanylphthalocyanine single crystals. *Angew. Chem.* 55, 5206–5209. doi: 10.1002/anie.201601065

Zhao, Y., Gumyusenge, A., He, J., Qu, G., McNutt, W. W., Long, Y., et al. (2018). Continuous melt-drawing of highly aligned flexible and stretchable semiconducting microfibers for organic electronics. *Adv. Funct. Mater.* 28:1705584. doi: 10.1002/adfm.201705584

Zhao, Y., Zhao, X., Roders, M., Gumyusenge, A., Ayzner, A. L., and Mei, J. (2017). Melt-processing of complementary semiconducting polymer blends for high performance organic transistors. *Adv. Mater.* 29:1605056. doi: 10.1002/adma.201605056

Zheng, S., Zhong, J., Matsuda, W., Jin, P., Chen, M., Akasaka, T., et al. (2018). Fullerene/cobalt porphyrin charge-transfer cocrystals: excellent thermal stability and high mobility. *Nano Res.* 11, 1917–1927. doi: 10.1007/s12274-017-1809-7

Zhu, W., Dong, H., Zhen, Y., and Hu, W. (2015). Challenges of organic "cocrystals." *Sci. China Mater.* 58, 854–859. doi: 10.1007/s40843-015-0099-1

Conflict of Interest Statement: The authors declare that the research was conducted in the absence of any commercial or financial relationships that could be construed as a potential conflict of interest.

frontiers in Chemistry

ORIGINAL RESEARCH
published: 28 June 2019
doi: 10.3389/fchem.2019.00467

Solvent-Induced Supramolecular Assembly of a Peptide-Tetrathiophene-Peptide Conjugate

Zongxia Guo[1], Yujiao Wang[2], Xiao Zhang[2], Ruiying Gong[3], Youbing Mu[4] and Xiaobo Wan[4]**

[1] College of Chemistry and Molecular Engineering, Qingdao University of Science and Technology, Qingdao, China, [2] Key Laboratory of Biobased Polymer Materials, Shandong Provincial Education Department, College of Polymer Science and Engineering, Qingdao University of Science and Technology, Qingdao, China, [3] Qingdao Institute of Bioenergy and Bioprocess Technology, Chinese Academy of Sciences, Qingdao, China, [4] Key Laboratory of Optoelectronic Chemical Materials and Devices, School of Chemical and Environmental Engineering, Jianghan University, Ministry of Education, Wuhan, China

The assembly of a peptide-tetrathiophene-peptide (PTP) conjugate has been investigated in mixed solvents, which has different polarities by changing the solvent proportions. It was found that PTP can form fibers in THF/hexane solutions with 40–80%v of hexane. The fibers were stable and did not change on time. On the other hand, PTP formed ordered structures in a mixed solution with the water content from 40 to 60%v. For the as-prepared solutions, two nanostructures vesicles and parallelogram sheets were obtained. The parallelogram sheets could transform into vesicles on time. The fibers showed supramolecular chirality, however, there was no Cotton effect for vesicles and parallelogram sheets. UV-vis, FL, XRD, FT-IR, and CD spectra together with SEM, AFM, TEM were used to characterize the nanostructures and properties of the assemblies. Molecular packing mechanism was proposed based on the experimental data.

Keywords: oligopeptide, oligothiophene, peptide-tetrathiophene-peptide, supramolecular assembly, supramolecular chirality

OPEN ACCESS

Edited by:
Takeharu Haino, Hiroshima University, Japan

Reviewed by:
Shiki Yagai, Chiba University, Japan
Liam Charles Palmer, Northwestern University, United States

****Correspondence:***
Zongxia Guo
zxguo@qust.edu.cn
Xiaobo Wan
wanxb@jhun.edu.cn

Specialty section:
This article was submitted to Supramolecular Chemistry, a section of the journal Frontiers in Chemistry

Received: *28 February 2019*
Accepted: *12 June 2019*
Published: *28 June 2019*

Citation:
Guo Z, Wang Y, Zhang X, Gong R, Mu Y and Wan X (2019) Solvent-Induced Supramolecular Assembly of a Peptide-Tetrathiophene-Peptide Conjugate. Front. Chem. 7:467. doi: 10.3389/fchem.2019.00467

INTRODUCTION

The performance of the functional materials based on these systems is largely affected by the nanostructures of the assemblies, therefore the manipulation of the nanostructures is one of the most important issue to tune their properties (Ajayaghosh et al., 2006; Zhang et al., 2009; George et al., 2012; Mitra et al., 2013; Shin et al., 2013; Baram et al., 2014; Liu et al., 2014). Especially, different nanostructures with distinct properties can be constructed from the same entity by adjusting the outside environment. Many strategies, such as guest induction (Janssen et al., 2010), light (Diegelmann et al., 2012; Samanta et al., 2012), pH (Mba et al., 2011; Draper et al., 2017), and solvent polarity (Hu et al., 2012; Guo et al., 2017a), have been used to assemble various superstructures based on the biomolecule-assisted self-assembly of π-conjugated systems.

The chiral property endows the materials with potential applications, such as chiral sensing, chiral switch, and asymmetric catalysis etc., (Zhang et al., 2014; Kim et al., 2015; Jiang et al., 2016; Jia et al., 2019). Supramolecular chirality is highly related to the packing mode of molecules, thus different packing styles may lead to diverse supramolecular chirality even when the chirality at the molecular level is the same. So, controlling the chiral properties of

self-assemblies based on the biomolecule-π-conjugated systems is an important issue. Bäuerle et al. have tuned the supramolecular chirality of the assembled oligothiophene nanostructures by decorating carbohydrate or amino acid with different chirality (Schmid et al., 2009; Digennaro et al., 2013; Schillinger et al., 2013). Wei and et al. reported a sugar-based amphiphilic perylene diimide derivative (PTCDI-HAG) which self-assembled into two kinds of fibers with opposite supramolecular chirality by using binary solvents (Huang et al., 2011). Yao and Zhan et al. showed that the chirality of nanohelices formed from a tripeptide-perylene diimide (PDI) conjugate could be reversed through heating and ultrasound treatment (Ke et al., 2013). In these previous reports, although the supramolecular chirality could be tuned, no distinct nanostructure change was observed, for example, fibers are still fibers although its twisting direction changed. On the other hand, distinct nanostructure change which is accompanied by supramolecular chirality change might provide alternative ways for chirality sensing materials. However, inspecting the relationship between distinct assembled nanostructure (Echue et al., 2015) and its supramolecular chirality is rarely reported especially based on the self-assembly of π-conjugated systems assisted by biomolecules (Shang et al., 2017).

Here, a peptide-tetrathiophene-peptide (PTP) conjugate (**Figure 1**) was used as a model object to explore the manipulation of morphology and supramolecular chirality of the assemblies via simply changing the solvent polarity. There are some significant features for PTP: Gly-(L-Val)-Gly-(L-Val) segments at both ends of the thiophene backbone are relatively hydrophilic than the thiophene core and can provide hydrogen bond sites through which β-sheet structures could be formed (Wall et al., 2011; Guo et al., 2013); the thiophene core decorated with two octyls in the middle is a hydrophobic part and can form π-π stacking as well (Lehrman et al., 2012; Guo et al., 2014); the linkers between the thiophene and peptide are flexible and then the spatial location of both hydrophilic and hydrophobic parts in the supramolecular assemblies can be freely tuned under certain conditions. Thus PTP gives chances to tune the self-assembly by verifying the solvent polarity, since H-bonding and π-π stacking are the driving forces for the self-assembly of peptide-thiophene conjugates (Guo et al., 2017b).

RESULTS AND DISCUSSIONS

The synthesis of PTP has been reported in our previous report (Guo et al., 2013). And it could form gels in some aprotic solvents (THF, dioxane, and acetone) and also protic solvents (methanol and ethanol) as reported in our previous work. Among these solvents, the critical gel formation concentration in THF is the highest, indicating the better solubility. In the present investigation, the assembly of PTP in solution were performed in pure THF, or mixed solvent composed of THF at very low concentration. The impact of different proportions of the mixed solvent on the nanostructures and properties were studied. Moreover, concentrations and time effect were also checked.

Solvent Induced Formation of Nanostructures

Firstly, the self-assembly of PTP was performed in THF with the concentration at 0.1 mg/mL (6.61×10^{-5} M). It was found that no well-organized nanostructures can be formed in THF solution **Figure S1**). Then the mixed solvent was used to detect if the nanostructures change when varying the solvent polarity. The solvent with high polarity (water) or low polarity (hexane) was added to THF to enhance or decrease the polarity of the mixed solvent. The proportions of the mixed solvent could be varied to obtain solvents with different polarities. For the preparation of the samples, PTP was dissolved in THF to make a parent solution and then water or hexane was added to get the solution with different volume ratio of the two solvents. The samples were stirred vigorously for 10 min and then kept at room temperature for a certain period of time.

For PTP in THF/hexane solution with a concentration at 0.1 mg/mL, it was observed that ordered nanostructures could be formed only in a certain range of hexane content (40–80%v). The morphology of the assembled PTP in THF/hexane (40–80%v) was always fiber structures (**Figure S2**). **Figure 2** shows the nanostructures in AFM and TEM images formed from the THF/hexane solution. It is clear that fibers were formed in the solvent with 50%v of hexane. PTP assembled into fibers with widths of 43 ± 15 nm and heights of 13 ± 6 nm (**Figures 2a,b**; **Figure S3**). The width of fibers was measured as 32 ± 17 nm. The difference for the above data might be due to the expansion effect

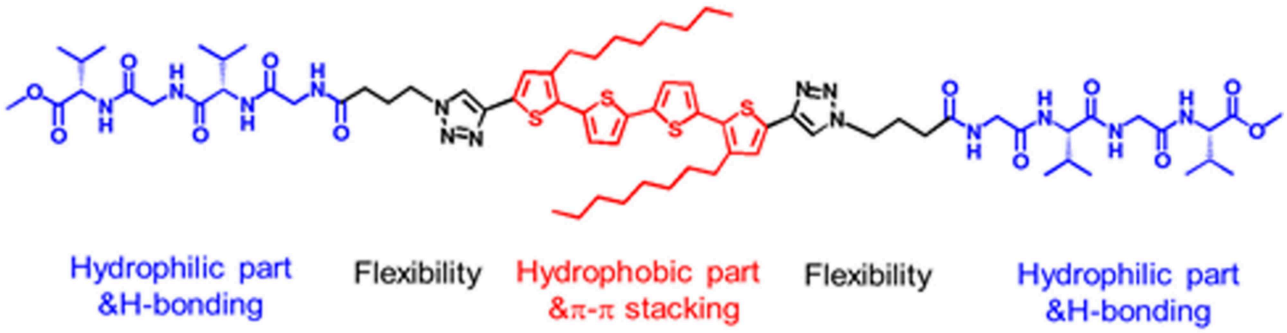

FIGURE 1 | Chemical structure of PTP.

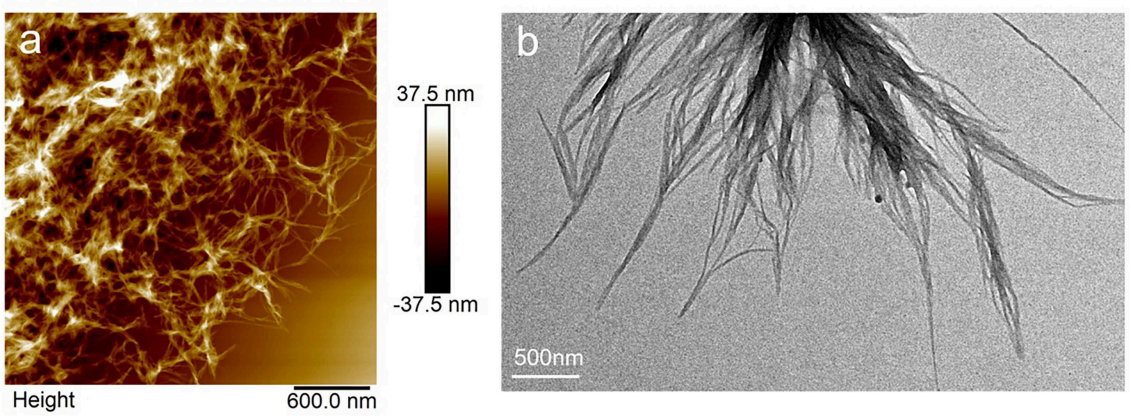

FIGURE 2 | AFM **(a)** and TEM **(b)** images of assembled structures of PTP in THF/hexane (1:1, v).

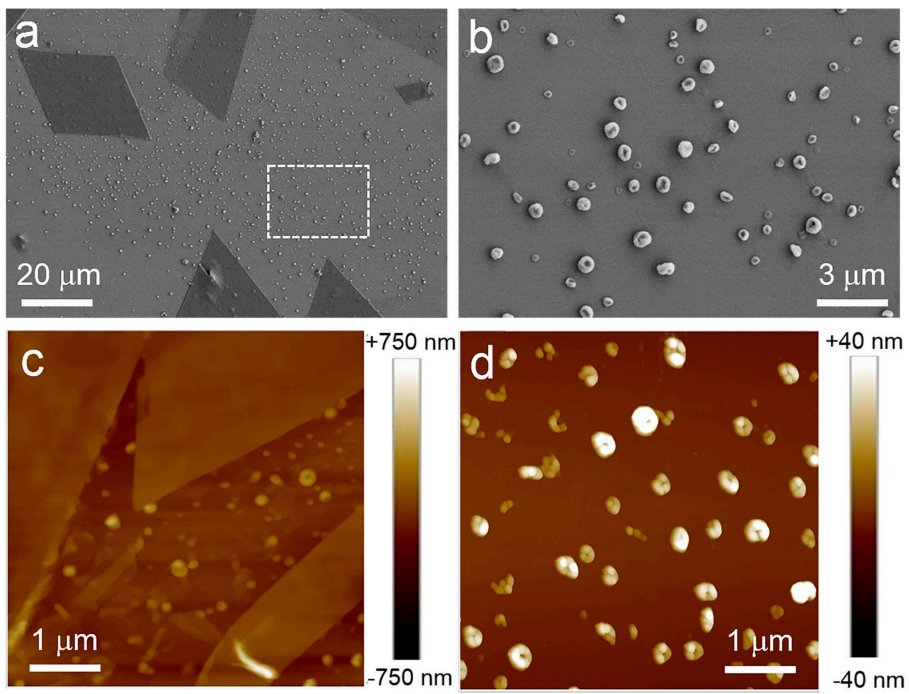

FIGURE 3 | SEM **(a,b)** and AFM **(c,d)** images of the as-prepared assembled structures of PTP in THF/water solution. **(b)** was zoomed in from the area enclosed by white dotted line in **(a)**. **(a,c)** showed the nanostructures composed of sheet structures and spherical ones. **(b,d)** indicated the spherical structures.

from the AFM tip and the possible drying effects on substrate. Inspecting the fibers carefully, thick ones were formed from thin ones as can be seen also in the SEM images (**Figure S2**). It should be noted that no obvious chiral structures could be observed indicating that the chirality from the peptide did not transfer into the assembled nanostructures (Yang et al., 2013; Wang et al., 2018), although supramolecular chirality might be formed in the assemblies. This formation of fiber in THF/hexane was also confirmed by SEM characterization (**Figure S2**). Aging treatment had no impact on such fiber structures.

It was the other case when mixed solvent composed of water was used. It was found that ordered structures can be formed in a narrow range of water content (40–60%v), and two nanostructures always could be formed in such range of water content for the as-prepared solutions. **Figure 3** showed SEM and AFM images obtained from THF/water solutions (water, 50%v). It is obvious that sheet and spherical structures were formed.

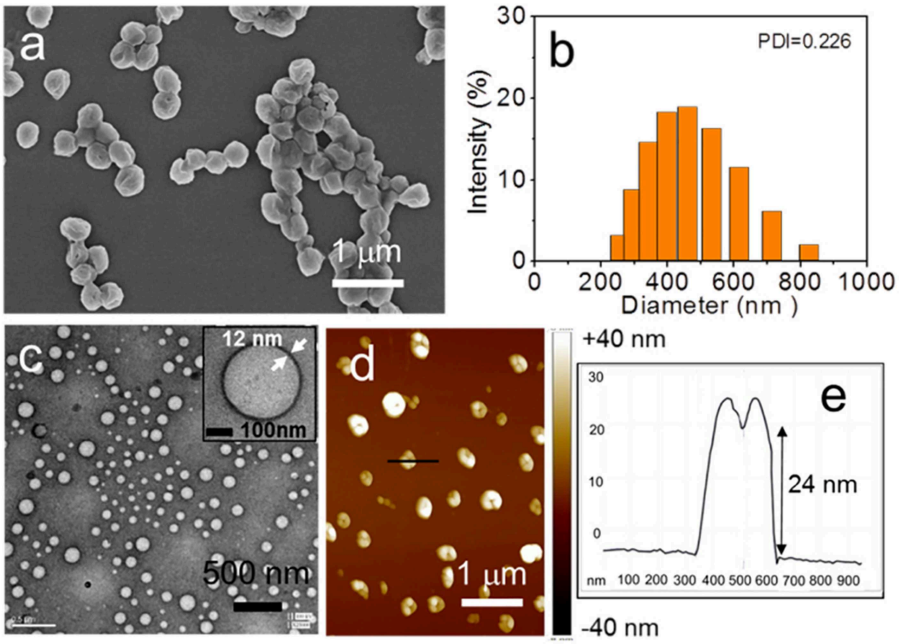

FIGURE 4 | The assembled structures of PTP in THF/water with 4 days of aging: **(a)** SEM image, **(c)** TEM image, and **(d)** AFM image. **(b)** Size distribution measurement of the vesicles by DLS. The section profile of one vesicle in **(d)** was shown in **(e)**.

Some sheets were parallelograms. The thickness of the sheets ranges from tens to hundreds of nanometers (**Figure S4**).

It should be noted that there is a time-dependent transformation of the nanostructures form sheet to spheres. As time went on, sheets structures gradually became into spheres. After 4 days of aging, only spherical aggregates were observed and their morphology was characterized by SEM, TEM, and AFM (**Figures 4a,c,d**; **Figure S5**). The diameter of the spheres ranges from 255 to 825 nm as evidenced by Dynamic Light Scattering (DLS) (**Figure 4b**). Furthermore, such sphere seems sunken from the SEM image, indicating that hollow spheres might be formed. This speculation was proved by TEM measurement, which clearly showed that the wall of sphere, as shown in the inset of **Figure 4c**. In addition, the morphology in AFM image is very similar to that obtained in the SEM image. Concave spheres were observed (**Figure 4d**). The section profile of a sphere shows that the ratio of horizontal distance (630–340 = 290 nm) to vertical distance (24 nm) is about 12. This high width to height ratio combined with the observation from SEM, TEM, and AFM images confirmed that vesicles were formed. The thickness of the vesicle wall was estimated to be about 12 nm by TEM image (**Figure 4c**). From AFM analysis, the thickness of double walls was measured as 22 ± 3 nm in accordance with the TEM results. A typical section profile of a vesicle was shown in **Figure 4e**.

The concentration impact on the nanostructures was detected as well for the two different mixed solvents. For the assembly of PTP in THF/Hexane (40–80%v), there was no obvious effect of the concentration on the fiber structures. However, it is the other case for the assembly in THF/water (40–80%v). On increasing the concentration of PTP to 0.2 mg/mL (THF/water, 1:1, v), the sheets became the major structures and the vesicles was almost disappeared for the as-prepared solutions (**Figure S6**). As discussed above, there is time-dependent transformation tendency from sheets to spheres. It is the same case for the high concentration solution. The sheets would transform into vesicles gradually. After 2 days of aging, vesicles appeared (**Figure S7**). And sheet structures can hardly be found for this solution after 4 days of aging, and only the vesicles showed up (**Figure S8**). Actually, it was found that the much-diluted solutions had the same tendency to from vesicles after long time of aging, although the number of vesicles was much less than that obtained from the high solutions. Based on the above investigation, it can be concluded that the sheets are dynamic controlled intermediate structures and the vesicles are thermodynamic stable ones.

Spectral Investigation of the Assembled Nanostructures

UV-Vis and FL Spectra

UV-vis and FL spectra were used to detect the aggregation of PTP (**Figure 5**). In THF, PTPs are in the molecularly dissolved state, the maximum absorption of PTP is at 412 nm which belongs to the π-π^* transition of the tetrathiophene backbone (Schillinger et al., 2009; Kumar et al., 2011). Two resolved emission peaks of PTP are observed at 498 and 529 nm, which again indicated the molecularly dissolved state of PTPs in THF. In the mixed solvents, absorption/emission band changes occurred and varied according to the polarity of the mixed solvents. In THF/hexane, the absorption was at 398 nm, showing a 14 nm blue-shift compared to that in the molecularly dissolved state, and the absorption intensity

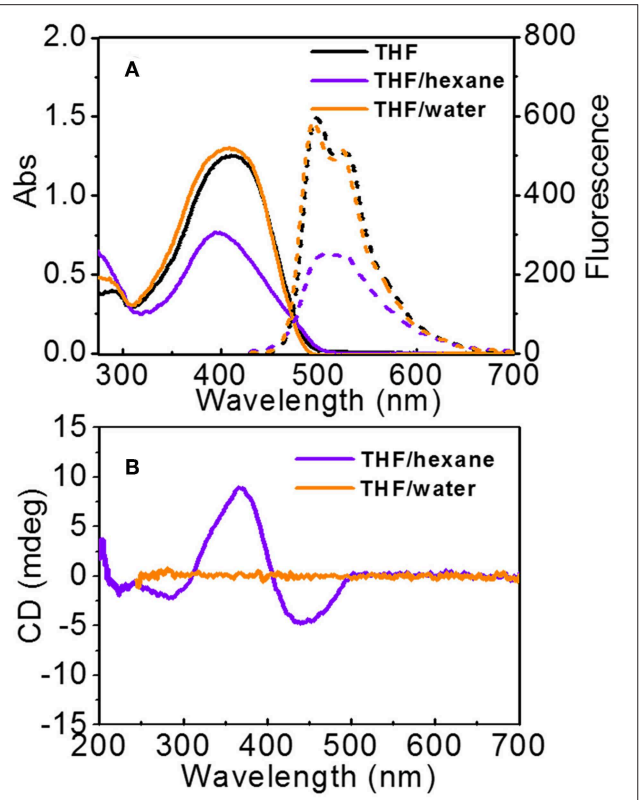

FIGURE 5 | (A) UV-vis (solid line) and FL spectra (dashed lines) of PTP in THF, THF/hexane (1:1, v), and THF/water (1:1, v). The excitation is 412 nm for all solutions. **(B)** CD spectra of PTP in THF/hexane and THF/water. [PTP] = 0.1 mg\mL.

decreased apparently. In FL spectra, the emission peaks became unresolved, and moreover, the intensity decreased by 50% with respect to that in THF. Based on the UV-vis and FL data, it was suggested that the PTP formed H-like aggregates in THF/hexane (Wall et al., 2011; Digennaro et al., 2013). While in THF/water, it is clear that the absorption spectrum is very close to that in THF, both in shape and intensity. The maximum absorption is at 409 nm, only a 3 nm of blue shift from that in the molecularly state (412 nm) was observed. The emission of PTP in THF/water was almost the same to that in THF. Only a very small blue shift occurred in accordance with the UV-vis spectra. It could be concluded that the interaction between thiophene backbones was weak and the chromophores were loosely packed in THF/water solution. Overall, spectroscopic data have proved that changing the solvent polarity could induce distinct aggregation modes of the molecules.

CD Spectra

Normally, the conjugates of peptide and thiophene will assemble into nanostructures with supramolecular chirality in thiophene parts if the peptide is chiral (Stone et al., 2009; Kumar et al., 2011; Lehrman et al., 2012). Thus, we explored the supramolecular chirality of the assembled vesicles and fibers (**Figure 5B**). The solution with fibers shows an obvious negative Cotton effect with a negative absorption at 442 nm, a positive absorption at 367 nm, and a crossover at 405 nm. A weak negative band at 284 nm was also found. Since the absorptions at about 400 and 280 nm were assigned to the tetrathiophene backbone, the CD signals should be due to the exciton coupling between thiophene chromophores (Cao et al., 2013). The small difference in the absorption positions in UV-vis and CD spectra would be due to the light scattering (Ajayaghosh et al., 2006). The CD spectrum was inconclusive about the presence of β-sheets in samples. Since molecularly PTP shows no chirality in the thiophene part (**Figure S9**), it indicated that the chirality of peptide was transferred to thiophene stacks which adopted a helical stacking way, in other words supramolecular chirality was formed consequently. Such helical stacks hierarchically assembled into fiber structures. However, the solution composed of vesicles was surprisingly CD silent from 270 to 700 nm. Only noise signal could be observed in the range from 200 to 250 nm. It was hardly to deduce the formation of regular β-sheets from the CD spectrum. It was indicated that the chirality transfer from peptide to thiophene was prohibited in THF/water solution. Based on the morphology and CD data, we can conclude that the different packing modes of PTP molecules in THF/hexane and THF/water lead to different chirality transfer behavior.

The above investigations were mainly focused on the packing of the thiophene core. FT-IR spectra were used to characterize the assembly of peptide segments (**Figure S10**). FT-IR data shows that the assemblies of the peptide segments in both cases are similar. Amide I and Amide II were found at 1,635 and 1,540 cm^{-1} in THF/hexane, and they were at 1,635 and 1,549 cm^{-1} in THF/water. Such absorptions indicate that β-sheets between peptide segments were formed in both cases (Diegelmann et al., 2008; Ke et al., 2013). The absorption at 3,289 cm^{-1} from the N-H stretching vibration further confirmed the formation of H-bonds for PTP in both solutions (Lehrman et al., 2012).

Based on the experimental data, molecular packing modes of PTP in THF/hexane and THF/water were proposed (**Figure 6**). In THF/hexane, it is speculated that the main driving force of self-assembly are hydrogen bond and π-π stacking, through which PTP assembled into H-like aggregates, and such H-like aggregates further hierarchically assembled into thin fibers. These thin fibers could further interact and twist with each other to form thicker ones. During such process of assembly, the chirality of peptide transferred to thiophene units, and helical thiophene stacks were formed. The chirality of peptide finally was expressed into the supramolecular chirality of the assembled nanostructures. On the other hand, since the polarity of the THF/water solution was much more polar than that of the THF/hexane solution, the hydrophobic part of PTP, that is the tetrathiophene core, tends to stay away from the polar solvent. Consequently, we postulated that the flexible linker between thiophene and peptide allows PTP to adopt a conformation different from that in THF/hexane: two octyl chains stay on one side and the two peptide segments stay on the opposite side with the tetrthiophene in the middle. Based on such conformation, octyl chains interdigitate with

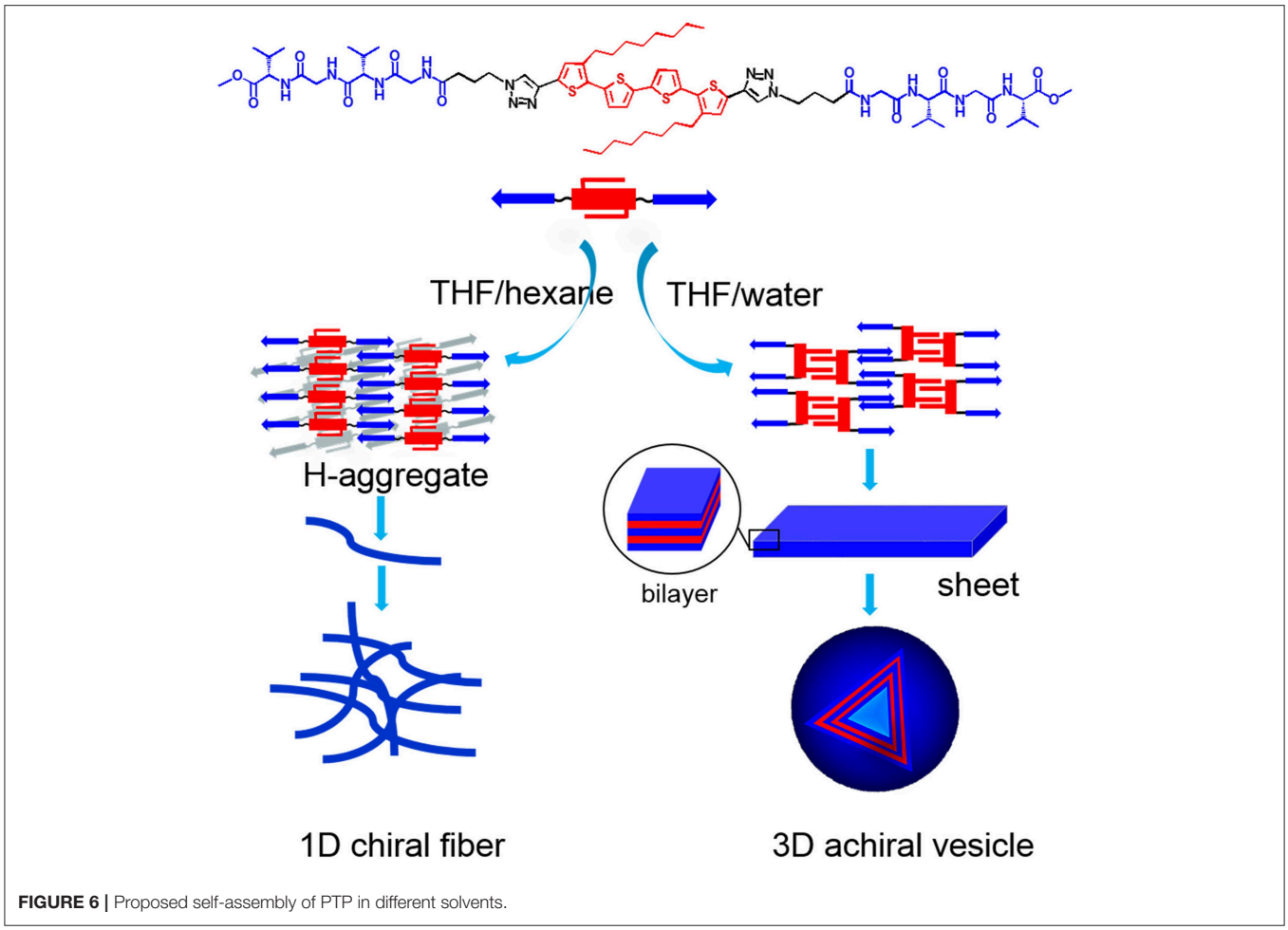

FIGURE 6 | Proposed self-assembly of PTP in different solvents.

octyl chains via van de Waals interactions, and peptide segments interdigitate with peptide segments from different PTPs via the hydrogen bonds, and finally 3D vesicles were formed. It is suggested that there are four PTP layers in the normal direction of the vesicle wall. It was estimated that such alignment will give a wall thickness of about 11 nm (**Figure S11**), which is in good agreement with the AFM and TEM data (12 nm). XRD was also used to check the molecular packing (**Figure S12**). XRD data of vesicles showed an obvious peak with *d* spacing of 12.7 and 6.2 nm for the vesicles, confirmed the bilayer signature. For the fibers, there was no such peaks. The small peaks with *d* spacing of 0.78 nm were both observed for vesicles and fibers should be from the π-π packing (0.78/2 = 0.39 nm). So, in THF/water, octyl chain-octyl chain interactions and H-bonding interactions between the peptide segments would play an important role in the formation of vesicles. It is interesting that the chirality transfer was blocked from peptide to thiophene in the vesicles. Two reasons might lead to such result in THF/water: (i) the chiral peptide segments prefer to stay on one side of the thiophene and in such conformation the peptide segment are somehow perpendicular to the long axis of thiophene, which might lead to the low possibility of chirality transfer; and (ii) UV-vis and FL spectral data showed very small changes in the aggregation state of PTP in THF/water compared to its dissolved state in THF, indicating that the interactions between thiophene units were not strong enough to generate exciton coupling between chromophores. Based on the above aspects, the chirality transfer was prohibited in the vesicles and supramolecular chirality formation did not occur either. It is clearly evidenced by the present investigation that there is a direct relationship between the assembled nanostructures and the formation of supramolecular chirality.

CONCLUSIONS

In summary, the self-assembly of a PTP conjugate in different solvents was systematically investigated. It reveals that the solvent polarity can induce different ways of hierarchical assembly, leading to different nanostructures and properties, especially the supramolecular chirality. In THF/hexane, chirality transfer from peptide to thiophene occurred and chiral fibers were formed. While in THF/water, vesicles were obtained and chirality transfer was prevented. This investigation highlighted that simple strategy could be used to manipulate the assembled nanostructures. Especially,

supramolecular chirality can be also tuned by forming different structures. The present strategy provides opportunities to fabricate assemblies with distinguished supramolecular chirality through manipulating the assembled nanostructures, therefore leading to diverse chiral functionalities, such as sensors or switches.

DATA AVAILABILITY

No datasets were generated or analyzed for this study.

AUTHOR CONTRIBUTIONS

ZG and XW contributed to the idea of the work and the preparation of the manuscript. ZG, YW, XZ, RG, and YM have done all experiments on the assembly and corresponding analysis.

FUNDING

The work has been supported by the National Natural Science Foundation of China (21573118) and the Natural Science Foundation of Shandong Province, China (ZR2016JL014, 2018GGX102026).

SUPPLEMENTARY MATERIAL

The Supplementary Material for this article can be found online at: https://www.frontiersin.org/articles/10.3389/fchem.2019.00467/full#supplementary-material

REFERENCES

Ajayaghosh, A., Varghese, R., George, S. J., and Vijayakumar, C. (2006). Transcription and amplification of molecular chirality to oppositely biased supramolecular pi helices. *Angew. Chem. Int. Ed.* 45, 1141–1144. doi: 10.1002/anie.200503142

Baram, J., Weissman, H., Tidhar, Y., Pinkas, I., and Rybtchinski, B. (2014). Hydrophobic self-assembly affords robust noncovalent polymer isomers. *Angew. Chem. Int. Ed.* 53, 4123–4126. doi: 10.1002/anie.201310571

Cao, H., Zhu, X., and Liu, M. (2013). Self-assembly of racemic alanine derivatives: unexpected chiral twist and enhanced capacity for the discrimination of chiral species. *Angew. Chem. Int. Ed.* 52, 4122–4126. doi: 10.1002/anie.201300444

Diegelmann, S. R., Gorham, J. M., and Tovar, J. D. (2008). One-dimensional optoelectronic nanostructures derived from the aqueous self-assembly of pi-conjugated oligopeptides. *J. Am. Chem. Soc.* 130, 13840–13841. doi: 10.1021/ja805491d

Diegelmann, S. R., Hartman, N., Markovic, N., and Tovar, J. D. (2012). Synthesis and alignment of discrete polydiacetylene-peptide nanostructures. *J. Am. Chem. Soc.* 134, 2028–2031. doi: 10.1021/ja211539j

Digennaro, A., Wennemers, H., Joshi, G., Schmid, S., Mena-Osteritz, E., and Bauerle, P. (2013). Chiral suprastructures of asymmetric oligothiophene-hybrids induced by a single proline. *Chem. Commun.* 49, 10929–10931. doi: 10.1039/c3cc44861d

Draper, E. R., Greeves, B. J., Barrow, M., Schweins, R., Zwijnenburg, M. A., and Adams, D. J. (2017). pH-Directed aggregation to control photoconductivity in self-assembled perylene bisimides. *Chem* 2, 716–731. doi: 10.1016/j.chempr.2017.03.022

Echue, G., Lloyd-Jones, G. C., and Faul, C. F. (2015). Chiral perylene diimides: building blocks for ionic self-assembly. *Chemistry* 21, 5118–5128. doi: 10.1002/chem.201406094

George, S. J., de Bruijn, R., Tomovic, Z., Van Averbeke, B., Beljonne, D., Lazzaroni, R., et al. (2012). Asymmetric noncovalent synthesis of self-assembled one-dimensional stacks by a chiral supramolecular auxiliary approach. *J. Am. Chem. Soc.* 134, 17789–17796. doi: 10.1021/ja3086005

Guo, Z., Gong, R., Mu, Y., Wang, X., and Wan, X. (2014). Oligopeptide-assisted self-assembly of oligothiophenes: co-assembly and chirality transfer. *Chem. Asian J.* 9, 3245–3250. doi: 10.1002/asia.201402646

Guo, Z., Song, Y., Gong, R., Mu, Y., Jiang, Y., Li, M., et al. (2013). Assembly of peptide–thiophene conjugates: the influence of peptide content and location. *Supramol. Chem.* 26, 383–391. doi: 10.1080/10610278.2013.844810

Guo, Z., Wang, K., Yu, P., Wang, X., Lan, S., Sun, K., et al. (2017a). Impact of linear alkyl length on the assembly of twisted perylene bisimides: from molecular arrangement to nanostructures. *Chem. Asian J.* 12, 2827–2833. doi: 10.1002/asia.201700984

Guo, Z., Wang, K., Yu, P., Zhang, S., Sun, K., and Li, Z. (2017b). Role of intrinsic hydrogen bonds in the assembly of perylene imide derivatives in solution and at the liquid-solid interface. *Phys. Chem. Chem. Phys.* 19, 23007–23014. doi: 10.1039/c7cp04928e

Hu, J., Kuang, W., Deng, K., Zou, W., Huang, Y., Wei, Z., et al. (2012). Self-assembled sugar-substituted perylene diimide nanostructures with homochirality and high gas sensitivity. *Adv. Funct. Mater.* 22, 4149–4158. doi: 10.1002/adfm.201200973

Huang, Y., Hu, J., Kuang, W., Wei, Z., and Faul, C. F. (2011). Modulating helicity through amphiphilicity-tuning supramolecular interactions for the controlled assembly of perylenes. *Chem. Commun.* 47, 5554–5556. doi: 10.1039/c1cc10220f

Janssen, P. G., Meeuwenoord, N., van der Marel, G., Jabbari-Farouji, S., van der Schoot, P., Surin, M., et al. (2010). ssPNA templated assembly of oligo(p-phenylenevinylene)s. *Chem. Commun.* 46, 109–111. doi: 10.1039/b913307k

Jia, T., Wang, M., and Liao, J. (2019). Chiral sulfoxide ligands in asymmetric catalysis. *Top. Curr. Chem.* 377:8. doi: 10.1007/s41061-019-0232-9

Jiang, J., Meng, Y., Zhang, L., and Liu, M. (2016). Self-assembled single-walled Metal-Helical Nanotube (M-HN): creation of efficient supramolecular catalysts for asymmetric reaction. *J. Am. Chem. Soc.* 138, 15629–15635. doi: 10.1021/jacs.6b08808

Ke, D., Tang, A., Zhan, C., and Yao, J. (2013). Conformation-variable PDI@beta-sheet nanohelices show stimulus-responsive supramolecular chirality. *Chem. Commun.* 49, 4914–4916. doi: 10.1039/c3cc42366b

Kim, J., Lee, J., Kim, W. Y., Kim, H., Lee, S., Lee, H. C., et al. (2015). Induction and control of supramolecular chirality by light in self-assembled helical nanostructures. *Nat. Commun.* 6:6959. doi: 10.1038/ncomms7959

Kumar, R. J., MacDonald, J. M., Singh, T. B., Waddington, L. J., and Holmes, A. B. (2011). Hierarchical self-assembly of semiconductor functionalized peptide alpha-helices and optoelectronic properties. *J. Am. Chem. Soc.* 133, 8564–8573. doi: 10.1021/ja110858k

Lehrman, J. A., Cui, H., Tsai, W. W., Moyer, T. J., and Stupp, S. I. (2012). Supramolecular control of self-assembling terthiophene-peptide conjugates through the amino acid side chain. *Chem. Commun.* 48, 9711–9713. doi: 10.1039/c2cc34375d

Liu, H., Cao, X., Wu, Y., Liao, Q., Jimenez, A. J., Wurthner, F., et al. (2014). Self-assembly of octachloroperylene diimide into 1D rods and 2D plates by manipulating the growth kinetics for waveguide applications. *Chem. Commun.* 50, 4620–4623. doi: 10.1039/c3cc49343a

Mba, M., Moretto, A., Armelao, L., Crisma, M., Toniolo, C., and Maggini, M. (2011). Synthesis and self-assembly of oligo(p-phenylenevinylene) peptide conjugates in water. *Chemistry* 17, 2044–2047. doi: 10.1002/chem.201002495

Mitra, A., Panda, D. K., Corson, L. J., and Saha, S. (2013). Controllable self-assembly of amphiphilic macrocycles into closed-shell and open-shell vesicles, nanotubes, and fibers. *Chem. Commun.* 49, 4601–4603. doi: 10.1039/c3cc40535d

Samanta, S., Qin, C., Lough, A. J., and Woolley, G. A. (2012). Bidirectional photocontrol of peptide conformation with a bridged azobenzene derivative. *Angew. Chem. Int. Ed.* 51, 6452–6455. doi: 10.1002/anie.201202383

Schillinger, E.-K., Kümin, M., Digennaro, A., Mena-Osteritz, E., Schmid, S., Wennemers, H., et al. (2013). Guiding suprastructure chirality of an oligothiophene by a single amino acid. *Chem. Mater.* 25, 4511–4521. doi: 10.1021/cm4020767

Schillinger, E.-K., Mena-Osteritz, E., Hentschel, J., Börner, H. G., and Bäuerle, P. (2009). Oligothiophene versusβ-sheet peptide: synthesis and self-assembly of an organic semiconductor-peptide hybrid. *Adv. Mater.* 21, 1562–1567. doi: 10.1002/adma.200803110

Schmid, S., Mena-Osteritz, E., Kopyshev, A., and Bauerle, P. (2009). Self-assembling carbohydrate-functionalized oligothiophenes. *Org. Lett.* 11, 5098–5101. doi: 10.1021/ol9022694

Shang, X., Song, I., Ohtsu, H., Lee, Y. H., Zhao, T., Kojima, T., et al. (2017). Supramolecular nanostructures of chiral perylene diimides with amplified chirality for high-performance chiroptical sensing. *Adv. Mater.* 29:1605828. doi: 10.1002/adma.201605828

Shin, S., Lim, S., Kim, Y., Kim, T., Choi, T. L., and Lee, M. (2013). Supramolecular switching between flat sheets and helical tubules triggered by coordination interaction. *J. Am. Chem. Soc.* 135, 2156–2159. doi: 10.1021/ja400160j

Stone, D. A., Hsu, L., and Stupp, S. I. (2009). Self-assembling quinquethiophene–oligopeptide hydrogelators. *Soft Matter* 5, 1990–1993. doi: 10.1039/b904326h

Wall, B. D., Diegelmann, S. R., Zhang, S., Dawidczyk, T. J., Wilson, W. L., Katz, H. E., et al. (2011). Aligned macroscopic domains of optoelectronic nanostructures prepared via shear-flow assembly of peptide hydrogels. *Adv. Mater.* 23, 5009–5014. doi: 10.1002/adma.201102963

Wang, J., Chen, L., Wu, J., Li, W., Liu, K., Masuda, T., et al. (2018). Supramolecular assembly of C3 -peptides into helical fibers stabilized through dynamic covalent chemistry. *Chem. Asian J.* 13, 3647–3652. doi: 10.1002/asia.201801310

Yang, Y., Zhang, Y., and Wei, Z. (2013). 25-Supramolecular helices: chirality transfer from conjugated molecules to structures. *Adv. Mater.* 25, 6039–6049. doi: 10.1002/adma.201302448

Zhang, L., Qin, L., Wang, X., Cao, H., and Liu, M. (2014). Supramolecular chirality in self-assembled soft materials: regulation of chiral nanostructures and chiral functions. *Adv. Mater.* 26, 6959–6964. doi: 10.1002/adma.201305422

Zhang, Y., Chen, P., Jiang, L., Hu, W., and Liu, M. (2009). Controllable fabrication of supramolecular nanocoils and nanoribbons and their morphology-dependent photoswitching. *J. Am. Chem. Soc.* 131, 2756–2757. doi: 10.1021/ja805891k

Conflict of Interest Statement: The authors declare that the research was conducted in the absence of any commercial or financial relationships that could be construed as a potential conflict of interest.

frontiers in Chemistry

ORIGINAL RESEARCH
published: 03 July 2019
doi: 10.3389/fchem.2019.00473

Synthesis and Supramolecular Assembly of a Terrylene Diimide Derivative Decorated With Long Branched Alkyl Chains

Zongxia Guo[1], Xiao Zhang[2], Lu Zhang[2], Yujiao Wang[2], Weisheng Feng[2], Kai Sun[3], Yuanping Yi[3] and Zhibo Li[2]**

[1] Key Laboratory of Optic-electric Sensing and Analytical Chemistry for Life Science, MOE, Key Laboratory of Biochemical Analysis, Shandong Province, College of Chemistry and Molecular Engineering, Qingdao University of Science and Technology, Qingdao, China, [2] Key Laboratory of Biobased Polymer Materials, Shandong Provincial Education Department, School of Polymer Science and Engineering, Qingdao University of Science and Technology, Qingdao, China, [3] Institute of Chemistry, Chinese Academy of Sciences, Beijing, China

OPEN ACCESS

Edited by:
Takeharu Haino,
Graduate School of Science,
Hiroshima University, Japan

Reviewed by:
Xiaodong Zhuang,
Shanghai Jiao Tong University, China
Hiromitsu Maeda,
Ritsumeikan University, Japan

***Correspondence:**
Zongxia Guo
zxguo@qust.edu.cn
Zhibo Li
zbli@qust.edu.cn

Specialty section:
This article was submitted to Supramolecular Chemistry, a section of the journal Frontiers in Chemistry

Received: 28 February 2019
Accepted: 20 June 2019
Published: 03 July 2019

Citation:
Guo Z, Zhang X, Zhang L, Wang Y, Feng W, Sun K, Yi Y and Li Z (2019) Synthesis and Supramolecular Assembly of a Terrylene Diimide Derivative Decorated With Long Branched Alkyl Chains. Front. Chem. 7:473. doi: 10.3389/fchem.2019.00473

Terrylene diimide derivatives are pigments for dyes and optoelectric devices. A terrylene diimide derivative N,N'-di(1-undecyldodecyl)terrylene-3,4:11,12-tetracarboxdiimide (DUO-TDI) decorated with long branched alkyl chains on both imide nitrogen atoms was designed and synthesized. The supramolecular assembly behaviors of DUO-TDI in solution and at the liquid-solid interface were both investigated. The assembled nanostructures and photophysical properties of TDI in solution were explored by varying solvent polarity with spectral methods (UV-Vis, FL and FT-IR) and morphological characterization (AFM). Depending on the solution polarities, fibers, disk structures and wires could be observed and they showed diverse photophysical properties. In addition, the interfacial assembly of DUO-TDI was further investigated at the liquid-Highly Oriented Pyrolytic Graphite (HOPG) interface probed by scanning tunneling microscope (STM). Long range ordered monolayers composed of lamellar structures were obtained. The assembly mechanisms were studied for DUO-TDI both in solution and at the interface. Our investigation provides alternative strategy for designing and manipulation of supramolecular nanostructures and corresponding properties of TDI based materials.

Keywords: terrylene diimides, supramolecular assembly, scanning tunneling microscope, aromatic systems, liquid-solid interface

INTRODUCTION

Rylene diimide dyes derivatives are famous for their outstanding photophysical and photochemical stability and their high fluorescence quantum yield (Zhao et al., 2016; Feng et al., 2017; Frankaer et al., 2019). They have not only shown importance as vat dyes in industrial olorants, but also have been proven to be excellent organic semiconductor candidate for opto-electronic applications (Geerts et al., 1998; Wolf-Klein et al., 2002; Jung et al., 2006). Terrylene diimides (TDIs) are a class of rylene diimide dye consisting of terrylene core, a large aromatic core along the long molecular axis. It shows brilliant blue color and emits fluorescence at long wavelengths with long fluorescence lifetime. Moreover, TDIs also show good thermal, chemical, and photochemical stabilities. TDIs are

potential candidates as excellent probes for bio-labeling, energy convertors for light concentrators, and functional materials in electronic devices (Peneva et al., 2008; Bai et al., 2011; Berberich and Würthner, 2012; Chen et al., 2014; Stappert et al., 2016). Then, the design and synthesis of TDI based molecules have been attracting increasing attention recently, although less research had been done compared to perylene diimides (PDIs) (Chen et al., 2015; Würthner et al., 2016; Guo et al., 2019), another kind of rylene diimides. TDI derivatives were mostly designed via the decoration of the parent TDI molecule with various functional groups on the imide positions or on the periphery of the terrylene core (Heek et al., 2013). Actually, the competition and cooperation of the π-π stacking from the terrylene cores and other weak interactions of added functional groups play a great role in the modulation of molecular packing and their nanostructures and properties. One of the strategies is by using flexible chains, especially the alkyl chains (Davies et al., 2011). The affiliation of alkyl chains could vary the solubility, processing ability, molecular arrangement way, and the corresponding properties of TDIs. The topological structures of the alkyl chains could affect the assembly of rylene imides as well (Balakrishnan et al., 2006). It was proved that branched alkyl chains were capable of promoting distinguished assembly than induced by normal alkyl chains (Liao et al., 2013). For TDIs, branched alkyl chains were indeed fixed on the aromatic core to study the assembly therefore (Nolde et al., 2006). It should be known that the length of the alkyl chains could greatly affect the molecular assembly even with only one methylene difference (Chesneau et al., 2010; Xu et al., 2013; Li et al., 2017). Here, we report on the synthesis and self-assembly of one terrylene imide derivative modified with alkyl chains. For this subjective, it has two branched long alkyl chains on both imide positions. The presence of long alkyl chains significantly enhances the solubility and inhibits the intermolecular interaction and aggregation. The modulation of the solution assembly of TDI was realized by changing the solvent polarity and monitored by spectral and morphological methods. It was found that different kinds of assembled nanostructures with various properties could be formed. In addition, the surface/interfacial assembly behaviors could provide insights into the design, select and optimizing of semiconductors for using in opto-electronic devices. Then the assembly of TDI at the liquid-HOPG interface was also explored by STM (Lee et al., 2014a,b).

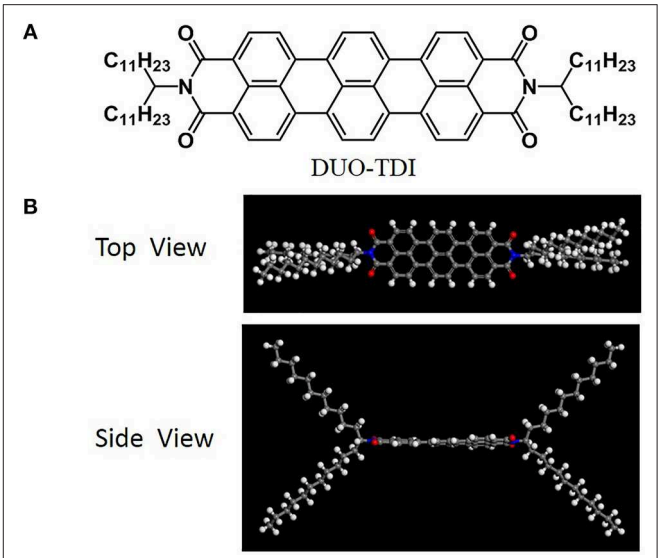

SCHEME 1 | (A) Molecular structure of DUO-TDI. **(B)** The top and side view of DUO-TDI molecule. The optimization was performed using the Forcite module of Materials Studio 7.0. The DREIDING force field was implemented for the geometry optimizations (Mayo et al., 1990).

RESULTS AND DISCUSSIONS

Synthesis and Properties of DUO-TDI

DUO-TDI was synthesized based on reported methods (Mayo et al., 1990; Nolde et al., 2006) (**Scheme 1**). Blue powder was obtained for DUO-TDI. The molecular structure was confirmed by ^{1}HNMR, ^{13}CNMR and MALDI TOF MS. As indicated in the **Scheme 1**, a large aromatic core exists between two branched alkyl chains. From the optimized molecular structure of TDI, the aromatic core is almost planar from the side view of the molecular structure. The distance between the two N atoms in the molecular skeleton is about 1.58 nm and such large π-conjugated core could provide strong π-π interactions with neighboring conjugated systems. The four undecyl chains with length about 1.39 nm in the periphery of the core structure not only change the solubility in usual organic solvents, but also offer van der Waals interactions among adjacent chains. It could be expected that the synergistic effect between π-π interactions from the core and the van der Waals interactions from such long alkyl chains could be effectively modulated by varying the conditions, thus leading to diverse assembly process, assembled nanostructures, and properties (Chen et al., 2015; Zhang et al., 2016).

Tetrahydrofuran (THF) is a good solvent for DUO-TDI. The absorption and emission properties of DUO-TDI in molecular state were investigated by UV-Vis and FL emission spectra. Firstly, the concentration-dependent UV-Vis absorption spectra of DUO-TDI in THF solutions were studied (**Figure 1A**). It can be seen that all the UV-Vis absorption spectra exhibited well-resolved vibronic structures when the concentration was varied from 4.3×10^{-6} to 3.5×10^{-5} M. With the concentration increasing, the absorbance intensity increased accordingly but without band shift. The relationship of absorbance intensity at 644 nm as a function of the concentration was shown in **Figure 1B**. From the fitted linear line, it was clear that DUO-TDI did not assemble into aggregates. In another words, DUO-TDI exists in molecularly state in THF within the above concentration range. In solution, the absorbance band from 450 to 700 nm was ascribed to the π-π* electronic transition of the chromophores in the monomeric state along with vibrational transitions (**Figure 1C**). Four characteristic vibration absorption bands centered at 644, 591, 546, and 505 nm were observed, and attributed to the 0-0, 0-1, 0-2, and 0-3 vibrational transitions, respectively (Nagao et al., 2002).

The cast film from THF solution of DUO-TDI was also studied to compare with the molecularly DUO-TDI. Two structureless bands at 670 and 597 nm were obtained for the cast film. The band at 597 nm should shift from that at 644 nm from diluted THF solution. Such blue shift indicated the formation of H-aggregates in the film (Davies et al., 2011). At the same time, the appeared shoulder band at 670 nm suggested the existence of J-aggregates in the cast film (Jung et al., 2006). From FL spectra, one emission peak at 672 nm and a shoulder band at 725 nm showed up for DUO-TDI in diluted solution. In contrast, the emission of DUO-TDI was completely quenched in the cast film, suggesting the main formation of H-type molecular packing in accordance with the results from UV-vis data (Jung et al., 2006).

Solvent Induced Assembly of DUO-TDI

Apart from the above discussions on the molecular behaviors in diluted solutions and in films, the self-assembly of TDI was further investigated in mixed solvent with varied polarity. In the present contribution, the mixed solvents were prepared by adding water into THF solutions. The volume percentage of water (Vw, v %) in the mixed solvent was altered to adjust the solvent polarity. Vw was changed from 0 to 75v% to study the solvent-dependent self-assembly of DUO-TDI, which was monitored by UV-vis and FL spectra firstly (**Figure 2**). With Vw = 25 v%, the absorption spectral lineshape was almost the same to that from monomeric DUO-TDI in THF (0 v%), while the absorbance intensity was slightly enhanced and the bands

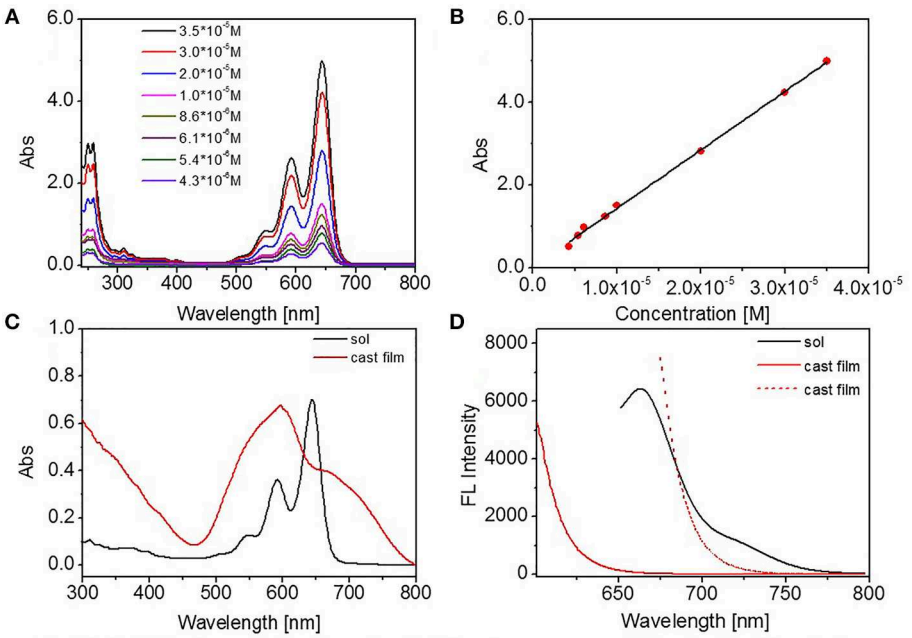

FIGURE 1 | (A) Concentration-dependent UV absorbance spectra of DUO-TDI in THF solutions, **(B)** The absorbance intensity at 644 nm as a function of concentration. The fitting R squared factor was 0.9966, **(C)** UV absorption spectra of DUO-TDI in THF solution (1.5×10^{-5} M) and cast film, **(D)** FL spectra of DUO-TDI in THF solution (1.5×10^{-5} M) and cast film. The excitation wavelength (λex) was 644 nm for solution. And Xex = 598 (red solid line) or 672 nm (red dashed line) for cast film.

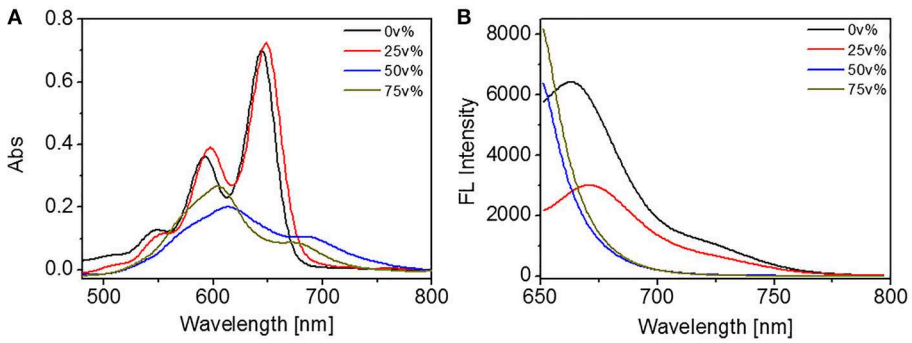

FIGURE 2 | (A) UV absorption and **(B)** FL emission spectra of DUO-TDI in solutions of water/THF. The concentration of all mixed solutions was 5.4×10^{-6} M. The excitation wavelength was 644 nm for all samples.

shifted to red. It can be seen that the three monomeric absorption bands at 546, 591, and 644 nm, which belong to the 0-2, 0-1, and 0-0 electronic transitions from the terrylene diimide cores red-shifted to 549, 597, and 648 nm. FL spectra were recorded to shed light on the self-assembly of DUO-TDI. It was shown that the emission was quenched greatly (about 50%) and the main emission band at around 662 nm red-shifted to 670 nm. It could be concluded that J-aggregates were formed with Vw = 25 v% (Jung et al., 2006). When Vw was raised to 50 v%, drastic changes of absorption band were observed. The absorption bands were broadened and turned into unresolved structures. Two main bands appeared at 600 and 690 nm, accompanied by incremental absorption at a wavelength longer than 700 nm. Clearly, the absorption at 612 nm was blue-shifted from the band at 644 nm, and the absorption at 690 nm was a newly appeared band. In addition, the emission was quenched as well. It was demonstrated that H-aggregates were mainly formed with J-aggregates in a minority in solution with Vw = 50 v%. With Vw = 75 v%, it showed similar spectral lineshape to that of 50 v%, however the two main peaks were centered at 600 and 680 nm (**Figure 2A**). It was obvious that the blue shift was enlarged compared to that from solution with Vw = 50 v%, indicating the increased π-π stacking. Apart from that, the relative intensity at about 600 and 690 nm was increased from 1.89 to 3.14, suggesting the increased relative amount of H- to J-aggregates. Besides, the fluorescence emission was completely quenched in accordance with the results from UV-vis spectra. Based on the above results, DUO-TDI could assemble into J- or H-type of aggregates relying on the solvent condition. Slightly increasing polarity of solvent, J-aggregates would be formed, and the elevation of polarity could facilatate the formation of H-aggregates. The molecular arrangement of DUO-TDI within the aggregates could be altered by changing solvent polarity.

FT-IR spectral method was used to detect alkyl chain packing in the molecular assemblies (**Figure 3**). It was reported that the alkyl chains with all trans-cis zigzag conformation could show an asymmetric stretching vibration of methylene group (CH_2) at 2,916–2,918 cm^{-1} (Wang et al., 1996; Zhang et al., 1997). For DUO-TDI powder, the asymmetric stretching vibration was at 2,918 cm^{-1}, which indicated all trans-cis zigzag conformation of alkyl chains. It was found that this peak shifted on varying V_W. The absorption of CH_2 from the branched undecyl groups were at 2,919 cm^{-1} from THF, indicating the relative disordered packing of alkyl chains. With the increase of polarity by the addition of water, the asymmetric vibrations of CH_2 shifted to longer wavenumbers, from 2,918 to 2,922 cm^{-1}, implying that gauche conformation or disordered packing of alkyl chains increased gradually. From the FT-IR and UV-Vis spectral data, both the π-π stacking and the alkyl chain packing were both varied on changing the solvent conditions.

Atomic force microscopy (AFM) measurements were carried out to investigate the polarity effect on the self-assembled nanostructures of DUO-TDI. **Figure 4** shows the AFM images of DUO-TDI nanostructures formed in different mixed solutions. It was evident that in the cast film from pure THF solution, no uniform structures could be observed. Amounts of amorphous structures existed on the surface with few thin fibers. The width of the fibers was around 18 nm. The observed fiber structures

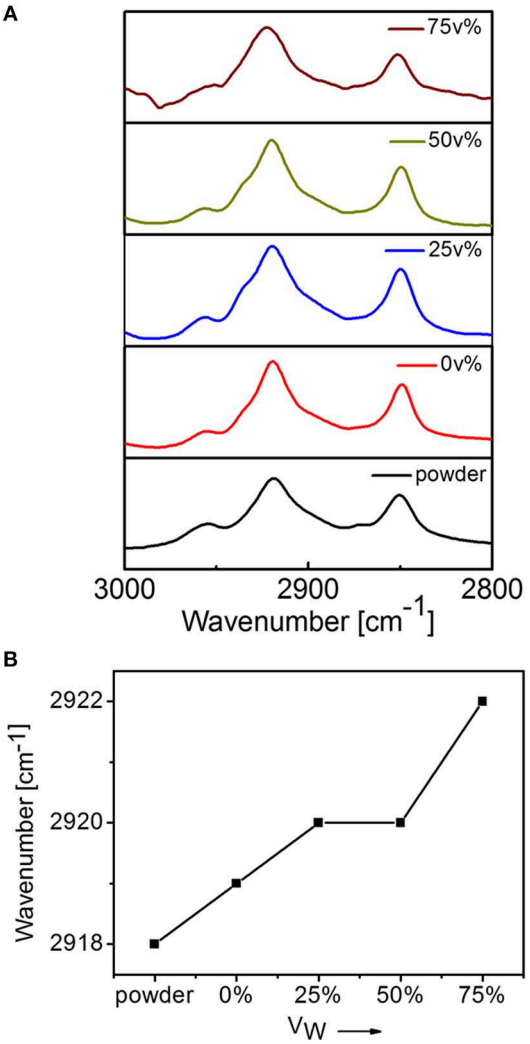

FIGURE 3 | (A) FT-IT spectra of DUO-TDI in solutions with variable V_W (0, 25, 50, and 75 v%). **(B)** Variation of peak positions of asymmetric stretching vibration of CH_2.

might be obtained due to the evaporation of THF on mica surface, since there was no obvious aggregation behaviors were found based on the solution spectral data. For V_W = 25 v%, helical fibers with left-handedness were mainly obtained. It means that chiral nanostructures were assembled, although DUO-TDI is an achiral building block (Shen et al., 2014). It was suggested that the J-aggregation manner facilitates DUO-TDI to hierarchically assemble into structures with handedness. The height of the helical fibers was around 13 nm. The width of the fibers was about 70 nm. It can be easily seen that thick fibers were entangled by thin fibers. With V_W = 50 v%, helical fibers almost disappeared, and there were sphere structures with diameters ∼1 μm and the height about 100 nm. Considering the high ratio (∼ 10) of width to height, it could be deduced that actually disk structures were formed. So, the emergence of both H- and J-aggregates could prevent the hierarchical growth of one dimensional fibers and the formation of chiral sense for the

nanostructures. On increasing the V_W to 75 v%, lots of wires with an average width of 50 nm showed up without obvious helical sense. Since H-aggregation manner was the major way of molecular packing with V_W = 75 v%, then it seems that the H-aggregates could promote the growth of one dimensional structures, but inhibit both chiral packing of molecules and hierarchical growth with chirality. It was clear that the solvent polarity indeed affected the assembled structures of DUO-TDI. The formation of helical fibers, disk structures and wires could be manipulated by controlling the solvent polarity and this further confirmed the different molecular packing modes and hierarchical ways within the assembled nanostructures. The AFM data was in accordance with that from the spectral results.

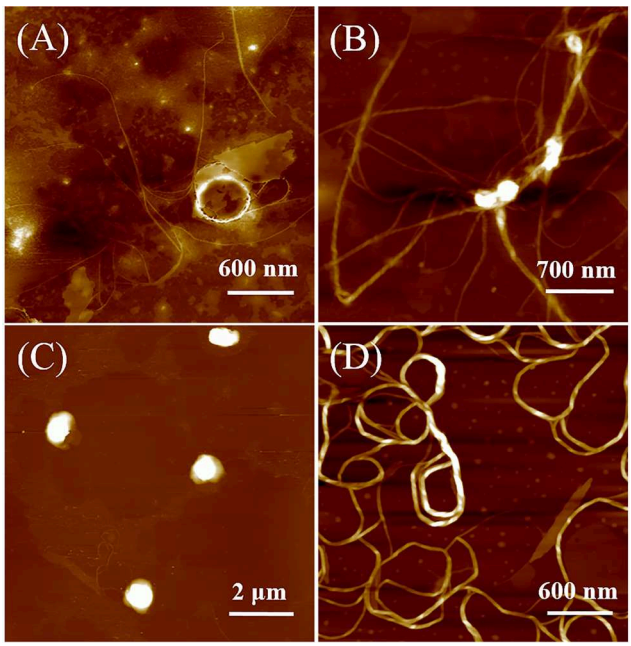

FIGURE 4 | AFM images of DUO-TDI films casted from solutions with varied Vw. **(A)** Vw = 0 v%, **(B)** Vw= 25 v%, **(C)** Vw = 50 v %, and **(D)** Vw= 75 v%. The concentration of all mixed solutions was 5.4 × 10^{-6} M.

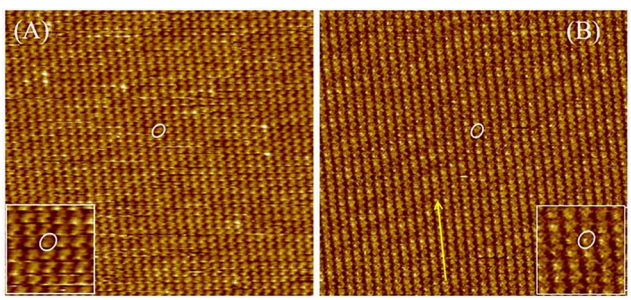

FIGURE 5 | Large-scale STM images (60 × 60 nm^2) of DUO-TDI at the **(A)** 1-Octanoic acid-HOPG interface and **(B)** 1-Phenyloctane-HOPG interface. Imaging conditions: **(A)** I_{set} = 70 pA, V_{bias} = −750 mV; **(B)** I_{set} = 75 pA, V_{bias} = −750 mV. One DUO-TDI is enclosed by a white oval in each image, and the inset indicates the magnified image for clarity. The yellow arrow points to the structure direction of the strip.

Assembly of DUO-TDI at the Liquid-HOPG Interface

We also reported the self-assembly of this n-type semiconductor at the liquid-HOPG interface. For DUO-TDI, the large π-conjugated core provides the π-π staking interactions with the substrate; and the four long alkyl chains offer potential good affinity with the HOPG surface and Van der Walls interactions among neighboring alkyl chains (Chen et al., 2014; Liu et al., 2015, 2016). Different solvents were tried, since the solvent may affect the self-assembly behaviors of molecules at the interface between the liquid and HOPG (Shen et al., 2010; Li et al., 2016). Here, 1-Octanoic acid and 1-Phenyloctane were used for detect the solvent effect. 1-Octanoic acid is a polar and protic solvent, and 1-Phenyloctane is an apolar and aprotic solvent.

In the first stage, the 2D crystallization behaviors of DUO-TDI at 1-Octanoic acid-HOPG interface were investigated. It was found that DUO-TDI could form ordered stable monolayers composed of lamellar structures (**Figure 5**). **Figure 5A** showed a large range of monolayers of DUO-TDI molecules. The relative bright dots were attributed to the π-conjugated core

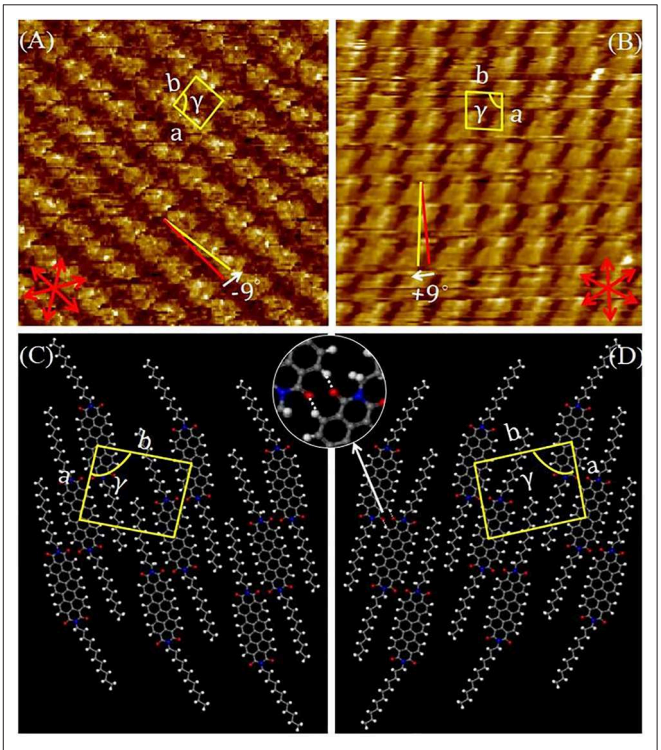

FIGURE 6 | (A,B) High-resolution STM images (15 × 15 mm^2, 4.3 × 10^{-6} M) of DUO-TDI at the 1-Octanoic acid-HOPG interface. Imaging conditions **(A)** I_{set} = 70 pA, V_{bias} = −750 mV; **(B)** I_{set} = 70 pA, V_{bias} = −750 mV. The graphite symmetry axes are shown in red. The yellow lines indicate the directions of the unit-cell vectors. **(C,D)** Tentative molecular packing models corresponding to the STM images. Hydrogen bonds are indicated by white dotted lines.

of DUO-TDI (**Figure S1**). Obviously, only two out of four alkyl chains of DUO-TDI adsorbed at the interface. One DUO-TDI core was enclosed by a white oval and enlarged in the inset of **Figure 5A** for clarity. The one well-ordered lamellar structure was indicated by a yellow arrow. Similar ordered stable monolayers were obtained for DUO-TDI at the 1-Phenyloctane-HOPG interface (**Figure 5B**).

To inspect the 2D molecular packing of this semiconductor in more detail, we recorded the high-resolution STM images. **Figure 6** showed a high-resolution image of DUO-TDI at the 1-Octanoic acid-HOPG interface. The unit cell parameters of the mirror patterns were the same within experimental error: $a = 1.53 \pm 0.01$ nm, $b = 1.96 \pm 0.02$ nm, and $\gamma = 86 \pm 2^{\circ}$ for the packing in **Figure 6A**; $a = 1.55 \pm 0.02$ nm, $b = 1.97 \pm 0.05$ nm, and $\gamma = 86 \pm 1^{\circ}$ for the packing in **Figure 6B**. In addition, the orientation angles of vector a with respect to the main symmetry axes of the underneath HOPG for the enantiomeric patterns were -9° and $+ 9^{\circ}$ (**Figures 6A,B**), respectively. Thus, 2D chirality was not only expressed within the monolayer plane, but also at the level of the monolayer orientation with respect to the HOPG substrate (Elemans et al., 2009; Guo et al., 2017). The tentative models for DUO-TDI are shown in **Figures 6C,D**, where the mirror-related patterns were clearly demonstrated. In rows, two DUO-TDI molecules were aligned in a shoulder-to-shoulder manner to form a dimer, indicated in the zoomed-in images of **Figure 6D**. Such dimers were connected with each other through two pairs of H-bonds (C-H$\cdots$O) within the same row. In STM images, the bright rows in the STM image corresponds to the molecular benzene ring skeleton in the model, and the dark rows corresponds to the alkyl chain in the model. The high resolution STM images at the 1-Phenyloctane-HOPG interface were also recorded and the monolayer composed of same nanopatterns with same unit cell parameters was obtained (**Figure S2**). However, it should be noted that the orientation angle of vector a with respect to the main symmetry axes of the underneath HOPG was 0° for both enantiomeric patterns. It can be seen that DUO-TDI molecules could form same long-term ordered nanostructures at both liquid-HOPG interface, but that the monolayer chirality was changed. Form above discussions, the formation of stable monolayers were attributed by the synergistic effect of H-bonds, π-π stacking, and Van der Walls interactions. And the solvent played an important role in the expression of supramolecular chirality, especially at the level of monolayers.

Actually, the bulk assemblies for DUO-TDI were examined by using the TGA and DSC **(Figure S3)**. TGA was used to characterize the thermal stability, and it was showed that DUO-TDI could be stable at the temperature lower than 360°C. DSC was performed to detect the phase transition of the DUO-TDI molecules. It was found that DUO-TDI showed two peaks at 145 and 137°C in the first cooling curve. It was obvious a thermotropic liquid crystal behavior was observed (reference). The systematic investigation of thermotropic liquid crystal behavior of DUO-TDI is undergoing.

CONCLUSIONS

The synthesis and the investigation of supramolecular assembly of a terylene diimide derivative DUO-TDI have been reported. DUO-TDI has a large π-conjugated core decorated with long branched 1-undecyldodecyl at both N positions. It was found that the supramolecular assembly could be manipulated by changing polarities of solutions consisting good solvent THF and poor solvent water. When varying the volume percentage of water (Vw) from 0 to 75v%, monomeric DUO-TDI, J-aggregates, H-aggregates with minor J-aggregates were obtained. Moreover, J-aggregates benefited for the formation of helical fibers, H-aggregates facilitated the fabrication of achiral nanostructures, such as nanodisks and wires. UV-vis, FL and FT-IR spectra confirmed that π-π stacking and alkyl chain packing were both altered within different nanostructures resulted from the difference in solvent polarity. The assembly of DUO-TDI at the liquid-HOPG interface was also studied. Stable monolayers composed of lamellar structures were observed. Chirality at the pattern level and monolayer level showed up for DUO-TDI at the 1-Octanoic acid-HOPG interface. While the monolayer level chirality disappeared at the 1-Phenyloctane-HOPG interface. The synergetic effect of π-π stacking from the large aromatic core and Van der Walls interactions from alkyl chains was proposed to contribute to the assembly of DUO-TDI in solutions and at the interface. The present investigation provides insight into the design of TDI based semiconductors for both academic research and potential opto-electronic devices or materials.

DATA AVAILABILITY

The raw data supporting the conclusions of this manuscript will be made available by the authors, without undue reservation, to any qualified researcher.

AUTHOR CONTRIBUTIONS

ZG and ZL contributed to the idea of the work and the preparation of the manuscript. XZ, LZ, and YW have done all experiments on the assembly and corresponding analysis. YW, WF, and YY did the simulation work. KS synthesized the molecule DUO-TDI.

FUNDING

The work has been supported by the National Natural Science Foundation of China (21573118, 21434008) and the Shandong Provincial Natural Science Foundation, China (ZR2016JL014, 2018GGX102026).

SUPPLEMENTARY MATERIAL

The Supplementary Material for this article can be found online at: https://www.frontiersin.org/articles/10.3389/fchem.2019.00473/full#supplementary-material

REFERENCES

Bai, Q., Gao, B., Ai, Q., Wu, Y., and Ba, X. (2011). Core-extended terrylene diimide on the bay region: synthesis and optical and electrochemical properties. *Org. Lett.* 13, 6484–6487. doi: 10.1021/ol202775b

Balakrishnan, K., Datar, A., Naddo, T., Huang, J., Oitker, R., Yen, M., et al. (2006). Effect of side-chain substituents on self-assembly of perylene diimide molecules: morphology control. *J. Am. Chem. Soc.* 128, 7390–7398. doi: 10.1021/ja061810z

Berberich, M., and Würthner, F. (2012). Terrylene bisimide-diarylethene photochromic switch. *Chem. Sci.* 3, 2771–2777. doi: 10.1039/c2sc20554h

Chen, L., Li, C., and Müllen, K. (2014). Beyond perylene diimides: synthesis, assembly and function of higher rylene chromophores. *J. Mater. Chem. C* 2, 1938–1956. doi: 10.1039/c3tc32315c

Chen, S., Slattum, P., Wang, C., and Zang, L. (2015). Self-Assembly of perylene imide molecules into 1D nanostructures: methods, morphologies, and applications. *Chem. Rev.* 115, 11967–11998. doi: 10.1021/acs.chemrev.5b00312

Chesneau, F., Schüpbach, B., Szelagowska-Kunstman, K., Ballav, N., Cyganik, P., Terfort, A., et al. (2010). Self-assembled monolayers of perfluoroterphenyl-substituted alkanethiols: specific characteristics and odd-even effects. *Phys. Chem. Chem. Phys.* 12, 12123–12137. doi: 10.1039/c0cp00317d

Davies, M., Jung, C., Wallis, P., Schnitzler, T., Li, C., Müllen, K., et al. (2011). Photophysics of new photostable rylene derivatives: applications in single-molecule studies and membrane labelling. *Chem. Phys. Chem.* 12, 1588–1595. doi: 10.1002/cphc.201000666

Elemans, J., De Cat, I., Xu, H., and De Feyter, S. (2009). Two-dimensional chirality at liquid-solid interfaces. *Chem. Soc. Rev.* 38, 722–736. doi: 10.1039/b800403j

Feng, J. J., Liang, N. N., Jiang, W., Meng, D., Xin, R., Xu, B. W., et al. (2017). Twisted terrylene dyes: synthesis and application in organic solar cells. *Org. Chem. Front.* 4, 811–816. doi: 10.1039/c7qo00118e

Frankaer, C. G., Hussain, K. J., Dörge, T. C., and Sorensen, T. J. (2019). Optical chemical sensor using intensity ratiometric fluorescence signals for fast and reliable pH determination. *ACS Sens.* 4, 26–31. doi: 10.1021/acssensors.8b01485

Geerts, Y., Quante, H., Platz, H., Mahrt, R., Hopmeier, M., Böhm, A., et al. (1998). Quaterrylenebis(dicarboximide)s: near infrared absorbing and emitting dyes. *J. Mater. Chem.* 8, 2357–2369. doi: 10.1039/a804337j

Guo, Z., Yu, P., Sun, K., Lei, S., Yi, Y., and Li, Z. (2017). Role of halogenhalogen interactions in the 2D crystallization of n-semiconductors at the liquid-solid interface. *Phys. Chem. Chem. Phys.* 19, 31540–31544. doi: 10.1039/c7cp06027k

Guo, Z., Zhang, X., Wang, Y., and Li, Z. (2019). Supramolecular self-assembly of perylene bisimide derivatives assisted by various groups. *Langmuir* 35, 342–358. doi: 10.1021/acs.langmuir.8b02964

Heek, T., Würthner, F., and Haag, R. (2013). Synthesis and optical properties of water-soluble polyglycerol-dendronized rylene bisimide dyes. *Chem.-Eur. J.* 19, 10911–10921. doi: 10.1002/chem.201300556

Jung, C., Müller, B. K., Lamb, D. C., Nolde, F., Müllen, K., and Brauchle, C. (2006). A new photostable terrylene diimide dye for applications in single molecule studies and membrane labeling. *J. Am. Chem. Soc.* 128, 5283–5291. doi: 10.1021/ja0588104

Lee, S. L., Yuan, Z., Chen, L., Mali, K. S., Müllen, K., and De Feyter, S. (2014a). Flow-assisted 2D polymorph selection: stabilizing metastable monolayers at the liquid-solid interface. *J. Am. Chem. Soc.* 136, 7595–7598. doi: 10.1021/ja503466p

Lee, S. L., Yuan, Z., Chen, L., Mali, K. S., Müllen, K., and De Feyter, S. (2014b). Forced to align: flow-induced long-range alignment of hierarchical molecular assemblies from 2D to 3D. *J. Am. Chem. Soc.* 136, 4117–4120. doi: 10.1021/ja5005202

Li, S. Y., Chen, T., Wang, L., Wang, D., and Wan, L. J. (2016). Turning off the majority-rules effect in two-dimensional hierarchical chiral assembly by introducing a chiral mismatch. *Nanoscale* 8, 17861–17868. doi: 10.1039/c6nr06341a

Li, Y., Wang, Y.-X., Ren, X.-K., and Chen, L. (2017). Synthesis and self-assembly of unconventional C3-symmetrical trisubstituted triphenylenes. *Mater. Chem. Front.* 1, 2599–2605. doi: 10.1039/c7qm00361g

Liao, Z., Hooley, E. N., Chen, L., Stappert, S., Müllen, K., and Vosch, T. (2013). Green emitting photoproducts from terrylene diimide after red illumination. *J. Am. Chem. Soc.* 135, 19180–19185. doi: 10.1021/ja407431w

Liu, M., Zhang, L., and Wang, T. (2015). Supramolecular chirality in self-assembled systems. *Chem. Rev.* 115, 7304–7397. doi: 10.1021/cr500671p

Liu, X.-P., Xue, L.-W., Wei, Q., Liang, M., Deng, K., Zhang, Z.-J., et al. (2016). Seeing modulability self-assembled monolayers of π-conjugated perylene derivatives by scanning tunneling microscopy. *J. Phys. Chem. C* 120, 18607–18615. doi: 10.1021/acs.jpcc.6b04975

Mayo, S. L., Olafson B. D., and Goddard, W. A. (1990). DREIDING: a generic force field for molecular simulations. *J. Phys. Chem.* 94, 8897–8909. doi: 10.1021/j100389a010

Nagao, Y., Iwawaki, H., and Kozawa, K. (2002). Synthesis and properties of terrylene-dicarboximide derivatives. *Heterocycles* 56, 331–340. doi: 10.3987/COM-01-S(K)43

Nolde, F., Pisula, W., Müller, S., Kohl, C., and Müllen, K. (2006). Synthesis and self-organization of core-extended perylene tetracarboxdiimides with branched alkyl substituents. *Chem. Mat.* 18, 3715–3725. doi: 10.1021/cm060742c

Peneva, K., Mihov, G., Nolde, F., Rocha, S., Hotta, J., Braeckmans, K., et al. (2008). Water-soluble monofunctional perylene and terrylene dyes: powerful labels for single-enzyme tracking. *Angew. Chem. Int. Ed.* 47, 3372–3375. doi: 10.1002/anie.200705409

Shen, Y. T., Deng, K., Zeng, Q. D., and Wang, C. (2010). Size-selective effects on fullerene adsorption by nanoporous molecular networks. *Small* 6, 76–80. doi: 10.1002/smll.200901601

Shen, Z., Wang, T., and Liu, M. (2014). Macroscopic chirality of supramolecular gels formed from achiral tris(ethyl cinnamate) benzene-1,3,5-tricarboxamides. *Angew. Chem. Int. Ed.* 53, 13424–13428. doi: 10.1002/anie.201407223

Stappert, S., Li, C., Müllen, K., and Basche, T. (2016). Synthesis of an acceptor-donor-acceptor multichromophore consisting of terrylene and perylene diimides for multistep energy transfer studies. *Chem. Mat.* 28, 906–914. doi: 10.1021/acs.chemmater.5b04602

Wang, Y., Nichogi, K., Iriyama, K., and Ozaki, Y. (1996). Thermal behavior of mixed-stack charge transfer films of 2-octadecyl-7,7,8,8-tetracyanoquinodimethane and 3,3‘,5,5‘-tetramethylbenzidine prepared by the langmuir–blodgett technique and donor doping. 2. Morphology and Annealing Effects of the Films Investigated by Atomic Force Microscopy and Ultraviolet–Visible–Near Infrared and Infrared Spectroscopies. *J. Phys. Chem.* 100, 17238–17242. doi: 10.1021/jp960751g

Wolf-Klein, H., Kohl, C., Müllen, K., and Paulsen, H. (2002). Biomimetic model of a plant photosystem consisting of a recombinant light-harvesting complex and a terrylene dye. *Angew. Chem. Int. Ed.* 41, 3378–3380. doi: 10.1002/1521-3773(20020916)41:18<3378::AID-ANIE3378>3.0.CO;2-#

Würthner, F., Saha-Möller, C. R., Fimmel, B., Ogi, S., Leowanawat, P., and Schmidt, D. (2016). Perylene bisimide dye assemblies as archetype functional supramolecular materials. *Chem. Rev.* 116, 962–1052. doi: 10.1021/acs.chemrev.5b00188

Xu, L., Miao, X., Zha, B., Miao, K., and Deng, W. (2013). Dipole-controlled self-assembly of 2,7-Bis(n-alkoxy)-9-fluorenone: odd–even and chain-length effects. *J. Phys. Chem. C* 117, 12707–12714. doi: 10.1021/jp403881t

Zhang, L., Wang, T., Shen, Z., and Liu, M. (2016). Chiral nanoarchitectonics: towards the design, self-assembly, and function of nanoscale chiral twists and helices. *Adv. Mater.* 28, 1044–1059. doi: 10.1002/adma.201502590

Zhang, Z., Verma, A. L., Yoneyama, M., Nakashima, K., Iriyama, K., and Ozaki, Y. (1997). Molecular orientation and aggregation in langmuir–blodgett films of 5-(4-N-Octadecylpyridyl)-10,15,20-tri-p-tolylporphyrin Studied by Ultraviolet–Visible and Infrared Spectroscopies. *Langmuir* 13, 4422–4427. doi: 10.1021/la970122d

Zhao, X., Xiong, Y., Ma, J., and Yuan, Z. (2016). Rylene and rylene diimides: comparison of theoretical and experimental results and prediction for high-rylene derivatives. *J. Phys. Chem. A* 120, 7554–7560. doi: 10.1021/acs.jpca.6b07552

Conflict of Interest Statement: The authors declare that the research was conducted in the absence of any commercial or financial relationships that could be construed as a potential conflict of interest.

frontiers in Chemistry

ORIGINAL RESEARCH
published: 11 July 2019
doi: 10.3389/fchem.2019.00493

A Cationic Tetraphenylethene as a Light-Up Supramolecular Probe for DNA G-Quadruplexes

Clément Kotras[1,2], *Mathieu Fosséprés*[2], *Maxime Roger*[1], *Virginie Gervais*[3], *Sébastien Richeter*[1], *Philippe Gerbier*[1], *Sébastien Ulrich*[4], *Mathieu Surin*[2]* and *Sébastien Clément*[1]*

[1] ICGM Institut Charles Gerhardt Montpellier, UMR 5253, CNRS, Université de Montpellier, ENSCM, Montpellier, France, [2] Laboratory for Chemistry of Novel Materials, Center of Innovation and Research in Materials and Polymers, University of Mons-UMONS, Mons, Belgium, [3] Institut de Pharmacologie et de Biologie Structurale, CNRS, IPBS, Université de Toulouse, Toulouse, France, [4] Institut des Biomolécules Max Mousseron, IBMM, UMR 5247, CNRS, Université de Montpellier, ENSCM, Montpellier, France

OPEN ACCESS

Edited by:
Penglei Chen,
Institute of Chemistry (CAS), China

Reviewed by:
Sriram Kanvah,
Indian Institute of Technology Gandhinagar, India
Jun Yin,
Central China Normal University, China
Ye Tian,
Nanjing University, China

***Correspondence:**
Mathieu Surin
mathieu.surin@umons.ac.be
Sébastien Clément
sebastien.clement1@umontpellier.fr

Specialty section:
This article was submitted to Supramolecular Chemistry, a section of the journal Frontiers in Chemistry

Received: 13 April 2019
Accepted: 26 June 2019
Published: 11 July 2019

Citation:
Kotras C, Fosséprés M, Roger M, Gervais V, Richeter S, Gerbier P, Ulrich S, Surin M and Clément S (2019) A Cationic Tetraphenylethene as a Light-Up Supramolecular Probe for DNA G-Quadruplexes. Front. Chem. 7:493. doi: 10.3389/fchem.2019.00493

Guanine-quadruplexes (G4s) are targets for anticancer therapeutics. In this context, human telomeric DNA (HT-DNA) that can fold into G4s sequences are of particular interest, and their stabilization with small molecules through a visualizable process has become a challenge. As a new type of ligand for HT-G4, we designed a tetraimidazolium tetraphenylethene (**TPE-Im**) as a water-soluble light-up G4 probe. We study its G4-binding properties with HT-DNA by UV-Visible absorption, circular dichroism and fluorescence spectroscopies, which provide insights into the interactions between **TPE-Im** and G4-DNA. Remarkably, **TPE-Im** shows a strong fluorescence enhancement and large shifts upon binding to G4, which is valuable for detecting G4s. The association constants for the **TPE-Im**/G4 complex were evaluated in different solution conditions via isothermal titration calorimetry (ITC), and its binding modes were explored by molecular modeling showing a groove-binding mechanism. The stabilization of G4 by **TPE-Im** has been assessed by Fluorescence Resonance Energy Transfer (FRET) melting assays, which show a strong stabilization ($\Delta T_{1/2}$ around +20°C), together with a specificity toward G4 with respect to double-stranded DNA.

Keywords: tetraphenylethene, G-quadruplexes, fluorescence, light-up probe, supramolecular

INTRODUCTION

G-quadruplexes (G4s) are secondary structures of DNA, formed by specific guanine-rich sequences in presence of monovalent cations. Guanine-rich sequences can self-assemble into square planar networks (called G-quartets) via Hoogsteen hydrogen-bonds, and these G-quartets can stack on top of each other, stabilized by monovalent alkali cations, to form G-quadruplexes (G4s) (Davis and Spada, 2007; Bochman et al., 2012; Doluca et al., 2013). Notably, it has been demonstrated that G4s are formed in human telomeres, made of DNA sequence d(TTAGGG)n (Balasubramanian and Neidle, 2009; Phan, 2010; Wu and Brosh, 2010; Lam et al., 2013; Hänsel-Hertsch et al., 2017). Telomeres are non-coding regions at the end of chromosomes that protect chromosomal ends from fusion during replication of DNA. A specific enzyme, the telomerase, add repetitions of d(TTAGGG)n at the end of telomeres, and it has been shown that in most cancer cells, this enzyme is overexpressed. The normal expression of telomerase into cells allows protection of

coding genes during the cell life, whereas when telomerase is overexpressed, the cell can no longer enter into senescence and start multiplying in a non-controlled manner, causing tumor growth (Phan, 2010; Wu and Brosh, 2010; Biffi et al., 2013; Maji and Bhattacharya, 2014). The challenge that emerge from these hypotheses in anti-cancer drug design is designing molecules that can bind/stabilize G4s and inhibit the telomerase activity in tumor cells (Monchaud and Teulade-Fichou, 2008; Balasubramanian and Neidle, 2009; Collie and Parkinson, 2011; Tucker et al., 2012; Neidle, 2017; Asamitsu et al., 2019). A large number of small molecules, such as porphyrin, perylene, and naphthalene diimide derivatives, have been prepared and demonstrated their ability to bind G4 (Zhao et al., 2013; Golub et al., 2015; Rubio-Magnieto et al., 2015). We have notably studied the interaction between imidazolium- or pyridinium-based tetracationic porphyrins and demonstrated their strong binding with G4s, and their selectivity to G4 over double-stranded DNA (dsDNA) (Rubio-Magnieto et al., 2015). Indeed, porphyrins have interesting UV-Vis absorption properties, but their fluorescence intensities in interaction with G4 are weak, hampering their use as fluorescent probes.

With the aim of evolving toward G4-DNA fluorescent probes, we synthesized a cationic tetraphenylethene (TPE) derivative, as recently reported by Hahn and coworkers (Sinha et al., 2017). The TPE core was selected due to its appropriate size in comparison to intramolecular human telomeric G4s (Hong et al., 2010). To promote multi-site interactions and solubility in aqueous media, four cationic groups were introduced into the TPE core as it has been achieved with porphyrins by us and others (Flynn et al., 1999; Trommel and Marzilli, 2001; Rubio-Magnieto et al., 2015). A remarkable characteristic of TPEs is their peculiar fluorescence properties: TPEs are poorly fluorescent when molecularly dissolved in solution due to the possible intramolecular rotations which lead to deexcitation through non-radiative pathways. However, when TPEs aggregate, a large increase of the fluorescence is noted because of the restriction of its intramolecular rotations by the aggregate formation (Mei et al., 2014; Yang et al., 2016). These Aggregation-Induced Emission (AIE) properties of TPE motivated us to conceive a "light-up" probe to stabilize and detect G4s with a very low detection limit. In contrast to another approach that make use of flexible alkylammonium groups (Hong et al., 2010; Zhang et al., 2015), we have selected imidazolium cationic groups directly connected to the TPE core (**Scheme 1**), as these were found to provide high affinity toward human telomeric G4s, through the combination of electrostatic interactions with the DNA backbone and π-type interactions with the nucleobases of the G4 loops (Rubio-Magnieto et al., 2015).

In this paper, we report on the synthesis and the optical properties of a novel compound **TPE-Im**, see **Scheme 1**. We study its G4 binding properties with human telomeric DNA (HT-DNA) sequences, by means of circular dichroism (CD), and fluorescence spectroscopies, and isothermal titration calorimetry (ITC). We have selected the (HT-DNA) sequences **Tel22** (5′-AGG GTT AGG GTT AGG GTT AGG G-3′) because of their relevance as G4 targets in cancer research, and because these sequences can adopt different intramolecular G-quadruplex structures depending on the solution conditions.

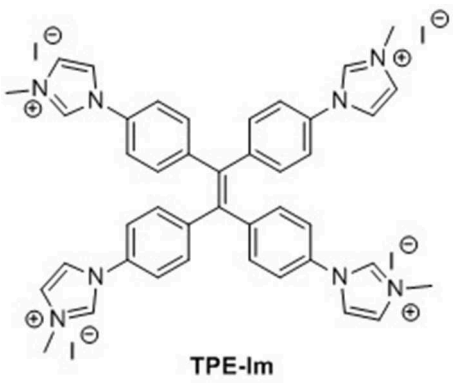

SCHEME 1 | Chemical structure of **TPE-Im**.

MATERIALS AND METHODS

Materials

Dry DMF and THF were obtained by a solvent purification system PureSolve MD5 from Innovative Technology. Preparative purifications were performed by silica gel flash column chromatography (Merck 40–60 mm). Solvents used as eluents are technical grade.

Synthesis

The synthesis of 1,1,2,2-tetrakis(4-bromophenyl)ethane (**TPE-Br**) was performed according to literature procedures (Schultz et al., 2003).

Synthesis of Tetra-Imidazole-Appended Tetrakis(*p*-phenylene)Ethylene (TIPE)

1,1,2,2-tetrakis(4-bromophenyl)ethene (0.500 g, 0,772 mmol), imidazole (0.42 g, 6.177 mmol; 8 eq.), potassium carbonate (0.750 g, 5.435 mmol; 7 eq.) and $CuSO_4$ (0.025 g, 0.157 mmol; 0.2 eq.) were placed into a Schlenk flask under an argon atmosphere and anhydrous DMF (2 mL) was added. The solid mixture was then heated to 140°C for 24 h. The reaction mixture was cooled to room temperature and was washed three times (3 × 20 mL) with distilled water. The remaining solid residue was extracted with methanol (3 × 10 mL) and the methanol solution was filtered and evaporated under vacuum. The crude product was then purified by column chromatography on silica gel eluting with a gradient of dichloromethane:methanol (98:2–90:10) to give **TIPE** as a colorless solid. Yield: 0.220 g (0.370 mmol, 48%). Spectroscopic data for **TIPE** are the same as previously described in the literature (Sinha et al., 2017). ^{1}H NMR (300 MHz, DMSO-d_6): $\delta = 8.27$ (s, 4H), 7.75 (s, 4H), 7.54 (d, $^3J_{H-H} = 8.5$ Hz, 8H), 7.19 (d, $^3J_{H-H} = 8.5$ Hz, 8H), 7.09 ppm (br. s, 4H) ppm.

Synthesis of TPE-Im

In a 50 mL Schlenk tube under an argon atmosphere, **TIPE** (0.100 g, 0.168 mmol) was dissolved in anhydrous DMF (15 mL). Iodomethane (5 mL, 0.800 mmol; 470 eq.) was added at once. The reaction mixture was stirred at room temperature for 72 h. **TPE-Im** is then precipitated in diethyl ether (400 mL) and filtered leading to a yellow solid. Yield: 0.180 g (0.146 mmol, 87%). ^{1}H NMR (300 MHz, CD_3OD) δ = 9.55 (s, 4H), 8.05 (t, J_{H-H} = 1.7 Hz, 4H), 7.76 (t, J_{H-H} = 1.8 Hz, 4H), 7.61 (d, $^{3}J_{H-H}$ =8.7 Hz, 8H), 7.42 (d, $^{3}J_{H-H}$ = 8.7 Hz, 8H), 4.03 (s, 12H, N-CH_3) ppm. $^{13}C\{^{1}H\}$ NMR (101 MHz, CD_3OD) δ = 143.8, 142.2, 135.3, 134.2, 125.7, 123.2, 122.6, 37.0 ppm. HR-MS (ESI-TOF^{+}): *m/z* calculated $C_{42}H_{40}N_8^{4+}$ 164.0844 $[M - 4I]^{4+}$, found 164.0845. UV-vis (H_2O) λ (ε L. mol^{-1}. cm^{-1}) = 260 (29 800), 293 (20 800), 322 (16 800) nm.

UV-Vis Absorption and Circular Dichroism Spectroscopy

UV-Vis absorption spectra of pure **TPE-Im** were recorded at 25°C on a JASCO V-750 spectrophotometer in 10 mm quartz cells (Hellma). The extinction coefficients were determined by preparing solutions of **TPE-Im** at different concentration, and the concentration range was judiciously chosen to remain in the linear range of the Beer-Lambert relationship (A $\sim$ 0.2–0.8). For **TPE-Im/G4** mixtures, UV-Vis absorption and Circular Dichroism (CD) measurements were recorded using a ChirascanTM Plus CD Spectrometer from Applied Photophysics. The measurements were carried out using 2 mm suprasil quartz cells from Hellma Analytics. The spectra were recorded at 20°C between 225 and 600 nm, with a bandwidth of 1 nm, time per point 1 s. The buffer water solvent was Tris-EDTA prepared from 1 M Tris-Cl and 0.5 M EDTA to achieve a 10 mM Tris-Cl and 1 mM EDTA final buffer at pH 7.5. The buffered water solvent reference spectra were used as baselines and were automatically subtracted from the CD and UV-Vis absorption of the samples. All the spectra were treated by using OriginPro 2018 software.

Fluorescence Spectroscopy

Emission spectra of pure **TPE-Im** were recorded at 25°C on a fluorescence spectrophotometer (FS920, Edinburgh Instruments) equipped with a calibrated photomultiplier in a Peltier (air cooled) housing (R928P, Hamamatsu), with a 450 W continuous xenon arc lamp as the excitation source for steady-state photoluminescence measurements using a quartz cuvette with 1.0 cm excitation path length. Emission spectra of **TPE-Im/G4** mixtures were recorded using a ChirascanTM Plus CD spectrophotometer from Applied Photophysics equipped for fluorescence measurements. The measurements were carried out using 4 mm by 10 mm suprasil quartz cells from Hellma Analytics. The spectra were recorded at 20°C between 270 and 700 nm, with a bandwidth of 2.0 nm, time per point 0.5 s. The buffer water solvent was Tris-EDTA at 10 mM Tris-Cl and 1 mM EDTA, pH 7.5, same as CD and UV-vis experiment. All the spectra were treated by using OriginPro 2018 software.

Molecular Docking

TPE-Im was built within the Avogadro molecular editor (Hanwell et al., 2012). Molecular mechanics calculations were then performed to optimize the geometry of the **TPE-Im** molecule. For this, a two-step minimization procedure, i.e., a steepest descent optimization followed by a conjugate gradient optimization, was performed with the General Amber Force Field (GAFF) (Wang et al., 2004). The energy convergence criterion was set at 10^{-5} kJ. mol^{-1} for the energy minimization. The coordinates of the two G-quadruplexes (G4) were obtained from the Protein Data Bank (PDB ID: 143d and PDB ID: 2hy9). For each G4, we extracted the different NMR conformations to perform ensemble docking calculations, i.e., six conformations for the 143D target and 10 conformations for the 2HY9 target. Docking calculations were performed with the AutoDock Vina package (Trott and Olson, 2009). As we have no *a priori* knowledge of the **TPE-Im** binding mode along the G4 structures, a sufficiently large grid was built around each G4 structure to allow the exploration of the entire G4 surface during the docking calculations. A large grid size of 100 × 100 × 100 Å^3 with a spacing of 0.375 Å was thus considered. The center of the grid box was located on the center-of-mass of the G4 targets. As the grid presents an important size, an exhaustiveness value of 32 was chosen, a larger one than the default value, i.e., eight (Jaghoori et al., 2016). **TPE-Im** was set as a flexible entity, and we considered various torsions between imidazolium and benzyl moieties. The 10 most energetically favorable complexes were retained for each docking calculation. The PyMOL molecular visualization system was used to depict illustrations of the **TPE-Im** docking calculations (Delano, 2002).

Fluorescence Resonance Energy Transfer (FRET) Melting Assays

FRET melting assays were performed according to Decian et al. (2007), Renciuk et al. (2012), and Rubio-Magnieto et al. (2015), using a synthetic double-dye labeled oligonucleotide called **F21T** 5′-FAM-GGG(T2AG3)3-TAMRA-3′ (purchased with the highest purity grade from Eurogentec, Belgium). The solutions were prepared at a concentration of around 0.3 μM (ODN concentration) in 10 mM lithium cacodylate buffer (pH = 7.2) in presence of 100 mM KCl. The solutions were first heated to 90°C for 315 min in the corresponding buffer conditions and then slowly cooled down at 1.5°C/min to 20°C to support the formation of G4 secondary structure. The mixtures were equilibrated at 25°C during 5 min. The FRET spectra were measured using a ChirascanTM Plus CD Spectrophotometer equipped for fluorescence measurements. The samples were excited at 492 nm and the fluorescence emission spectra were collected between 500 and 700 nm. The temperature was varied from 20 to 95°C at a rate of 0.3°C/min. The melting of the **F21T** was monitored by measuring the fluorescence of FAM (at 516 nm), as described in reference (Decian et al., 2007; Renciuk et al., 2012; Rubio-Magnieto et al., 2015). The FAM emission intensity was normalized and $\Delta T_{1/2}$ was defined as the temperature for which the normalized emission equals 0.5. For the selectivity studies, a solution of 10 molar equivalents of a

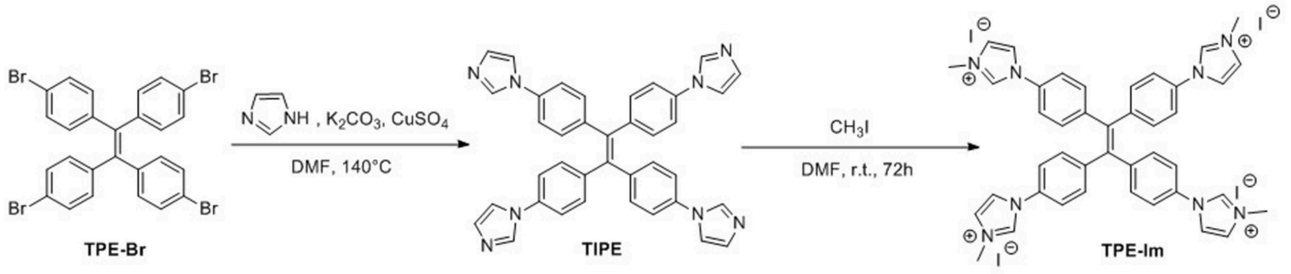

SCHEME 2 | Synthesis of **TPE-Im**.

dsDNA competitor (∼3 μM in double-strand) was added into the **F21T/TPE-Im** solution and the final solution was equilibrated at 25°C during 5 min. The dsDNA competitor (**ds43**) is a 43 base pairs with sequence: 5′-CGT CAC GTA AAT CGG TTA ACA AAT GGC TTT CGA AGC TAG CTT C-3′, hybridized with its complementary sequence. All the spectra were treated by using OriginPro 2018 software.

Isothermal Titration Calorimetry

Isothermal titration calorimetry (ITC) experiments were carried out at 20°C on a Microcal ITC200 instrument (Microcal). The titration cell was filled with a solution of 10–20 μM **Tel22** DNA and the syringe was loaded with a **TPE-Im** solution of 600–2,000 μM. Experiments consisted of a series of 26 injections of ligand from rotating syringe (speed 750 rpm) into the thermostatic cell (initial delay of 60 s, duration of 2 s and spacing of 120 s). Control experiments were carried out where the ligand solution was added into the buffer containing cell. The corrected ITC titrations were treated by using Origin 7.0 software.

RESULTS AND DISCUSSION

Synthesis

TPE-bridged tetraimidazolium salt (**TPE-Im**) was synthesized in two steps starting from 1,1,2,2-tetrakis(4-bromophenyl)ethene (**TPE-Br**) by using a slightly modified version of a previously reported procedure (**Scheme 2**) (Sinha et al., 2017). First, the imidazole was linked to the TPE core through Ulmann coupling reaction leading to **TIPE** in 47% yield (**Supplementary Figure 1**). Then, the alkylation of **TIPE** with an excess of iodomethane afforded the tetraimidazolium salt in a quantitative yield (**Supplementary Figures 2, 3**). The ^{1}H NMR spectrum of **TPE-Im** in CD_3OD clearly shows the downfield signal of the acidic proton (C-H) of the imidazolium ring at $\delta = 9.55$ ppm and the signal of N-CH_3 at $\delta = 4.03$ ppm (see **Supplementary Figure 2**). The molecular mass peak of **TPE-Im** was observed by using ESI-TOF mass spectrometry at $m/z = 164.0845$, as expected for this tetracationic species (calculated $m/z = 164.0844$ $[M-4I]^{4+}$).

Optical Properties

The optical properties of **TPE-Im** were studied by UV-Vis absorption and photoluminescence (PL) spectroscopies. The absorption and emission spectra of **TPE-Im** in water (0.8 % DMSO) are shown in **Figure 1A**. Two unstructured absorption bands are observed at 293 nm and 322 nm, which could be assigned to π-π* transition (Salimimarand et al., 2017; Kayal et al., 2018). In water, **TPE-Im** shows two emission bands: a structured one at ∼380 nm and another broader and weaker at ∼480 nm. The shape of the emission spectra, especially the ratio of the intensity of the two bands at ∼380 nm and ∼480 nm, is dependent on the nature of the solvent. **Figure 1B** shows the emission spectra of **TPE-Im** in polar aprotic (acetonitrile, DMF, DMSO) and protic (MeOH) solvents. A strong increase of the emission band at ∼480 nm in the emission spectra of **TPE-Im** in pure DMSO is noticed compared to water (0.8% DMSO). To understand the nature of the band at longer wavelength, the effect of concentration on the emission profile of pure **TPE-Im** in water is studied (from 10^{-5} to 10^{-3} M, see **Figure 1C**). At high concentration (5×10^{-4}–10^{-3} M), only the broad emission band at longer wavelength remains but its intensity gradually decreases. The solvatochromic and concentration effects may indicate that the broad peak at around 470 nm is due to a twisted intramolecular charge transfer (TICT) state, as previously observed for tetrapyridinium-based TPE (Grabowski et al., 2003; Shigeta et al., 2012). To investigate the potential AIE behavior of **TPE-Im**, emission spectra were then recorded in water/THF mixtures with different THF fractions in view of fine-tuning the THF content as well as the aggregation extent (**Figure 1D**). Adding a poorer solvent (THF) to the water solution results in the gradual disappearance of the broad emission band around 380 nm. Only the broad emission band around 480 nm remains at high THF content (90%). However, adding THF to a solution of **TPE-Im** in water not only leads to a modification of the emission profile but also to an important decrease of the emission intensity. These results clearly indicate that **TPE-Im** is AIE-inactive in THF/water solution conditions.

DFT B3LYP 6/31G* calculations have been carried out on **TPE-Im** to both get information about its optimized structure and its frontier orbitals plots (Frisch et al., 2009). As observed with other TPE derivatives, the optimized structure shows a four-winged propeller-like conformation with slightly different torsion angles between the ethylene core and the adjacent phenyl rings in the range of what is usually measured from the crystals ($\varphi_1 = 52.0°$, $\varphi_2 = 52.9°$, $\varphi_3 = 50.1°$, $\varphi_4 = 53.8°$, $\varphi_{av} = 52.2°$) (**Supplementary Figure 4** and **Supplementary Table 1**) (Cai et al., 2018; Zhang et al., 2019). Examination of the frontier

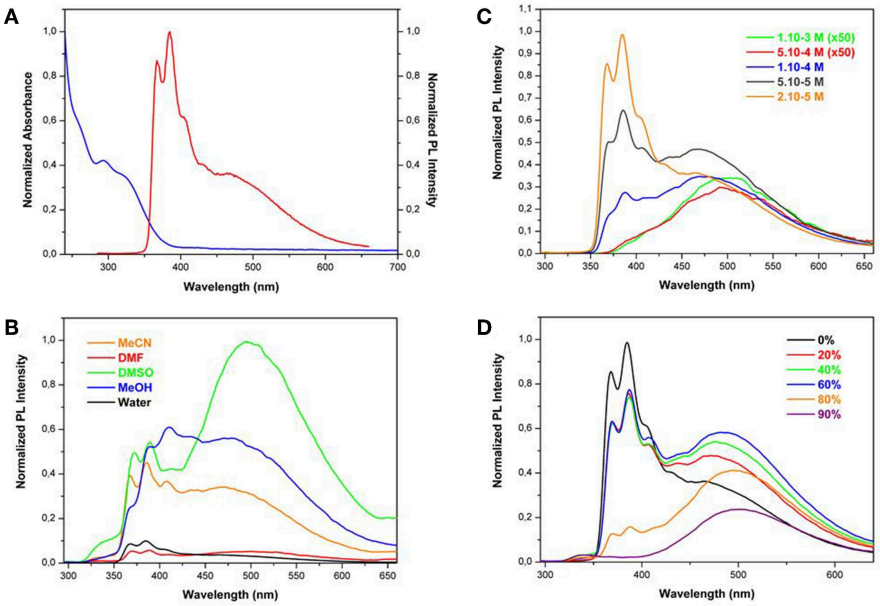

FIGURE 1 | (A) UV-Visible absorption (blue) and PL spectra (red) of **TPE-Im** in water (0.8 % DMSO) at 2×10^{-5} M ($\lambda_{exc} = 265$ nm). **(B)** PL spectra of **TPE-Im** in water (black), methanol (blue), acetonitrile (orange), DMF (red), and DMSO (green) at 2×10^{-5} M ($\lambda_{exc} = 265$ nm). **(C)** PL spectra of **TPE-Im** at different concentrations ($\lambda_{exc} = 265$ nm). **(D)** PL spectra of **TPE-Im** in water/THF mixtures with different THF fractions (Concentration: 2×10^{-5} M, $\lambda_{exc} = 265$ nm).

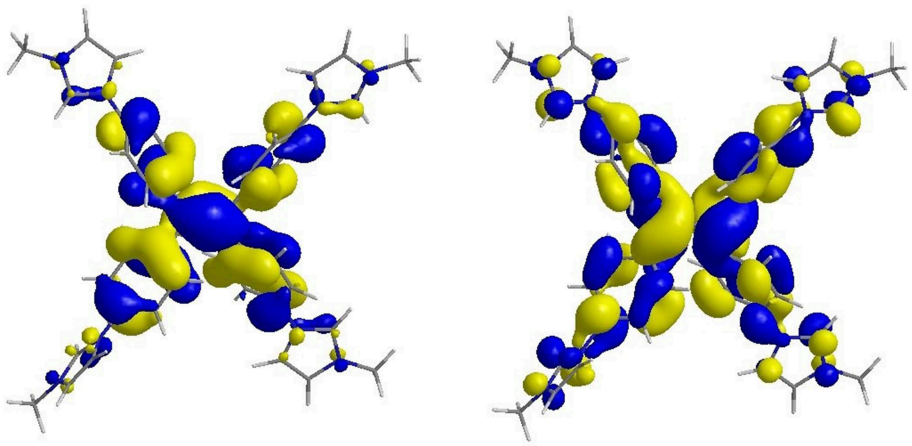

FIGURE 2 | Isosurface plots of frontier orbitals in the ground state: HOMO (left) and LUMO (right) orbitals of **TPE-Im**.

orbital plots indicates that HOMO and LUMO orbitals are mainly located on the TPE core with a relatively low contribution of the imidazolium rings, which suggests that the photophysical properties mainly arise from the TPE core (**Figure 2**).

Binding to Human Telomeric Sequence

The human telomeric sequence studied here was **Tel22** of $d[AG_3(T_2AG_3)]$ sequence, which presents different G4 loop structures depending on the nature of the alkali cation added in solution. With Na^+ at 100 mM, **Tel22** specifically folds into G4 parallel loop structure. In contrast, with K^+ at 100 mM, it folds into a mixture of parallel and anti-parallel G4 conformation, in a dynamic equilibrium between hybrid structures (Dai et al., 2008; Phan, 2010). CD spectra of **TPE-Im** in interaction with different **Tel22** in different aqueous solution media are presented in **Figure 3**. The CD spectra of **Tel22** in presence of KCl show a positive peak at 290 nm and a shoulder at 250 nm, which is typical of **Tel22** with K^+ (Rubio-Magnieto et al., 2015). In the **TPE-Im**/**Tel22** mixture (5:1), the CD bands related to the G-quadruplex are barely modified, with a slight decrease of the signal intensity. A weak negative peak appears at 315 nm, in the spectral range where only **TPE-Im** absorbs. Indeed, pure **TPE-Im** in aqueous solution does not show any CD signal. CD spectra of **Tel22**

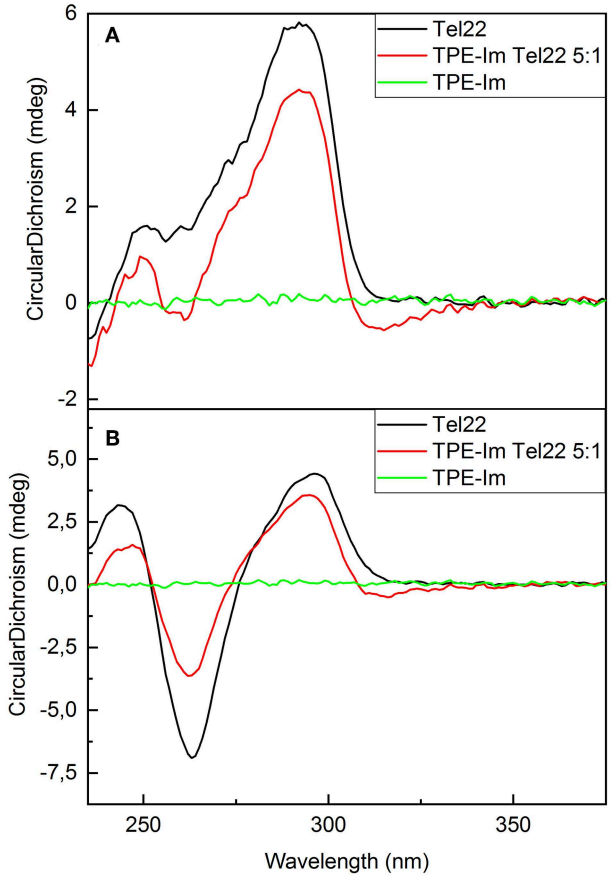

FIGURE 3 | CD spectra of **(A) TPE-Im:Tel22** in TE buffer + 100 mM KCl; B) **TPE-Im:Tel22** in TE buffer + 100 mM NaCl. The molar ratio for **(A)** and **(B)** is 5:1 in **TPE-Im:Tel22**.

in aqueous solution with NaCl show specific antiparallel G-quadruplex structure, with a positive peak at 295 nm and strong negative peak at 265 nm (Wang and Patel, 1993; Rubio-Magnieto et al., 2015). These signals are reduced in presence of **TPE-Im**, and a very weak negative signal at 315 nm is present. As the concentration of **Tel22** is maintained constant for both experiments (see **Supplementary Figure 5**), the modifications in the spectra seem to be directly linked to the interaction between **TPE-Im** and **Tel22**.

Molecular Modeling of TPE/G4 Binding Modes

To gain insights into the affinity and the binding modes of **TPE-Im** with **Tel22**, we perform docking calculations using the AutoDock Vina package (Trott and Olson, 2009), see computational details in the Supporting Information. We consider several conformations for both G4 targets (six conformations for the PDB IDs 143D with Na^+, and 10 conformations for 2HY9 with K^+) to take into account, in an implicit manner, the flexibility of the targets. The affinity, calculated on the 10 most stable docking solutions for each conformation of both G4 targets, are reported in **Supplementary Figure 10**. In **Supplementary Table 2**, we report the statistical analysis of the related docking calculations. For the G4 target in K^+ (2HY9), the best average affinity is found for the third conformation (model 3 in the NMR structure), with the global maximal affinity (lowest binding energy) of $E_b = -7.3$ kcal/mol (corresponding to the structure shown in **Figure 4** top). Let us note that the average RMSD of the 10 recorded docking solutions is also the lowest for the third conformation, which emphasizes a stable binding mode. For the G4 target in Na^+ (143D), the most stable set of docking solutions is found for the conformation #5 ($E_b = -7.1$ kcal/mol, **Supplementary Figure 10** and **Supplementary Table 2**), see its structure in **Figure 4** bottom.

The most energetically favorable docking solutions for **TPE-Im/Tel22** complex present similar calculated binding energies [$E_b = -7.3$ kcal/mol for the **TPE-Im**/G4(2HY9) complex and $E_b = -7.1$ kcal/mol for the **TPE-Im**/G4(143D)]. However, the superpositions of the 10 most stable docking solutions (**Supplementary Figures 11, 12**) depict different **TPE-Im**/G4 binding modes depending on the alkali cation. For the 2HY9 G4, docking solutions are well-superposed, indicating one clear binding mode of **TPE-Im** (**Supplementary Figure 11**). Nine of the ten **TPE-Im**/G4 (2HY9) docking solutions are grouped into only two clusters (**Supplementary Figure 11**). Moreover, these two clusters are similar between them regarding the weak RMSD value with respect to the most stable docking solution (**Supplementary Table 3**). Therefore, docking calculations show that **TPE-Im** ligand has a single, well-defined binding mode, as shown in **Figure 4** with **TPE-Im** buried at the bottom of the 2HY9 target. The close contacts of the most stable docking solution show that the charged nitrogen atoms of **TPE-Im** ligand are close to the phosphate groups of 2HY9. A proximity between aromatic nucleobases and aromatic ligand moieties is also observed. The affinity of the **TPE-Im** ligand to the G4 target (2HY9) arises from concomitant electrostatic interactions and stacking interactions.

The possible binding modes are different for the second G4 target (PDB ID: 143D). Although the **TPE-Im** is also bound in a wide groove of 143D, the 10 docking solutions are clearly much less superimposed than for 2HY9, illustrating various binding modes. The docking solutions are therefore grouped into clusters (**Supplementary Figure 12**), with high differences in RMSD values (**Supplementary Table 4**) compared to the case of **TPE-Im**/G4(2HY9) complex. The close contacts of the most stable docking mode do not involve phosphate groups (see **Figure 4** bottom), and the aromatic moieties of the **TPE-Im** are not in contact with nucleobases, with a quasi-perpendicular binding mode between the G4(143D) tetrad and the main plane of **TPE-Im**. Such a binding mode explains why the affinity of the **TPE-Im** ligand with the 143D target is lower compared to the 2HY9 target. Let us note that the most stable docking solution of **TPE-Im**/G4(143D) implies a particular conformation of the G4(143D) target, i.e., an opening of the G4 structure through disruption of some interactions between nucleobases. The docking calculations do not take into account the entropic effects, but such a binding mode could have a high entropic

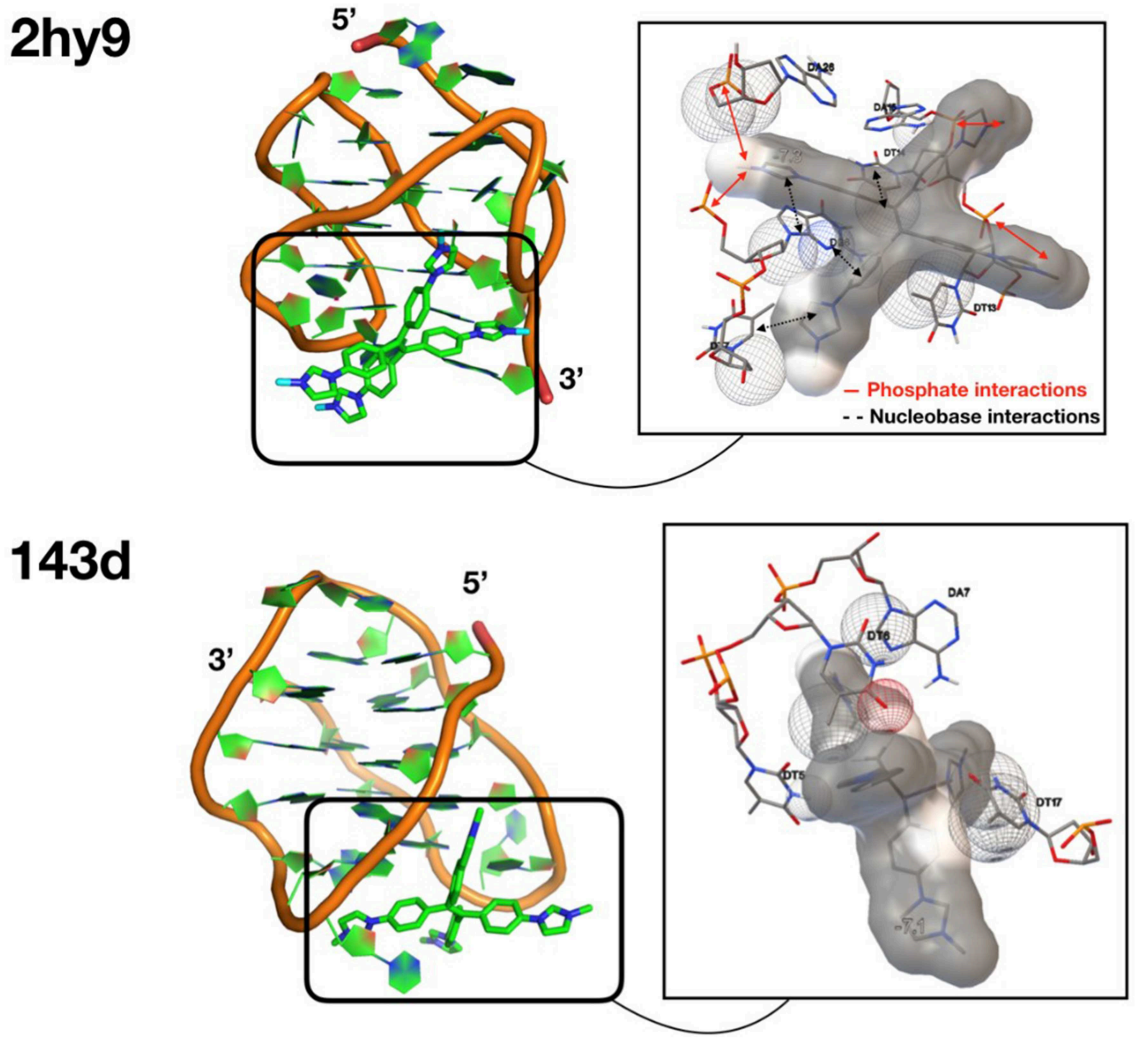

FIGURE 4 | Structures of the most stable docking solutions for each G4 target (see PDB ID on the left). The close contacts are shown on the right, with **TPE-Im** surrounded by its van der Waals surface. The spheres in dots represent van der Waals spheres of the atoms of G4 in contact with the **TPE-Im** ligand.

cost, needing an opening of 143D. These docking calculations indicate a groove-binding mechanism of **TPE-Im** to HT-G4, with more diverse possible binding modes for 2HY9 G4 compared to 143D G4.

Fluorescence Spectroscopy of TPE/G4

The interactions between **TPE-Im** and **Tel22** have also been studied by fluorescence spectroscopy, as shown in **Figure 5**. Pure **TPE-Im** in TE buffer (black lines **Figure 5**) reaches an emission maximum at 390 nm, with a broad shoulder at 470 nm. In the presence of salt or in physiological environment buffer, only minor changes are observed in the emission profile compared to pure **TPE-Im**: the intensity of the emission band at 390 nm is slightly modified whereas the emission band at 470 nm shows the same intensity with or without KCl in the solution (**Supplementary Figures 6, 7**). Adding **Tel22** to a solution containing NaCl, the emission peak at 470 nm of **TPE-Im** strongly increases while the peak at 390 nm vanishes. This increase of fluorescence for **TPE-Im** may be due to the concomitant electrostatic interactions and stacking interactions taking place with G4 (see above), which leads to restricted intramolecular rotations and thus, an exalted emission band around 480 nm; a typical value for TPE derivatives in aggregated state (Huang et al., 2012; Odabas et al., 2013; Sinha et al., 2017). The same behavior is observed with **Tel22** in an aqueous solution containing KCl, the shoulder at 390 nm decreases while the peak at 470 nm strongly increases, with about the same intensity than with NaCl. This "light-up" fluorescence effect is influenced by the presence of added salt in the mixture. Indeed, the increase of the fluorescence is significantly higher when no salt is added (note that pure **Tel22** form G-quadruplex structures even without adding salt to the solution, see **Supplementary Figure 8**), while it is lower with a concentration of added salt at 100 mM of NaCl or KCl (see green lines vs. red lines in **Figure 5**, respectively).

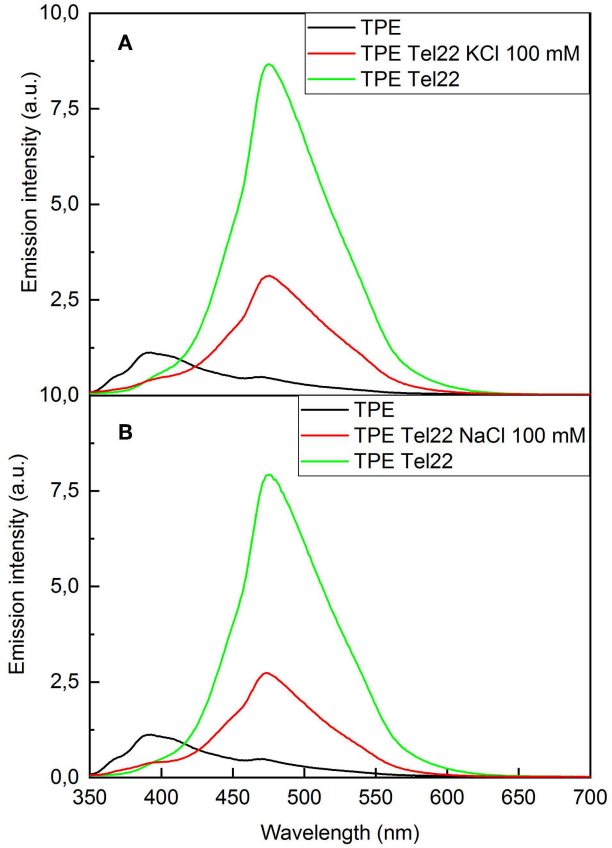

FIGURE 5 | Fluorescence spectra of **(A) TPE-Im:Tel22** in TE buffer (λ_{exc} = 265 nm). **(B) TPE-Im:Tel22** in TE buffer (λ_{exc} = 265 nm). The molar ratio for **(A)** and **(B)** is 5:1 in **TPE-Im:Tel22**.

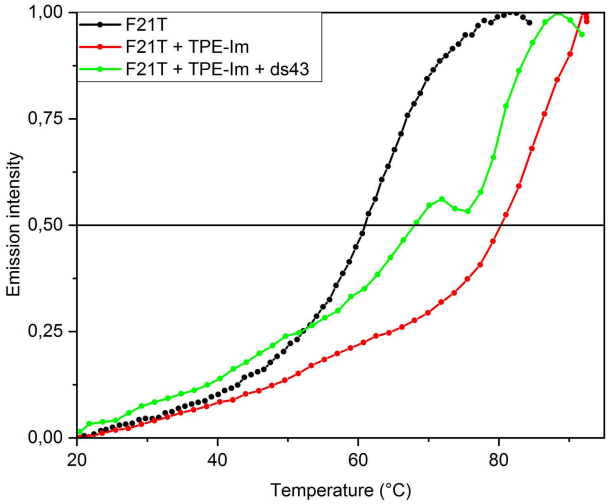

FIGURE 6 | FRET melting essay for solutions of pure **F21T** (200 nM), and in the presence of 1 μM **TPE-Im** with or without 10 equivalent of competitor double-stranded DNA (ds43). The emission intensity corresponds to normalized FAM fluorescence (λ_{exc} = 492 nm). All measurements were performed in a 10 mM lithium cacodylate buffer (pH = 7.2) with 100 mM KCl.

It is likely that G4 binding and further aggregation of **TPE-Im** over G4 is more favorable when the concentration of alkali cations is low, with a lesser extent of screening by alkali ions than for solutions with 100 mM of added salt. The selectivity of **TPE-Im** toward double stranded DNA (**dsR_{20}**) vs. G4 DNA (**Tel22**) was estimated through fluorescence measurements. Adding **Tel22** to **TPE-Im** results in a fluorescence exaltation three or five times higher than that with double-stranded DNA (see **Supplementary Figure 9**).

Stability and Specificity of TPE/G4 Interaction

Fluorescence Resonance Energy Transfer (FRET) melting assays were performed in order to assess the stability and selectivity of **TPE-Im** for G-quadruplex over double-stranded DNA (dsDNA). These experiments are based on the measurement of the melting temperature of double-dye labeled G4, by monitoring the FRET between two dyes located at 5′ and 3′ positions when the G4 goes from folded to unfolded states upon increasing the temperature of the solution. The oligonucleotide used here is a modified **Tel22** sequence end-capped with a fluorescein amidite dye (FAM) at 5′-end and a tetramethylrhodamine (TAMRA) at 3′-end, the labeled oligonucleotide FAM-5′-GGG(T2AG3)3-TAMRA-3′, referred to as **F21T**. This oligonucleotide has been widely studied in the literature for assessing stabilization of G4 and selectivity by ligands (Decian et al., 2007; Renciuk et al., 2012). After a preliminary heating/cooling cycle of **F21T** to make sure of its folding into a G4, **TPE-Im** is added and the emission of the donor dye (i.e., FAM, λ_{exc} = 492 nm) has been followed as a function of temperature, as it has already been done by us and others. This method has been shown to give more reproducible results than the sensitized emission of the acceptor (i.e., TAMRA). The G4 structure unfolds when the temperature increases and thereby the light emission of the donor (i.e., FAM) increases. The denaturation of G4 has been followed for pure **F21T**, for a mixture **F21T/TPE-Im** in a 1:5 molar ratio, and for a mixture **F21T/TPE-Im/ds43** in a 1:5:10 molar ratio in K^+ buffer conditions, as shown in **Figure 6**. The determination of the half-melting temperature difference ($\Delta T_{1/2}$) between the pure **F21T** and **F21T/TPE-Im** is a quantitative measurement of the stabilization effect due to the added ligand. The results show $T_{1/2}$ of 61.0 and 80.5°C for the pure **F21T** and **TPE-Im/F21T**, respectively. These results show a strong stabilization of G-quadruplex by **TPE-Im**, with a $\Delta T_{1/2}$ = 19.5°C. The addition of 10 equivalents of dsDNA competitor (**ds43**) disturbs the **TPE-Im/F21T** stabilization, with a $T_{1/2}$ of 68°C ($\Delta T_{1/2}$ = 7°C), despite the high content in competitor. This means that **TPE-Im** is more specific to **Tel22** G4 DNA conformation than to dsDNA conformation, even with 10 times the concentration of double-stranded DNA vs. G4 DNA. The **TPE-Im/F21T** complex seems disturbed by the high concentration on competitive double stranded DNA but we cannot see a complete drawback to pure **F21T** $T_{1/2}$. In comparison with the previous work of our group, the

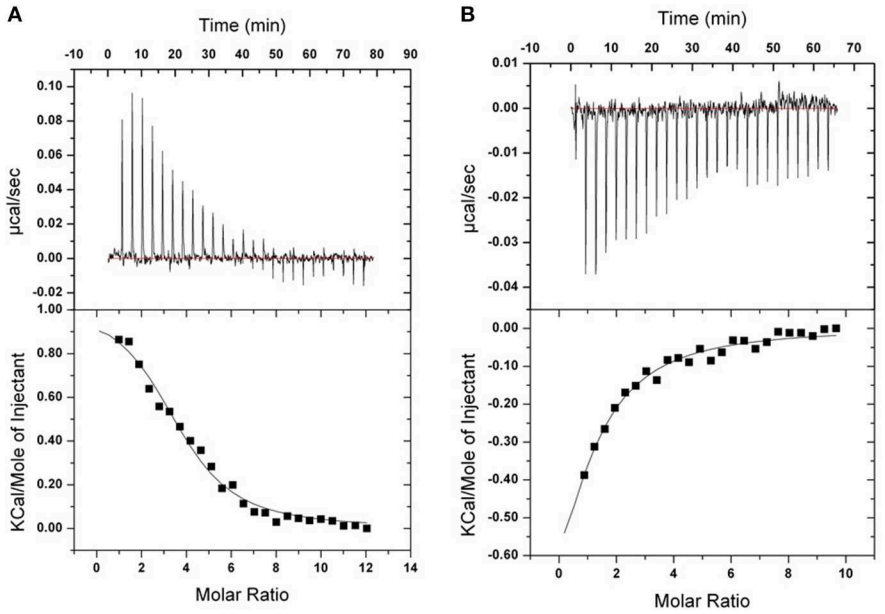

FIGURE 7 | ITC binding isotherms obtained at 20°C for **TPE-Im** in two different buffers. **(A)** 10 mM Tris, 1 mM EDTA, 100 mM KCl, pH 7.4. **(B)** 10 mM Tris, 1 mM EDTA, 100 mM NaCl, pH 7.4. The upper isotherms indicate **Tel22** DNA binding raw data. The lower curves are obtained after integration of individual heat flow signals as function of DNA/ligand molar ratio in the calorimeter cell.

TABLE 1 | Estimates of the association constants K_a and thermodynamic parameters, as determined by ITC.

	TPE-Im/HT-G4	
	in NaCl	**in KCl**
K_a (M^{-1})	3.2 (±1.1).10^5	2.4 (±1.0).10^5
ΔH (kcal.mol^{-1})	−0.3 (±0.06)	0.8 (±0.1)
$-T\Delta S$ (kcal.mol^{-1}.K^{-1})	−7.1 (±0.2)	−8 (±0.2)

TPE-Im/F21T complex is less disrupted than the porphyrin's one (Rubio-Magnieto et al., 2015). It is likely due to its geometry that is particularly adapted to the G4 structure (see above). Note that we observe a jump in the green curve at 72°C which may be due to a partial intercalation of **TPE-Im** in the unwound double stranded DNA (that has a melting temperature slightly under at 67°C).

Isothermal Titration Calorimetry

Isothermal titration calorimetry experiments were carried out to quantify the binding of **TPE-Im** to **Tel22** DNA in presence of NaCl or KCl, see **Figure 7** and **Table 1**. In both cases, binding seems to be strongly driven by favorable entropy changes to a much greater extent than with the flexible cationic TPE-based ligands previously described (Hong et al., 2010). This different behavior is possibly due to the dehydration of the larger aromatic surface of **TPE-Im** whereas entropic penalty occurs upon binding for the TPE-derivatives having flexible side-chains. While a small favorable enthalpy change is observed in the presence of NaCl, an endothermic binding occurs in the presence of KCl. It is possible that this small difference is due to the better pre-organization of **Tel22** in a single G4 parallel loop structure with NaCl and in a mixture of parallel and anti-parallel G4 conformation with KCl, but we interpret this with caution because of the small difference of measured association constants. Overall, the observed association constants reach $3.2 \pm 1.1\ 10^5\ M^{-1}$ in NaCl and $2.4 \pm 1.0\ 10^5\ M^{-1}$ in KCl (**Figure 7**), which are typical of TPE-based G-quadruplex ligands (Hong et al., 2010).

CONCLUSIONS

We have reported on the design of a novel TPE-based fluorophore that features methyl-imidazolium groups directly tethered to the TPE core, **TPE-Im**. We found that this original design endows peculiar optical properties and a significant shift from 380 to 480 nm in the fluorescence emission that is triggered by aggregation. Binding to a (HT-DNA) sequences **Tel22** was characterized by CD spectroscopy without and with salts (NaCl, KCl), and molecular modeling suggest a predominant *side-on* groove binding, with an opening of the grooves in the case of **Tel22** in KCl. Fluorescence spectroscopy demonstrates that the probe **TPE-Im** shows a turn-on fluorescence emission upon binding to **Tel22**, and interestingly, also displays a significant shift in fluorescence emission (380 to 480 nm). A FRET melting assay shows a strong stabilizing effects of **TPE-Im** on the secondary folded structure of **Tel22** ($\Delta T_{1/2} = 19.5$°C), with a good degree of selectivity to G4 against double-stranded DNA. Finally, ITC was used to determine the association constants, which are in the range $2.4–3.2 \times 10^5$ depending on the solution conditions. Overall, we believe these results set the stage for the further use of **TPE-Im** as a novel probe that display turn-on and ratiometric responses upon binding to DNA G-quadruplexes.

DATA AVAILABILITY

The raw data supporting the conclusions of this manuscript will be made available by the authors, without undue reservation, to any qualified researcher.

AUTHOR CONTRIBUTIONS

All authors listed have made a substantial, direct and intellectual contribution to the work, and approved it for publication.

FUNDING

Research in Mons was supported by the University of Mons—UMONS and by the Fund for Scientific Research (F.R.S.-FNRS), under the grants MIS No. F.4532.16 (SHERPA) and EOS No. 30650939 (PRECISION). Computational resources have been provided by the Consortium des Équipements de Calcul Intensif (CÉCI), funded by the F.R.S.-FNRS under Grant No. 2.5020.11 and by the Wallonia Region. CK and SR are grateful to the Région Languedoc-Roussillon (grant Chercheurs d'Avenir-2015, No. 005984) and the FEDER (Fonds Européen de Développement Régional) for financial support. CK acknowledges UMONS for a Ph.D. grant. The ITC equipment is part of the Integrated Screening Platform of Toulouse (PICT, IBiSA).

SUPPLEMENTARY MATERIAL

The Supplementary Material for this article can be found online at: https://www.frontiersin.org/articles/10.3389/fchem.2019.00493/full#supplementary-material

REFERENCES

Asamitsu, S., Bando, T., and Sugiyama, H. (2019). Ligand design to acquire specificity to intended G-quadruplex structures. *Chem. Eur. J.* 25, 417–430. doi: 10.1002/chem.201802691

Balasubramanian, S., and Neidle, S. (2009). G-quadruplex nucleic acids as therapeutic targets. *Curr. Opin. Chem. Biol.* 13, 345–353. doi: 10.1016/j.cbpa.2009.04.637

Biffi, G., Tannahill, D., McCafferty, J., and Balasubramanian, S. (2013). Quantitative visualization of DNA G-quadruplex structures in human cells. *Nat. Chem.* 5, 182–186. doi: 10.1038/nchem.1548

Bochman, M. L., Paeschke, K., and Zakian, V. A. (2012). DNA secondary structures: stability and function of G-quadruplex structures. *Nat. Rev. Genet.* 13, 770–780. doi: 10.1038/nrg3296

Cai, Y., Du, L., Samedov, K., Gu, X., Qi, F., Sung, H. H. Y., et al. (2018). Deciphering the working mechanism of aggregation-induced emission of tetraphenylethylene derivatives by ultrafast spectroscopy. *Chem. Sci.* 9, 4662–4670. doi: 10.1039/C8SC01170B

Collie, G. W., and Parkinson, G. N. (2011). The application of DNA and RNA G-quadruplexes to therapeutic medicines. *Chem. Soc. Rev.* 40, 5867–5892. doi: 10.1039/c1cs15067g

Dai, J., Carver, M., and Yang, D. (2008). Polymorphism of human telomeric quadruplex structures. *Biochimie* 90, 1172–1183. doi: 10.1016/j.biochi.2008.02.026

Davis, J. T., and Spada, G. P. (2007). Supramolecular architectures generated by self-assembly of guanosine derivatives. *Chem. Soc. Rev.* 36, 296–313. doi: 10.1039/B600282J

Decian, A., Guittat, L., Kaiser, M., Saccà, B., Amrane, S., Bourdoncle, A., et al. (2007). Fluorescence-based melting assays for studying quadruplex ligands. *Methods* 42, 183–195. doi: 10.1016/j.ymeth.2006.10.004

Delano, W. L. (2002). *The PyMOL Molecular Graphics System*. Available online at: https://ci.nii.ac.jp/naid/10020095229/en/

Doluca, O., Withers, J. M., and Filichev, V. V. (2013). Molecular engineering of guanine-rich sequences: Z-DNA, DNA triplexes, and G-Quadruplexes. *Chem. Rev.* 113, 3044–3083. doi: 10.1021/cr300225q

Flynn, S. M., George, S. T., White, L., Devonish, W., and Takle, G. B. (1999). Water-soluble, meso-substituted cationic porphyrins—a family of compounds for cellular delivery of oligonucleotides. *BioTechniques* 26, 736–746. doi: 10.2144/99264rr03

Frisch, M. J., Trucks, G. W., Schlegel, H. B., Scuseria, G. E., Robb, M. A., Cheeseman, J. R., et al. (2009). *Gaussian 09, Revision A.02.* Wallingford CT: Gaussian, Inc.

Golub, E., Lu, C.-H., and Willner, I. (2015). Metalloporphyrin/G-quadruplexes: from basic properties to practical applications. *J. Porphyr. Phthalocyan.* 19, 65–91. doi: 10.1142/S1088424615300025

Grabowski, Z. R., Rotkiewicz, K., and Rettig, W. (2003). Structural changes accompanying intramolecular electron transfer: focus on twisted intramolecular charge-transfer states and structures. *Chem. Rev.* 103, 3899–4032. doi: 10.1021/cr940745l

Hänsel-Hertsch, R., Di Antonio, M., and Balasubramanian, S. (2017). DNA G-quadruplexes in the human genome: detection, functions and therapeutic potential. *Nat. Rev. Mol. Cell Biol.* 18, 279–284. doi: 10.1038/nrm.2017.3

Hanwell, M. D., Curtis, D. E., Lonie, D. C., Vandermeersch, T., Zurek, E., and Hutchison, G. R. (2012). Avogadro: an advanced semantic chemical editor, visualization, and analysis platform. *J. Cheminform.* 4:17. doi: 10.1186/1758-2946-4-17

Hong, Y., Xiong, H., Lam, J. W., Häußler, M., Liu, J., Yu, Y., et al. (2010). Fluorescent bioprobes: structural matching in the docking processes of aggregation-induced emission fluorogens on DNA surfaces. *Chem. Eur. J.* 16, 1232–1245. doi: 10.1002/chem.200900778

Huang, J., Yang, X., Wang, J., Zhong, C., Wang, L., Qin, J., et al. (2012). New tetraphenylethene-based efficient blue luminophors: aggregation induced emission and partially controllable emitting color. *J. Mater. Chem.* 22, 2478–2484. doi: 10.1039/C1JM14054J

Jaghoori, M. M., Bleijlevens, B., and Olabarriaga, S. D. (2016). 1001 ways to run AutoDock Vina for virtual screening. *J. Comput. Aided Mol. Des.* 30, 237–249. doi: 10.1007/s10822-016-9900-9

Kayal, S., Roy, K., and Umapathy, S. (2018). Femtosecond coherent nuclear dynamics of excited tetraphenylethylene: ultrafast transient absorption and ultrafast Raman loss spectroscopic studies. *J. Chem. Phys.* 148:024301. doi: 10.1063/1.5008726

Lam, E. Y. N., Beraldi, D., Tannahill, D., and Balasubramanian, S. (2013). G-quadruplex structures are stable and detectable in human genomic DNA. *Nat. Commun.* 4:1796. doi: 10.1038/ncomms2792

Maji, B., and Bhattacharya, S. (2014). Advances in the molecular design of potential anticancer agents via targeting of human telomeric DNA. *Chem. Commun.* 50, 6422–6438. doi: 10.1039/C4CC00611A

Mei, J., Hong, Y., Lam, J. W. Y., Qin, A., Tang, Y., and Tang, B. Z. (2014). Aggregation-induced emission: the whole is more brilliant than the parts. *Adv. Mater.* 26, 5429–5479. doi: 10.1002/adma.201401356

Monchaud, D., and Teulade-Fichou, M.-P. (2008). A hitchhiker's guide to G-quadruplex ligands. *Org. Biomol. Chem.* 6, 627–636. doi: 10.1039/B714772B

Neidle, S. (2017). Quadruplex nucleic acids as targets for anticancer therapeutics. *Nat. Rev. Chem.* 1:0041. doi: 10.1038/s41570-017-0041

Odabas, S., Tekin, E., Turksoy, F., and Tanyeli, C. (2013). Inexpensive and valuable: a series of new luminogenic molecules with the tetraphenylethene core having excellent aggregation induced emission properties. *J. Mater. Chem. C* 1:7081–7091. doi: 10.1039/c3tc31427h

Phan, A. T. (2010). Human telomeric G-quadruplex: structures of DNA and RNA sequences. *FEBS J.* 277, 1107–1117. doi: 10.1111/j.1742-4658.2009.07464.x

Renciuk, D., Zhou, J., Beaurepaire, L., Guédin, A., Bourdoncle, A., and Mergny, J.-L. (2012). A FRET-based screening assay for nucleic acid ligands. *Methods* 57, 122–128. doi: 10.1016/j.ymeth.2012.03.020

Rubio-Magnieto, J., Di Meo, F., Lo, M., Delcourt, C., Clément, S., Norman, P., et al. (2015). Binding modes of a core-extended metalloporphyrin to human telomeric DNA G-quadruplexes. *Org. Biomol. Chem.* 13, 2453–2463. doi: 10.1039/C4OB02097A

Salimimarand, M., La, D. D., Kobaisi, M. A., and Bhosale, S. V. (2017). Flower-like superstructures of AIE-active tetraphenylethylene through solvophobic controlled self-assembly. *Sci. Rep.* 7:42898. doi: 10.1038/srep42898

Schultz, A., Laschat, S., Diele, S., and Nimtz, M. (2003). Tetraphenylethene-derived columnar liquid crystals and their oxidative photocyclization. *Eur. J. Org. Chem.* 2003, 2829–2839. doi: 10.1002/ejoc.200300118

Shigeta, M., Morita, M., and Konishi, G. (2012). Selective formation of twisted intramolecular charge transfer and excimer emissions on 2,7-bis(4-Diethylaminophenyl)-fluorenone by choice of solvent. *Molecules* 17, 4452–4459. doi: 10.3390/molecules17044452

Sinha, N., Stegemann, L., Tan, T. T., Doltsinis, N. L., Strassert, C. A., and Hahn, F. E. (2017). Turn-on fluorescence in tetra-NHC ligands by rigidification through metal complexation: an alternative to aggregation-induced emission. *Angew. Chem. Int. Ed.* 56, 2785–2789. doi: 10.1002/anie.201610971

Trommel, J. S., and Marzilli, L. G. (2001). Synthesis and DNA binding of novel water-soluble cationic methylcobalt porphyrins. *Inorg. Chem.* 40, 4374–4383. doi: 10.1021/ic010232e

Trott, O., and Olson, A. J. (2009). AutoDock vina: improving the speed and accuracy of docking with a new scoring function, efficient optimization, and multithreading. *J. Comput. Chem.* 31, 455–461. doi: 10.1002/jcc.21334

Tucker, W. O., Shum, K. T., and Tanner, J. A. (2012). G-quadruplex DNA aptamers and their ligands: structure, function and application. *Curr. Pharm. Des.* 18, 2014–2026. doi: 10.2174/138161212799958477

Wang, J., Wolf, R. M., Caldwell, J. W., Kollman, P. A., and Case, D. A. (2004). Development and testing of a general amber force field. *J. Comput. Chem.* 25, 1157–1174. doi: 10.1002/jcc.20035

Wang, Y., and Patel, D. J. (1993). Solution structure of the human telomeric repeat d[AG3(T2AG3)3] G-tetraplex. *Structure* 1, 263–282. doi: 10.1016/0969-2126(93)90015-9

Wu, Y., and Brosh, R. M. (2010). G-quadruplex nucleic acids and human disease. *FEBS J.* 277, 3470–3488. doi: 10.1111/j.1742-4658.2010.07760.x

Yang, Z., Qin, W., Leung, N. L. C., Arseneault, M., Lam, J. W. Y., Liang, G., et al. (2016). A mechanistic study of AIE processes of TPE luminogens: intramolecular rotation vs. *configurational isomerization. J. Mater. Chem. C.* 4, 99–107. doi: 10.1039/C5TC02924D

Zhang, H., Nie, Y., Miao, J., Zhang, D., Li, Y., Liu, G., et al. (2019). Fluorination of the tetraphenylethene core: synthesis, aggregation-induced emission, reversible mechanofluorochromism and thermofluorochromism of fluorinated tetraphenylethene derivatives. *J. Mater. Chem. C* 7, 3306–3314. doi: 10.1039/C9TC00511K

Zhang, Q., Liu, Y.-C., Kong, D.-M., and Guo, D.-S. (2015). Tetraphenylethene derivatives with different numbers of positively charged side arms have different multimeric G-quadruplex recognition specificity. *Chem. Eur. J.* 21, 13253–13260. doi: 10.1002/chem.201501847

Zhao, C., Wu, L., Ren, J., Xu, Y., and Qu, X. (2013). Targeting human telomeric higher-order DNA: dimeric G-quadruplex units serve as preferred binding site. *J. Am. Chem. Soc.* 135, 18786–18789. doi: 10.1021/ja410723r

Conflict of Interest Statement: The authors declare that the research was conducted in the absence of any commercial or financial relationships that could be construed as a potential conflict of interest.

Advantages of publishing in Frontiers

OPEN ACCESS
Articles are free to read for greatest visibility and readership

FAST PUBLICATION
Around 90 days from submission to decision

HIGH QUALITY PEER-REVIEW
Rigorous, collaborative, and constructive peer-review

TRANSPARENT PEER-REVIEW
Editors and reviewers acknowledged by name on published articles

Frontiers
Avenue du Tribunal-Fédéral 34
1005 Lausanne | Switzerland

Visit us: www.frontiersin.org
Contact us: info@frontiersin.org | +41 21 510 17 00

REPRODUCIBILITY OF RESEARCH
Support open data and methods to enhance research reproducibility

DIGITAL PUBLISHING
Articles designed for optimal readership across devices

FOLLOW US
@frontiersin

IMPACT METRICS
Advanced article metrics track visibility across digital media

EXTENSIVE PROMOTION
Marketing and promotion of impactful research

LOOP RESEARCH NETWORK
Our network increases your article's readership